Phase control and pulse shaping in Bragg diffraction for quantum atom optics : from matter-wave interferences to a Bell's inequality test

Charlie Leprince

▶ **To cite this version:**

Charlie Leprince. Phase control and pulse shaping in Bragg diffraction for quantum atom optics : from matter-wave interferences to a Bell's inequality test. Optics [physics.optics]. Université Paris-Saclay, 2024. English. ⟨NNT : 2024UPASP037⟩. ⟨tel-04658090⟩

HAL Id: tel-04658090

https://pastel.hal.science/tel-04658090v1

Submitted on 22 Jul 2024

HAL is a multi-disciplinary open access archive for the deposit and dissemination of scientific research documents, whether they are published or not. The documents may come from teaching and research institutions in France or abroad, or from public or private research centers.

L'archive ouverte pluridisciplinaire **HAL**, est destinée au dépôt et à la diffusion de documents scientifiques de niveau recherche, publiés ou non, émanant des établissements d'enseignement et de recherche français ou étrangers, des laboratoires publics ou privés.

HAL Authorization

université PARIS-SACLAY

Phase control and pulse shaping in Bragg diffraction for quantum atom optics

From matter-wave interferences to a Bell's inequality test

Thèse de doctorat de l'université Paris-Saclay

École doctorale n°572, Ondes et matière (EDOM)
Spécialité de doctorat : Physique
Graduate School : Physique. Référent : Institut d'Optique

Thèse préparée au **Laboratoire Charles Fabry** (Université Paris-Saclay, CNRS, Institut d'Optique Graduate School), sous la direction de **Christoph WESTBROOK**, Directeur de recherche, et le co-encadrement de **Denis BOIRON**, Professeur des universités.

Thèse soutenue à Palaiseau, le 5 juin 2024, par

Charlie Leprince

Composition du jury

Membres du jury avec voix délibérative

M. Jean-François ROCH Professeur des universités à l'Université Paris-Saclay (Laboratoire Lumière, Matière et Interfaces)	Président
Mme Caroline CHAMPENOIS Directrice de Recherche à Aix-Marseille Université (Laboratoire de Physique des Interactions Ioniques et Moléculaires)	Rapporteuse
M. Franck PEREIRA DOS SANTOS Directeur de Recherche à Sorbonne Université (Laboratoire SYRTE - Observatoire de Paris)	Rapporteur
Mme Juliette BILLY Maître de Conférences, à l'Université Paul Sabatier - Toulouse III (Laboratoire Collisions - Agrégats - Réactivité)	Examinatrice

THESE DE DOCTORAT
NNT : 2024UPASP037

université PARIS-SACLAY

ÉCOLE DOCTORALE
Ondes et matière (EDOM)

Titre : Contrôle de phase et façonnage d'impulsion de la diffraction de Bragg pour l'optique atomique quantique

Mots clés : Hélium métastable, Condensat de Bose-Einstein, Inégalités de Bell, Interférométrie atomique, Diffraction de Bragg

Résumé : La mécanique quantique prédit le phénomène d'intrication, qui prévoit que pour un système de deux particules dites intriquées, on observe de très fortes corrélations entre les propriétés des particules.

Une façon de caractériser un système intriqué est de réaliser un test d'inégalité de Bell. Le projet décrit dans cette thèse se propose de mettre en place un interféromètre de Bell mettant en jeu des atomes d'hélium métastables intriqués en impulsion. A partir d'atomes préparés dans un condensat de Bose-Einstein, des paires d'atomes fortement corrélées sont émises à des impulsions différentes par le processus de mélange à quatre ondes, puis les atomes sont envoyés dans un interféromètre à deux particules et quatre modes d'impulsion. Pour cela, on utilise la diffraction de Bragg, pour transférer de l'impulsion aux atomes de façon cohérente et ainsi former des miroirs et séparatrices à atomes.

Dans cette thèse, on étudie en détails la diffraction de Bragg et son influence dans la réalisation d'un interféromètre de Bell. On propose une méthode originale pour contrôler la différence de phase imprimée sur les atomes entre les deux doublets d'impulsion en jeu, en modulant temporellement l'amplitude de la pulsation de Rabi. Cette technique est également mise à profit pour façonner le profil temporel des miroirs et séparatrices Bragg afin d'améliorer leurs propriétés de réflectivité et de phase. De premiers tests interférométriques sont reportés (interféromètres de type Mach-Zehnder, Ramsey, Hong-Ou-Mandel), validant la technique de contrôle de phase notamment et donnant des résultats prometteurs quant à la réalisation prochaine d'un test de Bell.

Title : Phase control and pulse shaping in Bragg diffraction for quantum atom optics

Keywords : Metastable helium, Bose-Einstein Condensate, Bell's inequality, Atom interferometer, Bragg diffraction

Abstract : Quantum mechanics predicts the phenomenon of entanglement, which predicts thatthat for a system of two entangled particles, very strong correlations can be observed.

One way to characterize an entangled system is to perform a Bell inequality test. The project described in this thesis aims to set up a Bell interferometer involving metastable helium atoms entangled in momentum. Starting with atoms in a Bose-Einstein condensate, pairs of highly correlated atoms are emitted at different momenta through the four-wave mixing process. These atoms are then sent through a two-particle, four-momentum mode interferometer using Bragg diffraction to coherently transfer momentum to the atoms and create atom mirrors and beam splitters.

In this thesis, we study in detail Bragg diffraction and its influence on the realization of a Bell interferometer. We propose an original method to control the phase difference imprinted on the atoms between the two involved momentum doublets by temporally modulating the amplitude of the Rabi frequency. This technique is also used to shape the temporal profile of Bragg mirrors and beam splitters to improve their reflectivity and phase properties. Initial interferometric tests are reported (Mach-Zehnder, Ramsey, Hong-Ou-Mandel interferometers), validating the phase control technique in particular and showing promising results for the upcoming realization of a Bell test.

Phase control and pulse shaping in Bragg diffraction for quantum atom optics

From matter-wave interferences to a Bell's inequality test

Charlie Leprince

Friday 5$^{\text{th}}$ July, 2024

Remerciements

Ce manuscrit marque la fin de quatre ans de thèse et l'aboutissement de nombreuses années d'études, aussi j'aimerais remercier les personnes qui ont, de près ou de loin, contribué à rendre ce travail possible.

Je souhaite remercier les membres de mon jury, Caroline Champenois et Franck Pereira dos Santos, en tant que rapporteurs, et Juliette Billy et Jean-François Roch, en tant qu'examinateurs, pour avoir accepté d'évaluer mon travail et pour leurs retours sur mon manuscrit. Merci en particulier à Jean-François Roch, qui en cours de Licence m'avait fait découvrir l'intrication et les inégalités de Bell !

Il me faut bien sûr remercier Chris Westbrook et Denis Boiron, le binôme qui a encadré cette thèse, pour m'avoir fait confiance et permis de travailler sur une plateforme expérimentale exceptionnelle. Chris et Denis conduisent le projet de façon complémentaire, chacun à sa façon, mais toujours en laissant aux doctorants le soin de trouver leur place au sein de l'équipe dans une ambiance de travail chaleureuse. Chris a un sens physique remarquable et un enthousiasme à toute épreuve, et ne manque jamais de venir en salle de manip pour s'assurer que tout se passe bien. Quand ce n'est pas le cas (finalement assez souvent), il propose toujours des idées voire donne de sa personne quand c'est nécessaire. Denis assure le suivi expérimental de la manip au quotidien, et sa maîtrise impressionnante de chaque aspect de l'expérience a permis bien des fois d'avancer même si la manip avait l'air d'en avoir décidé autrement. Jamais avare d'un petit ordre de grandeur calculé sur un bout de tableau ou de quelque chose à tester, Denis est d'un dévouement sans failles et a marqué nombre de doctorants, dont j'ai la chance de faire partie, par la clarté de ses explications patientes. Je les remercie tous deux, et notamment pour leurs commentaires sur mon manuscrit, enrichi par leur connaissance étendue et leur compréhension profonde de la physique atomique.

Une thèse, particulièrement en atomes froids est un travail d'équipe, et les résultats présentés dans cette thèse n'auraient pas pu voir le jour sans les contributions indispensables de Quentin Marolleau et Victor Gondret (Gondre ?), à qui je tiens à exprimer ma reconnaissance. Quentin m'a pris sous son aile à mon arrivée dans l'équipe, dans une période parfois éprouvante où la manip n'était pas très en forme. C'est grâce aux conseils et explications toujours détaillées de Quentin que j'ai pu apprivoiser peu à peu la manip, appréhender ses humeurs et bizarreries et tenter de percer ses mystères. Quentin a joué un grand rôle dans le changement de paradigme de Matlab à Python, et je suis heureux d'avoir pu accompagner sa ferveur et sa découverte passionnée de ce nouveau langage. Victor a été mon compagnon d'aventure pendant toute ma thèse. Nous avons fait nos armes ensemble, de nos débuts prudents sur la manip (qui ont notamment consisté à déployer une fibre optique sans gaine protectrice sur 30 mètres, essayer de soulever le ralentisseur Zeeman, cramer une fibre haute puissance et faire une cinquantaine de joints de filasse...),

aux grandes réflexions sur la mise en évidence des corrélations ou la nature de l'intrication. Je tiens à le remercier pour son efficacité et sa force de proposition qui ont été des atouts constants pour l'équipe, l'expérience et l'ergonomie de notre environnement de travail.

Merci également à Marc Cheneau, qui a été jusqu'à récemment un consultant de luxe dans l'équipe, fournissant des conseils (notamment techniques) précieux, à Ziyad Amodjee, qui m'a appris à changer mon premier acousto juste avant le confinement covid, et à Alexandre Dareau, postdoc dans l'équipe à cette époque, qui a notamment éclairé mes premières réflexions sur la diffraction de Bragg.

Plusieurs étudiants en stage dans l'équipe ont apporté leur contribution à ce travail, et je les remercie chaleureusement pour leur aide : Flavien Barbe, Paul Paquiez, et Rui Dias. C'est Clothilde Lamirault, en stage puis en thèse, qui a repris depuis peu les rennes de la manip, et j'ai toute confiance dans le futur succès de l'expérience pendant son mandat de doctorante en chef !

Je remercie Patrick Georges, directeur du Laboratoire Charles Fabry, pour son accueil, sa disponibilité, et son soutien, notamment d'ordre administratif, ainsi que tous les membres du groupe gaz quantiques, au sein duquel il règne une très bonne ambiance. Les nombreuses discussions que j'ai eues dans le groupe m'ont toujours apporté un éclairage supplémentaire sur mon travail. Merci notamment à David et son équipe pour les nombreux échanges sur l'hélium et les calculs de corrélations. Merci à Isabelle et l'équipe Puce pour les discussions au Magnan et dans le bureau, pas toujours sur de la physique. Merci également aux deux Thomas, à Vincent, Alain et tous les étudiants que j'ai pu côtoyer pendant quatre ans.

Merci beaucoup à l'ensemble des services techniques (infra, méca, élec, optique) et administratifs (accueil, achats, missions, RH) du laboratoire, qui ont également contribué à ce travail de façons diverses et variées mais toujours bienveillantes. Merci notamment à Fabrice, Fabien, Jean-René, Patrick, Florence, Sophie, et Marc qui ont toujours su répondre rapidement à nos demandes parfois saugrenues.

Je remercie également Jacques Robert, Gaël Latour et Ariane Deniset avec qui j'ai pu enseigner pendant ma thèse dans différentes filières de l'Université Paris-Saclay. Merci également à Éric Jouguelet qui m'invite tous les ans aux Olympiades de physique et qui m'a fait l'amitié de venir assister à ma soutenance.

Mon parcours de physicien a d'ailleurs commencé avec de la diffraction de Bragg aux Olympiades de physique, auxquelles j'ai participé grâce à Marie-Christine Baurrier, ma prof de physique de lycée, qui m'a fait découvrir la démarche expérimentale et la rigueur scientifique. Ses conseils de l'époque m'accompagnent encore aujourd'hui ! Merci aussi à Olivier Joachim, prof de prépa en 5/2, dont la force tranquille a renforcé mon goût pour la physique. Je remercie aussi Pierre Encrenaz, qui m'a fait confiance et m'a introduit au passionnant monde de la recherche dès ma sortie du lycée.

Merci à la dream team de bénévoles de l'association La Rue Tourne, grâce à qui j'ai pu passer des moments de solidarité dans la jovalité, lors des maraudes et en-dehors. L'occasion aussi de garder un pied sur le terrain et dans la réalité, malgré ma participation un peu sporadique ces derniers mois. Merci pour leur soutien sans faille ! Je reviens bientôt pour les chouquettes.

Je remercie mes amis, avec qui j'ai passé du (bon !) temps en-dehors de la thèse,

lors des week-ends, des vacances, souvent autour de bons repas. Merci aux camarades cachanais, Paul, Théo, Gentón, Thomas, Benjamin, Piwi, Rémi, Haëck et Pellet, ainsi qu'à Marie, Jessie, Rémy et Sarah. Merci à Peter et Manon, Malek et Damien, Pauline et Avotra, à Lyna et au Mag, et à tous les autres, pour tous ces beaux souvenirs en votre compagnie.

Enfin, j'aimerais adresser des remerciements particuliers à ma famille, qui m'a toujours encouragé dans mon long parcours scolaire et universitaire. Leur soutien et leur approbation comptent beaucoup pour moi. Merci à mes parents, ma soeur, mes grand-parents, et Pascal et Brigitte pour leur accompagnement depuis toujours. Et merci à ma belle famille pour leurs encouragements !

Élodie, je ne sais pas si je saurais te remercier assez pour m'aider au quotidien à donner le meilleur de moi-même. Réaliser nos thèses en parallèle n'a pas été de tout repos, mais ta façon de travailler et de t'interroger ont été pour moi des sources constantes d'admiration et d'inspiration. Merci de me supporter. Merci pour tout.

Résumé

La mécanique quantique prédit que pour un système de deux particules dites intriquées, on ne peut pas décrire chaque particule indépendamment : la mesure d'une observable physique sur une particule affecte également l'autre, quelle que soit la distance entre les particules, donnant lieu à l'observation de très fortes corrélations. Une façon de mettre en évidence un système intriqué consiste à réaliser ce qu'on appelle un test d'inégalité de Bell, dont le principe est de mettre en évidence des interférences à deux particules en pilotant les corrélations entre ces particules à l'aide d'un paramètre de contrôle. La théorie quantique prévoit l'observation de corrélations très fortes, plus fortes que ce qu'on pourrait obtenir avec la théorie classique. Ainsi, si le contraste de l'interférence est suffisant, alors non seulement le système est intriqué, mais en plus il n'existe aucune théorie physique qui puisse expliquer l'observation de corrélations aussi fortes tout en faisant l'hypothèse de localité, selon laquelle des actions effectuées à un endroit de l'espace ne peuvent pas influencer instantanément un autre endroit de l'espace. On dit alors qu'il y a violation d'inégalité de Bell.

Si des violations d'inégalité de Bell, dont le principe est rappelé dans le chapitre 1 de ce manuscrit, ont été mises en évidence sur différents types de systèmes depuis les années 1980 (sur des photons intriqués en polarisation, des particules massives intriquées en spin, ou encore des photons intriqués en impulsion), il n'existe à ce jour aucune preuve expérimentale d'une violation d'inégalité de Bell avec des particules massives intriquées en impulsion. L'étude de tels systèmes représente un enjeu important, car ils font directement intervenir l'intrication, propriété purement quantique, et la masse, propriété gravitationnelle. Observer une violation d'inégalité de Bell avec des particules massives intriquées via un tel degré de liberté externe constituerait une première étape vers la réalisation d'expériences visant à établir les liens entre mécanique quantique et gravitation. Dans cette optique, le projet décrit dans cette thèse se propose de mettre en place un interféromètre de Bell mettant en jeu des atomes d'hélium métastables intriqués en impulsion.

Pour cela, l'idée consiste à s'inspirer de l'interféromètre réalisé en 1990 par J. Rarity et P. Tapster qui a donné lieu à une violation d'inégalité de Bell avec des photons intriqués en impulsion. Pour adapter ce dispositif avec des atomes, plusieurs éléments sont nécessaires : une source de paires d'atomes, des miroirs et séparatrices à atomes avec un paramètre de contrôle permettant de piloter les corrélations, et un dispositif de détection d'atomes uniques permettant de calculer les impulsions des atomes détectés et leurs corrélations.

L'équipe Optique atomique quantique du Laboratoire Charles Fabry, dans laquelle j'ai effectué ma thèse, est spécialisée dans la réalisation de condensats de Bose-Einstein avec des atomes d'hélium dans son premier état excité, état métastable dont la grande énergie interne permet d'arracher des électrons à une surface métallique, et donc de détecter des atomes uniques. Grâce à un système de détection ingénieux constitué d'une galette de

micro-canaux et de lignes à retard, il est possible de déterminer la position et le temps d'arrivée des atomes d'hélium qui tombent (par gravité) sur le détecteur, placé sous le site du piégeage des atomes. Comme le détecteur est suffisamment éloigné du piège initial, on peut alors calculer les impulsions initiales des atomes avant leur chute sur la galette (mesure par temps de vol). Ce dispositif expérimental, présenté dans le chapitre 2, constitue ainsi la plateforme idéale pour réaliser des mesures de corrélations en impulsion entre atomes individuels.

Le condensat constitue le réservoir d'atomes cohérent à partir duquel des paires d'atomes fortement corrélées sont émises à des impulsions différentes par le processus de mélange à quatre ondes (analogue à un processus de conversion de fréquence dans un cristal non linéaire en optique). Les paires émises doivent vérifier les conditions d'accord de phase, qui correspondent à la conservation de l'impulsion et de l'énergie. Pour émettre des paires de façon accordable, on place le condensat dans un potentiel périodique à l'aide d'un réseau optique mobile, de façon à exploiter le diagramme de bande du réseau et ainsi ajuster les impulsions des paires émises en pilotant la vitesse du réseau. Comme il n'y a pas conservation stricte de l'énergie (on applique le réseau optique pendant une durée finie), on obtient alors une source multimode émettant plusieurs doublets d'impulsion, de manière à ce que l'état du système corresponde à une superposition d'états comprimés à deux modes d'impulsion. Si la population par mode est suffisamment faible, alors on peut utiliser cet état comme état d'entrée d'un interféromètre de Bell.

Cette méthode est utilisée dans l'équipe depuis une dizaine d'années et a donné lieu à l'observation de fortes corrélations entre les paires créées. Suite à divers problèmes expérimentaux, il a été nécessaire pendant ma thèse de paramétrer et caractériser à nouveau ce dispositif d'émission de paires, en termes d'amplitude de corrélation locale et croisée, de largeur de mode, de population par mode. Ainsi, l'étude de la fonction de corrélation d'ordre 2 et une analyse statistique du nombre d'atomes détectés, présentées dans le chapitre 3, ont permis de caractériser un mode d'impulsion et de mettre en évidence des corrélations entre paires. Pour de faibles populations par mode, nous avons mis en évidence une variance de la différence du nombre d'atomes sub-poissonienne et une violation d'inégalité de Cauchy-Schwarz, qui sont des signatures de corrélations quantiques fortes entre modes d'impulsion de différentes paires.

On peut considérer en bonne approximation que la source émet deux atomes jumeaux, soit dans les modes dénotés p et $-p$, soit dans les modes q et $-q$. Cette superposition quantique des états à deux particules $|p,-p\rangle$ et $|q,-q\rangle$ constitue l'état intriqué dont on va chercher à piloter les corrélations à l'aide d'un interféromètre. Pour cela, on va mélanger des atomes issus de chaque paire pour les faire interférer. On formera ainsi deux sous-parties de l'interféromètre, appelées boucles, l'une mélangeant les atomes des modes p et $-q$ (boucle B), et l'autre mélangeant les atomes des modes q et $-p$ (boucle A). En pilotant la différence de phase entre les atomes de chaque boucle, la mécanique quantique prévoit que l'on observe une interférence à deux atomes, c'est-à-dire une oscillation de la probabilité de mesurer simultanément un atomes dans un mode de la boucle A et un atome dans un mode de la boucle B.

On réalise ainsi des miroirs et des séparatrices à atomes en effectuant des transferts cohérents d'impulsion aux atomes à l'aide de la diffraction de Bragg. On peut ainsi transférer aux atomes d'une certaine classe d'impulsion p une impulsion $2\hbar k$, fixée par la longueur d'onde du laser et l'angle entre les faisceaux. Ce processus de transfert peut être modélisé comme un système à deux niveaux couplé par une pulsation de Rabi à deux photons. On sélectionne le doublet résonant $(p, p+2\hbar k)$ en ajustant la différence de

fréquence entre les faisceaux. Un tel couplage permet ainsi de contrôler les populations dans les deux modes couplés pour former des miroirs et des séparatrices à atomes. De plus, lors d'une séparatrice Bragg, la différence de phase entre les atomes transmis et réfléchis est égale à la différence de phase entre les faisceaux lasers. C'est ce processus d'impression de phase qui va permettre de contrôler la phase imprimée entre les deux doublets d'impulsion A et B couplés par diffraction de Bragg dans l'interféromètre de Bell, et donc jouer le rôle de paramètre de contrôle des corrélations. Un contrôle précis de la réflectivité, de la sélectivité et de la phase imprimée par la diffraction de Bragg est nécessaire à la bonne réalisation d'un test de Bell. Étudier l'influence de ces paramètres sur le signal de Bell et vérifier que l'on est capable de les contrôler a été au coeur de mon travail de thèse, présenté dans ce manuscrit.

Au cours de ma thèse, la diffraction de Bragg et son influence dans la réalisation d'un interféromètre de Bell ont ainsi été étudiées en détails. Le chapitre 4 présente le schéma de principe de l'interféromètre à deux particules et quatre modes que l'on cherche à réaliser. Le dispositif est comparé avec un autre interféromètre récemment rapporté dans la littérature par un autre groupe de recherche, qui a observé des interférences à deux atomes mais dont le contraste n'était pas suffisant pour qu'il y ait violation d'inégalité de Bell. Dans notre cas, l'objectif principal est de parvenir à imprimer deux phases différentes sur les deux doublets qui forment l'interféromètre de Bell, ce qui constitue la difficulté majeure de notre dispositif. Pour ce faire, le chapitre 4 détaille le formalisme de transition à deux photons qui décrit la diffraction de Bragg, et ce formalisme est appliqué aux interféromètres atomiques dans le but de déterminer les phases en jeu dans l'interféromètre de Bell.

Dans le chapitre 5 est décrite la stratégie originale que nous avons élaborée afin d'assurer le contrôle de la phase relative entre les deux doublets A et B. Le principe consiste à utiliser le fait que les deux doublets couplés par la diffraction de Bragg n'ont pas la même fréquence de résonance. De cette façon, lors de la séparatrice, une modulation de la pulsation de Rabi à deux photons permet d'être résonant avec deux doublets, dont l'écart est fixé en choisissant la fréquence de la fonction de modulation. Une même séparatrice Bragg joue alors le rôle de deux séparatrices, chacune résonante avec un doublet. On peut alors, en ajoutant une phase à l'origine à cette pulsation de Rabi à deux photons, piloter la différence de phase imprimée entre les deux doublets. Un point important est que cette différence de phase est le paramètre de contrôle qui permet de piloter les interférences à deux particules de l'interféromètre de Bell. Ainsi, en modifiant la phase à l'origine de la fonction de modulation, on peut contrôler cette différence de phase entre les deux doublets et ainsi piloter les corrélations entre les particules détectées.

En utilisant les mêmes faisceaux pour les deux doublets, cette stratégie de contrôle de phase assure que la différence de phase imprimée entre les deux doublets ne dépend pas de la différence de phase entre les lasers. Cette réjection de mode commun constitue un avantage pour l'observation d'une interférence avec un bon contraste, car l'interféromètre est ainsi, par construction, insensible aux fluctuations de phase relatives entre les faisceaux Bragg, susceptibles de diminuer le contraste des interférences.

On peut résoudre l'équation de Schrödinger numériquement pour ces séparatrices Bragg modulées afin d'estimer le contraste des interférences Bragg que l'on peut chercher à obtenir. En prenant en compte l'influence de la classe de vitesse sur le profil de réflectivité, on trouve que l'oscillation du paramètre de Bell, qui quantifie la force des corrélations, n'est pas maximale. En effet, les séparatrices résonantes avec chacun des deux doublets ne sont pas indépendantes du fait du profil de réflectivité évasé de chaque séparatrice en

fonction de la classe de vitesse. Pour améliorer ce contraste, on montre qu'il est possible de réaliser des séparatrices et des miroirs dont le profil temporel a une forme de sinus cardinal.

Dans le chapitre 6, on décrit la mise en place expérimentale des impulsions Bragg en forme de sinus cardinal, qui nécessite un asservissement de la puissance des faisceaux ainsi qu'un dispositif appelé phase shifter qui permet d'ajouter des phases de π entre les faisceaux lasers de façon contrôlée. Pour démontrer notre capacité à contrôler la phase imprimée sur les atomes, on réalise une expérience de Ramsey, qui consiste à faire interférer sur le MCP deux condensats qui ont la même impulsion mais qui ne sont pas tombés de la même hauteur. La figure d'interférence ainsi observée peut alors être décalée en ajustant la tension dans le phase shifter.

On réalise alors des impulsions Bragg façonnées, en forme de sinus cardinal, ou modulées sinusoïdalement, que l'on caractérise en détails. Les résultats démontrent notre capacité à contrôler très finement la classe de vitesse sélectionnée pour le transfert Bragg, et valident le principe des séparatrices modulées pour avoir deux fréquences de résonance. En réalisant une interférence de Ramsey avec de telles séparatrices modulées, on montre que les interférences se décalent dans des sens opposées entre les doublets A et B quand on fait varier la phase à l'origine de la fonction de modulation, ce qui valide la stratégie de contrôle de phase puisqu'on arrive bien à imprimer une phase opposée sur chaque doublet.

Enfin, on réalise une expérience d'interférences à deux particules de type Hong-Ou-Mandel à l'aide de la source de paires, de façon à déterminer les temps auxquels on doit appliquer les impulsions Bragg pour l'expérience de Bell. Réalisée pour la première fois avec des impulsions en forme de sinus cardinal, cette expérience permet en effet de repérer à quel moment on doit appliquer la séparatrice de Bragg pour que les particules soient indiscernables. Après cette calibration, présentée dans le chapitre 7, l'expérience de Bell a été lancée mais n'a pas donné lieu à l'observation de corrélations à deux atomes. Depuis, des causes probables ont été identifiées pour expliquer pourquoi le signal de Bell n'a pas été observé. Les résultats sont encourageants, et notre capacité à contrôler très finement la diffraction de Bragg constitue une étape importante vers la réalisation prochaine d'un nouveau test de Bell.

Contents

Introduction **16**

1 Quantum atom optics experiments as probes of non classical correlations **22**
1.1 Correlations in classical and quantum optics . . . 23
1.1.1 Correlations in classical optics . . . 23
1.1.2 Entanglement and correlations in quantum optics . . . 26
1.2 Experimental evidence of non classical correlations in optics . . . 30
1.2.1 Sub-shot-noise measurements . . . 30
1.2.2 Cauchy-Schwarz inequality violation . . . 32
1.2.3 Hong-Ou-Mandel effect . . . 33
1.3 Bell tests . . . 38
1.3.1 EPR argument . . . 38
1.3.2 Bell inequality . . . 40
1.3.3 The momentum degree of freedom: Rarity-Tapster experiment . . . 43
1.3.4 From photons to atoms . . . 45
1.4 Quantum atom optics with metastable helium . . . 45
1.4.1 Bose-Einstein condensation and single atom detection . . . 45
1.4.2 Pairs emission and non-classical correlations . . . 47
1.4.3 Bragg diffraction and atom interferometers . . . 50
1.4.4 Towards a Bell test . . . 52

2 Experimental setup: preparation of a metastable Helium Bose-Einstein Condensate **54**
2.1 Metastable helium: interest and detection . . . 55
2.1.1 Metastable helium . . . 55
2.1.2 Micro-Channel Plate . . . 57
2.1.3 Delay lines . . . 59
2.1.4 Reconstruction . . . 62
2.2 Cooling procedure . . . 64
2.2.1 Source . . . 64
2.2.2 Cooling atoms down to Bose-Einstein Condensation . . . 65
2.2.3 Raman transfer and protective copper plate beam dump . . . 69
2.2.4 Imaging system . . . 73
2.3 BEC characterization . . . 75
2.3.1 Stability . . . 75
2.3.2 Number of atoms, temperature, size and chemical potential . . . 76

3 Emission of momentum pairs of atoms **80**
3.1 Four-wave mixing . . . 81
3.1.1 Simple model: emission of two coupled modes . . . 81

3.1.2 Phase-matching conditions in a periodic potential . . . 82
3.1.3 Output state, density and correlations . . . 85
3.1.4 Multimode description . . . 86
3.2 Experimental procedure and results . . . 89
3.2.1 Experimental procedure . . . 89
3.2.2 Density and phase-matching . . . 91
3.3 Second order correlation fonctions . . . 93
3.3.1 Correlations computation . . . 93
3.3.2 Auto-correlation . . . 98
3.3.3 Cross-correlation . . . 101
3.4 Counting statistics . . . 104
3.4.1 Detection probabilities . . . 104
3.4.2 Joint detection probabilities . . . 107
3.5 Towards non classical correlation effects . . . 110
3.5.1 Sub shot-noise variance . . . 110
3.5.2 Cauchy-Schwartz violation . . . 111
3.5.3 Experimental results . . . 112

4 Interferometer theory: from Bragg diffraction to Bell tests 115
4.1 Description of the Bell interferometer . . . 116
4.1.1 Principle . . . 116
4.1.2 Assessment of assumptions and visibility of the Bell correlator . . . 120
4.1.3 Comparison with another setup . . . 127
4.2 Theoretical description of the Bragg pulses . . . 133
4.2.1 Bragg diffraction of atoms in an optical lattice . . . 133
4.2.2 Bragg regime, Kapitza-Dirac regime and Raman-Nath approximation . 137
4.2.3 Off-resonance Bragg diffraction . . . 142
4.3 Phase involved in an interferometer . . . 145
4.3.1 Propagation phase shifts . . . 146
4.3.2 Light-matter interaction phase shifts . . . 151
4.3.3 Conclusion . . . 156
4.4 Application to the Mach-Zehnder interferometer . . . 158
4.4.1 Resonant case with short pulses . . . 158
4.4.2 Off-resonant corrective terms - finite duration pulses . . . 163
4.5 Application to the Bell interferometer . . . 166
4.5.1 Propagation phase . . . 166
4.5.2 Center of mass-dependent imprinted phase . . . 168
4.5.3 Off-resonant terms . . . 169

5 Bragg pulses shaping and phase control for a Bell test 172
5.1 Bell oscillation in an off-resonant HOM experiment . . . 173
5.1.1 Description of the Hong-Ou-Mandel effect . . . 175
5.1.2 Analytical results for the Bell correlator . . . 176
5.1.3 Numerical simulation . . . 184
5.1.4 Discussion of previous results . . . 186
5.2 Bell phase control . . . 188
5.2.1 Principle: two-frequency pulses . . . 188
5.2.2 Experimental implementation . . . 190
5.2.3 Reflectivity and phase of Bragg pulses for a Bell test . . . 195
5.2.4 Bell correlator . . . 201

5.3 Bragg pulse shaping . . . 204
5.3.1 State of the art, motivation and criteria . . . 204
5.3.2 Sinc-shaped mirror . . . 207
5.3.3 Modulated sinc-shaped beam splitter . . . 211
5.3.4 Oscillation of the Bell correlator . . . 214

6 Experimental preparation of the Bragg pulses: interferometric experiments 219
6.1 Setup of the Bragg pulses . . . 220
6.1.1 Optical setup . . . 220
6.1.2 Alignment and two-photon resonances . . . 221
6.1.3 Compensating gravity . . . 222
6.1.4 Rabi oscillations . . . 223
6.1.5 Bragg diffraction in the Kapitza-Dirac regime . . . 225
6.1.6 Experimental setup for the pulses shaping . . . 226
6.2 Ramsey interferometer . . . 228
6.2.1 Principle . . . 228
6.2.2 Calculation . . . 229
6.2.3 Experimental results . . . 234
6.2.4 Phase shifter calibration . . . 237
6.3 Shaped Bragg pulses . . . 239
6.3.1 Sinc pulses . . . 239
6.3.2 Shaped pulse equivalent time . . . 243
6.3.3 Modulated pulses . . . 245
6.3.4 Phase control . . . 247
6.4 Mach-Zehnder gravimeter . . . 250
6.4.1 Principle . . . 250
6.4.2 Gravity measurement attempt . . . 251
6.5 Conclusion and outlook . . . 253

7 Hong-Ou-Mandel experiment and Bell inequality test 254
7.1 The Hong-Ou-Mandel effect with atoms . . . 255
7.1.1 Generalization for any input state . . . 255
7.1.2 Tuning indistinguishability . . . 257
7.2 Observation of an atomic Hong-Ou-Mandel effect . . . 259
7.2.1 Experimental preparation . . . 259
7.2.2 Results: analysis of the HOM dip . . . 262
7.2.3 Ramsey fringes . . . 267
7.3 First Bell test attempt . . . 268
7.3.1 Parameters and procedure . . . 268
7.3.2 Sensitivity to the interferometer closure . . . 270
7.3.3 Sensitivity to the detuning . . . 272
7.3.4 Sensitivity to the initial cloud position . . . 273

Conclusion and outlook 276

Appendices 281
A. Experimental sequences used for the figures . . . 282
B. Timeline . . . 283
C. Experimental setup for a Bell test with global phase control . . . 288

Bibliography **290**

Introduction

A brief history of entanglement

In the 1920s, a group of physicists embarked on the development of quantum theory to explain certain perplexing observations that defied classical models. It was M. Planck in 1900 who initially introduced the concept of quantized energy to account for blackbody radiation[1]. Subsequently, A. Einstein proposed a model in 1905 to explain the photoelectric effect[2], employing the idea of light particles and building on Planck's notion of energy quantization. In 1913, N. Bohr incorporated energy quantization into his renowned atomic model[3], aiming to elucidate atomic spectra.

Gradually, a mathematical framework emerged to describe a quantum system, characterize its evolution and properties, and account for experimental observations. E. Schrödinger and W. Heisenberg significantly contributed to formalizing quantum mechanics in complementary ways around 1925, with Heisenberg using matrix notation and Schrödinger employing a wave function formulation defined in a complex vector space called a Hilbert space, and governed by the equation now bearing his name. Schrödinger demonstrated the equivalence of their two formalisms, and with the contribution of M. Born in 1926, they established that observables in quantum mechanics are represented by Hermitian operators, and the squared modulus of the wave function can be interpreted as measurement probabilities. Shortly thereafter, J. von Neumann formulated a first axiomatization of quantum mechanics and Dirac introduced the bra-ket notation, simplifying the mathematical description of quantum concepts.

Thus, a quantum system is represented by a state defined in a Hilbert space, and its evolution is determined by a Hamiltonian, a Hermitian operator that describes the energies involved between the system and its environment. Very importantly, in quantum mechanics, not only does the measurement result of an observable have a certain probability, equal to one of the eigenvalues of the measured observable, but also the measurement projects the state of the system onto the associated eigenstate. The future evolution of the system is described by the Schrödinger equation, but now with the system's state that has been projected by the measurement.

The establishment of this formalism by the physicists now recognized as the pioneers of quantum mechanics was marked not only by a constant concern to account for experimental results but also by a determination to draw implications from this nascent theory. One of its strengths lies in its ability to predict experimental outcomes. It is indeed possible to describe sometimes very simply the evolution of a simple quantum system subject to constraints characterized by a potential term in the system's Hamiltonian, which represents

its energy. Numerous experiments have confirmed predictions of quantum theory, such as the Stern–Gerlach experiment (1922) which demonstrated the quantization of the spatial orientation of angular momentum, and which has allowed, through the measurement of a particle's spin, for the verification of quantum theory predictions related to the projection of a quantum state by measurement.

One of the most striking results of quantum mechanics is the phenomenon of entanglement, which occurs when a system of two (or more) particles cannot be independently described but must be considered as an inseparable whole, regardless of the distance between them. An important consequence is that the measurement result of an observable on one of these particles will be correlated with the measurement result on the other particle, sometimes perfectly correlated. This means that, for an entangled system, measuring an observable on only one of the two particles affects the entire system. This can lead to the observation of very strong correlations in the measurements of the physical properties of both particles, so strong that they cannot be explained classically.

In 1935, A. Einstein, B. Podolsky, and N. Rosen published a paper[4] in which they emphasized the inherently counterintuitive nature of this theory, in which the result of a measurement is intrinsically probabilistic. They gave the example of entangled particles (a term introduced shortly afterward by Schrödinger): if one measures the position of one of the two particles, then one can predict with certainty the position of the other, and likewise if one measures the momentum of one, one can predict the momentum of the other, as if the information about the measurement could be instantaneously transmitted from one particle to the other, which would violate the principle of special relativity, according to which no information can propagate faster than the speed of light. They drew important consequences regarding the very nature of quantum theory: either it is incomplete and there exist hidden variables to which we do not have access and which would allow for deterministic predictions of measurement outcomes, or the theory is complete, but one must abandon the assumption of locality, meaning the idea that changes made in one region of space cannot instantaneously influence another distant region. This gave rise to a famous debate between Einstein and Bohr, advocates of the first and second options, respectively.

The debate remained solely philosophical and a matter of interpretation until 1964 when J. Bell mathematically proved that the assumption of locality is inherently incompatible with the predictions of quantum theory[5]. This breakthrough paved the way for experiments that could settle the dispute between Einstein and Bohr, known as Bell tests. The idea is, of course, to use a system of entangled particles and highlight correlations so strong that even a hidden-variable model would not be able to explain them. To achieve this, one should determine a quantity (called the Bell parameter), from measurements of correlation properties of the system, that has a limit for local theories but which can be exceeded by quantum mechanics. It is then said that there is a violation of the Bell inequality.

It is noteworthy that while quantum mechanics can, in specific cases, lead to a violation of the Bell inequality, this is generally not the case. It is not straightforward to demonstrate quantum measurements outcomes that do not verify the Bell inequality, and special efforts are required to achieve it. Following an article by J. Clauser, M. Horne, A. Shimony, and R. Holt[6], which formulates a Bell inequality in a practical form for experimental testing, the first Bell tests were conducted using photons in the 1970s in the United States by J. Clauser[7], and E. Fry[8], yielding early results that tended to confirm the non-local nature of quantum mechanics. However, these tests had shortcomings, and it was only with the

experiments conducted by A. Aspect in Orsay from 1975 to 1982[9][10], using a high flux source of entangled photons, that the experimental results highlighted a violation of the Bell inequality by 40 standard deviations.

Following a scheme initially introduced by D. Bohm, the experiment involves generating two photons with entangled polarization degrees of freedom. The photons then move away from each other, and correlations between the polarization measurements of one photon and the other are studied. With quantum mechanics, it can be shown that the joint probabilities of measuring both photons in the same polarization state (for instance) varies sinusoidally with the angle between the two polarizers used for the measurement. To ensure the fundamentally non-local nature of the measurement result, it is crucial to separate the two measurement sites by a space-like interval. To do so, the time between the choice of measurement parameters and the measurement itself must be shorter than the time it takes for light to travel from one site to the other. To achieve this, Aspect and his team implemented an ultra-fast switch which would change the polarizer's angles so that the choice of the measurement angle could be made during the time of flight of the photons[11]. They exhibited a Bell violation by 6 standard deviations, providing, for the first time, solid experimental evidence for the non-local nature of the measurement, as predicted by quantum mechanics.

Over time, with scientific and technological advancements, it became possible to conduct further experiments to confirm this result, using particles other than photons and exploring different degrees of freedom for entanglement. Let us mention, for example, the experiment conducted by J. Rarity and P. Tapster[12] in 1990, who successfully performed a Bell inequality test involving pairs of photons with the same polarization but following four different optical paths, following an interferometric scheme proposed by M. Horne, A. Shimony, and A. Zeilinger[13]. In this experiment, the photons are entangled in momentum, marking the first Bell test involving an external degree of freedom of the particles. In 1998, the team of Zeilinger conducted a Bell test similar to the one of Aspect, but using a quantum process to randomize the choice of the measurement during the time of flight, definitely closing the so-called locality loophole[14]. This progress continued until 2015 when three independent experiments[15][16][17] provided evidence of Bell inequality violations that ruled out any loopholes. The current consensus is that quantum theory, never proven wrong so far, has successfully challenged the principle of locality in space-time through the strong correlation properties inherent in entangled states. Beyond being mere subjects of study, these states have such unique properties that they can be harnessed in technological applications, ranging from quantum cryptography to quantum computing.

The ideas of quantum mechanics have progressed, and simultaneously the properties of quantized light have been studied and used, leading to the emergence of quantum optics, and to technological developments such as the laser. Not only do we now have a better understanding of how to prepare, control, and detect photons, but there is also an improved understanding of the interaction mechanisms between light and matter. This has paved the way for atomic physics, involving the manipulation of atoms and the study of their quantum properties. The laser cooling of atoms resulted in the observation in 1995 of a phenomenon predicted by A. Einstein and S. Bose, a phase transition of a bosonic atomic gas at very low temperature into a state of matter where almost all atoms are in the same quantum state[18]. This state, known as the Bose-Einstein condensate, enables the formation of a coherent reservoir of atoms in a specific quantum state, making it possible to conduct experiments that were once merely thought experiments during the development of quantum theory in the 1920s and 30s.

Similar to photons, it is then possible to study the quantum properties of atoms, including entanglement. But observing non-classical correlations with atoms remains an experimental challenge, especially when attempting to do so using an external degree of freedom for entanglement. While successful Bell tests have been conducted with atoms using their spin, it has not been the case with atoms entangled in momentum, as originally envisioned by Einstein, Podolsky, and Rosen.

Description of the thesis project

This historically rich context is the framework of my thesis project. The Quantum Atomic Optics team at the Charles Fabry Laboratory of the Institute d'Optique, that I joined in March 2020, is specialized in manipulating ultra-cold metastable helium atoms. These atoms possess the unique feature of having high internal energy, allowing their detection when they collide onto a metallic surface, thereby extracting electrons from it. An ingenious detection system, called a microchannel plate, then amplifies the detection signal using an electron cascade. Coupled with the use of so-called delay lines[19], this system not only enables the detection of individual atoms but also allows retrieving the particle velocities before their impact on the plate. This detailed knowledge of the momentum distribution of helium atoms can be leveraged to study their correlation properties. The experimental platform thus makes it feasible to conduct experiments historically performed with photons, but this time using atoms: this is what is called quantum atomic optics.

For the past few years, the team has been able to create pairs of twin atoms with different momenta from a Bose-Einstein condensate using a process called four-wave mixing[20]. These atom pairs have led to the observation of non-classical correlations[21], suggesting that momentum modes are entangled. The goal of my thesis is to implement a Bell interferometer, inspired by the scheme of Rarity and Tapster, to demonstrate a violation of the Bell inequality with atoms entangled in momentum.

While this experiment is situated in a context with significant implications for the nonlocal nature of spacetime, we will not delve into such considerations here. The stringent experimental constraints do not allow closing the locality loophole. Nevertheless, demonstrating a violation of the Bell inequality remains an important objective, serving both as a test for quantum mechanics and as a clear affirmation that the system subjected to the Bell interferometer is entangled and exhibits correlations stronger than what could be obtained classically. Such a result would pave the way for a new generation of experiments, which could further close loopholes and verify the possibility of violating Bell inequalities with entangled massive particles via an external degree of freedom. This aspect also sparks the curiosity of another scientific community, aiming to study and conduct experiments involving both entanglement and gravity to analyze gravitational decoherence mechanisms, aiming to develop a theory unifying quantum physics and gravity[22].

My work has involved setting up a Bell interferometer, an objective pursued by the team for several years but delayed due to technical issues and breakdowns in the experimental platform, which has been in place for many years. I contributed to the upgrade and modernization of the experiment, aiming to achieve a stable Bose-Einstein condensate to facilitate the reliable and reproducible execution of interferometric experiments. Subsequently, our team gradually implemented the necessary components for constructing the interferometer: the atom pairs emission process and the study of their correlations, followed by the setting up of atom mirrors and beam splitters. I particularly contributed

to the development of the latter, involving the realization of two-photon transitions to transfer momentum to atoms through a coherent process known as Bragg diffraction. The initial interferometric results for testing these mirrors and splitters yielded conclusive outcomes detailed in this thesis. A first Bell test was conducted in October 2023, but no correlation signal was observed. Encouraging avenues to explain this and continue our quest for Bell inequality violation will be discussed at the end of this manuscript.

Outline of the manuscript

This manuscript is divided into 7 chapters.

1. Quantum atom optics experiments as probes of non-classical correlations

This introductory chapter presents the framework within which this thesis is situated. We introduce the concept of correlation in quantum systems along with suitable tools for their study. The principle of a Bell test is presented using the example of photons, as this experiment is designed to highlight correlations so strong that they constitute the signature of the purely quantum phenomenon of entanglement. We show that the recent developments of quantum atom optics, in particular with metastable helium, make it possible to perform a similar test with momentum correlated atoms.

2. Experimental setup: preparation of a metastable Helium Bose-Einstein Condensate

In this chapter, we present the experimental setup through which a Bose-Einstein condensate of metastable helium can be obtained, marking the initial step towards the realization of a Bell test. The use of a microchannel plate (MCP) combined with delay lines makes it possible to have a three-dimensional single-atom detector, which enables the determination of the momentum of each detected atom before their fall on the MCP, as detailed in this chapter. Additionally, we provide some characteristics of the obtained condensates through an analysis of the clouds after time of flight.

3. Emission of momentum pairs of atoms

In order to emit pairs of correlated atoms, we use the interactions between atoms in the condensate, which we subject to an optical lattice. We exploit the dispersion relation of atoms in the lattice to generate pairs of atoms, emitted from the condensate at different momenta. This phenomenon, known as four-wave mixing, is presented in this chapter, along with the results obtained during this thesis to characterize the emitted pairs and to highlight correlations between coupled momentum modes.

4. Interferometer theory: from Bragg diffraction to Bell tests

In this chapter, we delve into greater detail regarding the strategy adopted to set up a Bell interferometer with momentum correlated atoms, which involves the use of mirrors and beam splitters that transfer momentum to atoms by Bragg diffraction. After discussing a recent test conducted in another configuration, we provide a presentation of Bragg diffraction. An important aspect of our setup consists in exploiting the fact that the two momentum doublets involved in the Bell interferometer do not have the same

resonance frequency, thus we place particular importance on the spectral dimension of the Bragg mirrors and beam splitters. To calculate the phase involved in the Bell interferometer, we present basic concepts of atom interferometry allowing for the general calculation of phase shifts that occur in interferometers, due to the propagation of wavepackets along with the interaction with light. The results are applied to the well-known case of the Mach-Zehnder interferometer before being applied to the case of the Bell interferometer.

5. Bragg pulses shaping and phase control for a Bell test

A preliminary step towards the realization of a Bell test is to perform of a Hong-Ou-Mandel (HOM) interferometer, which allows for the detection of the interferometer closure. It turns out that, thanks to our multimode source, we can simultaneously implement Bell interferometers alongside an HOM interferometer. Despite the fact that the Bell phase cannot be controlled, it can provide useful information regarding the possibility of observing Bell correlations. In this chapter, we use this idea along with the formalism developed in the previous chapter to discuss past results obtained within the team, before detailing the strategy adopted to control the Bell phase in a genuine Bell test, which involves imprinting on the atoms a tunable phase by modulating the amplitude of the Bragg beam splitter pulse. We also show that it is possible to enhance the Bell correlation signal by realizing sinc-shaped Bragg pulses. These discussions are based on the results of simulations I developed during the thesis, which consist in numerically solving the Bragg coupling equations between momentum states.

6. Experimental preparation of the Bragg pulses: interferometric experiments

In this chapter, we describe the experimental setup of the Bragg pulses and provide proof of principle of their proper functioning. Using a power feedback control and a phase shifter, we can shape a Bragg pulse into any desired form, resulting in a Rabi frequency that can be negative or even complex. To ensure that we control the phase imprinted on the atoms as desired, we interfere two condensates using a Ramsey-type interferometer, demonstrating that we can shift the observed interference pattern in a controlled and reproducible manner. Additionally, we present the results obtained with sinc-shaped pulses, which we employ in a Mach-Zehnder interferometer in an attempt to measure the value of gravity.

7. Hong-Ou-Mandel experiment and Bell inequality test

Finally, this last chapter describes the preliminary results recently obtained for an HOM interferometer realized with sinc-shaped Bragg pulses. A HOM dip has been observed, and its characteristics are discussed. Following these encouraging results, a first Bell test was conducted in October 2023 but did not lead to the observation of Bell correlations. Several possible explanations are provided to try to explain the absence of signal as several potential sources of errors have been identified since then.

Chapter 1

Quantum atom optics experiments as probes of non classical correlations

1.1 Correlations in classical and quantum optics 23
1.1.1 Correlations in classical optics 23
1.1.2 Entanglement and correlations in quantum optics 26
1.2 Experimental evidence of non classical correlations in optics 30
1.2.1 Sub-shot-noise measurements 30
1.2.2 Cauchy-Schwarz inequality violation 32
1.2.3 Hong-Ou-Mandel effect 33
1.3 Bell tests 38
1.3.1 EPR argument 38
1.3.2 Bell inequality 40
1.3.3 The momentum degree of freedom: Rarity-Tapster experiment . . 43
1.3.4 From photons to atoms 45
1.4 Quantum atom optics with metastable helium 45
1.4.1 Bose-Einstein condensation and single atom detection 45
1.4.2 Pairs emission and non-classical correlations 47
1.4.3 Bragg diffraction and atom interferometers 50
1.4.4 Towards a Bell test 52

In this chapter, we will introduce the concepts and tools developed by quantum optics to study light sources and their properties. It will be demonstrated that these tools can also be employed to describe atomic sources, and we will justify the significance of conducting quantum optics experiments with atoms.

1.1 Correlations in classical and quantum optics

1.1.1 Correlations in classical optics

Interferences in classical optics

Let us consider a light source that we use as an input in an interferometric device, whether it be a Michelson interferometer (using amplitude division) or a Young's double-slit interferometer (using wavefront division). A light detector, capable of measuring light intensity, is placed at a fixed location in the interference zone (Figures 1.1 and 1.2).

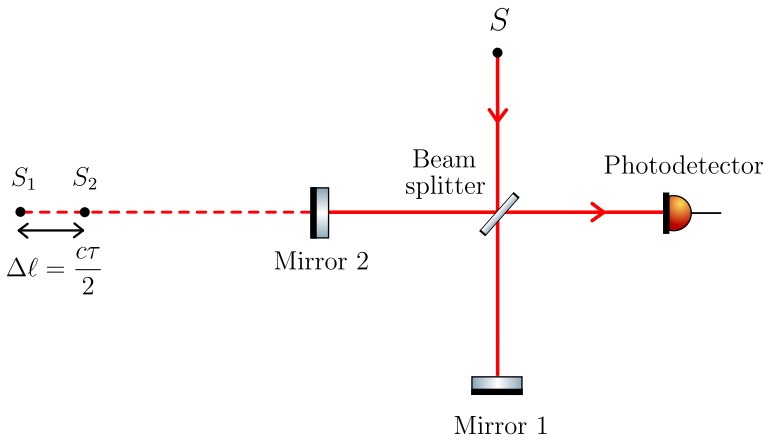

Figure 1.1: Scheme of a Michelson interferometer. A light source sends light onto a 50/50 beam splitter. The two resulting beams are each reflected off a mirror and then recombined at the beam splitter. A photodetector collects the resulting light.

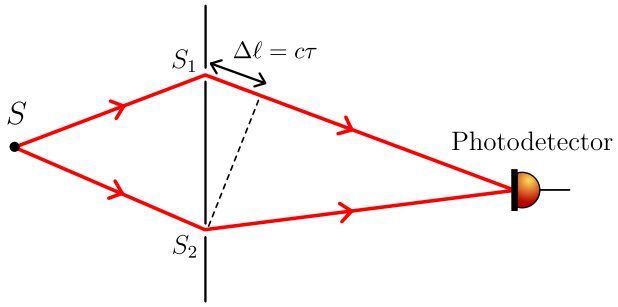

Figure 1.2: Scheme of a Young interferometer. Two light rays originating from the same source are diffracted by two slits. A detector collects the beams emanating from the two slits.

The total electric field at the detector is the sum of the two electric fields originating from the two secondary sources permitted by the interferometric device. Let's assume a non-zero path length difference between the two light paths, resulting in a time delay τ

between the interfering waves. The electric intensity at the detector is then expressed as:

$$I = \langle |E(t) + E(t+\tau)|^2 \rangle \tag{1.1}$$

where $\langle \ldots \rangle$ corresponds to the time averaging of the detector. Expanding this expression, we obtain

$$I = \langle |E(t)^2| \rangle + \langle |E(t+\tau)|^2 \rangle + 2\,\mathrm{Re}\,\langle E(t)E^*(t+\tau) \rangle \tag{1.2}$$

For a stationary source for which $\langle |E(t)^2| \rangle = \langle |E(t+\tau)|^2 \rangle = \langle |E|^2 \rangle = I_0$, this can be rewritten:

$$I = 2I_0 \left[1 + \mathrm{Re}\left(g^{(1)}(\tau) \right) \right] \tag{1.3}$$

where

$$g^{(1)}(\tau) = \frac{\langle E(t)E^*(t+\tau) \rangle}{\langle |E|^2 \rangle} \tag{1.4}$$

This function $g^{(1)}$ is called the normalized first order correlation function, and contains crucial information for characterizing the coherence properties of the source. For interference to occur, it is necessary for $g^{(1)}$ to be different from 0. If $E(t)$ and $E(t+\tau)$ are independent random variables, then $\langle E(t)E(t+\tau) \rangle = \langle E(t) \rangle \langle E(t+\tau) \rangle$ and so $g^{(1)} = 0$. This highlights the fact that the first order correlation function thus quantifies the temporal correlation between these two quantities.

Note that $g^{(1)}$ is directly related to the spectral properties of the light source. Indeed, if we consider a source containing multiple spectral components, there is complete blurring of interferences beyond a certain delay τ, which occurs more quickly as the source is spectrally rich in spectral components. This is the Wiener-Khintchine theorem, which expresses the first order correlation function as the Fourier transform of the normalized spectral density $s(\omega)$ through the relationship:

$$g^{(1)}(\tau) = \int_{-\infty}^{+\infty} s(\omega)\, \mathrm{e}^{\mathrm{i}\omega\tau} \mathrm{d}\omega \tag{1.5}$$

Thus, by using only a light sensor and detecting the intensity resulting from an interference signal, one can measure correlation properties related to the amplitude of the electric field. This allows the deduction information about the coherence of the source.

The Hanbury Brown and Twiss experiment

Now, it is possible to go even further by looking at intensity correlations, involving four values of the electric field. This method, introduced by R. Hanbury Brown in order to measure the angular diameter of stars, involves two detectors and enables the probing of higher-order correlations. Together with R. Twiss, they conducted a famous experiment, now known as the Hanbury Brown and Twiss (HBT) experiment[23], to demonstrate the validity of the idea.

The principle of the experiment is as follows. One studies the light from a star, considered as an incoherent source with a certain spatial extent. Using filters, the light signal is made monochromatic. A beam splitter is used to divide the light beam into two, directed towards two separate detectors. The light intensity is then measured at two points, $\mathbf{r}_1$ and $\mathbf{r}_2$, as close to each other than one wants (Figure 1.3).

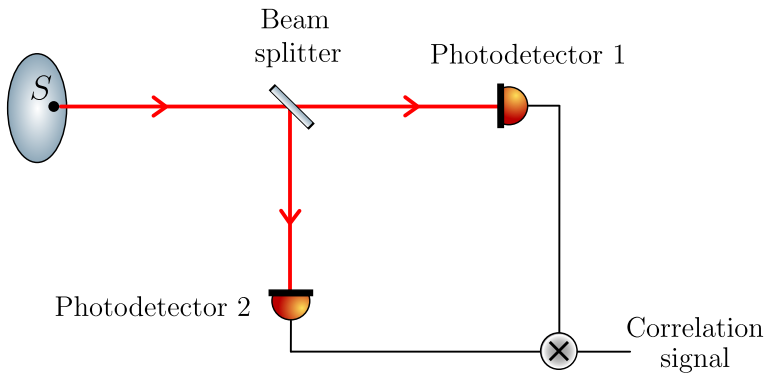

Figure 1.3: Scheme of the Hanbury Brown and Twiss setup. A spatially extended source emits light onto a 50/50 beam splitter. The intensity is collected at each output of the beam splitter, and a detection system allows access to the correlation signal between these two intensities.

The electrical signals from these two detectors are then combined, providing access to the second-order correlation function, defined as:

$$G^{(2)}(\mathbf{r}_1, \mathbf{r}_2) = \langle I(\mathbf{r}_1) I(\mathbf{r}_2) \rangle = \langle E(\mathbf{r}_1) E^*(\mathbf{r}_1) E(\mathbf{r}_2) E^*(\mathbf{r}_2) \rangle \tag{1.6}$$

To describe the light emitted by the star, one can use the Fraunhofer integral, which characterizes the electric field emitted by a collection of incoherent sources when the observation distance D is much greater than the wavelength λ and the size S of the source:

$$E(\mathbf{r}) = \int_S E(\mathbf{s})\, \mathrm{e}^{\frac{\mathrm{i}\pi}{\lambda D}|\mathbf{r}-\mathbf{s}|^2} \mathrm{d}\mathbf{s} \tag{1.7}$$

where $\mathbf{s}$ designates a point from the star, which is assumed to be uncorrelated with the others. It is then possible to apply the central limit theorem to show that the total electric field at each point $\mathbf{r}$ results from a Gaussian random process. As a result, $G^{(2)}(\mathbf{r}_1, \mathbf{r}_2)$ can be rewritten[1]

$$G^{(2)}(\mathbf{r}_1, \mathbf{r}_2) = \langle I(\mathbf{r}_1) \rangle \langle I(\mathbf{r}_2) \rangle + \langle E(\mathbf{r}_1) E^*(\mathbf{r}_2) \rangle \langle E(\mathbf{r}_2) E^*(\mathbf{r}_1) \rangle \tag{1.8}$$

From the second term, we can identify the spatial analogue of the first-order correlation function defined earlier. Using 1.7, we get:

$$G^{(1)}(\mathbf{r}_1, \mathbf{r}_2) = \langle E(\mathbf{r}_1) E^*(\mathbf{r}_2) \rangle = \iint_S \langle E(\mathbf{s}_1) E^*(\mathbf{s}_2) \rangle\, \mathrm{e}^{-\frac{\mathrm{i}\pi}{\lambda D}\left(|\mathbf{r}_2-\mathbf{s}_2|^2 - |\mathbf{r}_1-\mathbf{s}_1|^2\right)} \mathrm{d}\mathbf{s}_1 \mathrm{d}\mathbf{s}_2 \tag{1.9}$$

Using the fact that each point has no phase relation with another due to the source incoherence, we have $\langle E(\mathbf{s}_1) E^*(\mathbf{s}_2) \rangle = I(\mathbf{s}_1)\, \delta_{\mathbf{s}_1,\mathbf{s}_2}$, so that

$$G^{(1)}(\mathbf{r}_1, \mathbf{r}_2) = \int_S I(\mathbf{s}_1)\, \mathrm{e}^{-\frac{2\mathrm{i}\pi}{\lambda D}(\mathbf{r}_2-\mathbf{r}_1).\mathbf{s}_1} \mathrm{d}\mathbf{s}_1 \tag{1.10}$$

This is the van Cittert–Zernike theorem, which expresses the first-order spatial correlation function as the Fourier transform of the spatial intensity profile. Similarly to the temporal case, the first order correlation function contains the information about the

[1] Using the Gaussian Moment Theorem for this fourth order correlation function in terms of electric field.

coherence of the source. Indeed, for a homogeneous source intensity, $G^{(1)}(\mathbf{r}_1 - \mathbf{r}_2)$ decays on a scale ℓ_c called the correlation length of the source, inversely proportional to its size L.

The expression of the second order correlation function can be normalized by the product $\langle I(\mathbf{r}_1)\rangle \langle I(\mathbf{r}_2)\rangle$ of the mean intensities, which defines the normalized second-order correlation function, given by:

$$g^{(2)}(\mathbf{r}_1, \mathbf{r}_2) = 1 + |g^{(1)}(\mathbf{r}_1, \mathbf{r}_2)|^2 \tag{1.11}$$

The shape of $g^{(2)}(\mathbf{r}_1 - \mathbf{r}_2)$ is depicted in Figure 1.4. When $\mathbf{r}_1 = \mathbf{r}_2$, it reaches 2, and decreases gradually as $\mathbf{r}_1 - \mathbf{r}_2$ increases. When $\mathbf{r}_1 - \mathbf{r}_2 \geq \ell_c$, then $g^{(2)} = 1$. The Hanbury Brown and Twiss method thus provides a means to access information about the spatial coherence of the source. By varying the position of the detectors, one can obtain the coherence length of the star and consequently deduce its size, which they used to successfully measure the diameter of Sirius.

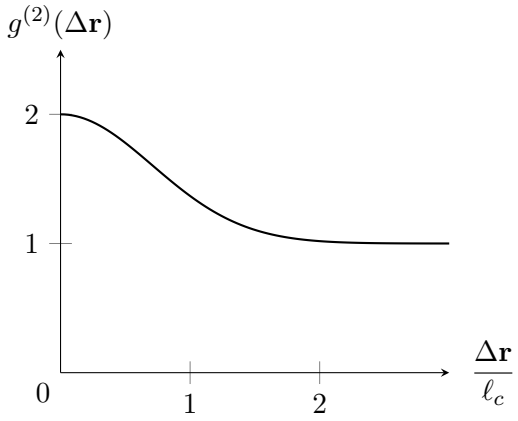

Figure 1.4: Shape of the second order correlation function $g^{(2)}$ as a function of the detectors position difference $\Delta\mathbf{r} = \mathbf{r}_1 - \mathbf{r}_2$ in the HBT experiment.

1.1.2 Entanglement and correlations in quantum optics

Quantum interpretation of the Hanbury Brown and Twiss effect

In the 1950s, the HBT experiment faced significant skepticism[24] due to its surprising interpretation in terms of photons. With the advent of light detectors based on the photoelectric effect, it was now possible to treat the current received by a sensor as the probability of detecting a photon, so that $I(\mathbf{r}) \propto \mathcal{P}(\mathbf{r})$, where $\mathcal{P}(\mathbf{r})$ designates the probability of measuring one photon at position $\mathbf{r}$. Thus, we can reinterpret the second-order correlation function in the form:

$$g^{(2)}(\mathbf{r}_1, \mathbf{r}_2) = \frac{\mathcal{P}(\mathbf{r}_1, \mathbf{r}_2)}{\mathcal{P}(\mathbf{r}_1)\mathcal{P}(\mathbf{r}_2)} \tag{1.12}$$

where $\mathcal{P}(\mathbf{r}_1, \mathbf{r}_2)$ is the joint probability to detect simultaneously one photon at position $\mathbf{r}_1$ and one photon at position $\mathbf{r}_2$.

Surprisingly, when $\mathbf{r}_1 = \mathbf{r}_2$, as we showed that $g^{(2)} = 2$, this would mean that the probability of detecting two photons at the same position is two times greater than the probability of detecting them independently, suggesting that the photons "come in pairs". This can seem false at first, since photons emitted at different, possibly very distant, points of a star, would be *a priori* considered to be independent.

An explanation of this phenomenon was provided in 1961 by U. Fano[25], using a simple model consisting of only two points from the source, noted A and B. Two photons are considered to be emitted from these two source points. When a particle is detected by one of the two sensors, it is impossible to know which path it took; it could have been emitted by A or B (Figure 1.5).

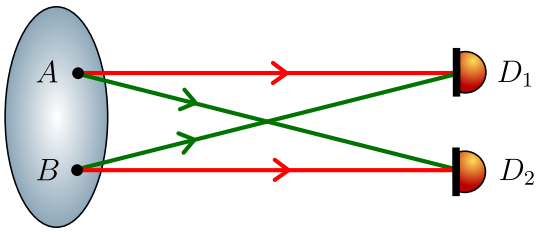

Figure 1.5: Input and ouput modes of the beam-spitter.

To account for this, the two-particle state at the detector level must be written as the superposition of both possibilities, namely:

$$|\psi\rangle = \frac{1}{\sqrt{2}}(|A,B\rangle + |B,A\rangle) \tag{1.13}$$

In this two-particle basis, $|A,B\rangle = |A\rangle_1 \otimes |B\rangle_2$ means that particle 1 was emitted by source A while particle 2 was emitted by source B. Note that the expression of the state 1.13 is directly related to the indistinguishability of the two particles. Since photons are bosons, the state must be symmetric with respect to the interchange of the particles, which justifies the + sign between the two terms (it would be a − sign for fermions).

The probability of detecting atoms in both detectors noted D_1 and D_2 is therefore $\mathcal{P}(D_1, D_2) = |\langle D_1, D_2|\psi\rangle|^2$ so that

$$\begin{aligned}\mathcal{P}(D_1,D_2) = \frac{1}{2}\big(&|\langle D_1,D_2|A,B\rangle|^2 + |\langle D_1,D_2|B,A\rangle|^2 \\ &+ 2\,\mathrm{Re}\,\langle D_1,D_2|A,B\rangle\langle D_1,D_2|B,A\rangle\big)\end{aligned} \tag{1.14}$$

We observe the emergence of an interference term, which depends on the phase relationship between the particles. If the two photons are statistically independent, then this term vanishes when averaging over all the points from the source and we have:

$$\mathcal{P}_{\mathrm{ind}}(D_1,D_2) = \mathcal{P}(D_1)\mathcal{P}(D_2) = \frac{1}{2}\left(|\langle D_1,D_2|A,B\rangle|^2 + |\langle D_1,D_2|B,A\rangle|^2\right) \tag{1.15}$$

If the two photons are coherent and the distance between the detectors is small enough, then the interference term is not zero but depends on the distance between the two detectors. When this distance is zero, we get $\langle D_1, D_2|B,A\rangle = \langle D_1, D_2|A,B\rangle$, so the interference is constructive and we obtain

$$\mathcal{P}(D_1 = D_2) = |\langle D_1,D_2|A,B\rangle|^2 + |\langle D_1,D_2|B,A\rangle|^2 = 2\,\mathcal{P}_{\mathrm{ind}}(D_1,D_2) \tag{1.16}$$

which is the result we found using a classical reasoning by treating light as a wave.

With this simple two-photon interference model, we can understand the HBT result as a consequence of the bosonic nature of the two-particle state, leading to what is known as a bosonic bunching effect. Thermal bosons tend to be emitted in pairs, resulting in significant correlations. This correlation is related to expressing the two-particle state as the sum of two inseparable terms, leading to interference. Such a state corresponds, in fact, to what is commonly referred to as an entangled state. This example highlights the importance of entangled states when studying the correlation properties of quantum systems.

Second quantization formalism

To demonstrate this effect by treating light in a quantum manner, it is possible to use the formalism of second quantization by introducing the creation and annihilation operators $\hat{a}^\dagger$ and $\hat{a}$. By modeling the process of photodetection as the transition of an electron from a bound state to a continuum state in a semiconductor material, it is possible to show, using the Hamiltonian of the light-atom interaction and Fermi's golden rule, that the mean transition rate w (and thus the associated photocurrent) for a given state of light $|\psi\rangle$ is given by[26]:

$$w \propto \langle \hat{a}^\dagger \hat{a} \rangle = \langle \psi | \hat{a}^\dagger \hat{a} | \psi \rangle \tag{1.17}$$

Here, the notation $\langle \ldots \rangle$ designates the quantum measurement, i.e., the quantum average of an operator over a state $|\psi\rangle$. Note that w is actually the quantum version of the normalized first order correlation function $g^{(1)}$ for the annihilation operator, which ultimately involves counting the number of photons received by a detector, as it can be observed by introducing the number operator $\hat{N} = \hat{a}^\dagger \hat{a}$.

Similarly, the joint measurement of photons in two detectors 1 and 2 is related to the normalized second order correlation function, defined as

$$g^{(2)}(1,2) = \frac{\langle \hat{a}_1^\dagger \hat{a}_2^\dagger \hat{a}_2 \hat{a}_1 \rangle}{\langle \hat{a}_1^\dagger \hat{a}_1 \rangle \langle \hat{a}_2^\dagger \hat{a}_2 \rangle} \tag{1.18}$$

where $\hat{a}_i^\dagger$ and $\hat{a}_i$ are the creation and annihilation operators of a photon in detector i, respectively.

This is the formalism developed by R. Glauber to describe the HBT experiment[27]. More generally, he introduced normalized n-th order correlation functions as

$$g^{(n)}(1,2,\ldots,n) = \frac{\langle \hat{a}_1^\dagger \hat{a}_2^\dagger \cdots \hat{a}_{n-1}^\dagger \hat{a}_n^\dagger \hat{a}_n \hat{a}_{n-1} \cdots \hat{a}_2 \hat{a}_1 \rangle}{\langle \hat{a}_1^\dagger \hat{a}_1 \rangle \langle \hat{a}_2^\dagger \hat{a}_2 \rangle \cdots \langle \hat{a}_n^\dagger \hat{a}_n \rangle} = \frac{G^{(n)}(1,2,\ldots,n)}{\langle \hat{a}_1^\dagger \hat{a}_1 \rangle \langle \hat{a}_2^\dagger \hat{a}_2 \rangle \cdots \langle \hat{a}_n^\dagger \hat{a}_n \rangle} \tag{1.19}$$

where $G^{(n)}(1,2,\ldots,n)$ is the non normalized n-th order correlation function.

Let us conclude on the Hanbury Brown and Twiss experiment. When the two detectors are at the same position ($\mathbf{r}_1 = \mathbf{r}_2$), the second order correlation function is

$$g^{(2)}(\mathbf{r}_1, \mathbf{r}_2 = \mathbf{r}_1) = \frac{\langle \hat{a}^\dagger \hat{a}^\dagger \hat{a} \hat{a} \rangle}{\langle \hat{a}^\dagger \hat{a} \rangle^2} \tag{1.20}$$

Using the commutation relation for bosons $[\hat{a}\hat{a}^\dagger] = 1$, we get

$$g^{(2)}(\mathbf{r}_1, \mathbf{r}_2 = \mathbf{r}_1) = \frac{\langle \hat{a}^\dagger(\hat{a}\hat{a}^\dagger - 1)\hat{a}\rangle}{\langle \hat{a}^\dagger\hat{a}\rangle^2} = \frac{\langle \hat{N}^2\rangle - \langle \hat{N}\rangle}{\langle \hat{N}\rangle^2} = 1 + \frac{\sigma_N^2 - \langle \hat{N}\rangle}{\langle \hat{N}\rangle^2} \tag{1.21}$$

where σ_N^2 is the variance of the number of photons. We can see that $g^{(2)}$ depends on the distribution statistics of the source. For a thermal light following Planck's distribution, it can be shown that the variance is

$$\sigma_N^2 = \langle N\rangle^2 + \langle N\rangle \tag{1.22}$$

By inserting this in equation 1.20, we find the bosonic bunching relation:

$$g^{(2)}(\mathbf{r}_1, \mathbf{r}_2 = \mathbf{r}_1) = 2 \tag{1.23}$$

Note that, for a laser, the number of photons follows a Poisson law for which $\sigma_N^2 = \langle \hat{N}\rangle$, so that $g^{(2)}(\mathbf{r}_1, \mathbf{r}_2) = 1$.

Notion of entanglement

Let us briefly present and discuss the concept of entanglement, previously introduced to describe the bosonic state of two particles. We consider a physical system with two degrees of freedom, denoted as A and B[28]. The space in which to describe the system is a tensor product Hilbert space, denoted as $\mathcal{E} = \mathcal{E}_A \otimes \mathcal{E}_B$. The factorized state

$$|\psi\rangle = |\alpha\rangle \otimes |\beta\rangle \tag{1.24}$$

belongs to this space. This means that sub-system A is in state α and sub-system B is in state β. Due to the properties of the Hilbert space, the following state

$$|\psi\rangle = \frac{1}{\sqrt{2}}\left(|\alpha_1\rangle \otimes |\beta_1\rangle + |\alpha_2\rangle \otimes |\beta_2\rangle\right) = \frac{1}{\sqrt{2}}\left(|\alpha_1, \beta_1\rangle + |\alpha_2, \beta_2\rangle\right) \tag{1.25}$$

also represents a state of the system (where the $1/\sqrt{2}$ factor is just a normalization factor). This remark may appear trivial, but its consequences are of utmost significance. Indeed, this state results in very strong correlations between the degrees of freedom A and B.

Indeed, if we measure both the degrees of freedom A and B, we find either α_1 for A and β_1 for B, with a probability of $1/2$, or α_2 for A and β_2 for B, with a probability of $1/2$, but the probability of measuring α_1 for A and α_2 for B is zero:

$$\begin{cases} \mathcal{P}(\alpha_1, \beta_1) = |\langle \alpha_1, \beta_1|\psi\rangle|^2 = \dfrac{1}{2} \\ \mathcal{P}(\alpha_2, \beta_2) = |\langle \alpha_2, \beta_2|\psi\rangle|^2 = \dfrac{1}{2} \\ \mathcal{P}(\alpha_1, \beta_2) = |\langle \alpha_1, \beta_2|\psi\rangle|^2 = 0 \\ \mathcal{P}(\alpha_2, \beta_1) = |\langle \alpha_2, \beta_1|\psi\rangle|^2 = 0 \end{cases} \tag{1.26}$$

Note that the probability of measuring α_1 is given by:

$$\mathcal{P}(\alpha_1) = \mathcal{P}(\alpha_1, \beta_1) + \mathcal{P}(\alpha_1, \beta_2) = \frac{1}{2} \tag{1.27}$$

and so on for the other probabilities of measuring α_2, β_1, β_2. Now, it is important to highlight that the conditional probability of measuring β_1, given that α_1 has been measured, is equal to

$$\mathcal{P}(\beta_1|\alpha_1) = \frac{\mathcal{P}(\alpha_1, \beta_1)}{\mathcal{P}(\alpha_1)} = 1 \tag{1.28}$$

This mathematically evident result nevertheless has very important consequences. Indeed, if we now consider that the two degrees of freedom are two different particles, possibly widely separated from each other, it is striking to note that, regardless of the outcome of the measurement on one of the two particles, the result of the other particle can be predicted with a probability of 1. This very strong correlation, inherent to the entangled state in quantum mechanics, lies at the heart of the discussions that took place between Einstein and Bohr.

As a consequence, one sub-system cannot be described independently from the other, the system must be considered as an inseparable whole. This non-separability is proper to quantum mechanics and can be taken as a definition for entanglement.

1.2 Experimental evidence of non classical correlations in optics

There are different ways of demonstrating that the correlations in systems of multiple particles cannot be explained by classical physics. We will mention just a few of them, which will be of particular importance in the subsequent sections of this manuscript.

1.2.1 Sub-shot-noise measurements

Let us consider a classical source of light, characterized by a Poissonian distribution law, like a laser. Light can be described as a coherent state $|\alpha\rangle$, where α is the parameter of the Poissonian distribution. Recall that $|\alpha\rangle$ is an eigenstate of the annihilation operator $\hat{a}$.

Due to the distribution statistics of the source, when using a photodetector to detect its light, the rate of photon detection will change from one realization to the other. Its mean value w is

$$w = \langle \hat{a}^\dagger \hat{a} \rangle = \langle \alpha | \hat{a}^\dagger \hat{a} | \alpha \rangle = |\alpha|^2 \tag{1.29}$$

This is, by definition, the value of the mean number of photons $\langle N \rangle$ involved in the measurement. On the other hand, the variance of w is

$$V(w) = (\sigma_w)^2 = \langle (\hat{a}^\dagger \hat{a})^2 \rangle - \langle \hat{a}^\dagger \hat{a} \rangle^2 = \langle \hat{a}^\dagger \hat{a}^\dagger \hat{a} \hat{a} + \hat{a}^\dagger \hat{a} \rangle - |\alpha|^4 = |\alpha|^2 \tag{1.30}$$

where σ_w is the standard deviation of the intensity measurement. Therefore, the relative precision of a measurement of w is:

$$\frac{\sigma_w}{w} = \frac{1}{|\alpha|} = \frac{1}{\sqrt{\langle N \rangle}} \tag{1.31}$$

As we can see, the precision is limited by the square root of the number of detected photons. Even the most stable classical flux exhibits such noise. This intrinsic limitation is called shot noise.

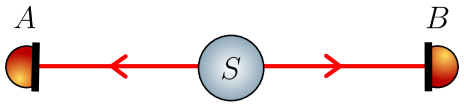

Figure 1.6: Scheme of a source emitting particles in two opposite directions.

Similarly, let us consider a classical system emitting particles in two different directions, on which we place two detectors A and B (Figure 1.6).

In each direction, an average of $\langle N \rangle$ particles are emitted. The source follows a Poissonian distribution law, so that the variance of the particles number in each beam is also equal to $\langle N \rangle$, as shown previously. If we consider the photon difference $\Delta N = N_A - N_B$ measured between the two detectors, the variance of this observable is equal to the sum of the two variances of the particles number detected in both beams, so $V(\Delta N) = N + N = 2N$. Again, this boundary is due to shot noise because of the intrinsic fluctuations of the number of photons emitted by the source.

In quantum mechanics, some highly quantum states make it possible to surpass this classical limit, leading to the observation of what is called a sub-shot noise variance. Let us consider for instance the twin-Fock state

$$|\psi\rangle = |N\rangle_A \otimes |N\rangle_B = |N, N\rangle \tag{1.32}$$

for which there are exactly N photons in beam A and N photons in beam B. For this state, the average photon number difference is obviously

$$\langle \Delta\hat{N} \rangle = \langle \hat{N}_A \rangle - \langle \hat{N}_B \rangle = N - N = 0 \tag{1.33}$$

but more importantly, its variance is

$$V(\Delta\hat{N}) = \langle \Delta\hat{N}^2 \rangle - \langle \Delta N \rangle^2 = \langle \hat{N}_A^2 \rangle - 2 \langle \hat{N}_A \hat{N}_B \rangle + \langle \hat{N}_B^2 \rangle = 0 \tag{1.34}$$

The variance then drops to zero (for a detector with a perfect quantum efficiency), which clearly beats the classical limit.

In practice, achieving such a state is experimentally challenging. However, it is possible to create states that are linear combinations of Fock states[29][30]. They can be expressed in the form:

$$|\psi\rangle = \sum_{n=0}^{+\infty} \gamma^n |n, n\rangle \tag{1.35}$$

Such states are called two-mode squeezed state. Like twin-Fock states, they lead to a variance equal to zero for perfect detectors. Note that, in general, it is possible to reduce the fluctuation in the number of atoms thanks to what is referred to as squeezing, which consist in reducing the range of variation in the number of atoms. Such states have many applications in metrology, since they enable better-than-classical precision measurements[31][32].

A criterion to determine whether a two-particle state beats the shot-noise limit in this situation is to look at the normalized variance $\tilde{V}(\Delta N)$ of the photon difference:

$$\tilde{V}(\Delta N) = \frac{\langle \Delta\hat{N}^2 \rangle - \langle \Delta N \rangle^2}{\langle \hat{N}_A + \hat{N}_B \rangle} \tag{1.36}$$

The limit for a classical source is therefore

$$\tilde{V} \geq 1 \tag{1.37}$$

If $\tilde{V} < 1$, this is the evidence of a non classical correlation.

1.2.2 Cauchy-Schwarz inequality violation

Let us express the normalized variance in terms of correlation functions. To do so, we will consider again that both beams are equivalent, so that they have the same mean number of photons ($\langle \hat{N}_A \rangle = \langle \hat{N}_B \rangle$) and the same variance ($\langle \hat{N}_A^2 \rangle = \langle \hat{N}_B^2 \rangle$). We have therefore

$$\tilde{V}(\Delta N) = \frac{\langle (\hat{N}_A - \hat{N}_B)^2 \rangle - (\langle \hat{N}_A \rangle - \langle \hat{N}_B \rangle)^2}{\langle \hat{N}_A + \hat{N}_B \rangle} = \frac{\langle \hat{N}_A^2 \rangle - \langle \hat{N}_A \hat{N}_B \rangle}{\langle \hat{N}_A \rangle} \tag{1.38}$$

Note that it can be expressed in terms of second-order correlation function. Indeed, we have shown previously that

$$G^{(2)}(A,A) = \langle \hat{a}_A^\dagger \hat{a}_A^\dagger \hat{a}_A \hat{a}_A \rangle = \langle \hat{N}_A^2 \rangle - \langle \hat{N}_A \rangle \tag{1.39}$$

using the commutation relation of $\hat{a}_A$ and $\hat{a}_A^\dagger$ for bosons. This is the auto-correlation function for beam A.

Now, the cross second-order correlation function between the two beams is, when $A \neq B$,

$$G^{(2)}(A,B) = \langle \hat{a}_A^\dagger \hat{a}_B^\dagger \hat{a}_B \hat{a}_A \rangle = \langle \hat{N}_A \hat{N}_B \rangle \tag{1.40}$$

since the creation and annihilation operators of A and B commute.

The apparent asymmetry between the two formulas 1.39 and 1.40 arises from considering the order of operators in the definition of the correlation functions. When $A = B$, this results in subtracting a term from the correlation, which is actually equal to the shot noise. A general way to express correlation functions in terms of number operators is to specify the preservation of the order of operators, which is written as:

$$G^{(2)}(A,B) = \langle : \hat{N}_A \hat{N}_B : \rangle \tag{1.41}$$

where the notation $\langle : \cdots : \rangle$ indicates the normal ordering of the creation and annihilation operators.

Finally, it can be easily shown that

$$\tilde{V}(\Delta N) = \frac{\langle \hat{N}_A^2 \rangle - \langle \hat{N}_A \hat{N}_B \rangle}{\langle \hat{N}_A \rangle} = 1 + \frac{G^{(2)}(A,A) - G^{(2)}(A,B)}{\langle \hat{N}_A \rangle} \tag{1.42}$$

which can be written:

$$\tilde{V}(\Delta N) = 1 + (1 - \mathcal{C}) \frac{G^{(2)}(A,A)}{\langle \hat{N}_A \rangle} \tag{1.43}$$

where

$$\mathcal{C} = \frac{G^{(2)}(A,B)}{G^{(2)}(A,A)} = \frac{G^{(2)}(A,B)}{\sqrt{G^{(2)}(A,A) G^{(2)}(B,B)}} \tag{1.44}$$

Thus, having a sub-shot noise variance is equivalent to having a coefficient $\mathcal{C} > 1$, which corresponds to satisfying the inequality:

$$G^{(2)}(A,B) > \sqrt{G^{(2)}(A,A)G^{(2)}(B,B)} \tag{1.45}$$

This is what is referred to as a violation of the Cauchy-Schwarz inequality. Indeed, in classical physics, if we consider two random variables X_A and X_B, then we necessarily have:

$$\langle X_A X_B \rangle \leq \sqrt{\langle X_A^2 \rangle \langle X_B^2 \rangle} \tag{1.46}$$

which, in terms of correlation functions, is equivalent to

$$G^{(2)}(A,B) \leq \sqrt{G^{(2)}(A,A)G^{(2)}(B,B)} \tag{1.47}$$

With a classical model, it cannot be explained that the cross-correlation is greater than the square root of the auto-correlations product. A violation of this inequality is then a signature of a purely quantum effect[33][34].

Note that exhibiting a violation of the Cauchy-Schwarz inequality or a sub-shot noise variance, despite the fact that this means that the correlation is stronger than classical, is actually not sufficient to claim that the state at play is entangled, as discussed in reference [35] where the authors formulate the Busch-Parentani criterion of entanglement: apart from exhibiting a violation of the Cauchy Schwarz inequality, one should also show that the statistics of the system is Gaussian on the one side, and that $\langle \hat{a}_A^\dagger \hat{a}_B \rangle = \langle \hat{a}_B^\dagger \hat{a}_A \rangle = 0$.

1.2.3 Hong-Ou-Mandel effect

As discussed in the introduction, another way to probe the correlations of a system is to perform interference experiments. Thus, there are interferometers which make it possible to exhibit purely quantum interferences, meaning that the amplitude of the correlation cannot be explained by classical physics. Among them, one can mention, for example, the Hong-Ou-and Mandel (HOM) experiment.

Principle

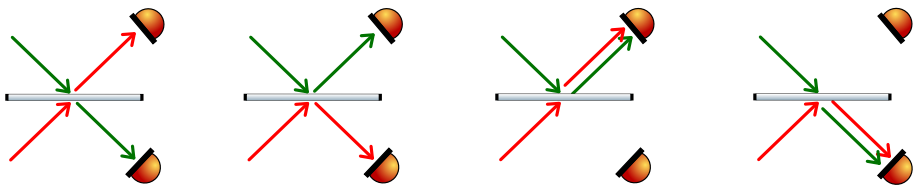

Figure 1.7: Four equiprobable possibilities in a classical point of view.

The Hong-Ou-Mandel effect is a two-particle interference phenomenon that occurs when two indistinguishable bosons are sent into the two input modes of a 50/50 beam splitter. From a classical point of view, the four possibilities represented in Figure 1.7 are equiprobable, and one would expect the probability of measuring two particles in different output modes to be equal to the probability of measuring two particles in the same mode. However, quantum theory can predict a result contrary to classical expectations: the output modes of the particles will always be identical, meaning that the two bosons

will emerge from the same output port. In this case, if one measures the probability of detecting two particles simultaneously at detectors placed on each output port, this probability must go to zero.

This effect was first experimentally observed by Hong, Ou, and Mandel in 1987[36] with pairs of photons emitted by parametric down-conversion (Figure 1.8). The experiment was designed so that the indistinguishability of the two emitted photons could be tuned by controlling the optical path of the photons with the position of the beam splitter. If the photons do not overlap on the beam splitter, the particle's paths are distinguishable. Therefore, by plotting the coincidence count rate in the output ports as a function of the beam-splitter position, the authors observed a dip in the coincidence count rate, which approaches zero when the photons are indistinguishable, a result now known as the HOM dip. The width of the dip is directly related to the temporal width of the photon wavepacket, which was what the authors aimed at measuring.

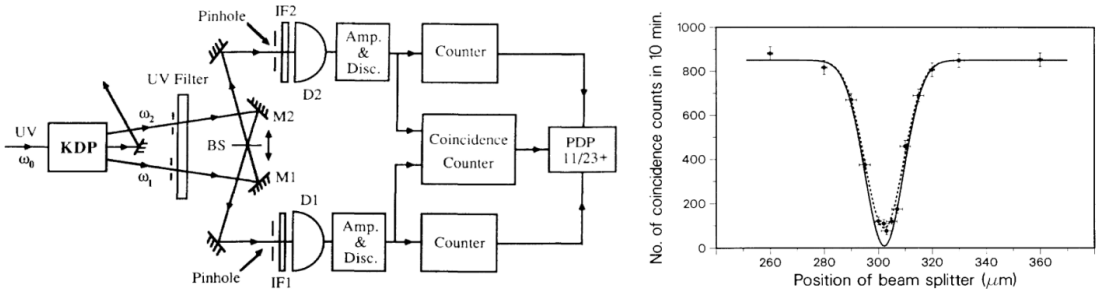

Figure 1.8: Original scheme of the classical HOM experiment (left) and result of the number of coincidence count as a function of the position of the beam splitter (right). Taken from [36].

Since this historic experiment, the HOM effect has become a textbook example of quantum interference that cannot be explained by a classical or semi-classical model.

Simple two-particle model

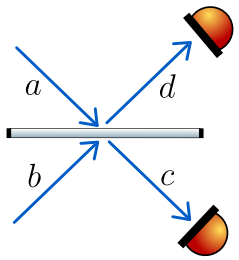

Figure 1.9: Input and ouput modes of the beam-spitter.

Let us consider the situation illustrated in Figure 1.9, where two identical particles in the two input modes a and b are mixed on a 50/50 splitter. Two detectors are places at the ouput modes of the beam splitter, written c and d. The input state is

$$|\Psi_{\text{in}}\rangle = \hat{a}^\dagger \hat{b}^\dagger |0,0\rangle \tag{1.48}$$

where $|0,0\rangle$ denotes the vacuum and $\hat{a}^\dagger$ (respectively $\hat{b}^\dagger$) is the particle creation operator in the mode a (respectively b).

In accordance with the second quantization formalism, one can establish a relationship between input and output modes using the beam splitter matrix:

$$\begin{pmatrix}\hat{c}^\dagger\\ \hat{d}^\dagger\end{pmatrix} = \hat{S}\begin{pmatrix}\hat{a}^\dagger\\ \hat{b}^\dagger\end{pmatrix} \qquad \text{with} \qquad \hat{S} = \frac{1}{\sqrt{2}}\begin{pmatrix}1 & \mathrm{i}e^{\mathrm{i}\phi}\\ \mathrm{i}e^{-\mathrm{i}\phi} & 1\end{pmatrix} \tag{1.49}$$

The unitary character of the matrix $\hat{S}$ reflects the conservation of the particle number between the input and output states. By inverting $\hat{S}$, the input modes can be expressed in terms of $\hat{c}^\dagger$ and $\hat{d}^\dagger$:

$$\begin{pmatrix}\hat{a}^\dagger\\ \hat{b}^\dagger\end{pmatrix} = \hat{S}^{-1}\begin{pmatrix}\hat{c}^\dagger\\ \hat{d}^\dagger\end{pmatrix} = \frac{1}{\sqrt{2}}\begin{pmatrix}1 & -\mathrm{i}e^{\mathrm{i}\phi}\\ -\mathrm{i}e^{-\mathrm{i}\phi} & 1\end{pmatrix}\begin{pmatrix}\hat{c}^\dagger\\ \hat{d}^\dagger\end{pmatrix} \tag{1.50}$$

where $\hat{S}^{-1}$ is equal to the conjugate transpose of $\hat{S}$ as it is a Hermitian matrix. The final state of the two-particle system after passing the beam splitter can be expressed as follows:

$$|\Psi_{\text{out}}\rangle = \frac{1}{2}\left(\hat{c}^\dagger - \mathrm{i}e^{\mathrm{i}\phi}\hat{d}^\dagger\right)\left(-\mathrm{i}e^{-\mathrm{i}\phi}\hat{c}^\dagger + \hat{d}^\dagger\right)|0,0\rangle$$

from which we get

$$|\Psi_{\text{out}}\rangle = \frac{1}{2}\left(-\mathrm{i}e^{-\mathrm{i}\phi}\hat{c}^\dagger\hat{c}^\dagger + \hat{c}^\dagger\hat{d}^\dagger - \hat{d}^\dagger\hat{c}^\dagger - \mathrm{i}e^{\mathrm{i}\phi}\hat{d}^\dagger\hat{d}^\dagger\right)|0,0\rangle \tag{1.51}$$

So far, we have not taken into account the fermionic or bosonic nature of the considered particles. However, at this stage, it is crucial to note that the commutation relations differ depending on whether the particles are bosons or fermions. For bosons, we have $\hat{c}^\dagger\hat{d}^\dagger = \hat{d}^\dagger\hat{c}^\dagger$, so the crossed terms cancel out and equation 1.51 can be rewritten

$$|\Psi_{\text{out}}\rangle = \frac{1}{2}\left(-\mathrm{i}e^{-\mathrm{i}\phi}\hat{c}^\dagger\hat{c}^\dagger - \mathrm{i}e^{\mathrm{i}\phi}\hat{d}^\dagger\hat{d}^\dagger\right)|0,0\rangle \tag{1.52}$$

The output state is therefore

$$|\Psi_{\text{out}}\rangle = -\frac{\mathrm{i}}{\sqrt{2}}\left(e^{-\mathrm{i}\phi}|2,0\rangle + e^{\mathrm{i}\phi}|0,2\rangle\right) \tag{1.53}$$

From this expression, it is immediately apparent that the probability of measuring both particles in two different modes is zero, since the remaining terms are squared creation operators: this is the destructive interference known as the HOM effect.[2] The number of joint coincidences in modes c and d can be determined using the second-order correlation function $G^{(2)}_{cd}$, for which we have :

$$G^{(2)}_{cd} = \langle\hat{c}^\dagger\hat{d}^\dagger\hat{d}\hat{c}\rangle = 0 \tag{1.55}$$

[2]In the case of fermions, Pauli's exclusion principle prohibits two particles from occupying the same mode. The commutation relations are then given by

$$\hat{c}^\dagger\hat{c}^\dagger = \hat{d}^\dagger\hat{d}^\dagger = 0 \qquad \text{and} \qquad \hat{c}^\dagger\hat{d}^\dagger = -\hat{d}^\dagger\hat{c}^\dagger$$

and equation 1.51 becomes:

$$|\Psi_{\text{out}}\rangle = \hat{c}^\dagger\hat{d}^\dagger|0,0\rangle \tag{1.54}$$

As expected for fermions, and contrarily to what is observed for bosons, the output particles are never in the same mode. This effect was observed experimentally with single electrons[37] in 2013.

Indistinguishability

In the previously presented model, the indistinguishability of the two particles is slightly hidden in the way we express the input state $\hat{a}^\dagger \hat{b}^\dagger |0,0\rangle$, without distinguishing particle 1 from particle 2.

Now, suppose that the input particles, for example photons, have orthogonal polarizations denoted as H (for the particule in mode a) and V (for the particule in mode b). In this case, they are no longer indistinguishable because we have introduced an additional degree of freedom that would allow us to differentiate them after measurement. In this case, the input state would be $\hat{a}_H^\dagger \hat{b}_V^\dagger |0,0\rangle$, leading to

$$|\Psi_{\text{out}}\rangle = \frac{1}{2}\left(-\mathrm{i}e^{-\mathrm{i}\phi}\hat{c}_H^\dagger \hat{c}_V^\dagger + \hat{c}_H^\dagger \hat{d}_V^\dagger - \hat{d}_H^\dagger \hat{c}_V^\dagger - \mathrm{i}e^{\mathrm{i}\phi}\hat{d}_H^\dagger \hat{d}_V^\dagger\right)|0,0\rangle \tag{1.56}$$

The crossed terms $\hat{c}_H^\dagger \hat{d}_V^\dagger$ and $\hat{d}_H^\dagger \hat{c}_V^\dagger$ no longer commute, and we do not observe the destructive interference leading to the Hong-Ou-Mandel effect.

Alternatively, we can highlight the distinguishable or indistinguishable character of the particles by using the formalism of first quantization. Again, let us note a and b the input modes. At the output of the beam splitter, the one-particle input states $|a\rangle$ and $|b\rangle$ are transformed into output states through the matrix relationships

$$\begin{cases} \hat{S}\,|a\rangle = \dfrac{1}{\sqrt{2}}(|a\rangle + \mathrm{i}e^{\mathrm{i}\phi}\,|b\rangle) \\ \hat{S}\,|b\rangle = \dfrac{1}{\sqrt{2}}(\mathrm{i}e^{-\mathrm{i}\phi}\,|a\rangle + |b\rangle) \end{cases} \tag{1.57}$$

Now, let us write the two-particle input state in the form:

$$|\Psi_{\text{in}}^{\text{dis}}\rangle = |a\rangle_1 \otimes |b\rangle_2 = |a,b\rangle \tag{1.58}$$

where the indices 1 and 2 correspond to the considered particles. This input state corresponds to the distinguishable case, since we know without any ambiguity that the particle 1 is in mode a and particle 2 is in mode b. The output state writes :

$$|\Psi_{\text{out}}^{\text{dis}}\rangle = \hat{S}\,|a\rangle_1 \otimes |b\rangle_2 = \frac{1}{2}(|a\rangle_1 + \mathrm{i}e^{\mathrm{i}\phi}\,|b\rangle_1)(\mathrm{i}e^{-\mathrm{i}\phi}\,|a\rangle_2 + |b\rangle_2)$$

therefore

$$|\Psi_{\text{out}}^{\text{dis}}\rangle = \frac{1}{2}(\mathrm{i}e^{-\mathrm{i}\phi}\,|a,a\rangle + |a,b\rangle - |b,a\rangle + \mathrm{i}e^{\mathrm{i}\phi}\,|b,b\rangle) \tag{1.59}$$

where $|a,b\rangle$ and $|b,a\rangle$ represent two different physical situations: particle 1 in mode a and particle 2 in mode b on one hand, and particle 1 is in mode b and particle 2 is in mode a on the other hand. Here, we retrieve the four equiprobable situations corresponding to the classical intuition.

Similarly, we get

$$\hat{S}\,|b\rangle_1 \otimes |a\rangle_2 = \frac{1}{2}(\mathrm{i}e^{-\mathrm{i}\phi}\,|a,a\rangle - |a,b\rangle + |b,a\rangle + \mathrm{i}e^{\mathrm{i}\phi}\,|b,b\rangle) \tag{1.60}$$

Now, let us consider the case of indistinguishable particles. The states $|a,b\rangle$ and $|b,a\rangle$ are equiprobable. For bosons, the wavefunction must be symmetric under the exchange of the two particles, so that the input state is

$$|\Psi_{\text{in}}^{\text{bos}}\rangle = \frac{1}{\sqrt{2}}(|a\rangle_1 \otimes |b\rangle_2 + |b\rangle_1 \otimes |a\rangle_2) = \frac{1}{\sqrt{2}}(|a,b\rangle + |b,a\rangle) \tag{1.61}$$

The output state is equal, up to a normalization factor, to the sum of equations 1.59 and 1.60, so in the case of bosons, we find:

$$|\Psi_{\text{out}}^{\text{bos}}\rangle = \frac{1}{\sqrt{2}}(\mathrm{i}e^{-\mathrm{i}\phi}\,|a,a\rangle + \mathrm{i}e^{\mathrm{i}\phi}\,|b,b\rangle) \tag{1.62}$$

We see that the two particles are always in the same output mode. Writing the input state as a bosonic wavefunction of indistinguishable particles made it possible to retrieve the Hong-Ou-Mandel effect.[3]

This formalism highlights well both the indistinguishability and the bosonic nature of the Hong-Ou-Mandel effect.

Classical limit

In this paragraph, we will compare the HOM effect, so far regarded as a purely quantum phenomenon, with a classical model. We have previously seen that a naive model featuring two incoming classical particles on a beam splitter results in four equiprobable situations, and consequently, no observed decrease in the number of coincidences between the two output modes. However, we will demonstrate that such a decrease can actually be predicted with a classical wave model, up to a certain point. Indeed, let's consider two incident waves on the beam splitter, with amplitudes denoted as E_a and E_b, such as

$$E_a = E_0\,\mathrm{e}^{\mathrm{i}\phi_a} \qquad \text{and} \qquad E_b = E_0\,\mathrm{e}^{\mathrm{i}\phi_b} \tag{1.64}$$

where ϕ_a and ϕ_b are random phases. The amplitude of the outcoming waves is

$$E_c = \frac{1}{\sqrt{2}}(E_a + \mathrm{i}e^{\mathrm{i}\phi_s}E_b) \qquad \text{and} \qquad E_d = \frac{1}{\sqrt{2}}(\mathrm{i}e^{-\mathrm{i}\phi_s}E_a + E_b) \tag{1.65}$$

The intensity at the output ports, averaged over the random phases ϕ_a and ϕ_b, is then

$$\langle I_c\rangle = \langle I_d\rangle = I_0 \tag{1.66}$$

while the product intensity is

$$\langle I_c I_d\rangle = \frac{I_0^2}{2} \tag{1.67}$$

This shows that the amplitude of the product intensity is smaller than the square of the output intensity from one of the two ports of the beam splitter. This implies that such a classical wave model allows for the observation of a decrease in the joint detection probability on channels c and d.

To quantify this destructive interference, we introduce the visibility V of the HOM signal detection, defined as

$$V = 1 - \frac{G^{(2)}_{cd,\text{Ind}}}{G^{(2)}_{cd,\text{Dis}}} \tag{1.68}$$

[3]For fermions, the wavefunction must be antisymmetric under the exchange of the two particles, leading to

$$|\Psi_{\text{in}}^{\text{fer}}\rangle = \frac{1}{\sqrt{2}}(|a,b\rangle - |b,a\rangle) \qquad \text{and} \qquad |\Psi_{\text{out}}^{\text{fer}}\rangle = \frac{1}{\sqrt{2}}(|a,b\rangle - |b,a\rangle) \tag{1.63}$$

The quantum model with two indistinguishable bosons ensures that $G^{(2)}_{cd,\mathrm{Ind}} = 0$, hence $V = 1$: the visibility of the HOM dip is maximal. In the previous classical model, we have:

$$V = 1 - \frac{\langle I_c I_d \rangle}{\langle I_c \rangle \langle I_d \rangle} = 1 - \frac{I_0^2/2}{I_0^2} = 0.5 \tag{1.69}$$

Therefore, the visibility of the HOM dip with this classical model cannot exceed 0.5, establishing a classical threshold: an experiment exhibiting visibility greater than 0.5 ensures the quantum nature of the input state.

In chapter 7, we will generalize the quantum HOM effect for an input state which can be written in the basis of twin-Fock states. We will see that the visibility of the dip can actually be related to the Cauchy-Schwarz inequality, such that having $\mathcal{C} > 1$ is equivalent to getting $V > 0.5$: this is again an evidence of a stronger-than-classical correlation. Still, the most effective way to claim that a quantum state is entangled consists in exhibiting a violation of Bell inequality.

1.3 Bell tests

The intrinsically probabilistic nature of quantum mechanics has consistently sparked debates among the pioneers of this theory. In particular, starting from a two-particle entangled state, it is possible to highlight strong correlation between sub-systems, so that each system cannot be described independently, leading to a famous debate between A. Einstein and N. Bohr.

1.3.1 EPR argument

In 1935, Einstein, Podolsky, and Rosen published a famous article untitled "Can Quantum-Mechanical Description of Physical Reality be Considered Complete?" In this article, they used the formalism of quantum mechanics to highlight a particularly perplexing aspect of this theory, known now as the "EPR paradox." In the following, we will quickly present the EPR argument in its version formulated by D. Bohm[38]. The following discussion was inspired by a talk by A. Aspect[39].

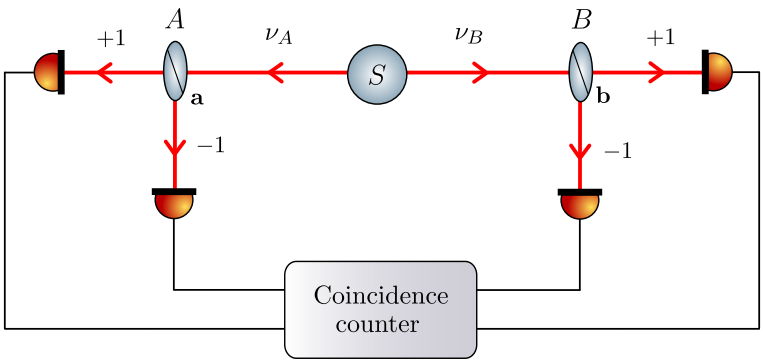

Figure 1.10: Scheme of the Einstein-Podolsky-Rosen-Bohm experiment. A source emits polarized photons in two opposite directions. Polarizers placed along each photon's path allow measurement of its polarization relative to the polarizers' axes. The detection system makes it possible to determine the coincidence rates between measurement outcomes on both sides.

Let us consider a source that emits two linearly polarized photons ν_A and ν_B in two different directions, such that the state of the system is given by:

$$|\psi\rangle = \frac{1}{\sqrt{2}} \left(|H, H\rangle + |V, V\rangle \right) \tag{1.70}$$

where the system is defined in a Hilbert space $\mathcal{E} = \mathcal{E}_A \otimes \mathcal{E}_B$ and H and V represent two orthogonal linear polarization orientations (horizontal and vertical). As seen previously, this is an entangled state, since none of the two particles has a well-defined polarization state.

In each direction, a polarizer makes it possible to measure the polarization of each photon (Figure 1.10). Let **a** and **b** denote the polarization axes of each polarizers. Depending on its polarization, the photons will then follow a different path after the polarizers, denoted as $+1$ if the photon polarization is found parallel to the axis of the polarizer, or -1 in the other case. Therefore, it is possible to measure the probabilities of single or joint detections in the output channels of the polarizers. Using the notations defined in Figure 1.11, a simple projection gives

$$\begin{cases} |+\rangle_a = \dfrac{1}{\sqrt{2}} \left(\cos\theta_a |H\rangle + \sin\theta_a |V\rangle \right) \\ |-\rangle_a = \dfrac{1}{\sqrt{2}} \left(-\sin\theta_b |H\rangle + \cos\theta_b |V\rangle \right) \end{cases} \tag{1.71}$$

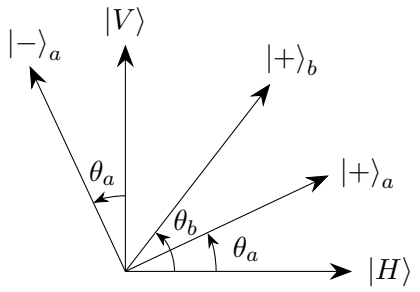

Figure 1.11: Orientation of the polarizers axes.

The joint probability of measuring $+1$ in A and $+1$ in B is

$$\mathcal{P}_{++}(\mathbf{a}, \mathbf{b}) = |\langle ++ |\psi\rangle|^2 \tag{1.72}$$

where

$$\begin{aligned} |++\rangle &= \frac{1}{2} \left(\cos\theta_a |H\rangle + \sin\theta_a |V\rangle \right) \otimes \left(\cos\theta_b |H\rangle + \sin\theta_b |V\rangle \right) \\ &= \frac{1}{2} \left(\cos\theta_a \cos\theta_b |H, H\rangle + \cos\theta_a \sin\theta_b |H, V\rangle + \sin\theta_a \cos\theta_b |V, H\rangle + \sin\theta_a \sin\theta_b |V, V\rangle \right) \end{aligned} \tag{1.73}$$

Therefore, we get

$$\mathcal{P}_{++}(\mathbf{a}, \mathbf{b}) = \frac{1}{2} |\cos\theta_a \cos\theta_b + \sin\theta_a \sin\theta_b|^2 = \frac{1}{2} \cos^2(\theta_a - \theta_b) = \frac{1}{2} \cos^2(\mathbf{a}, \mathbf{b}) \tag{1.74}$$

Similarly, we find

$$\begin{cases} \mathcal{P}_{++}(\mathbf{a},\mathbf{b}) = \mathcal{P}_{--}(\mathbf{a},\mathbf{b}) = \dfrac{1}{2}\cos^2(\mathbf{a},\mathbf{b}) \\ \mathcal{P}_{+-}(\mathbf{a},\mathbf{b}) = \mathcal{P}_{-+}(\mathbf{a},\mathbf{b}) = \dfrac{1}{2}\sin^2(\mathbf{a},\mathbf{b}) \end{cases} \tag{1.75}$$

One can also deduce that the single probability of measuring $+1$ in A is

$$\mathcal{P}_{+}(\mathbf{a}) = \mathcal{P}_{++}(\mathbf{a},\mathbf{b}) + \mathcal{P}_{+-}(\mathbf{a},\mathbf{b}) = \frac{1}{2} \tag{1.76}$$

and similarly

$$\begin{cases} \mathcal{P}_{+}(\mathbf{a}) = \mathcal{P}_{-}(\mathbf{a}) = \dfrac{1}{2} \\ \mathcal{P}_{+}(\mathbf{b}) = \mathcal{P}_{-}(\mathbf{b}) = \dfrac{1}{2} \end{cases} \tag{1.77}$$

It is worth noting that, while an individual polarization measurement yields a random outcome, there is a clear correlation between the measurements on A and B, which depends on the relative angle between both polarizers.

Again, this can be explained by the fact that when a polarization measurement is made at A, the state of the system is immediately projected onto the corresponding eigenstate. As a result, the polarization measurement at B is then directly determined.

In this whole scheme, the distance between the two measurements does not play any role. This means that, according to quantum theory, theses results hold true even if the polarizers are separated by a space like interval. In a way, the instantaneous quantum projection of the state leads to wonder if the information of the measurement travelled faster than light between both detectors. This idea was rejected by Einstein, who saw in this picture an incompatibility with relativity.

In order to overcome this paradox, Einstein's proposed explanation asserts that the state vector does not contain all the necessary information for the system's description. According to this concept, often referred to as a hidden variables theory, there would be parameters that are inaccessible to us, determining the outcomes of a measurement (determined for instance when the photons pair is created). This would restore the idea that the result of a measurement is deterministic, while quantum theory is intrinsically probabilistic, but, as proposed by EPR, incomplete. Additionally, it would explain the correlation between measurement outcomes on two different sub-systems, akin to two celestial objects whose trajectories are linked by initial conditions. To reconcile the observed results with the probabilities predicted by quantum mechanics, it is then sufficient to average over the additional variables.

1.3.2 Bell inequality

Although N. Bohr responded to EPR by rejecting the idea that quantum mechanics is incomplete, he did not provide conclusive proof. He pointed out that the assumption of local realism had to be dropped out, so that it can happen that the measurement on one sub-system can affect the other, no matter the distance between the two. For a few decades, the debate remained a matter of opinion and interpretation, as EPR arguments do not invalidate the predictions of quantum mechanics but rather attempt to provide an explanation for the nature of the observed results.

But this changed in 1964 when J. Bell found a way to experimentally highlight a contradiction between quantum mechanics and a hidden variables theory[5].

Demonstration of a Bell inequality

We introduce a set of parameters denoted as λ for hidden variables, in the sense of EPR, which would thereby ensure that the theory predicting measurement outcomes satisfies the locality assumption. These parameters are characterized by a probability density $\rho(\lambda)$, defined such that

$$\int \rho(\lambda)\mathrm{d}\lambda = 1 \tag{1.78}$$

The result of a polarization measurement in A for instance is then given by a function $A(\mathbf{a}, \lambda, \lambda_a)$, which is entirely determined by the parameters $\mathbf{a}$, λ, and λ_a, which respectively represent the orientation of the polarizer, a hidden variable linking A and B, and an additional hidden variable related to the detector that could influence the measurement outcome. The function $A(\mathbf{a}, \lambda, \lambda_a)$ can take the values $+1$, -1, or 0 in the case of a measurement failure that does not yield a result. Performing the measurement of an observable involves averaging the function A over the hidden variables, weighted by their density. Thus, by first averaging over the variables λ_a associated with the detector, we get

$$\bar{A}(\mathbf{a}, \lambda) = \int \rho_a(\lambda_a) A(\mathbf{a}, \lambda, \lambda_a)\mathrm{d}\lambda_a \tag{1.79}$$

Noticeably, as ρ_a is a probability density, one can deduce the following inequality

$$|\bar{A}(\mathbf{a}, \lambda)| \leq 1 \tag{1.80}$$

Similarly, the same reasoning being applied in B, we have

$$\bar{B}(\mathbf{b}, \lambda) = \int \rho_b(\lambda_b) B(\mathbf{b}, \lambda, \lambda_b)\mathrm{d}\lambda_b \qquad \text{and} \qquad |\bar{B}(\mathbf{b}, \lambda)| \leq 1 \tag{1.81}$$

and consequently

$$|\bar{A}(\mathbf{a}, \lambda)\bar{B}(\mathbf{b}, \lambda)| \leq 1 \tag{1.82}$$

One way of characterizing the correlation between the measurements outcomes in A and B is to define the Bell correlator E as

$$E(\mathbf{a}, \mathbf{b}) = \langle A \cdot B \rangle \tag{1.83}$$

So that we get immediately

$$E(\mathbf{a}, \mathbf{b}) = \int \rho(\lambda)\bar{A}(\mathbf{a}, \lambda)\bar{B}(\mathbf{b}, \lambda)\mathrm{d}\lambda \tag{1.84}$$

Let us consider a second set of orientations of the polarizers $\mathbf{a}'$ and $\mathbf{b}'$. It is interesting to look at the quantity $s(\lambda, \mathbf{a}, \mathbf{a}', \mathbf{b}, \mathbf{b}')$, defined as

$$\begin{aligned} s(\lambda, \mathbf{a}, \mathbf{a}', \mathbf{b}, \mathbf{b}') &= \bar{A}(\mathbf{a}, \lambda)\bar{B}(\mathbf{b}, \lambda) - \bar{A}(\mathbf{a}, \lambda)\bar{B}(\mathbf{b}', \lambda) + \bar{A}(\mathbf{a}', \lambda)\bar{B}(\mathbf{b}, \lambda) + \bar{A}(\mathbf{a}', \lambda)\bar{B}(\mathbf{b}', \lambda) \\ &= \bar{A}(\mathbf{a}, \lambda)\left[\bar{B}(\mathbf{b}, \lambda) - \bar{B}(\mathbf{b}', \lambda)\right] + \bar{A}(\mathbf{a}, \lambda)\left[\bar{B}(\mathbf{b}, \lambda) + \bar{B}(\mathbf{b}', \lambda)\right] \end{aligned} \tag{1.85}$$

Since $\bar{A}(\mathbf{a},\lambda)$ and $\bar{B}(\mathbf{b},\lambda)$ range between -1 and +1 (which is also true for $\mathbf{a'}$ and $\mathbf{b'}$), then the last expression of s leads to the inequality

$$-2 \leq s(\lambda,\mathbf{a},\mathbf{a'},\mathbf{b},\mathbf{b'}) \leq 2 \tag{1.86}$$

This inequality is also verified by the average S of s over the hidden variables λ:

$$-2 \leq S(\mathbf{a},\mathbf{a'},\mathbf{b},\mathbf{b'}) = \int \rho(\lambda) s(\lambda,\mathbf{a},\mathbf{a'},\mathbf{b},\mathbf{b'}) \mathrm{d}\lambda \leq 2 \tag{1.87}$$

Let us name S the Bell parameter. Using equation 1.84, it can be expressed as a function of the Bell correlators

$$S(\mathbf{a},\mathbf{a'},\mathbf{b},\mathbf{b'}) = E(\mathbf{a},\mathbf{b}) - E(\mathbf{a},\mathbf{b'}) + E(\mathbf{a'},\mathbf{b}) + E(\mathbf{a'},\mathbf{b'}) \tag{1.88}$$

This demonstration allows us to show that if the outcome of a measurement can be predicted by a local hidden variable theory, then the result of the measurement of S for any quadruplet of angles $(\mathbf{a},\mathbf{a'},\mathbf{b},\mathbf{b'})$ must necessarily satisfy the inequality:

$$-2 \leq S(\mathbf{a},\mathbf{a'},\mathbf{b},\mathbf{b'}) \leq 2 \tag{1.89}$$

Thus, any experiment yielding a Bell parameter that violates this inequality serves to verify that the result is not dictated by a local hidden variable theory. Any experiment aimed at demonstrating a violation of this inequality is then referred to as a Bell test.

It is noteworthy that we have demonstrated here a certain form of Bell inequality derived by J. Clauser, M. Horne, A. Shimony, and R. Holt[40] (often referred to as the CHSH version of the Bell inequality), but there exist other versions, involving different observables. An experimenter may choose to employ a Bell inequality version that is more favorable given the experimental constraints, as discussed in the thesis of Q. Marolleau[41], former PhD student in the team.

Violation of Bell inequality predicted by quantum theory

Let us use the definition 1.83 of the Bell correlator to calculate what quantum mechanics predicts:

$$\begin{aligned} E(\mathbf{a},\mathbf{b}) &= \langle A \cdot B \rangle \\ &= (+1)\cdot(+1)\cdot|\langle ++|\psi\rangle|^2 + (-1)\cdot(+1)\cdot|\langle -+|\psi\rangle|^2 \\ &\quad + (+1)\cdot(-1)\cdot|\langle +-|\psi\rangle|^2 + (-1)\cdot(-1)\cdot|\langle --|\psi\rangle|^2 \\ &= \mathcal{P}_{++}(\mathbf{a},\mathbf{b}) + \mathcal{P}_{--}(\mathbf{a},\mathbf{b}) - \mathcal{P}_{+-}(\mathbf{a},\mathbf{b}) - \mathcal{P}_{-+}(\mathbf{a},\mathbf{b}) \end{aligned} \tag{1.90}$$

We showed earlier the expressions of the joint probabilities of detection (equation 1.75) from which we get easily:

$$E(\mathbf{a},\mathbf{b}) = \cos(2(\mathbf{a},\mathbf{b})) = \cos(2(\theta_a - \theta_b)) \tag{1.91}$$

where θ_a and θ_b are the angles corresponding to the orientations of the polarizers $\mathbf{a}$ and $\mathbf{b}$. If we take the following angles:

$$\theta_a = 0 \qquad \theta_b = \frac{\pi}{8} \qquad \theta_{a'} = \frac{\pi}{4} \qquad \theta_{b'} = \frac{3\pi}{8} \tag{1.92}$$

then we obtain

$$S(\theta_a,\theta_{a'},\theta_b,\theta_{b'}) = 2\sqrt{2} \tag{1.93}$$

This means that quantum mechanics predicts a violation of the Bell inequality by more than 40%. This highlights the highly non local character of quantum theory.

The experiments conducted by A. Aspect[9][10][11] experimentally demonstrated a clear violation of Bell's inequality with a setup similar to the one previously presented. The most famous one is certainly the experiment reported in 1982[11], during which the Orsay team implemented a device making it possible to choose the orientation angle of polarizers *during* the flight time of photons, in order to separate the two polarization measurements at A and B by a space-like interval. Thus, relativity prohibits the transmission of information between A and B: if there is a violation of Bell's inequality, then it definitively implies that the results of the experiment cannot be associated with a theory assuming locality, and this is precisely what was observed at that time.

Note that the choice of the polarizers angles was not fully random, introducing a potential bias in the experiment. The experiment has been reiterated and improved upon since then, notably in Innsbruck in 1998, where genuine random number generators were utilized, resulting in a violation of Bell's inequality by several tens of standard deviations[42].

1.3.3 The momentum degree of freedom: Rarity-Tapster experiment

The setup described in the previous sections involves pairs of photons whose polarization degree of freedom is entangled. It is worth noting that the Bell test involves four detection modes: two ($+1$ and -1) for the measurement in A, and two others ($+1$ and -1) for the measurement in B. Here, a mode is any possible value taken by a degree of freedom for a single-particle wavefunction. The $+$ and $-$ modes for A and B are distinct because they involve different subsystems, making the modes distinguishable.

In this regard, the system designed to demonstrate a violation of Bell's inequalities differs from the one that would be used to highlight the HOM effect or a violation of Cauchy-Schwarz inequalities. Although these experiments also involve two-particle interference, they only involve two modes, which do not stress out the contradiction between quantum mechanics and relativity. A two-particle Bell test must involve a two-dimensional space on each side for each particle, as the measurement should allow the choice between two non-commuting observables.[4]

While the Orsay experiments used a source of pairs of correlated photons generated by non-linear laser excitations of an atomic radiative cascade[44], technological advancements have led to the emergence of new efficient sources of entangled photons. For instance, non-linear splitting of ultraviolet photons has been employed to produce pairs of correlated photons by optical parametric down conversion[45]. These sources have enabled the implementation of Bell tests on continuous variables[46].

In 1989, M. Horne, A. Shimony, and A. Zeilinger[13] proposed a new scheme of Bell test involving the momentum of photons instead of an internal degree of freedom like polarization. The corresponding experiment was successfully conducted shortly thereafter by J. Rarity and P. Tapster[12], who observed a violation of Bell's inequality by several standard deviations ($S = 2.21 \pm 0.02$). The principle of the experimental setup will be briefly discussed in the following.

In this setup (Figure 1.12), the idea is that all photons have the same polarization, but their optical paths are different. A source emits pairs of photons through parametric down

[4]Note that this is only true for a system of two particles, as shown in reference [43].

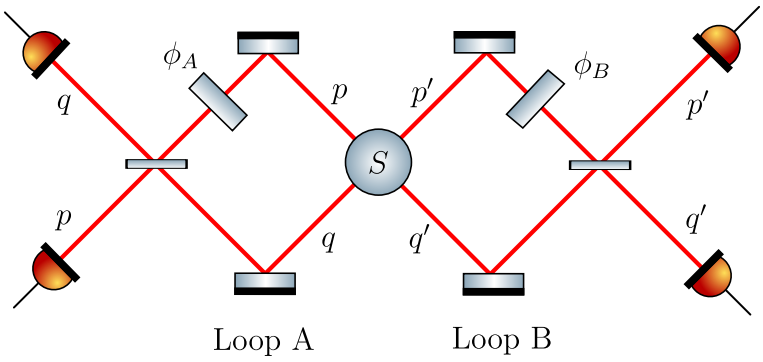

Figure 1.12: Scheme of the Rarity-Tapster setup for a Bell experiment with momentum entangled photons. A source emit two pairs of photons (p, p') and (q, q'). The photons from a pair are directed to two different beam splitter, where they are mixed with the photons from the other pair, forming loops A and B. Photodetectors are placed at each output of the beam splitters and make it possible to measure the coincidence count rates. In each loop, a phase plate can add a tunable path length difference.

conversion, where the phase-matching conditions (momentum and energy conservation) implies that the created pairs have different momenta, denoted as p and p' on one hand, and q and q' on the other hand (as mentioned earlier, a Bell test must involve four modes). In this configuration, the input state is expressed as follows:

$$|\psi\rangle = \frac{1}{\sqrt{2}}\left(|p, p'\rangle + |q, q'\rangle\right) \tag{1.94}$$

Then, photons from each pair are made to interfere with photons from the other pair at two beam splitters, spatially separated. Therefore, there are two loops in the interferometers, denoted as A and B. These loops are equivalent, except that a phase plate is added to each loop, inducing a path length difference. After that, a detection system and correlation counter makes it possible to measure the joint probabilities of detection and then to compute the Bell signal.

As we will see later in this manuscript with a similar setup using atoms, it is easy to demonstrate that if one looks at the correlations between two modes within the same loop (for example, p and q), then there is no interference signal observed. However, if one examines the joint detection probabilities between two modes from two different loops, then the latter oscillates based on the phase difference between the two loops:

$$\begin{aligned} \mathcal{P}_{p,q}(\phi_A, \phi_B) = \mathcal{P}_{-p,-q}(\phi_A, \phi_B) &= \frac{1}{2}\cos^2(\phi_A - \phi_B) \\ \mathcal{P}_{p,-q}(\phi_A, \phi_B) = \mathcal{P}_{q,-p}(\phi_A, \phi_B) &= \frac{1}{2}\sin^2(\phi_A - \phi_B) \end{aligned} \tag{1.95}$$

In the same manner that tuning the relative orientation of the polarizers leads to a two-particle interference involving polarization, here the relative phase difference between the two loops of the interferometer plays the same role with the momentum degree of freedom and leads to the oscillation of the Bell correlator. These are two analogous systems, for which quantum mechanics predicts that they can demonstration a violation of Bell's inequality.

Let us summarize the key elements necessary for setting up experimental platforms that can lead to the observation of Bell inequalities.

- Firstly, a source of two-particle entangled pairs is required.[5]
- Secondly, an interferometric set up is needed to observe four-mode correlations, along with a tunable parameter to control the interference.
- Finally, single-particle detectors are required to calculate the correlations between the different output ports of the experiment.

These are the three elements that we will need to bring together to conduct a Bell experiment involving atom pairs entangled in momentum.

1.3.4 From photons to atoms

Following the pioneer experiments with photons, Bell tests have been conducted with massive particles, leading to the observation of Bell inequality violations. One can for instance mention Bell inequality violation with mesons in 1999[49], ions in 2001[50], composite systems consisting of an atom and a photon in 2004 [51], atoms in 2007[52] and nitrogen-vacancy (NV) defects in diamond in 2011[53]. All these experiments involve internal degrees of freedom of the particles.

Beyond discussing the question of the local or non-local nature of spacetime, which is increasingly clear since the loophole-free tests of 2015[15][16][17], Bell tests now provide an effective way to study the correlations properties of two-particle quantum sources. Observing a violation of Bell's inequality implies that the system's state is non-separable, indicating that the involved modes are entangled. This represents the strongest way to demonstrate non-classical correlations.

This becomes particularly interesting when involving external degrees of freedom of entangled massive particles, as they are subject to gravity. This opens the way to experiments involving both entanglement and gravitation. Some theoreticians indeed suggest that gravitational interaction induces a decoherence phenomenon leading to the disappearance of entanglement[22][54]. An experimental test of this theory involves the use of systems with a mass much greater than that of two atoms. However, performing a Bell test with a pair of momentum entangled atoms would represent a significant milestone.

1.4 Quantum atom optics with metastable helium

In this section, we will focus on the experimental realization of the elements necessary for the Bell interferometer. We will demonstrate that the metastable helium experiment on which I worked is an ideal experimental platform for conducting so-called quantum atomic optics experiments, which consist in carrying out with atoms experiments that were historically performed with photons.

1.4.1 Bose-Einstein condensation and single atom detection

Before creating entangled pairs of atoms, it is essential to have a source of atoms that can serve as a coherent reservoir of particles in a well-defined momentum state. Having such a source is a fundamental building block when manipulating quantum states. Thanks

[5] It is worth noting that it is possible to use systems with more than two particles to demonstrate a violation of Bell's inequality, and there are Bell inequalities specifically designed for such cases [47][48].

to laser cooling and trapping and evaporative cooling methods developed from the 1980s onward, it is now possible to form a state of matter called a Bose-Einstein condensate (BEC) from bosonic atoms[55]. In a BEC, the typical size of the wave function of a particle is of the same order of magnitude as the typical distance between these particles, forming a macroscopically degenerate wave function for all particles. This phase transition to a state with purely quantum properties occurs when the de Broglie wavelength λ_{dB} associated with each particle and the atoms density n satisfy the relationship

$$n\lambda_{\mathrm{dB}}^3 \approx 1 \tag{1.96}$$

with

$$\lambda_{\mathrm{dB}} = \frac{h}{\sqrt{2\pi m k_{\mathrm{Boltz}} T}} \tag{1.97}$$

where m is the mass of the particles, k_{Boltz} the Boltzmann constant and T the temperature.

Under standard temperature and pressure conditions, this parameter is on the order of 10^{-8} to 10^{-6} for a gas. Thus, one has to decrease the temperature while ensuring that the density remains sufficiently low to avoid the formation of condensed phases. To achieve this, laser cooling methods are employed, using the radiation pressure exerted by photons to slow down atoms.

Thus, the choice of the atomic species to be cooled determines the laser cooling setup, as one needs to select one (or more) atomic transition for efficient atom-light interaction. Depending on the physical phenomena one aims to study, the choice of atom can vary. Rubidium is particularly easy to cool and is widely used in the ultracold atom community. Other alkali atoms possess what is known as Feshbach resonances, allowing control of atomic interactions by manipulating a magnetic field, making them particularly interesting[56].

The atom chosen by the team for conducting quantum atomic optics experiments is the helium atom ^{4}He in its 2^3S_1 metastable state. In addition to having atomic transitions suitable for laser cooling and trapping, this state of helium has a very high internal energy of 19.82 eV, which is sufficient to extract an electron from a metallic surface when an atom falls onto it. With an amplification system, it becomes possible to detect individual atoms. This is the principle behind detectors known as Micro-Channel Plates (MCPs), which are used to detect energetic particles in various contexts, particularly in high-energy physics[57].

Under the MCP, it is possible to place conductive lines called delay lines. These lines transform the electric pulse amplified by the MCP into four signals, whose time of propagation in each line is recorded. This allows determining the arrival time and position of the detected particle. By knowing the atom's fall time, one can then calculate its momentum values in all three spatial directions, as time can be converted into a vertical position in the free-falling cloud.

Thus, with this detector developed in the early 2000s by the team led by C. Westbrook, D. Boiron, and A. Aspect at the Laboratoire Charles Fabry of the Institut d'Optique, there is now a detection technique capable of resolving the momentum of each detected atom. This makes it an efficient experimental platform for studying the correlation properties in momentum of quantum systems composed of multiple particles.

Although helium is more challenging to cool compared to other alkali atoms, the team successfully achieved a metastable helium condensate in 2001[58]. This quickly led to the study of correlations in quantum systems, such as a Hanbury-Brown and Twiss experiment, where a bunching effect was observed in a thermal gas but not in a coherent BEC[59].

Several other experimental platforms have also succeeded in forming helium Bose-Einstein condensates, at the École Normale Supérieure in Paris[60], in Harvard[61], in Vienna [62], in Canberra[63], and a second experiment at the Institut d'Optique[64] in the team led by D. Clément. The experiments still in use aim at studying systems exhibiting quantum correlations.

1.4.2 Pairs emission and non-classical correlations

Now that we have described how to get a reservoir of atoms in a specific momentum state thanks to the helium BEC (more details about our experimental setup are provided in Chapter 2), the next step is to generate momentum-correlated pairs of atoms if we want to use them as the input state for a Bell interferometer. There are various ways to generate such pairs and to demonstrate quantum correlations on momentum degrees of freedom.

In the C. Regal group, two independent atoms are cooled and trapped in optical tweezers, enabling control of their momentum[65]. If the optical tweezers are brought close enough, the resulting double-well trapping potential acts as a beam splitter for the atoms due to tunnel coupling. This setup was used to demonstrate a Hong-Ou-Mandel effect with independently prepared massive bosons[66], by measuring the number of atoms in each well after the tweezers were separated again.

According to a protocol from the group of J. Schmiedmayer, it is possible to perform a similar experiment by adding an additional degree of freedom in order to have a two-particle four-mode state[67]. Indeed, twin atoms can be emitted at opposite momenta due to collisions from a 1D BEC in the quasicondensate regime subjected to phase fluctuations[68]. By putting this system in a double-well potential where tunnel coupling occurs, a two-particle interference was observed when studying the correlations between atoms with opposite momenta. Such a two-particle, four-mode state could theoretically lead to a violation of Bell inequality[69], however the observed signal was not significant enough.

A recent paper by the team of C. Klempt in Hannover[70] reports the creation of entangled momentum pairs starting from entangled spin pairs of rubidium atoms. An entanglement transfer[71] is achieved using a two-photon Raman transition that selects atoms in one of the two entangled magnetic sublevels and transfers them momentum, thus converting a spin-entangled pair into a momentum-entangled pair. This setup has exhibited sub-shot noise correlations but, to our knowledge, has not yet been attempted for a Bell test. Note that they work in a regime with a lot of atoms and do not detect single particles.

More recently, the group of T. Esslinger in Zürich demonstrated a new way of emitting momentum pairs, by coupling atoms from a BEC via a superradiant photon-exchange process in an optical cavity[72]. The emitted pairs are correlated both in spin and momentum and the process is reported to be fast and tunable. The authors showed a good correlation between the emitted modes, although without exhibiting a purely quantum correlation.

Another approach involves performing parametric excitation, which means periodically varying the intensity of the trapping laser at a certain frequency to modulate the trapping frequencies[73][74]. This technique induces the creation of pairs of phonons with opposite momenta from the BEC and constitutes an acoustic analogue to the dynamic Casimir effect. This technique, first demonstrated in our team in 2012[73], has been employed again in recent years as part of a project that will not be described in this manuscript but

in the one of V. Gondret, also a PhD student in the team.

Another way of creating pairs is to perform so-called four-wave mixing. This is a process similar to parametric down conversion, often used with photons to generate entangled pairs[75]. The principle behind these techniques is to use a nonlinear process (a $\chi^{(2)}$ or $\chi^{(3)}$ nonlinearity for light) to generate entanglement. Whereas parametric down conversion requires only a single pump photon to generate two correlated photons, four-wave mixing[76], first used with photons in 1985 to generate squeezed states[30], requires two pump photons to generate two correlated photons.

The four-wave mixing process in a Bose-Einstein condensate will be discussed in more detail in Chapter 3. Nevertheless, it is possible at this point to identify two distinct regimes of use for this process, which, like parametric down conversion, must verify energy conservation and momentum conservation, commonly referred to as phase-matching conditions. For a process involving four atoms, with momenta denoted as $\mathbf{p}_A$ and $\mathbf{p}_B$ for the atoms in the BEC, and $\mathbf{p}_1$ and $\mathbf{p}_2$ for the twin atoms emitted by the process, the following equations must be satisfied:

$$\begin{cases} \mathbf{p}_A + \mathbf{p}_B = \mathbf{p}_1 + \mathbf{p}_2 & \text{Momentum conservation} \\ E(\mathbf{p}_A) + E(\mathbf{p}_B) = E(\mathbf{p}_1) + E(\mathbf{p}_2) & \text{Energy conservation} \end{cases} \tag{1.98}$$

Consider a BEC in an optical dipole trap, for instance. All atoms are in the same momentum state, i.e., $\mathbf{p}_A = \mathbf{p}_B = \mathbf{p}_0$. When turning off the trap, the atoms in the BEC are in free fall. Apart from gravity, the only energy involved is their kinetic energy $E = \mathbf{p}^2/2m$. The phase-matching conditions can then be expressed as follows:

$$\begin{cases} \mathbf{p}_0 + \mathbf{p}_0 = \mathbf{p}_1 + \mathbf{p}_2 \\ \dfrac{\mathbf{p}_0^2}{2m} + \dfrac{\mathbf{p}_0^2}{2m} = \dfrac{\mathbf{p}_1^2}{2m} + \dfrac{\mathbf{p}_2^2}{2m} \end{cases} \tag{1.99}$$

Under these conditions, it is obvious that $\mathbf{p}_1 = \mathbf{p}_2 = \mathbf{p}_0$, and the four-wave mixing is a trivial process that re-emits atoms in the same mode as the condensate. Therefore, an additional element is needed to generate pairs of atoms in momentum modes different from that of the BEC.

A first approach involves having two condensates with different momenta. In this way, having $\mathbf{p}_A \neq \mathbf{p}_B$ allows the formation of pairs of atoms with distinct momenta. To achieve this, starting from an initial BEC, one can create a copy using a two-photon transition (involving two laser beams) that transfers half of the atoms to a different momentum state. Before moving apart, there is an overlap between the two clouds, making possible the emission of pairs through four-wave mixing.

The principle of the two-photon transition enabling the creation of a copy of a condensate, known as Bragg diffraction, will be detailed later. In the center-of-mass frame of the two condensates, whose momenta are respectively $\mathbf{p}_A = \mathbf{p}$ and $\mathbf{p}_B = -\mathbf{p}$, the phase-matching conditions can be expressed as follows:

$$\begin{cases} \mathbf{p}_A + \mathbf{p}_B = \mathbf{0} = \mathbf{p}_1 + \mathbf{p}_2 \\ 2\dfrac{p^2}{2m} = \dfrac{p_1^2}{2m} + \dfrac{p_2^2}{2m} \end{cases} \tag{1.100}$$

where $p = ||\mathbf{p}||$ is the norm of vector $\mathbf{p}$, and so on.

From the first equation, we deduce $\mathbf{p}_1 = -\mathbf{p}_2$, suggesting that the correlated pairs have an opposite momentum, and from the second equation, we get that the norms $p_1 = p_2$

are equal to p. This means that this process emits pairs along a sphere, whose center of mass is the center of mass of the two BEC (Figure 1.13). This sphere is often called a scattering halo, since four-wave mixing can actually be interpreted in terms of collisions between the atoms from the two condensates.

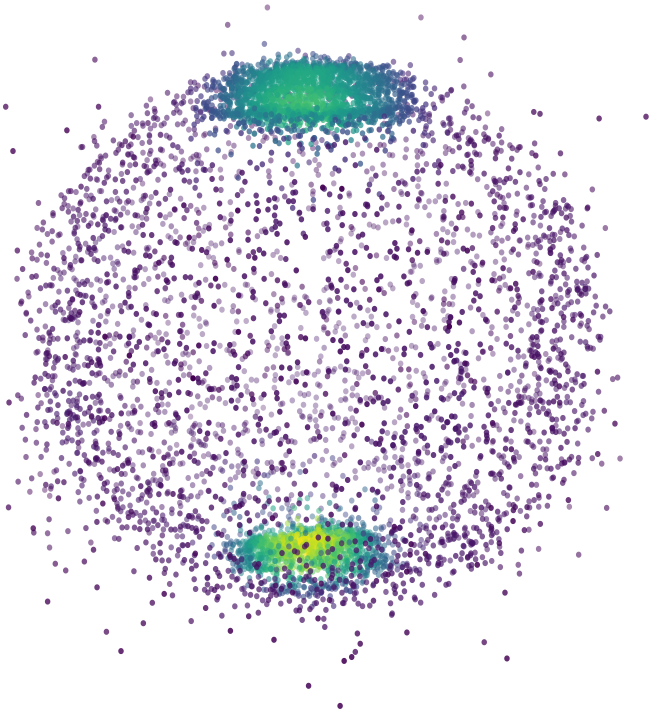

Figure 1.13: Scattering halo resulting from the collision of two BEC. Experimental result for a single run, where a Bragg $\pi/2$ pulse is applied to a condensate for 10 µs immediately after the trap cutoff. Each dot corresponds to a detected atom. The high-density regions at the poles are the two condensates.

The collision of BEC was achieved in our team in 2007[77] and resulted in the observation of non-classical correlations, such as sub-shot noise variance in the difference of the number of atoms detected in two diametrically opposite regions of the sphere[78], as well as a violation of the Cauchy-Schwarz inequality between these two regions [79].

There is another way to generate pairs through four-wave mixing. In 2005, a theoretical article[80] suggests that it would be possible, starting from a single condensate, to manipulate the phase-matching conditions using an optical lattice. Indeed, by subjecting the BEC to a standing wave, the energy conservation relation is dictated by the energy band structure of the lattice, so that the phase matching conditions are

$$\begin{cases} 2p_0 = p_1 + p_2 \\ 2E(p_0) = E(p_1) + E(p_2) \end{cases} \tag{1.101}$$

where the momenta are expressed along the direction of the lattice.

This technique, first experimentally demonstrated in 2006 by W. Ketterle's group[81], was implemented in our experiment in 2012[20]. It will be discussed in more detail in Chapter 3, but it presents several advantages that can be leveraged in a Bell experiment. Instead of being emitted on a sphere, the correlated pairs are emitted along a single axis.

The pair source is multimode, ensuring the possibility of working with at least a quadruplet of momenta, as required in a Bell experiment. The number of atoms emitted in the pairs is easily controllable by adjusting the duration of the optical lattice application. Additionally, one can control the emission density profile of the pairs by adjusting the detuning between the two beams of the optical lattice. This flexible and tunable source thus provides the opportunity to conduct interferometric experiments.

1.4.3 Bragg diffraction and atom interferometers

How to make atom mirrors and beam splitters? Looking at the design of the Rarity Tapster interferometer, we can see that mirrors transfer the photons from one momentum state to another, while beams splitter enable the mixing of two momentum states. This concept can be applied to atoms: optics for atoms consist in transferring them momentum.

To vary the momentum of an atom, a two-photon momentum transfer can be achieved by subjecting atoms to two detuned laser beams with the same polarization, which make it possible to exchange recoil momentum between photons and atoms. Indeed, an atom can absorb a photon from one of the beams and re-emit a photon into the other laser via stimulated emission while de-exciting (Figure 1.14). In doing so, its internal energy remains the same as the initial state, and the energy difference between the absorbed and emitted photons is converted into kinetic energy, altering its momentum. This process, called Bragg diffraction, enables to exclusively manipulating the external degrees of freedom of the atom while maintaining it in the same electronic state[6].

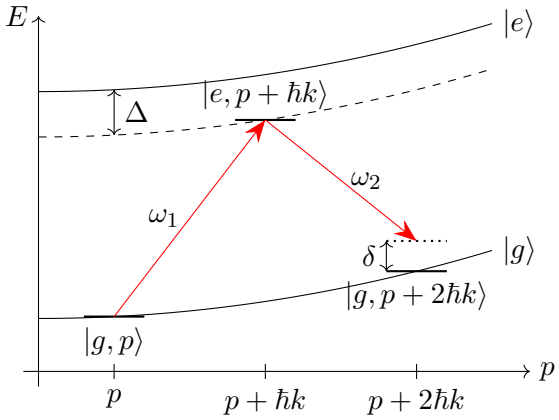

Figure 1.14: Scheme of the two-photon transition process. The atoms are initially in the momentum state $|p\rangle$ along the direction of the lattice. Δ is the detuning with the excited state, while δ is the two-photon detuning with the fundamental state $|p+2\hbar k\rangle$.

If the lasers are significantly detuned from the transition with the intermediate excited state, then this state is not populated. In this case, the two ground states can be considered as a two-level system coupled by an effective Rabi frequency. Consequently, starting with atoms in a momentum state p_i, Rabi oscillations can be performed with the momentum state p_f. Depending on the duration of the application of the Bragg beams, a beam splitter

[6]Note that a similar two-photon coherent process called Raman transition involving two beams of different polarization is also possible but changes the internal state of the atom.

for atoms can be achieved by transferring half of the initial population, or a mirror can be created by transferring the entire initial population.

In this manner, if two laser beams with a wavelength λ are directed onto the atoms in a plane (x, z) and separated by an angle θ, the beams form an optical lattice at the intersection where atoms move along the z direction. Following a single two-photon process (absorption followed by stimulated emission), the momentum of an atom has been altered by twice the momentum of a photon projected along the z-axis of the lattice. We denote

$$k = \frac{2\pi}{\lambda} \sin(\theta/2) \tag{1.102}$$

the recoil wavevector of a photon projected onto the lattice axis. Consequently, a momentum $k_{\mathrm{B}} = 2k$ is exchanged during the process. In the following of the manuscript, we will consider that the momentum transfers occur along the vertical direction (because the lattices were aligned this way), so that the momenta will be written as scalars, equal to the projections of the corresponding vectors along this z-axis.

The conservation of energy condition for this two-photon process states that the detuning between the beams must be equal to the difference between the final kinetic energy and the initial kinetic energy of the atom:

$$\hbar(\omega_1 - \omega_2) = \frac{p_{\mathrm{f}}^2}{2m} - \frac{p_{\mathrm{i}}^2}{2m} \tag{1.103}$$

where $p_{\mathrm{i}} = p = \hbar k_{\mathrm{i}}$ is the initial momentum of the atom and $p_{\mathrm{f}} = \hbar(k_{\mathrm{i}} + k_{\mathrm{B}})$ its momentum after exchanging two photons. Therefore, we get the resonance condition

$$\hbar(\omega_1 - \omega_2) = \frac{\hbar^2 k_{\mathrm{B}}^2}{2m} + \frac{\hbar k_{\mathrm{B}}}{m} p_{\mathrm{i}} \tag{1.104}$$

This relation indicates that it is possible to select the resonant momentum class p_{i} by adjusting the detuning between the two lasers.

Finally, note that this is a process during which the phase difference between the two laser beams can also be transferred to the atoms. This mechanism, known as phase imprinting, can be leveraged in order to vary the phase involved in an atom interferometer. For a Bell test, it can be used as a way to introduce a control parameter to observe a two-particle interference between the atoms and allowing the oscillation of the Bell correlator. A significant part of my thesis work involved determining how to experimentally achieve this phase control for a Bell interferometer.

Bragg diffraction will be the subject of a detailed study in Chapter 4. First observed with sodium atoms in 1988[82], it was experimentally tested with condensates in 1999[83]. It is noteworthy that the width of the Bragg resonance varies depending on the power and duration of the beams. Consequently, Bragg diffraction has been employed to investigate the momentum distribution of BEC in cases where the resonance width is smaller than the momentum distribution width of the BEC[84].

The use of Bragg diffraction (as well as Raman transitions) has played a crucial role in the development of atomic interferometers with light gratings since the 1990s. Following initial proof-of-concept demonstrations[85][86][87], their application in diverse contexts and configurations has facilitated fundamental tests, including studies of BEC, decoherence mechanisms, and tests of relativity, as well as the rise of atomic clocks and highly precise measurements of gravity, rotations, and the fine-structure constant for instance (a general introduction to atom interferometry and its applications can be found in reference[88]).

Finally, it should be mentioned that the precision of the measurement achieved by counting the number of particles in the output port of an interferometer is a priori limited by shot noise, a limit known as the Standard Quantum Limit (SQL). As previously discussed, it is possible to surpass this limit by employing squeezed states, which leverage entanglement to exceed the SQL by more than 20 dB[89], theoretically approaching the fundamental Heisenberg limit.

1.4.4 Towards a Bell test

A few references in the literature describe attempts to measure EPR-type correlations with entangled momentum states of atoms. A proposal by the team of A. Zeilinger in Vienna[90] investigated the possibility of demonstrating two-atom interference in four momentum modes using a double-double-split experiment setup. Pairs are generated through four-wave mixing from colliding BECs and directed onto a material grating with four openings, beneath which lies a MCP. Sizing the slits based on their metastable helium experiment, the authors showed that the feasibility of observing interference was highly constrained. However, some experimental constraints could be relaxed with the use of a ghost imaging setup, a technique that utilizes correlations between two beams to reconstruct an image in one beam from particles that do not interact with the imaged object. Although this technique was recently first implemented with metastable helium atoms[91], there has been no attempt to implement the four-momentum-mode correlation observation proposal, to our knowledge. It is worth noting that the proposal does not constitute a genuine Bell test but rather a way to observe a quantum two-atom interference.

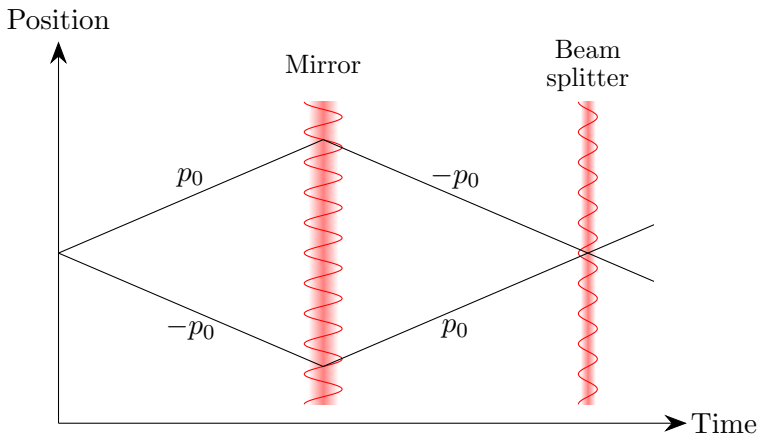

Figure 1.15: Scheme of the atomic Hong-Ou-Mandel interferometer. This representation corresponds to the trajectories of the atoms in the interferometer. The atoms are labeled p_0 and $-p_0$ corresponding to their momenta in the center-of-mass frame of the pairs. The atoms actually fall on the MCP due to gravity, but this scheme is represented in the falling frame.

In our team, Bragg diffraction has been implemented to conduct a Hong-Ou-Mandel type experiment. In this setup, atoms with opposite momenta $(p_0, -p_0)$ are emitted in pairs (in the center-of-mass reference frame of the emitted atoms) through four-wave mixing using an optical lattice at 1064 nm. For the interferometer, we use another pair of beams at 1083 nm to couple the atoms at momenta p_0 and $-p_0$, so that a Bragg mirror directs the atoms towards a beam splitter (Figure 1.15) where a two-particle inter-

ference is observed, revealing a distinct Hong-Ou-Mandel dip indicative of non-classical correlations[92]. This experiment serves as the foundation for a Bell test, where a momentum quadruplet will be involved instead of a pair.

The idea for a Bell test with our setup is to leverage the multimode nature of the pair source to conduct an experiment similar to the Hong-Ou-Mandel interferometer, but with an input state composed of two pairs of correlated modes, represented as:

$$|\psi_{\text{in}}\rangle = \frac{1}{\sqrt{2}}(|p, -p\rangle + |q, -q\rangle) \tag{1.105}$$

Subsequently, a Bragg mirror pulse redirects the atoms towards two different Bragg beam splitters, forming loops A and B, where $-p$ and q are coupled in loop A while $-q$ and p are coupled in loop B. This configuration is similar to the setup of the Rarity and Tapster interferometer for photons. As we will show in Chapter 4, in this case the two-particle interference can be controlled by tuning the differential phase between the atoms from loops A and B. The challenge lies in how to create two distinct beam splitters for A and B, on which different phases must be imprinted. This aspect will be extensively discussed in the following of this manuscript. The difficulty in achieving this differential phase control is the reason why a Bell experiment with atoms is a lot more challenging to perform than a Hong-Ou-Mandel experiment, where it is only necessary to couple the correct momentum modes through Bragg diffraction.

To circumvent this difficulty, a first solution is to use the same beam splitter for both A and B, with its resonance set to a doublet $(p_0, -p_0)$, akin to a HOM experiment. The underlying idea is to investigate correlations within non-resonant Bell quadruplets. Indeed, it will be shown later that Bragg diffraction imprints a phase on non-resonant atoms that depends on the detuning from resonance, and thus on the momentum class according to relation 1.104. Therefore, if the correlator varies with the momentum class, one can hope to measure different correlator values by calculating it for several successive quadruplets that gradually move away from the resonant doublet. This is not a Bell test since no control parameter is tuned, but this can lead to a proof of concept.

This study was conducted in our team in 2017 and led to the observation of non-zero correlators[93], suggesting that the phase imprinted on the atoms is stable and that a Bell experiment is feasible. These results will be discussed further in the manuscript in light of new theoretical developments that I have undertaken during my thesis.

Another attempt to perform a Bell test has been recently reported in the literature[94] by the team of A. Truscott in Canberra, also using a helium BEC for similar reasons as ours. In this article, pairs are created through collisions between condensates. The originality lies in using two scattering halos to emit pairs, resulting in a configuration where it is not the phase difference between A and B that is involved in the Bell correlator, but rather the sum of these two phases. This allows for a Bell test using the same pulse for both A and B, by varying the phase imprinted on the atoms during the beam splitter pulse. The results show a clear oscillation of the Bell correlator, but the amplitude is not sufficient for a violation of the Bell inequality. This setup will also be discussed later in this manuscript (section 4.1.3) and compared to our configuration. It will be demonstrated that while its main advantage is using the same beam splitter for both A and B, it may introduce phase sensitivity issues that might be responsible for the low contrast in the two-atom interference.

Chapter 2

Experimental setup: preparation of a metastable Helium Bose-Einstein Condensate

2.1 Metastable helium: interest and detection 55
2.1.1 Metastable helium 55
2.1.2 Micro-Channel Plate 57
2.1.3 Delay lines 59
2.1.4 Reconstruction 62
2.2 Cooling procedure 64
2.2.1 Source 64
2.2.2 Cooling atoms down to Bose-Einstein Condensation 65
2.2.3 Raman transfer and protective copper plate beam dump 69
2.2.4 Imaging system 73
2.3 BEC characterization 75
2.3.1 Stability 75
2.3.2 Number of atoms, temperature, size and chemical potential 76

In this chapter, we will briefly introduce the experimental setup. A more exhaustive presentation can be found in the thesis of Q. Marolleau[41], previous PhD student in the team. We will limit ourselves to a general presentation of the detector and the major cooling steps.

My doctoral work was marked by various experimental difficulties and challenges that impeded the progress of the experiment towards the realization of a Bell test. In particular, having a systematic and stable Bose-Einstein condensate with the correct number of atoms posed a significant challenge. It was necessary to develop new strategies and replace crucial equipment to ensure the right behavior of each cooling stage. A detailed timeline is provided in appendix B. The majority of the results in this thesis were obtained during two periods: the first for pair data with a large population in May 2022, and the second for pair data with a small population and interferometric measurements from April to September 2023.

2.1 Metastable helium: interest and detection

2.1.1 Metastable helium

Spectroscopy of $^4_2$He

The most common isotope of helium on Earth is bosonic helium $^4_2$He. Despite having two electrons, it behaves like a one-electron atom because a state with two excited electrons would always have higher energy than its auto-ionization energy (24.59 eV). ^{4}He has no nuclear spin and has two configurations, *para* or *ortho*, where the two electrons respectively have spins that are anti-parallel (total spin $S = 0$) or parallel (total spin $S = 1$).

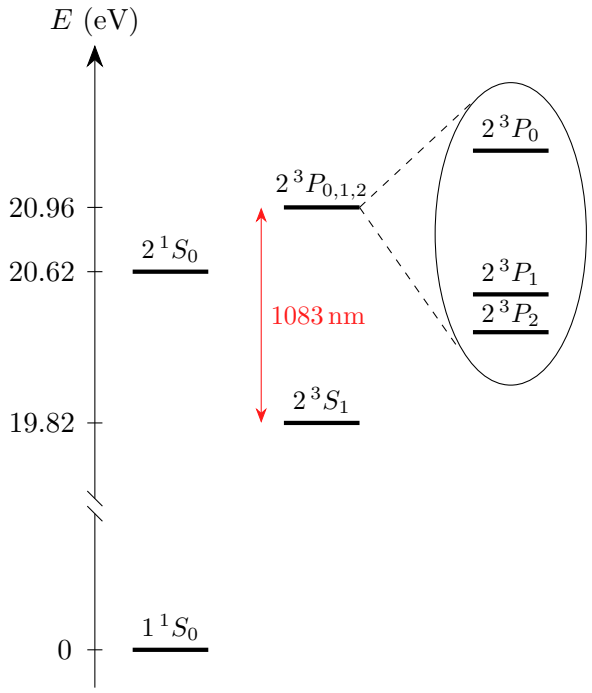

Figure 2.1: Simplified energy diagram of ^{4}He.

A simplified energy diagram is provided in Figure 2.1, using spectroscopic notations $n\,^{2S+1}L_j$[95]. The transition between *para* and *ortho* states is prohibited as it does not

conserve the total spin. Consequently, both states $2\,^1S_0$ and $2\,^3S_1$ are metastable states, but the singlet state has a lifetime of only 195 ms, whereas the triplet state has a lifetime on the order of 2 hours[96]. For similar reasons of spin conservation, excited triplet states preferentially de-excite to the $2\,^3S_1$ state, which can be considered as the ground state in our experiments, sometimes denoted as He*.

This is the state that is used for a BEC. On one hand, the spin-induced magnetic dipole of this state enables the use of magnetic trapping techniques. Furthermore, the transition $2\,^3S_1 \longrightarrow 2\,^3P_{0,1,2}$ has a wavelength of 1083 nm, for which commercial lasers (such as diode lasers or fiber lasers) are available. In particular, the $J \to J+1$-type $2\,^3S_1 \longrightarrow 2\,^3P_2$ transition is employed for the first cooling stages, allowing for a classical Magneto-Optical Trap (MOT) scheme. Some characteristics of He* and the cooling transition are given in Table 2.1.

Quantity	**Symbol**	**Value**
Mass[97]	m	$6.646 \times 10^{-27}\,\mathrm{kg}$
Lifetime[96]	τ	$7870(510)\,\mathrm{s}$
Transition wavelength[98]	λ	$1083.33\,\mathrm{nm}$
Transition width[95]	Γ	$2\pi \times 1.63\,\mathrm{MHz}$
Lifetime	$\tau = 1/\Gamma$	$98\,\mathrm{ns}$
Saturation intensity	$I_{\mathrm{sat}} = \dfrac{\pi h c \Gamma}{3\lambda^3}$	$0.167\,\mathrm{mW.cm^{-2}}$
Doppler limit temperature	$T_{\mathrm{D}} = \dfrac{\hbar\Gamma}{2k_{\mathrm{Boltz}}}$	$39\,\mu\mathrm{K}$
Recoil momentum	$k_{\mathrm{rec}} = \dfrac{2\pi}{\lambda}$	$5.8\,\mu\mathrm{m^{-1}}$
Recoil velocity	$v_{\mathrm{rec}} = \dfrac{\hbar k_{\mathrm{rec}}}{m}$	$92.0\,\mathrm{mm.s^{-1}}$
Recoil energy	$E_{\mathrm{rec}} = \dfrac{\hbar^2 k_{\mathrm{rec}}^2}{2m}$	$1.8{\times}10^{-10}\,\mathrm{eV}$
Recoil temperature	$T_{\mathrm{rec}} = \dfrac{E_{\mathrm{rec}}}{k_{\mathrm{Boltz}}}$	$2.0\,\mu\mathrm{K}$

Table 2.1: Properties of ^{4}He and cooling characteristics of the $2\,^3S_1 \longrightarrow 2\,^3P_0$ transition.

Note that the transition $2\,^3S_1 \longrightarrow 2\,^3P_0$ is also used in our experiment for Raman and Bragg transitions. These points will be detailed further in the manuscript.

It is noteworthy that, in comparison to most other atoms used in experiments involving ultracold atoms, the mass of helium atom is particularly low. Consequently, the recoil velocity of helium is high when interacting with a resonant laser beam, resulting in improved spatial separation of different velocity classes after time of flight. Using an atom with a low mass is advantageous for the resolution of an experiment which aims at studying correlations between different velocity classes.

Collisions

Due to the high atom density in a cold cloud, a frequent mechanism is the occurrence of collisions between atoms. There are several types of collisions, depending on whether they are elastic (in this case the total kinetic energy and momentum of the system are conserved) or inelastic (for which there is a transfer of kinetic energy between the involved atoms, leading to changes in the energy states of the atoms), and they can induce important atom losses in the system.

It is noteworthy that a crucial step in forming a BEC is evaporative cooling[55]. This process involves expelling the hottest atoms from a trap by adiabatically lowering the trap depth and allowing the remaining atoms to rethermalize through elastic collisions. If there are too many inelastic collisions, evaporative cooling becomes less effective. Therefore, understanding the collisional mechanisms at play in a cold cloud is essential, especially in BEC where collisions play a significant role in the atomic cloud properties.

At low temperatures, elastic collisions are exclusively characterized by s-wave scattering. For He^*, it was estimated that this is the case when the temperature is smaller than 8 mK[99]. Below this temperature, the elastic collision rate only depends on the scattering length $a = 7.5\,\text{nm}$, and the scattering cross-section is $\sigma_0 = 8\pi a^2$.

An important feature of He^* is an inelastic process called Penning collisions, which consist of two-body collisions between metastable atoms leading to the creation of ions:

$$\begin{cases} He^* + He^* \rightarrow He + He^+ + e^- \\ He^* + He^* \rightarrow He_2^+ + e^- \end{cases} \tag{2.1}$$

This process is characterized by the collision constant β, defined as the time constant related to the two-body losses:

$$\frac{dn}{dt} = -2\beta(T)n^2 \tag{2.2}$$

where n is the atom density.

The value of β strongly depends on whether the gas is magnetically polarized or not. If the gas is non-polarized, the β constant is $10^{-10}\,\text{cm}^3.\text{s}^{-1}$[100], which is too high to allow for Bose-Einstein condensation. However, if the gas is polarized through a magnetic field (in an $m = 1$ state), the previous collisions are strongly inhibited as they do not conserve spin[101]. In this case, β equals $10^{-14}\,\text{cm}^3.\text{s}^{-1}$. This losses reduction by four orders of magnitude is sufficient to enable the formation of a BEC.

Moreover, when the density is high (in a BEC for instance, or close to condensation), there are also three-body collisions that need to be considered and lead to additional losses:

$$He^* + He^* + He^* \rightarrow He + He^+ + He^*|_{\approx \text{mK}} + e^- \tag{2.3}$$

The collision constant L associated to this process was measured in our group[102], and is small enough so that the three body collisions have a small effect as long as the density is below $10^{13}\,\text{cm}^{-3}$.

2.1.2 Micro-Channel Plate

The internal energy of a metastable helium atom is significant enough to extract an electron from a metallic surface. To detect an atom, it is therefore necessary to amplify

this electron signal, and this is the role of the Micro-Channel Plate.

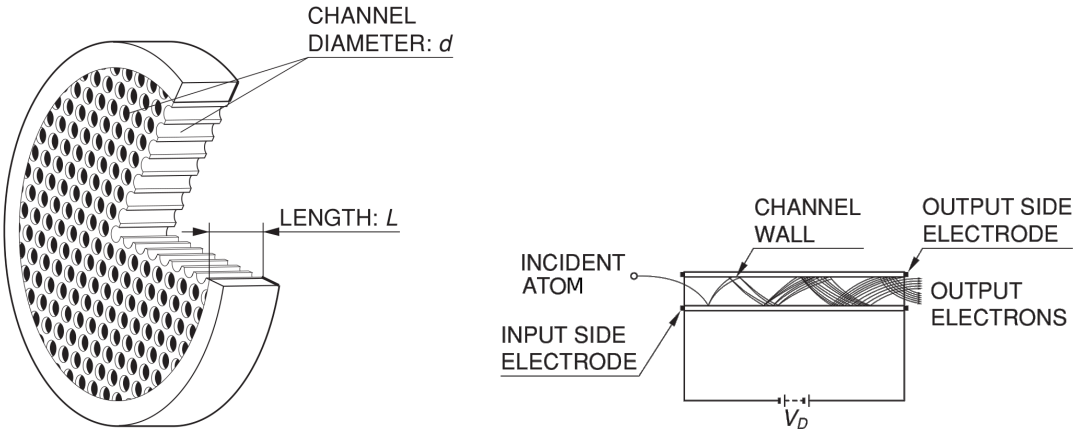

(a) Cutaway drawing of a MCP. **(b)** Schematic of the electronic cascade inside a channel.

Figure 2.2: Schematic representation of the detector. Images provided by Hamamatsu Photonics.

A MCP consists of a set of regularly spaced hollow cylindrical channels bonded together (Figure 2.2). The front (onto which the atoms fall) and back faces are metallized, allowing for the application of a potential difference on the order of 1 kV. Consequently, when an electron is extracted from the surface by an atom, it is accelerated by the electric field and collides again with the channel wall, inducing the ejection of additional electrons. This process continues, forming an electron cascade that results in a macroscopic signal. The typical amplification gain is on the order of 10^4. The channels are tilted relative to the vertical axis, allowing atoms, which arrive vertically in a good approximation, to fall directly onto the channel walls.

Like any detector, the MCP has limitations in terms of detection efficiency, resolution, and saturation. The quantitative estimation of these features will be discussed later, but we can already identify some sources of limitation.

- After an electronic discharge, a channel takes some time to become available again for the detection of a new atom, as it has lost many electrons. This dead time is responsible for a saturation effect in the detector, especially significant when the atom flux is high.
- The MCP indeed has a certain efficiency, meaning that not all atoms that fall onto the detector are converted into a useful signal. This is related, on the one hand, to a quantum efficiency associated with the process by which an atom leads to the emission of an electron (measurements have shown a quantum efficiency on the order of 60 %[103]), and on the other hand, to the fact that some atoms do not fall into the channels but onto the solid surface that connects them, and therefore, they are not amplified. The latter limitation is characterized by the open area ratio (OAR), which is the fraction of the total MCP surface composed of open channels relative to the total surface, including the solid walls between the channels. For our current MCP, this ratio is 90 %. The entrance apertures of the channels are precisely flared to enhance the OAR.

- The resolution of the MCP is constrained by the geometry of the channels: the larger the diameter of a channel, the more it covers a significant area. Since the detected signal is the same for each atom that falls into the same channel, this limits the transverse resolution of the detector.

The MCP we currently work with was installed in 2019. It has a 8 cm diameter, and its quantum efficiency was estimated by the constructor (Hamamatsu) to be around 50%. The channel diameter is 12 µm and each channel is tilted by 20°. The longitudinal resolution is estimated to be 33 µm, while the transverse resolution is 50 µm[41].

2.1.3 Delay lines

The MCP is not the only component necessary for a single-atom detection. Actually in our experiment two MCPs are used in series, concatenated in such a way that each channel is bent. In this manner, the total gain is 10^8, meaning that a metastable atom, at the output of the MCP, generates a cascade of 10^8 electrons. Beneath the MCP, two long copper wires, called delay lines, are positioned, wound along the X and Y axes, respectively (Figure 2.3). When the electrons reach the delay lines, they induce an electrical pulse that propagates along the lines.

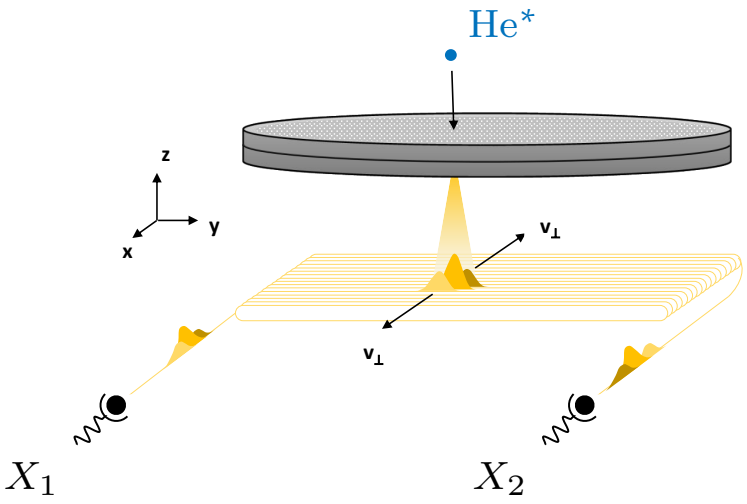

Figure 2.3: Scheme of the detection process. A helium atom falling on the MCP leads to an electronic cascade within a microchannel, resulting in an electric pulse which propagates along the delay lines. Taken and modified from [104].

At each end of a line, pulse detectors are placed to determine, through a non-linear process, the moment at which a pulse is detected. For a given pulse, the detection instants $(t_{X_1}, t_{X_2}, t_{Y_1}, t_{Y_2})$ are then measured. Depending on the position and time of the atom's fall, the distance traveled by the pulse along the line varies, leading to different detection times. In this way, one can deduce the values of the position and the detection time. The signal propagation speed along the copper line is $c/3$, so the transverse speed is

$$v_\perp = \frac{c}{3N} \tag{2.4}$$

where N is the number of loops (approximately 100 in our setup). In practice, due to slight differences between the lines, the transverse speeds are a bit different. They were

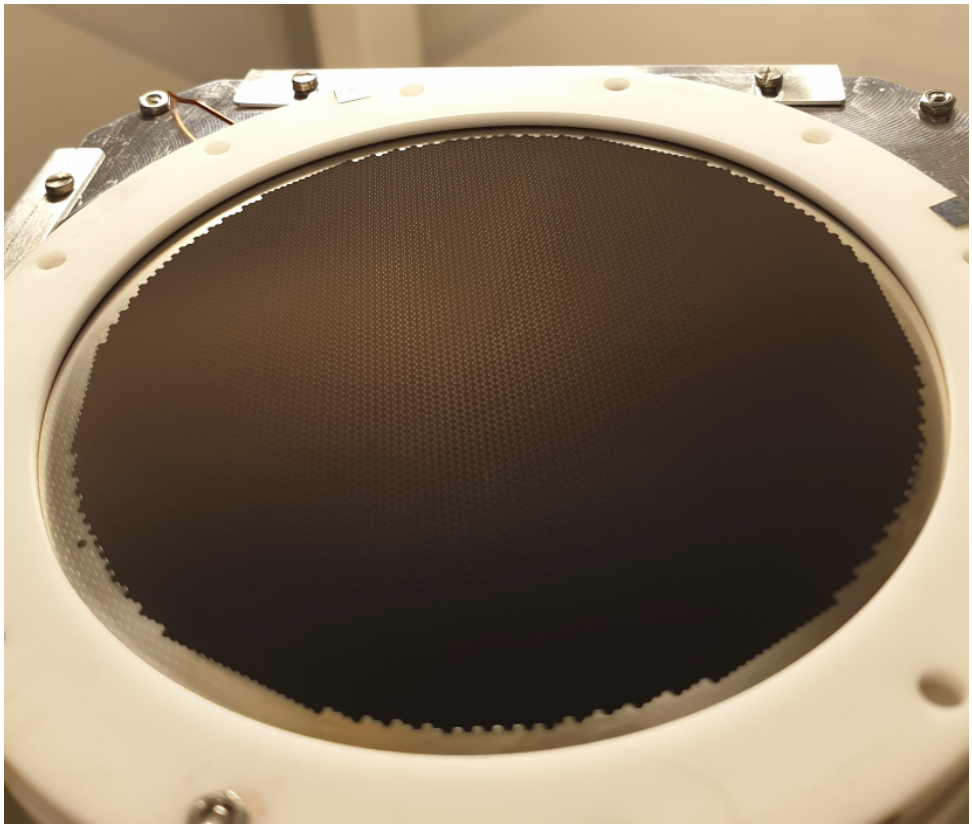

(a) Top view of the MCP.

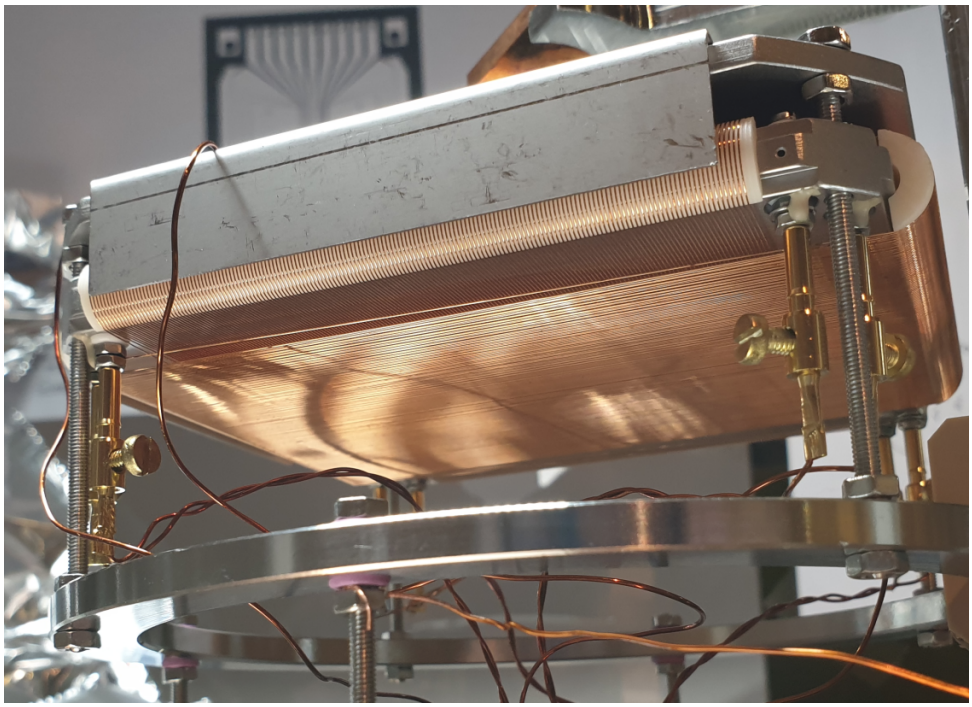

(b) Delay lines below the MCP

Figure 2.4: Pictures of the detector.

calibrated by the constructor:

$$\begin{cases} v_\perp^x = 1.02\,\text{mm.ns}^{-1} \\ v_\perp^y = 1.13\,\text{mm.ns}^{-1} \end{cases} \tag{2.5}$$

Using these values, one can get the instant and position of the impact of a metastable atom, according to the relations

$$\begin{cases} X = \dfrac{v_\perp^x}{2}(t_{X_1} - t_{X_2}) \\ Y = \dfrac{v_\perp^y}{2}(t_{Y_1} - t_{Y_2}) \\ T = \dfrac{1}{2}(t_{X_1} + t_{X_2}) \\ T = \dfrac{1}{2}(t_{Y_1} + t_{Y_2}) \end{cases} \tag{2.6}$$

The process to get the detection times of the electrical pulses corresponding to the fall of an atom is not trivial. The idea is to use a discriminator to detect the arrival time of a pulse caused by an atom. This pulse is pre-amplified, but the amplification process is noisy. Importantly, using a simple threshold with a peak detector to deduce the arrival time of a pulse is not satisfying because the electrical pulses do not all have the same amplitude (the gain can vary depending on the amplification chain), and such a system would yield different arrival times for two signals of different amplitudes arriving at the same moment. To counteract this effect, a Constant Fraction Discriminator (CFD) is employed, leveraging the fact that all pulses have the same shape and allowing access to the timing at which the input signal is at a certain fraction of its maximum value. This makes the process independent of the amplitude of the input signal. A logical signal is then generated, which equals 1 when an electrical pulse above the threshold reaches this fraction. The signal is then digitally converted using a Time-to-Digital Converter (TDC). The complete process is represented in Figure 2.5. The details of this detection system are provided in the thesis of Q. Marolleau[41], along with the procedure to set up the parameters leading to an efficient detection of atoms.

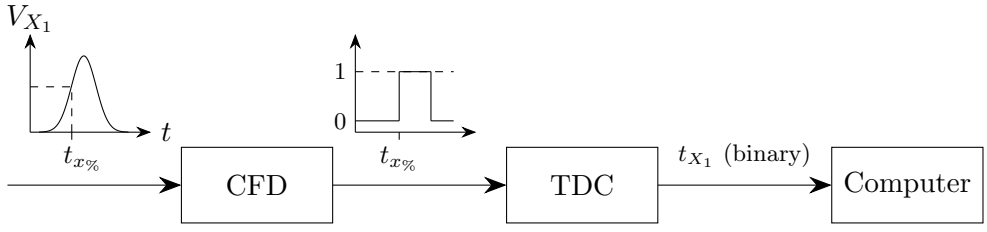

Figure 2.5: Simplified representation of the electronic detection process.

This detection process is linear only as long as the atom flux is not too high. Otherwise, for dense clouds, an excessively high atom flux induces electronic saturation, making atom counting impossible. In the context of conducting a Bell experiment, this saturation is not an issue as we will be working with only a few pairs emitted by the condensate.

Therefore, we can effectively proceed with a regime of single-atom detection.

2.1.4 Reconstruction

Once the TDC returns a list of events on each line to the computer, corresponding to the moments of detection of different pulses, a reconstruction algorithm compares the detected timings on the four channels to identify correlated events that could be caused by the arrival of an atom. Indeed, it is possible that a noisy signal exceeds the threshold and is counted as an event on a channel. Additionally, what is referred to as pulse rebounds can occur, meaning that when a pulse reaches the end of a line, part of its energy is reflected (due to impedance mismatch) and can be detected again. It is common to observe, after the detection of an atom, another signal of lower amplitude, shifted by a duration corresponding to twice the propagation time on a line. Most of these rebounds are eliminated by the detection threshold, but some may persist, counting as false events that should not be considered.

For this reason, an event reconstruction algorithm is necessary, which seeks genuine events and consists of a series of filters and conditions related to the timings on each channel. The idea is simply to create nested loops to consider all possible quadruplets that could correspond to an event and ensure that the events meet the following criteria:

- The maximum duration between two events detected on different channels is given by the propagation time of an electrical signal over a distance equal to the diameter of the MCP.
- The position (X, Y) of the atom, calculated from the relationships 2.6, must be such that the atom is within the disc formed by the MCP.
- The instant T of the atom detection can be calculated in two different ways (equations 2.6), so we have to ensure that the difference between these two calculated quantities remains below a certain threshold.

This algorithm has been improved in recent years by V. Gondret, who enhanced the last point to account for additional geometric constraints. Indeed, according to equations 2.6, the quantity

$$S_{\mathrm{MCP}} = (t_{X_1} + t_{X_2}) - (t_{Y_1} + t_{Y_2}) \tag{2.7}$$

should be equal to zero. But due to geometry and electronic defects (because of an imperfect winding of the delay lines for instance), this value, called offset, has a slight spatial dependency over the MCP. Since the variations of S_{MCP} are stable over time, it is possible to make a reference offset map and to compare the value of the offset for a candidate quadruplet to the corresponding value on the map. If the difference between the two is too high, then the quadruplet is rejected.

At the end of this reconstruction algorithm, which occurs in real-time during data acquisition, we have a list of events presumed to correspond to the detection of single atoms, represented in the form of a list of coordinates (X, Y, T) specifying the position and arrival time of the atoms.

In practice, atoms are trapped in a region of space approximately 46 cm above the MCP, either by a magnetic trap or an optical dipole trap. The trap is abruptly switched off and the atoms fall on the MCP due to gravity (Figure 2.6). One can then deduce the speed of an atom right after the trap is abruptly switched off from its position and arrival

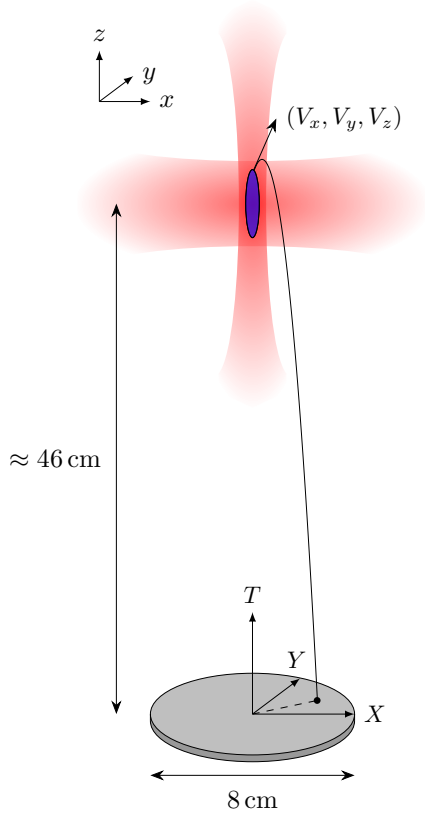

Figure 2.6: Schematic representation of atom detection after time of flight. A crossed optical dipole trap (in red) traps a cold atoms cloud (in blue). An atom emitted with a certain initial velocity from this cloud is detected, after time of flight, at precise coordinates on the MCP.

time. Indeed, a simple classical mechanics calculation makes it possible to determine the initial velocity of the atom before its fall based on its arrival coordinates (X, Y, T) on the MCP. By setting the spatial origin at the center of the MCP and the temporal origin at the moment of trap cutoff, we have the following relationships:

$$\begin{cases} V_x = \dfrac{X}{T} \\ V_y = \dfrac{Y}{T} \\ V_z = \dfrac{1}{2}gT - \dfrac{L}{T} \end{cases} \tag{2.8}$$

where L is the vertical distance between the trap and the MCP. It can be obtained by identifying the mean arrival time of a BEC for instance, which corresponds to an initial vertical speed equal to zero. Note that to get these equations, gravity was the only force considered. Although L can be determined using the center of a BEC, these equations cannot be used to calculate the velocity distribution of a BEC, since its expansion dynamics is governed by interactions between atoms. As a consequence, relationships 2.8 can only be used for thermal clouds or dilute gases.

The typical size of the BEC is on the order of 100 µm, so that the distance L is sufficiently large to consider that the MCP is in the far-field regime, ensuring that the detection of atoms emitted from the BEC constitutes more of a measurement of the initial

momentum than a measurement of the initial position of the atoms. Actually, in the previous calculation, it is assumed that the initial position is identical for all atoms (the center of the cloud) which is a good approximation up to a certain point which will be discussed later in this manuscript (section 7.3.4).

This calculation also assumes that the only force acting on the atoms is gravity. In reality, we mentioned that atoms are trapped in the magnetic sublevel $m = 1$, so the atoms are sensitive to any residual magnetic field that may remain in the chamber. Therefore, just after cutting off the trap, a Raman transfer is performed using two laser beams and a so-called compensation coil to define the direction of the magnetic field. This enables a coherent two-photon transfer to the magnetic sublevel $m = 0$, to make sure that the falling atoms are not sensitive to magnetic fields. A few details about the Raman transfer will be given in section 2.2.3.

2.2 Cooling procedure

In this section, we will recapitulate the key steps that allow us to get a BEC. Once again, these steps are more detailed in the theses of the previous PhD students in the team, and are presented here only as an overview. This also provides an opportunity to mention the technological changes made during my thesis.

2.2.1 Source

In order to prepare helium in the metastable 2^3S_1 state from a bottle of gaseous $^4_2$He in the ground state, it is not possible to use a laser beam due to the significant energy difference between the two levels. Instead, the idea is to make a plasma using an electrical discharge, which populates many different excited states, including the desired metastable state[105].

Ground state helium is transported into a vacuum chamber through a pipe to a glass tube, in the middle of which there is a conductive tip serving as the cathode. The anode is a skimmer (a funnel-shaped metal plate with a central hole) positioned opposite the tip, and the discharge occurs between these two ends (Figure 2.7).

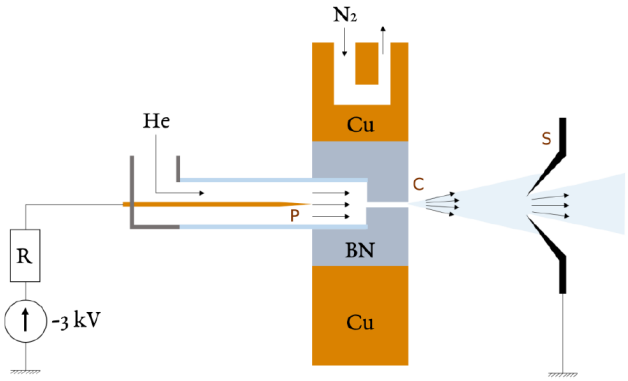

Figure 2.7: Schematic representation of the source. Taken from [41].

To prevent excessive heating of the atoms during plasma creation, the gas passes through a piece of boron nitride with a small hole, held in place by a copper plate through which liquid nitrogen circulates. Boron nitride, an electrical insulator but a good thermal conductor, provides an initial cooling stage, limiting the particle velocity to 1200 $\mathrm{m.s^{-1}}$

instead of 2600 m.s^{-1}[106]. This results in a divergent atom flux, which can then be further cooled using optical methods.

In September 2022, a leak occurred between the pipes transporting liquid nitrogen and the vacuum chamber. Due to significant thermal constraints, the leak could not be sealed with vacuum glue. Consequently, the source had to be extracted so that a welding could be made on a part of the vacuum chamber outside the laboratory. During this operation, and after approximately 10 years of proper functioning, the source was damaged (the glass tube and the boron nitride piece are particularly fragile) and had to be replaced.

2.2.2 Cooling atoms down to Bose-Einstein Condensation

After obtaining a helium atom jet, we can interact with the small fraction of atoms in the metastable state (evaluated at approximately one out of ten thousand) using a laser tuned to the transition $2\,^3S_1 \longrightarrow 2\,^3P_2$. The other atoms do not interact with the light and are gradually absorbed by the vacuum pumps during the process.

To achieve Bose-Einstein condensation, several cooling steps are necessary. The general principle of these steps is described in references [55] and [107], for example. The specific steps followed in our experiment are detailed in [41].

- First, a pair of retro-reflected beams is used to form a so-called transverse molasses. The wavefront of the beams is curved, which leads to a greater reduction of the transverse velocity of the atoms than a plane wave and thus increase the spatial density of the atomic jet along the y axis[108].

- The atoms then enter a Zeeman slower: a long tube (2.4 m) in which atoms interact with a beam opposite to their propagation direction, decelerating them through radiation pressure. To stay at resonance with the decelerated atoms and continue cooling them during their propagation in the slower, we compensate for the Doppler effect using a solenoid with a varying radius. The magnetic field thus created compensates, through the Zeeman effect, for the Doppler shift of the slowing atoms. At the end of the Zeeman slower, the speed of the atoms is about 70-100 m.s^{-1}.

- Then, we can load the atoms in a Magneto-Optical Trap (MOT), consisting of three retro-reflected beams near resonance and a magnetic field generated by a pair of coils in an anti-Helmholtz configuration. In this so-called science chamber, an infrared camera is used for imaging the atomic cloud through fluorescence/absorption, providing information about the size and number of atoms during successive cooling stages. The MOT loading step takes about 1.5 seconds, resulting in approximately 2.10^9 atoms at a temperature of around 1 mK.

- At the end of the MOT loading, we compress the trap by bringing the frequency of the beams closer to resonance and reducing their power, further reducing the phase space density as both the temperature and the volume of the cloud are reduced[109].

- Following the MOT compression, the same beams are employed to create an optical molasses close to resonance, further cooling the atoms. This step lasts for a few milliseconds and results in obtaining clouds on the order of 100-200 µK.

- The atoms are then transferred into a magnetic trap (without optical confinement), in what is called a Ioffe-Pritchard trap[110] in a cloverleaf configuration, composed of two symmetrical clusters of coils located on either side of the vacuum chamber. Each cluster consists of one quadrupole with four elliptic coils and two concentric

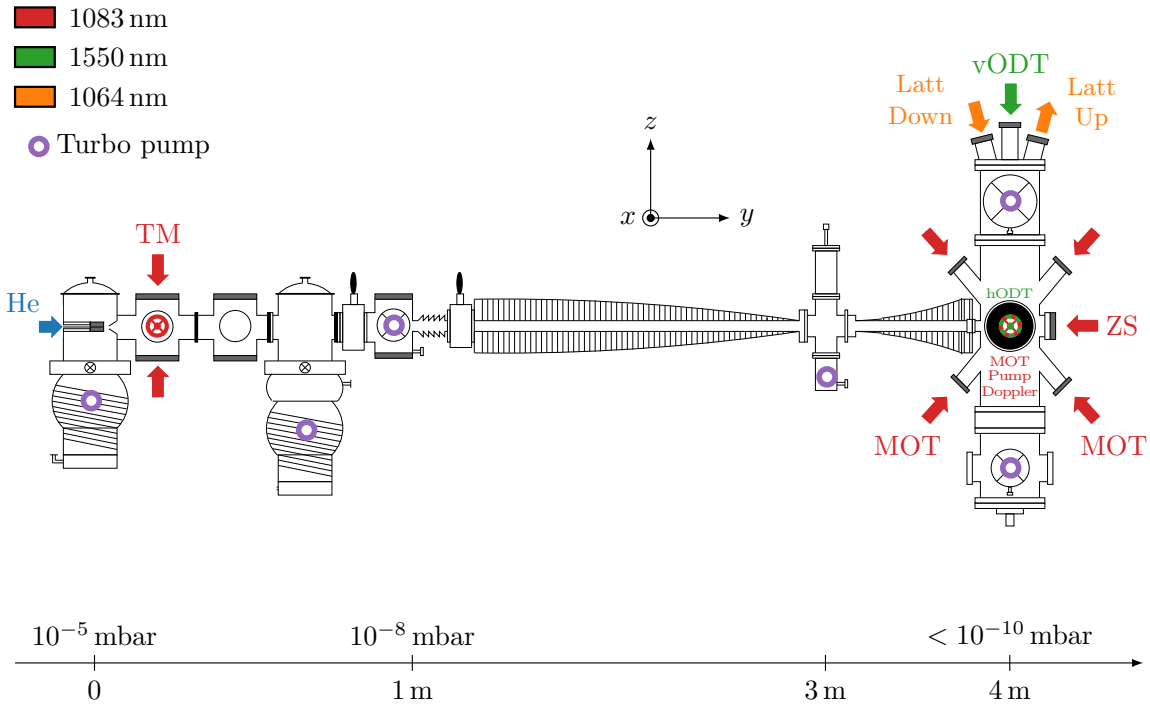

Figure 2.8: Schematic representation of the experiment. The helium atoms are brought in the vacuum chamber from the left of the image where the discharge occurs to form a helium plasma. The transverse molasses (TM) reduces the transverse velocity of the atoms, which go to the Zeeman slower (ZS). Once in the science chamber, they are trapped in a magneto-optical trap (MOT), then in a magnetic trap, and finally in an optical dipole trap consisting of a vertical (vODT) and a horizontal (hODT) beam. In the following, we will see that an optical lattice is used to generate pairs of atoms, with the beams (Latt Down and Latt Up) oriented at a 7° angle from the vertical axis. After the trap cutoff, the atoms fall onto the MCP placed in the vacuum chamber beneath the science chamber.

circular coils of different diameters (Figure 2.9). This trap enables the formation of a quasi-harmonic confining magnetic field at the center of the chamber. The originality of this configuration lies in the ability to control the value of the minimum magnetic field, referred to as the bias field. This bias controls the transverse confinement of the trap[106].

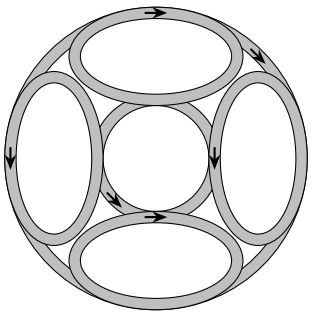

Figure 2.9: Geometry of a cluster from the Magnetic Trap.

- At the beginning of the magnetic trap, an intense and short laser pulse is used as an optical pumping beam in order to transfer in the magnetic sub-level $m = 1$, which

is the only state within which the atoms are trapped.

- The magnetic trap is then compressed by ramping down the bias field, and a low-intensity 1D retro-reflected Doppler beam is applied for 1 s. This results in a temperature decrease as well as an increase of density[111]. At this step, the 3D temperature of the cloud (100 µK) is close to the Doppler limit of 39 µK.

- A second compression of the magnetic trap is then performed to increase the transverse trapping frequency once again. Subsequently, an evaporative cooling step is carried out using a radiofrequency antenna located within the science chamber, coupling atoms from the sub-level $m = 1$ to the untrapped sub-level $m = 0$. By adiabatically lowering the RF frequency, progressively removing the most energetic atoms from the trap, the remaining atoms rethermalize through elastic collisions and the cloud gets colder and colder.

  At this stage, it is possible to evaporate until there is a transition towards a Bose-Einstein Condensate (Figure 2.10). The trapping frequencies at this point are $\omega_x = 2\pi \times 45$ Hz and $\omega_{y,z} = 2\pi \times 930$ Hz. This is how the first metastable helium condensate was obtained in our team[58]. However, some magnetic instabilities in our setup lead to fluctuations in the bias field, resulting in sometimes significant variations in atomic density and even the cloud's position. Consequently, achieving a stable condensate over several hours is not optimal under these conditions, which is why the atoms are transferred in an optical dipole trap, at a temperature of 30 µK, before condensation.

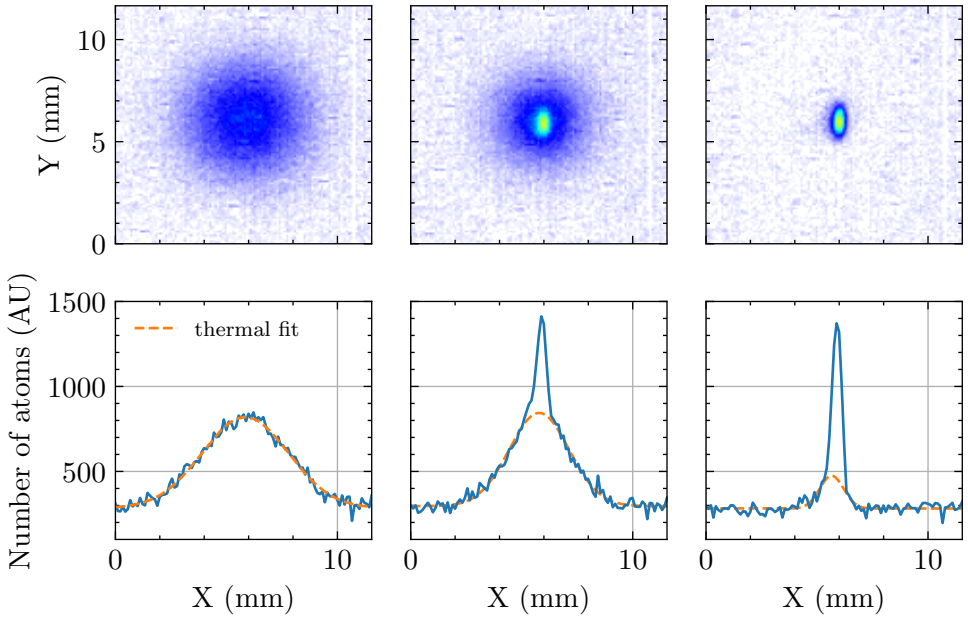

Figure 2.10: Bose-Einstein Condensation in the Magnetic Trap. Each column corresponds to a given final frequency of evaporative cooling, decreasing from left to right. Pictures from the camera are shown on the top row, while a Y-fixed transverse cut is depicted on the bottom row. We can see, from left to right as the trap depth decreases, a thermal cloud, a thermal/condensate bimodal profile, and a BEC.

- The atoms are then transferred into an intense (a few Watts) and highly red-detuned ($\lambda = 1550$ nm) vertical beam, which plays the role of an optical dipole trap (ODT). After a 500 ms overlap with the magnetic trap, the latter is adiabatically turned off,

and approximately 4.10^7 atoms are loaded without heating the cloud, which remains at 30 µK. A compensation coil is employed to maintain the atoms in the $m = 1$ magnetic sub-level.

- Then, a second horizontal laser beam at 1550 nm is turned on and intersects the vertical beam at the location of the atoms. Subsequently, evaporation is carried out in the crossed trap by adiabatically lowering the power of the beams and, consequently, the trap depth. The role of the horizontal beam is twofold: firstly, to compensate for gravity when the power of the vertical beam becomes too low, and secondly, to increase the oscillation frequency in the vertical axis. Indeed, the longitudinal trapping frequency of the vertical beam alone is on the order of $\omega_z = 10\,\text{Hz}$ after evaporation (compared to $\omega_{x,y} = 1.5\,\text{kHz}$ for the transverse frequency). As a result, with only a vertical beam, the highly elongated condensate obtained is actually in a quasi-condensate 1D regime, exhibiting physics distinct from that of 3D condensates.

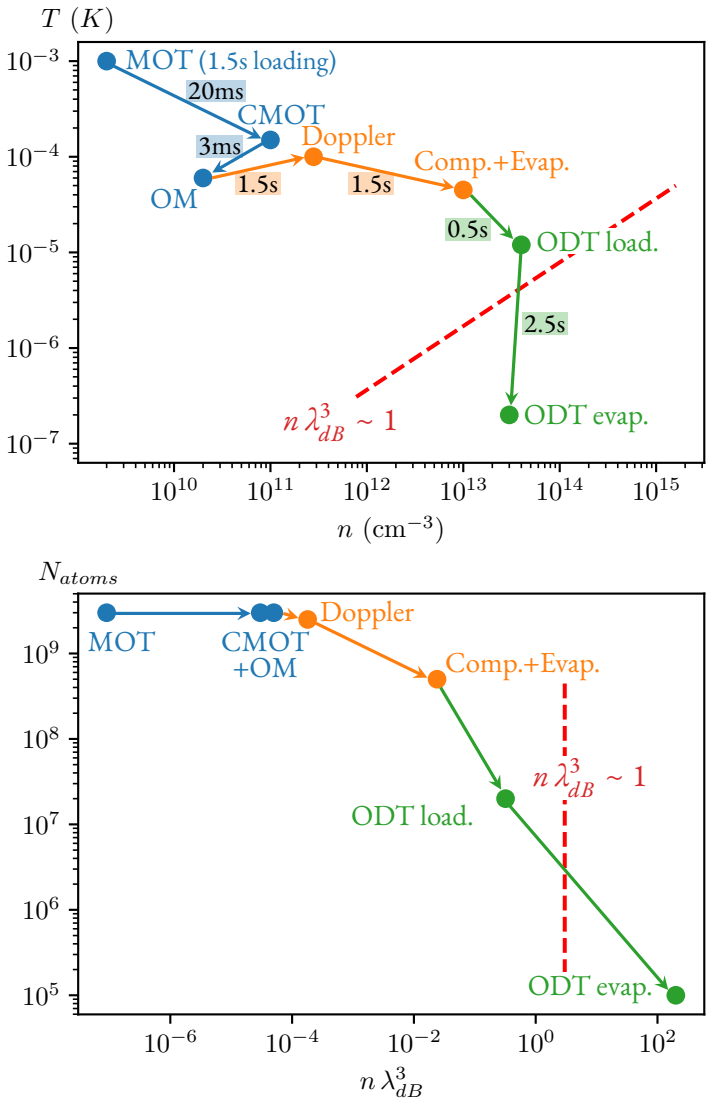

Figure 2.11: Summary of the cooling procedure. Above: Temperature as a function of the density. Below: Number of atoms as a function the the phase space density. Taken from [41].

A summary graph of the various cooling stages is presented in Figure 2.11, providing the temperature and atom number at each step. These steps are computer-controlled using a sequencer that sends instructions and signals to different devices to ensure the sequential progression of the cooling stages. Thanks to the work of the previous PhD students on the experiment[112], obtaining a BEC in the ODT now takes approximately 10 to 12 seconds, compared to around thirty seconds in 2015 when the team conducted the Hong-Ou-Mandel experiment (and 45 seconds for the "historical" BEC in the magnetic trap). During this time frame, the experiment faced various breakdowns and technical issues, delaying the progress of the experiment and preventing the realization of other interference experiments, including the Bell test, which was the clear objective after HOM.

Particularly, after my arrival in the team, the experiment faced significant fluctuations of the atom number of various origins (computer bugs, frequency instabilities, power and polarization fluctuations), hindering even the loading of a stable MOT. In February 2021, it was decided to make substantial changes, during which we replaced the diode laser, responsible for the cooling transition, with a narrowband and stable fiber laser. We specifically revamped the frequency locking optical setup. Additionally, we replaced the aging sequencer, controlled in Matlab and historically developed by the laboratory's electronic workshop, with a Python-controlled ADWIN sequencer. The development of object-oriented code to control the experiment took some time, but these changes significantly improved the stability of the atomic clouds.

The transition to Python for the sequencer control code was also seized as an opportunity to write a new program for visualizing and processing data in the laboratory room. This task was primarily carried out by A. Dareau, a postdoctoral researcher in the team, for the images received by the camera. I developed the software component responsible for visualizing the data received from the MCP.

2.2.3 Raman transfer and protective copper plate beam dump

In August 2019, while the team managed to have a BEC in the ODT, the vertical beam was left at full power (8W at the time) for several seconds. The MCP, positioned below, could not dissipate the received thermal energy, resulting in a complete and irreversible loss of detectivity at the center of the detector. The MCP was then replaced by a new model, which is the one we currently use, expected to increase quantum efficiency from 25% to 50%. However, even by reducing the initial power and following a standard evaporation ramp, the new MCP was damaged again in January 2020, just before my arrival in the team. It turned out that the new MCP is also more sensitive to thermal stress. Additionally, the hole radius kept increasing while evaporative cooling was performed, without any visible asymptotic limit.

After an initial unsuccessful attempt to change the geometry of the ODT (without using a powerful vertical beam), which proved too sensitive to fluctuations in the center of the magnetic trap for stable loading of the optical trap, the solution we opted for involved two elements:

- adding a copper plate above the MCP, held by a stainless steel arm, to dissipate thermal energy without deteriorating the detector, like a beam dump in high vacuum ;

- implementing a momentum transfer along the X-direction during the Raman transfer, in order to shift the atoms away from the center of the MCP and let them fall next to the hole and the "shadow" of the copper plate.

Copper plate beam dump

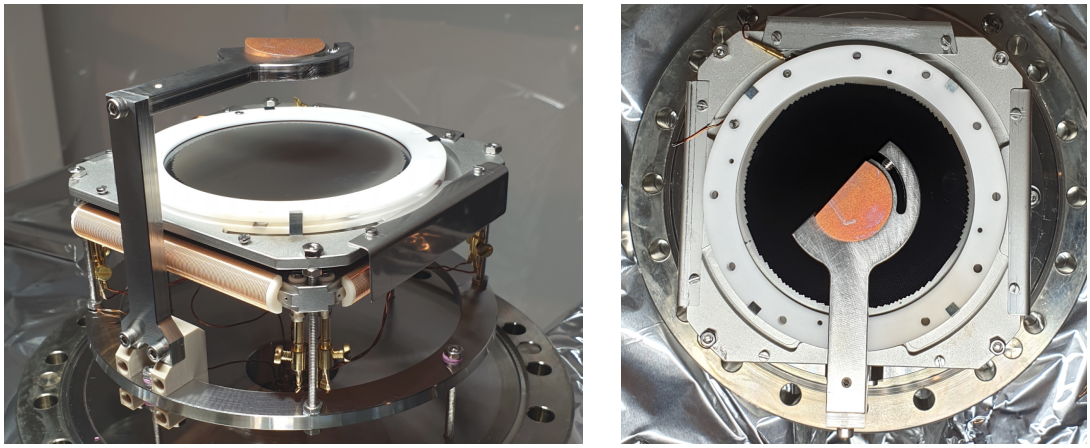

(a) Side view. **(b)** View from above.

Figure 2.12: Pictures of the copper plate beam dump, held by a stainless steal arm.

The copper plate consists of a one-inch diameter disk, 6 mm wide, with a surface treated to diffuse laser light. Copper was chosen after preliminary tests on other surfaces (such as a mirror with a diffusing gold coating) due to its excellent thermal conduction properties. The piece was cut to avoid obstructing the useful area of the MCP and is held by a stainless steel arm that tilts it 7° relative to the MCP plane, preventing the reflection of light onto the atoms.

The piece was installed on the MCP in December 2021. By studying the MCP detectivity map, obtained by allowing a hot cloud to fall across the entire detector, it became apparent that the copper plate with its stainless steel mounting arm disrupted the electromagnetic environment around the MCP, resulting in detectivity variations in the vicinity of the piece, likely caused by atom deviations. This can be observed by allowing a hot cloud to fall on the MCP: if its temperature is high enough, the spatial extension of the cloud after time of flight covers the entire detector. It should have very few atoms to prevent saturation. In practice, we use atoms from a MOT without transverse molasses. A typical example is given in Figure 2.13.

Initially, it was considered that this effect might be of electrical origin. Consequently, we opened the vacuum chamber again and the stainless steel arm was connected to the ground, since it was originally in contact with the high-voltage part of the MCP. However, this change had no effect. It was then observed that the detectivity decrease at the vicinity of the piece was much more pronounced for $m = 1$ clouds than for $m = 0$ clouds, suggesting that the effect is, in reality, magnetic (Figure 2.13). The SAE 304 stainless steel used, while less magnetic than conventional stainless steel, is not entirely non-magnetic, which could explain this observation. It was decided to retain this setup since the atoms of interest are those transferred by Raman into the $m = 0$ state.

Nevertheless, a deterioration in detectivity around the piece was observed after a year of operation. The cause of this deterioration is unknown, and regular checks are conducted to ensure that it does not significantly impact our study of condensates in the useful area.

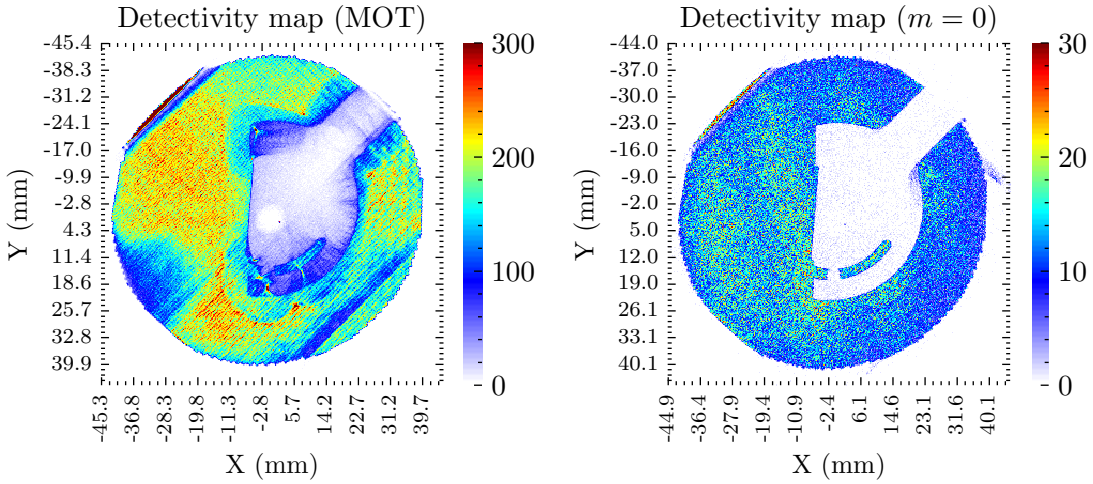

Figure 2.13: Detectivity maps of the MCP with the copper plate. Left: Map obtained with MOT clouds ($m = 1$). Data averaged over 560 runs. A clear spatial dependency of the detectivity is observed, especially around the shadow of the beam dump. Right: Map obtained with cold clouds transferred in $m = 0$. Data averaged over 29 runs. Despite a lack of statistics, the spatial effects on the detectivity are less visible.

Raman transfer

Like a Bragg transfer, a Raman transfer is a coherent two-photon transition, but it couples two internal states of the atom. This allows us to transfer atoms from the $m = 1$ state (which allows for the trapping of the atoms in the magnetic trap and has a low Penning collision rate) to the $m = 0$ state when they are released from the trap (making them insensitive to any residual magnetic fields in the chamber during their fall towards the MCP). We employ a diode laser at 1083 nm and address the $2^3S_1 \rightarrow 2^3P_0$ transition with σ^- and π polarized beams (Figure 2.14).

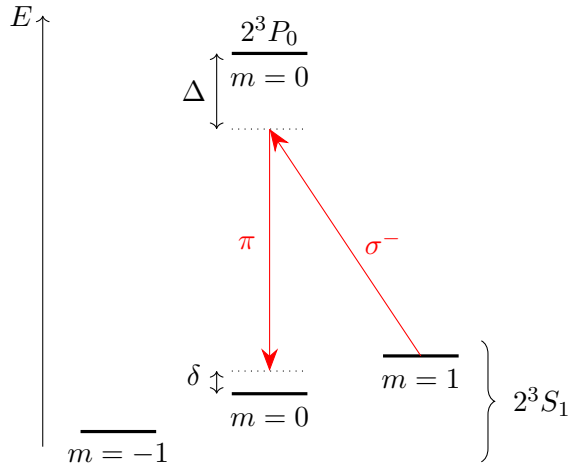

Figure 2.14: Energetic diagram of the two-photon transition process.

The amplitude of the compensation magnetic field determines the splitting between the magnetic sublevels, and consequently, the two-photon resonance condition. The detuning

Δ from the excited state is 800 MHz, allowing for adiabatic elimination of the excited state population to reduce the system to a two-level configuration between $m = 0$ and $m = 1$. This system is coupled by an effective Rabi frequency given by:

$$\Omega_{2\text{ph}} = \frac{\Omega_{\sigma^-}\Omega_{\pi}}{2\Delta} \tag{2.9}$$

where Ω_{σ^-} and Ω_{π} are the Rabi frequencies of each beam.

It is possible to use the Raman transition to transfer momentum to the atoms. Indeed, if both beams make an angle of $\theta/2$ with the y axis, momentum conservation imposes that the transferred atoms acquire an additional momentum along x equal to $2\hbar k \sin(\theta)$, where $\hbar k = 2\pi\hbar/\lambda$ is the one photon recoil momentum. This effect is used to "kick" the atoms from the BEC along x, so that after a time of flight of 300 ms, they are shifted by 13.5 mm along x (Figure 2.15) for an angle of $\theta = 28°$. This displacement is sufficient to avoid the hole and the shadow of the protective arm while remaining within the MCP diameter.

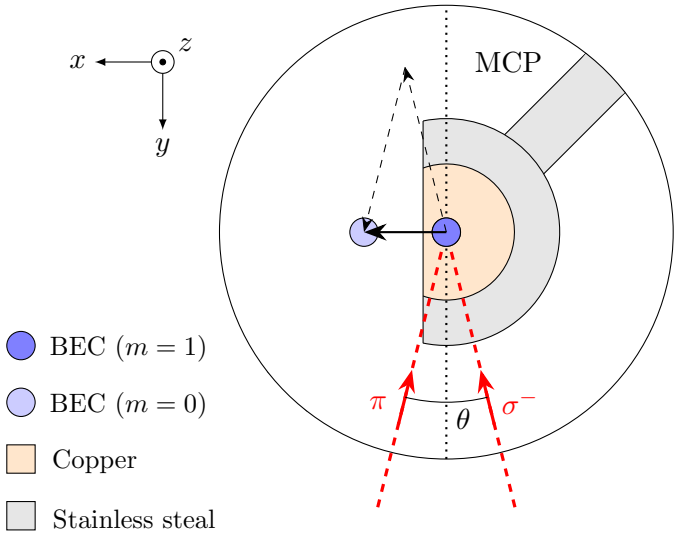

Figure 2.15: Schematic representation of the two-photon Raman kick as seen from above the science chamber.

We can therefore detect $m = 0$ atoms on the MCP. The implementation of the copper plate above the MCP introduces a constraint for characterizing the Raman transfer because $m = 1$ atoms falling onto it are not observable. Nevertheless, residual magnetic fields induce non-trivial motion in $m = 1$ atoms, leading to the detection of some magnetic atoms on the useful part of the MCP. The acceleration caused by residual magnetic fields further results in this signal not being detected simultaneously with the atoms transferred into $m = 0$.

Subsequently, a Rabi oscillation between the two levels can be realized by varying the duration of the Raman beam application. The data from the MCP provides a list of atoms identified by their coordinates (X, Y, T). To observe the Rabi oscillation with the $m = 0$ atoms, one simply needs to count the atoms falling onto the MCP within a short time range centered 308 ms after the trap is turned off. For the $m = 1$ atoms, we count the number of events within the spatiotemporal range corresponding to the residual atoms. An example is shown in Figure 2.16. By finely scanning the duration of the Raman pulse around the value for which all atoms are transferred, one can precisely determine the

duration required to achieve the optimal transfer. At resonance, it is possible to transfer approximately 98% of the atoms for a duration of around 15 µs.

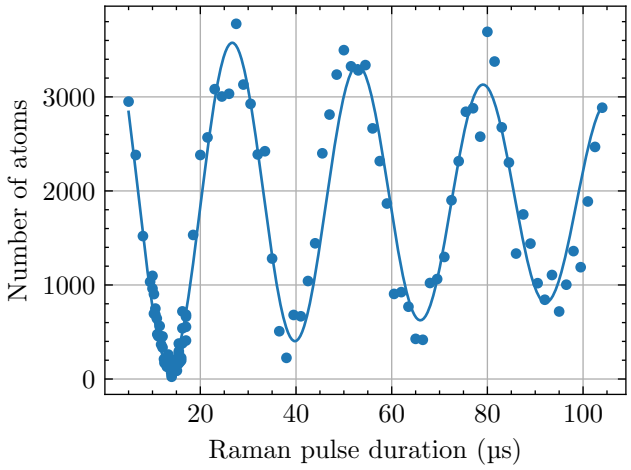

Figure 2.16: Rabi oscillations with the Raman beams.

2.2.4 Imaging system

As previously mentioned, an infrared camera is used to image the atoms in the science chamber (Figure 2.17), providing information on the number of atoms and the cloud size to ensure the proper progress of the different cooling stages, as long as the size of the cloud is not too small (which is the case for a BEC in the crossed dipole trap) or the number of atoms too low.

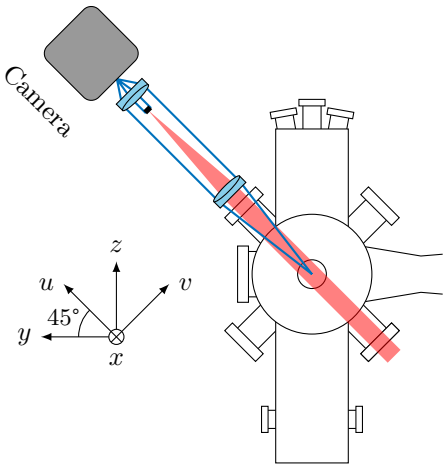

Figure 2.17: Schematic representation of the imaging setup. Taken and adapted from [41].

The camera is a short-wave infrared InGaAs model (Xeva 320 by Xenics), installed in 2017 on the experiment. It is positioned at a 45° angle relative to the experiment's vertical axe, along one of the MOT beams direction (a motorized arm makes it possible to deploy a retroreflection mirror during the MOT). A telescope is employed to conjugate the atoms with the camera CCD sensor. The camera can be used either in fluorescence or absorption imaging modes.

In the case of fluorescence imaging, resonant light with the transition $2^3S_1 \rightarrow 2^3P_2$ is directed onto the atoms for a duration of $\tau = 200\,\mu s$ using the MOT beams (except the one along the camera axis). The atoms are then excited and subsequently emit photons via spontaneous emission, with a rate given by:

$$\gamma = \frac{\Gamma}{2}\frac{s}{1+s} \tag{2.10}$$

where $s = I/I_{\text{sat}}$ is the resonance saturation parameter. By ensuring that the beam intensity is sufficient, we have $\gamma = \Gamma/2$.

It is possible to estimate the number of atoms in the cloud based on the number of photons N_p detected by the camera, as the number of emitted photons is directly proportional to the number of atoms N according to the simple relation

$$N_p = \frac{\Gamma}{2}\tau N \tag{2.11}$$

In practice, obtaining a reliable estimation is challenging because it requires estimating the fraction of emitted photons reaching the detector, and determining the corresponding solid angle is not straightforward. Additionally, the camera provides an image in grayscale rather than a count of photons, so a detailed understanding of the camera's (non linear) conversion chain is necessary. Thus far, this has been the method used to calculate the number of atoms in a cold cloud, but there is suspicion that the result is consistently overestimated. Furthermore, the significant duration of the fluorescence pulse has a mechanical effect on the cloud, causing its size to increase significantly for atoms trapped in the dipole trap, thereby distorting the cloud size estimation and therefore potentially the temperature measurements.

During my thesis, I contributed to the implementation of imaging in an absorption mode. In this technique, the atoms are illuminated using the beam employed for the MOT along the camera axis for $18\,\mu s$. The intensity transmitted after the light passes through the cloud is directly related to the cloud density by Beer-Lambert's law:

$$I(x,v) = I_0(x,v)\exp\left(-\sigma\int n(x,v,u)\,\mathrm{d}u\right) \tag{2.12}$$

where I_0 is the incident intensity, n the atomic density and $\sigma = \frac{3\lambda^2}{2\pi}$ the absorption cross section at resonance. In order to measure the density $n(x,v)$ of a given cloud integrated along the u axis, a common way consists in taking three consecutive pictures, a first one in order to collect the intensity $I(x,v)$ with atoms, a second one to measure $I_0(x,v)$ with light but without atoms, and finally one without light and without atoms in order to cancel any background noise $I_{\text{b}}(x,v)$. The density of the cloud is then given by

$$n(x,v) = \frac{1}{\sigma}\ln\frac{I_0(x,v) - I_{\text{b}}(x,v)}{I(x,v) - I_{\text{b}}(x,v)} \tag{2.13}$$

Implementing this type of absorption imaging will enable the camera to be calibrated more accurately than with fluorescence, for example by comparing the number of atoms N calculated by integrating $n(x,v)$ with that expected when N is thermodynamically fixed (typically a thermal cloud at the condensation threshold). During the Spring of 2022, this work has been conducted by C. Lamirault, new PhD student in the team, during her Master internship[113].

One of the main goal is to use this calibration to determine the quantum efficiency of the MCP, by dropping onto it a known fraction of atoms by Raman transfer. Preliminary

results suggest that the quantum efficiency is of the order of 50%, as measured by the team of D. Clément[114], but our study needs to be continued at this stage.

2.3 BEC characterization

2.3.1 Stability

One way to monitor the stability of the experiment and the reproducibility of condensate realization consists in iteratively releasing identical clouds onto the MCP and study the statistics of the detected atoms. In the following, we analyze a dataset for which we produced a very cold condensate in order to achieve a very low temperature (potentially at the expense of atom number).

As seen before, a BEC is so dense that it inevitably saturates the detector, making it impossible to directly determine the number of atoms. Although the total number of atoms is significantly underestimated, the spatial delineation of the condensate is not affected by saturation. Therefore, it is possible to determine the size and position of the detected cloud after time of flight by fitting the density of detected atoms in each direction.

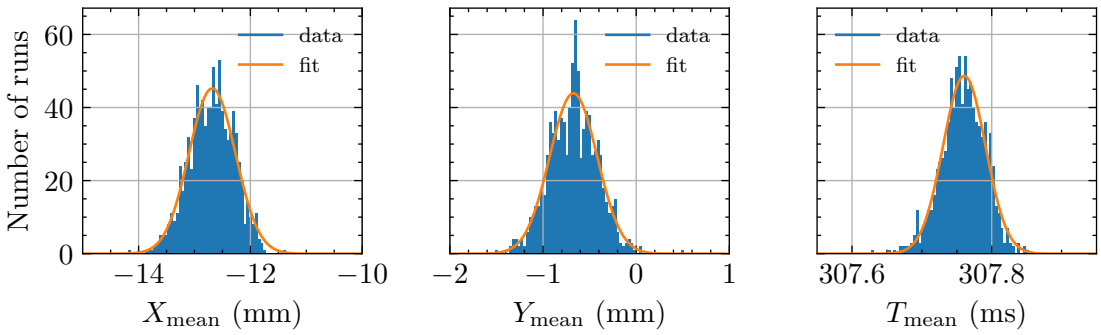

Figure 2.18: Stability histograms of the BEC. For each experimental run, the center of the BEC in each direction is determined by a density fit. The histograms show the distribution of the position and arrival time of this center for the 922 runs considered.

Figure 2.18 shows the statistical distribution of the center of the BEC, which was determined by a Gaussian fit in each direction. The average value and the standard deviation of the center of the cloud (along with its size) are given in Table 2.2. The space origin is the center of the MCP, while the time origin corresponds to the time at which the optical dipole trap is switched off. A Raman pulse is performed a few milliseconds after in order to transfer the atoms in $m = 0$ and kick them along X. The center of the BEC is located 12.7 mm away from the center of the MCP, which corresponds to what we expect given the angle between the two Raman beams.

For our future Bell experiment, we will show that the correlated pairs of atoms are emitted from the condensate (in an optical lattice) in the vertical direction. Therefore, it is crucial to have good stability along this axis because instability of the BEC leads to instability of the pairs, resulting in a significant limitation of our longitudinal resolution. The arrival time of the cloud should vary little compared to the width of a momentum mode, which will be determined later in this manuscript. A first reference value is provided in R. Lopes's thesis[115], which estimates the standard deviation of arrival times from the crossed optical dipole trap to be $\sigma(T_{\mathrm{mean}}) = 0.04\,\mathrm{ms}$ (in a setup that allowed observation

Quantity	Mean	Standard deviation
X_{mean}	-12.7 mm	0.4 mm
Y_{mean}	-0.7 mm	0.3 mm
T_{mean}	307.76 ms	0.03 ms
σ_X	3.1 mm	0.2 mm
σ_Y	3.4 mm	0.2 mm
σ_T	0.15 ms	0.02 ms

Table 2.2: Results of the stability measurements. Mean and standard deviation of the center of the MCP (up) and of its size (down) in every direction.

of the HOM effect with atoms). In our case, we measure $\sigma(T_{\text{mean}}) = 0.03\,\text{ms}$, which is satisfying.

2.3.2 Number of atoms, temperature, size and chemical potential

For a condensate, one cannot simply deduce the momentum distribution using classical mechanics relations 2.8 because the expansion dynamics of a BEC are governed by interactions within the cloud, which cannot be neglected. Nevertheless, it is possible to infer certain properties of the BEC.

Figure 2.19 presents the density of the detected atoms when a BEC falls onto the MCP, averaged over 922 runs, in the transverse plane and along the longitudinal axis. On this latter curve, four zones can be distinguished. In gray, one can observe a residual atom noise. The blue plateau corresponds to a few atoms emitted via spontaneous emission from the Raman beam slightly too close to resonance. In green, we observe atoms originating from a thermal cloud, here fitted by a Gaussian distribution, and in red, the density peak corresponds to the condensate, which is significantly dominant.

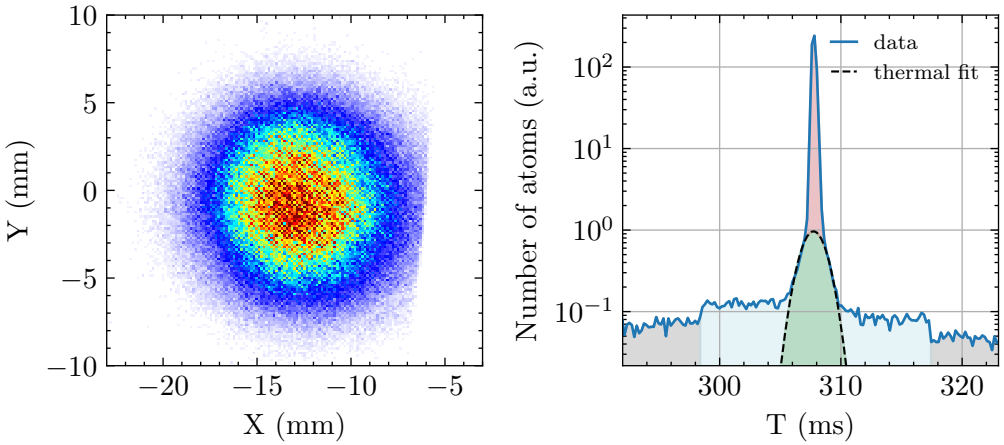

Figure 2.19: BEC after time of flight, averaged over 922 runs. Left: Transverse density profile, integrated along the vertical direction. The colormap highlights a Thomas-Fermi parabolic profile. Right: Vertical density profile in terms of arrival time, integrated along the transverse directions. In gray: noise. In light blue: atoms emitted by spontaneous emission. In green: atoms from the thermal fraction. In red: BEC.

From this profile, one can estimate in particular the temperature of the thermal frac-

tion. Indeed, for an ideal gas where we neglect interactions between atoms, the size of a thermal cloud after a time of flight t is given by a ballistic expansion expression[116]:

$$\sigma_i(t) = \sigma_i(0)\sqrt{1+\omega_i^2 t^2} \tag{2.14}$$

where $i \in \{x, y, z\}$ and ω_i is the trapping frequency along i. The initial size of the cloud writes

$$\sigma_i(0) = \sqrt{\frac{k_{\text{Boltz}}T}{m\omega_i^2}} \tag{2.15}$$

For a long time of flight, i.e. when $\omega_i^2 t^2 \gg 1$, we get

$$\sigma_i(t) = \sqrt{\frac{k_{\text{Boltz}}T}{m}}\, t \tag{2.16}$$

Along the vertical axis, the size of the cloud is converted into a detection duration on the MCP, given by $\sigma_t(t) = \frac{\sigma_z(t)}{gt}$. The temperature is then equal to

$$T = \frac{mg^2\sigma_t^2}{k_{\text{Boltz}}} \tag{2.17}$$

The fitted size from Figure 2.19 equals $0.99 \pm 0.08\,\text{ms}$, which corresponds to a temperature of $T = 45 \pm 8\,\text{nK}$. Note that, by integrating the area of the thermal fit, one can deduce an estimation of the number of detected thermal atoms per run, which is equal to $N_{\text{therm}} = 12 \pm 4$.

For a BEC, the ballistic expansion expression is not valid because of the interactions in the cloud, characterized by the chemical potential μ. It can be considered that when the BEC is trapped, the kinetic energy of the atoms is negligible compared to the interaction energy, so that the BEC is in the so-called Thomas-Fermi regime and the in-trap density profile is given by an inverted parabola:

$$\Phi_{\text{TF}}(\mathbf{r}) = \left(\frac{\mu - U(\mathbf{r})}{g_{\text{GP}}N}\right)^{1/2} \tag{2.18}$$

where N is the number of atoms, $U(\mathbf{r})$ the trapping potential (considered to be harmonic in our case) and g_{GP} is a coupling constant, proportional to the s-wave scattering length a:

$$g_{\text{GP}} = \frac{4\pi\hbar^2 a}{m} \tag{2.19}$$

The chemical potential μ is then given by

$$\mu = \frac{\hbar\bar{\omega}}{2}\left(15\frac{aN}{\bar{\sigma}}\right)^{2/5} \tag{2.20}$$

where

$$\bar{\omega} = (\omega_x\omega_y\omega_z)^{1/3} \qquad \text{and} \qquad \bar{\sigma} = \sqrt{\frac{\hbar}{m\bar{\omega}}} \tag{2.21}$$

When the trap is switched off, the BEC expands and the interaction energy is converted into kinetic energy. The expansion dynamics was studied in references [117] and [118]. In particular, Y. Castin and R. Dum developed an analytic model in the case of a very

anisotropic trap, for which $\omega_{\parallel} \ll \omega_{\perp}$. In this case, the radius $R(t)$ of the BEC in each direction is given by a scaling law:

$$\begin{cases} R_{\perp}(t) = R_{\perp}(0)\sqrt{1+\tau^2} \\ R_{\parallel}(t) = R_{\parallel}(0)\left[1+\varepsilon^2\left(\tau\arctan(\tau) - \ln\sqrt{1+\tau^2}\right)\right] \end{cases} \tag{2.22}$$

where

$$R_i(0) = \sqrt{\frac{2\mu}{m\omega_i^2}}\,, \qquad \varepsilon = \frac{\omega_{\parallel}}{\omega_{\perp}}\,, \qquad \tau = \omega_{\perp}t \tag{2.23}$$

The size of the cloud after expansion is entirely determined by the chemical potential and the oscillation frequencies. In our case where the BEC is elongated along the vertical direction, $\omega_{x,y} = \omega_{\perp}$ while $\omega_z = \omega_{\parallel}$. Therefore, fitting the condensate with a parabolic function in each direction using these three parameters as fitting parameters allows us to infer the characteristics of the BEC. The clouds are fitted for each experimental run. The results are given in Table 2.3.

Quantity	Value
$\omega_{x,y}$	$2\pi \times (1010 \pm 200)$ Hz
ω_z	$2\pi \times (87 \pm 20)$ Hz
μ	149 ± 9 nK
$R_{x,y}(0)$	4 ± 1 µm
$R_z(0)$	45 ± 13 µm
N	15300 ± 5000

Table 2.3: Oscillation frequencies in the crossed optical dipole trap and characteristics of the BEC.

The oscillation frequencies found are compatible with measurements performed by quenching the cloud. From the fitted data, one can deduce the size of the cloud inside the trap, along with an estimation of the number of atoms, given by

$$N = \frac{\bar{\sigma}}{15a}\left(\frac{2\mu}{\hbar\bar{\omega}}\right)^{5/2} \tag{2.24}$$

We find $N = 15300 \pm 800$, which is the expected order of magnitude. Note that one can also deduce the number of atoms in the thermal part of the cloud, from the estimated temperature and the oscillation frequencies, according to the relationship[119]:

$$N_{\text{therm}} = 1.202\left(\frac{k_{\text{Boltz}}T}{\hbar\bar{\omega}}\right)^3 \tag{2.25}$$

This gives $N_{\text{therm}} = 11 \pm 6$, which is the same order of magnitude at what was estimated experimentally by fitting the thermal fraction of the atoms (one should expect to find half of this number due to the quantum efficiency of the MCP supposed to be around 50%, this is not exactly the case here but the low number of atoms found in both cases confirms the order of magnitude).

Note that these results indicate a very small thermal fraction, on the order of 0.1%. Such a result may seem surprising, as it can be challenging to have so few thermal atoms.

In practice, measuring temperatures smaller than the chemical potential, as in our case, is rare, which explains the significantly condensed fraction we obtain. It is possible that the temperature of the thermal fraction has been underestimated. Indeed, the elongated shape of the BEC is such that we are close to a quasi-1D regime, for which the expansion laws are known to be different from a 3D BEC. Nevertheless, this reinforces the idea that we are capable of achieving very cold clouds, so cold that we can neglect any thermal atoms when working in the crossed dipole trap. In particular, we will see that we can emit atom pairs from the condensate, sufficiently far from the BEC so that there are no thermal atom in the region of emission.

Chapter 3

Emission of momentum pairs of atoms

3.1 Four-wave mixing 81
3.1.1 Simple model: emission of two coupled modes 81
3.1.2 Phase-matching conditions in a periodic potential 82
3.1.3 Output state, density and correlations 85
3.1.4 Multimode description 86
3.2 Experimental procedure and results 89
3.2.1 Experimental procedure 89
3.2.2 Density and phase-matching 91
3.3 Second order correlation fonctions 93
3.3.1 Correlations computation 93
3.3.2 Auto-correlation 98
3.3.3 Cross-correlation 101
3.4 Counting statistics 104
3.4.1 Detection probabilities 104
3.4.2 Joint detection probabilities 107
3.5 Towards non classical correlation effects 110
3.5.1 Sub shot-noise variance 110
3.5.2 Cauchy-Schwartz violation 111
3.5.3 Experimental results 112

The parametric conversion process has been employed in our team in a collision regime between two condensates since 2007 [120], leading to the observation of non-classical correlations[21]. As discussed in the introduction, the pairs are then produced on a collision sphere. The volume of the sphere is determined by the conservation of energy and momentum, while the number of produced atoms depends on the condensate density, which remains concentrated at the poles of the sphere. Such a geometry is quite constraining as it results in the emission of many momentum modes across 4π steradians. An interesting alternative is to use a one-dimensional optical lattice to generate two correlated atomic beams. Initially proposed by in 2005 [80] and first observed in 2006[81], the idea is to use the lattice to modify the dispersion relation of the atoms, thus enabling the spontaneous creation of correlated pairs. This technique was implemented in our experiment in 2012.

In this section, we will present the process of pair creation. An analytical model is detailed in P. Dussarrat's thesis[121], from which we will summarize the main results here. We will also present the results obtained from the experiment, consisting of mainly two datasets. One dataset was obtained in the spring of 2022, with a significant population of atoms per mode, while the other was obtained in the spring-summer of 2023, with a much smaller population. We will see that the results have revealed non-classical correlations, which is encouraging for conducting a Bell test.

3.1 Four-wave mixing

3.1.1 Simple model: emission of two coupled modes

Let us consider a condensate in a dilute regime, meaning that the distance between atoms is much greater than the typical range of interatomic interaction. This gas is described by the Gross-Pitaevskii Hamiltonian, which can be expressed in the Heisenberg picture as follows:

$$\hat{H} = \int \mathrm{d}^3\mathbf{r}\, \hat{\Psi}^\dagger \left(-\frac{\hbar^2}{2m}\Delta + V(\mathbf{r},t) + \frac{g}{2}\hat{\Psi}^\dagger\hat{\Psi} \right) \hat{\Psi} \tag{3.1}$$

where, $\hat{\Psi}(\mathrm{r},t)$ is the field operator, m is the mass of the atoms, $V(\mathbf{r},t)$ is an external potential, and g is the interaction strength, related to the s-wave scattering length a through the relation

$$g = \frac{4\pi\hbar^2 a}{m} \tag{3.2}$$

The interactions within the condensate, described by the interaction Hamiltonian

$$\hat{H}_\mathrm{I} = \frac{g}{2}\hat{\Psi}^\dagger\hat{\Psi}^\dagger\hat{\Psi}\hat{\Psi} \tag{3.3}$$

can be responsible for the emission of correlated atom pairs. Indeed, let us index by 0 the momentum mode of the atoms in the condensate, we aim to emit a pair of atoms with momentum modes indexed by 1 and 2, respectively. Let us decompose the field operator into these three modes, in the form

$$\hat{\Psi} = \psi_0\hat{a}_0 + \psi_1\hat{a}_1 + \psi_2\hat{a}_2 \tag{3.4}$$

The term $\psi_0\hat{a}_0$ correspond to the BEC, which can be interpreted as a pump signal which will lead to the emission of scattered modes $\psi_1\hat{a}_1$ and $\psi_2\hat{a}_2$. By injecting this field operator into the interaction Hamiltonian 3.3, we obtain many terms. By retaining only the ones that verify momentum conservation, the remaining terms are:

- mean-field interaction terms

$$\hat{H}_{\mathrm{MF}} = 2g \sum_{i \neq j} \int \mathrm{d}^3\mathbf{r}\, |\psi_i|^2 |\psi_j|^2 \hat{a}_i^\dagger \hat{a}_i \hat{a}_j^\dagger \hat{a}_j + \frac{g}{2} \sum_i \int \mathrm{d}^3\mathbf{r}\, |\psi_i|^4 \hat{a}_i^\dagger \hat{a}_i^\dagger \hat{a}_i \hat{a}_i \tag{3.5}$$

- two four-wave mixing terms

$$\hat{H}_{\mathrm{FWM}} = g \int \mathrm{d}^3\mathbf{r}\, \psi_0^2 \psi_1^* \psi_2^*\, \hat{a}_1^\dagger \hat{a}_2^\dagger \hat{a}_0 \hat{a}_0 + g \int \mathrm{d}^3\mathbf{r}\, \psi_0^{*2} \psi_1 \psi_2\, \hat{a}_0^\dagger \hat{a}_0^\dagger \hat{a}_1 \hat{a}_2 \tag{3.6}$$

Note that the process $\hat{a}_1^\dagger \hat{a}_2^\dagger \hat{a}_0 \hat{a}_0$ actually corresponds to the desired pair emission, where two atoms from the BEC are annihilated while two atoms in momentum modes 1 and 2 are created. More particularly, if we express $\hat{a}_0$ using the Bogoliubov description $\hat{a}_0 = \sqrt{N_0}\,\hat{\mathbb{1}}$ (where N_0 is the number of atoms in the BEC, assumed to remain constant), then the Four-wave mixing Hamiltonian can be written:

$$\hat{H}_{\mathrm{FWM}} = \hbar\kappa_{1,2} \hat{a}_1^\dagger \hat{a}_2^\dagger + \hbar\kappa_{1,2}^* \hat{a}_1 \hat{a}_2 \tag{3.7}$$

where

$$\kappa_{1,2} = \frac{gN_0}{\hbar} \int \mathrm{d}^3\mathbf{r}\, \psi_0^2 \psi_1^* \psi_2^* \tag{3.8}$$

This the typical expression of a so-called squeezing Hamiltonian, resulting in the emission of correlated pairs[26], expressed with an associated gain of the process $\kappa_{1,2}$, depending on the density, the strength of the interaction, and the overlap integral between the involved momentum modes.

3.1.2 Phase-matching conditions in a periodic potential

As mentioned, the emitted modes must satisfy the conservation of energy and momentum. This is where the lattice comes into play since the atoms are placed in a periodic potential. To achieve this, two laser beams are used, forming an angle θ between them and intersecting at the BEC to interfere in the z direction, so that the lattice wavevector is

$$k_{\mathrm{lat}} = \frac{2\pi}{\lambda} \sin(\theta) \tag{3.9}$$

The beams do not have the same frequency, so that the instantaneous intensity profile in the BEC is

$$I(z,t) = I_0 \sin^2\left(k_{\mathrm{lat}} z - \frac{\delta}{2} t\right) \tag{3.10}$$

where δ is the beams detuning. The lattice is moving at a speed $v_{\mathrm{lat}} = \delta / 2k_{\mathrm{lat}}$. In the lattice reference frame, the atoms (trapped in the optical dipole trap with a zero velocity in the laboratory frame), acquire a speed equal to $v_0 = -v_{\mathrm{lat}}$, so that the momentum of the atoms in the BEC is

$$\hbar k_0 = -\frac{m\delta}{2k_{\mathrm{lat}}} \tag{3.11}$$

In this frame, the potential due to the lattice is

$$V(\mathbf{r}, t) = V_0 \sin^2(k_{\mathrm{lat}} z) \tag{3.12}$$

Let us neglect (at first) the interactions in the condensate. It can be shown that this is assumption is well verified, provided that a corrective mean-field energy is added[122]. Assuming that the optical dipole trap is an infinite well between $-L_z/2$ and $L_z/2$, where L_z is the size of the BEC, the 1D Schrödinger equation can then be expressed as:

$$-\frac{\hbar^2}{2m}\frac{\partial^2\Psi}{\partial z^2} + V_0 \sin^2(k_{\text{lat}} z)\Psi = E\Psi \tag{3.13}$$

The dispersion relation is periodic with a period of $2k_{\text{lat}}$. We then restrict ourselves to the first Brillouin zone and work with the quasi-momentum $q \in [-\hbar k_{\text{lat}}, \hbar k_{\text{lat}}]$ rather than the momentum in real space. According to Bloch's theorem, we can look for periodic solutions. So it is possible to decompose the wavevectors of the system in a basis of plane waves, so that:

$$\Psi_q(z) = \mathrm{e}^{\frac{\mathrm{i}qz}{\hbar}} \sum_j C_j(q)\mathrm{e}^{2\mathrm{i}k_{\text{lat}}jz} \tag{3.14}$$

By inserting $\Psi_q(z)$ in the Schrödinger equation, one gets the system of coupled equations

$$\frac{E(q)}{E_{\text{lat}}}C_j = \left[\left(\frac{q}{\hbar k_{\text{lat}}} + 2j\right)^2 + \frac{V_0}{2E_{\text{lat}}}\right] C_j - \frac{V_0}{4E_{\text{lat}}}\left[C_{j-1} + C_{j+1}\right] \tag{3.15}$$

where

$$E_{\text{lat}} = \frac{\hbar^2 k_{\text{lat}}^2}{2m} \tag{3.16}$$

The numerical resolution of these equations equation yields the band structure of the atoms in the lattice (Figure 3.1). It is possible to limit ourselves to $j \in [-3, 3]$ for solving the system if the lattice is shallow ($V_0 \leq E_{\text{lat}}$) because the amplitude of the coefficients C_j then rapidly decreases with $|j|$.

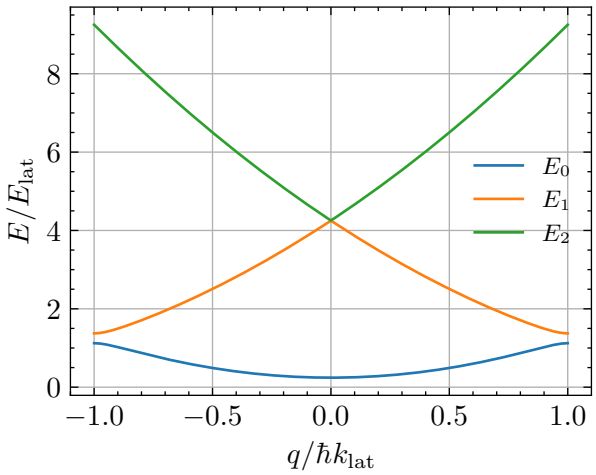

Figure 3.1: Band structure of the atoms in a lattice ($V_0 = 0.5E_{\text{lat}}$).

Let us suppose that the atoms remain in the fundamental band. The atoms in the BEC have a quasi-momentum q_0 and emit a pair with quasi-momenta q_1 and q_2. Conservation of energy and quasi-momentum in the lattice then can be expressed as:

$$\begin{cases} 2E(q_0) = E(q_1) + E(q_2) \\ \quad 2q_0 = q_1 + q_2 \ [2\hbar k_{\text{lat}}] \end{cases} \tag{3.17}$$

In this simple two-mode model, the pair creation process can be interpreted as follows: the condensate, with quasi-momentum q_0, creates two atoms of momenta q_1 and q_2 satisfying the above relations. For different values of q_0, such a solution exists with q_1 and q_2 different from q_0 due to the periodicity of the dispersion relation (Figure 3.2). In the lattice, we remain within the first Brillouin zone, so the atom for which $|q| < \hbar k_{\mathrm{lat}}$ actually corresponds to a quasi-momentum refolded into the quasi-momentum range $[-\hbar k_{\mathrm{lat}}, \hbar k_{\mathrm{lat}}]$.

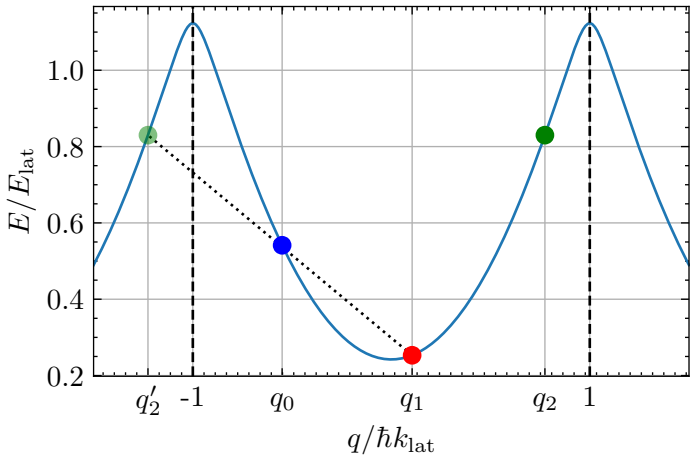

Figure 3.2: Schematic representation of the pair creation process. In the lattice frame, the condensate has a quasi-momentum q_0 (blue dot). The blue curve is the fundamental band of the atoms in the lattice ($V_0 = 0.5E_{\mathrm{lat}}$). Phase matching conditions allow for the emission of a pair of atoms with quasi-momenta q_1 (red dot) and q_2' (light green dot). Since $q_2' < -\hbar k_{\mathrm{lat}}$, the corresponding quasi-momentum of the atom in the first Brillouin zone is $q_2 = q_2' + 2\hbar k_{\mathrm{lat}}$ (green dot).

When the lattice is adiabatically turned off, a so-called band mapping phenomenon occurs, where the eigenfunction of quasi-momentum q is projected into real space as a plane wave of momentum p, where p is the quasi-momentum of the lattice restricted to the first Brillouin zone. An important consequence is that the two atoms are not emitted on opposite sides of the condensate but on the same side, due to the conservation of quasi-momentum rather than momentum.

So far, we have neglected interactions in the condensate, but in reality, they must be taken into account as they are responsible for pair creation. One approach is to add a mean-field term in the energy conservation equation. It can be shown that this approximation allows us to consider that the non-interacting eigenvectors are the eigenvectors of the system with good approximation[122]. The mean-field corrective interaction term is in this case $2gn_0$, where n_0 is the density of the BEC, so that the energy conservation relation is actually

$$2E(q_0) = E(q_1) + E(q_2) + 2gn_0 \tag{3.18}$$

The previous reasoning remains valid, but the energy value given by the band diagram is shifted by an amount that depends on the density of the BEC.

One can then numerically solve the phase-matching conditions to determine the quasi-momentum of the created pairs for a condensate with initial quasi-momentum q_0, a density n_0 and a potential depth V_0 (Figure 3.3).

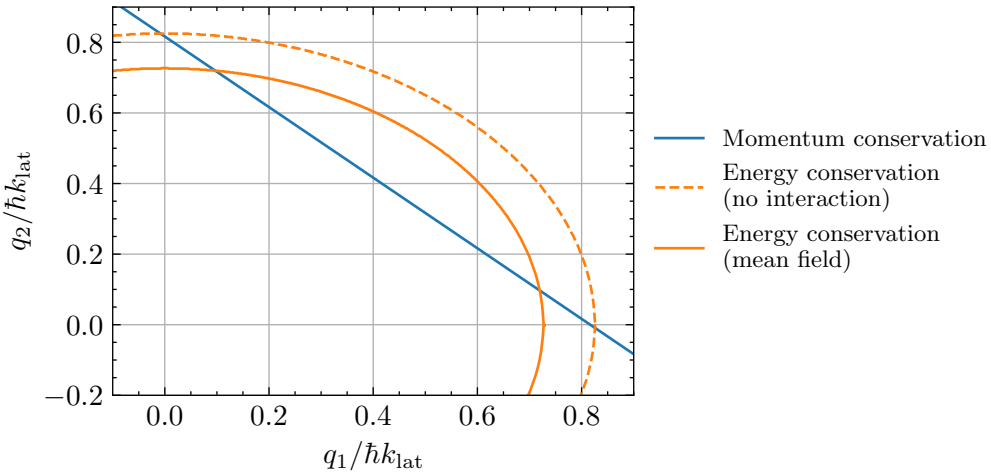

Figure 3.3: Phase matching conditions. The momentum conservation curve (in blue) is given by $q_2 = 2q_0 - q_1 + 2\hbar k_{\mathrm{lat}}$ for $q_0 = -0.58\hbar k_{\mathrm{lat}}$. The energy conservation curve (in orange) is obtained by numerically solving the equation 3.18 for $q_0 = -0.58\,\hbar k_{\mathrm{lat}}$, and $V_0 = 0.5\,E_{\mathrm{lat}}$, in the case where the mean-field term due to interactions is not considered (dashed line) and in the case where we take it into account with $n_0 = 1.3 \times 10^{13}\,\mathrm{cm}^{-3}$ (solid line). The intersection points between these two curves yield the quasi-momenta of the emitted atoms. The graph is symmetric with respect to the exchange $q_2 \leftrightarrow q_1$.

Thus, interactions within the BEC, modeled by the mean-field term $2gn_0$, have the effect of shifting the energy conservation curve as the density increases. Note that, knowing q_0, the density n_0 can be determined by measuring the momenta of the pair of atoms.

3.1.3 Output state, density and correlations

Recall that the previous results were obtained by decomposing "by hand" the Hamiltonian, introducing modes 0, 1 and 2. Within the framework of this ansatz where we consider strict conservation of momentum and energy, there is an easy analytical resolution of the problem. In the Schrödinger picture, one can solve the 1D Schrödinger equation to determine the output state of the system[121], which can be written:

$$|\psi(T)\rangle = \frac{1}{\cosh(|\kappa|T)} \sum_{n=0}^{+\infty} \mathrm{e}^{\mathrm{i}n\phi_\kappa} \tanh^n(|\kappa|T)\,|n,n\rangle \tag{3.19}$$

where $\phi_\kappa = \arg(\kappa)$ and T the duration of the optical lattice. This is the expression of a two-mode squeezed state (TMS), which can be rewritten in the general form:

$$|\psi(T)\rangle = \sqrt{1-|\alpha|^2} \sum_{n=0}^{+\infty} \alpha^n\,|n,n\rangle \tag{3.20}$$

where α, called the squeezing parameter, is related to the average population $\langle N\rangle$ in the emitted modes through the relationship:

$$\langle N\rangle = \frac{|\alpha|^2}{1-|\alpha|^2} \tag{3.21}$$

This quantum state is of particular interest because it is a superposition of twin Fock states, which are quantum states with very strong correlation properties. In particular,

as discussed in Chapter 1, the Fock state $|1,1\rangle$ can lead to the observation of a sub-shot noise variance or a HOM dip whose contrast cannot be explained by a classical model. However, experimentally producing twin Fock states is challenging, unlike TMS states. In practice, since the coefficients' weight decreases rapidly with n, it is interesting to produce TMS states with a low population, in order to approach a Fock state $|1,1\rangle$.

Similarly, it is possible to determine the expression of the creation and annihilation operator expressions. In the Heisenberg picture, on gets

$$\begin{cases} \hat{a}_1(t) = \hat{a}_1(0)\cosh(|\kappa|t) - \mathrm{i}e^{\mathrm{i}\phi_\kappa}\hat{a}_0^\dagger(0)\sinh(|\kappa|t) \\ \hat{a}_2(t) = \hat{a}_2(0)\cosh(|\kappa|t) - \mathrm{i}e^{\mathrm{i}\phi_\kappa}\hat{a}_1^\dagger(0)\sinh(|\kappa|t) \end{cases} \tag{3.22}$$

From these expressions, typical of the squeezing Hamiltonian 3.7, it is possible to determine the mean values of several observables of interest. Thus, we find again that the average number of atoms in the pairs is given by:

$$\langle N\rangle = \langle\hat{a}_1^\dagger\hat{a}_1\rangle = \langle\hat{a}_2^\dagger\hat{a}_2\rangle = \sinh^2(|\kappa|T) \tag{3.23}$$

The population in the pairs must therefore increase exponentially with the duration of the lattice. Of course, this process will be limited by a saturation phenomenon, primarily related to the depletion of the condensate.

It is also possible to calculate the correlations between the emitted pairs. The local correlation (or auto-correlation) $g^{(2)}_{\mathrm{loc}} = g^{(2)}_{1,1} = g^{(2)}_{2,2}$ and the cross-correlation between the emitted pairs $g^{(2)}_{\mathrm{cross}} = g^{(2)}_{1,2}$ are given by

$$\begin{cases} g^{(2)}_{\mathrm{loc}} = \dfrac{\langle\hat{a}_1^\dagger\hat{a}_1^\dagger\hat{a}_1\hat{a}_1\rangle}{\langle\hat{a}_1^\dagger\hat{a}_1\rangle^2} = \dfrac{\langle\hat{a}_2^\dagger\hat{a}_2^\dagger\hat{a}_2\hat{a}_2\rangle}{\langle\hat{a}_2^\dagger\hat{a}_2\rangle^2} = 2 \\ \\ g^{(2)}_{\mathrm{cross}} = \dfrac{\langle\hat{a}_2^\dagger\hat{a}_1^\dagger\hat{a}_1\hat{a}_2\rangle}{\langle\hat{a}_1^\dagger\hat{a}_1\rangle\langle\hat{a}_2^\dagger\hat{a}_2\rangle} = 2 + \dfrac{1}{\langle N\rangle} \end{cases} \tag{3.24}$$

The normalized local correlation is equal to 2, which corresponds to bosonic bunching. Indeed, the pair creation process follows a thermal distribution, thus reproducing the Hanbury Brown and Twiss effect.

On the contrary, the cross-correlation is greater than 2, and increases as the average population decreases. This state intrinsically violates the Cauchy-Schwarz inequality, since $g^{(2)}_{\mathrm{cross}} > g^{(2)}_{\mathrm{loc}}$. Again, this suggests that we will have to work with a low population in the pairs in order to exhibit strong correlations.

3.1.4 Multimode description

In the previous discussion, we have only considered pairs (q_1, q_2) that strictly satisfy energy and momentum conservation. Thus, for a condensate at a given velocity in the lattice's reference frame, only two modes are emitted. In practice, this is not the case, and the previous reasoning must be generalized to the emission of pairs that do not strictly conserve energy and momentum. Indeed, the finite size of the BEC relaxes the momentum conservation condition, while the finite duration of the lattice relaxes the energy conservation.

The four-wave mixing Hamiltonian is then written in a more general form as follows:

$$\hat{H}_{\mathrm{FWM}} = \sum_{q_1,q_2} \hbar\kappa(q_1,q_2)\hat{a}^\dagger_{q_1}\hat{a}^\dagger_{q_2} + \hbar\kappa^*(q_1,q_2)\hat{a}_{q_1}\hat{a}_{q_2} \tag{3.25}$$

where the gain κ is given by

$$\kappa(q_1,q_2) = \frac{gN_0}{\hbar}\int \mathrm{d}^3\mathbf{r}\,\psi(q_0)^2\psi^*(q_1)\psi^*(q_2) \tag{3.26}$$

Numerical simulations were conducted by J. Ruaudel[122], and P. Dussarrat developed in his thesis a perturbative analytical multimode 1D model for a shallow lattice where the BEC density profile can be considered uniform[121]. Recently, P. Paquiez, intern in the team, conducted new numerical analyses to characterize the pair source with as few approximations as possible to best account for experimental observations[123]. In this paragraph, we will briefly summarize the results of the uniform analytical model, which provides valuable physical insights.

In this model, we can approximate the wavefunction of atoms with quasi-momentum q as plane waves restricted to the volume of the BEC, which allows for easy calculation of the gain:

$$\kappa(q_1,q_2) = \frac{gn_0}{\hbar}\,\mathrm{sinc}\left(\Delta q(q_1,q_2)\frac{L}{2\hbar}\right) \tag{3.27}$$

where

$$\Delta q(q_1,q_2) = 2q_0 - q_1 - q_2 \tag{3.28}$$

which is actually the conservation of quasi-momentum condition. This time, the modulo does not appear because in a multimode model, a given mode can *a priori* interact with all other modes. It can be shown that adding "by hand" a modulo $2\hbar k$ would lead to the emission of pairs when $V_0 = 0$, which is not physical.

Subsequently, by considering non-strict conservation of energy using a perturbative expansion (where the gain of the process is low, so that $\kappa T \ll 1$), we can show that the number of emitted atoms can be written as

$$N(q) = \int \frac{\mathrm{d}q'}{\delta q}|\kappa(q,q')|^2|\varepsilon(q,q')|^2 \tag{3.29}$$

where $\delta q = \frac{2\pi\hbar}{L}$ and

$$\varepsilon(q,q') = T\,\mathrm{sinc}\left(\Delta E(q,q')\frac{T}{2\hbar}\right) \tag{3.30}$$

with

$$\Delta E(q,q') = 2E(q_0) - E(q_1) - E(q_2) - 2gn_0 \tag{3.31}$$

The formula 3.29 illustrates that the deviation from both strict conservation of momentum and conservation of energy naturally intervene in the problem to weigh the emission of pairs. The functions κ and ε (and hence the number of emitted atoms) are maximal when the phase-matching conditions are strictly satisfied, but other modes are emitted due to the size L of the BEC and the duration T of the lattice.

Note that $\delta q = \frac{2\pi\hbar}{L}$ can be interpreted as the size of a (quasi)-momentum mode since it is the typical scale for the cancellation of the overlap integral between two wavefunctions:

$$\langle\Psi(q)|\Psi(q')\rangle = \int_{-L/2}^{L/2}\mathrm{d}z\,\mathrm{e}^{\frac{\mathrm{i}qz}{\hbar}}\,\mathrm{e}^{-\frac{\mathrm{i}q'z}{\hbar}} \propto \mathrm{sinc}\left((q-q')\frac{L}{2\hbar}\right) \tag{3.32}$$

We have seen that the typical length scale of the BEC in the vertical axis is on the order of 100 µm. For a lattice wavevector equal to 5.9 µm^{-1} like in our case, the size of a mode is then on the order of $\delta q = 0.01\,\hbar k_{\mathrm{lat}}$.

The density profile as a function of quasi-momentum is shown in Figure 3.4 with parameters close to the experimental ones. We clearly observe the predominance of two peaks, corresponding to the strict phase matching conditions. The peaks are much broader than the typical size of a mode, which also confirms that the pair source is highly multimode. Similarly to the previous toy model, the number of atoms emitted in pairs grows exponentially with the duration T of the lattice.

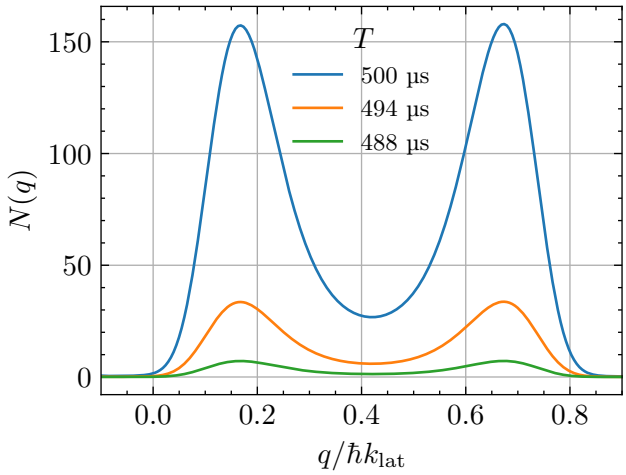

Figure 3.4: Density profile along the vertical direction. For each value of q, the number of atoms is calculated using the relation 3.29 with $q_0 = -0.58\hbar k_{\mathrm{lat}}$, $V_0 = 0.5E_{\mathrm{lat}}$ and a mean-field energy term with $n_0 = 1.6 \times 10^{13}\,\mathrm{cm}^{-3}$, for three values of T.

One can also determine the consequences of the multimode nature of the source on the correlations. The correlation functions can also be calculated analytically, provided that we assume a strict conservation of quasi-momentum (it can be showed numerically that the correlation decreases quickly when quasi-momentum is not conserved), and write:

$$\begin{cases} g^{(2)}_{\mathrm{loc}} = g^{(2)}(q_1, q_1 + \Delta q) = 1 + \mathrm{sinc}^2\left(\Delta q \dfrac{L}{2\hbar}\right) \\ g^{(2)}_{\mathrm{cross}} = g^{(2)}(q_1, q_2 + \Delta q) = 1 + \dfrac{1}{N(q_1)}\mathrm{sinc}^2\left(\Delta q \dfrac{L}{2\hbar}\right) \end{cases} \tag{3.33}$$

where $q_2 = 2q_0 - q_1$. Note that these expressions are only true in the limit where $N(q_1) \ll 1$ (which is why we do not find $g^{(2)} = 2$ when $N(q_1) \to \infty$).

Interestingly, we observe that the width of the correlation (both local and cross) is given by the size of a mode. For local correlation, this could be expected because it is essentially a Hanbury Brown and Twiss-type experiment, where the correlation width corresponds to the coherence length of the source. We can use this relation to experimentally determine the size of a mode, which in our case is inversely proportional to the size of the BEC. We can then use this parameter as a control parameter to adjust the size of a mode, making our source more or less multimode. As we will see later, an advantage of having a multimode source is the ability to perform multiple interferometers in parallel. It is worth noting that the width of the cross-correlation is the same as that of the local

correlation, suggesting that a mode is correlated with only one other mode, given by the quasi-momentum conservation.

We can still expect to observe stronger cross-correlations than local correlations, allowing us to observe a violation of the Cauchy-Schwarz inequality.

3.2 Experimental procedure and results

3.2.1 Experimental procedure

We use a laser at 1064 nm, far detuned from the atomic transition $2^3S_1 \rightarrow 2^3P_2$, in order to neglect spontaneous emission when using long pulses on the order of a millisecond. Typical parameters used for the optical lattice are given in Table 3.1.

Quantity	Symbol	Value
Wavelength	λ_{lat}	1064 nm
Angle between the beams	θ	83°
Lattice wavevector	$k_{\text{lat}} = \frac{2\pi}{\lambda_{\text{lat}}} \sin\theta$	$5.9\,\mu\text{m}^{-1}$
Lattice periodicity	$a_{\text{lat}} = \frac{\pi}{k_{\text{lat}}}$	536 nm
Detuning with the excited state	$\Delta = c\left(\frac{1}{\lambda_{\text{lat}}} - \frac{1}{\lambda}\right)$	4.9 THz
Lattice depth	V_0	$0.5E_{\text{lat}}$
Lattice duration	T	$\approx 400 - 800\,\mu\text{s}$
Lattice detuning	δ	$\approx 100\,\text{kHz}$
Lattice speed	$v_{\text{lat}} = \frac{\delta}{2k_{\text{lat}}}$	$53\,\text{mm.s}^{-1}$
BEC quasi-momentum (lattice frame)	$q_0 = \frac{m\delta}{2\hbar k_{\text{lat}}}$	$-0.58\,k_{\text{lat}}$

Table 3.1: Typical values used for the pair creation lattice.

After alignment onto the atoms, we can perform Rabi oscillations between two (ground) momentum states by using the two beams in the Bragg regime (the principle of which will be detailed in the next chapter). One can indeed exhibit an oscillation of the population in each state as a function of the lattice duration. This experimentally allows to determine the depth of the lattice, given simply by the relation

$$V_0 = 2\hbar\Omega \tag{3.34}$$

where Ω is the effective two-photon Rabi frequency of this process.

The detuning δ between the two beams is controlled by two acousto-optic modulators (AOMs), each of which receives an RF frequency generated by a synthesizer. The power of the beams is also controlled by the AOMs because the RF signals pass through RF attenuators, allowing us to modulate the signal amplitude.

The lattice is switched on when the BEC is in the optical dipole trap, because the high density in the cloud makes it possible to have enough collisions for the four-wave mixing to be efficient. Note that the power of the lattice beams increases adiabatically, in order

to smoothly load the atoms in the lowest energy band of the lattice. This rising time is of the order of 50 µs.

The lattice is then maintained at constant power for a duration T on the order of several hundred microseconds, during which the pair creation process occurs. Varying this duration allows control over the number of emitted atoms per momentum mode.

Then, the beams are turned off adiabatically, so that the Bloch's states in the lattice associated to atoms of quasi-momentum q are slowly projected onto free space plane waves of momentum p. This band mapping is efficient due to the fact that the lattice depth is quite shallow so that Bloch's states and plane waves match well. In the following, we will consider that a mode emitted with a quasi-momentum q in the lattice reference frame is exactly projected into an atom with momentum $p = q - q_0$ in the laboratory reference frame.

Experimentally, it is observed that the rising duration and the extinction duration have a non-trivial influence on the density profile of emitted atoms, particularly in the transverse plane where complex structures may appear. In practice, these two durations are empirically adjusted to ensure that the density profile is anisotropic and denser at the center. A more quantitative discussion on the adiabaticity condition and the influence of ramps can be found in references [115], [121] and [41].

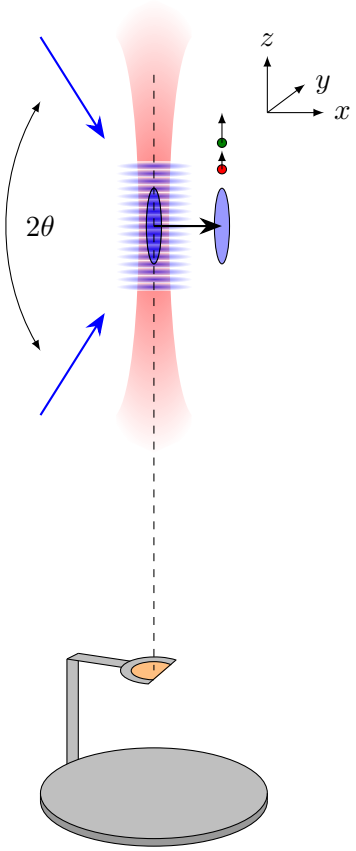

Figure 3.5: Schematic representation of the process of emission and detection of pairs. The BEC (in blue) is trapped in an optical dipole trap (in red) and subjected to an optical lattice, leading to the emission of a pair of atoms (red and green dots). After switching off the trap, the atoms and the condensate are kicked along the x-axis by a Raman transfer (black arrow), to move away from the copper plate beam dump before falling onto the MCP (in gray).

Once the pairs are emitted and the lattice is turned off, the optical dipole trap is switched off abruptly. Right after, a Raman transfer is performed so that most of the atoms are transferred into the $m = 0$ state, insensitive to the magnetic field, with an additional momentum along x, which makes it possible to detect them on the MCP after time of flight next to the "shadow" of the copper beam dump (Figure 3.5).

3.2.2 Density and phase-matching

As mentioned previously, due to various experimental issues, a long time has passed between the last pair production runs on the experiment in 2017 and the reinstallation of the lattice in the spring of 2022. At that time, we initially worked in a regime where many pairs were emitted per mode compared to the values used previously.

In the spring of 2023, for a new set of pair data collection, the atom population was reduced to approach a quantum behavior that could lead to the observation of non-classical correlations.

We typically obtain the density profiles depicted in Figures 3.6 and 3.7. We clearly observe two main peaks, as predicted by energy and momentum conservation (see Figure 3.4). These peaks are broad and contain many modes, as expected. In this example, atoms from the pairs fall after the BEC, but we can also change the sign of the detuning, so that q_0 is positive: this way, the folding of the quasi-momentum in the first Brillouin zone occurs in the opposite direction, so that q_1 and $q_2 < q_0$, and the pairs fall before the BEC.

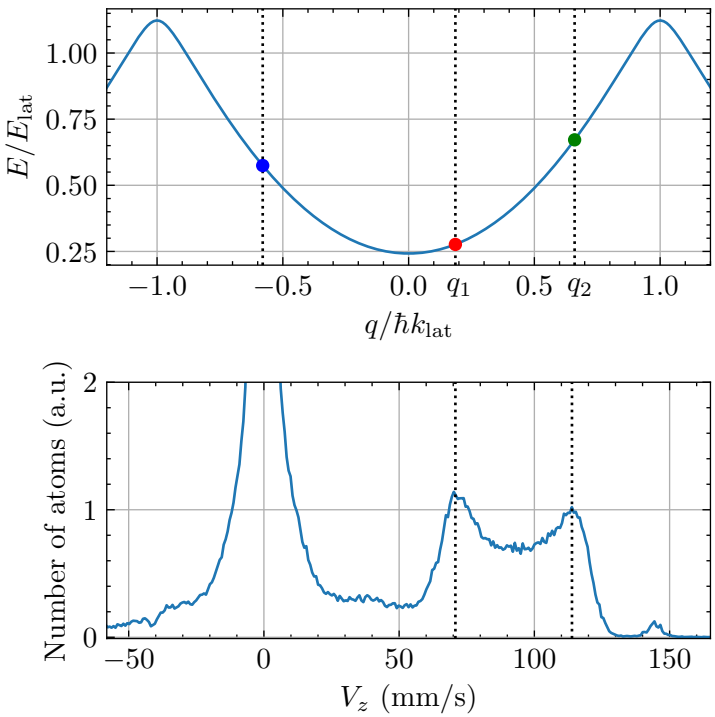

Figure 3.6: Density profile along the vertical direction. Up: fundamental band of atoms in the lattice ($V_0 = 0.5E_{\mathrm{lat}}$). Down: Number of atoms measured as a function of their velocity before time of flight. Data averaged over 1600 runs, and integrated along the transverse directions. The BEC corresponds to a zero velocity in the laboratory frame.

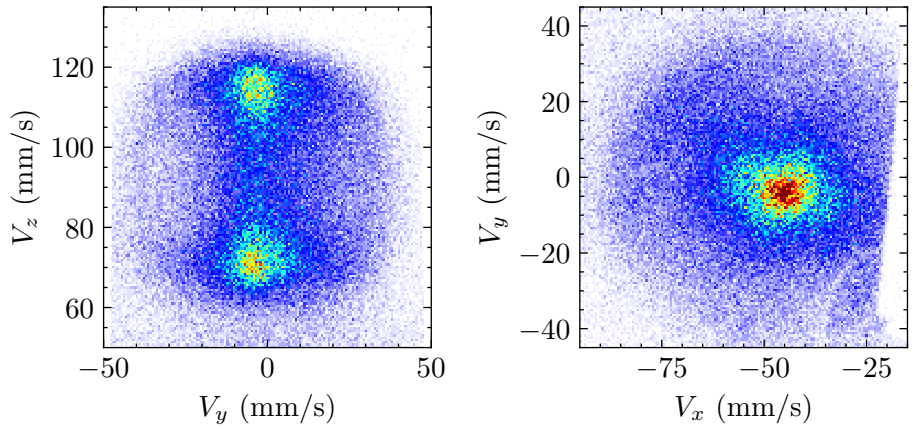

Figure 3.7: Density profiles of the emitted pairs. 2D histograms of the pairs' density in momentum space. Data averaged over 1600 runs, and integrated along the third direction.

From a BEC at $q_0 = -0.58\,\hbar k_{\mathrm{lat}}$, we get the values of q_1 and q_2 from a fit of the density peaks. We find $q_1 = 0.19 \pm 0.02\,\hbar k_{\mathrm{lat}}$ and $q_2 = 0.66 \pm 0.02\,\hbar k_{\mathrm{lat}}$, which are compatible with quasi-momentum conservation. In the BEC reference frame, the pairs velocities are $V_1 = 70.8\,\mathrm{mm.s^{-1}}$ and $V_2 = 113.9\,\mathrm{mm.s^{-1}}$. The expected values given by the phase matching conditions depend on the BEC density through the mean field term in the energy conservation (equation 3.18).

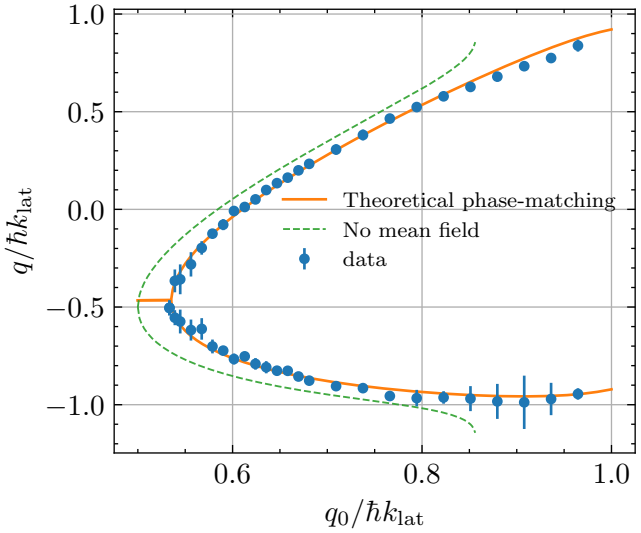

Figure 3.8: Experimental phase-matching diagram. Quasi-momenta of the pairs as a function of the quasi-momentum of the BEC. The pairs momenta were determined with Gaussian fits of the density profile and converted in quasi-momentum in the lattice reference frame. The orange and green lines depict the numerical resolution of the phase matching conditions, with $V_0 = 0.54 E_{\mathrm{lat}}$ (a value determined by a two-photon Rabi oscillation of the lattice beams), in the case where interactions are not considered (green dashed line) and in the case where we add a mean-field term $2gn_0$ in the energy conservation, with $n_0 = 1.3 \times 10^{13}\,\mathrm{cm^{-3}}$.

As we have seen, changing the detuning allows us to vary q_0. By scanning the detuning, one can then plot the phase matching graph, which shows the emitted modes as a function of q_0. The results are given Figure 3.8 in the lattice reference frame, along

with the theoretical predictions for the quasi-momenta of the emitted pairs without mean-field (green curve) and with a mean-field term determined with a fit. The values of q_1 and q_2 were estimated using Gaussian fits to the density envelope of pairs along the z-axis.

This measurement enables to estimate the atom density n_0 in the condensate using the mean-field term that appears in the energy conservation condition. The fit result leads to a density $n_0 = 1.3 \pm 0.2 \times 10^{13}\,\mathrm{cm}^{-3}$. This value is the expected order of magnitude and corresponds to what was first measured in 2013[20].

The ability to tune the momentum of emitted atoms represents a major advantage of this pair creation technique. Indeed, by simply changing the detuning, one can select which momentum modes are most populated. Thus, we benefit from a tunable multimode source of pairs, a property that can be leveraged for experiments such as HOM and Bell. In the laboratory frame, if one specifically chooses the value of δ (hence q_0) for which the difference $p_2 - p_1$ between pairs corresponds to the momentum transferred by a Bragg pulse, then this ensures that the momentum classes coupled by Bragg are those that best satisfy the phase matching conditions. This not only ensures that the coupled modes are the most populated, but also aims to involve pairs with the strongest correlations.

3.3 Second order correlation fonctions

Studying correlations between pairs is a preliminary step to ensure that our atom beams can be used for a Bell test or any other experiment aiming to exhibit stronger-than-classical correlations. This not only provides an estimation of the strength of cross-correlations by examining the second-order correlation function between the atoms from a pairs, but it also experimentally helps us determine the size of a mode (and thus the population of atoms per mode) by examining the width of the local correlation.

In the following sections, we will present typical correlation results obtained over the past months.

3.3.1 Correlations computation

Let us recall that the definitions of the correlation functions between atoms of speeds V_1 and V_2, respectively non normalized and normalized, are

$$G^{(2)}(V_1, V_2) = \langle \hat{a}^\dagger_{V_1} \hat{a}^\dagger_{V_2} \hat{a}_{V_2} \hat{a}_{V_1} \rangle = \langle : \hat{N}_{V_1} \hat{N}_{V_2} : \rangle \tag{3.35}$$

$$g^{(2)}(V_1, V_2) = \frac{\langle \hat{a}^\dagger_{V_1} \hat{a}^\dagger_{V_2} \hat{a}_{V_2} \hat{a}_{V_1} \rangle}{\langle \hat{a}^\dagger_{V_1} \hat{a}_{V_1} \rangle \langle \hat{a}^\dagger_{V_2} \hat{a}_{V_2} \rangle} = \frac{\langle : \hat{N}_{V_1} \hat{N}_{V_2} : \rangle}{\langle \hat{N}_{V_1} \rangle \langle \hat{N}_{V_2} \rangle} \tag{3.36}$$

where the notation $\langle : \cdots : \rangle$ indicate the normal ordering of the annihilation and creation operators. Here, we suppose that V_1 and V_2 correspond to speeds along the vertical direction.

Of course, the value of the non normalized correlation function depends on the population, and thus on the density envelope, whereas this is not the case for the normalized correlation function. Therefore, in our study, we will prefer to use this second quantity, which does not depend on the quantum efficiency of the detector (which is presumably around 50% but has not been precisely determined to date). We have already seen that the value of $g^{(2)}_{\mathrm{loc}}$ should be equal to 2 for pairs emitted via a thermal distribution process.

Similarly, the value of cross-correlation $g^{(2)}_{\text{cross}}$ should be equal to $2 + 1/\langle N \rangle$, where $\langle N \rangle$ is the number of atoms per mode.

There are different ways to represent correlations and to compute them. This is not a straightforward issue: although the previous definitions were given in one dimension (along z which is the axis of interest for us), the $g^{(2)}$ function depends on 6 variables, corresponding to the momentum coordinates of two vectors $\mathbf{V}_1$ and $\mathbf{V}_2$. It is necessary to simplify the problem by eliminating dimensions, which is usually done by averaging over certain regions of the momentum space, but one has to ensure that a sufficient signal with a correct signal-to-noise ratio can be obtained.

Counting atoms in momentum boxes

A first way to verify that the correlations correspond to what is expected and to identify modes that are correlated with each other is to create a two-dimensional map showing $g^{(2)}$ as a function of V_1 and V_2. In the pairs center of mass reference frame (i.e. in the frame where the velocity reference is located at the midpoint of the segment separating the two density peaks), the diagonal then corresponds to the local correlation $g^{(2)}(V_1, V_1)$, while the anti-diagonal corresponds, in principle, to correlated modes.

For this purpose, we define an integration volume, which corresponds to a three-dimensional box in momentum space, within which we count the detected atoms. Since the MCP provides us with a list (V_x, V_y, V_z) of 3D momenta corresponding to the detected atoms per cycle, it is easy to determine if an atom belongs to a certain range of three-dimensional velocity, and thus to calculate the number of atoms in that case.

A box corresponds to specifying three widths ΔV_x, ΔV_y and ΔV_z and three centers V_x, V_y, and V_z in each direction, so the volume in momentum space is given by:

$$\mathcal{V} = \left[V_x - \frac{\Delta V_x}{2}, V_x + \frac{\Delta V_x}{2}\right] \times \left[V_y - \frac{\Delta V_y}{2}, V_y + \frac{\Delta V_y}{2}\right] \times \left[V_z - \frac{\Delta V_z}{2}, V_z + \frac{\Delta V_z}{2}\right] \quad (3.37)$$

In each experimental cycle, we then calculate, within two boxes centered on velocities V_{z_1} and V_{z_2}, the number of atoms $N(V_{z_1})$ and $N(V_{z_2})$, as well as the product $N(V_{z_1}) \times N(V_{z_2})$. The center of the boxes in the transverse directions $V_{x_1} = V_{x_2}$ and $V_{y_1} = V_{y_2}$ are chosen to match the peak density of the emitted pairs. After repeating this process for all cycles, we compute the average of these three quantities, from which we derive the value of $g^{(2)}$, according to the relations

$$\begin{cases} g^{(2)}(V_{z_1}, V_{z_2}) = \dfrac{\langle N(V_{z_1}) N(V_{z_2}) \rangle}{\langle N(V_{z_1}) \rangle \langle N(V_{z_2}) \rangle} \\ g^{(2)}(V_{z_1}, V_{z_1}) = \dfrac{\langle N(V_{z_1})^2 \rangle}{\langle N(V_{z_1}) \rangle^2} - \dfrac{1}{\langle N(V_{z_1}) \rangle} \end{cases} \quad (3.38)$$

where $\langle \cdots \rangle$ designates the average over all cycles. In the case of the auto-correlation, we need to subtract a term corresponding to the shot noise.

The choice of the integration volume is particularly important.

- If the integration volume is small, then there will be, on average, few atoms per box, leading to significant noise and requiring a large number of experimental cycles

to achieve a good signal-to-noise ratio. Since modes have a certain width, it is essential not to choose a box with a width much smaller than the size of the mode, as this would result in losing information about the correlation. Additionally, the computation time can be long, and significant memory depth is required for storing the lists $N(V_{z_i})$ and $N(V_{z_i})N(V_{z_j})$ for each cycle.

- If the integration volume is too large, especially larger than the size of a mode, then there is a risk of averaging atoms that are not correlated, leading to a decrease in the correlation signal.

In practice, the optimal box size corresponds roughly to the size of a mode. To probe the correlation along a particular axis, in our case the vertical axis, one can choose boxes along z slightly smaller than the size of a mode. For ease of reading $g^{(2)}$ maps, it is also possible to oversample by scanning V_z with a step smaller than the size of the box along this axis.

A typical example of a $g^{(2)}$ map obtained using this method is shown in Figure 3.9. We have placed ourselves in the pair reference frame, in which atoms with velocity V_{z_i} are presumed to be correlated with atoms with velocity $-V_{z_i}$.

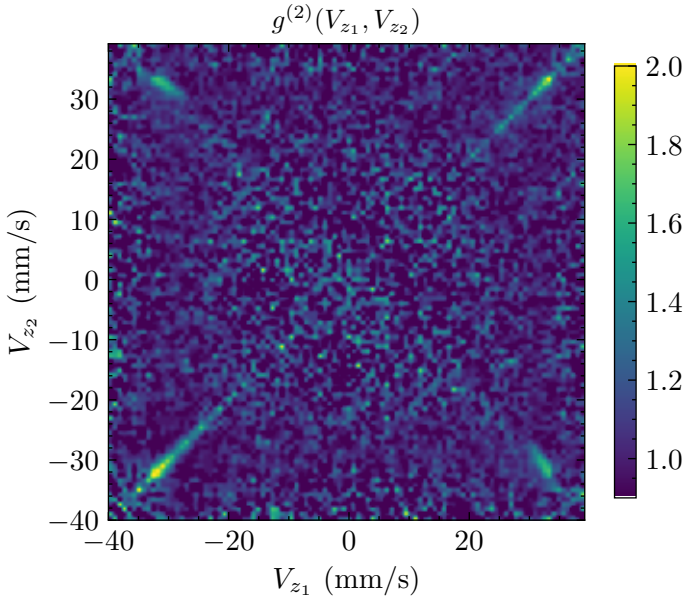

Figure 3.9: 2D Correlation map in the pairs reference frame. The integration boxes are $\Delta V_z = 1\,\mathrm{mm.s^{-1}}$, $\Delta V_x = \Delta V_y = 10\,\mathrm{mm.s^{-1}}$. The map is symmetric with respect to the exchange $V_{z_1} \leftrightarrow V_{z_2}$. The diagonal corresponds to $V_{z_1} = V_{z_2}$, highlighting local correlations, and the antidiagonal corresponds to $V_{z_1} = -V_{z_2}$, highlighting cross-correlations. Dataset of 1012 experimental runs.

In this example, the density peaks are located at $\pm 32\,\mathrm{mm.s^{-1}}$, which can be seen on the map, where the signal-to-noise ratio is better between 25 and 35 $\mathrm{mm.s^{-1}}$ than between 0 and 20 $\mathrm{mm.s^{-1}}$. This map was obtained with a dataset with a significant number of atoms per mode, as we will see later.

A diagonal line corresponding to auto-correlation and an anti-diagonal line corresponding to cross-correlations are observed, while the average value of the rest of the map (apart from these lines) is around 1, validating the overall appearance of the graph in light of the

expected results. Thus, our atom source produces atoms correlated in momentum. However, it is noteworthy that the cross-correlation is not greater than the local correlation, which seems to tend towards 2 as expected. Indeed, as previously observed in the team, we never manage to demonstrate a cross-correlation greater than 1.5. This point will be discussed in the following.

In order to make the analysis more quantitative and get the correlation amplitude and width (to deduce the mode size), we can then plot one-dimensional curves from the $g^{(2)}$ map. To calculate the local $g^{(2)}$ curve, for example, the idea is to integrate the correlation signal with diagonal slices at constant $V_{z_1} - V_{z_2}$ in a certain velocity range (in the zone of maximum density, for example) and plot the averaged value along an anti-diagonal axis. The result is a curve showing $g^{(2)}$ as a function of $V_{z_1} - V_{z_2}$.

Note that this integration operation is performed on the non normalized $G^{(2)}$ map, and converted into $g^{(2)}$ by performing the same integration on the densities, otherwise the correlation signal decreases. Mathematically, this corresponds to calculating an integrated $g^{(2)}$ as

$$g^{(2)}_{\mathrm{loc}}(\delta V_z = V_{z_1} - V_{z_2}) = \frac{\int_\Omega \langle \hat{a}^\dagger_{V_z} \hat{a}^\dagger_{\delta V_z - V_z} \hat{a}_{\delta V_z - V_z} \hat{a}_{V_z} \rangle \, \mathrm{d}V_z}{\int_\Omega N(V_z) N(\delta V_z - V_z) \mathrm{d}V_z} \tag{3.39}$$

where Ω is the integration volume in momentum space.

One can proceed similarly in the opposite direction to plot the cross-correlation function, by integrating the correlation along anti-diagonal slices at constant $V_{z_1} + V_{z_2}$ in a given velocity range and plotting the averaged value along a diagonal axis. In this case, one gets $g^{(2)}$ as a function of $V_{z_1} + V_{z_2}$, so that

$$g^{(2)}_{\mathrm{cross}}(\delta V'_z = V_{z_1} + V_{z_2}) = \frac{\int_\Omega \langle \hat{a}^\dagger_{V_z} \hat{a}^\dagger_{\delta V'_z - V_z} \hat{a}_{\delta V'_z - V_z} \hat{a}_{V_z} \rangle \, \mathrm{d}V_z}{\int_\Omega N(V_z) N(\delta V'_z - V_z) \mathrm{d}V_z} \tag{3.40}$$

Note that $\delta V'_z = 0$ when $V_{z_1} = -V_{z_2}$, corresponding to the anti-diagonal where we expect to find the cross-correlation in the pair reference frame.

Loops over the detected atoms

There is another method for calculating correlations, this time without using boxes, but rather by directly determining, for each atom, the histogram of velocity differences. This method is described in the theses of M. Schellekens[124], H. Cayla[125] or in reference [126]. This second way of computing the correlation, potentially longer in computation time, has the advantage of increasing the signal-to-noise ratio: in the previous method, by defining small density boxes, one potentially excludes correlated atoms that lie beyond the box boundaries, whereas they can be taken into account in this second approach.

The idea is to consider the correlation function $g^{(2)}(\delta V_z)$ as a histogram of the velocity difference between atoms. Once again, we calculate separately the numerator and denominator of the normalized correlation function. The numerator calculation proceeds as follows:

- Consider a dataset containing N_{runs} experimental cycles, and suppose we want to determine the correlation function along z. We start by defining two large density

regions (in three dimensions), corresponding to the two pairs of beams created with the lattice, denoted A and B, defining subsets A and B.

- For a given experimental cycle, we choose an atom labeled 1 in beam A, for example. Then we select another atom labeled 2 (in subset A if we want to study local correlations, or subset B if we want to study cross-correlations).

- We define velocity difference thresholds ΔV_x and ΔV_y such that if $|V_{x_1} - V_{x_2}| \leq \Delta V_x$ and $|V_{y_1} - V_{y_2}| \leq \Delta V_y$, then we note $\delta V_z = |V_{z_1} - V_{z_2}|$ and increment a histogram $H_1(\delta V_z)$ (or similarly $\delta V_z' = |V_{z_1} + V_{z_2}|$ if one aims at plotting the cross-correlation).

- We repeat the previous operation for all atoms 2 of subset B: we obtain a full histogram of velocity differences $H_1(\delta V_z)$ with respect to atom 1.

- We choose a new atom 1 in subset A and repeat the operation to obtain a new histogram of velocity differences. We then obtain a set of histograms for all atoms, which we average to obtain the histogram $H_{\mathrm{r}}(\delta V_z)$ of velocity differences between the two beams for one experimental run:

$$H_{\mathrm{r}}(\delta V_z) = \sum_{i=1}^{N_{\mathrm{runs}}} \frac{H_{1,i}(\delta V_z)}{N_A} \tag{3.41}$$

- We repeat the operation for each experimental cycle and then average the obtained histograms. The resulting histogram gives the non normalized correlation function $G^{(2)}$ as a function of the velocity difference δV_z.

The binning δV_z of the histogram along z plays a similar role as the size of the box along z in the previous algorithm: if the binning is too small, the signal-to-noise ratio is low, and if it is too large, there is a risk of decreasing the correlation amplitude. The transverse thresholds ΔV_x and ΔV_y also help increase the correlation signal: the smaller they are, the more assured we are of counting atoms whose velocity difference is small, indicating potential correlation. However, this also reduces the signal-to-noise ratio. This second method for computing the correlation converges towards the first when selecting density beams A and B that are the size of a box.

Note that the algorithm developed in the team according to this method by V. Gondret allows for performing the previous operation directly in all three spatial directions, by storing a three-dimensional array $G^{(2)}(\delta V_x, \delta V_y, \delta V_z)$. This enables obtaining correlations along each axis by integrating over the other two while considering the corresponding thresholds.

The calculation of the denominator is performed in the same way as the numerator, but with a dataset where atoms do not exhibit correlations and have the same average density. Indeed, we have $\langle N(V_{z_1})N(V_{z_2})\rangle = \langle N(V_{z_1})\rangle \langle N(V_{z_2})\rangle$ in the case where we consider independent atoms. To achieve this, we mix the different experimental cycles into a large dataset containing all atoms. The calculation of $G^{(2)}$ is the same as the numerator, except that for an atom from a given experimental run, atoms from the same run are not considered (to ensure they do not introduce correlations). Even without this precaution, with a sufficient number of runs, the correlations arising from atoms from the same run are negligible, allowing to proceed with the previous calculation to determine the denominator.

In practice, as this procedure can be very time-consuming, it is possible to randomly select a subset of the mixed dataset. We can then deduce the normalized correlation function by dividing the histogram of the numerator by that of the denominator, and multiplying the result by a normalization factor as the total number of atoms involved in the calculation of the denominator differs from that of the numerator.

Computing the error bars: bootstrapping technique

We need a way to estimate the uncertainty on the computed correlation values. Suppose we want to determine an error bar on the $G^{(2)}$ function from a dataset of N_{runs} experimental runs. One method is to express the error bars as the inverse of the square root of the number of events per bin.

Alternatively, one can use a technique called bootstrapping[127], which works as follows: for each run, we perform a random sampling *with replacement* with the same number of atoms as the original run. From this sampled run, we then calculate the value of G2. We repeat this process a certain number of times, and the error bar is then given by the standard deviation of all the $G^{(2)}$ values obtained in this manner. One can check that the error bar converges towards a value which is not very different from the one given by the inverse of the square root of the number of atoms.

This technique can be applied to the calculation of other statistical quantities as well.

3.3.2 Auto-correlation

The results showing the local correlation functions are presented in Figure 3.10. They were computed using the second method on the same dataset as those appearing on the $g^{(2)}$ map. Error bars are evaluated using bootstrapping. Note that the curves are symmetric because we actually plot $g^{(2)}(|\Delta V|)$. Beam A corresponds to the density peak center on $-32\,\text{mm.s}^{-1}$ while beam B corresponds to the density peak center on $+32\,\text{mm.s}^{-1}$.

Clear local correlations are observed in all three spatial directions. The data are fitted with Gaussian functions written as follows:

$$g^{(2)}_{\text{fit}}(|\Delta V_i|) = 1 + A_i\, \mathrm{e}^{-\frac{(\Delta V_i)^2}{2(\sigma_i)^2}} \tag{3.42}$$

where A_i and σ_i correspond to the amplitude and width of the correlation, respectively.

As mentioned previously, we expect A_i to reach 1 for the local correlation when $\Delta V_i = 0$. This is not exactly the case, although the value of the correlation clearly exceeds 1.5. This can be explained by the fact that what we compute is an average over atoms whose velocity difference is not exactly zero.

This effect can be easily highlighted by gradually reducing the velocity difference thresholds, as depicted in Figure 3.11. Of course, this has the effect of decreasing the signal-to-noise ratio, but successive fits show that the amplitude A_i tends toward 1 in each case as the size of the integration volume in the transverse plane is reduced.

This validates our HBT-like experiment, which clearly demonstrates that the local correlation tends toward 2 as ΔV approaches zero. We can then use this measurement to determine the size of a mode using the width of the correlation function.

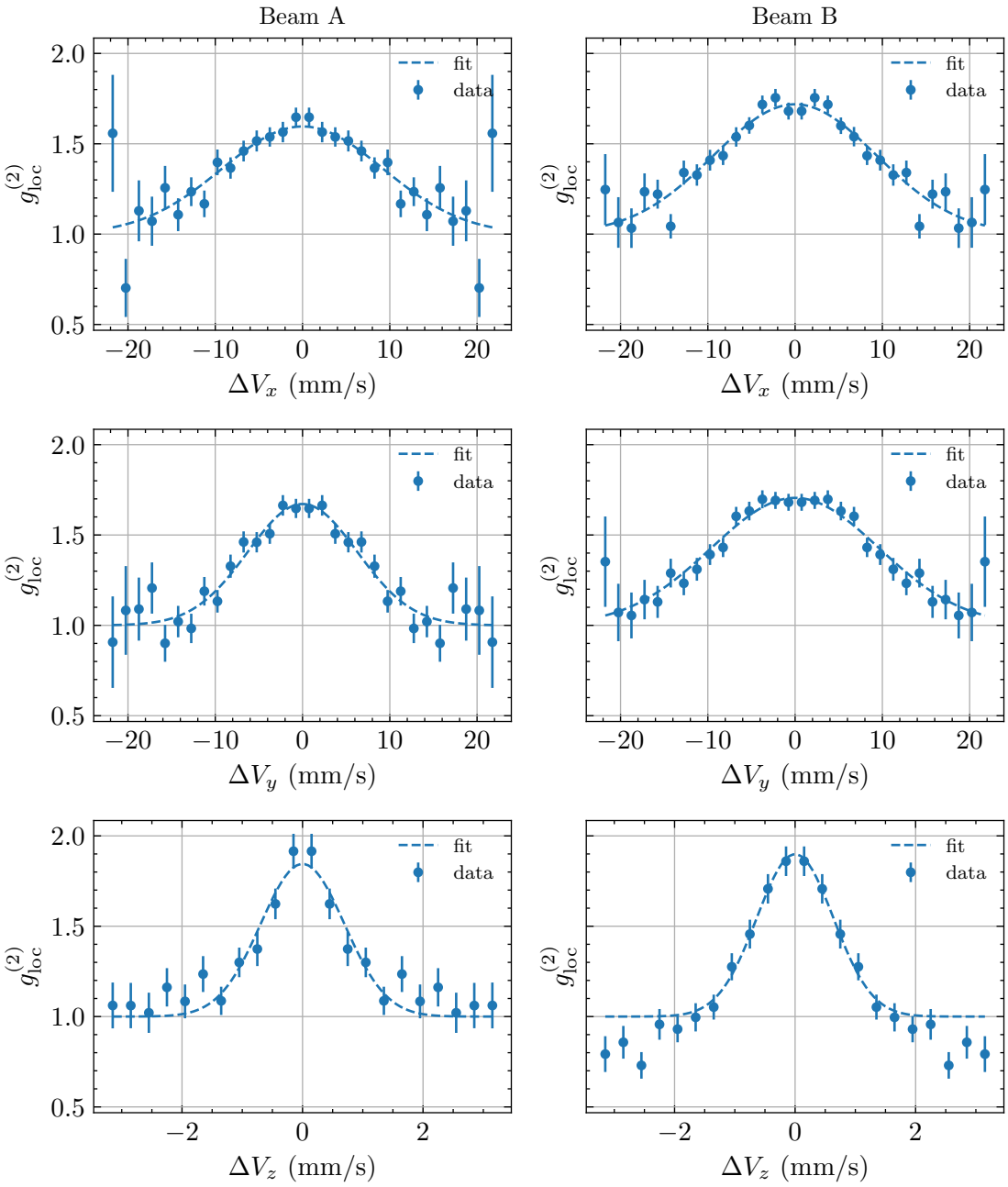

Figure 3.10: Normalized local correlation functions. The $g^{(2)}$ function is calculated using the velocity difference histogram algorithm. The histogram is calculated for both atomic beams A (left) and B (right) and in each direction, using a velocity difference threshold in the other axes of $\Delta V_{x,y} = 2\,\mathrm{mm.s^{-1}}$ and $\Delta V_z = 1\,\mathrm{mm.s^{-1}}$. Dataset of 1012 experimental runs.

Again, it is important to note that both the width of the correlation and the amplitude, depends on the integration range. Therefore, we will consider the width of the correlation as the value toward which σ_i tends when ΔV approaches zero. Although it is expected that the amplitude size of the correlation depends on the integration range in the other directions (since uncorrelated atoms are taken into account if the velocity difference is too large), it is not obvious to understand why this is also the case (to a lesser extent) for the correlation function widths.

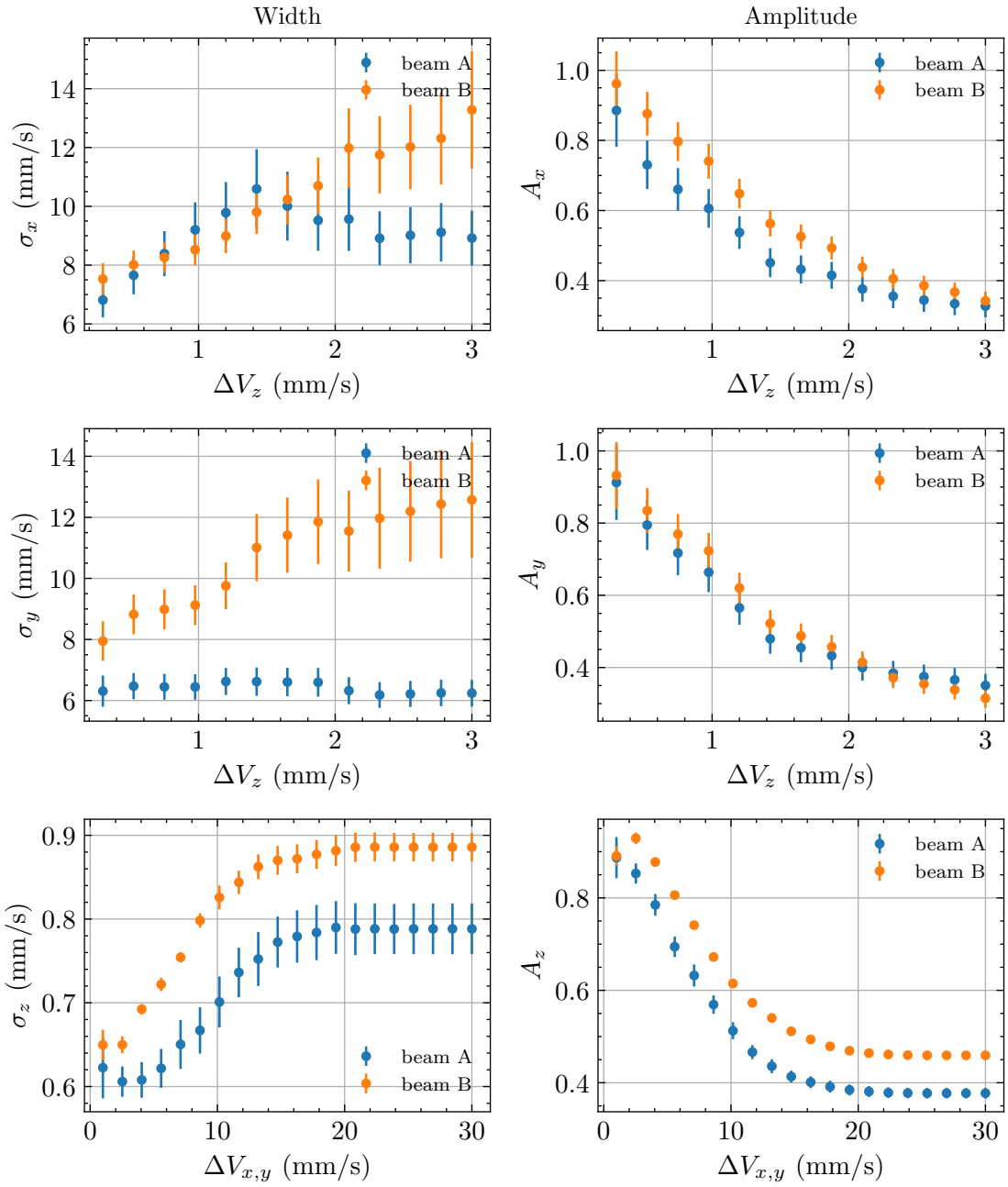

Figure 3.11: Effect of the integration thresholds on the correlation amplitude and width. Each point corresponds to a 1D correlation function similar to that plotted in Figure 3.10, for which a Gaussian fit was performed to determine both the width σ_i and the amplitude A_i of the $g^{(2)}$ function. The velocity difference threshold is scanned along z for the correlation functions along x and y, while it is varied along x and y for the correlation functions along z.

The results providing the sizes of the modes and the amplitudes for $\Delta V = 0$ are presented in Table 3.2, estimated from the curves in Figure 3.11. Slight differences are observed between beams A and B, but in the transverse plane, the correlation widths in x and y for the same beam are identical.

Since we have estimated that the size of a mode is inversely proportional to the size of the BEC in the corresponding direction, we should recover the ratio between the oscillation frequencies from the ratio between the mode sizes. As seen above, the oscillation

Quantity	Beam A	Beam B
σ_x (mm.s^{-1})	6.5 ± 0.6	7.4 ± 0.6
σ_y (mm.s^{-1})	6.2 ± 0.6	7.5 ± 0.7
σ_z (mm.s^{-1})	0.61 ± 0.06	0.65 ± 0.05
$\sigma_{x,y}/\sigma_z$	10.4 ± 0.8	11.5 ± 0.7
A_x	0.95 ± 0.08	1.00 ± 0.08
A_y	0.92 ± 0.08	0.96 ± 0.08
A_z	0.93 ± 0.07	0.92 ± 0.13

Table 3.2: Local correlation results.Values obtained by when the velocity difference thresholds tend towards zero.

frequencies $\omega_{x,y} = 2\pi \times 870\,\text{Hz}$ and $\omega_z = 2\pi \times 78\,\text{Hz}$ were estimated, giving a ratio of the order of 11.2, which is compatible with the ratio found between the transverse correlation width and the correlation width along z.

It is not particularly straightforward to determine the absolute size of a mode from the width of the correlation. The analytical model suggested a sinc^2-shaped correlation resulting from many approximations. We performed Gaussian fits to account for the correlation width, but in some cases, it is empirically observed that Lorentzian fits are sometimes more appropriate for describing the correlation evolution. It should be noted that there is an alternative way to determine the size of a mode by studying the pair emission statistics, which will be addressed in section 3.4.1.

3.3.3 Cross-correlation

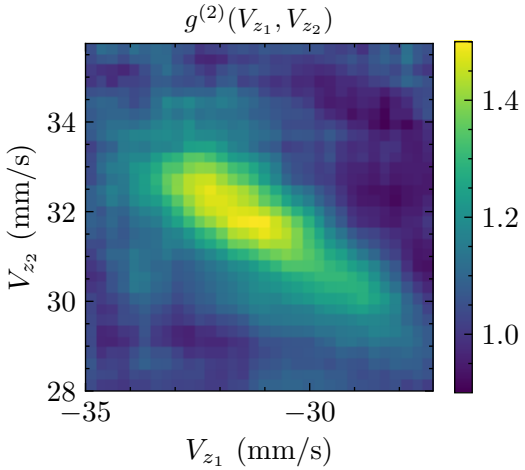

Figure 3.12: Cross-correlation map. The integration boxes are $\Delta V_z = 1\,\text{mm.s}^{-1}$, $\Delta V_x = \Delta V_y = 10\,\text{mm.s}^{-1}$. The calculation step is four times smaller than the size of a box, meaning that the data is oversampled. Dataset of 1012 experimental runs.

Next, we can analyze the cross-correlation between pairs from beam A and those from beam B. A zoom-in on the $g^{(2)}$ map presented earlier is shown in Figure 3.12, clearly indicating a cross-correlation along an antidiagonal. For our future Bell test, it is important to note that we observe a significant cross-correlation signal over a range of several mm.s^{-1}, indicating coupling between multiple modes. We can then use this source

as a reservoir of correlated pairs that can be used in a four-mode Bell-type interferometer in a Rarity-Tapster configuration (this point will be presented in details in section 4.1.1).

The 1D cross-correlation signal (in the z direction) is depicted in Figure 3.13. In practice, cross-correlation can also be discerned in other directions, but with a poor signal-to-noise ratio that does not make it possible to conduct a quantitative analysis. However, along the z direction, we typically obtain the curve shown in the figure, where a clear cross-correlation is observed, reaching up to 1.4 ± 0.2 as $\Delta V'$ tends towards zero.

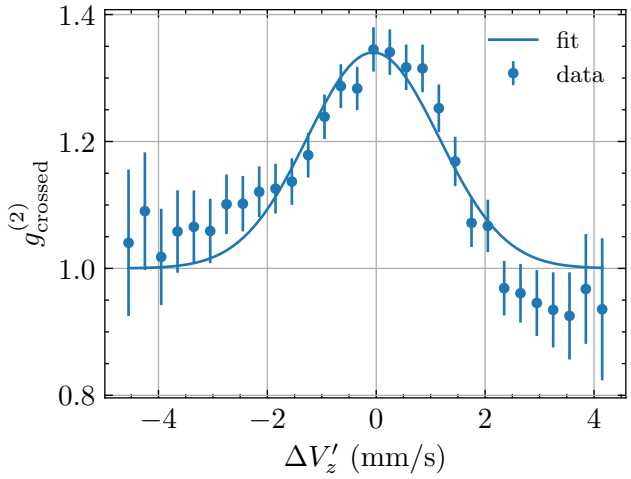

Figure 3.13: Normalized cross-correlation function along z. The transverse velocity difference threshold is $\Delta V_{x,y} = 3\,\text{mm.s}^{-1}$.

Theoretically, it was predicted that for a two-mode squeezed state, the cross-correlation should rise to $2 + 1/\langle N \rangle$, where $\langle N \rangle$ is the mean number of atoms per mode. However, we never measure a signal greater than 1.5, and the cross-correlation is systematically weaker than the local correlation. Data taken with a low atom population did not increase the value of the observed correlation signal. This may suggest that the pair creation model differs from the one presented previously, and that the system's state cannot truly be approximated by a superposition of TMS states. However, it is worth noting that the maximum value obtained in our case is higher than the values obtained by the team a few years ago, which exhibited correlations on the order of 1.2.

Noticeably, the width of the cross-correlation is larger than the width of the local correlation in all datasets we have taken, with different population regimes. Here, we find $\sigma_{z,\text{crossed}} = 1.21 \pm 0.08\,\text{mm.s}^{-1}$. The reasons behind this observed effect are not known: is one mode actually correlated with multiple others? Is there a mechanism between pair creation and detection that diminishes the amplitude of correlation but widens it?

It is possible that this effect is partly due to fluctuations in the arrival time of the condensate. Indeed, if q_0 varies, then the doublet (q_1, q_2) of correlated atoms differs. This effect is not visible in local correlations (since q_1 is always coupled to q_1, regardless of q_0), but it may be responsible for the broadening of the cross-correlation. A thorough analysis was conducted by rescaling, for each experimental run, the velocity reference with respect to the arrival time of the condensate in that particular run, rather than with respect to the average arrival time as is the case in the analyses presented in this manuscript. However, this rescaling of arrival times did not significantly reduce the width of the cross-correlation.

Obtaining a cross-correlation signal weaker than local correlation signals prevents

demonstrating a violation of the Cauchy-Schwarz inequality in the form:

$$g^{(2)}_{\text{cross}}(\Delta V' = 0) \geq \sqrt{g^{(2)}_{\text{loc},A}(\Delta V = 0)\, g^{(2)}_{\text{loc},B}(\Delta V = 0)} \tag{3.43}$$

But is worth noting that it is possible to use an integrated version of this inequality, where we consider not just the value of correlation at one point but rather the integral of the correlation signal within a certain volume of momentum space. By comparing the integrated cross-correlation value in a box to the local $g^{(2)}$ values in boxes of similar size, it is possible to demonstrate a violation of the Cauchy-Schwarz inequality. The observation of a cross-correlation wider than the local correlation supports this approach, which was used in our team to exhibit a violation of the Cauchy-Schwarz inequality with atoms emitted by four-wave mixing on collision halos[21]. Such a measurement with our data will be the subject of section 3.5.2.

3.4 Counting statistics

3.4.1 Detection probabilities

In this section, we will focus on the population distribution of the atomic beams emitted by four-wave mixing. This study was conducted by the team a few years ago[128], using a dataset in a regime with fewer atoms, as we will see in the following.

We have already mentioned that the final state of the system could be modeled as a superposition of TMS states, where each pair of modes is described by:

$$|\psi\rangle = \sqrt{1-|\alpha|^2}\sum_{n=0}^{+\infty}\alpha^n\,|n\rangle_{p_1}\,|n\rangle_{p_2} \tag{3.44}$$

where p_1 and p_2 are the coupled modes, and the squeezing parameter α is related to the average population $\langle N\rangle$ in each mode through

$$\langle N\rangle = \frac{|\alpha|^2}{1-|\alpha|^2} \tag{3.45}$$

It is easy to determine the distribution associated with this process for only one mode[129] by tracing the density matrix corresponding to the TMS state over the other mode. One gets the probability $\mathcal{P}(n)$ of measuring n atoms in one mode, which writes

$$\mathcal{P}(n) = (1-|\alpha|^2)|\alpha|^{2n} = \frac{\langle N\rangle^2}{(1+\langle N\rangle)^{n+1}} \tag{3.46}$$

which is a thermal distribution. Note that this thermal law remains valid when the detector efficiency η is not equal to 1: in this case, one has only to replace the average number of atoms $\langle N\rangle$ by the average *detected* number of atoms $\eta\langle N\rangle$.

Our detector's ability to detect single atoms enables us to highlight this distribution law: for a dataset consisting of a certain number of experimental runs, we can count, within a given box, the probability of obtaining n atoms. This even provides us with a means to estimate the size of a mode, as we will observe a thermal distribution if the size of the box is smaller or equal to the size of one mode.

We can even go further by examining the statistical distribution for boxes larger than the size of a mode. Indeed, it is possible to demonstrate that the distribution law obtained by considering an integration volume containing m modes of identical mean number is given by[130]

$$\mathcal{P}_{\text{multimode}}(n) = \frac{\Gamma(n+m)}{\Gamma(n+1)\Gamma(m)}\left(1+\frac{m}{\langle N\rangle}\right)^{-n}\left(1+\frac{\langle N\rangle}{m}\right)^{-m} \tag{3.47}$$

where Γ is the Euler Gamma function. Noticeably, this distributions tends to a Poisson distribution when m is large

$$\mathcal{P}_{\text{Poisson}}(n) = \frac{\langle N\rangle^n}{n!}\mathrm{e}^{-\langle N\rangle} \tag{3.48}$$

This suggests that in a large momentum volume the counting events are no more correlated.

The results are presented in Figure 3.14 for the same dataset as before. The distribution statistics were calculated within a box of transverse size $\Delta V_{x,y} = 12\,\text{mm.s}^{-1}$ and of size along z successively equal to $\Delta V_z = 1$, 3, and $10\,\text{mm.s}^{-1}$. The box was centered on

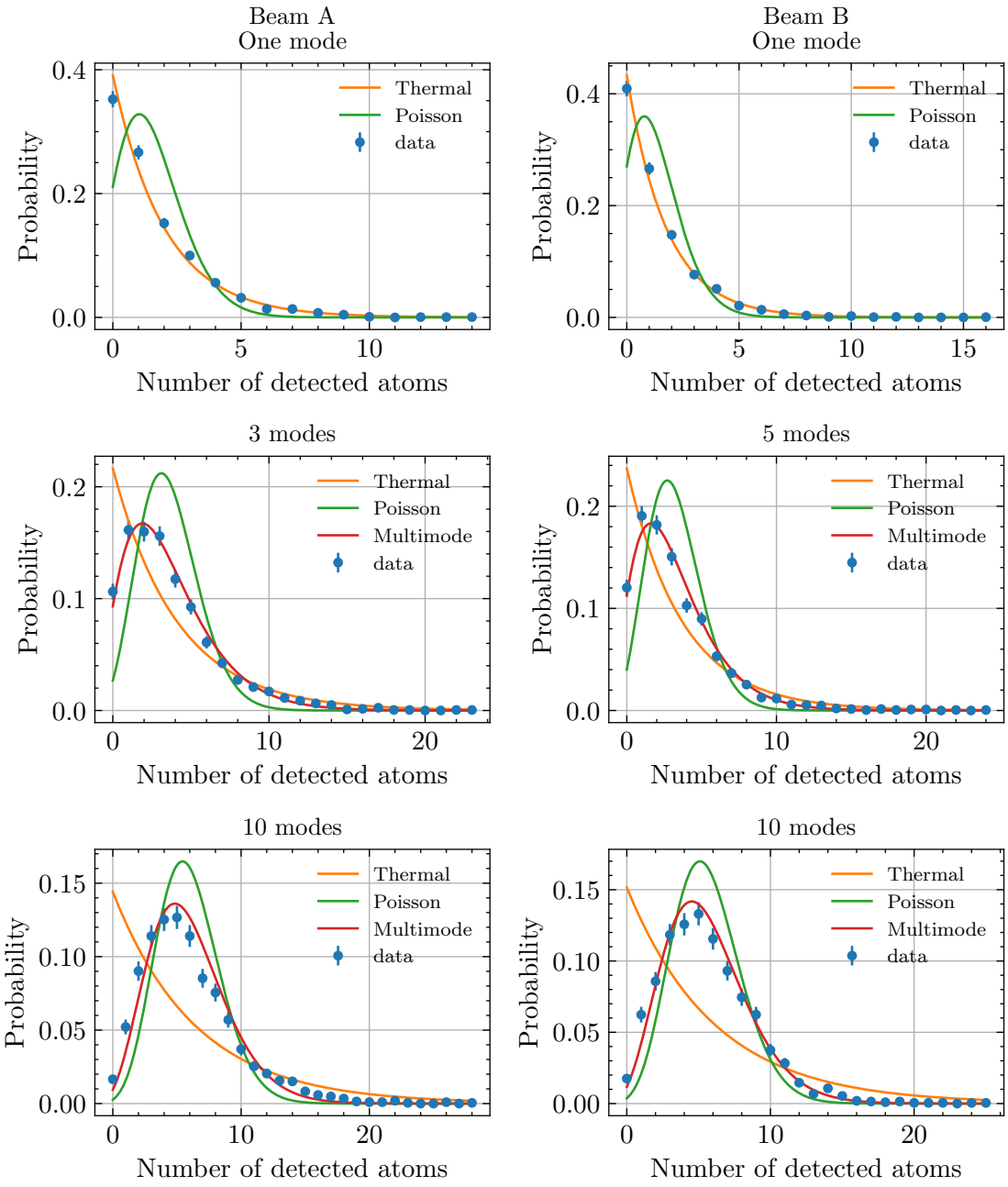

Figure 3.14: Counting statistics for different boxes sizes. For the entire dataset, we determine the number of occurrences for which n atoms were detected in a given momentum box, and divide by the total number of experimental runs. The result is averaged over two boxes of the same size, juxtaposed along the z-axis so that they have the same average population. The transverse size of the box is $12\,\mathrm{mm.s^{-1}}$. The size of the box along z is $1\,\mathrm{mm.s^{-1}}$ (top), $3\,\mathrm{mm.s^{-1}}$ (middle), $10\,\mathrm{mm.s^{-1}}$ (bottom). The data are compared with the expected theoretical distribution laws for a similar mean number of atoms with no adjustable parameter. Dataset of 1012 experimental runs.

the peak density[1]. The experimental results are compared with thermal, Poissonian, and multimode distribution laws in the last two cases, where we took respectively $m = 3$ modes and $m = 10$ modes. These are not fits but theoretical laws that depend solely on

[1]In reality, for better statistics, we averaged over two successive boxes with similar average populations.

the average number of atoms detected in the box, which we took as a fixed parameter in each case.

We observe that the results are consistent with a mode size of 1 mm/s along the z-axis and 12 mm/s along the x and y axes. A clear thermal distribution law is observed when the size of the box fits the size of a mode, while the multimode law matches well the experimental data when the degeneracy parameter m equals the number of boxes taken into account. Therefore, this is a strong evidence that the process is characterized by a thermal distribution law. The ratio between the transverse and longitudinal sizes of the mode is similar to what we estimated by studying the width of the local correlation function.

From these results, we can easily estimate the number of atoms per mode in each beam as well as the total number of emitted modes by counting the number of atoms in a box of the size of one mode, whose position is scanned. The results are presented in Figure 3.15. We find a maximum detected atom number per mode of around 1.7, which is ten times larger than the average number measured by the team in 2019 (0.158). At that time, the detector had a quantum efficiency estimated at 25%, while it is estimated at 50% with the MCP currently in place in the experiment. The "real" population in our case is thus on the order of 3.4 atoms per mode, compared to 0.6 in the dataset studied in reference [128]. We thus observe that the pair creation process remains thermal even for a larger number of atoms.

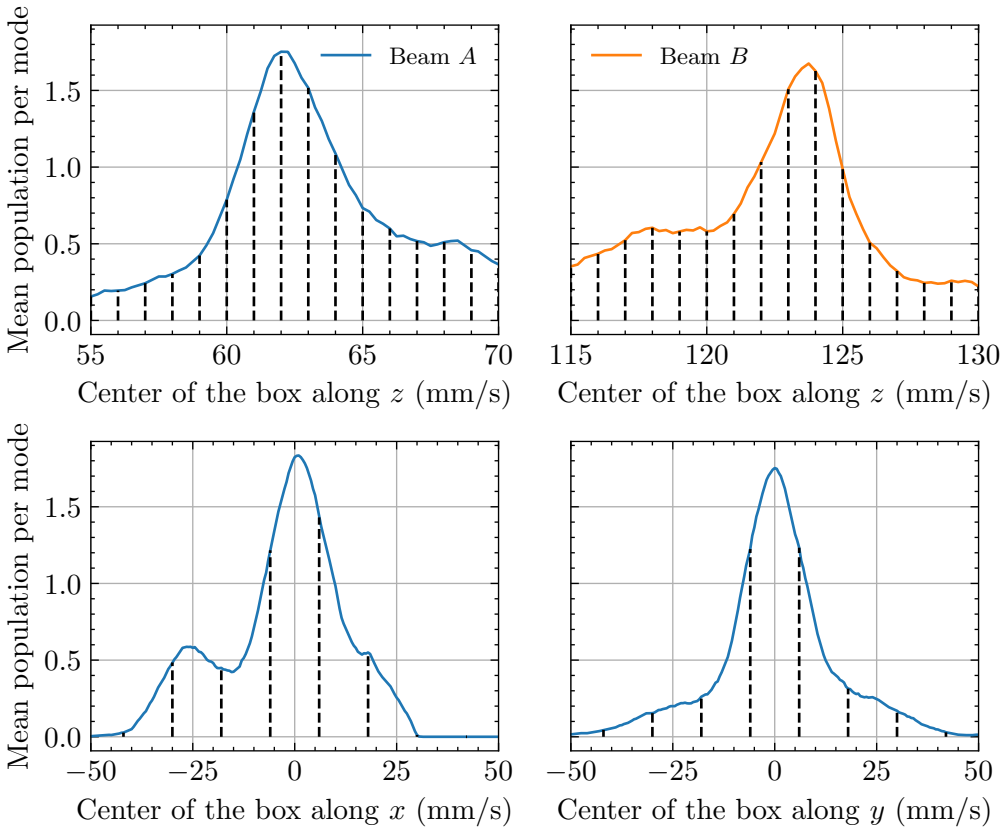

Figure 3.15: Mean population per mode. Number of atoms in a box of 1 mm.s^{-1} along z and 12 mm.s^{-1} along x and y.

Furthermore, the multimode character of the source is particularly highlighted when comparing the width of the population density envelop with the size of one mode: we

can observe numerous modes in the z direction, and around 5 modes in the transverse directions. However, it should be noted that the population per mode decreases rapidly if the box is not located at the density peak.

3.4.2 Joint detection probabilities

Of course, the distribution statistics of atoms in each beam are expected to be correlated. The formula of the TMS state directly provides access to the joint detection probability, which is expressed as:

$$\begin{cases} \mathcal{P}(n,n) = (1-|\alpha|^2)|\alpha|^{2n} = \dfrac{\langle N\rangle^2}{(1+\langle N\rangle)^{n+1}} = \mathcal{P}(n) \\ \mathcal{P}(n, m\neq n) = 0 \end{cases} \tag{3.49}$$

For a TMS state, if there are n atoms in a mode, there are necessarily n atoms in the coupled mode. This statistic can be compared, for example, to that given by two independent thermal processes, given by

$$\mathcal{P}_{\text{thermal}}(n_1,n_2) = \frac{\langle N_A\rangle^2}{(1+\langle N_A\rangle)^{n_1+1}}\frac{\langle N_B\rangle^2}{(1+\langle N_B\rangle)^{n_2+1}} \tag{3.50}$$

or by the statistic arising from two independent Poisson processes

$$\mathcal{P}_{\text{Poisson}}(n_1,n_2) = \frac{\langle N_A\rangle^{n_1}}{n_1!}\mathrm{e}^{-\langle N_A\rangle}\frac{\langle N_B\rangle^{n_2}}{n_2!}\mathrm{e}^{-\langle N_B\rangle} \tag{3.51}$$

where $\langle N_B\rangle$ and $\langle N_B\rangle$ are the mean number of atoms involved in each process. These distributions laws are plotted in Figure 3.16 for a mean population of $\langle N\rangle = 3.4$.

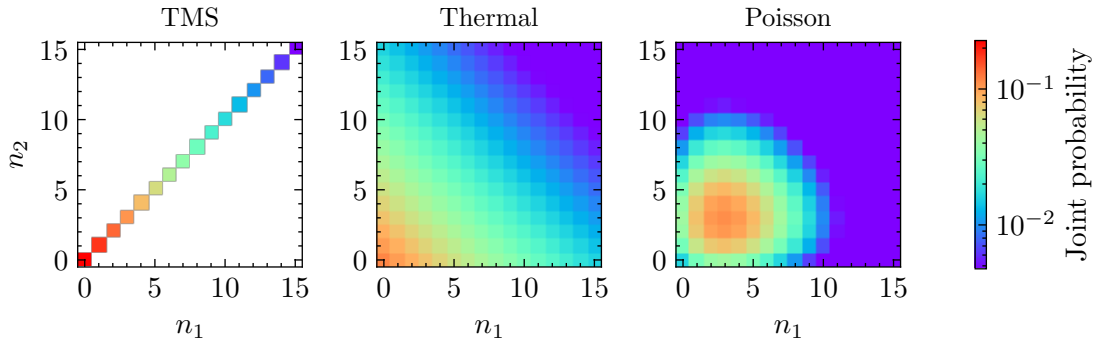

Figure 3.16: Joint counting statistics. Theoretical joint probabilities of measuring n_1 atoms in a given mode and n_2 atom in a second mode, in the case where the modes are coupled modes of a TMS (left), independent thermal modes (middle), independent Poissonian modes (right).

However, we must take into account the efficiency $\eta < 1$ of our detector. For the Poisson and thermal distribution, we only have to replace the absolute number of atoms by the detected number of atoms, so the behavior of the distribution will not change. On the contrary, this imperfection of the detector will broaden the joint probability profile of the TMS state: even if we detect n atoms in one mode, we may detect $n+1$ or $n-1$ atoms in the other mode (and so on) because not all atoms are always detected.

In his thesis, Q. Marolleau[41] derived the expression giving the joint probability of detection for a TMS state and a detector of quantum efficiency η, which is expressed as:

$$\begin{aligned}\mathcal{P}(n_1, n_2 \leq n_1) = (1-|\alpha|^2)|\alpha|^{2n_1}\eta^{n_1+n_2}(1-\eta)^{n_1-n_2} \\ \times \binom{n_1}{n_2}\, {}_2F_1\left(n_1+1, n_1+1, n_1-n_2+1; (1-\eta)^2|\alpha|^2\right)\end{aligned} \tag{3.52}$$

where $\binom{n_1}{n_2}$ is a binomial coefficient and ${}_2F_1$ is a hypergeometric function defined, for $|z|<1$, by

$${}_2F_1(a,b,c,;z) = \sum_{n=0}^{\infty} \frac{a^{\bar{n}}b^{\bar{n}}}{c^{\bar{n}}}\frac{z^n}{n!} \tag{3.53}$$

with $z^{\bar{n}}$ is the rising factorial, such that

$$z^{\bar{n}} = z(z+1)(z+2)\cdots(z+n-1) \tag{3.54}$$

Figure 3.17 shows various joint probability distributions for different values of η (for an average population equal to 3.4 atoms per mode) and shows the broadening of the signature diagonal of the TMS state.

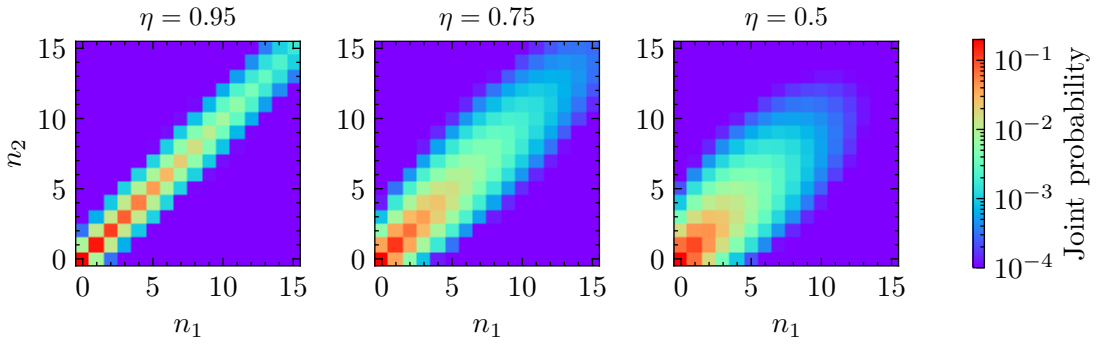

Figure 3.17: Joint counting statistics for two coupled modes of a TMS state, for different quantum efficiencies of the detector. The total average population equals 3.4.

The creation pair datasets allow us to experimentally access this quantity, although a lot of experimental runs are required to have a clear measurement. We choose two boxes, labeled 1 and 2, each the size of one mode, centered on speeds which exhibited cross-correlation on the correlation function analysis. Then, we count the number of occurrences where we simultaneously measure n_1 and n_2 atoms, and divide the result by the total number of experimental runs.

The result is shown in Figure3.18 and compared to the expected joint distribution for two independent Poisson distributions and for a TMS state with a quantum efficiency of 0.5, in both cases with an average detected population of 1.7. Note that since we only have a thousand experimental runs, only the most populated points are accessible as the others are highly improbable.

The distribution obtained experimentally does not allow for a clear distinction between the distributions. The overall appearance resembles that of a Poisson distribution, but $\mathcal{P}(0,0)$ is the most populated, like for the TMS state. The low statistics do not allow for

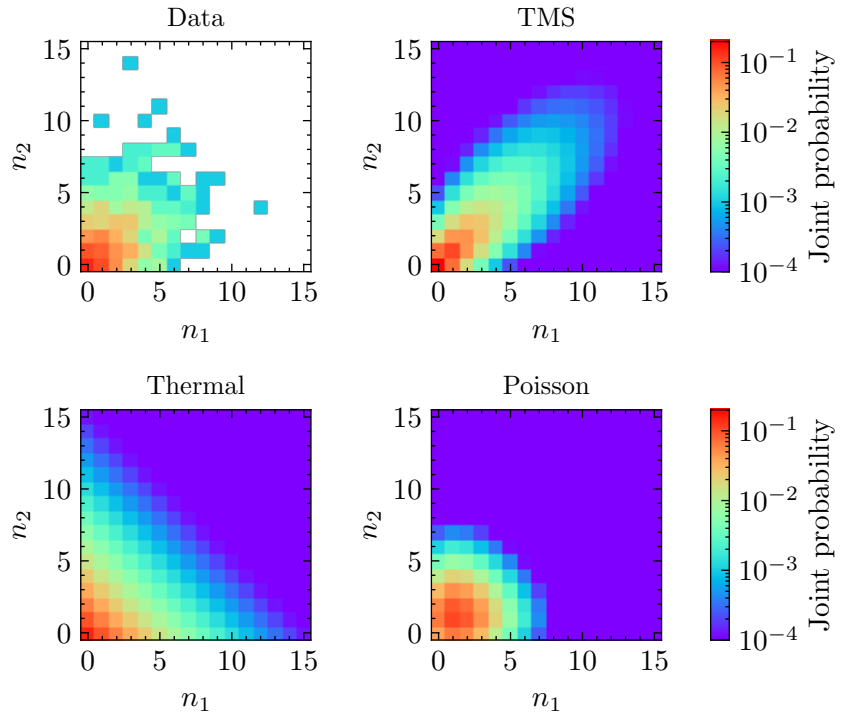

Figure 3.18: Measured joint counting statistics in boxes of the size of a mode (upper left), compared to the expected joint distribution statistics for a TMS state with a quantum efficiency of 50% (upper right), independent thermal processes (lower left) and independent Poissonian processes (lower right). The detected average population is 1.7.

observing additional points on the diagonal, as expected for a TMS state.

In order to increase sensitivity to more atoms, an alternative approach involves considering larger boxes and averaging the joint detection measurements over several consecutive boxes. The expected outcome is no longer the distribution of a TMS, but rather that of a multimode sample characterized by a distribution 3.47 for one mode. However, this formula has not been generalized for two output modes at an imperfect detector, so there is no theoretical model that we know of to match the expected joint measurements analysis. Instead, a comparison of the experimental results can be made with the joint distributions obtained by averaging several TMS and Poissonian distributions in boxes whose population is equal to those measured experimentally. The expected theoretical behavior of the joint distribution should lie between the two.

We typically get the result shown in Figure 3.19, computed for 11 consecutive boxes (along z) with sizes of $\Delta V_z = 7\,\mathrm{mm.s^{-1}}$ and $\Delta V_{x,y} = 12\,\mathrm{mm.s^{-1}}$, which correspond to seven modes.

The obtained result indeed exhibits a trend that lies between the TMS state and the Poisson distribution. The width of the distribution leans more towards that given by Poisson, which could be explained by the fact that we considered a box that contains multiple modes or by a potential overestimation of the quantum efficiency. Nevertheless, we still have a non zero probability of measuring atoms along a diagonal trend for high values of n_1 and n_2, suggesting that we are indeed observing a stronger correlation than that expected for two independent Poissonian processes.

A more quantitative analysis, along with datasets containing more experimental runs,

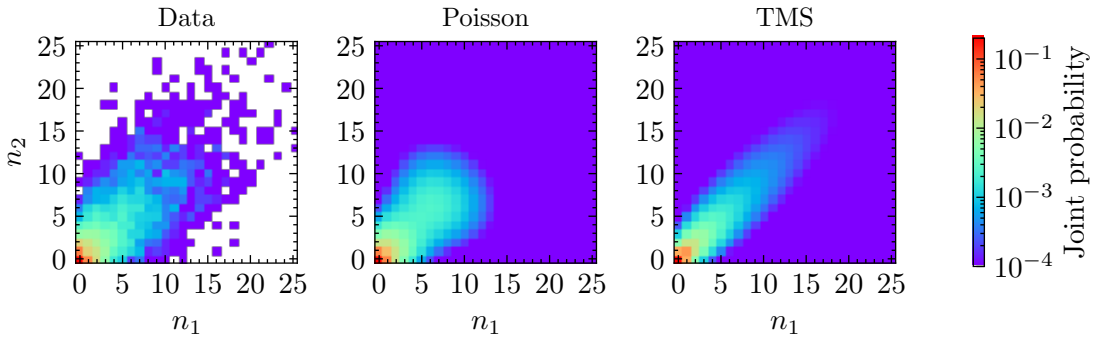

Figure 3.19: Measured joint counting statistics in 11 boxes of the size of 7 modes (left), compared to the expected equivalent joint distribution statistics for an independent Poissonian process (center), and a TMS state with a quantum efficiency of 50%. The theoretical profiles are calculated by averaging the joint statistics for processes with the same average population.

is necessary to further pursue this study.

3.5 Towards non classical correlation effects

3.5.1 Sub shot-noise variance

As mentioned in the first chapter, it is possible to highlight stronger correlations from TMS states than what could be observed with a classical system.

A first approach involves highlighting sub-Poissonian variance, also called sub-shot noise variance. Specifically, we study the variance of the difference in the number of detected atoms in two different regions A and B of momentum space, normalized by the mean number of detected atoms:

$$\tilde{V}(\Delta N) = \frac{\langle \Delta N^2 \rangle - \langle \Delta N \rangle^2}{\langle N_A + N_B \rangle} \tag{3.55}$$

with $\Delta N = N_A - N_B$. For a classical source, this quantity can not go below 1.

For a TMS state, for which there are consistently as many atoms in one mode as in its twin mode, this variance is strictly zero when counting the atoms received in a box of the size of one mode with a perfect detector. However, in practice, one must again take into account the quantum efficiency of the detector. In this case, the normalized variance no longer drops to zero.

In order to account for the imperfect detection efficiency, one often models the losses as an additional beam splitter placed before a perfect detector (Figure 3.20). The output mode $\hat{a}'$ can be expressed as a function of the input mode $\hat{a}$, using

$$\begin{pmatrix} \hat{a}' \\ \hat{a}'' \end{pmatrix} = \begin{pmatrix} \sqrt{\eta} & \sqrt{1-\eta} \\ -\sqrt{1-\eta} & \sqrt{\eta} \end{pmatrix} \begin{pmatrix} \hat{a} \\ \hat{O} \end{pmatrix} \tag{3.56}$$

where $\hat{O}$ designates the vacuum operator at the other input of the beam splitter. The expression of the annihilation operator $\hat{a}'$ is therefore

$$\hat{a}' = \sqrt{\eta}\,\hat{a} + \sqrt{1-\eta}\,\hat{O} \tag{3.57}$$

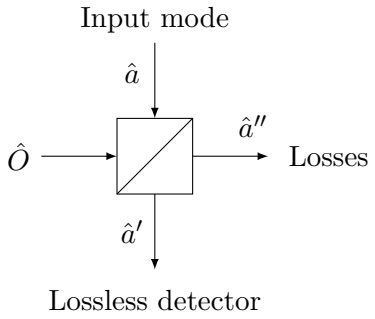

Figure 3.20: Model of an imperfect detector. The atoms are sent to one of two input ports of a beam splitter, while the other input is the vacuum operator. The beam splitter reflects a portion of the input atoms to an output mode $\hat{a}''$ where they are lost and thus not measured, while the remaining portion of atoms (mode $\hat{a}'$) heads towards a perfect detector which counts all of them.

from which we get:

$$\langle \hat{N}'_A \rangle = \langle \hat{a}'^{\dagger} \hat{a}' \rangle = \eta \langle \hat{a}^{\dagger} \hat{a} \rangle = \eta \langle \hat{N}_A \rangle \tag{3.58}$$

and

$$\langle \hat{N}'^2_A \rangle = \eta^2 \langle \hat{N}^2_A \rangle + \eta(1-\eta) \langle \hat{N}_A \rangle \tag{3.59}$$

By applying the same reasoning to the detection the atoms from region B, we also get

$$\langle \hat{N}'_A \hat{N}'_B \rangle = \eta^2 \langle \hat{N}_A \hat{N}_B \rangle \tag{3.60}$$

One can then determine the variance of the number difference between A and B, which writes

$$V(\hat{N}'_A - \hat{N}'_B) = (1-\eta)(\langle \hat{N}'_A \rangle + \langle \hat{N}'_B \rangle) \tag{3.61}$$

We observe that the normalized variance is thus equal to $1-\eta$. For $\eta = 1$, we recover the limit $\tilde{V} = 0$. For a quantum efficiency detector of 50%, we therefore expect this normalized variance to decrease to 0.5. In 2010, the team demonstrated sub-shot noise variance from pairs of atoms emitted by four-wave mixing on collision spheres[78]. By taking increasingly smaller diametrically opposed boxes, the normalized variance decreased to 0.75, which was consistent with the quantum efficiency of the detector then estimated at 25%. This is the kind of effect we want to highlight.

3.5.2 Cauchy-Schwartz violation

An equivalent formulation of obtaining sub-shot noise variance is the observation of a violation of the Cauchy-Schwarz inequality. As we have seen, we never observe a cross-correlation greater than the local correlation; however, we can use an integrated version of the inequality[21], which can be expressed as:

$$\bar{g}^{(2)}_{\text{cross}} \geq \sqrt{\bar{g}^{(2)}_{\text{loc},A}\, \bar{g}^{(2)}_{\text{loc},B}} \tag{3.62}$$

where $\bar{g}^{(2)}$ are average values of $g^{(2)}(\Delta V_z)$ integrated over momentum boxes of the same size:

$$\bar{g}^{(2)} = \int_{\mathcal{V}} \mathrm{d}^3 V\, g^{(2)}(\Delta V) \tag{3.63}$$

As we have seen, the algorithm that computes the value of $g^{(2)}$ in boxes directly provides the corresponding values. In practice, we compute the quantity:

$$\mathcal{C} = \frac{\bar{g}^{(2)}(V_{z_1}, V_{z_2})}{\sqrt{\bar{g}^{(2)}(V_{z_1}, V_{z_1})\bar{g}^{(2)}(V_{z_2}, V_{z_2})}} = \frac{\langle : N_1 N_2 : \rangle}{\sqrt{\langle : N_1^2 : \rangle \langle : N_2^2 : \rangle}} \tag{3.64}$$

where $\bar{g}^{(2)}(V_{z_1}, V_{z_2})$ is the value of the normalized correlation function between two boxes centered on vertical speeds V_{z_1} and V_{z_2}. N_1 and N_2 are the atoms counted within these two boxes. If $\mathcal{C} > 1$, then the cross-correlation is stronger than the local correlations, indicating a violation of the inequality.

The results of the Cauchy-Schwarz violation analysis will be conducted jointly with those of the normalized variance, as they represent two equivalent formulations for highlighting quantum correlations, yielding similar outcomes.

3.5.3 Experimental results

First, we can plot maps of the normalized variance and the Cauchy-Schwarz coefficient, defined as a function of two boxes centered on two velocities V_{z_1} and V_{z_2} that are scanned over the momentum space. The results are presented in Figure 3.21 and exhibit similar outcomes in both cases.

Note that the dataset presented here is different than the one analyzed before which does not exhibit any sub-shot noise variance or Cauchy-Schwarz violation, as we will explain in the following.

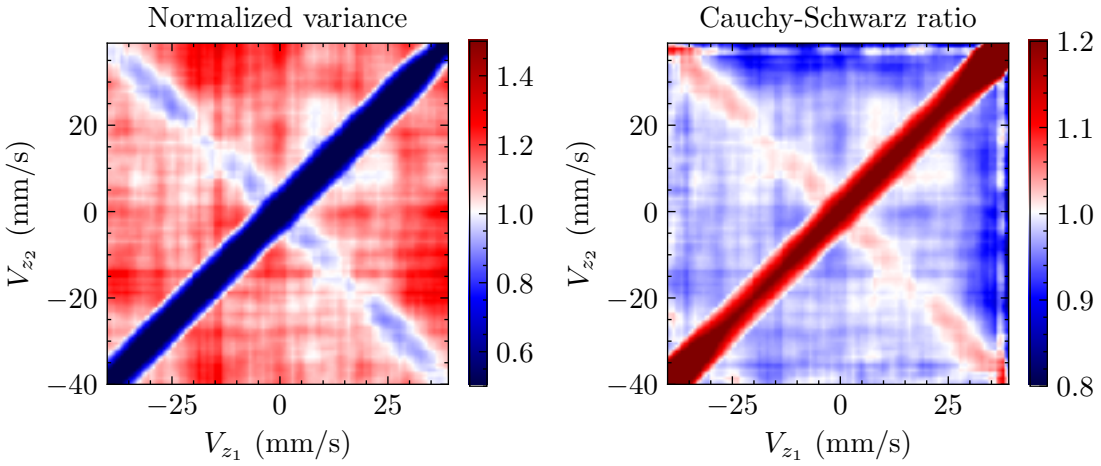

Figure 3.21: 2D maps of normalized variance and Cauchy-Schwarz coefficient. The size of a momentum box is $\Delta V_z = 7\,\mathrm{mm.s^{-1}}$ and $\Delta V_{x,y} = 30\,\mathrm{mm.s^{-1}}$. In each box, we calculate both the normalized variance $\tilde{V}(V_{z_1}, V_{z_1})$ (left) and the Cauchy-Schwarz ratio $\mathcal{C}(V_{z_1}, V_{z_1})$ (right). The shot noise is not removed from the $g^{(2)}$ calculation for the Cauchy-Schwarz ratio, since this process is not trivial when oversampling.

Along the diagonal, the normalized variance naturally tends towards zero since we are comparing the difference between two similar boxes. We observe a clear effect of cross-correlation along the anti-diagonal, where the normalized variance descends below 1. It is noteworthy that this effect is observed across the entire anti-diagonal, not just at the peaks of density. This confirms that we have a highly multimode source with correlations extending beyond high-density zones.

It is also worth mentioning that these data were obtained with a dataset containing fewer atoms per mode (on the order of 0.2 detected atoms per mode), as we never observe

a sub-shot noise variance when the population is high. As the population decreases (which can be achieved by reducing the duration of the lattice), we begin to detect sub-shot noise signals at the extremity of the density peaks, in regions of low density, and eventually across the entire anti-diagonal, as shown in the Figure 3.21. This highlights that the model asserting the final state induced by four-wave mixing is a superposition of TMS states is a perturbative model: if the population is too significant, this assumption cannot be maintained. Specifically, we cannot demonstrate correlations stronger than classical when the population is too high. In order to demonstrate a violation of Bell's inequalities, it will therefore be necessary to work with a set of atoms with few atoms per mode, typically with the population that allowed the observation of this sub-Poissonian variance. In the next chapter, we will demonstrate criteria regarding the population per mode to observe a violation of Bell's inequality with TMS states.

To observe such a signal, it was necessary to choose boxes significantly larger than the size of a mode ($\Delta V_z = 7\,\mathrm{mm.s^{-1}}$, $\Delta V_{x,y} = 30\,\mathrm{mm.s^{-1}}$). This was also the case in the data from 2015 presented by R. Lopes in his thesis[115] and is not fully understood to date. Furthermore, the variance does not decrease to 0.5 as expected with a quantum efficiency detector of 50%. It is uncertain whether this implies that the quantum efficiency of the MCP is lower than expected because it aligns with observations using correlation functions: the observed cross-correlations are not as strong as expected. This could be due to excessive averaging effects, to an unidentified mechanism that weakens correlations between pairs, or to the fact that even with a low population the atom source is not exactly a superposition of TMS states.

The map displaying the Cauchy-Schwarz coefficient exhibits a similar pattern: a violation of the Cauchy-Schwarz inequality is discernible along the anti-diagonal. Note that the diagonal should be equal to 1, but this is not the case as we did not remove the shot noise term, which is a non trivial operation when oversampling.

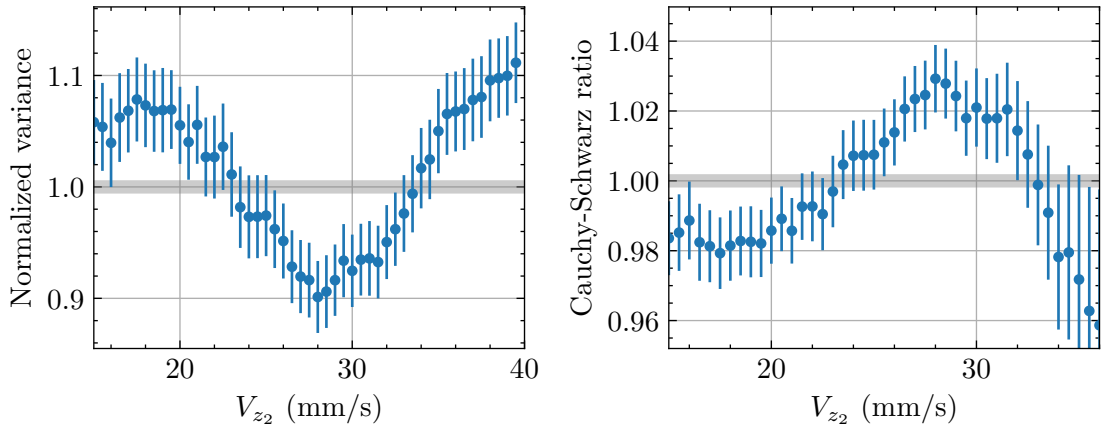

Figure 3.22: 1D normalized variance and Cauchy-Schwarz coefficient. The size of a momentum box is $\Delta V_z = 7\,\mathrm{mm.s^{-1}}$ and $\Delta V_{x,y} = 30\,\mathrm{mm.s^{-1}}$. One box is fixed, while the position of the other is scanned. The error bars are evaluated by bootstrapping.

One can also plot 1D curves with the same algorithm: a box is centered on a velocity V_{z_1}, and we calculate the value of the normalized variance and the coefficient $\mathcal{C}$ relative to a box centered on a velocity V_{z_2}, whose position is scanned. The results are shown in

Figure 3.22 for $V_{z_1} = 28\,\mathrm{mm.s^{-1}}$ (in the pair's frame), corresponding to the density peak. The results confirm that we obtain sub-shot noise variance, which decreases to 0.9 when the scanned box is centered on $-28\,\mathrm{mm.s^{-1}}$, confirming the strong correlation between the two. The error bars, estimated by bootstrap, unequivocally demonstrate the quantum nature of the correlation.

Despite the aforementioned points, we have successfully and reproducibly demonstrated sub-shot noise variance and a violation of the Cauchy-Schwarz inequality, which are signatures of a process with purely quantum correlations. Therefore, there is hope for the realization of a Bell test.

Chapter 4

Interferometer theory: from Bragg diffraction to Bell tests

4.1 Description of the Bell interferometer 116
4.1.1 Principle 116
4.1.2 Assessment of assumptions and visibility of the Bell correlator . . 120
4.1.3 Comparison with another setup 127
4.2 Theoretical description of the Bragg pulses 133
4.2.1 Bragg diffraction of atoms in an optical lattice 133
4.2.2 Bragg regime, Kapitza-Dirac regime and Raman-Nath approximation 137
4.2.3 Off-resonance Bragg diffraction 142
4.3 Phase involved in an interferometer 145
4.3.1 Propagation phase shifts 146
4.3.2 Light-matter interaction phase shifts 151
4.3.3 Conclusion 156
4.4 Application to the Mach-Zehnder interferometer 158
4.4.1 Resonant case with short pulses 158
4.4.2 Off-resonant corrective terms - finite duration pulses 163
4.5 Application to the Bell interferometer 166
4.5.1 Propagation phase 166
4.5.2 Center of mass-dependent imprinted phase 168
4.5.3 Off-resonant terms 169

In this section, we will introduce the Bell interferometer that we aim to implement. Previous chapters have focused on the source of twin atoms, emitted by four-wave mixing from a Bose-Einstein condensate. Subsequent chapters will specifically focus on the interferometric sequence itself, which will be executed using Bragg mirrors and beam splitters that ensure the coherent transfer of momentum between the modes involved in the interferometer. The ultimate goal is to conduct a Bell inequality test to confirm or refute the predictions of quantum mechanics, which anticipates a sinusoidal oscillation of the Bell correlator as a function of a phase difference between the Alice and Bob loops of the interferometer. The experiment has a dual purpose: to enable a precise control of this phase and to ensure that the contrast of the two-particle interference is sufficient to exhibit a violation of the Bell inequality. We will demonstrate that the interferometer configuration that we chose offers inherent advantages in terms of contrast, but it requires a meticulous control of the phase involved in the interferometer as a function of the momentum class.

This chapter is divided into five parts:

- The first section outlines the principle of the Bell interferometer with atoms and the configuration we chose, compared to another one already reported in the literature.
- The second part provides a theoretical description of Bragg diffraction, which will be used to create atom separators and mirrors.
- The third describes how to theoretically address the phase shifts involved in atomic interferometers, considering especially the phase imprinted on the atoms by the Bragg pulses out of resonance.
- In the fourth part, the results of the previous section are applied to the well-known case of a Mach-Zehnder interferometer as an example.
- The final part applies the results to the case of the Bell interferometer. The objective is to determine the phase involved in our Bell test, taking into account the non-resonant phase shifts, within a model where the wave functions of the atoms are treated as plane waves.

4.1 Description of the Bell interferometer

4.1.1 Principle

The design of the interferometer we aim to implement is inspired by the one used by Rarity and Tapster, who conducted a Bell inequality test with momentum entangled photons[12], as outlined in Chapter 1. In our case, photons are replaced by atoms, therefore two major elements differ. Firstly, mirrors and beam splitters for atoms consist in performing two-photon transitions that transfer momentum to atoms. Secondly, a method is needed to independently control the phase imposed on the loop A of the interferometer and the phase on the loop B. In the Rarity and Tapster's scheme, a phase plate provided such a phase control. Here, we will see that the phase imprinted by the Bragg beams on the atoms achieves this phase control.

The scheme of the interferometer is shown in Figure 4.1 in the falling frame, where the trajectories of the atoms are linear. The atoms are emitted from the BEC by four-wave mixing at a time that will be considered as the reference time $t = 0$, at which the

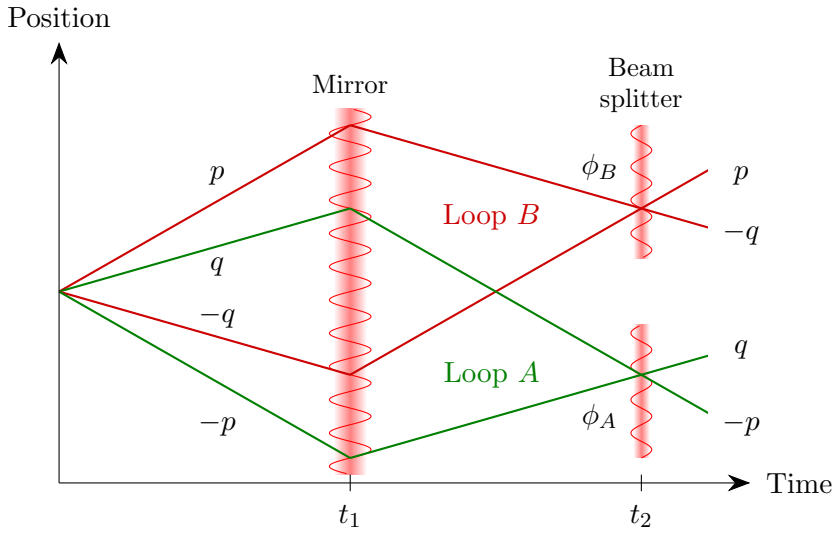

Figure 4.1: Schematic representation of the Bell interferometer, in the falling frame. The modes $(q, -p)$ and $(p, -q)$ are coupled pairwise by Bragg diffraction, forming loops A and B of the interferometer. For each loop, the beam splitter imparts a specific phase onto the atoms.

trap is switched off. From this moment, the atoms are in free fall. Although our pair source is largely multimode (as seen in Chapter 3), only four modes are necessary for the implementation of the Bell interferometer. Indeed, these two pairs of atoms will, according to quantum mechanics, exhibit stronger correlations than what could be obtained with any classical model. In the following, we will only represent these two pairs of momenta, since our detector allows us to perform post-selection to focus only on these specific modes.

Let us consider a doublet of correlated modes p_0 and $-p_0$ (with opposite momenta in the lattice frame), whose momentum difference corresponds to the Bragg momentum p_B transferred to the atoms by a Bragg two-photon transition. This implies that during a Bragg beam splitter or mirror, these two modes will interchange some or all of their populations. In practice, we will ensure that modes p_0 and $-p_0$ correspond to the maximum population of emitted pairs by adjusting the frequency of the lattice (cf section 3.2.2). As showed in Figure 4.2, due to the properties of the source, the modes involved in the Bell interferometer are pairs of correlated modes, denoted as $(p, -p)$ on one hand and $(q, -q)$ on the other, symmetric with respect to the doublet $(p_0,\ -p_0)$, such that:

$$\begin{cases} p = p_0 + \Delta p \\ q = p_0 - \Delta p \\ -p = -p_0 - \Delta p \\ -q = -p_0 + \Delta p \end{cases} \quad \text{and} \quad \begin{cases} p_0 = -p_0 + p_\mathrm{B} \\ p = -q + p_\mathrm{B} \\ q = -p + p_\mathrm{B} \end{cases} \tag{4.1}$$

where Δp is larger than the size of a mode. Note that the existence Δp such that a quadruplet $(-p, -q, q, p)$ verifies equations 4.1 is not evident *a priori*, but is due to the symmetry properties of our multimode source.

The input state is therefore:

$$|\psi_\mathrm{in}\rangle = \frac{1}{\sqrt{2}}(|-p, p\rangle + \mathrm{e}^{\mathrm{i}\phi_0}\,|-q, q\rangle) \tag{4.2}$$

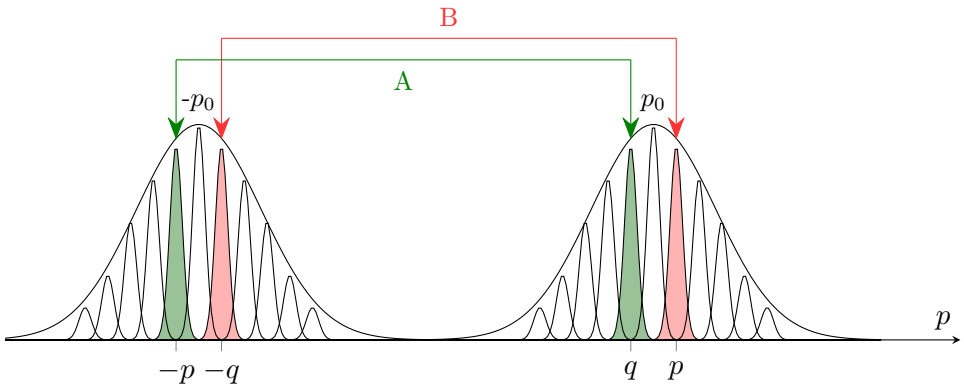

Figure 4.2: Schematic representation of the momentum modes involved in the interferometer. The modes are depicted by Gaussians within a density envelope. We are working in the pair's reference frame, meaning that two modes of opposite momenta are pairwise correlated by the pair creation process. The Bragg pulses couple modes $-p$ and q (loop A) and $-q$ and p (loop B).

where ϕ_0 is a phase between the correlated doublets which depends on the pair creation mechanism, and that we will assume to remain the same over many repetitions of the experiment. It may depend on the considered quadruplet, and therefore on p and q.

This two-particle four-mode state is the coherent superposition of a state for which one atom is in mode p while the other in the mode $-p$, and a state for which one atom is in mode q while the other in the mode $-q$.

At time t_1, a Bragg mirror is applied. Modes $-p$ and q are coupled by Bragg diffraction, as well as modes p and $-q$. This configuration forms two loops in the interferometer, labeled A and B, respectively (Figure 4.1). In both cases, the trajectories of the modes intersect at the same moment t_2 at which a Bragg beam splitter is applied. The overlap between the wavepackets of each modes will result in a two-particle interference. It is important to note that each loop of the interferometer involves two modes that do not belong to the same pair.

In order to show that this interferometer should theoretically lead to a violation of Bell inequality, let us calculate the output state of the interferometer. To do so, we will treat each momentum doublet coupled by Bragg diffraction as a two-level system. A given doublet is denoted as:

$$|\psi\rangle = C_0 \left|\tilde{p}\right\rangle + C_2 \left|\tilde{p} + \hbar k_\mathrm{B}\right\rangle = \begin{pmatrix} C_0 \\ C_2 \end{pmatrix}_{\{|\tilde{p}\rangle, |\tilde{p}+\hbar k_\mathrm{B}\rangle\}} \tag{4.3}$$

where C_0 and C_2 are the amplitudes related to the population of states $|\tilde{p}\rangle$ and $|\tilde{p} + \hbar k_\mathrm{B}\rangle$. In our case, this basis is either $A = \{|-p\rangle, |q\rangle\}$ or $B = \{|-q\rangle, |p\rangle\}$. By convention, we will consider that the state with the lowest momentum corresponds to the 0th order of diffraction.

The input state $|\psi_\mathrm{in}\rangle$ is therefore

$$|\psi_\mathrm{in}\rangle = \frac{1}{\sqrt{2}} \left[\begin{pmatrix} 1 \\ 0 \end{pmatrix}_A \otimes \begin{pmatrix} 0 \\ 1 \end{pmatrix}_B + \mathrm{e}^{\mathrm{i}\phi_0} \begin{pmatrix} 0 \\ 1 \end{pmatrix}_A \otimes \begin{pmatrix} 1 \\ 0 \end{pmatrix}_B \right] \tag{4.4}$$

As we will demonstrate later in the manuscript, for a given momentum doublet (labeled D with $D = A$ or B), the transfer matrix of a beam splitter between two resonant modes can be written

$$\hat{U}_{\mathrm{S}}^{(D)} = \frac{1}{\sqrt{2}} \begin{pmatrix} 1 & \mathrm{i}\mathrm{e}^{\mathrm{i}\phi_D} \\ \mathrm{i}\mathrm{e}^{-\mathrm{i}\phi_D} & 1 \end{pmatrix} \tag{4.5}$$

where ϕ_D is the phase difference between the two lasers used for the two-photon transfer involved in the loop $D = A$ or B[1]. This phase is imprinted on the atoms, meaning that the phase difference between the lasers beams will lead to an equal phase difference between the reflected atoms and the transmitted ones. Similarly, the evolution matrix of a mirror is

$$\hat{U}_{\mathrm{M}}^{(D)} = \begin{pmatrix} 0 & \mathrm{i}\mathrm{e}^{\mathrm{i}\phi'_D} \\ \mathrm{i}\mathrm{e}^{-\mathrm{i}\phi'_D} & 0 \end{pmatrix} \tag{4.6}$$

In the interferometer, after the two Bragg pulses, the output state is

$$|\psi_{\mathrm{out}}\rangle = \hat{U}^{(A)} \otimes \hat{U}^{(B)} |\psi_{\mathrm{in}}\rangle \tag{4.7}$$

with

$$\hat{U}^{(A)} = \hat{U}_{\mathrm{S}}^{(A)} \hat{U}_{\mathrm{M}}^{(A)} \qquad \text{and} \qquad \hat{U}^{(B)} = \hat{U}_{\mathrm{S}}^{(B)} \hat{U}_{\mathrm{M}}^{(B)} \tag{4.8}$$

Given that

$$\hat{U}^{(D)} = \frac{1}{\sqrt{2}} \begin{pmatrix} -\mathrm{e}^{\mathrm{i}(\phi_D - \phi'_D)} & \mathrm{i}\mathrm{e}^{\mathrm{i}\phi'_D} \\ \mathrm{i}\mathrm{e}^{-\mathrm{i}\phi'_D} & -\mathrm{e}^{\mathrm{i}(\phi'_D - \phi_D)} \end{pmatrix} \tag{4.9}$$

the output state can be easily determined, and we find[2]

$$\begin{aligned} |\psi_{\mathrm{out}}\rangle = \frac{1}{2} \Big[& -\mathrm{i} \left(\mathrm{e}^{\mathrm{i}(\phi_B - \phi'_B + \phi'_A)} + \mathrm{e}^{\mathrm{i}(\phi_0 + \phi_A - \phi'_A + \phi'_B)} \right) |-p, -q\rangle \\ & + \left(-\mathrm{e}^{\mathrm{i}(\phi_0 + \phi'_B - \phi'_A)} + \mathrm{e}^{\mathrm{i}(\phi_B - \phi'_B + \phi'_A - \phi_A)} \right) |q, -q\rangle \\ & + \left(\mathrm{e}^{\mathrm{i}(\phi'_B - \phi_B + \phi_A - \phi'_A + \phi_0)} - \mathrm{e}^{\mathrm{i}(\phi'_A - \phi'_B)} \right) |p, -p\rangle \\ & -\mathrm{i} \left(\mathrm{e}^{\mathrm{i}(\phi'_A - \phi_A - \phi'_B)} + \mathrm{e}^{\mathrm{i}(\phi_0 + \phi'_B - \phi_B - \phi'_A)} \right) |p, q\rangle \Big] \end{aligned} \tag{4.10}$$

Let us assume that the Bragg mirror acts similarly on atoms from loops A and B. Specifically, we have $\phi'_A = \phi'_B$, so the previous expression simplifies to

$$\begin{aligned} |\psi_{\mathrm{out}}\rangle = \frac{1}{2} \Big[& -\mathrm{i} \left(\mathrm{e}^{\mathrm{i}\phi_B} + \mathrm{e}^{\mathrm{i}(\phi_0 + \phi_A)} \right) |-p, -q\rangle + \left(-\mathrm{e}^{\mathrm{i}\phi_0} + \mathrm{e}^{\mathrm{i}(\phi_B - \phi_A)} \right) |q, -q\rangle \\ & + \left(\mathrm{e}^{\mathrm{i}(-\phi_B + \phi_A + \phi_0)} - 1 \right) |p, -p\rangle - \mathrm{i} \left(\mathrm{e}^{-\mathrm{i}\phi_A} + \mathrm{e}^{\mathrm{i}(\phi_0 - \phi_B)} \right) |p, q\rangle \Big] \end{aligned} \tag{4.11}$$

From this expression, we can calculate the joint probabilities of detection, that is to say the probabilities to measure, after the beam splitter, two atoms in different modes. Note

[1] For now, we only consider this phase term, without taking into account the phase shifts due to the position of the center of mass, the detuning, or the wave packet propagation.

[2] Using

$$\begin{pmatrix} a \\ b \end{pmatrix}_{\{|-p\rangle, |q\rangle\}} \otimes \begin{pmatrix} c \\ d \end{pmatrix}_{\{|-q\rangle, |p\rangle\}} = ac\,|-p, -q\rangle + ad\,|-p, p\rangle + bc\,|q, -q\rangle + bd\,|q, p\rangle$$

that the joint probabilities $\mathcal{P}(p,-q)$ and $\mathcal{P}(-p,q)$ of finding two atoms within the same loop of the interferometer are zero, which is why the loops A and B are not interferometers themselves. If we consider the joint probabilities involving modes from each loop, we have:

$$\mathcal{P}(p,q) = |\langle p,q|\psi_{\text{out}}\rangle|^2 = \frac{1}{2}\cos^2\left(\frac{\phi_A-\phi_B}{2}+\frac{\phi_0}{2}\right) \tag{4.12}$$

$$\mathcal{P}(-p,-q) = |\langle -p,-q|\psi_{\text{out}}\rangle|^2 = \frac{1}{2}\cos^2\left(\frac{\phi_A-\phi_B}{2}+\frac{\phi_0}{2}\right) \tag{4.13}$$

$$\mathcal{P}(p,-p) = |\langle p,-p|\psi_{\text{out}}\rangle|^2 = \frac{1}{2}\sin^2\left(\frac{\phi_A-\phi_B}{2}+\frac{\phi_0}{2}\right) \tag{4.14}$$

$$\mathcal{P}(q,-q) = |\langle q,-q|\psi_{\text{out}}\rangle|^2 = \frac{1}{2}\sin^2\left(\frac{\phi_A-\phi_B}{2}+\frac{\phi_0}{2}\right) \tag{4.15}$$

We can see that these joint probabilities of detection oscillate as a function of the phase difference $\phi_A - \phi_B$ (for a given value of ϕ_0, which, again, we assume to remain constant over the realizations of the interferometer). Note that there is no interference effect when looking at the single atom detection probabilities, which are constant:

$$\mathcal{P}(p) = \mathcal{P}(p,q) + \mathcal{P}(p,-p) = \frac{1}{2} \tag{4.16}$$

The oscillation of the joint probabilities of detection is a quantum two-particle interference which can lead to a violation of Bell inequality. A standard version of this inequality (called the CHSH version)[40] consists in defining a Bell correlator E, as

$$E = \mathcal{P}(p,q) + \mathcal{P}(-p,-q) - \mathcal{P}(p,-p) - \mathcal{P}(q,-q) \tag{4.17}$$

Using the previous expressions for the probabilities, we get

$$E(\phi_A,\phi_B) = \cos\left(\phi_A - \phi_B + \phi_0\right) = \cos\Phi \tag{4.18}$$

We expect that the interferometer leads to an oscillation of the Bell correlator as a function of $\phi_A - \phi_B$. This requires us to be able to control the difference of imprinted phases between the loops A and B. This crucial point will be discussed in detail later in the manuscript. The unknown value of ϕ_0 adds a phase offset in the oscillation of E.

By choosing specific values of $\phi_A - \phi_B$, and therefore tuning Φ, it is possible to obtain a Bell parameter S greater than 2:

$$S = E\left(\phi_A^{(1)},\phi_B^{(1)}\right) - E\left(\phi_A^{(1)},\phi_B^{(2)}\right) + E\left(\phi_A^{(2)},\phi_B^{(1)}\right) + E\left(\phi_A^{(2)},\phi_B^{(2)}\right) = 2\sqrt{2} \tag{4.19}$$

where we took $\phi_A^{(1)} - \phi_B^{(1)} = 45°$, $\phi_A^{(1)} - \phi_B^{(2)} = 135°$, $\phi_A^{(2)} - \phi_B^{(1)} = 315°$ and $\phi_A^{(2)} - \phi_B^{(2)} = 45°$.

The interferometer therefore should lead to a violation of Bell inequality according to the laws of quantum mechanics.

4.1.2 Assessment of assumptions and visibility of the Bell correlator

At this stage, let us highlight the crucial assumptions made during the previous proof of principle. It is essential to assess their validity in order to estimate the deviation from the ideal model that would arise in our experimental setup.

Input state

The first hypothesis to discuss is that of the initial state. It was considered that the initial state could be written as $|p,-p\rangle + \mathrm{e}^{i\phi_0}|q,-q\rangle$. However, as seen in the previous chapter, the state resulting from the four-wave mixing is more appropriately described as a superposition of two-mode squeezed states, which can be expressed particularly in the following form:

$$|\psi_{\mathrm{in}}\rangle = \left(\sqrt{1-|\alpha|^2}\sum_{n=0}^{+\infty}\alpha^n\,|n\rangle_p\,|n\rangle_{-p}\right)\otimes\left(\sqrt{1-|\beta|^2}\sum_{n=0}^{+\infty}\beta^n\,|n\rangle_q\,|n\rangle_{-q}\right) \tag{4.20}$$

where we restrict ourselves to the mode pairs involved in the Bell interferometer. α and β are related to the average population per mode through the following relationships:

$$\langle n\rangle_p = \frac{|\alpha|^2}{1-|\alpha|^2} \qquad \text{and} \qquad \langle n\rangle_q = \frac{|\beta|^2}{1-|\beta|^2} \tag{4.21}$$

We now assume that the population of modes p, $-p$, and q, $-q$ is the same (in practice, the frequency of the pair network is chosen to make this the case) so that $|\alpha| = |\beta|$. As we can see, when the population tends toward zero, the initial state can be rewritten by retaining only the first-order terms in α, such as:

$$|\psi_{\mathrm{in}}\rangle \underset{\langle n\rangle\to 0}{=} (1-|\alpha|^2)\left[|0\rangle + \alpha\left(|1\rangle_p\,|1\rangle_{-p} + \mathrm{e}^{i\phi_0}\,|1\rangle_q\,|1\rangle_{-q}\right)\right] \tag{4.22}$$

with $\phi_0 = \arg(\beta/\alpha)$. By omitting the vacuum part, we recover the Bell state used in the previous section.

This demonstrates that the ideal case is approached when the population of the two-mode squeezed states tends towards zero. Indeed, as it will also be demonstrated for the HOM effect, our aim here is to exhibit a two-particle interference effect. Thus, the probability of having two particles in modes p and $-p$ will inevitably lead to a reduction in the visibility of this interference effect.

In practice, in order to exhibit a violation of Bell's inequality, experiments are conducted iteratively. In each experimental cycle, the number of atoms N_{p_i} detected in each mode p_i is recorded. The joint probability $\mathcal{P}(p,-q)$ of detecting atoms in the modes p and $-q$ for instance are thus defined such that

$$\mathcal{P}(p,-q) = \frac{\langle N_p N_{-q}\rangle}{\langle N_p N_{-p}\rangle + \langle N_q N_{-q}\rangle + \langle N_p N_{-q}\rangle + \langle N_q N_{-p}\rangle} \tag{4.23}$$

and so on for $\mathcal{P}(p,-p)$, $\mathcal{P}(q,-p)$ and $\mathcal{P}(q,-q)$.

These probabilities can be calculated analytically by taking the superposition of two-mode squeezed states as the input state, as defined in equation 4.20, without truncating the sum over Fock states. This yields[121] the expression for the Bell correlator in the form:

$$E = V(\langle N\rangle)\cos\Phi \qquad \text{with} \qquad V(\langle N\rangle) = \frac{1+\langle N\rangle}{1+3\langle N\rangle} \tag{4.24}$$

A visibility term V emerges that tends to reduce the amplitude of the Bell correlator oscillation as the average population $\langle N\rangle$ increases. Consequently, the maximum value of

the Bell parameter S which can be achieved is

$$S = 2\sqrt{2}\,\frac{1+\langle N\rangle}{1+3\,\langle N\rangle} \tag{4.25}$$

The graph of $S(\langle N\rangle)$ is presented in Figure 4.3. When working with two-mode squeezed states, one needs to operate within a specific population regime if the goal is to measure a violation of Bell's inequality.

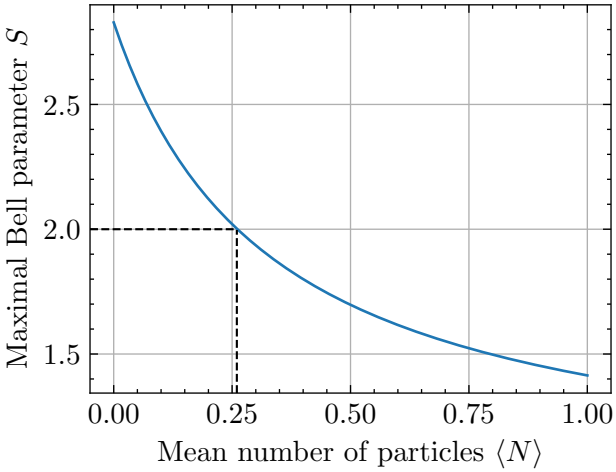

Figure 4.3: Visibility of the Bell parameter as a function of the mean population, for a two mode squeezed input state.

In practice, to achieve $S > 2$, the oscillation amplitude of the correlator $V(\langle N\rangle)$ must be greater than $1/\sqrt{2}$, which corresponds to a population which needs to be lower than 0.26.

The major challenge in experiments aiming to demonstrate a violation of Bell inequalities is ensuring that the visibility of the signal is sufficient to surpass the classical limit of $S = 2$. This requires the preparation of an initial state that closely resembles a Bell state. In the case of TMS states, this implies working with a low population. However, this choice will impact the signal-to-noise ratio, as operating below the population limit of 0.26 atoms per mode means that more than three-quarters of the realizations will occur without any atoms, thus not contributing to the useful signal.

Note that there are other forms of Bell inequalities than the CHSH inequality used here[41][131], involving different correlators, which can be exploited to enhance the visibility of the associated Bell correlator.

Reflectivity of the Bragg pulses

Another potential cause of a decreased visibility of the Bell correlator is a poor quality of the mirror and Bragg beam splitter properties, meaning transition probabilities that differ from 100% for the mirror and 50% for the beam splitter. Analogous to optics, these parameters are referred to as the "reflectivity" properties of the Bragg pulses. In practice, this involves expressing the Bragg transfer matrices in the form:

$$\hat{U}^{(D)}_{\mathrm{M,S}} = \begin{pmatrix} t & r\mathrm{e}^{\mathrm{i}\phi_D} \\ r\mathrm{e}^{-\mathrm{i}\phi_D} & t \end{pmatrix} \tag{4.26}$$

where r and t are reflectivity and transmittivity coefficients. We will show in a following section of the chapter how to write the coefficients r and t and their impact on the visibility of the Bell correlator.

Regardless of the specific Bell experiment being conducted, this issue is common to all atomic interferometers, which involve Bragg (or Raman) transitions whose resonance depends on the momentum class. As the atom source has a certain momentum coherence width, the reflectivity of the pulses needs to remain high within a momentum range corresponding to the source width in order to optimize the signal. In our case, this requires the reflectivity of the Bragg pulses to be good at the scale of a momentum mode, which determines the integration volume within which the atoms will be counted.

As we will see, Bragg transitions (unlike Raman transitions) enable diffraction towards more than one diffraction order, in the case where the Bragg power is high, which may be responsible for an additional reflectivity decrease which needs to be avoided.

Same mirror but different splitters for A and B

In the chosen configuration for the interferometer, the decision was made to use the same Bragg mirror for loops A and B, while two different beam splitters need to be performed. This has important implications for the constraints on the Bragg pulses. Specifically, the momentum doublet involved in loop A does not have the same Bragg resonance frequency as beam splitter B, since the resonance frequency depends linearly on the momentum class.

This implies that the Bragg mirror's resonance width must be sufficiently broad to effectively transfer atoms from doublet A *and* doublet B without a loss of reflectivity. For the mirror, the Bragg resonance must remain effective not just over the range of one momentum mode but at least over a range of three momentum modes, considering that the chosen modes $-p$, $-q$, p, and q are the neighboring modes of the doublet $(p_0, -p_0)$ (Figure 4.4).

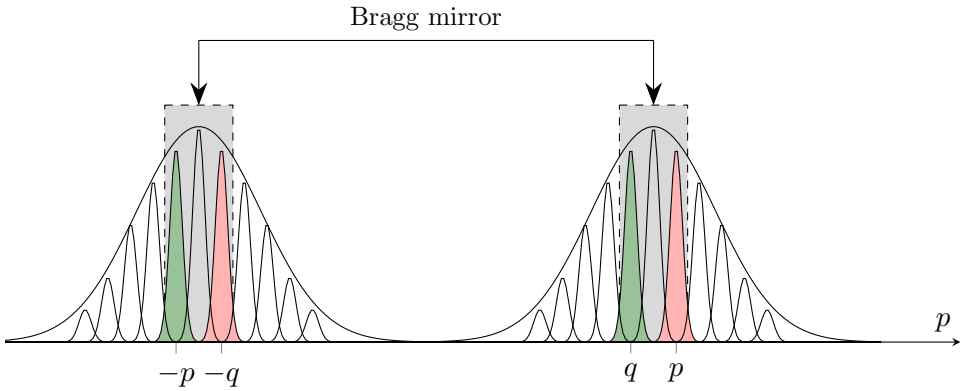

Figure 4.4: Schematic representation of the chosen Bragg transfer for the mirror. The resonant range of the Bragg transfer is depicted in gray. The same pulse couples modes $-p$ and q of loop $A$and modes $-q$ and p of loop B.

Furthermore, we imposed the phase imprinted by the mirror on the atoms to be the same for loops A and B. We will show that this is actually not necessary, provided that the phase difference between A and B imprinted by the mirror remains constant. Similar to the reflectivity, the phase must remain constant for a given mode, since we will average

the measured joint probabilities over an integration range corresponding to the size of a mode: if the phase varies too much within a mode, the Bell interference might vanish.

Regarding the beam splitter, the chosen configuration is different. In contrast to the mirror, we aim to imprint different phases on the atoms in loops A and B. Therefore, it is necessary to make two distinct beam splitters. One possible approach would be to align two different sets of beams on the spatial regions where the atoms of loops A and B intersect since these regions are distinct. In practice, these two intersections are only a few µm apart, making this approach technically very challenging in terms of beam waist and alignment.

Instead, we will leverage the fact that doublets A and B have different resonance frequencies. This will allow us to use the same set of beams for A and B. The objective is to ensure that these beams have two distinct resonance frequencies, and that the resonance widths are sufficiently narrow to enable efficient coupling of one doublet without affecting the other (Figure 4.5). One could also apply this principle to make two resonant mirrors, each interacting with either the atoms from loop A or B, in the event that the reflectivity obtained with a single mirror proves to be insufficient.

Additionally, we must be able to control the relative phase imprinted between the doublets A and B. This is a crucial constraint, as this phase difference is the one involved in the Bell correlator and plays the role of the control parameter of the Bell test. Addressing this challenge is at the core of the design approach for the Bragg pulses, which will be further detailed in the following sections of this chapter.

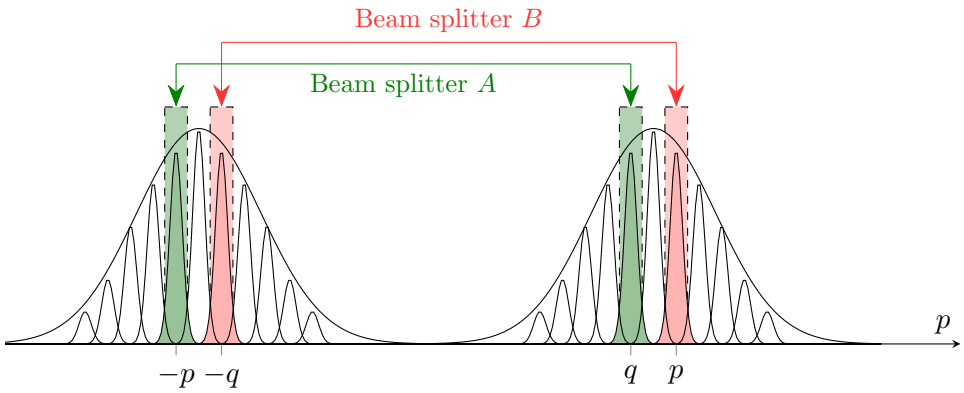

Figure 4.5: Schematic representation of the chosen Bragg transfer for the beam splitter. Two distinct beam splitters are actually applied, each resonant with a doublet: $-p$ and q for doublet A (in green), $-q$ and p for doublet B (in red).

Note that, so far, we have only discussed the control of the phase difference $\phi_A - \phi_B$. However, to perform a genuine Bell test in the sense of a test of quantum mechanics, the formal demonstration presented in the introduction requires independent control of both degrees of freedom, in our case the phases ϕ_A and ϕ_B. It will be shown later that achieving such phase control is experimentally more demanding than controlling only the phase difference. In the following, we will thus specifically focus on controlling the phase difference between A and B.

Multiplexing

It is worth noting that we can leverage the multimode nature of the pair source to conduct multiple Bell experiments in parallel. If the Bragg coupling performance allows, we could use not just a single quadruplet at a given Δp, but several quadruplets for different values of Δp. This would enable a form of multiplexing, where a single experimental cycle involves conducting multiple Bell experiments, providing a significant statistical advantage.

However, averaging the results obtained with one quadruplet and those obtained with another would not be feasible because the phase ϕ_0 arising from the pair creation process depends *a priori* on the specific quadruplet considered. Thus, when varying the control parameter $\phi_A - \phi_B$ for a given quadruplet, the Bell correlator $E = V\cos(\phi_A - \phi_B + \phi_0)$ oscillates with an initial phase that depends on the specific quadruplet under consideration.

Nevertheless, if we manage to observe distinct oscillations with different initial phases but with a sufficient oscillation amplitude, then it might be feasible to average the results. This would only be meaningful in observing the oscillation of the Bell correlator, as during a measurement of the Bell parameter S, the four sets of phases $\phi_A - \phi_B$ leading to a maximal S would vary depending on the momentum quadruplet. Let us highlight again that implementing a multiplexing scheme requires maintaining good reflectivity of the Bragg mirrors and beam splitters over a momentum range that encompasses all involved modes.

Additional phases and closure of the interferometer

Even when considering the nature of the quantum input state and the influence of the momentum class on the reflectivity and the phase imprinted on the atoms by the Bragg pulses in the Bell interferometer, the previous model remains incomplete. Indeed, it does not take into account any spatial effects. The effects neglected by this model are of various kinds.

We have not yet accounted for the fact that in atomic interferometers, the phase imprinted on atoms during the Bragg pulse is not solely equal to the phase difference between the lasers, there is also a term corresponding to the product of the Bragg wavevector and the center of mass of the atoms. This term is, in fact, at the heart of atomic interferometry, as it enables the measurement of gravity in Mach-Zehnder-type gravimeters.

There is also an additional phase accumulated by the atoms during their free fall, which depends on their position in the gravitational field, hence both their position and momentum.

We will demonstrate that both these terms can be analytically calculated in simple cases using a formalism involving wave packets evolving under the influence of propagators that account for gravity and interaction with light.

We will see that these additional phases vanish in the case where the interferometer is closed, that is to say when the duration between the mirror and the beam splitter is equal to the duration between the emission of the pairs and the mirror, which gives, with the previous conventions, $t_2 = 2t_1$. This is the application time of the beam splitter for which the wavepackets overlap, resulting in the best visibility of two-particle interference. This idea is similar in other types of interferometers such as the Mach-Zehnder interferometer, for example.

In practice, several factors complicate the exact determination of the delay at which to apply the beam splitter to close the interferometer.

- Firstly, the pair creation process has a duration on the order of a few hundred µs. Although this is a process with an exponentially increasing gain with the duration of the optical lattice, leading to the expectation that most pairs are created towards the end of the lattice application, it is not straightforward to pinpoint a precise moment when the pairs are emitted (due to saturation effects of the four-wave mixing process, for instance).

- Secondly, the Bragg pulses have a finite duration. Typically, in atomic interferometry experiments, their duration remains small compared to the free propagation durations of the atoms. However, if one considers the pulse duration (even assuming that the emission time of the pairs is precisely known), should the time of applying the beam splitter be referenced to the beginning, end, or middle of the mirror pulse?

To address these issues experimentally, it is possible to precisely determine the delay of the beam splitter to close the interferometer by using the same source of pairs and the same mirror, conducting another two-particle interference experiment involving only two correlated momentum modes, p_0 and $-p_0$: the Hong-Ou-Mandel experiment. As mentioned in Chapter 1, such an experiment allows for one to determine conditions under which two bosons are indistinguishable. By sending two bosons through a beam splitter and by varying the beam splitter delay, one can identify the delay that achieves the best overlap between the wave packets by counting coincidences between the modes. Quantum theory predicts that the coincidence rate $G^{(2)}(p_0, -p_0)$ tends toward zero when the interferometer is closed, at low population. A more detailed discussion of the HOM effect will be presented in Chapter 6 of this manuscript, and a comprehensive presentation can also be found in the thesis of R. Lopes[115], who reported the first HOM experiment with atoms in our team.

Thus, a preliminary step in the implementation of the Bell interferometer will involve conducting an HOM experiment, serving as temporal calibration to determine the timings ensuring the closure of the interferometer.

Additionally, in the previous model, the Bragg beams are treated as plane waves. But the wavefront of the Bragg beams can only be considered planar over a limited region of space, essentially within a cylinder whose length corresponds to the Rayleigh length and the radius to the beam waist. If atoms move away from this region, it can induce a differential light shift and affect the reflectivity of the pulses and the phase imprinted on the atoms. This effect will be neglected in the following discussions, assuming that the interferometer is implemented over a sufficiently short time for the atoms to remain within a region where the wavefront is planar.

A few words about non-locality

In the first chapter, it was mentioned that a major contribution of Aspect was to establish a so-called "sensitive" experiment, capable of potentially violating Bell inequalities while challenging the locality assumption of the EPR argument. In our experiment, the two beam splitters are not separated by a spacelike interval. Indeed, considering pairs p_0 and $-p_0$ emitted at speeds of 65 and 115 mm^{-1} in the laboratory reference frame, we can estimate the trajectories of the atoms involved in the Bell interferometer with a classical model. Assuming a velocity difference of $\pm 3\,\mathrm{mm.s}^{-1}$ relative to the HOM doublet,

infinitely thin Bragg pulses, and a typical free propagation time of 1.5 ms, we find that the distance between the atoms from loops A and B is on the order of 20 µm at the final beam splitter (Figure 4.6).

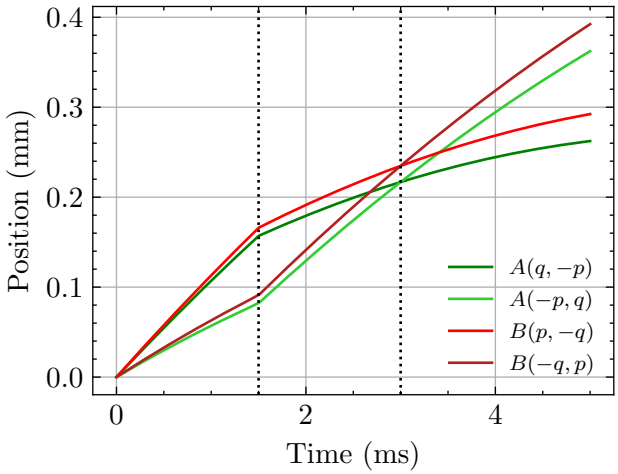

Figure 4.6: Trajectories of the atoms involved in the Bell interferometer in the laboratory reference frame. The legend indicates, for the considered trajectory, the corresponding loop of the interferometer as well as the successive momenta of the atoms.

Our experiment will not challenge the locality assumption, even if we achieve a setup allowing independent control of the phases ϕ_A and ϕ_B. This is not the goal here. Nevertheless, demonstrating a weak version of Bell inequalities would validate the principle of Bell interferometers with atoms involving an external degree of freedom, paving the way for next-generation experiments that could separate the beam splitters by a larger distance to test the issues of locality.

Our goal in observing a violation of Bell inequality is that it is a strong evidence of entanglement of the input state, which in itself would be a significant result, since observing a direct evidence of entanglement in massive particles entangled in momentum is challenging, as discussed in section 1.4.2.

4.1.3 Comparison with another setup

In this section, we will compare our interferometric setup with another recently reported in the literature that has observed an oscillation of the Bell correlator with a visibility $V = 0.42 \pm 0.09$. This Bell interferometer is described in the article "A Matter Wave Rarity-Tapster Interferometer to Demonstrate Non-Locality"[94] published in 2022 by K. Thomas et al. from the He* BEC group at the Australian National University (Canberra). Similar to our team, they employ an experiment involving ultra-cold metastable helium atoms detected by a Microchannel Plate. This article follows a theoretical proposal published in 2015 by R. Lewis-Swan and K. Kheruntsyan[132].

The fundamental difference between our two experiments lies in the pair creation process. In both cases, pairs are generated by four-wave mixing due to collisions in the condensate. In our case, we manipulate the conservation of energy relation using the the optical lattice's fundamental band to emit pairs along a vertical axis. In the experiment reported by Thomas et al., on the other hand, pairs are created by collisions between two condensates[77]. This phenomenon, discussed in the first chapter, involves using Bragg

diffraction to create two condensates moving away from each other, thus generating pairs of opposing momentum in the center-of-mass frame.

The originality here lies in the fact that the Bragg diffraction resonance is sufficiently broad to allow the emission of two scattering halos: one between the initial BEC and the +1 diffraction order, and the other between the BEC and the -1 diffraction order (Figure 4.7). This aspect differs from the initial proposal by Lewis-Swan and Kheruntsyan, who only consider atoms from one scattering halo.

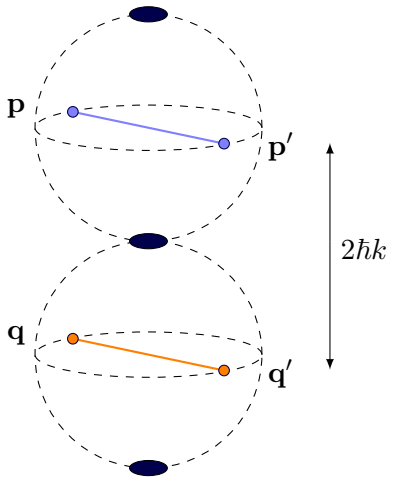

Figure 4.7: Schematic representation of the pair creation process used by Thomas et al. for a Bell interferometer. The dark blue ellipses at the poles of the spheres represent the BECs. A Bragg pulse applied just after the trap is turned off allows the transfer of atoms from an initial BEC (at the center) to two other BECs (at the top and bottom of the spheres). Collisions between the clouds result, through four-wave mixing, in the emission of atom pairs on spheres whose center is the center of mass of the two condensates. Two diametrically opposite modes of a sphere are correlated modes.

The state produced by four-wave mixing results from the same interaction Hamiltonian as the one used in the previous chapter, so the input state of the interferometer is, as in our case, a superposition of TMS states. This imposes similar constraints on mode populations to achieve good correlation properties, along with a good visibility of the Bell correlator. The emitted pairs occur here in all three dimensions of space within a spherical shell. Such a system has led to the observation of strong crossed correlations between pairs of opposite momentum with high $g^{(2)}$ correlation functions[120][133] (up to 10^2 at low population) and violations of the Cauchy-Schwartz inequality[133][21].

Here, two scattering halos are emitted and share a pole along the vertical direction formed by the three BECs (this axis is defined by the Bragg transfer, which transfers to the atoms some momentum in a specific direction).

The momentum modes involved in the Bell interferometer are described in Figure 4.7. The idea is to take a pair of correlated modes $\mathbf{p}$ and $\mathbf{p}'$ from the upper sphere and a pair of modes $\mathbf{q}$ and $\mathbf{q}'$ from the lower sphere, with opposite momentum in the initial BEC reference frame, such that $\mathbf{q}' = -\mathbf{p}$ and $\mathbf{q} = -\mathbf{p}'$. The input state is therefore:

$$|\psi_{\text{in}}\rangle = \frac{1}{\sqrt{2}}(|\mathbf{p}, \mathbf{p}'\rangle + |\mathbf{q}, \mathbf{q}'\rangle) \tag{4.27}$$

The authors do not take into account a possible quadruplet-dependent phase ϕ_0 be-

tween the two coupled modes, considering that this phase is the same for all quadruplets.

The Bell interferometer must involve two momentum doublets, each involving atoms in modes that do not belong to the same correlated pair. The velocity difference along the vertical axis between modes $\mathbf{p}$ and $\mathbf{q}$ is the same as the one between modes $\mathbf{p}'$ and $\mathbf{q}'$. Therefore, these modes can be coupled pairwise by the same pair of Bragg beams. At a time t_1 after the emission of the pairs, a mirror Bragg pulse is sent to the atoms and couples $\mathbf{p}$ and $\mathbf{q}$ in the so-called Left loop, and $\mathbf{p}'$ and $\mathbf{q}'$ in the Right loop (Figure 4.8). At time t_2 a Bragg beam splitter pulse mixes the modes involved in each of these loops, and then the atoms fall freely before being detected by the MCP.

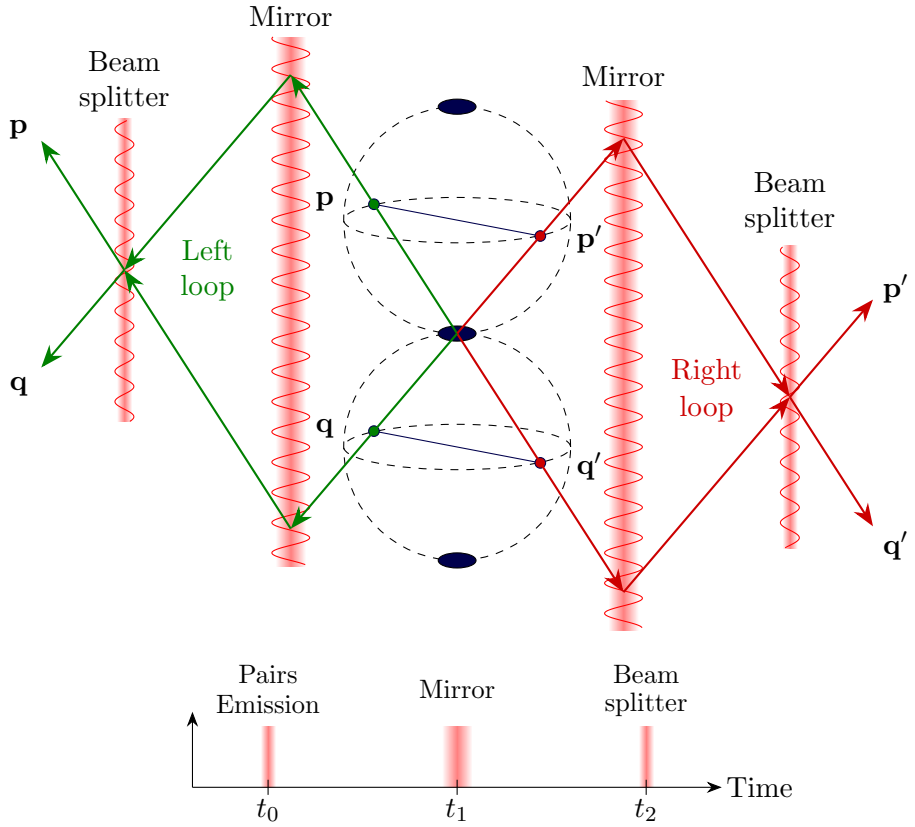

Figure 4.8: Schematic representation of the Bell interferometer presented in Thomas et al.[94]. A first Bragg pulse at $t = t_0$ emits pairs of atoms in two collision halos. Then, a mirror pulse is applied at t_1 followed by a beam splitter pulse at $t - 2$. The diametrically opposed atoms from the two spheres are thereby coupled by Bragg diffraction, forming a Left loop for atoms with momenta $\mathbf{q}$ and $\mathbf{p}$, and a Right loop for atoms with momenta $\mathbf{p}'$ and $\mathbf{q}'$.

By using the same notation conventions as in the previous section, where we expressed a momentum doublet coupled by Bragg as a column matrix, the initial state $|\psi_{\text{in}}\rangle$ writes as follows:

$$|\psi_{\text{in}}\rangle = \frac{1}{\sqrt{2}}\left[\begin{pmatrix}0\\1\end{pmatrix}_L \otimes \begin{pmatrix}0\\1\end{pmatrix}_R + \begin{pmatrix}1\\0\end{pmatrix}_L \otimes \begin{pmatrix}1\\0\end{pmatrix}_R\right] \tag{4.28}$$

where $L = \{|\mathbf{q}\rangle, |\mathbf{p}\rangle\}$ and $R = \{|\mathbf{q}'\rangle, |\mathbf{p}'\rangle\}$ are the basis of the two loops.

Notably, this state differs from the input state of our interferometer (equation 4.4). Here, the first term of the sum involves two atoms that are in the highest momentum state ($\mathbf{p}$ and $\mathbf{p}'$) relative to its Bragg doublet, and the second term includes two atoms that are in the lowest momentum state ($\mathbf{q}$ and $\mathbf{q}'$). In our geometry, on the other hand, each term involved one atom in the lowest momentum state and one atom in the highest momentum state. This difference has a significant consequence, because if we continue the calculation as was done in the first part of this chapter, then we find that this time the joint detection probabilities and the Bell correlator are expressed in the form:

$$\mathcal{P}(p,q) = \mathcal{P}(-p,-q) = \frac{1}{2}\cos^2\left(\frac{\phi_L + \phi_R}{2}\right) \tag{4.29}$$

$$\mathcal{P}(p,-p) = \mathcal{P}(q,-q) = \frac{1}{2}\sin^2\left(\frac{\phi_L + \phi_R}{2}\right) \tag{4.30}$$

where ϕ_L and ϕ_R are the phases imprinted by the lasers on the atoms from loops L and R respectively. We assumed that the phase imprinted by the Bragg mirror was the same for each doublet. From these expressions we get

$$E = \cos(\phi_L + \phi_R) \tag{4.31}$$

In this configuration, the Bell correlator does not depend on the phase difference imposed between the two loops, but on their sum. This difference lies in the geometry of the created pairs relative to how modes are coupled by Bragg: the topology of the interferometer is different from ours (Table 4.1), it is not possible to go continuously from one configuration to another.

Configuration	**Input state**	**Bell correlator**
Thomas et al.[94]	$\lvert\psi_{\text{in}}\rangle = \frac{1}{\sqrt{2}}\left[\begin{pmatrix}0\\1\end{pmatrix}_L \otimes \begin{pmatrix}0\\1\end{pmatrix}_R + \begin{pmatrix}1\\0\end{pmatrix}_L \otimes \begin{pmatrix}1\\0\end{pmatrix}_R\right]$	$\phi_L + \phi_R$
Our setup[93]	$\lvert\psi_{\text{in}}\rangle = \frac{1}{\sqrt{2}}\left[\begin{pmatrix}1\\0\end{pmatrix}_A \otimes \begin{pmatrix}0\\1\end{pmatrix}_B + \begin{pmatrix}0\\1\end{pmatrix}_A \otimes \begin{pmatrix}1\\0\end{pmatrix}_B\right]$	$\phi_A - \phi_B$

Table 4.1: Comparison between the two configurations of Bell interferometers. The input state of each interferometer is given in the adapted basis for Bragg diffraction, such that the top row of each matrix represents the state with the lowest momentum. In the geometry of the interferometer by Thomas et al., $L = \{|\mathbf{q}\rangle, |\mathbf{p}\rangle\}$ and $R = \{|\mathbf{q}'\rangle, |\mathbf{p}'\rangle\}$, while in our configuration, $A = \{|-p\rangle, |q\rangle\}$ and $B = \{|-q\rangle, |p\rangle\}$. The sign between the two phases involved in the interferometer is not the same in the two configurations.

The major advantage is that the same beam splitter can be applied to both loops ($\phi_R = \phi_L$). The Bragg beams are resonant with both doublets, selected to belong to the equatorial plane of each of the two collision spheres. The phase control is performed by a two-output RF generator sending a signal to two different acousto-optics modulators controlling the frequency of each Bragg beam.

The Bell experiment was performed for 9 values of the phase $\Phi = 2\phi_L$ from a BEC with $14(4).10^4$ atoms. The mode population is $\langle N\rangle = 0.15$[133], which should be efficient to exhibit a violation of Bell inequality for a two-mode squeezed state. The duration between each Bragg pulse is 240 µs, and the intensity profiles of the Bragg mirror and beam

splitter are Gaussian-shaped. Their peak reflectivity is 0.984. The results are given in Figure 4.9 after averaging over momentum quadruplet located in the equatorial plane of the scattering halos. Each data point corresponds to about 2900 experimental runs. The authors emphasize that at the time of the Bragg splitter, the distance between the atoms from each loop is 62.4 µm, corresponding to about four times the correlation length of a momentum mode.

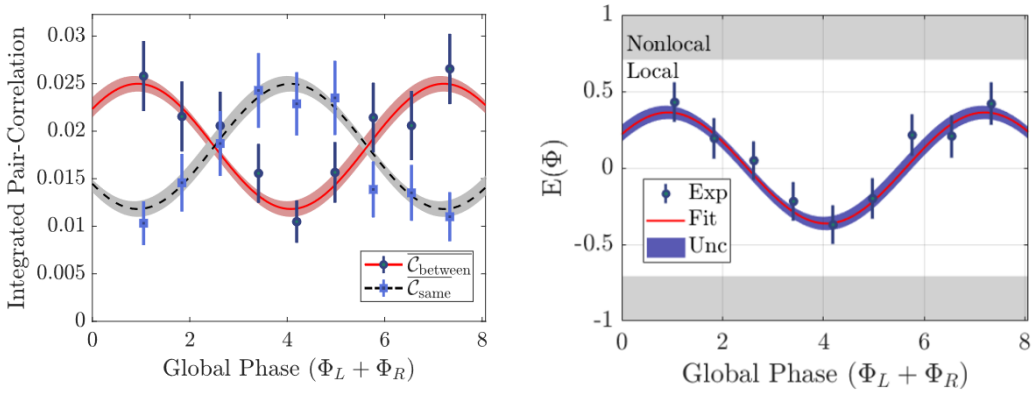

Figure 4.9: Results of the Bell experiment conducted by the ANU team. Taken from [94].

The results show a significant oscillation of the joint probabilities of detection as a function of the global phase Φ, leading to an oscillation of the Bell correlator, but the visibility of 0.42(9) does not make it possible to reach the value of S for which a violation of Bell inequality is observed, despite the low estimated mode population. The authors find indeed $S = 1.1(1)$.

A model presented in the article takes into account the finite momentum mode width by modeling the second order function correlation $G^{(2)}$ as Gaussians. The model also considers the effects of momentum box integration and detector resolution. This led to an estimated visibility of the Bell correlator which depends on mode population, height and width of the correlation between opposite momentum modes, along with integration bin size and detector resolution, which are all experimentally accessible quantities. Nevertheless, these refinements are not sufficient to explain the low measured visibility. The other possibilities mentioned by the authors (Bragg pulse reflectivity, false positives dark counts on the MCP) to account for this low oscillation amplitude appear to have relatively minor effects on the visibility of the Bell signal.

A major drawback of this interferometer, as we understand it, is its high sensitivity to phase fluctuations. As previously mentioned, it is the global phase that plays a role in the Bell signal, i.e., the phase difference between the two Bragg laser beams. Since the two beams do not have the same frequency and ultimately have a certain angle between them (which determines the Bragg momentum $\hbar k_{\mathrm{B}}$), there is inevitably a part of their path where they are in a different free space. Therefore, the slightest relative phase fluctuation between the two beams, typically caused by a mirror vibration on the path of one of the beams, then appears with a factor of two in the Bell correlator, adding a significant averaging effect.

This effect can be estimated by averaging a cosine function within an integration range corresponding to twice the typical estimated phase fluctuation. The expected visibility for a TMS whose mode population is 0.15 is $V = 0.79$. In order to estimate the effect of phase

fluctuations, it is possible to the compute the averaged function $\langle V\cos\Phi\rangle$ as a function of Φ, where $\langle\cdots\rangle$ represents the average of the function $V\cos\Phi$ between $\Phi-\Delta\Phi/2$ and $\Phi+\Delta\Phi/2$. By considering a typical phase fluctuations between different experimental runs of $\Delta\Phi=\pi/2\,\mathrm{rad}$, we find that the visibility decreases to $V=0.50$, which is close to the measured value. Since the authors do not mention any effort on stabilizing or measuring the phase from one experimental run to another, we think that this averaging effect could be part of the reason why the measured visibility is not as high as expected.

Let us point out that this averaging effect cannot be explained by phase fluctuations of the laser itself, since the Bell correlator depends on the phase difference between the phases of the two beams, so the possible phase fluctuations of the laser cancel out.

The phase involved in our interferometer, on the contrary, depends on the relative phase between the two loops $\phi_A-\phi_B$. Since we aim at using the same laser beams for A and B, any phase fluctuation between the two beams present for the atoms from loop A is also present for the atoms from loop B, and this fluctuation cancels out. This effect is called common mode rejection and makes the interferometer we intend to perform more robust to the various phase fluctuations that could occur in a laboratory. Despite the experimental challenges of designing different beam splitters for A and B by exploiting the fact that the doublets do not have the same resonance frequency, the advantage is significant in the quest to demonstrate a violation of Bell's inequality.

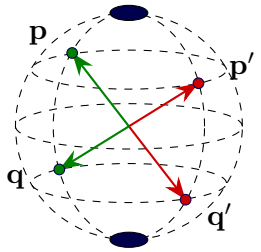

Figure 4.10: Schematic representation of the pairs involved in the Bell proposal by Lewis-Swan et al[132]. The atoms coupled by Bragg are located at two latitudes within the same collision halo. The correlated atoms are $\mathbf{p}$ and $\mathbf{q}'=-\mathbf{p}$ on one hand, and $\mathbf{q}$ and $\mathbf{p}'=-\mathbf{q}$ on the other hand. $\mathbf{p}$ and $\mathbf{q}$ form the Left loop of the interferometer, while $\mathbf{p}'$ and $\mathbf{q}'$ form the Right loop.

In summary, the interferometer presented by Thomas et al. exhibited the oscillation of the Bell correlator, but its visibility is not sufficient to claim a violation of Bell inequality. One potential explanation for this visibility lower than expected is the significant sensitivity of the interferometer to phase fluctuations. This effect is inherent to the chosen interferometer geometry, especially the involved momentum modes, for which the Bell correlator depends on the global phase. It is worth noting that the initial proposal[132], on which the authors rely, has a different geometry, with pairs originating from a single scattering halo (Figure 4.10). In this case, the interferometer's input state is

$$|\psi_{\mathrm{in}}\rangle=\frac{1}{\sqrt{2}}\left[\begin{pmatrix}0\\1\end{pmatrix}_L\otimes\begin{pmatrix}1\\0\end{pmatrix}_R+\begin{pmatrix}0\\1\end{pmatrix}_L\otimes\begin{pmatrix}1\\0\end{pmatrix}_R\right] \tag{4.32}$$

and the correlator then depends on the phase difference between the loops. The Bell correlator is therefore $E=\cos(\phi_L-\phi_R)$. Such an interferometer does not have the sensitivity to phase fluctuations like that of the Thomas et al. interferometer, due to common mode rejection. But it is also more challenging to implement because it requires

addressing different phases to loops L and R, either by using different beams (but with very demanding geometric alignment) or by employing different resonance frequencies (which necessitates a very precise spectral control and doublets L and R at different latitudes)

4.2 Theoretical description of the Bragg pulses

In this section, we will introduce the theoretical model describing Bragg diffraction, which we will use for simulations to determine the characteristics of the mirror and beam splitter pulses for the Bell interferometer. We focus here on the coherent momentum transfer process at a given position, without considering the propagation of wave packets, which will be addressed in section 4.3 about interferometers.

4.2.1 Bragg diffraction of atoms in an optical lattice

Let us consider a BEC of helium atoms in the metastable state $2^3S_1\,(m = 0)$, in free space and without interactions. Two laser beams are directed onto these atoms in the (x, z) plane, separated by an angle θ_B (Figure 4.11). Both beams are π polarized (corresponding to an amplitude of the electric field along the y direction) and originate from the same laser source with a wavelength $\lambda = 1083\,\mathrm{nm}$ but have been separated and prepared at different frequencies ω_1 and ω_2. They intersect on the atoms and interfere, creating an optical lattice in the vertical direction.

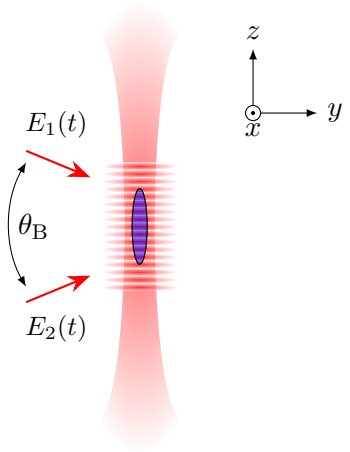

Figure 4.11: Schematic representation of the optical geometry used for the Bragg beams. The two beams are inclined at an angle $\theta_\mathrm{B}/2$ with respect to the y-axis in the (y, z) plane and interfere at the location of the BEC in the optical dipole trap.

The total electric field on the atoms is

$$\mathbf{E} = \mathbf{E_1} + \mathbf{E_2} = E_{1,0} \sin\left(\mathbf{k_1}.\mathbf{r} - \omega_1 t + \varphi_1\right) \mathbf{u_y} + E_{2,0} \sin\left(\mathbf{k_2}.\mathbf{r} - \omega_2 t + \varphi_2\right) \mathbf{u_y} \qquad (4.33)$$

where

$$\mathbf{k_1} = \frac{2\pi}{\lambda}\left(\cos\frac{\theta_\mathrm{B}}{2}\mathbf{u_y} - \sin\frac{\theta_\mathrm{B}}{2}\mathbf{u_z}\right) \qquad \text{and} \qquad \mathbf{k_2} = \frac{2\pi}{\lambda}\left(\cos\frac{\theta_\mathrm{B}}{2}\mathbf{u_y} + \sin\frac{\theta_\mathrm{B}}{2}\mathbf{u_z}\right) \qquad (4.34)$$

Provided that the amplitude of both electric fields is the same ($E_{1,0} = E_{2,0} = E_0$), the resulting intensity is

$$I(z) = |\mathbf{E}|^2 = 2I_0 \left[1 + \sin\left(2kz - \phi(t)\right)\right] = 4I_0 \sin^2\left(kz - \frac{\phi(t)}{2}\right) \tag{4.35}$$

where we defined $I_0 = E_0^2$ and

$$k = \frac{2\pi}{\lambda} \sin\frac{\theta_\mathrm{B}}{2} \qquad \text{and} \qquad \phi(t) = (\omega_2 - \omega_1)t + \varphi_2 - \varphi_1 \tag{4.36}$$

It is worth noting that $\hbar k$ is the elementary momentum exchanged between the photons and the atoms in the lattice along the vertical direction. The period of the lattice is

$$a_\mathrm{lat} = \frac{\lambda}{2\sin\left(\theta_B/2\right)} \tag{4.37}$$

In our case, the angle between the beams is $\theta_\mathrm{B} \approx 31°$, giving an interfringe of $a_\mathrm{lat} \approx 2\,\mu\mathrm{m}$, which is small compared to the estimated size of the BEC along the vertical direction.

In order to characterize the dipole atom-light interaction $\hat{H}_i = -\hat{\mathbf{d}}.\mathbf{E_i}$, one can introduce the (one-photon) Rabi frequency Ω_i for each beam ($i = 1, 2$), which is defined as

$$\Omega_i = -\frac{\langle g|\hat{\mathbf{d}}.\mathbf{E_i}|e\rangle}{\hbar} = -\frac{d_0 E_i}{\hbar} \mathrm{e}^{-\mathrm{i}\varphi_i} \tag{4.38}$$

where $|g\rangle$ and $|e\rangle$ are respectively the ground state and the excited state of the $2^3S_1 \rightarrow 2^3P_0$ transition, d_0 is the associated reduced atomic dipole, and φ_i is the laser phase.

One can show[134] that, if the detuning Δ between the laser frequencies and the atomic transition resonance frequency is high enough, then the population of the excited state is negligible. The atoms in the standing wave are therefore subject to a potential $\hat{H}_\mathrm{I}$ which is proportional to the local light intensity and can be written

$$\hat{H}_\mathrm{I} = 2\hbar|\Omega_\mathrm{R}| \sin^2\left(k\hat{z} - \frac{\phi(t)}{2}\right) \tag{4.39}$$

where we defined the two-photon Rabi frequency Ω_R:

$$\Omega_\mathrm{R} = \frac{\Omega_1 \Omega_2^*}{2\Delta} \tag{4.40}$$

Note that $|\Omega_\mathrm{R}|$ is proportional to the intensity of the light on the atoms and can depend both on time and position. In the following, we will neglect the spatial dependence of Ω_R, assuming that the light is uniform on the atoms (as well as $|\Omega_1| = |\Omega_2|$), but we will keep the assumption that this quantity can be time-dependent.

A detailed calculation of the adiabatic elimination of the excited state in our case can be found in the manuscript of M. Perrier[104]. With $\Delta = 2\pi \times 800\,\mathrm{MHz}$, we will consider that the approximation is well verified and we will neglect the atoms in the excited state, as well as spontaneous emission (see section 6.1.4).

We will also neglect the interactions in the BEC, since the Bragg lattice is performed at least a few hundreds of microseconds after the release of the atoms from the trap, thus after the time for which the dynamics is dominated by the interactions in the BEC.

Consequently, by taking into account the gravity field, the full Hamiltonian of an atom in the lattice is

$$\hat{H} = \frac{\hat{p}^2}{2m} + mg\hat{z} + 2\hbar|\Omega_{\mathrm{R}}|\sin^2\left(k\hat{z} - \frac{\phi(t)}{2}\right) \tag{4.41}$$

Using a unitary transformation, it is possible to work in a basis where the gravitational potential does not appear[135]. Basically this corresponds to work in the reference frame of the atoms in free fall. After shifting the energy reference by $\hbar|\Omega_{\mathrm{R}}|$, the Hamiltonian can then be rewritten

$$\hat{H} = \frac{\hat{p}^2}{2m} - \frac{\hbar|\Omega_{\mathrm{R}}|}{2}\left(\mathrm{e}^{2\mathrm{i}k\hat{z}-\mathrm{i}\phi(t)} + \mathrm{e}^{-2\mathrm{i}k\hat{z}+\mathrm{i}\phi(t)}\right) \tag{4.42}$$

The operators $\mathrm{e}^{\pm 2\mathrm{i}k\hat{z}}$ are translation operators by $\pm 2\hbar k$ in the momentum space:

$$e^{\pm 2\mathrm{i}k\hat{z}}\,|p\rangle = |p \pm 2\hbar k\rangle \tag{4.43}$$

We can see from equation 4.42 that the interaction term allows for a momentum transfer of $2\hbar k$ to the atoms. Bragg diffraction between a momentum state $|p\rangle$ and a momentum state $|p + 2\hbar k\rangle$ can actually be interpreted as a two-photon process: one photon from beam 1 is absorbed by an atom, which excites it while transferring it a momentum $\hbar k$, then this atom emits a photon by stimulated emission in beam 2, which deexcites it to the ground state while transferring it again a momentum $\hbar k$.

In order to determine the evolution of the system, we will expand the state of the atoms in the basis of momentum states:

$$|\psi(t)\rangle = \sum_{n=-\infty}^{+\infty} C_{2n}(t)\mathrm{e}^{-\mathrm{i}\frac{E_{2n}}{\hbar}t}\,|p + 2n\hbar k\rangle \tag{4.44}$$

where

$$E_{2n} = \frac{(p + 2n\hbar k)^2}{2m} \tag{4.45}$$

is the kinetic energy of the atom in the momentum state $|p + 2n\hbar k\rangle$. Note that C_{2n} is the amplitude of probability to find an atom in the associated momentum state, and n is the diffraction order.

By inserting the state 4.44 into the Schrödinger equation with the Hamiltonian 4.42, one can establish the following relationship between the C_{2n} coefficients:

$$\mathrm{i}\hbar\dot{C}_{2n}\mathrm{e}^{-\mathrm{i}\frac{E_{2n}}{\hbar}t} = -\frac{\hbar|\Omega_{\mathrm{R}}|}{2}\left(C_{2n-2}\mathrm{e}^{-\mathrm{i}\frac{E_{2n-2}}{\hbar}t}\mathrm{e}^{-\mathrm{i}\phi(t)} + C_{2n+2}\mathrm{e}^{-\mathrm{i}\frac{E_{2n+2}}{\hbar}t}\mathrm{e}^{\mathrm{i}\phi(t)}\right) \tag{4.46}$$

which can be rewritten

$$\dot{C}_{2n} = \mathrm{i}\frac{|\Omega_{\mathrm{R}}|}{2}\left(C_{2n-2}\mathrm{e}^{-\mathrm{i}\frac{E_{2n-2}-E_{2n}}{\hbar}t}\mathrm{e}^{-\mathrm{i}\phi(t)} + C_{2n+2}\mathrm{e}^{-\mathrm{i}\frac{E_{2n+2}-E_{2n}}{\hbar}t}\mathrm{e}^{\mathrm{i}\phi(t)}\right) \tag{4.47}$$

Let us recall that $\phi(t) = (\omega_2 - \omega_1)t + \varphi_2 - \varphi_1$. The exponential terms can be expressed in terms of detuning between the laser frequency difference and the Bragg coupling frequency between the energy levels (Figure 4.12), by defining, for each momentum state:

$$\delta_{2n} = \omega_2 - \omega_1 - \frac{E_{2n+2} - E_{2n}}{\hbar} \tag{4.48}$$

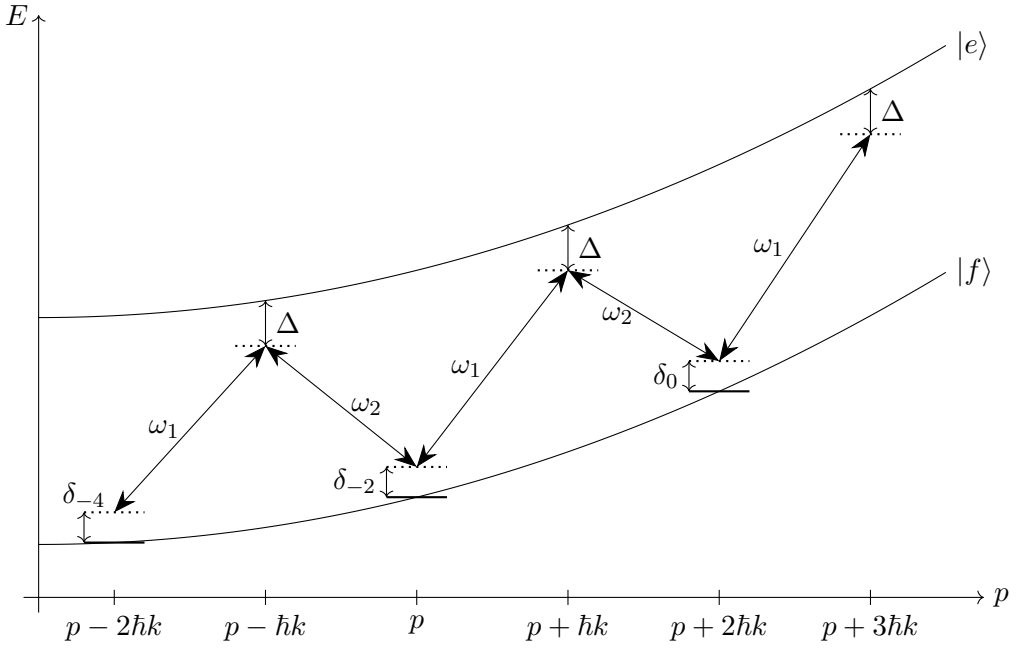

Figure 4.12: Energy diagram of the Bragg diffraction process.

This way, equation 4.47 reads

$$\dot{C}_{2n} = \mathrm{i}\frac{|\Omega_\mathrm{R}|}{2}\left(C_{2n-2}\mathrm{e}^{-\mathrm{i}\delta_{2n-2}t}\mathrm{e}^{-\mathrm{i}(\varphi_2-\varphi_1)} + C_{2n+2}\mathrm{e}^{\mathrm{i}\delta_{2n}t}\mathrm{e}^{\mathrm{i}(\varphi_2-\varphi_1)}\right) \tag{4.49}$$

which can be simplified to give

$$\dot{C}_{2n} = \mathrm{i}\frac{\Omega_\mathrm{R}^*}{2}C_{2n-2}\mathrm{e}^{-\mathrm{i}\delta_{2n-2}t} + \mathrm{i}\frac{\Omega_\mathrm{R}}{2}C_{2n+2}\mathrm{e}^{\mathrm{i}\delta_{2n}t} \tag{4.50}$$

where we used the definition 4.40 of the two-photon Rabi frequency. Therefore the dynamics of the system can be described by the following matrix equation:

$$\begin{pmatrix}\dot{C}_{-4}\\ \dot{C}_{-2}\\ \dot{C}_0\\ \dot{C}_2\\ \dot{C}_4\end{pmatrix} = \mathrm{i}\begin{pmatrix} 0 & \frac{\Omega_\mathrm{R}}{2}\mathrm{e}^{\mathrm{i}\delta_{-4}t} & 0 & 0 & 0\\ \frac{\Omega_\mathrm{R}^*}{2}\mathrm{e}^{-\mathrm{i}\delta_{-4}t} & 0 & \frac{\Omega_\mathrm{R}}{2}\mathrm{e}^{\mathrm{i}\delta_{-2}t} & 0 & 0\\ 0 & \frac{\Omega_\mathrm{R}^*}{2}\mathrm{e}^{-\mathrm{i}\delta_{-2}t} & 0 & \frac{\Omega_\mathrm{R}}{2}\mathrm{e}^{\mathrm{i}\delta_0 t} & 0\\ 0 & 0 & \frac{\Omega_\mathrm{R}^*}{2}\mathrm{e}^{-\mathrm{i}\delta_0 t} & 0 & \frac{\Omega_\mathrm{R}}{2}\mathrm{e}^{\mathrm{i}\delta_2 t}\\ 0 & 0 & 0 & \frac{\Omega_\mathrm{R}^*}{2}\mathrm{e}^{-\mathrm{i}\delta_2 t} & 0\end{pmatrix}\begin{pmatrix}C_{-4}\\ C_{-2}\\ C_0\\ C_2\\ C_4\end{pmatrix} \tag{4.51}$$

The system was truncated to 5 diffraction orders for readability. This expression shows that the different momentum states are coupled two by two. The detuning δ_{2n} quantifies the deviation from resonance between two levels, and can be expressed as a function of the initial momentum p:

$$\hbar\delta_{2n} = \hbar(\omega_2 - \omega_1) - \left(\frac{\hbar^2 k_\mathrm{B}^2}{2m}(2n+1) + \frac{\hbar k_\mathrm{B}}{m}p\right) \tag{4.52}$$

where $\hbar k_\mathrm{B} = 2\hbar k$ is the momentum transferred during the two-photon transition. When $\delta_{2n} = 0$, the resonance condition is fulfilled between the momentum states $|p + 2n\hbar k\rangle$ and

$|p + (2n + 2)\hbar k\rangle$, leading to an efficient transfer between the two momentum levels, as we will see in the following. δ_{2n} can easily be expressed as a function of the δ_0 and n:

$$\delta_{2n} = \delta_0 - 4n\Omega_\mathrm{r} \tag{4.53}$$

where we defined

$$\Omega_\mathrm{r} = \frac{\hbar k^2}{m} \qquad \text{and} \qquad \hbar\delta_0 = \hbar(\omega_2 - \omega_1) - \left(\frac{\hbar^2 k_\mathrm{B}^2}{2m} + \frac{\hbar k_\mathrm{B}}{m} p\right) \tag{4.54}$$

The energy $\hbar\Omega_\mathrm{r}$ corresponds to the two-photon recoil energy transferred to the atoms by the Bragg lattice. Note that, when $\delta_0 = 0$, we recover the resonance condition 1.104 derived in Chapter 1 from momentum and conservation.

Let us highlight that the detuning depends linearly on the initial momentum p of the atoms. This means that for a given value of $\omega_2 - \omega_1$, solving the Schrödinger equation for one initial momentum class p as a function of the detuning δ_0 gives the information about how the off-resonant momentum classes will behave in the Bragg process. Experimentally, it is possible to tune the frequency difference $\omega_2 - \omega_1$ (using one acousto-optic modulator for each beam for instance) in order to select a specific momentum class which will be resonant for the Bragg transition.

4.2.2 Bragg regime, Kapitza-Dirac regime and Raman-Nath approximation

In this section, we will numerically solve the Bragg system of equations 4.51 and briefly discuss the limiting cases in the simple case where Ω_R is constant and the detuning is fixed. The goal is to determine the atom population after a Bragg pulse of duration T. We will assume that the phase difference between the lasers $\varphi_1 - \varphi_2$ is constant over the duration of a Bragg pulse, so that the term $\mathrm{e}^{\mathrm{i}(\varphi_1 - \varphi_2)}$ in the two-photon Rabi frequency is a global phase which does not play a role in the population evolution of the system. We will write, in all the manuscript, $\Omega_\mathrm{R}(t) = \Omega_\mathrm{M}$ for a constant Bragg pulse, where Ω_M is a real number corresponding to the amplitude of the two-photon Rabi frequency.

The equation 4.51 can be numerically solved by providing an initial condition and truncating the matrix to a number of orders to be considered.

We will start from a situation where an atom is in the momentum state $|p\rangle$, which determines the order 0 of diffraction. The system is arbitrarily truncated to 11 diffraction orders, and we will stay in a range of parameters for which Bragg pulses do not transfer atoms beyond orders -5 and 5. The initial condition for the numerical solution is therefore $(C_{-10}, \ldots, C_{-2}, C_0, C_2, \ldots, C_{10}) = (0, \ldots, 0, 1, 0, \ldots, 0)$.

Let us consider at first the case for which the detuning between orders 0 and 1 is $\delta_0 = 0$. The system 4.51 was solved in three cases for different values of Ω_M compared to the two-photon recoil frequency Ω_r. The population evolution dynamics $|C_{2n}(t)|^2$ is given as a function of time, which was nondimensionalized by diving it by the typical evolution time given by the two-photon Rabi frequency π/Ω_M. The results are plotted in Figure 4.13.

Two diffraction regimes can be distinguished:

- If the Rabi frequency is small compared to the recoil frequency, only the 0th and first diffraction orders are populated, and their population oscillates regularly over time. This regime is referred to as the Bragg regime, and we will see later that in

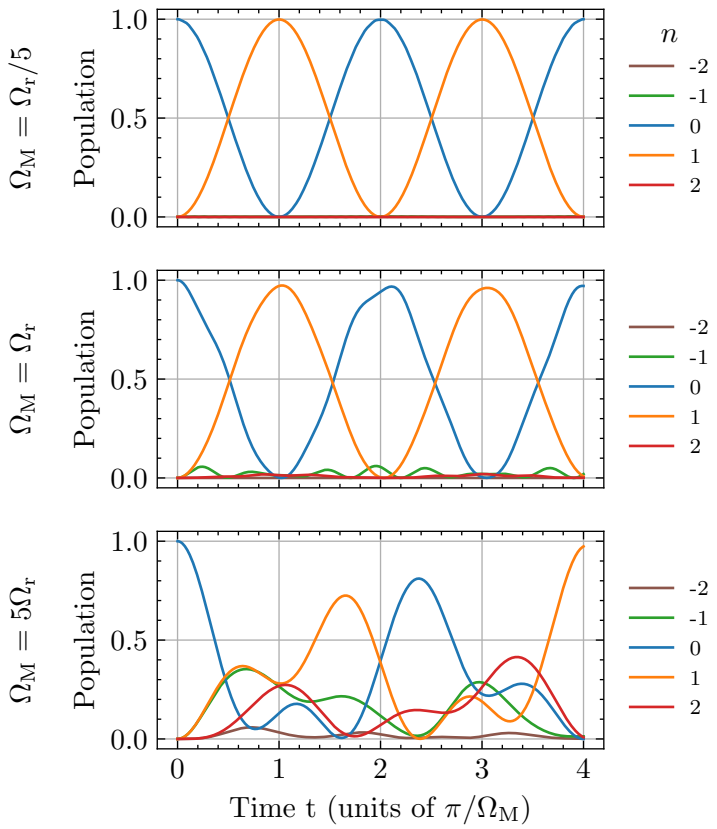

Figure 4.13: Evolution of the population of 5 diffraction orders as a function of the pulse duration for different two-photon Rabi frequencies. The results are obtained by solving equations 4.51. Time is normalized by π/Ω_M, so a similar value on the abscissa does not correspond to the same duration for each plot.

this regime, it is possible to simplify the problem into a two-level system coupled by Rabi oscillations.

- If the Rabi frequency is large compared to the recoil frequency, more diffraction orders are populated, and the populations fluctuate in a non-trivial manner. This regime is called the Kapitza-Dirac regime (or diffractive regime), named after the two physicists who predicted a similar diffraction effect of light by electrons[136], a principle now more widely used to describe the diffraction of a particle by a standing wave. While some authors refer to this effect as diffraction in general, we will limit ourselves here to stating that this regime corresponds to the case where diffraction is observed into more than two diffraction orders.

In our case, the Bragg regime is the most suitable for transferring a specific momentum to the atoms in a controlled manner. It is already evident that, in this regime, depending on the duration of the pulse, it is possible to implement π and $\pi/2$ pulses, thereby realizing atom mirrors and beam splitters, respectively. Moreover, in the Bell interferometer, transferring a part of the atoms into other diffraction orders would be considered as losses since these atoms would not be involved in the two-atom interference leading to the oscillation of the Bell parameter. As seen in Figure 4.13, a two-photon Rabi frequency of the same order of magnitude as the recoil frequency corresponds to the threshold beyond which diffraction towards higher orders cannot be neglected.

Observing many diffraction orders in the Kapitza-Dirac regime can still be useful experimentally in order to measure precisely the momentum transferred by Bragg diffraction.

Kapitza-Dirac in the Raman-Nath regime

Under some conditions, it is possible to derive an analytical solution for the Bragg diffraction in the Kapitza-Dirac regime. Indeed, if we suppose that the duration t of the pulse is small enough to neglect the detuning variation in equation 4.51 (hypothesis on which we will come back later), then the amplitude coefficients are given by

$$\dot{C}_{2n} = \mathrm{i}\frac{\Omega_\mathrm{M}}{2}\left(C_{2n-2} + C_{2n+2}\right) \tag{4.55}$$

The solutions of these coupled equations are known and can be written

$$C_{2n} = \mathrm{i}^n\, J_n(\Omega_\mathrm{M} t) \tag{4.56}$$

where J_n is the Bessel function of first kind.[3] The population of the nth diffraction order is therefore

$$\mathcal{P}_{2n}(t) = |J_n(\Omega_\mathrm{M} t)|^2 \tag{4.57}$$

Figure 4.14 shows a comparison of the numerical solution for the populations with $\Omega_\mathrm{M} = 5\Omega_\mathrm{r}$ with the analytic solution from equation 4.57. One can see that the small duration approximation holds true for $t \ll \pi/\Omega_\mathrm{M}$. This is referred to as the Raman-Nath regime, named after the equation that characterizes the system with slightly different conventions.[4]

The Raman-Nath approximation actually consists in neglecting the kinetic energy term in the Hamiltonian, thus assuming that the atoms do not have time to move in the optical lattice during their interaction. This is much true as long as t is smaller than the typical oscillation period τ_osc of the atoms in the lattice. By approximating the interaction Hamiltonian 4.39 by a squared potential ($\hat{H}_I \approx \hbar\Omega_\mathrm{M} k^2 z^2$), we see that the typical oscillation frequency ω_osc is such that

$$\omega_\mathrm{osc}^2 = \frac{2\hbar\Omega_\mathrm{M} k^2}{m} = 2\Omega_\mathrm{M}\Omega_\mathrm{r} \tag{4.58}$$

from which we obtain

$$t \ll \tau_\mathrm{osc} = \frac{1}{\sqrt{2\Omega_\mathrm{M}\Omega_\mathrm{r}}} \tag{4.59}$$

which is more general than the condition $t \ll \pi/\Omega_\mathrm{M}$ that we conjectured from the particular case where $\Omega_\mathrm{M} = 5\Omega_\mathrm{r}$.

[3] The Bessel functions verify the relationship

$$2J_n'(t) = J_{n-1}(t) - J_{n+1}(t)$$

[4] Starting from Hamiltonian 4.42 in the space representation, and by decomposing the solution in the basis of plane waves

$$\psi(z) = \sum_n C_{2n}(t)\mathrm{e}^{2\mathrm{i}nkz}$$

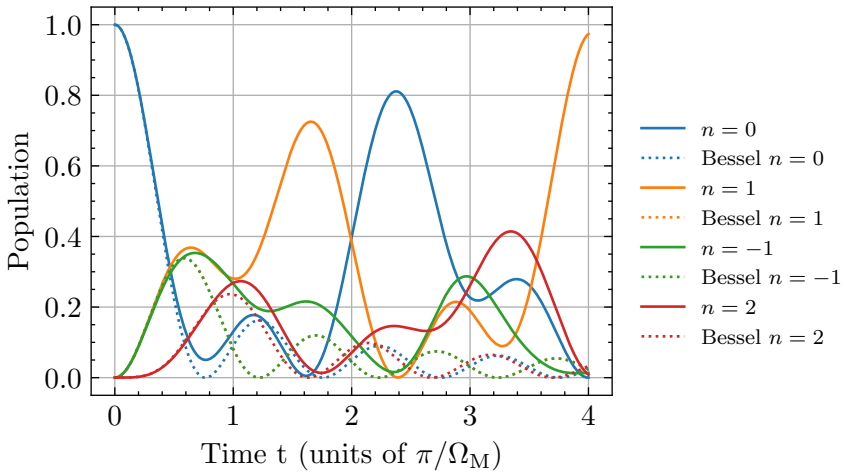

Figure 4.14: Comparison of the population evolution of 3 diffraction orders between the numerical (solid lines) and the analytical solution (dashed lines) for $\Omega_M = 5\Omega_r$.

Bragg regime: a two-level system

In this section, we will focus on the Bragg regime, for which only two states are populated. Let us suppose that the amplitude Ω_M of the two-photon Rabi frequency Ω_R is small enough to prevent diffraction towards orders other than 0 and 1. We assume an arbitrary detuning δ_0, but within a range where only orders 0 and 1 are populated. The multi-level system 4.51 can be truncated to a two-level system, so that

$$\begin{pmatrix} \dot{C}_0 \\ \dot{C}_2 \end{pmatrix} = \mathrm{i} \begin{pmatrix} 0 & \frac{\Omega_R}{2} e^{\mathrm{i}\delta_0 t} \\ \frac{\Omega_R^*}{2} e^{-\mathrm{i}\delta_0 t} & 0 \end{pmatrix} \begin{pmatrix} C_0 \\ C_2 \end{pmatrix} \tag{4.60}$$

This can be analytically solved when Ω_R and δ_0 are constant (laser intensity and frequency difference held constant). The temporal origin is set at $t = 0$, corresponding to the moments when the lasers are turned on. Initially, all the atoms are in the 0th order of diffraction, so that $C_0(0) = 1$ and $C_2(0) = 0$.

Starting from equation 4.60, it is possible to express $\dot{C}_0$ as a function of C_2 and vice versa. By differentiating either of these two relations and using the second one, we obtain a second-order differential equation involving only one of the coefficients:

$$\ddot{C}_n + \mathrm{i}\epsilon\,\delta\,\dot{C}_n + \frac{|\Omega_R|^2}{4} C_n = 0 \tag{4.61}$$

with $\epsilon = -1$ if $n = 0$ and $\epsilon = +1$ if $n = 2$. By solving these two decoupled equations, we get the relationship:

$$\begin{pmatrix} C_0(t) \\ C_2(t) \end{pmatrix} = U(t) \begin{pmatrix} C_0(0) \\ C_2(0) \end{pmatrix} \tag{4.62}$$

where

$$U(t) = \begin{pmatrix} \left[\cos\left(\frac{\Omega t}{2}\right) - \mathrm{i}\frac{\delta_0}{\Omega}\sin\left(\frac{\Omega t}{2}\right)\right] e^{\frac{\mathrm{i}\delta_0 t}{2}} & \mathrm{i}\frac{\Omega_R}{\Omega}\sin\left(\frac{\Omega t}{2}\right) e^{\frac{\mathrm{i}\delta_0 t}{2}} \\ \mathrm{i}\frac{\Omega_R^*}{\Omega}\sin\left(\frac{\Omega t}{2}\right) e^{-\frac{\mathrm{i}\delta_0 t}{2}} & \left[\cos\left(\frac{\Omega t}{2}\right) + \mathrm{i}\frac{\delta_0}{\Omega}\sin\left(\frac{\Omega t}{2}\right)\right] e^{-\frac{\mathrm{i}\delta_0 t}{2}} \end{pmatrix} \tag{4.63}$$

with $\Omega = \sqrt{|\Omega_\mathrm{R}|^2 + \delta_0^2}$.

This is the evolution matrix of a two-level system subject to Rabi oscillations. With the initial conditions previously mentioned, the probability $\mathcal{P}_2(t) = |C_2(t)|^2$ of measuring atoms in the 1st diffraction order after a pulse of duration t is given by the well known Rabi formula:

$$\mathcal{P}_2(t) = \frac{|\Omega_\mathrm{R}|^2}{|\Omega_\mathrm{R}|^2 + \delta_0^2} \sin^2\left(\frac{\sqrt{|\Omega_\mathrm{R}|^2 + \delta_0^2}\, t}{2}\right) \tag{4.64}$$

Let us write the two-photon Rabi frequency in the form $\Omega_\mathrm{R} = \Omega_\mathrm{M} \mathrm{e}^{\mathrm{i}\phi}$, where Ω_M is a real number and $\phi = \varphi_1 - \varphi_2$ is the phase difference between the two Bragg beams. In the resonant case, for which $\delta_0 = 0$, the evolution matrix is

$$U(t) = \begin{pmatrix} \cos\left(\dfrac{\Omega_\mathrm{M} t}{2}\right) & \mathrm{i}\sin\left(\dfrac{\Omega_\mathrm{M} t}{2}\right)\mathrm{e}^{\mathrm{i}\phi} \\ \mathrm{i}\sin\left(\dfrac{\Omega_\mathrm{M} t}{2}\right)\mathrm{e}^{-\mathrm{i}\phi} & \cos\left(\dfrac{\Omega_\mathrm{M} t}{2}\right) \end{pmatrix} \tag{4.65}$$

This expression highlights the fact that at fixed Ω_M, varying the duration t of the Bragg pulse makes it possible to coherently transfer the atoms from the state $|p\rangle$ to a superposition of $|p\rangle$ and $|p + 2\hbar k\rangle$, or even to the state $|p + 2\hbar k\rangle$ only:

- If $\Omega_M t = \pi/2$, the resonant atoms are transferred from state $|p\rangle$ to an equiprobable superposition of states $|p\rangle$ and $|p + 2\hbar k\rangle$. This is called a $\pi/2$ pulse, for which the transfer matrix writes:
$$U_\mathrm{S}(t) = \frac{\sqrt{2}}{2}\begin{pmatrix} 1 & \mathrm{i}\mathrm{e}^{\mathrm{i}\phi} \\ \mathrm{i}\mathrm{e}^{-\mathrm{i}\phi} & 1 \end{pmatrix} \tag{4.66}$$
This is the operator we used in section 4.1 to describe an atom beam splitter.

- Similarly, if $\Omega_M t = \pi$, the resonant atoms are transferred from state $|p\rangle$ to state $|p + 2\hbar k\rangle$. This is called a π pulse, and the transfer matrix writes:
$$U_\mathrm{M}(t) = \begin{pmatrix} 0 & \mathrm{i}\mathrm{e}^{\mathrm{i}\phi} \\ \mathrm{i}\mathrm{e}^{-\mathrm{i}\phi} & 0 \end{pmatrix} \tag{4.67}$$
Again, this is the operator we used to describe an atom mirror.

We therefore showed that the Bragg beams act on the atoms like optics would act on photons, by transferring them momentum in a controlled manner. Furthermore, we see that Bragg diffraction imprints a phase onto the atoms, corresponding to the phase difference between the two beams at the moment of the Bragg pulse. Starting from atoms in the 0th diffraction order, C_0 can be called the transmission coefficient while C_2 can be called the reflection coefficient, by analogy with optics.

Ultimately, our goal is to determine the evolution of the Bell correlator as a function of the momentum class. To this end, the first step is to have a look at the Bragg transfer properties (reflectivity and phase) as a function of the detuning, due to the linear relationship between the two. From the propagation matrix 4.63, we can clearly see that out of resonance, the reflection and transmission coefficients will depend on the detuning δ_0, both in terms of amplitude and phase.

4.2.3 Off-resonance Bragg diffraction

From now on, we will consider a multi-level system characterized by equation 4.51. In Figure 4.15, we plot the probabilities of finding the atoms in different diffraction orders for a π pulse (for which the duration T of the pulse is $T = \pi/\Omega_{\mathrm{M}}$) with different values of $\Omega_{\mathrm{M}}/\Omega_{\mathrm{r}}$ as a function of detuning δ_0 (again, $\delta_0 = 0$ corresponds to a resonance between the orders 0 and +1), obtained by solving numerically equation 4.51 for each value of detuning.

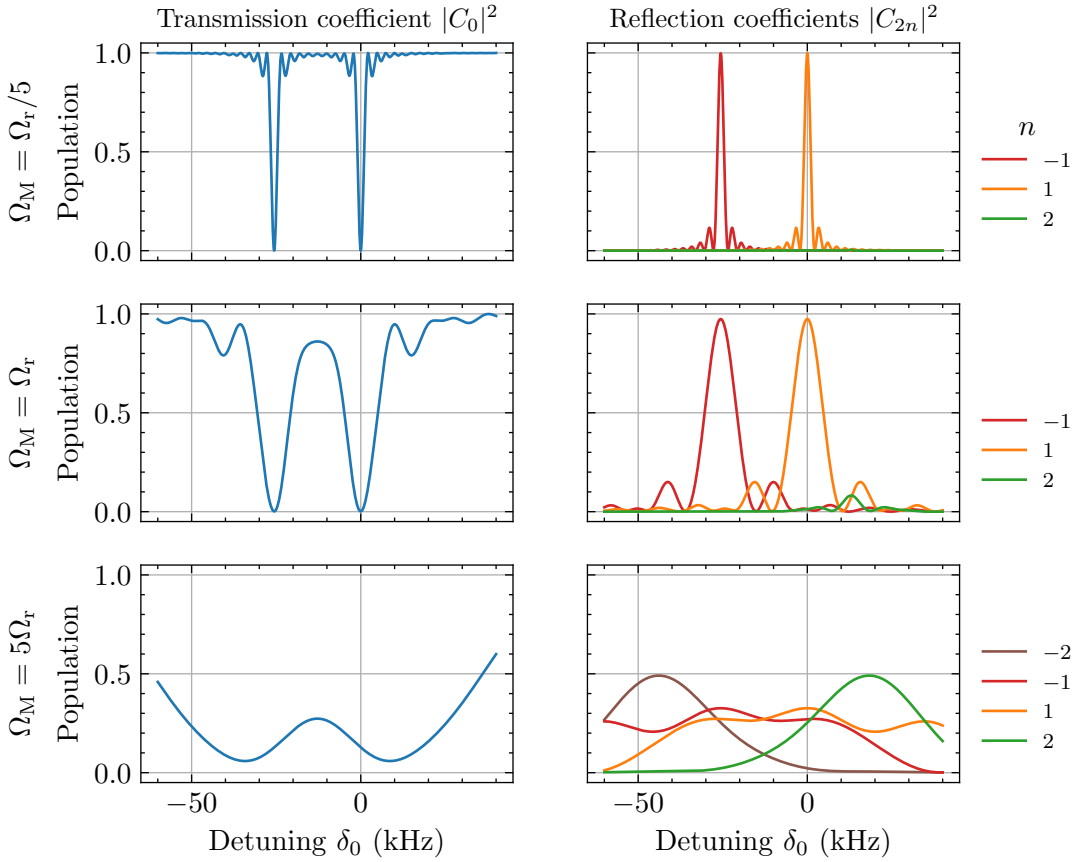

Figure 4.15: Populations as a function of detuning for different values of the two-photon Rabi frequency. The duration of the pulse is $T = \pi/\Omega_{\mathrm{M}}$. The transmission and reflection coefficients C_{2n} are calculated from solving equation 4.51. We use a recoil frequency $\Omega_{\mathrm{r}} = 2\pi \times 6.3\,\mathrm{kHz}$, corresponding to the experimental value.

In the Bragg regime ($\Omega_{\mathrm{M}} = \Omega_{\mathrm{r}}/5$), the resonant atoms ($\delta_0 = 0$) are transferred to the +1 diffraction order. The reflectivity profile (i.e., the probability $|C_2|^2$ of finding the atoms in the $n = 1$ diffraction order) as a function of detuning has a sinc-squared shape. By varying the detuning, one can reach a value of δ_0 for which the Bragg transition occurs between the 0 order and the −1 order. In this case, $\delta_{-2} = 0$, and the reflectivity profile is identical to the one observed for the +1 order, both situations being symmetrical. There is no detuning for which atoms are diffracted to other diffraction orders.

As the two-photon Rabi frequency increases ($\Omega_{\mathrm{M}} = \Omega_{\mathrm{r}}$), the resonance peak widths also increase. The reflectivity of the +1 order becomes broadened to the point of being close to the resonance peak of the −1 order. Under these limiting conditions, there are detunings for which the population towards, for example, the +2 diffraction order is non-zero.

In the Kapitza-Dirac regime, it no longer makes sense to define the Bragg pulse as

a π pulse, as even the resonant atoms are transferred to states other than the $+1$ order. The resonance peak is broadened to the extent that it overlaps with the resonance towards the -1 order and so on, leading to the population of additional diffraction orders.

We see that the distinction between the Bragg regime and the Kapitza-Dirac regime can be interpreted in terms of resonance width. In the Bragg regime, the two-photon Rabi frequency is low, so the resonance is well-resolved, and the reflectivity is narrow around a well-defined momentum level, which is the only one coupled to the initial state. In the Kapitza-Dirac regime, the Rabi frequency is high, resulting in a broad resonance that encompasses multiple levels that can be populated because coupling with the initial state is permitted.

In the following, we will only focus on the Bragg regime. We make sure that the Rabi frequency remains lower than the recoil frequency (with our parameters, we have $\Omega_\mathrm{r} = 2\pi \times 6.3\,\mathrm{kHz}$), so that we work in this regime and can neglect diffraction towards diffraction orders otherthan the resonant one.

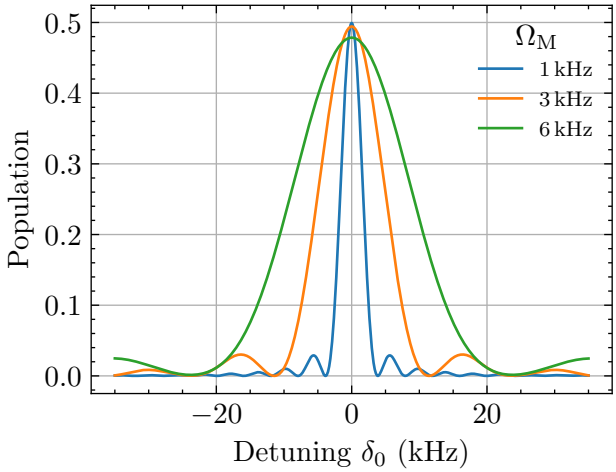

Figure 4.16: Reflected population $|C_2|^2$ as a function of detuning for different values of the two-photon Rabi frequency. The duration of the pulse is $T = \pi/2\Omega_\mathrm{M}$. We use a recoil frequency $\Omega_\mathrm{r} = 2\pi \times 6.3\,\mathrm{kHz}$, corresponding to the experimental value.

A similar behavior is observed with $\pi/2$ pulses, as seen in Figure 4.16 representing the population of the $+1$ diffraction orders for different values of Ω_M. The reflectivity profile has a sinc-squared shape, reaching 0.5 at resonance. As the two-photon Rabi frequency increases, the width of the resonance peak also increases. Approaching the recoil frequency Ω_r, the resonance reflectivity decreases, indicating that there is also diffraction of atoms towards other diffraction orders.

Expression of the reflection coefficient in a perturbative model

The width of the reflectivity profile is, for a constant pulse, entirely determined by the two-photon Rabi frequency. It is possible to formally show this relationship in a general case (without assuming that $\Omega_\mathrm{R}(t)$ is constant) by expressing analytically the coefficients C_{2n} in a perturbative approach.

We consider again the case where $C_0(0) = 1$ and $C_{2n}(0) = 0$ for $n \neq 0$. We define the initial instant as the limit $t \to -\infty$ and the final instant as the limit $t \to +\infty$. Making this choice is not restrictive because the pulses have a finite duration T, and $\Omega_R = 0$ if $t \notin [0, T]$, so that the only non-zero contribution of the two-photon Rabi frequency contributes to the result. To determine the final state of the system, we integrate equation 4.47, so that we get

$$C_{2n}(t \to +\infty) = \frac{\mathrm{i}}{2} \int_{-\infty}^{+\infty} C_{2n-2}(t)\Omega_{\mathrm{R}}^*(t)\mathrm{e}^{-\mathrm{i}\delta_{2n-2}t}\mathrm{d}t + \frac{\mathrm{i}}{2} \int_{-\infty}^{+\infty} C_{2n+2}(t)\Omega_{\mathrm{R}}(t)\mathrm{e}^{\mathrm{i}\delta_{2n}t}\mathrm{d}t \tag{4.68}$$

Let us assume that the coupling is weak, so that at any given time, we can consider the population of order 0 to be predominant: $|C_{2n}(t)| \ll |C_0(t)| \approx 1$. In particular, for $n = 1$, we can neglect $|C_4(t)|$ compared to $|C_0(t)|$ to obtain an analytical expression for the coefficient C_2 at the final state:

$$C_2(t \to +\infty) \approx \frac{\mathrm{i}}{2} \int_{-\infty}^{+\infty} \Omega_{\mathrm{R}}^*(t)\mathrm{e}^{-\mathrm{i}\delta_0 t}\mathrm{d}t \tag{4.69}$$

Interestingly, this expression shows that the reflection coefficient $C_2(t)$ can be expressed as the Fourier transform of the temporal profile of the two-photon Rabi frequency:

$$C_2(t \to +\infty) \approx \frac{\mathrm{i}}{2}\mathrm{FT}[\Omega_{\mathrm{R}}^*(t)](\delta_0) \tag{4.70}$$

where we defined the Fourier transform as

$$\mathrm{FT}[f(t)](\omega) = \int_{-\infty}^{+\infty} f(t)\mathrm{e}^{-\mathrm{i}\omega t}\mathrm{d}t \tag{4.71}$$

This relationship sheds light on the reflectivity curves shown earlier for constant pulses. Indeed, the Fourier transform of a square signal is a sinc function. The probability of reflection $|C_2|^2$ as a function of detuning, corresponding to the squared modulus of the Fourier transform of the Bragg pulse profile, thus follows a squared sinc profile. This also explains why the width of the resonance peak is larger when the Rabi frequency is greater, as the duration of a $\pi/2$ pulse (for instance) is inversely proportional to the Rabi frequency: if Ω_{M} is high, then the duration T of the pulse is small, making its Fourier transform broader.

Let us discuss the assumption that led to the derivation of the relation 4.70. It was necessary to assume that $C_0(t) \approx 1$. In general, this holds true only for Bragg pulses for which the population of the excited state remains low, i.e., for short interaction times. Strictly speaking, this assumption is not satisfied for a $\pi/2$ pulse, and even less so for a π pulse. In these two cases, we cannot assert that the reflectivity as a function of detuning is rigorously equal to the Fourier transform of the temporal pulse.

However, we empirically observe that the difference between the simulated reflectivity profile and the profile calculated using the Fourier transform 4.70 formula is small. This will be discussed later in the manuscript when considering time-varying Bragg pulses. In the case of a constant pulse, the analytical solution of equation 4.63 shows that this relation is indeed exact, provided that we neglect diffraction towards higher orders (Figure 4.17).

Thus, this perturbative development, even if not rigorously valid for significant transfers, provides an intuitive understanding of the reflectivity profile as a function of detuning.

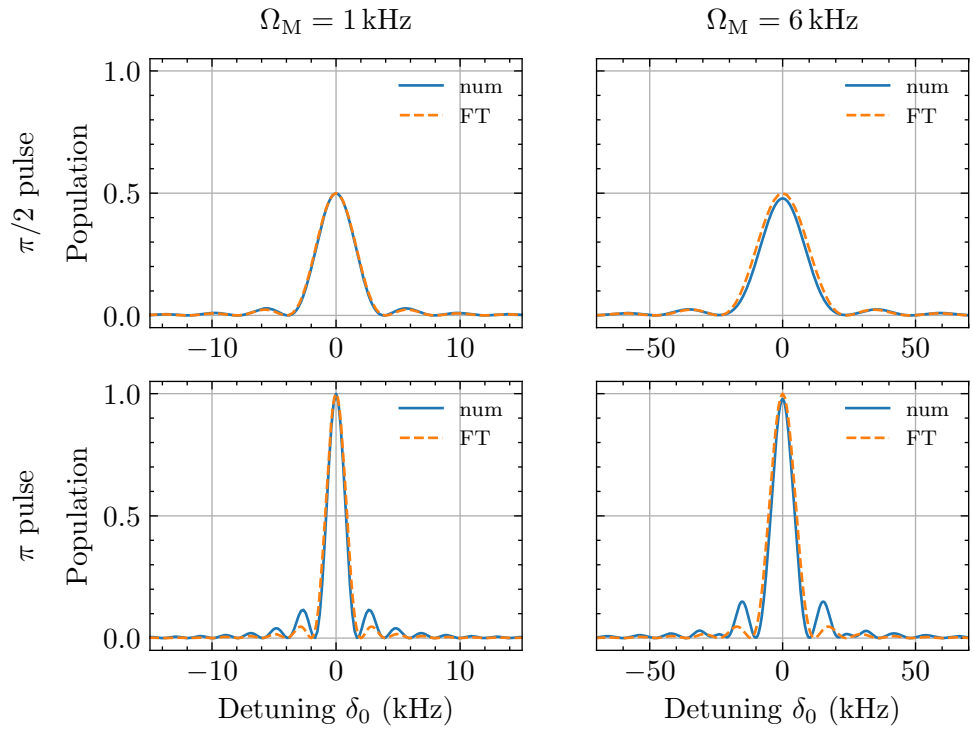

Figure 4.17: Comparison between the reflected population $|C_2|^2$ with the perturbative analytical formula 4.70 as a function of detuning for different values of the two-photon Rabi frequency. The analytical Fourier relation matches well the numerically solved reflection coefficient, even for a mirror. The difference increases when a high two-photon Rabi frequency is responsible for diffraction into other diffraction orders.

4.3 Phase involved in an interferometer

As we have seen, the interferometer we aim to realize involves the phase imprinted by the lasers on the atoms. This is the key parameter we seek to control in order to induce an oscillation of the Bell parameter. This is why it is crucial to consider the phase shift that have been neglected so far and will play a role in the interferometer.

In the literature, several theoretical studies can be found to provide tools to calculate the phases involved in interferometers, especially in a Mach-Zehnder configuration. In this section, we will introduce the various terms responsible for interferometric phase shifts and apply them initially to the Mach-Zehnder interferometer, and subsequently to the Bell interferometer. This will allow us to highlight the similarities and differences between these two interferometers. The advantage of the Mach-Zehnder configuration is that it has been extensively studied, both theoretically and experimentally, providing us with a benchmark for comparison with the Bell interferometer.

Experimentally, a first goal in the implementation of custom Bragg pulses for a Bell test will consist in realizing a Mach-Zehnder interferometer to make sure that the Bragg pulses behave as expected.

In order to express the phase difference between two arms of an interferometer, we will use the formalism employed since the 2000s by S. Chu and M. Kasevich[137][138]. The convention is to categorize the phase shifts into three groups: the phase shifts Φ_{lasers} resulting from the light-matter interaction during Bragg pulses (or Raman pulses in some

cases), the phase shifts Φ_{prop} due to the propagation of wave packets in a given potential (often a gravitational field) between pulses, and the phase shifts Φ_{sep} due to a possible final spatial separation of the interfering wavepackets at the output port.

$$\Phi = \Phi_{\text{lasers}} + \Phi_{\text{prop}} + \Phi_{\text{sep}} \tag{4.72}$$

There are various methods to calculate these phases. One alternative approach involves using the formalism developed by C. Bordé, who generalized the ABCD matrix formulation used in optics to the case of atomic interferometers[139][140]. The method presented here involves calculating the accumulated phase on each arm of an interferometer using path integrals, a formalism developed by R. Feynman[141] and subsequently applied to atom interferometers, notably by P. Storey and C. Cohen-Tannoudji[142].

4.3.1 Propagation phase shifts

In this section, we will develop the tools for calculating the accumulated phase of a wave packet as it propagates through a given potential.

Principle

Let us first consider an atom in the momentum mode p propagating without gravity. The dynamics of the system is governed by the Schrödinger equation, where the Hamiltonian is here only kinetic energy:

$$\mathrm{i}\hbar\frac{\mathrm{d}\,|\psi(t)\rangle}{\mathrm{d}t} = \hat{H}\,|\psi(t)\rangle = \frac{\hat{p}^2}{2m}\,|\psi(t)\rangle \tag{4.73}$$

Assuming that the initial state is $|\psi(0)\rangle = |p\rangle$, the solution to this equation is simply

$$|\psi(t)\rangle = \exp\left(-\mathrm{i}\frac{p^2}{2m\hbar}t\right)|p\rangle \tag{4.74}$$

This is the well-known result where a phase accumulates while rotating at a frequency $\omega_0 = \frac{p^2}{2m\hbar}$. Thus, there is a phase associated with the propagation of a particle in time. This phase varies depending on the particle's momentum, and these phase shifts need to be considered when calculating the phase involved in an interferometer.

Standard approach

The previous approach does not account for the spatial dimension. To address the problem more rigorously, one must consider the propagation of a wave packet in both space and time. The wave function of the atom has a certain spatial extension σ, implying that the momentum also has a width proportional to $1/\sigma$, due to the Heisenberg uncertainty principle.

To calculate the wave function at a point z in space at time t, it is common to define the evolution operator $\hat{U}$ through the relation

$$|\psi(t)\rangle = \hat{U}(t)\,|\psi(0)\rangle \tag{4.75}$$

The wave function evaluated at a point z is then given by

$$\psi(z,t) = \langle z|\hat{U}(t)|\psi(0)\rangle \tag{4.76}$$

In the case where the Hamiltonian of the system does not depend on time, the evolution operator is simply expressed as

$$\hat{U}(t) = \exp\left(-\frac{\mathrm{i}}{\hbar}\hat{H}\,t\right) \tag{4.77}$$

Let us discuss again the simple case of free propagation without gravity. Once again, the Hamiltonian contains only a term of kinetic energy, and the most straightforward way to calculate the wave function at time t from equation 4.76 is to employ a closure relation using the momentum operator, which is an eigenstate of the system.

$$\psi(z,t) = \int \mathrm{d}p\ \langle z|\hat{U}(t)|p\rangle\,\langle p|\psi(0)\rangle = \int \mathrm{d}p \exp\left(-\mathrm{i}\frac{p^2 t}{2m\hbar}\right)\langle z|p\rangle\,\langle p|\psi(0)\rangle \tag{4.78}$$

from which we get

$$\psi(z,t) = \int \mathrm{d}p \exp\left(-\mathrm{i}\frac{p^2 t}{2m\hbar}\right)\exp\left(\mathrm{i}\frac{pz}{\hbar}\right)\tilde{\psi}(p,0) \tag{4.79}$$

where $\tilde{\psi}(p,0)$ is the Fourier transform of the initial wavefunction, i.e., $|\psi(0)\rangle$ in the p-basis representation.

Let us assume that the initial wavefunction is a Gaussian wave packet, described by the following relation:

$$\psi(z,0) = \exp\left(-\frac{(z-z_0)^2}{2\sigma^2}\right)\exp\left(\mathrm{i}\frac{p_0}{\hbar}(z-z_0)\right) \tag{4.80}$$

meaning that the center of mass of the wave packet is at position $z = z_0$ and its momentum is $p = p_0$.

The Fourier transform of the initial wavefunction can be easily obtained, and we find

$$\tilde{\psi}(p,0) = \int \mathrm{d}z\,\psi(z,0)\exp\left(-\mathrm{i}\frac{pz}{\hbar}\right) = \exp\left(-\mathrm{i}\frac{pz_0}{\hbar}\right)\exp\left(-\sigma^2\frac{(p-p_0)^2}{2\hbar^2}\right) \tag{4.81}$$

Finally, after dropping the normalization factor, we get from equation 4.79:

$$\psi(z,t) = \exp\left(-\frac{p_0^2\sigma^2}{2\hbar^2}\right)\exp\left(-\frac{1}{2}\frac{(z-z_0)^2}{\sigma^2+\mathrm{i}\frac{\hbar t}{m}}\right)\exp\left(\frac{p_0^2}{2\hbar^2}\frac{\sigma^4}{\sigma^2+\mathrm{i}\frac{\hbar t}{m}}\right)\exp\left(\mathrm{i}\frac{p_0}{\hbar}\frac{\sigma^2(z-z_0)}{\sigma^2+\mathrm{i}\frac{\hbar t}{m}}\right) \tag{4.82}$$

This expression does not provide any intuition on the propagation of the wave packet since the center of mass $z_c = z_0 + \frac{p_0 t}{m}$ does not appear clearly.

Center of mass approach

An alternative is to use a trick presented in reference [143], which involves introducing "by hand" the center of mass by defining an operator $\hat{G}$ such that

$$\hat{G}(t) = \exp\left(\frac{\mathrm{i}}{\hbar}\int_\Gamma \mathcal{L}_\mathrm{c}\,\mathrm{d}t\right)\exp\left(-\mathrm{i}\frac{\hat{p}z_\mathrm{c}}{\hbar}\right)\exp\left(\mathrm{i}\frac{p_\mathrm{c}\hat{z}}{\hbar}\right) \tag{4.83}$$

where z_c, p_c and $\mathcal{L}_c$ are the classical position, momentum and Lagrangian of the system. The latter is integrated over the classical path Γ.

$\hat{G}$ is a Galilean transformation operator, which consists of a momentum boost, a position translation, and a phase shift. For any Hamiltonian at most quadratic in $\hat{z}$ and $\hat{p}$, it can be shown that the state at time t is given by

$$|\psi(t)\rangle = \hat{G}(t)\,|\psi_{\mathrm{CM}}(t)\rangle \tag{4.84}$$

where $|\psi_{\mathrm{CM}}(t)\rangle$ is the state in the atom's rest frame. $|\psi_{\mathrm{CM}}(t)\rangle$ does not contain any information about the center of mass of the system but quantifies the expansion of the wave packet. It satisfies $\langle\hat{z}\rangle = 0$ and $\langle\hat{p}\rangle = 0$ and

$$|\psi_{\mathrm{CM}}(t)\rangle = \exp\left(-\mathrm{i}\frac{\hat{p}^2}{2m\hbar}t\right)|\psi_{\mathrm{CM}}(0)\rangle \tag{4.85}$$

The final wavefunction can be calculated by projecting 4.84 on a position operator, from which we get, after using two closure relations:

$$\psi(z,t) = \exp\left(\frac{\mathrm{i}}{\hbar}\int_\Gamma \mathcal{L}_c\,\mathrm{d}t\right)\exp\left(\mathrm{i}\frac{p_c(z-z_c)}{\hbar}\right)\psi_{\mathrm{CM}}(z-z_c,t) \tag{4.86}$$

This expression actually corresponds to a traveling wave with a de Broglie wavelength equal to $\hbar/p_c$, multiplied by an envelope function $\psi_{\mathrm{CM}}(z)$ which expresses the expansion of the wavefunction. The envelope moves along the classical path z_c and the wave packet accumulates a phase, given by the classical action of the particle.

Let us consider again the case of a Gaussian wave packet propagating without gravity. The momentum of the center of mass is $p_c(t) = p_0$ and its position is $z_c(t) = z_0 + \frac{p_0}{m}t$. The only term in the Lagrangian is again the kinetic energy, so that

$$\exp\left(\frac{\mathrm{i}}{\hbar}\int_\Gamma \mathcal{L}_c\,\mathrm{d}t\right) = \exp\left(\frac{\mathrm{i}}{\hbar}\int_\Gamma \frac{p_0^2}{2m}\mathrm{d}t\right) = \exp\left(\frac{\mathrm{i}p_0^2 t}{2m\hbar}\right) \tag{4.87}$$

Now we only have to determine $\psi_{\mathrm{CM}}(z-z_c,t)$. Assuming that the initial wavefunction is given by equation 4.80, we can identify the initial center of mass wavefunction using 4.86 at $t=0$ so that

$$\psi_{\mathrm{CM}}(z,0) = \exp\left(-\frac{z}{2\sigma^2}\right) \tag{4.88}$$

from which we get

$$\tilde{\psi}_{\mathrm{CM}}(p,0) = \exp\left(-\frac{\sigma^2 p^2}{2\hbar^2}\right) \tag{4.89}$$

The center of mass wavefunction at any time t can be calculated easily using $\tilde{\psi}_{\mathrm{CM}}$ as seen in equation 4.79:

$$\psi_{\mathrm{CM}}(z,t) = \int \mathrm{d}p \exp\left(-\mathrm{i}\frac{p^2 t}{2m\hbar}\right)\exp\left(\mathrm{i}\frac{pz}{\hbar}\right)\tilde{\psi}_{\mathrm{CM}}(p,0) = \exp\left(-\frac{1}{2}\frac{z^2}{\sigma^2+\mathrm{i}\frac{\hbar}{m}t}\right) \tag{4.90}$$

One can then deduce the expression of the wavefunction from 4.86:

$$\psi(z,t) = \exp\left(\mathrm{i}\frac{p_0^2 t}{2m\hbar}\right)\exp\left(\mathrm{i}\frac{p_0}{\hbar}\left(z - z_0 - \frac{p_0}{m}t\right)\right)\exp\left(-\frac{1}{2}\frac{\left(z-z_0-\frac{p_0}{m}t\right)^2}{\sigma^2+\mathrm{i}\frac{\hbar}{m}t}\right) \tag{4.91}$$

Although it may not be obvious at the first look, this expression is equivalent to the relation 4.82 obtained with the previous method, and one expression can mathematically be deduced from the other. The advantage here is that the result from equation 4.91 is much more physically insightful than the previous way of writing the wavefunction. Indeed, as expected, we recover the expression for a Gaussian wave packet with momentum p_0, and with its center of mass shifted by $\frac{p_0}{m}t$. We also see that the atom has accumulated a phase with frequency $\omega_0 = \frac{p_0^2}{2m\hbar}$, corresponding to its kinetic energy (this term arises from the integral of the Lagrangian). It is noteworthy that, apart from the phase of the center of mass, an additional phase must be considered due to the expansion of the wave packet. But this term is mostly negligible compared to the initial size of the wave packet, provided that the propagation time t remains small (such that $\sigma^2 \gg \hbar t/m$).

While this calculation may not be particularly useful for calculating the accumulated phase of a free particle in the absence of gravity, it is a convenient way to introduce the center of mass in an intuitive way. Note that this method remains valid for Hamiltonians that contain no terms higher than second order in $\hat{x}$ and $\hat{p}$.

Path integral approach

One can extend the previous approach without assuming that the wave packet is Gaussian. The most widely used approach, developed in a paper by Storey and Cohen-Tannoudji[142], involves expressing the wave function in terms of the evolution operator in position representation:

$$\psi(z,t) = \int \mathrm{d}z' \ \langle z|\hat{U}(t)|z'\rangle \langle z'|\psi(0)\rangle = \int \mathrm{d}z' \, K(z,t,z',0)\psi(z',0) \tag{4.92}$$

where $K(z,t,z',0) = \langle z|\hat{U}(t)|z'\rangle$ is the quantum propagator, which translates the probability amplitude of the particle to arrive at position z at time t, given that it started at position z' at $t = 0$.

Feynman's idea is to express this propagator as an integral of the action S over all possible paths Γ connecting the points (z,t) and $(z',0)$.

$$K(z,t,z',0) = \int_{(z',0)}^{(z,t)} \mathcal{D}z(t) \exp\left(\mathrm{i}\frac{S_\Gamma}{\hbar}\right) \tag{4.93}$$

It can then be shown that the paths with the most weight are paths in the vicinity of the classical trajectory, in the (classical) limit where $S \gg \hbar$. For a Lagrangian (or a Hamiltonian) that is at most a quadratic function of $\hat{z}$ and $\hat{p}$, the propagator is given by

$$K(z,t,z',0) = F(t,0) \exp\left(\frac{\mathrm{i}}{\hbar} S_{\mathrm{cl}}(z,t,z',0)\right) \tag{4.94}$$

where the factor $F(t,0)$ only depends on time, so it will not add a phase shift between two different trajectories in an interferometer. Indeed, atomic interferometers consist of alternating periods of free propagation and pulses where atoms interact with light: in an interferometer, atoms interact with light at the same time even if they do not have the same trajectory.

Since the classical action is equal to the integral of the Lagrangian of the system's center of mass, we retrieve the term introduced in the previous approach which was responsible

for the phase accumulated by the wave packet. Consequently, the wavefunction can be expressed as

$$\psi(z,t) = F(t,0)\int \mathrm{d}z' \exp\left(\frac{\mathrm{i}}{\hbar}S_{\mathrm{cl}}(z,t,z',0)\right)\psi(z',0) \tag{4.95}$$

Now, if we assume that the initial wavefunction is a plane wave, which can be written

$$\psi(z',0) = \exp\left(\frac{\mathrm{i}p_0 z'}{\hbar}\right) \tag{4.96}$$

then it can be shown, using an expansion of both the wavefunction and the classical action around the classical position of the center of mass z_0, that the final wavefunction is

$$\psi(z,t) = \tilde{F}(t,0)\exp\left(\frac{\mathrm{i}}{\hbar}S_{\mathrm{cl}}(z,t,z_0,0)\right)\psi(z_0,0) \tag{4.97}$$

This expression clearly shows that the phase accumulated by the final wave function is given by the action along the classical path. This result is exact in the case of a plane wave at $t = 0$, and we will consider it to be approximately valid for any initial wave function, neglecting other phase terms due to the expansion of the wave packet as discussed in the previous paragraph.

Thus, to calculate the phase of the wavefunction associated with the propagation of a particle in a given potential, we need to determine the action, i.e., the integral of the system's Lagrangian, along the classical path:

$$\phi_{\mathrm{path}} = \frac{1}{\hbar}S_{\mathrm{cl}}(z,t,z_0,0) = \frac{1}{\hbar}\int \mathcal{L}_{\mathrm{c}}[z(t),\dot{z}(t)]\,\mathrm{d}t \tag{4.98}$$

We will only consider a particle in a gravitational field (without considering a rotating reference frame for instance), so that the action is

$$S_{\mathrm{cl}} = \int \mathcal{L}_{\mathrm{c}}\,\mathrm{d}t = \int (T-V)\,\mathrm{d}t = \int (p\,\mathrm{d}x - E\,\mathrm{d}t) \tag{4.99}$$

where $T = \frac{1}{2}mv^2$ and $V = -mgz$ are the kinetic potential energies, while $p = mv$ and E are the momentum and the total energy of the center of mass.

We note $p_0 = mv_0$ the initial momentum and z_0 the initial position, so that the trajectories and speeds are

$$z(t) = -\frac{1}{2}gt^2 + v_0 t + z_0 \qquad \text{and} \qquad v(t) = v_0 - gt \tag{4.100}$$

from which we get the phase associated to the classical path for a wavepacket propagating from z_0 with a speed v_0 for a duration t:

$$\phi_{\mathrm{path}} = \frac{m}{\hbar}\left(\frac{v_0^2}{2} + gz_0\right)t \tag{4.101}$$

In the end, to calculate the phase shift associated with the propagation of wave packets in the interferometer, one will need to compare the accumulated phases along each path of the interferometer using the relation 4.101.

Note that the separation phase Φ_{sep} also arises from this Lagrangian propagation formalism, as will be demonstrated later on.

This latter method using path integrals allows for easy calculation of the phase associated with the trajectory of atoms in an interferometer and is commonly used. However, it is not general as it neglects phase shifts related to the spatial extension of the wave packet by essentially considering atoms as plane waves. The corrective terms become apparent when describing the wave packet using the method outlined by Hogan et al.[143], which consists in "following" the center of mass of the wave packet.

4.3.2 Light-matter interaction phase shifts

Principle: phase imprinted on plane waves

First, let us revisit the simple case of plane waves discussed in the first section of this chapter, without considering any terms related to space. This will enable us to determine some of the phase shifts included in Φ_{lasers}, resulting from the interaction between an atom with light

The goal is to provide tools to generalize the results found in section 4.1.1 in the case where the matrices describing Bragg mirrors and beam splitters are expressed in any form.

In our description of the Bell interferometer, we mentioned the principle of phase imprinting, which we will discuss again in this section. Let us consider the matrix of a Bragg beam splitter 4.5 for instance, taken at resonance for a $\pi/2$ pulse, acting on an initial state consisting of an atom in mode p. The output state is

$$|\psi_{\text{out}}\rangle = \begin{pmatrix} C_0 \\ C_2 \end{pmatrix} = \frac{\sqrt{2}}{2} \begin{pmatrix} 1 & \mathrm{i}\mathrm{e}^{\mathrm{i}\phi} \\ \mathrm{i}\mathrm{e}^{-\mathrm{i}\phi} & 1 \end{pmatrix} \begin{pmatrix} 1 \\ 0 \end{pmatrix} = \frac{\sqrt{2}}{2} \left(|p\rangle + \mathrm{i}\mathrm{e}^{-\mathrm{i}\phi} |p + 2\hbar k\rangle \right) \tag{4.102}$$

where $\phi = \varphi_1 - \varphi_2$ is the phase difference between the lasers during the pulse duration. The phase difference between modes $p + 2\hbar k$ and p is

$$\Delta\phi = \arg(C_2) - \arg(C_0) = \varphi_2 - \varphi_1 \left(+ \frac{\pi}{2} \right) \tag{4.103}$$

The $\pi/2$ term from the i factor can be dropped since it cancels out in most interferometer geometries, and it can be said that the phase difference between the lasers is imprinted on the atoms.

It is possible to calculate the phase shifts induced by Bragg transfers in a more general case, still within the Bragg regime but without assuming resonance. To this end, we only need to write the transfer matrix of a Bragg doublet in the general form:

$$U(T) = \begin{pmatrix} t\mathrm{e}^{\mathrm{i}\phi'} & \mathrm{i}r\mathrm{e}^{\mathrm{i}\phi} \\ \mathrm{i}r\mathrm{e}^{-\mathrm{i}\phi} & t\mathrm{e}^{-\mathrm{i}\phi'} \end{pmatrix} \tag{4.104}$$

where r and t are real numbers corresponding to the amplitude reflection and transmission coefficients of the pulse. They depend on the duration T of the pulse and on the detuning δ_0, and so do the phases ϕ and ϕ'. Similarly, we find

$$|\psi_{\text{out}}\rangle = \begin{pmatrix} C_0 \\ C_2 \end{pmatrix} = \begin{pmatrix} t\mathrm{e}^{\mathrm{i}\phi'} & \mathrm{i}r\mathrm{e}^{\mathrm{i}\phi} \\ \mathrm{i}r\mathrm{e}^{-\mathrm{i}\phi} & t\mathrm{e}^{-\mathrm{i}\phi'} \end{pmatrix} \begin{pmatrix} 1 \\ 0 \end{pmatrix} = \begin{pmatrix} t\mathrm{e}^{\mathrm{i}\phi'} \\ \mathrm{i}r\mathrm{e}^{-\mathrm{i}\phi} \end{pmatrix} \tag{4.105}$$

so the imprinted phase is, in a general case:

$$\Delta\phi = \arg(C_2) - \arg(C_0) = \phi' + \phi \tag{4.106}$$

For instance, in the specific case of a Bragg pulse with a constant two-photon Rabi frequency, we showed the expression 4.63 of the evolution operator as a function of the detuning δ_0. The corresponding phase terms can be identified with 4.104, and we find

$$\phi' = \frac{\delta_0 T}{2} + \tan^{-1}\left[-\frac{\delta_0}{\Omega}\tan\left(\frac{\Omega T}{2}\right)\right] \qquad \text{and} \qquad \phi = \varphi_1 - \varphi_2 + \frac{\delta_0 T}{2} \tag{4.107}$$

where $\Omega = \sqrt{|\Omega_\mathrm{R}|^2 + \delta_0^2}$ and T is the duration of the pulse. The phase difference between modes $p + 2\hbar k$ and p, assuming that the atom is initially in mode p, is

$$\Delta\phi = \varphi_2 - \varphi_1 - \delta_0 T + \tan^{-1}\left[\frac{\delta_0}{\Omega}\tan\left(\frac{\Omega T}{2}\right)\right] \tag{4.108}$$

As we can see, additional phase shifts appear when considering out of resonance momentum classes.

An additional phase shift which depends on the center of mass

In this paragraph, we will show that there is an additional phase imprinted to the atoms by the Bragg pulse, which depends on the position of the center of mass. To this end, we will once again employ the formalism of Hogan et al.[143], as presented previously, which conveniently brings out the center of mass in the equations. This time, we will consider the case where the potential only consists of the light interaction term (gravity is not considered for simplicity, but the same reasoning remains valid and could be applied similarly).

We will assume that we work in the Bragg regime, so that only two Bragg momentum levels need to be considered. We will write $|0\rangle = |p\rangle$ and $|2\rangle = |p + 2\hbar k\rangle$ these coupled levels, as well as $E_0 = \frac{p^2}{2m}$ and $E_2 = \frac{(p+2\hbar k)^2}{2m}$ their kinetic energy. The interaction term $V(\hat{z})$ in the Hamiltonian was given in equation 4.42:

$$V(\hat{z}) = -\frac{\hbar|\Omega_\mathrm{R}|}{2}\left(\mathrm{e}^{2\mathrm{i}k\hat{z} - \mathrm{i}\phi(t)} + \mathrm{e}^{-2\mathrm{i}k\hat{z} + \mathrm{i}\phi(t)}\right) \tag{4.109}$$

with $\phi(t) = (\omega_2 - \omega_1)t + \varphi_2 - \varphi_1$ where $\omega_2 - \omega_1$ is the frequency difference between the two laser beams.

Here, for a two-level system, we will assume that $\mathrm{e}^{2\mathrm{i}k\hat{z}}\,|2\rangle = \mathrm{e}^{-2\mathrm{i}k\hat{z}}\,|0\rangle = |\mathrm{vac}\rangle$ where $|\mathrm{vac}\rangle$ is a vacuum state, so that the atom stays within the two-level system.

We will proceed in a manner similar to when introducing Bragg diffraction, i.e., we will express the wavefunction in the $\{|0\rangle, |2\rangle\}$ basis and then apply the Schrödinger equation. The distinction lies in the fact that this time we will use the operator $\hat{G}$, defined earlier as a Galilean transformation operator which explicitly involves the system's center of mass.

$$|\psi(t)\rangle = C_0(t)\,\mathrm{e}^{-\frac{\mathrm{i}E_0 t}{\hbar}}\hat{G}(t)\,|0\rangle + C_2(t)\,\mathrm{e}^{-\frac{\mathrm{i}E_2 t}{\hbar}}\hat{G}(t)\,|2\rangle \tag{4.110}$$

In this case, the states $|0\rangle$ and $|2\rangle$ play the role of the center of mass states $|\psi_\mathrm{CM}\rangle$. This notation can seem misleading as these momentum states are plane waves with a delocalized center of mass. However, we can later generalize the results by decomposing any wave function onto these momentum states[5].

[5] A more general formulation consists in writing

$$|\psi(t)\rangle = \int \mathrm{d}p\,\tilde{C}_0^{(p)}(t)\,\mathrm{e}^{-\mathrm{i}\frac{p^2 t}{2m\hbar}}\hat{G}(t)\,|p\rangle + \int \mathrm{d}p\,\tilde{C}_2^{(p)}(t)\,\mathrm{e}^{-\mathrm{i}\frac{(p+2\hbar k)^2 t}{2m\hbar}}\hat{G}(t)\,|p + 2\hbar k\rangle$$

The time derivative of $\mathrm{i}\hbar\,|\psi\rangle$ is

$$\mathrm{i}\hbar\,|\dot{\psi}(t)\rangle = \sum_{j\in\{0,2\}} \left(\mathrm{i}\hbar\dot{C}_j\hat{G} + E_jC_j\hat{G} + \mathrm{i}\hbar C_j\dot{\hat{G}}\right)\mathrm{e}^{-\frac{\mathrm{i}E_jt}{\hbar}}\,|j\rangle \tag{4.111}$$

Now, using the fact that $\mathrm{i}\hbar\dot{\hat{G}} = \dfrac{\hat{p}^2}{2m}\hat{G} - \hat{G}\dfrac{\hat{p}^2}{2m}$, we get from the Schrödinger equation the following relation:

$$\mathrm{i}\hbar\sum_{j\in\{0,2\}} \dot{C}_j\hat{G}\,\mathrm{e}^{-\frac{\mathrm{i}E_jt}{\hbar}}\,|j\rangle = \sum_{j\in\{0,2\}} C_j\,\mathrm{e}^{-\frac{\mathrm{i}E_jt}{\hbar}}\,V(\hat{z})\hat{G}\,|j\rangle \tag{4.112}$$

Then, we left multiply this expression by $\hat{G}^\dagger$. On the left-hand side, we obtain the identity, and on the right-hand side, we get the operator $\hat{G}^\dagger V(\hat{z})\hat{G}$, which can be demonstrated to be written as:

$$\hat{G}^\dagger V(\hat{z})\hat{G} = V(\hat{z} - z_c) \tag{4.113}$$

where z_c is the center of mass of the wave packet, since $\hat{G}$ is the Galilean transformation which moves an operator to the center of mass reference frame. The interaction potential $V(\hat{z} - z_c)$ can then be rewritten

$$V(\hat{z} - z_c) = -\frac{\hbar|\Omega_\mathrm{R}|}{2}\left(\mathrm{e}^{2\mathrm{i}k\hat{z} - 2\mathrm{i}kz_c - \mathrm{i}\phi(t)} + \mathrm{e}^{-2\mathrm{i}k\hat{z} + 2\mathrm{i}kz_c + \mathrm{i}\phi(t)}\right) \tag{4.114}$$

For our two-level system $\{|0\rangle, |2\rangle\}$, we have in particular

$$V(\hat{z} - z_c) = -\frac{\hbar\Omega_\mathrm{R}}{2}\mathrm{e}^{-2\mathrm{i}kz_c + \mathrm{i}(\omega_2 - \omega_1)t}\,|2\rangle\langle 0| - \frac{\hbar\Omega_\mathrm{R}^*}{2}\mathrm{e}^{2\mathrm{i}kz_c - \mathrm{i}(\omega_2 - \omega_1)t}\,|0\rangle\langle 2| \tag{4.115}$$

with $\Omega_\mathrm{R} = |\Omega_\mathrm{R}|\mathrm{e}^{\mathrm{i}(\varphi_2 - \varphi_1)}$.

In the end, we get from the Schrödinger equation 4.112 the following relationships:

$$\begin{cases} \mathrm{i}\hbar\dot{C}_0\mathrm{e}^{-\frac{\mathrm{i}E_0t}{\hbar}} = -\dfrac{\hbar\Omega_\mathrm{R}}{2}\,C_2\,\mathrm{e}^{-\frac{\mathrm{i}E_2t}{\hbar}}\mathrm{e}^{-2\mathrm{i}kz_c + \mathrm{i}(\omega_2 - \omega_1)t} \\ \mathrm{i}\hbar\dot{C}_2\mathrm{e}^{-\frac{\mathrm{i}E_2t}{\hbar}} = -\dfrac{\hbar\Omega_\mathrm{R}^*}{2}\,C_0\,\mathrm{e}^{-\frac{\mathrm{i}E_0t}{\hbar}}\mathrm{e}^{2\mathrm{i}kz_c - \mathrm{i}(\omega_2 - \omega_1)t} \end{cases} \tag{4.116}$$

leading to

$$\begin{cases} \dot{C}_0 = \mathrm{i}\dfrac{\hbar\Omega_\mathrm{R}}{2}\,C_2\,\mathrm{e}^{\mathrm{i}\delta_0 t}\mathrm{e}^{-2\mathrm{i}kz_c} \\ \dot{C}_2 = \mathrm{i}\dfrac{\hbar\Omega_\mathrm{R}^*}{2}\,C_0\,\mathrm{e}^{-\mathrm{i}\delta_0 t}\mathrm{e}^{2\mathrm{i}kz_c} \end{cases} \tag{4.117}$$

where we used the definition of δ_0:

$$\hbar\delta_0 = \hbar(\omega_2 - \omega_1) - (E_2 - E_0) \tag{4.118}$$

The system 4.117 is identical to the system 4.60 obtained previously for the two-level system, except for the addition of a phase term $2kz_c$ dependent on the system's center of mass. This phase will be imprinted onto the atoms, like the phase difference of the lasers $\varphi_2 - \varphi_1$, which plays a similar role mathematically.

So far, we have only performed a change of basis. However, we can view this change of reference frame as the operation of following the wave packet during its propagation. In

contrast, the previous model developed in section 4.2 allowed the calculation of the wave packet phase at a fixed location, independent of its propagation. To determine what phase is imprinted to the wave packet, it is necessary to calculate the wavefunctions associated with the transmitted and reflected waves.

Transmitted and reflected wave packets

In the case where the detuning δ_0 between the lasers is time-independent and the Bragg pulse is constant ($\Omega_{\mathrm{R}}(t) = \Omega_{\mathrm{M}}$), we have shown that the system 4.117 could be solved analytically. Therefore, we use the analytical formula 4.65, only adding the phase term which depends on the center of mass. Let us assume that initially, the atoms are in the $|0\rangle$ momentum state ($C_0(0) = 1$, $C_2(0) = 0$). The coefficients C_0 and C_2 at the end of the pulse, in the resonant case ($\delta_0 = 0$), are given by

$$\begin{cases} C_0(t) = \cos\left(\dfrac{\Omega_{\mathrm{M}} t}{2}\right) C_0(0) \\ C_2(t) = \mathrm{i}\sin\left(\dfrac{\Omega_{\mathrm{M}} t}{2}\right) \mathrm{e}^{-\mathrm{i}(\varphi_2-\varphi_1)} e^{2\mathrm{i}kz_c}\, C_0(0) \end{cases} \tag{4.119}$$

Now, let us return to the case of Gaussian wavefunctions, which consist in integrating the previous expressions over p, along with a gaussian density envelope (again, we omit the normalization factors). We recall that the initial wavefunction can be written as

$$\psi(z,0) = \mathrm{e}^{-\frac{(z-z_0)^2}{2\sigma^2}} \mathrm{e}^{\mathrm{i}\frac{p_0}{\hbar}(z-z_0)} \tag{4.120}$$

where z_0 and p_0 are the (mean) position and momentum of the wavepacket at the initial time.

We will consider separately the transmitted part (staying at momentum p_0) and the reflected part (with momentum $p_0 + 2\hbar k$) of the wavefunction, which will be noted $|\psi_{\mathrm{t}}\rangle$ and $|\psi_{\mathrm{r}}\rangle$, respectively.

$$|\psi(t)\rangle = |\psi_{\mathrm{t}}(t)\rangle + |\psi_{\mathrm{r}}(t)\rangle \tag{4.121}$$

The transmitted part of the total output state is

$$|\psi_{\mathrm{t}}(t)\rangle = \int \mathrm{d}p\, \tilde{C}_0^{(p)}(t)\, \mathrm{e}^{-\mathrm{i}\frac{p^2 t}{2m\hbar}}\, \hat{G}(t)\, |p\rangle \tag{4.122}$$

where $\tilde{C}_0^{(p)}(t)$ is the amplitude coefficient at a momentum p. It is both related to the Bragg coupling and the momentum distribution of the wave packet. In particular at $t = 0$, $\tilde{C}_0^{(p)}(0)$ is the initial momentum distribution at the center of mass (since the operator $\hat{G}$ moves to the center of mass reference frame), which is the Fourier transform of $\psi_{\mathrm{CM}}(z,0)$, so that

$$\tilde{C}_0^{(p)}(0) = \tilde{\psi}_{\mathrm{CM}}(p,0) = \mathrm{e}^{-\frac{\sigma^2 p^2}{2\hbar^2}} \tag{4.123}$$

We use the definition 4.83 of the Galilean transformation operator $\hat{G}$ to get

$$\hat{G}(t)\, |p\rangle = \mathrm{e}^{\mathrm{i}\frac{p_0^2}{2m\hbar}t} \mathrm{e}^{-\mathrm{i}\frac{(p+p_c)z_{\mathrm{c}}}{\hbar}}\, |p + p_c\rangle \tag{4.124}$$

Therefore, we have

$$|\psi_{\mathrm{t}}(t)\rangle = \mathrm{e}^{\mathrm{i}\frac{p_0^2}{2m\hbar}t} \int \mathrm{d}p\, \tilde{C}_0^{(p)}(t)\, \mathrm{e}^{-\mathrm{i}\frac{p^2 t}{2m\hbar}}\, \mathrm{e}^{-\mathrm{i}\frac{(p+p_c)z_{\mathrm{c}}}{\hbar}}\, |p + p_c\rangle \tag{4.125}$$

Here, we will assume that all the atoms from the wave packet are resonant with the Bragg coupling, neglecting the detuning effects, so that the Bragg transfer does not depend on p, and then $\tilde{C}_0^{(p)}(t)$ is the product of the Bragg transmittivity (given by equation 4.119) with the momentum density envelope:

$$\tilde{C}_0^{(p)}(t) = \cos\left(\frac{\Omega_{\mathrm{M}} t}{2}\right) \tilde{C}_0^{(p)}(0) = \cos\left(\frac{\Omega_{\mathrm{M}} t}{2}\right) \mathrm{e}^{-\frac{\sigma^2 p^2}{2\hbar^2}} \tag{4.126}$$

By writing $p_c = p_0$ and $z_c = z_0 + \frac{p_0 t}{m}$, we find

$$|\psi_{\mathrm{t}}(t)\rangle = \cos\left(\frac{\Omega_{\mathrm{M}} t}{2}\right) \mathrm{e}^{\mathrm{i}\frac{p_0^2}{2m\hbar}t} \int \mathrm{d}p\, \mathrm{e}^{-\frac{\sigma^2 p^2}{2\hbar^2}} \mathrm{e}^{-\mathrm{i}\frac{p^2 t}{2m\hbar}} \mathrm{e}^{-\mathrm{i}\frac{(p+p_0)\left(z_0+\frac{p_0 t}{m}\right)}{\hbar}} |p+p_0\rangle \tag{4.127}$$

from which we can deduce the wavefunction

$$\psi_{\mathrm{t}}(z,t) = \cos\left(\frac{\Omega_{\mathrm{M}} t}{2}\right) \mathrm{e}^{\mathrm{i}\frac{p_0^2}{2m\hbar}t} \mathrm{e}^{\frac{\mathrm{i}p_0}{\hbar}\left(z-z_0-\frac{p_0 t}{m}\right)} \int \mathrm{d}p\, \mathrm{e}^{-\frac{\sigma^2 p^2}{2\hbar^2}} \mathrm{e}^{-\mathrm{i}\frac{p^2 t}{2m\hbar}} \mathrm{e}^{\frac{\mathrm{i}p}{\hbar}\left(z-z_0-\frac{p_0 t}{m}\right)} \tag{4.128}$$

Apart from the Bragg transmittivity factor, this is exactly the same calculation as what was done previously in equation 4.91 to determine the wavefunction of a free wave packet.

So, as expected, the transmitted part of the wave packet at the end of a Bragg pulse is equal to what we would find without any Bragg pulse, up to a population modulation determined by the Bragg pulse duration.

The same reasoning can be applied to the part of the wavefunction that is reflected by the Bragg pulse:

$$|\psi_{\mathrm{r}}(t)\rangle = \int \mathrm{d}p\, \tilde{C}_2^{(p)}(t)\, \mathrm{e}^{-\mathrm{i}\frac{(p+2\hbar k)^2 t}{2m\hbar}} \hat{G}(t)\, |p+2\hbar k\rangle \tag{4.129}$$

Thus, we find a similar expression for the reflected wavefunction

$$\psi_{\mathrm{r}}(z,t) = \mathrm{i}\sin\left(\frac{\Omega_{\mathrm{M}} t}{2}\right) \mathrm{e}^{-\mathrm{i}\phi_{\mathrm{L}}} \mathrm{e}^{\mathrm{i}\frac{(p_0+2\hbar k)^2}{2m\hbar}t} \mathrm{e}^{\frac{\mathrm{i}(p_0+2\hbar k)}{\hbar}(z-z_{\mathrm{c}})} \int \mathrm{d}p\, \mathrm{e}^{-\frac{\sigma^2 p^2}{2\hbar^2}} \mathrm{e}^{-\mathrm{i}\frac{(p+2\hbar k)^2 t}{2m\hbar}} \mathrm{e}^{\frac{\mathrm{i}p}{\hbar}(z-z_{\mathrm{c}})} \tag{4.130}$$

where $\phi_{\mathrm{L}} = \varphi_2 - \varphi_1 - 2kz_{\mathrm{c}}$.

This yields the expression for a wave packet propagating at the momentum $p_0 + 2\hbar k$, with a center of mass z_{c}. The only difference with the propagation of a wave packet at the same momentum is the Bragg reflectivity factor $\sin(\Omega_{\mathrm{M}} t/2)$ and the additional phase ϕ_{L} imprinted by the lasers on the atom, which depends on the center of mass of the wave packet at the time of the pulse. It appears that this phase must be considered in the calculation of the phase shifts that come into play in an interferometer.

Note that we have not explicitly specified the expression of the center of mass (although we have assumed that the wave packet has a classical momentum $p_{\mathrm{c}} = p_0 + 2\hbar k$). If we do not consider the interaction term in the Hamilton equations to get the classical trajectory, we get $z_{\mathrm{c}} = z_0 + \frac{(p_0+2\hbar k)t}{m}$, meaning that the diffracted wave packet departs from the location of the incident wave packet when the light is turned on.

In fact, it can be shown, by taking into account the off-resonant effects, that the interaction with light during the pulse alters the trajectory of the center of mass compared

to the case without light. As a consequence, the reflected and transmitted wave packets, if their trajectories after the pulse are extended towards the initial time, do not intersect at the position of the center of mass of the initial wave packet when the light is turned on. This point will not be discussed further in the manuscript, but the previous formalism allows for simulations to account for this effect, and analyses are underway in the team to determine to what extent this deviation by light is measurable with our setup.

In most interferometers, especially the Mach-Zehnder interferometers reported in the literature, the duration of the Bragg pulses is much shorter than the free propagation time. Consequently, the interaction time with light is considered negligible. In this case, the position of the center of mass corresponds to the classical position at the time of the Bragg pulse.

Atoms in a gravitational potential

In our case, the Bell interferometer occurs along the vertical axis. Therefore, it is necessary to consider the gravitational potential in the Hamiltonian. An important consequence is that as atoms fall, they will detune with respect to the Bragg resonance. This Doppler detuning can be corrected by applying a frequency ramp to one of the lasers.

As mentionned in reference [143], the same formalism can be applied when adding gravity. Starting from the Bragg coupled system from equation 4.117, we have:

$$\begin{cases} \dot{C}_0 = \mathrm{i}\dfrac{\hbar\Omega_\mathrm{R}}{2}\, C_2\, \mathrm{e}^{\mathrm{i}\delta_0 t}\mathrm{e}^{-2\mathrm{i}k\left(z_0+\frac{p_0 t}{m}-\frac{1}{2}gt^2\right)} \\ \dot{C}_2 = \mathrm{i}\dfrac{\hbar\Omega_\mathrm{R}^*}{2}\, C_0\, \mathrm{e}^{-\mathrm{i}\delta_0 t}\mathrm{e}^{2\mathrm{i}k\left(z_0+\frac{p_0 t}{m}-\frac{1}{2}gt^2\right)} \end{cases} \tag{4.131}$$

where the additional term $-\frac{1}{2}gt^2$ arises from the acceleration due to gravity. This system is equivalent to having a detuning which varies linearly with time $\tilde{\delta_0} = \delta_0 + kgt$, which reflects the fact that during their fall, the momentum of the atoms changes, causing them to shift away from resonance.

To counteract this effect, it is immediately apparent that if a linear ramp is applied to the detuning, typically by performing a frequency sweep on one of the two lasers, then one can compensate for this loss of resonance. The phase that must be added to compensate for gravity is therefore $\phi_\mathrm{comp} = -kgt^2$. Thus, the corresponding frequency ramp to be applied is given by:

$$f_\mathrm{comp} = \frac{\mathrm{d}\phi_\mathrm{comp}}{\mathrm{d}t} = -2kgt \tag{4.132}$$

The gravity term is compensated when the slope α of the frequency sweep is $\alpha = -2kg = -k_\mathrm{B}g$. In practice, unless in specific cases[6], efforts are made to ensure that this condition is satisfied so that the Bragg resonant momentum class moves with the atoms.

4.3.3 Conclusion

In the preceding paragraphs, we have shown the expression of the phase shifts to be taken into account when calculating the phase involved in an interferometer. We can differentiate between the phase shifts Φ_prop resulting from the propagation of a wave packet in a gravitational potential and the phase shifts Φ_laser arising from the interaction between the wave packet and light.

[6]For instance, in Mach-Zehnder gravimeters aiming at measuring g, the value of the slope α is finely scanned in order to precisely spot its value when gravity is compensated.

- Two wave packets that separate from a certain point and propagate at different momenta acquire different phases during their respective propagation. Therefore, there is a phase difference associated with this propagation difference when the wave packets meet again to interfere.

  We have seen that the phase accumulated by a wave packet can be expressed in the form:

$$\phi_{\text{path}} = \frac{1}{\hbar} S_{\text{cl}}(z, t, z_0, 0) = \frac{1}{\hbar} \int_{\Gamma} \mathcal{L}_{\text{c}}[z(t), \dot{z}(t)] \, \mathrm{d}t \tag{4.133}$$

  where

$$\frac{1}{\hbar} \int_{\Gamma_0} \mathcal{L}_{\text{c}}[z(t), \dot{z}(t)] \, \mathrm{d}t = \frac{m}{\hbar} \left(\frac{v_0^2}{2} + g z_0 \right) t \tag{4.134}$$

  for a wavepacket propagating on a path Γ_0 at a speed v_0 from a position z_0 for a duration t in a gravitational potential.

  The phase difference between two wave packets is then

$$\Phi_{\text{prop}} = \phi_{\text{path},2} - \phi_{\text{path},1} \tag{4.135}$$

- Furthermore, we have seen that when an atom interacts with light during a Bragg pulse, there is a phase imprinted by the lasers onto the atoms (or more precisely, a phase difference between the transmitted and reflected atomic beams). At resonance, this phase can be expressed in the form:

$$\Phi_{\text{lasers}} = -k_{\text{B}} z_{\text{c}} + (\varphi_2 - \varphi_1) \tag{4.136}$$

  where $k_{\text{B}} = 2k$ is the Bragg momentum transferred to the atoms, z_{c} is the center of mass of the wave packet and $\varphi_2 - \varphi_1$ is the phase difference between the lasers at the time of the pulse. Note that in addition to the instantaneous phases φ_i, a similar reasoning for a Bragg pulse starting at $t = t_i$ also implies the existence of a term written as $(\omega_2 - \omega_1)t_i = \Delta\omega_{\text{L}} t_i$ where $\omega_{1,2}$ are the laser beams frequencies. This term must be considered in the calculations, and we will see that it cancels out in the case of closed interferometers.

  Out of resonance, additional terms emerge. For example, we have seen that for a constant two-photon Rabi frequency beam splitter in a plane wave model, a correction must be taken into account:

$$\Phi_{\text{lasers}} = -k_{\text{B}} z_{\text{c}} + \varphi_2 - \varphi_1 + \Delta\omega_{\text{L}} t_i - \delta_0 T + \tan^{-1}\left[\frac{\delta_0}{\Omega} \tan\left(\frac{\Omega T}{2} \right) \right] \tag{4.137}$$

  where T is the duration of the pulse.

The objective of this section was to formally highlight the phase shifts involved in atomic interferometers. The derived expressions will now be used in two different cases: at resonance and for short pulse durations on one hand, and off-resonance for finite-duration pulses within a model where atoms are treated as plane waves on the other hand.

4.4 Application to the Mach-Zehnder interferometer

The previous results will be applied to a Mach-Zehnder type interferometer, as depicted in Figure 4.18. Starting from an initial atomic cloud at a given momentum p, a first beam splitter pulse is applied to split the cloud into two parts, with a momentum p or $p + 2\hbar k$. Subsequently, a mirror pulse is introduced to bring the two wave packets together onto a final beam splitter, where the two momentum modes are mixed. The idea is to have two clouds interfering at a beam splitter, which justifies the geometry of the interferometer: the initial pulse allows for amplitude splitting interference by emitting two coherent clouds from the same atomic source. The mirror pulse is employed to close the interferometer, so that the two wave packets overlap.

We assume that the interferometer is in a spatial configuration where the momentum transferred by Bragg diffraction is in the vertical axis, for which gravity needs to be taken into account.

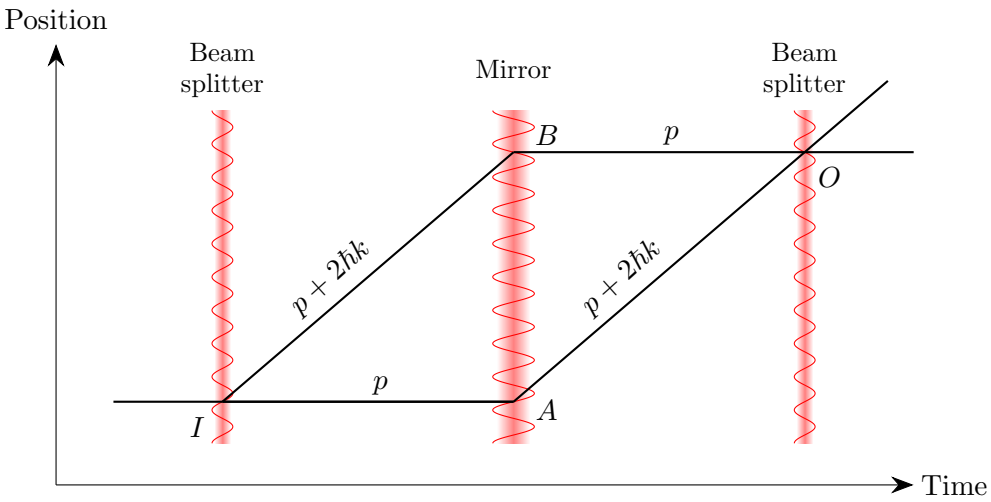

Figure 4.18: Schematic representation of the Mach-Zehnder interferometer in the falling frame.

This atomic interferometer was initially realized by S. Chu and M. Kasevich[86] with cold atom clouds and Raman beams, and then successfully replicated a few years later using Bragg diffraction[144] and BECs[145]. It can be used to measure gravitational acceleration[146], as we will show in the following.

4.4.1 Resonant case with short pulses

First, we will focus on the simple case where all atoms are resonant for the Bragg pulses in a "closed" interferometer (a concept that will naturally emerge). We assume that the Bragg pulses are short, meaning that their duration is negligible compared to the free propagation duration. For now, we do not assume that the atomic wavefunction is a plane wave, and use the results from the previous section.

Laser phase

Let us determine the phase due to the interaction between the atoms and the light pulses.

We have shown that for a given momentum doublet in the basis $\{p, p+2\hbar k\}$, the Bragg transfer matrices of a mirror and a beam splitter can respectively be written, at resonance,

$$U_{\mathrm{M}} = \begin{pmatrix} 0 & \mathrm{i}e^{\mathrm{i}\phi} \\ \mathrm{i}e^{-\mathrm{i}\phi} & 0 \end{pmatrix} \qquad \text{and} \qquad U_{\mathrm{S}} = \frac{\sqrt{2}}{2}\begin{pmatrix} 1 & \mathrm{i}e^{\mathrm{i}\phi} \\ \mathrm{i}e^{-\mathrm{i}\phi} & 1 \end{pmatrix} \tag{4.138}$$

where

$$\phi = -k_{\mathrm{B}} z_{\mathrm{c}} + \Delta\omega_{\mathrm{L}} t_i + (\varphi_2 - \varphi_1) \tag{4.139}$$

Here, z_{c} is the center of mass of the wavepacket subjected to a Bragg pulse. Note that, in this formalism, the center of mass is obviously not the same for the wave packet initially transmitted by the first Bragg splitter, compared to the one of the wave packet initially reflected. Even if we consider only two momentum modes, the same mode can be involved in the interferometer through two spatially decoupled paths (as seen in Figure 4.19, mode p is involved in paths α and β, and similarly, mode $p+2\hbar k$ is involved in paths α' and β').

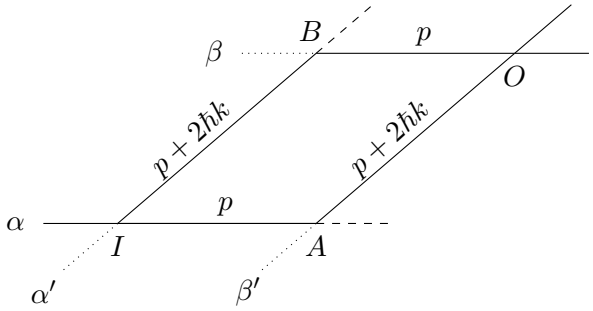

Figure 4.19: Schematic representation of the modes involved in the Mach-Zehnder interferometer. We distinguish modes with the same momentum but spatially separated. Strictly speaking, this is a four-input, four-output interferometer, but we only consider one input mode (α) and two output modes (β and β').

Strictly speaking, mode $(p)_\alpha$ is coupled with mode $(p+2\hbar k)_{\beta'}$, while mode $(p+2\hbar k)_{\alpha'}$ is coupled with mode $(p)_\beta$ during the Bragg mirror pulse, when accounting for the spatial dimension, so that two mirror matrices are necessary to describe the whole system:

$$\begin{cases} \begin{pmatrix} C_{0,\alpha}(t) \\ C_{2,\beta'}(t) \end{pmatrix} = \begin{pmatrix} 0 & \mathrm{i}e^{\mathrm{i}\phi_A} \\ \mathrm{i}e^{-\mathrm{i}\phi_A} & 0 \end{pmatrix} \begin{pmatrix} C_{0,\alpha}(0) \\ C_{2,\beta'}(0) \end{pmatrix} \\ \begin{pmatrix} C_{0,\beta}(t) \\ C_{2,\alpha'}(t) \end{pmatrix} = \begin{pmatrix} 0 & \mathrm{i}e^{\mathrm{i}\phi_B} \\ \mathrm{i}e^{-\mathrm{i}\phi_B} & 0 \end{pmatrix} \begin{pmatrix} C_{0,\beta}(0) \\ C_{2,\alpha'}(0) \end{pmatrix} \end{cases} \tag{4.140}$$

To address this issue, it is natural to use 4×4 matrices, so we can write, for the mirror,

$$\begin{pmatrix} C_{0,\alpha}(t) \\ C_{2,\alpha'}(t) \\ C_{0,\beta}(t) \\ C_{2,\beta'}(t) \end{pmatrix} = \frac{\sqrt{2}}{2} \begin{pmatrix} 0 & 0 & 0 & \mathrm{i}e^{\mathrm{i}\phi_{2A}} \\ 0 & 0 & \mathrm{i}e^{-\mathrm{i}\phi_{2B}} & 0 \\ 0 & \mathrm{i}e^{\mathrm{i}\phi_{2B}} & 0 & 0 \\ \mathrm{i}e^{-\mathrm{i}\phi_{2A}} & 0 & 0 & 0 \end{pmatrix} \begin{pmatrix} C_{0,\alpha}(0) \\ C_{2,\alpha'}(0) \\ C_{0,\beta}(0) \\ C_{2,\beta'}(0) \end{pmatrix} \tag{4.141}$$

where the index 2 designates the mirror, and the index A or B indicates the path of the interferometer under consideration, upon which the center of mass depends. In the same basis, the matrices for the two splitters are therefore:

$$U_{\mathrm{S1}} = \frac{\sqrt{2}}{2} \begin{pmatrix} 1 & \mathrm{i}e^{\mathrm{i}\phi_1} & 0 & 0 \\ \mathrm{i}e^{-\mathrm{i}\phi_1} & 1 & 0 & 0 \\ 0 & 0 & 0 & 0 \\ 0 & 0 & 0 & 0 \end{pmatrix} \quad \text{and} \quad U_{\mathrm{S3}} = \frac{\sqrt{2}}{2} \begin{pmatrix} 0 & 0 & 0 & 0 \\ 0 & 0 & 0 & 0 \\ 0 & 0 & 1 & \mathrm{i}e^{\mathrm{i}\phi_3} \\ 0 & 0 & \mathrm{i}e^{-\mathrm{i}\phi_3} & 1 \end{pmatrix} \tag{4.142}$$

Starting from a certain initial state $|\psi_{\mathrm{in}}\rangle$, the final state is

$$|\psi_{\mathrm{out}}\rangle = \hat{U}_{\mathrm{S3}}\,\hat{U}_{\mathrm{M}}\,\hat{U}_{\mathrm{S1}}\,|\psi_{\mathrm{in}}\rangle \tag{4.143}$$

It can be easily demonstrated that in the case of a single input mode, under the considered conditions where atoms are perfectly resonant and there is no atom leakage (perfect reflectivity of the mirror), then it is possible to determine the output state using 2×2 matrices in a $\{p, p+2\hbar k\}$ basis (without specifying the spatial mode), provided that the mirror matrix is written as follows:

$$\begin{pmatrix} C_0(t) \\ C_2(t) \end{pmatrix} = \begin{pmatrix} 0 & \mathrm{i}e^{\mathrm{i}\phi_{2A}} \\ \mathrm{i}e^{-\mathrm{i}\phi_{2B}} & 0 \end{pmatrix} \begin{pmatrix} C_0(0) \\ C_2(0) \end{pmatrix} \tag{4.144}$$

The beam splitter matrices are in the usual form given in equation 4.138.

One can then calculate the final state for an input state where the atoms are in the momentum mode p:

$$|\psi_{\mathrm{out}}\rangle = \hat{U}_{\mathrm{S3}}\,\hat{U}_{\mathrm{M}}\,\hat{U}_{\mathrm{S1}} \begin{pmatrix} 1 \\ 0 \end{pmatrix} = \frac{1}{2} \begin{pmatrix} -e^{\mathrm{i}(\phi_{2A}-\phi_1)} - e^{\mathrm{i}(\phi_3-\phi_{2B})} \\ -\mathrm{i}e^{\mathrm{i}(\phi_{2A}-\phi_1-\phi_3)} + \mathrm{i}e^{-\mathrm{i}\phi_{2B}} \end{pmatrix} \tag{4.145}$$

The probability of measuring an atom in modes p and $p+2\hbar k$ are then respectively

$$\begin{cases} \mathcal{P}_0 = \cos^2\left(\dfrac{\phi_1 - \phi_{2A} - \phi_{2B} + \phi_3}{2}\right) \\ \mathcal{P}_2 = \sin^2\left(\dfrac{\phi_1 - \phi_{2A} - \phi_{2B} + \phi_3}{2}\right) \end{cases} \tag{4.146}$$

As expected, the populations of the output modes oscillate as a function of the phase $\Phi_{\mathrm{lasers}} = \phi_1 - \phi_{2A} - \phi_{2B} + \phi_3$ of the interferometer, i.e.,

$$\begin{aligned} \Phi_{\mathrm{lasers}} = -k_{\mathrm{B}}(z_{\mathrm{c},1} - z_{\mathrm{c},2A} - z_{\mathrm{c},2B} + z_{\mathrm{c},3}) + \Delta\omega_{\mathrm{L}}(t_1 - 2t_2 + t_3) \\ + \Delta\varphi_1 - 2\Delta\varphi_2 + \Delta\varphi_3 \end{aligned} \tag{4.147}$$

where $\Delta\varphi_i = (\varphi_2 - \varphi_1)_i$ is the phase difference between the lasers at the time t_i of the pulse i, and $z_{\mathrm{c},1}$ is the center of mass of the initial wave packet during the first beam splitter, while $z_{\mathrm{c},2A}$ and $z_{\mathrm{c},2B}$ are the centers of mass of the clouds in both paths during the mirror, and $z_{\mathrm{c},3}$ is the center of mass of the recombined cloud during the second beam splitter.

To give an explicit expression of this phase where each term is given by $\phi_i = -k_{\mathrm{B}} z_{\mathrm{c},i} + (\varphi_{2,i} - \varphi_{1,i})$, it is necessary to determine the position of the wave packets during the Bragg pulses, based on their classical trajectories. Let us note T_1 the duration between the first two pulses and T_2 the duration between the mirror and the second splitter. The time origin is set at the moment of the first pulse, such that $t_1 = 0$, $t_2 = T_1$ and $t_2 = T_1 + T_2$. We also write the speeds $v_0 = \frac{p}{m}$ and $v_{\mathrm{B}} = \frac{2\hbar k}{m}$ and the initial position of the wavepacket is z_0. With these notations, we have

$$\begin{cases} z_{\mathrm{c},1} = z_1 \\ z_{\mathrm{c},2\mathrm{A}} = z_1 + v_0 T_1 - \dfrac{1}{2} g T_1^2 \\ z_{\mathrm{c},2\mathrm{B}} = z_1 + (v_0 + v_{\mathrm{B}}) T_1 - \dfrac{1}{2} g T_1^2 \end{cases} \tag{4.148}$$

Note that there are two ways of writing the position of the wave packets during the second beam splitter, each being given by the path of each cloud:

$$\begin{cases} z_{\mathrm{c},3\mathrm{A}} = z_{\mathrm{c},2\mathrm{A}} + (v_{\mathrm{c},2\mathrm{A}} + v_{\mathrm{B}}) T_2 - \dfrac{1}{2} g T_2^2 \\ z_{\mathrm{c},3\mathrm{B}} = z_{\mathrm{c},2\mathrm{B}} + (v_{\mathrm{c},2\mathrm{B}} - v_{\mathrm{B}}) T_2 - \dfrac{1}{2} g T_2^2 \end{cases} \tag{4.149}$$

Here, we consider the case where there is a perfect overlap between the wave packets during the second beam splitter, corresponding to $z_{\mathrm{c},3\mathrm{A}} = z_{\mathrm{c},3\mathrm{B}} = z_{\mathrm{c},3}$, i.e., $T_1 = T_2 = T$. The interferometer is then said to be closed, ensuring maximal interference contrast. We have therefore:

$$z_{\mathrm{c},3} = z_1 + (2v_0 + v_{\mathrm{B}}) T - 2gT^2 \tag{4.150}$$

Since, in this case, $t_1 - 2t_2 + t_3 = 0$, the phase involved in the Mach-Zehnder interferometer is then:

$$\Phi_{\mathrm{lasers}} = k_{\mathrm{B}} g T^2 + \Delta\varphi_1 - 2\Delta\varphi_2 + \Delta\varphi_3 \tag{4.151}$$

This important result shows that the interference phase depends on gravity and the duration between successive Bragg pulses. Actually, the atoms are detuned from the Bragg transition while falling, due to the Doppler effect. As mentioned earlier, it is possible to compensate for this effect by sweeping the frequency between the two lasers. As mentioned earlier, if we note α as the sweep slope, then the additional phase imposed during a pulse i is expressed as:

$$\phi_{\mathrm{sw},i} = \int_0^{t_i} \delta_0(t)\mathrm{d}t = \int_0^{t_i} \alpha t^2 \mathrm{d}t = \alpha \frac{t_i^2}{2} \tag{4.152}$$

with $t_1 = 0$ for the first splitter, $t_2 = T$ for the mirror, and $t_3 = 2T$ for the second splitter. The phase thus added to the total phase Φ is given by:

$$\Phi_{\mathrm{sw}} = \frac{\alpha}{2}(t_1^2 - 2t_2^2 + t_3^2) = \alpha T^2 \tag{4.153}$$

so that

$$\Phi_{\text{lasers}} = (k_{\text{B}}g + \alpha)T^2 + \Delta\varphi_1 - 2\Delta\varphi_2 + \Delta\varphi_3 \tag{4.154}$$

If the value of the frequency ramp slope α is equal to $-k_{\text{B}}g$, then the loss of resonance of the atoms is compensated. This is, in fact, the principle behind cold atom gravimeters, which involve precisely determining the value of this slope to deduce g.

One can then observe an oscillation of the population in each of the modes: for instance if the phase differences $\Delta\varphi_1$ and $\Delta\varphi_2$ are kept the same during the first two pulses, it can be done by varying the phase difference $\Delta\varphi_3$ at the third pulse between each realization of the experiment. Note that it is necessary for the phase differences $\Delta\varphi_i$ not to vary during an experiment, otherwise the interference vanishes.

Propagation phase

Between the pulses, the atoms also acquire a phase. To account for this effect, we must add a term that corresponds to the phase difference accumulated by each wave packet in the gravitational field during its propagation.

To do this, as shown earlier, we will calculate the action associated with each path, maintaining the notations from Figure 4.20, in order to compare the phase accumulated by each wave packet until the second beam splitter where they interfere.

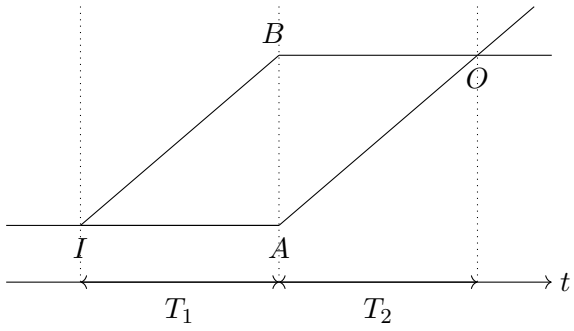

Figure 4.20: Schematic representation of the interferometer. Atoms follow either path A or path B. Here, we assume that the propagation durations are equal, so that $T_1 = T_2$.

On one hand, the phase accumulated by the wave packet that passes through point A is expressed as:

$$\phi_{\text{path,A}} = \frac{1}{\hbar}\int_{\text{IAO}} \mathcal{L}_{\text{c}}\,\mathrm{d}t = \frac{1}{\hbar}\int_{\text{IA}} \mathcal{L}_{\text{c}}\,\mathrm{d}t + \frac{1}{\hbar}\int_{\text{AO}} \mathcal{L}_{\text{c}}\,\mathrm{d}t \tag{4.155}$$

Using 4.134 and assuming that $T_1 = T_2 = T$, we get:

$$\phi_{\text{path,A}} = \frac{m}{\hbar}\left(\frac{v_0^2}{2} + gz_0\right)T + \frac{m}{\hbar}\left(\frac{(v_0 + v_{\text{B}} - gT)^2}{2} + gz_{\text{c,A}}\right)T \tag{4.156}$$

where $z_{\text{c,A}} = z_0 + v_0T - \frac{1}{2}gT^2$ and v_{B} is the Bragg velocity transferred to the atoms by the Bragg pulse.

Similarly, we find for the other path

$$\phi_{\text{path,B}} = \frac{m}{\hbar}\left(\frac{(v_0 + v_{\text{B}})^2}{2} + gz_0\right)T + \frac{m}{\hbar}\left(\frac{(v_0 - gT)^2}{2} + gz_{\text{c,B}}\right)T \tag{4.157}$$

where $z_{\mathrm{c,B}} = z_0 + (v_0 + v_\mathrm{B})T - \frac{1}{2}gT^2$.

At this stage, it can be noted that an order of magnitude of the action is $S \approx 1.5 \times 10^{-32}\,\mathrm{J.s}$ (with $z_0 = 0$, $v_0 = 0$ and $T = 1\,\mathrm{ms}$). Therefore, we have $S \gg \hbar$, justifying that the dominant contribution in the path integral calculation is the classical solution, as discussed earlier.

The phase difference between the wave packets at the second beam splitter is

$$\Phi_\mathrm{prop} = \phi_\mathrm{path,B} - \phi_\mathrm{path,A} = \frac{m}{\hbar}\left(-v_\mathrm{B}gT^2 + gT(z_\mathrm{c,B} - z_\mathrm{c,A})\right) = 0 \tag{4.158}$$

Thus, in the case where the interferometer is closed, the phases accumulated by the two wave packets are equal, and there is no phase shift associated with the propagation of the wave packets in the population oscillation.

This result is actually general: as long as an interferometer is closed, no phase related to the propagation of the wave packets comes into play. On the contrary, if the interferometer is not closed, additional phase shifts appear that tend to decrease the contrast of interferences, eventually leading to total blurring.

4.4.2 Off-resonant corrective terms - finite duration pulses

In section 4.2 presenting the Bragg diffraction model, we showed that the matrices 4.138 employed to model the mirror and Bragg beam splitter are, in fact, specific cases of Bragg transfer matrices in the case of resonant square pulses in the Bragg regime. As mentioned earlier, it is possible to calculate the phases induced by the Bragg transfers in a general case, still within the Bragg regime but without assuming resonance.

In this section, we will then consider an off-resonance model with finite-duration Bragg pulses. We assume that a frequency sweep on one of the two lasers compensates for gravity. Furthermore, we will assume that atoms behave like plane waves to focus solely on the corrective phase shifts due to laser-induced phase imprinting. At first, we do not assume that the interferometer is closed.

We write the transfer matrix 4.63 for a Bragg pulse of duration T in the general form:

$$U(T) = \begin{pmatrix} t\mathrm{e}^{\mathrm{i}\phi'} & \mathrm{i}r\mathrm{e}^{\mathrm{i}\phi} \\ \mathrm{i}r\mathrm{e}^{-\mathrm{i}\phi} & t\mathrm{e}^{-\mathrm{i}\phi'} \end{pmatrix} \tag{4.159}$$

We recall that r and t are real numbers and depend on the duration T of the pulse and on the detuning δ_0, and so do the phases ϕ and ϕ'.

Note that the expression of a Bragg matrix 4.63 was derived in the rotating frame, meaning that we had written $|\psi(t)\rangle = C_0\mathrm{e}^{-\mathrm{i}\omega_0 t}\,|p\rangle + C_2\mathrm{e}^{-\mathrm{i}\omega_2 t}\,|p + 2\hbar k\rangle$, where $\omega_i = \frac{E_i}{\hbar}$. In a plane wave model, we need to return to the laboratory frame in order to take into account the propagation phase shift, i.e., the phase accumulated by the atoms due to their kinetic energy. Therefore, we can rewrite the expression for the evolution matrix as follows:

$$U(T) = \begin{pmatrix} t\mathrm{e}^{\mathrm{i}\phi'}\mathrm{e}^{-\mathrm{i}\omega_0 T} & \mathrm{i}r\mathrm{e}^{\mathrm{i}\phi}\mathrm{e}^{-\mathrm{i}\omega_0 T} \\ \mathrm{i}r\mathrm{e}^{-\mathrm{i}\phi}\mathrm{e}^{-\mathrm{i}\omega_2 T} & t\mathrm{e}^{-\mathrm{i}\phi'}\mathrm{e}^{-\mathrm{i}\omega_2 T} \end{pmatrix} \tag{4.160}$$

Specifically, in the case where there is no light interacting with the atoms, the matrix U

represents the free propagation matrix

$$U_{\mathrm{F}}(T) = \begin{pmatrix} \mathrm{e}^{-\mathrm{i}\omega_0 T} & 0 \\ 0 & \mathrm{e}^{-\mathrm{i}\omega_2 T} \end{pmatrix} \tag{4.161}$$

For better clarity of the results, we will assume that no atoms are transmitted through the mirrors by setting the diagonal terms to zero. This strong assumption will be relaxed later when we will proceed numerically to calculate the phase involved in the Bell interferometer. Under this assumption, the propagation matrix for a mirror is

$$U_{\mathrm{M}}(T) = \begin{pmatrix} 0 & \mathrm{i}r_{\mathrm{M}}\mathrm{e}^{\mathrm{i}\phi_{\mathrm{M}}}\mathrm{e}^{-\mathrm{i}\omega_0 T} \\ \mathrm{i}r_{\mathrm{M}}\mathrm{e}^{-\mathrm{i}\phi_{\mathrm{M}}}\mathrm{e}^{-\mathrm{i}\omega_2 T} & 0 \end{pmatrix} \tag{4.162}$$

and for a beam splitter, we have

$$U_{\mathrm{S}}(T) = \begin{pmatrix} t_{\mathrm{S}}\mathrm{e}^{\mathrm{i}\phi'_{\mathrm{S}}}\mathrm{e}^{-\mathrm{i}\omega_0 T} & \mathrm{i}r_{\mathrm{S}}\mathrm{e}^{\mathrm{i}\phi_{\mathrm{S}}}\mathrm{e}^{-\mathrm{i}\omega_0 T} \\ \mathrm{i}r_{\mathrm{S}}\mathrm{e}^{-\mathrm{i}\phi_{\mathrm{S}}}\mathrm{e}^{-\mathrm{i}\omega_2 T} & t_{\mathrm{S}}\mathrm{e}^{-\mathrm{i}\phi'_{\mathrm{S}}}\mathrm{e}^{-\mathrm{i}\omega_2 T} \end{pmatrix} \tag{4.163}$$

Thus, to determine the output state $|\psi_{\mathrm{out}}\rangle$ of a Bragg doublet in a Mach-Zehnder interferometer, constituted by a sequence of beam-splitter - mirror - beam splitter pulses, one needs to calculate the product

$$|\psi_{\mathrm{out}}\rangle = U_{\mathrm{S}_2}(T_{\mathrm{S}2})U_{\mathrm{F}_2}(T_2)U_{\mathrm{M}}(T_{\mathrm{M}})U_{\mathrm{F}_1}(T_1)U_{\mathrm{S}_1}(T_{\mathrm{S}1})\,|\psi_{\mathrm{in}}\rangle \tag{4.164}$$

where $T_{\mathrm{S}1}$, T_{M} and $T_{\mathrm{S}2}$ are the durations of the successive Bragg pulses, and T_1 and T_2 are the durations of the free propagation (Figure 4.21).

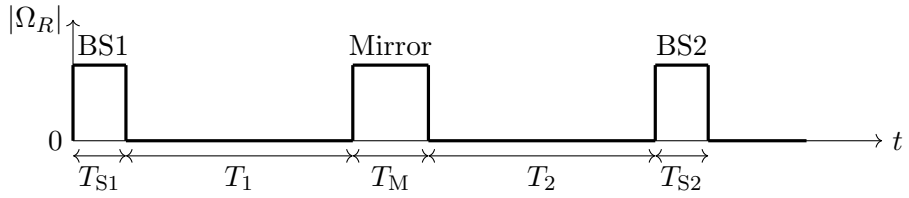

Figure 4.21: Temporal representation of the Mach-Zehnder interferometer.

Starting from an input state where all the atoms are in momentum p, we find

$$\begin{aligned} \langle p|\psi_{\mathrm{out}}\rangle = &-r_{\mathrm{M}}r_{\mathrm{S1}}t_{\mathrm{S2}}\mathrm{e}^{\mathrm{i}\left(\phi'_{\mathrm{S2}}+\phi_{\mathrm{M}}-\phi_{\mathrm{S1}}-\omega_0(T_{\mathrm{S2}}+T_{\mathrm{M}}+T_2)-\omega_2(T_{\mathrm{S1}}+T_1)\right)} \\ &- r_{\mathrm{M}}r_{\mathrm{S2}}t_{\mathrm{S1}}\mathrm{e}^{\mathrm{i}\left(\phi_{\mathrm{S2}}-\phi_{\mathrm{M}}+\phi'_{\mathrm{S1}}-\omega_0(T_{\mathrm{S1}}+T_1+T_{\mathrm{S2}})-\omega_2(T_{\mathrm{M}}+T_2)\right)} \end{aligned} \tag{4.165}$$

Assuming that the reflectivity and transmittivity coefficients are the same for the first and the second beam splitter ($r_{\mathrm{S1}} = r_{\mathrm{S2}} = r_{\mathrm{S}}$ and $t_{\mathrm{S1}} = t_{\mathrm{S2}} = t_{\mathrm{S}}$), we obtain the oscillation of the population of the p momentum state (for instance):

$$\mathcal{P}_0(t) = |\,\langle p|\psi_{\mathrm{out}}\rangle\,|^2 = r_{\mathrm{M}}^2\, r_{\mathrm{S}}^2\, t_{\mathrm{S}}^2 \cos^2\left(\frac{\Phi}{2}\right) \tag{4.166}$$

where

$$\Phi = \phi'_{\mathrm{S1}} + \phi_{\mathrm{S1}} - 2\phi_{\mathrm{M}} - \phi'_{\mathrm{S2}} + \phi_{\mathrm{S2}} + (T_{\mathrm{M}} + T_2 - T_{\mathrm{S1}} - T_1)(\omega_0 - \omega_2) \tag{4.167}$$

We thus obtain a somewhat more general result for the phase involved in the Mach-Zehnder interferometer, with a term related to the phase accumulation due to the kinetic energy of the atom, and phases originating from the interaction with light.

The phase term due to propagation cancels out in the case where $T_{S1} + T_1 = T_M + T_2$. This seems to mean that, in this model, the interferometer is closed when the duration between the start of the first pulse and the start of the second pulse is equal to the duration between the start of the second pulse and the start of the third pulse. This result may seem counterintuitive, as the closure condition for an interferometer with pulses of a certain duration is typically represented in relation to the half-duration of a pulse (so that $T_1 = T_2$) rather than its start. This raises the question of the classical time equivalent to a pulse with a non-zero duration, which originates from a fully quantum phenomenon. Recall that we do not take into account any spatial effect, although they would lead to a additional phase shifts through the center of mass.

In the model presented here, it is not surprising that this condition related to the propagation of the wave packets involves the beginning of each pulse. Let us take the example of a resonant mirror pulse. When expressing the transfer matrix in the form 4.163, if the input state corresponds to an atom in state p, one can see that the transferred mode starts accumulating phase at the frequency ω_2 as soon as $t > 0$, regardless of the fact that the transferred population is nearly zero:

$$|\psi_{\text{out}}\rangle = \begin{pmatrix} 0 & \mathrm{i}e^{\mathrm{i}\phi}e^{-\mathrm{i}\omega_0 t} \\ \mathrm{i}e^{-\mathrm{i}\phi}e^{-\mathrm{i}\omega_2 t} & 0 \end{pmatrix} \begin{pmatrix} 1 \\ 0 \end{pmatrix} = \mathrm{i}e^{-\mathrm{i}\phi}e^{-\mathrm{i}\omega_2 t} |p + 2\hbar k\rangle \tag{4.168}$$

For any finite-duration pulse, the phase accumulated in the reflected mode (for instance) begins to accrue right from the start of the pulse. This is why this initial moment is involved in the condition $T_{S1} + T_1 = T_M + T_2$. But one has to keep in mind that there is another term related to the beginning of the pulses when taking into account the interaction with light, through the phase terms $\Delta\omega_L t_i$. In equation 4.167, we should add

$$\Delta\omega_L(t_1 - 2t_2 + t_3) = \Delta\omega_L(T_M + T_2 - T_{S1} - T_1) \tag{4.169}$$

so that the Mach-Zehnder phase is actually

$$\Phi = \phi'_{S1} + \phi_{S1} - 2\phi_M - \phi'_{S2} + \phi_{S2} + \delta_0(T_M + T_2 - T_{S1} - T_1) \tag{4.170}$$

where we used the definition 4.118 of the detuning, i.e. $\delta_0 = \Delta\omega_L - (\omega_0 - \omega_2)$.

This result is valid regardless of the type of pulse applied, no matter its temporal shape. In the specific case of a constant pulse, we derived an analytical expression for the propagation matrix $\hat{U}$, which can be used to identify the expressions of the phases ϕ and ϕ'. Using the results from equation 4.107, we have:

$$\phi' = \frac{\delta_0 T}{2} + \tan^{-1}\left[-\frac{\delta_0}{\Omega}\tan\left(\frac{\Omega T}{2}\right)\right] \qquad \text{and} \qquad \phi = \Delta\varphi + \frac{\delta_0 T}{2} \tag{4.171}$$

Assuming that we have $T_{S1} = T_{S2} = T_S$, we find

$$\phi'_{S1} + \phi_{S1} - 2\phi_M - \phi'_{S2} + \phi_{S2} = \Delta\varphi_1 - 2\Delta\varphi_2 + \Delta\varphi_3 + \delta_0(T_S - T_M) + \delta_0(T_M + T_2 - T_{S1} - T_1) \tag{4.172}$$

from which we can deduce the phase of the interferometer

$$\Phi = \Delta\varphi_1 - 2\Delta\varphi_2 + \Delta\varphi_3 + \delta_0(T_2 - T_1) \tag{4.173}$$

We recover the resonant case when $\delta_0 = 0$. Note that the well known closure condition $T_1 = T_2$ naturally emerges from this calculation when trying to be less sensitive to the resonance condition (even without considering the wave packets). It appears that the condition for the interferometer to be closed is achieved when

$$\frac{\mathrm{d}\Phi}{\mathrm{d}\delta_0} = 0 \tag{4.174}$$

4.5 Application to the Bell interferometer

In this section, we will apply the formalism developed earlier to the case of the Bell interferometer. The ideal case with perfect resonant beam splitters and mirrors was analyzed in the first section of this chapter. The input state is the two-particle four-mode state

$$|\psi_{\mathrm{in}}\rangle = \frac{1}{\sqrt{2}}(|-p,p\rangle + \mathrm{e}^{\mathrm{i}\phi_0}\,|-q,q\rangle) \tag{4.175}$$

where ϕ_0 is the phase difference between the two input momentum doublets.

We found that, at resonance, the phase involved in the Bell interferometer is $\Phi = \phi_A - \phi_B + \phi_0$, where ϕ_A and ϕ_B are the phases imprinted by the splitter on each loop of the interferometer.

Here, we will incorporate into our analysis the propagation phase, the phase imprinted by the mirror, the center of mass-dependent phase shift. We will also discuss, in a second part, the non-resonant corrective terms to be added to the phase involved in the Bell interferometer in a plane wave model. This last information is crucial for us since we aim to exploit the fact that the A and B Bragg doublets do not have the same resonance frequency. Therefore, it is necessary to understand the effects of a pulse on all velocity classes.

4.5.1 Propagation phase

Let us begin by discussing the phase associated with the propagation of the wave packets. In the case of Mach-Zehnder interferometers, only two momentum modes are at play. The term related to the propagation of the wave packets that comes into play in the interferometer's phase is then equal to the phase difference between the two wave packets when they interfere. We have shown that this phase cancels out when the interferometer is closed. In contrast, the Bell interferometer involves four momentum modes, and we have seen that interference can only be observed by looking at two-particle states. How then can we account for the propagation phase?

If we return to the case of the Mach-Zehnder interferometer, we can write the state of the system just before the second beam splitter as $\psi = C_0\,|p\rangle + C_2\,\mathrm{e}^{\mathrm{i}\Phi_{\mathrm{prop}}}\,|p+2\hbar k\rangle$, where Φ_{prop} is the propagation phase difference between the two wave packets. The coefficients C_0 and C_2 contain all the phase shifts due to the phase imprinted by the first beam splitter and the mirror pulses. After the second beam splitter, the output state is written as follows:

$$|\psi_{\mathrm{out}}\rangle = \frac{1}{\sqrt{2}}\begin{pmatrix} 1 & \mathrm{i}\mathrm{e}^{\mathrm{i}\phi_3} \\ \mathrm{i}\mathrm{e}^{-\mathrm{i}\phi_3} & 1 \end{pmatrix}\begin{pmatrix} C_0 \\ C_2\,\mathrm{e}^{\mathrm{i}\Phi_{\mathrm{prop}}} \end{pmatrix} = \frac{1}{\sqrt{2}}\begin{pmatrix} C_0 + \mathrm{i}C_2\,\mathrm{e}^{\mathrm{i}\phi_3}\mathrm{e}^{\mathrm{i}\Phi_{\mathrm{prop}}} \\ \mathrm{i}C_0\,\mathrm{e}^{-\mathrm{i}\phi_3} + C_2\,\mathrm{e}^{\mathrm{i}\Phi_{\mathrm{prop}}} \end{pmatrix} \tag{4.176}$$

This is where the propagation phase comes into play: we can see that it plays a role similar to the phase imprinted by the third beam splitter. This is the reason why the propagation phase is often treated independently and then added to the laser phase.

Similarly, for each loop A or B of the Bell interferometer, the phase difference due to the propagation of the wave packets associated with each loop plays a role similar to that of the beam splitter. We can express it as follows, for the loop A for instance:

$$|\psi_{\text{out}}^{(A)}\rangle = \frac{1}{\sqrt{2}} \begin{pmatrix} C_0 + \mathrm{i}C_2\, \mathrm{e}^{\mathrm{i}\phi_A} \mathrm{e}^{\mathrm{i}\Phi_{\text{prop}}^{(A)}} \\ \mathrm{i}C_0\, \mathrm{e}^{-\mathrm{i}\phi_3} + C_2\, \mathrm{e}^{\mathrm{i}\Phi_{\text{prop}}^{(A)}} \end{pmatrix} \tag{4.177}$$

So, following the same steps as before, the phase that we need to consider for the Bell interferometer is given by:

$$\Phi = \phi_A - \phi_B + \Phi_{\text{prop}}^{(A)} - \Phi_{\text{prop}}^{(B)} + \phi_0 \tag{4.178}$$

The propagation phases can be calculated in the same manner as for the Mach-Zehnder interferometer. Consider loop A, for example. Let z_0 be the initial position and v_q and v_{-p} the initial velocities, with $v_q = v_{-p} + v_{\text{B}}$. We calculate the phase accumulated by the two wave packets, one going through path D and the other going through path F (Figure 4.22). We note z_D and z_F the position of the center of mass of each wave packet at the time of the mirror. The pulses are considered short enough to be neglected, and the duration between each pulse is T.

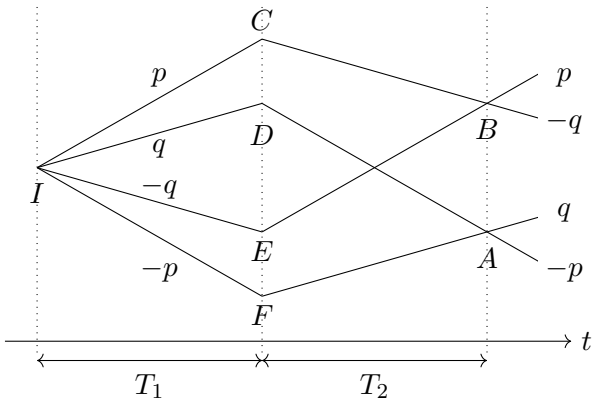

Figure 4.22: Schematic representation of the Bell interferometer.

The propagation phases are

$$\phi_{\text{path,D}}^{(A)} = \frac{m}{\hbar}\left(\frac{v_q^2}{2} + gz_0\right)T + \frac{m}{\hbar}\left(\frac{(v_p - gT)^2}{2} + gz_D\right)T \tag{4.179}$$

$$\phi_{\text{path,F}}^{(A)} = \frac{m}{\hbar}\left(\frac{v_p^2}{2} + gz_0\right)T + \frac{m}{\hbar}\left(\frac{(v_q + gT)^2}{2} - gz_F\right)T \tag{4.180}$$

so the phase difference for loop A is:

$$\Phi_{\text{prop}}^{(A)} = \phi_{\text{path,D}}^{(A)} - \phi_{\text{path,F}}^{(A)} = gT^2(v_p - v_q) + gT(z_D - z_F) \tag{4.181}$$

This expression is unsurprisingly similar to the one obtained for the Mach-Zehnder interferometer. Again, since $z_D - z_F = (v_q - v_p)T$ (due to the fact that the duration between each pulse is the same), we get

$$\Phi_{\text{prop}}^{(A)} = 0 \tag{4.182}$$

Similarly, it can be shown that, for the same reasons, we have $\Phi_{\text{prop}}^{(B)} = 0$.

Again, we find that for a closed interferometer, the phase related to the propagation of the wave packets cancels out. We will assume this condition to be satisfied in the rest of this manuscript. However, it is worth noting that this formalism would allow the calculation of the phase involved in a non-closed Bell interferometer. This suggests that the closure condition is not necessary to perform a Bell test, even though it represents the most favorable scenario (since, of course, in a non-closed interferometer, there is a reduction of the interference contrast due to partial overlap of the wave packets). Finally, let us just mention that we have expressed a classical closure condition, by neglecting the effects related to interaction with light.

4.5.2 Center of mass-dependent imprinted phase

Before determining the phase terms related to non-resonant momentum classes, let us determine the role of the wave packets center-of-mass phase in the Bell interferometer. As a reminder, it has been demonstrated that during the interaction with Bragg beams, the phase difference between the reflected and transmitted beams includes a term written as $-k_{\text{B}}z$, where z is the position of the center of mass of the wave packet.

Therefore, we will once again compute the output state of the interferometer in the resonant case, but this time by expressing the propagation matrices in a non-unitary form (assuming that at resonance, no atoms are transmitted through the mirror). As mentioned earlier, this approach allows us to account for the spatial position of the momentum modes involved in the interferometer. We express the mirror and beam splitter matrices for loop A as follows:

$$\hat{U}_{\text{M}}^{(A)} = \begin{pmatrix} 0 & \mathrm{i}e^{\mathrm{i}\phi_{\text{M}}^{A}(z_F)} \\ \mathrm{i}e^{-\mathrm{i}\phi_{\text{M}}^{A}(z_D)} & 0 \end{pmatrix} \quad \text{and} \quad \hat{U}_{\text{S}}^{(A)} = \frac{1}{\sqrt{2}} \begin{pmatrix} 1 & \mathrm{i}e^{\mathrm{i}\phi_{\text{S}}^{A}(z_A)} \\ \mathrm{i}e^{-\mathrm{i}\phi_{\text{S}}^{A}(z_A)} & 1 \end{pmatrix} \tag{4.183}$$

where each phase term $\phi^A(z_i)$ is the sum of the laser imprinted phase and the center-of-mass z_i imprinted phase. Similarly, we have

$$\hat{U}_{\text{M}}^{(B)} = \begin{pmatrix} 0 & \mathrm{i}e^{i\phi_{\text{M}}^{B}(z_E)} \\ \mathrm{i}e^{-i\phi_{\text{M}}^{B}(z_C)} & 0 \end{pmatrix} \quad \text{and} \quad \hat{U}_{\text{S}}^{(B)} = \frac{1}{\sqrt{2}} \begin{pmatrix} 1 & i\mathrm{e}^{\mathrm{i}\phi_{\text{S}}^{B}(z_B)} \\ i\mathrm{e}^{-\mathrm{i}\phi_{\text{S}}^{B}(z_B)} & 1 \end{pmatrix} \tag{4.184}$$

Thus, starting from the initial state

$$|\psi_{\text{in}}\rangle = \frac{1}{\sqrt{2}} \left[\begin{pmatrix} 1 \\ 0 \end{pmatrix}_A \otimes \begin{pmatrix} 0 \\ 1 \end{pmatrix}_B + \mathrm{e}^{\mathrm{i}\phi_0} \begin{pmatrix} 0 \\ 1 \end{pmatrix}_A \otimes \begin{pmatrix} 1 \\ 0 \end{pmatrix}_B \right] \tag{4.185}$$

we can calculate the output state $|\psi_{\text{out}}\rangle$ using the relation

$$|\psi_{\text{out}}\rangle = \hat{U}_{\text{S}}^{(A)} \hat{U}_{\text{M}}^{(A)} \otimes \hat{U}_{\text{S}}^{(B)} \hat{U}_{\text{M}}^{(B)} |\psi_{\text{in}}\rangle \tag{4.186}$$

from which we deduce the phase Φ on which the Bell interference depends, by calculating $\mathcal{P}(p,-p)$ for instance. We find:

$$\Phi = \phi_{\mathrm{S}}^{A}(z_A) - \phi_{\mathrm{S}}^{B}(z_B) + \phi_0 + \phi_{\mathrm{M}}^{B}(z_C) - \phi_{\mathrm{M}}^{A}(z_D) + \phi_{\mathrm{M}}^{B}(z_E) - \phi_{\mathrm{M}}^{A}(z_F) \tag{4.187}$$

Let us calculate only the phase term Φ_{com} related to the contribution of the center of mass of the wave packets at play ($\Phi = \Phi_{\mathrm{com}} + \Phi_{\mathrm{light}}$). We have

$$-\frac{\Phi_{\mathrm{com}}}{k_{\mathrm{B}}} = z_A - z_B + z_C - z_D + z_E - z_F \tag{4.188}$$

Using the same notation as before, we have

$$\begin{cases} z_C = z_0 + v_p T - \dfrac{1}{2} g T^2 \\ z_D = z_0 + v_q T - \dfrac{1}{2} g T^2 \\ z_E = z_0 + v_{-q} T - \dfrac{1}{2} g T^2 \\ z_F = z_0 + v_{-p} T - \dfrac{1}{2} g T^2 \end{cases} \quad \text{and} \quad \begin{cases} z_A = z_0 + (v_q + v_{-p}) T - g T \\ z_A = z_0 + (v_p + v_{-q}) T - g T \end{cases} \tag{4.189}$$

Finally, we find

$$\Phi_{\mathrm{com}} = 0 \tag{4.190}$$

Thus, we conclude that the center-of-mass phase of the interferometer is zero. This is due to the geometric configuration of the Bell interferometer, which essentially involves taking the difference between two loops. For the same reason, the phase terms related to the laser frequency difference $\Delta\omega_{\mathrm{L}}$ cancel out.

Similarly, if a frequency ramp is added to compensate for the Doppler shift due to gravity, then the additional phase introduced[7] cancels out because the phase shift due to the ramp is the same for A and B, and the equation 4.187 only involves differences between the phases of A and B.

4.5.3 Off-resonant terms

As emphasized several times before, additional phase terms come into play in the phase imprinted on atoms whose momentum class is not resonant with the Bragg transition. Using the previous formalism, it is possible to determine a general expression for the Bell phase for any momentum class, as a function of the phase imprinted by light on the atoms.

The interest of this formulation is to facilitate the understanding of the phases involved, in order to design Bragg pulses that yield the most efficient Bell signal. Indeed, non-resonant terms tend to blur the Bell interference signal, and one of our objectives is to minimize this effect to ensure that the Bell phase does not vary too much with the detuning as we move away from resonance.

We will proceed in the same way as in Section 4.4.2 for the Mach-Zehnder interferometer. The atom wavefunction is considered as a plane wave, so that we do not take into account the off-resonant effects related to the center of mass of the wave packets. Once

[7] For a pulse at $t = t_i$, we have shown that $\phi_{\mathrm{sw},i} = \alpha \dfrac{t_i^2}{2}$ where α is the slope of the frequency ramp.

again, we will start by assuming that the mirror's transmissivity is zero, forcing its diagonal coefficients to zero. This is a strong assumption, certainly not valid off-resonance, but it will lead to a simpler analytical result for interpretation.

To calculate the Bell phase, we again use the relationship 4.186, but this time the matrices for mirrors and beam splitters have the more general form:

$$U_{\mathrm{M}}^{(A)}(T) = \begin{pmatrix} 0 & \mathrm{i}r_{\mathrm{M}}^{A}\mathrm{e}^{\mathrm{i}\phi_{\mathrm{M}}^{A}}\mathrm{e}^{-\mathrm{i}\omega_{0}^{A}T} \\ \mathrm{i}r_{\mathrm{M}}^{A}\mathrm{e}^{-\mathrm{i}\phi_{\mathrm{M}}^{A}}\mathrm{e}^{-\mathrm{i}\omega_{2}^{A}T} & 0 \end{pmatrix} \tag{4.191}$$

and

$$U_{\mathrm{S}}^{(A)}(T) = \begin{pmatrix} t_{\mathrm{S}}^{A}\mathrm{e}^{\mathrm{i}\phi_{\mathrm{S}}'^{A}}\mathrm{e}^{-\mathrm{i}\omega_{0}^{A}T} & \mathrm{i}r_{\mathrm{S}}^{A}\mathrm{e}^{\mathrm{i}\phi_{\mathrm{S}}^{A}}\mathrm{e}^{-\mathrm{i}\omega_{0}^{A}T} \\ \mathrm{i}r_{\mathrm{S}}^{A}\mathrm{e}^{-\mathrm{i}\phi_{\mathrm{S}}^{A}}\mathrm{e}^{-\mathrm{i}\omega_{2}^{A}T} & t_{\mathrm{S}}^{A}\mathrm{e}^{-\mathrm{i}\phi_{\mathrm{S}}'^{A}}\mathrm{e}^{-\mathrm{i}\omega_{2}^{A}T} \end{pmatrix} \tag{4.192}$$

where T is the duration of the pulse. We included propagation terms $\mathrm{e}^{-\mathrm{i}\omega T}$ due to the kinetic energy of the atoms in order to discuss the interferometer closure condition with finite duration pulses. Since the momentum doublets involved are different for A and B, we have $\omega_0^A = \omega_{-p}$ and $\omega_2^A = \omega_q$, while $\omega_0^B = \omega_{-q}$ and $\omega_2^B = \omega_p$. T is the duration of the pulse, and all the variables are detuning-dependent, from the reflectivity r and transmittivity t coefficients to the phases ϕ and ϕ'.

The interferometric sequence is represented in Figure 4.23, where T_{M} and T_{S} are the durations of the Bragg mirror and beam splitter pulses, and T_1 and T_2 are the free propagation times.

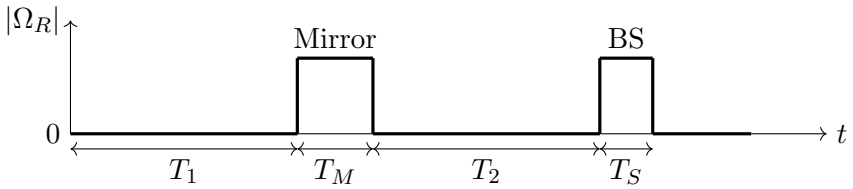

Figure 4.23: Temporal representation of the Bell interferometer.

We obtain

$$\begin{aligned}\langle -p, -q|\psi_{\mathrm{out}}\rangle = &-\mathrm{i}r_{\mathrm{M}}^{A}\, r_{\mathrm{S}}^{A}\, r_{\mathrm{M}}^{B}\, t_{\mathrm{S}}^{B}\, \mathrm{e}^{\mathrm{i}\left(\phi_{\mathrm{S}}^{A}-\phi_{\mathrm{M}}^{A}+\phi_{\mathrm{S}}'^{B}+\phi_{\mathrm{M}}^{B}-T_1(\omega_q+\omega_{-q})-(T_{\mathrm{M}}+T_2)(\omega_{-p}+\omega_p)\right)} \\ &-\mathrm{i}r_{\mathrm{M}}^{A}\, t_{\mathrm{S}}^{A}\, r_{\mathrm{S}}^{B}\, r_{\mathrm{M}}^{B}\, \mathrm{e}^{\mathrm{i}\left(\phi_{\mathrm{S}}'^{A}+\phi_{\mathrm{M}}^{A}+\phi_{\mathrm{S}}^{B}-\phi_{\mathrm{M}}^{B}+\phi_0-T_1(\omega_p+\omega_{-p})-(T_{\mathrm{M}}+T_2)(\omega_q+\omega_{-q})\right)}\end{aligned} \tag{4.193}$$

Assuming that $r_{\mathrm{S}}^{A} = r_{\mathrm{S}}^{B}$ and $t_{\mathrm{T}}^{A} = t_{\mathrm{S}}^{B}$, we get the Bell phase, which can be written:

$$\Phi = \phi_{\mathrm{S}}^{A} - \phi_{\mathrm{S}}^{B} - \phi_{\mathrm{S}}'^{A} + \phi_{\mathrm{S}}'^{B} + 2\phi_{\mathrm{M}}^{B} - 2\phi_{\mathrm{M}}^{A} + (\omega_q + \omega_{-q} - \omega_p - \omega_{-p})(T_{\mathrm{M}} + T_2 - T_1) + \phi_0 \tag{4.194}$$

We distinguish three kinds of phase shifts.

- First, the phase shifts $\phi_{S,M}^{A,B}$ and $\phi_{S,M}'^{A,B}$ are related to the interaction of the atoms with light. They are known analytically for constant squared pulses, or can be determined in a more general case by solving the Bragg coupling equation 4.60 of each momentum doublet A and B for a given pulse.

- Second, the phase shift proportional to $T_\mathrm{M} + T_2 - T_1$ is related to the propagation of wavepackets, and corresponds to the phase difference accumulated by loops A and B in the different momentum modes involved. This phase shift only originates from the $\mathrm{e}^{\mathrm{i}\omega t}$ terms in the evolution matrices. Interestingly, this propagation phase shift vanishes for $T_1 = T_\mathrm{M} + T_2$. This appears to be a "closure" relation based on the beginning of the pulses, meaning that the duration between the spatial separation of the atoms (at the beginning of the interferometer) and the start of the mirror pulse must be equal to the duration between the start of the mirror pulse and the start of the beam splitter pulse. The discussion is similar to the case of the Mach-Zehnder interferometer: in our formalism, the reflected momentum modes start acquiring phase as soon as the pulse starts, no matter how small the transferred population is. So, if we do not consider the additional phase shifts due to the interaction with light, the modes cross each other at the beginning of the beam splitter pulse. The interpretation in terms of interferometer closure will be further discussed in the next chapter, when we will aim at determining the closure relation for the Hong-Ou-Mandel interferometer.

- Finally, the phase shift ϕ_0 is due to the initial phase shift between the two pairs of twin momentum modes emitted by the four-wave mixing process. This phase can *a priori* depend on the momentum quadruplet considered, but remains constant for a given quadruplet, whose momentum width corresponds to the size of a mode.

Chapter 5

Bragg pulses shaping and phase control for a Bell test

5.1 Bell oscillation in an off-resonant HOM experiment 173
5.1.1 Description of the Hong-Ou-Mandel effect 175
5.1.2 Analytical results for the Bell correlator 176
5.1.3 Numerical simulation 184
5.1.4 Discussion of previous results 186
5.2 Bell phase control 188
5.2.1 Principle: two-frequency pulses 188
5.2.2 Experimental implementation 190
5.2.3 Reflectivity and phase of Bragg pulses for a Bell test 195
5.2.4 Bell correlator 201
5.3 Bragg pulse shaping 204
5.3.1 State of the art, motivation and criteria 204
5.3.2 Sinc-shaped mirror 207
5.3.3 Modulated sinc-shaped beam splitter 211
5.3.4 Oscillation of the Bell correlator 214

In this chapter, we will describe the strategy we adopted to carry out a Bell inequality test and the Bragg pulses we aim at performing.

A first attempt to observe a Bell correlator oscillation consists in conducting a HOM-type experiment to ensure the closure of the interferometer, and to use the data when the interferometer is closed to focus on non-resonant momentum classes, as the Bell correlator was shown to depend on the detuning. This experiment was conducted by our team in 2017, and we will briefly discuss the results obtained at that time.

The terminology used throughout the rest of the manuscript will be as follows: we will describe an HOM experiment as an interferometer with a single beam splitter, while in a Bell experiment there are two distinct beam splitters for the A and B momentum doublets. In the first section, we will describe the Bell-type correlations that can be highlighted with a HOM interferometer. Subsequent sections will be dedicated to the implementation of a proper Bell interferometer.

Indeed, following this initial test using a HOM interferometer, which provides an insight into the expected amplitude of the Bell correlator oscillation, the Bell test we aim to perform requires a control of the phase difference between A and B, as mentioned in section 4.1.2. The main idea is to leverage the fact that the momentum doublets involved in loops A and B do not share the same resonance frequency. By implementing a "two-frequency" beam splitter pulse, we can have two different beam splitters whose characteristics can be independently controlled, specifically the phase imprinted by the light to the atoms of each doublet.

We will see that a convenient way to realize such two-frequency pulses without being sensitive to phase fluctuations consists in shaping the temporal profile of the beam splitter pulse. It also makes it possible to control the phase difference imprinted on doublets A and B. This technique can be used to perform negative or even complex two-photon Rabi frequencies, which we will also leverage to enhance the resonance width of mirror and beam splitter pulses.

The final section of this chapter is dedicated to applying these pulses to a Bell interferometer in a numerical simulation that calculates the Bell oscillator.

5.1 Bell oscillation in an off-resonant HOM experiment

As mentioned in the introduction, a Hong-Ou-Mandel interferometer can be used to identify conditions under which two particles are indistinguishable.

In the case under consideration here, two twin atoms are emitted through four-wave mixing in two different momentum modes, denoted as p_0 and $-p_0$ (in the center of mass reference frame). The momentum difference between the two is set equal to the momentum $\hbar k_\mathrm{B}$ transferred during a two-photon Bragg transition, such that a mirror pulse couples p_0 and $-p_0$. Following this mirror pulse, the two wave packets then approach each other. When looking at the probabilities of detection after time of flight, maximum amplitude interference is observed when a beam splitter is applied at the moment when the wave packets perfectly overlap. This results in a decrease of the probability of measuring two atoms in the two modes (to zero in the ideal case of a Fock state, as will be discussed in Chapter 7). Therefore, the time of application of the beam splitter at which this joint probability of measuring one atom in each mode p_0 and $-p_0$ is minimal ensures that the interferometer is closed.

This is strong evidence of two-atom interference, a phenomenon only explainable by quantum theory when the probability of jointly measuring p_0 and $-p_0$ falls below 0.5.

This experiment was first conducted by our team in 2014[92] and successfully replicated in 2016[121].

The indistinguishability of interfering particles when the beam splitter is applied at the HOM "dip" ensures that the interferometer is closed. Otherwise, partial overlap between the wave packets would lead to a loss of contrast. We can then leverage the fact that the emission of our pair source is multimode to notice that alongside the HOM interferometer, involving only a doublet $(p_0, -p_0)$, we also realize a Bell-type interferometer when considering a quadruplet $(p, -p, q, -q)$ where the momentum modes p and q are symmetric with respect to the mode p_0 (Figure 5.1).

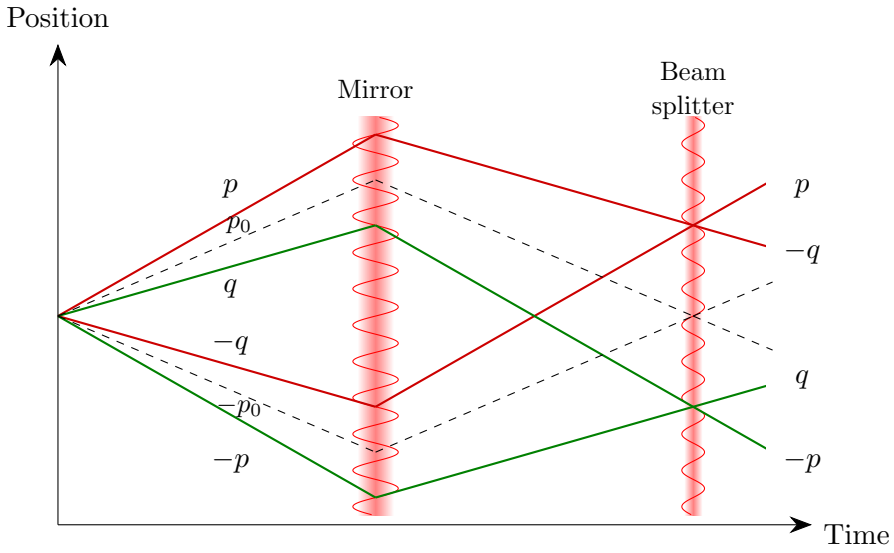

Figure 5.1: Schematic representation of a Bell-type interferometer realized in parallel with a HOM interferometer. Representation in the falling frame. The modes p_0 and $-p_0$ involved in the HOM interferometer are depicted with dashed lines. The coupled neighboring modes p and $-p$ on one hand, and q and $-q$ on the other hand, form a Bell interferometer, for which there is no control parameter. The observation of a HOM dip ensures that the interferometer is closed.

In fact, our pairs source produces a set of momentum quadruplets corresponding to various values of Δp, where $\Delta p = p - p_0 = p_0 - q$. For each value of Δp, the associated quadruplet $(p, -p, q, -q)$ is detuned by $\delta_0 = -\frac{k_B}{m}\Delta p$ with respect to the Bragg resonance, which corresponds to the momentum doublet $(p_0, -p_0)$ used for the HOM experiment.

This is not a Bell test in the strict sense, as we cannot control the phases imprinted on A and B. However, an idea to exhibit Bell correlations is to use the fact that the phase imprinted by a Bragg pulse depends on the considered momentum classes. Thus, since the different quadruplets correspond to different detunings, we could measure the Bell correlator for each available quadruplet to observe a variation of the Bell correlator as a function of the detuning.

An analysis in this spirit was conducted using the data from the 2016 HOM interferometer, leading to an article published in 2017[93], that will be discussed in the following. In this article, three correlator values were calculated for three different quadruplets, and indeed, a significant variation in the correlator with the momentum quadruplet was observed.

The new theoretical developments I have conducted during my thesis and presented in this chapter alter the interpretation of these results, as we will demonstrate that the closure of the interferometer precisely corresponds to the case where the Bell correlator does not depend on the detuning. Any variation in the correlator would thus arise from a quadruplet-dependent phase shift other than that due to the detuning imprinted by the Bragg pulses.

5.1.1 Description of the Hong-Ou-Mandel effect

First, let us demonstrate the HOM effect. We will use the same formalism as before, but, for the sake of simplicity, we will not consider in this section the phase terms associated with the accumulation of kinetic phase in each mode (in this section only). Therefore, the resonant matrices for the mirror and the beam splitter are once again:

$$\hat{U}_{\mathrm{M}} = \begin{pmatrix} 0 & \mathrm{i}e^{\mathrm{i}\phi_{\mathrm{M}}} \\ \mathrm{i}e^{-\mathrm{i}\phi_{\mathrm{M}}} & 0 \end{pmatrix} \qquad \text{and} \qquad \hat{U}_{\mathrm{S}} = \frac{1}{\sqrt{2}} \begin{pmatrix} 1 & \mathrm{i}e^{\mathrm{i}\phi_{\mathrm{S}}} \\ \mathrm{i}e^{-\mathrm{i}\phi_{\mathrm{S}}} & 1 \end{pmatrix} \tag{5.1}$$

The input state of the HOM interferometer is composed of a pair of atoms in the states p_0 and $-p_0$.

$$|\psi_{\mathrm{in}}\rangle = |p_0, -p_0\rangle \tag{5.2}$$

However, as will be discussed in detail in the HOM chapter, this expression is incomplete as it does not account for the bosonic nature of atoms. Indeed, the emitted atoms are indistinguishable, and writing the input state as $|p_0, -p_0\rangle = |p_0\rangle_1 \otimes |-p_0\rangle_2$ implicitly suggests that particle 1 is in mode p_0, and particle 2 is in mode $-p_0$, which corresponds to treating the particles as distinguishable. To make the input state indistinguishable, and since our atoms are bosons, the state must be symmetrized:

$$|\psi_{\mathrm{in}}\rangle = \frac{1}{\sqrt{2}} \left(|1 : p_0, 2 : -p_0\rangle + |1 : -p_0, 2 : p_0\rangle \right) \tag{5.3}$$

If we express this initial state as column matrices in the basis of states coupled by Bragg scattering, we have:

$$|\psi_{\mathrm{in}}\rangle = \frac{1}{\sqrt{2}} \left[\begin{pmatrix} 1 \\ 0 \end{pmatrix}_1 \otimes \begin{pmatrix} 0 \\ 1 \end{pmatrix}_2 + \begin{pmatrix} 0 \\ 1 \end{pmatrix}_1 \otimes \begin{pmatrix} 1 \\ 0 \end{pmatrix}_2 \right] \tag{5.4}$$

$$\hat{U}_{\mathrm{S}}\hat{U}_{\mathrm{M}} \begin{pmatrix} 1 \\ 0 \end{pmatrix} = \frac{1}{\sqrt{2}} \begin{pmatrix} -e^{\mathrm{i}(\phi_{\mathrm{S}} - \phi_{\mathrm{M}})} \\ \mathrm{i}e^{-\mathrm{i}\phi_{\mathrm{M}}} \end{pmatrix} \qquad \text{and} \qquad \hat{U}_{\mathrm{S}}\hat{U}_{\mathrm{M}} \begin{pmatrix} 0 \\ 1 \end{pmatrix} = \frac{1}{\sqrt{2}} \begin{pmatrix} \mathrm{i}e^{\mathrm{i}\phi_{\mathrm{M}}} \\ -e^{\mathrm{i}(\phi_{\mathrm{M}} - \phi_{\mathrm{S}})} \end{pmatrix} \tag{5.5}$$

Note that $|\psi_{\mathrm{in,dis}}\rangle = \begin{pmatrix} 1 \\ 0 \end{pmatrix}_1 \otimes \begin{pmatrix} 0 \\ 1 \end{pmatrix}_2$ a state of distinguishable particles. At the output of the interferometer, the state is

$$\begin{aligned} \hat{U}_{\mathrm{M}}\hat{U}_{\mathrm{S}} \begin{pmatrix} 1 \\ 0 \end{pmatrix}_1 \otimes \begin{pmatrix} 0 \\ 1 \end{pmatrix}_2 &= \frac{1}{\sqrt{2}} \begin{pmatrix} -e^{\mathrm{i}(\phi_{\mathrm{S}} - \phi_{\mathrm{M}})} \\ \mathrm{i}e^{-\mathrm{i}\phi_{\mathrm{M}}} \end{pmatrix}_1 \otimes \frac{1}{\sqrt{2}} \begin{pmatrix} \mathrm{i}e^{\mathrm{i}\phi_{\mathrm{M}}} \\ -e^{\mathrm{i}(\phi_{\mathrm{M}} - \phi_{\mathrm{S}})} \end{pmatrix}_2 \\ &= \frac{1}{2} \left[-\mathrm{i}e^{\phi_{\mathrm{S}}} |-p_0, -p_0\rangle + |-p_0, p_0\rangle - |p_0, -p_0\rangle - \mathrm{i}e^{-\mathrm{i}\phi_{\mathrm{S}}} |p_0, p_0\rangle \right] \end{aligned} \tag{5.6}$$

If we calculate the probabilities associated with each basis state, we find

$$\mathcal{P}(p_0, p_0) = \mathcal{P}(-p_0, p_0) = \mathcal{P}(p_0, -p_0) = \mathcal{P}(-p_0, -p_0) = \frac{1}{4} \tag{5.7}$$

We can see that the output state is associated with four equiprobable probabilities of finding the two particles in different output states, as in the intuitive result with classical particles. In particular, experimentally, the probability $\mathcal{P}_{\text{diff}}$ of finding two particles in the two different modes is

$$\mathcal{P}_{\text{diff}} = \mathcal{P}(-p_0, p_0) + \mathcal{P}(p_0, -p_0) = \frac{1}{2} \tag{5.8}$$

For this state corresponding to distinguishable particles at the input of the HOM interferometer, no decrease in the joint probability of detecting atoms in different modes is observed.

Similarly,

$$\begin{aligned} \hat{U}_{\text{S}}\hat{U}_{\text{M}} \begin{pmatrix} 0 \\ 1 \end{pmatrix}_1 \otimes \begin{pmatrix} 1 \\ 0 \end{pmatrix}_2 &= \frac{1}{\sqrt{2}} \begin{pmatrix} \text{i}e^{\text{i}\phi_{\text{M}}} \\ -e^{\text{i}(\phi_{\text{M}}-\phi_{\text{S}})} \end{pmatrix}_1 \otimes \frac{1}{\sqrt{2}} \begin{pmatrix} -e^{\text{i}(\phi_{\text{S}}-\phi_{\text{M}})} \\ \text{i}e^{-\text{i}\phi_{\text{M}}} \end{pmatrix}_2 \\ &= \frac{1}{2}\left[-\text{i}e^{\phi_{\text{S}}} |-p_0, -p_0\rangle - |-p_0, p_0\rangle + |p_0, -p_0\rangle - \text{i}e^{-\text{i}\phi_{\text{S}}} |p_0, p_0\rangle\right] \end{aligned} \tag{5.9}$$

Therefore, the output state $|\psi_{\text{out}}\rangle$ of the HOM interferometer for the indistinguishable input state 5.4 is equal to the sum of expressions 5.6 and 5.9. We then obtain:

$$|\psi_{\text{out}}\rangle = \frac{1}{\sqrt{2}}\left[-\text{i}e^{\phi_{\text{S}}} |-p_0, -p_0\rangle - \text{i}e^{-\text{i}\phi_{\text{S}}} |p_0, p_0\rangle\right] \tag{5.10}$$

Thus, we can see that the probability of finding two particles in two different momentum modes is zero:

$$\mathcal{P}_{\text{diff}} = \mathcal{P}(-p_0, p_0) + \mathcal{P}(p_0, -p_0) = 0 \tag{5.11}$$

This is the HOM effect, which, as observed, is linked to the indistinguishable nature of bosonic particles. Note that, to account for this effect, it was necessary to symmetrize the input bosonic state.

5.1.2 Analytical results for the Bell correlator

Analytical expression of the Bell correlator

In the following, we return to a more general description of Bragg pulses as discussed in the previous chapter, where atoms are treated as plane waves, taking into account the finite duration of Bragg pulses as well as the off-resonance terms. As discussed earlier, the question here is to determine the expression of the Bell correlator associated with the non-resonant terms of the HOM interferometer.

Calculating the Bell phase involved in the HOM interferometer is a particularly simple case because, as the Bragg pulses used are constant pulses and similar for A and B, we have an analytical expression for the transfer matrices and, consequently, for the Bell correlator. We will reuse the results from the previous chapter, in which we derived a general expression for the Bell phase, expressed in terms of phases associated with the reflection and transmission coefficients of the Bragg pulse.

$$\Phi = \phi_{\text{S}}^{A} - \phi_{\text{S}}^{B} - \phi_{\text{S}}^{\prime A} + \phi_{\text{S}}^{\prime B} + 2\phi_{\text{M}}^{B} - 2\phi_{\text{M}}^{A} + (\omega_q + \omega_{-q} - \omega_p - \omega_{-p})(T_{\text{M}} + T_2 - T_1) + \phi_0 \tag{5.12}$$

where the phase terms $\phi_{\mathrm{S,M}}^{A,B}$ correspond to the phase imprinted on the reflected part of the state while the terms $\phi_{\mathrm{S}}^{\prime A,B}$ are the phase shifts imprinted on the transmitted part. Recall that this result was obtained for a mirror with a transmission coefficient being zero for any momentum class, which is a strong assumption that is valid only over a narrow range of momentum, as we will see later. We will later numerically calculate the Bell phase without relying on this assumption. ϕ_0 is the phase difference between the two pairs of the input modes.

For square pulses, we have analytical expressions for the phase shifts due to the interaction with light. The distinction between doublet A and doublet B will only lie in the detuning considered. For the HOM experiment, the resonant doublet (for which $\delta_0 = 0$) is $(p_0, -p_0)$, so that $\delta_0 = +\delta$ for doublet A and $\delta_0 = -\delta$ for doublet B. Note that ϕ_0, determined by the pairs creation process, can also depend on the momentum quadruplet considered, and therefore on δ.

Then, like for the Mach-Zehnder interferometer (equation 4.171), we identify the phases ϕ and ϕ' using the matrix 4.63 obtained for a constant pulse of duration T and two-photon Rabi frequency Ω, leading to the expression:

$$\phi' = \frac{\delta_0 T}{2} + \tan^{-1}\left[-\frac{\delta_0}{\tilde{\Omega}}\tan\left(\frac{\tilde{\Omega}T}{2}\right)\right] \qquad \text{and} \qquad \phi = \Delta\varphi + \frac{\delta_0 T}{2} \tag{5.13}$$

with $\tilde{\Omega} = \sqrt{\Omega^2 + \delta_0^2}$ and $\Delta\varphi$ is the laser phase difference between the two beams of the Bragg pulse. Here, we will consider that the two Bragg pulses have the same two-photon Rabi frequency, so $\Omega_{\mathrm{S}} = \Omega_{\mathrm{M}} = \Omega$.

If we apply this formula to the mirror and beam splitter pulses, indexed respectively by M and S, we obtain:

$$\begin{cases} \phi_{\mathrm{S}}^{A} = \Delta\varphi_{\mathrm{S}}^{A} + \dfrac{\delta T_{\mathrm{S}}}{2} \\ \phi_{\mathrm{S}}^{B} = \Delta\varphi_{\mathrm{S}}^{B} - \dfrac{\delta T_{\mathrm{S}}}{2} \\ \phi_{\mathrm{M}}^{A} = \Delta\varphi_{\mathrm{M}}^{A} + \dfrac{\delta T_{\mathrm{M}}}{2} \\ \phi_{\mathrm{M}}^{B} = \Delta\varphi_{\mathrm{M}}^{B} - \dfrac{\delta T_{\mathrm{M}}}{2} \end{cases} \qquad \text{and} \qquad \begin{cases} \phi_{\mathrm{S}}^{\prime A} = \dfrac{\delta T_{\mathrm{S}}}{2} - \tan^{-1}\left[\dfrac{\delta}{\tilde{\Omega}}\tan\left(\dfrac{\tilde{\Omega}T_{\mathrm{S}}}{2}\right)\right] \\ \phi_{\mathrm{S}}^{\prime B} = -\dfrac{\delta T_{\mathrm{S}}}{2} + \tan^{-1}\left[\dfrac{\delta}{\tilde{\Omega}}\tan\left(\dfrac{\tilde{\Omega}T_{\mathrm{S}}}{2}\right)\right] \end{cases} \tag{5.14}$$

The Bell phase is therefore

$$\begin{aligned} \Phi = {} & \Delta\varphi_{\mathrm{S}}^{A} - \Delta\varphi_{\mathrm{S}}^{B} + 2\Delta\varphi_{\mathrm{M}}^{A} - 2\Delta\varphi_{\mathrm{S}}^{B} - 2\delta T_{\mathrm{M}} + 2\tan^{-1}\left[\frac{\delta}{\tilde{\Omega}}\tan\left(\frac{\tilde{\Omega}T_{\mathrm{S}}}{2}\right)\right] \\ & + (\omega_q + \omega_{-q} - \omega_p - \omega_{-p})(T_{\mathrm{M}} + T_2 - T_1) + \phi_0(\delta) \end{aligned} \tag{5.15}$$

Recall that $\Delta\varphi$ represents the phase difference between the lasers. Since the same pulses are used for both A and B, we have $\Delta\varphi^A = \Delta\varphi^B$, and the laser phase terms cancel out. Moreover, the propagation phase shift can be expressed in terms of detuning, using the definition $\omega_p = \frac{p^2}{2m\hbar}$, so that:

$$\hbar(\omega_q + \omega_{-q} - \omega_p - \omega_{-p}) = -\frac{2\hbar k_{\mathrm{B}}}{m}\Delta p = +2\hbar\delta \tag{5.16}$$

Finally, the phase shifts in $2\delta T_{\mathrm{M}}$ cancel out and the Bell phase is

$$\Phi = 2\tan^{-1}\left[\frac{\delta}{\sqrt{\Omega^2+\delta^2}}\tan\left(\sqrt{\Omega^2+\delta^2}\frac{T_{\mathrm{S}}}{2}\right)\right] + 2\delta(T_2 - T_1) + \phi_0(\delta) \tag{5.17}$$

It is possible to calculate analytically not only the phase involved in the interferometer but also the amplitude of the Bell correlator. To do so, the previous formalism can be applied: the output state is calculated using transfer matrices 4.63 whose analytical expressions are known. Again, for this calculation, we assume the transmission coefficient of the mirror to be zero. We obtain:

$$\begin{cases} \mathcal{P}(p,q) = \mathcal{P}(-p,-q) = \dfrac{1}{2}R_{\mathrm{M}}^2\left(1-4\varepsilon_{\mathrm{S}}^2\right)\cos^2\left(\dfrac{\Phi}{2}\right) \\ \mathcal{P}(p,-p) = \mathcal{P}(q,-q) = \dfrac{1}{2}R_{\mathrm{M}}^2\left(\sin^2\left(\dfrac{\Phi}{2}\right) + 4\varepsilon_{\mathrm{S}}^2\cos^2\left(\dfrac{\Phi}{2}\right)\right) \end{cases} \tag{5.18}$$

where we defined

$$\varepsilon_{\mathrm{S}} = \frac{1}{2} - \frac{\Omega^2}{\tilde{\Omega}^2}\sin^2\left(\frac{\pi\tilde{\Omega}}{4\Omega}\right) \qquad \text{and} \qquad R_{\mathrm{M}} = \frac{\Omega^2}{\tilde{\Omega}^2}\sin^2\left(\frac{\pi\tilde{\Omega}}{2\Omega}\right) \tag{5.19}$$

Ideally (i.e. at the limit to the resonant case where $\delta_0 = 0$), $\varepsilon = 0$ and $R_{\mathrm{M}} = 1$. Finally, we get the full expression of the Bell correlator:

$$E = \mathcal{P}(p,q) + \mathcal{P}(-p,-q) - \mathcal{P}(p,-p) - \mathcal{P}(q,-q) = R_{\mathrm{M}}^2\left[\left(1-4\varepsilon_{\mathrm{S}}^2\right)\cos\Phi - 4\varepsilon_{\mathrm{S}}^2\right] \tag{5.20}$$

Let us define

$$A(\delta) = R_{\mathrm{M}}^2\left(1-4\varepsilon_{\mathrm{S}}^2\right) \tag{5.21}$$

the amplitude of the Bell oscillation. Note that, as the considered quadruplet gets further from the Bragg resonance (i.e. as δ, or equivalently Δp, increases), the amplitude of the Bell oscillation will decrease due to the less favorable reflectivity properties of the mirror and the beam splitter.

Using the expression 5.20, the Bell correlator can be calculated as a function of the detuning. However, this requires knowing the durations T_1 and T_2 for which the interferometer is closed. In the following paragraphs, we will study an arbitrary choice of $T_2 - T_1$ to discuss the variation of the correlator before determining in the next section the closure condition.

As a first example, let us consider the case $T_2 = T_1 - T_{\mathrm{M}}$. Choosing this condition consists in studying the case where the phase term of the correlator related to the kinetic energy of wave packet propagation is canceled out. We take $T_1 = 800\,\mu\mathrm{s}$, which corresponds to the order of magnitude used in the article [93]. The Bell phase Φ also depends on the two-photon Rabi frequency of the beam splitter pulse, so we used the characteristics of the Bragg pulses described in the article to plot the Bell phase, the joint probabilities of detection and the Bell correlator (Figure 5.2). The two pulses have a two-photon Rabi frequency of 5 kHz, so the mirror π pulse is 100 µs long while the beam-splitter $\pi/2$ pulse is 50 µs long.

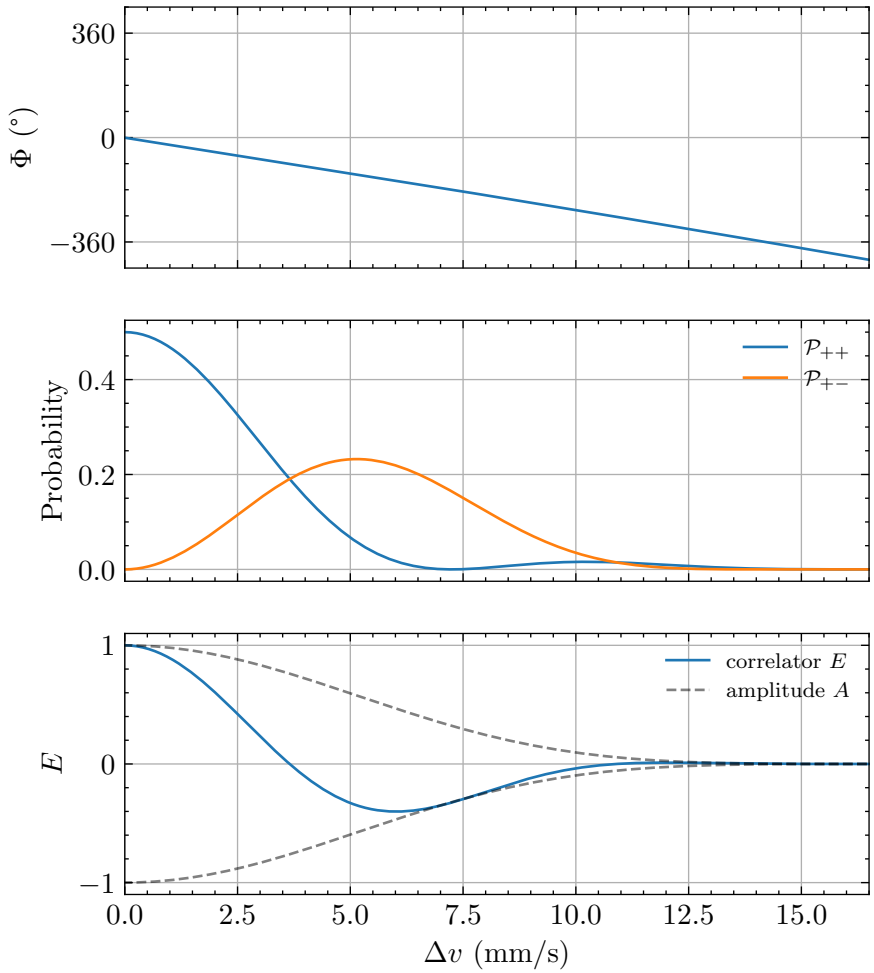

Figure 5.2: Analytical solution of the Bell interferometer for square pulses. The atoms transmitted by the mirror are not taken into account. We calculate the Bell phase Φ that appears in the Bell correlator, the joint probabilities $\mathcal{P}_{++} = \mathcal{P}(p,q) + \mathcal{P}(-p,-q)$ and $\mathcal{P}_{+-} = \mathcal{P}(p,-q) + \mathcal{P}(q,-p)$, and the Bell correlator E. Each value corresponds to the analytical solution at a fixed detuning, and the results are plotted as a function of the velocity class Δv using $\delta = -k_\mathrm{B}\Delta v$. The phase ϕ_0 between the pairs is supposed to be zero. The two-photon Rabi frequency of each pulse is $\Omega_\mathrm{M} = 5\,\mathrm{kHz}$, the duration of the first free propagation is $T_1 = 800\,\mu\mathrm{s}$, and the duration of the second free propagation is $T_2 = T_1 - \pi/\Omega_\mathrm{M}$.

For now, we also assume that the phase ϕ_0 between the two pairs of emitted modes is zero. The curves are plotted as a function of the velocity class, Δv with respect to resonance, which depends on the detuning according to the relation $\delta = -k_\mathrm{B}\Delta v$. Note that, for our Bragg wavevector k_B, we have $\Delta v\,(\mathrm{mm.s^{-1}}) \approx -2\delta\,(\mathrm{kHz})$.

It can be observed that the Bell phase seems to vary linearly with the detuning. The slope is such that the phase varies by a bit less than 2π over the velocity range for which the amplitude $A(\Delta v)$ of the HOM signal, depicted as dashed lines, remains non-zero. This velocity range, along with the size of a mode over which to integrate the signal, determines the number of quadruplets that can be used to observe a non-zero correlator. The challenge of measuring the correlator E in parallel with a HOM experiment is to ensure that it is possible to measure non-zero values of the correlator, with the maximum attainable value being determined by the correlator's amplitude, which depends only on

the reflection and transmission coefficients of the Bragg pulses. As seen in section 4.2.2, the two-photon Rabi frequency of 5 kHz used in the experiment allows the widest resonance width possible while remaining within the framework of a two-level system without losses towards higher diffraction orders.

Note also that resonance corresponds to the HOM effect, so that $\mathcal{P}_{+-}$ vanishes, as will be discussed in the following paragraph.

Closure of the interferometer

Now, let us ask under what conditions the interferometer is closed, or rather, how to translate, in our model, the fact that the interferometer is closed (since this is what the HOM interferometer detects). This question is crucial because, for a fixed value of T_1, it determines the value of T_2, which corresponds to the delay at which the beam splitter is applied. Knowing $T_2 - T_1$ is essential for calculating the correlator of the Bell interferometers realized in the HOM dip for various momentum quadruplets.

The previous model used to calculate the output state of the Bell interferometer can also be used to determine the HOM dip when operating at resonance. Indeed, our initial state is a two-particle state with four modes that can be expressed as:

$$\begin{aligned} |\psi_{\text{in}}\rangle &= \frac{1}{\sqrt{2}}(|p,-p\rangle + |q,-q\rangle) \\ &= \frac{1}{\sqrt{2}}\left[\begin{pmatrix}1\\0\end{pmatrix}_A \otimes \begin{pmatrix}0\\1\end{pmatrix}_B + \begin{pmatrix}0\\1\end{pmatrix}_A \otimes \begin{pmatrix}1\\0\end{pmatrix}_B\right] \end{aligned} \tag{5.22}$$

When the momentum difference with the HOM doublet $\Delta p = p - p_0 = p_0 - q$ equals zero, the previous expression becomes

$$\begin{aligned} |\psi_{\text{in}}\rangle &= \frac{1}{\sqrt{2}}(|p_0,-p_0\rangle + |p_0,-p_0\rangle) \\ &= \frac{1}{\sqrt{2}}\left[\begin{pmatrix}1\\0\end{pmatrix} \otimes \begin{pmatrix}0\\1\end{pmatrix} + \begin{pmatrix}0\\1\end{pmatrix} \otimes \begin{pmatrix}1\\0\end{pmatrix}\right] \end{aligned} \tag{5.23}$$

There is no phase term ϕ_0 between the two pairs of the quadruplet since they consist in the same momentum pair. However, the two terms are not the same, as shown in the second equality, because the state is symmetrized. At resonance, there is no longer a distinction between doublet A and doublet B, both being subject to the same propagation matrix, but, the state is symmetrized since, in one term, particle 1 is in mode $-p_0$ and particle 2 is in mode p_0, and vice versa in the other term.

This state is actually the initial state 5.4 that we used to describe the HOM effect in the previous section. For $\phi_0 = 0$, this formalism allows us to go continuously from HOM to Bell as Δp increases.

We can then use the previous formalism to simulate an HOM experiment, by taking into account the off-resonant terms due to the interaction with light. It has been demonstrated that, regardless of the value of T_2, at resonance, the joint probability $\mathcal{P}_{+-}$ of detecting two atoms in two different modes will always be zero. However, in a real experiment, one does not selectively choose the resonant class with Bragg pulses with infinite precision: the signal is always integrated over a certain integration volume, which includes some values of momentum that are not strictly resonant. Therefore, for a fixed value of T_2, we can

compute the average value $\tilde{\mathcal{P}}_{+-}$ of $\mathcal{P}_{+-}$ within a velocity range Δv_0 centered on resonance and of the size of a mode. We take $\Delta v_0 = 2.5\,\mathrm{mm.s^{-1}}$, which is the size of a mode at the time of the 2016 HOM experiment (the optical dipole trap was less elongated at that time than it is nowadays). The graph of $\tilde{\mathcal{P}}_{+-}$ as a function of T_2, given in Figure 5.3, then simulates the HOM experiment.

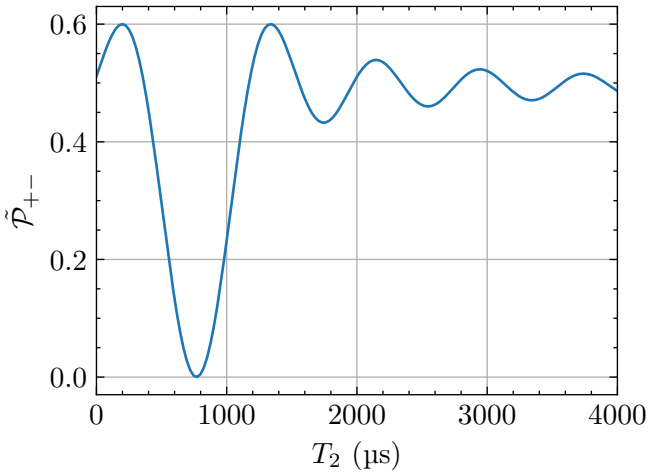

Figure 5.3: Simulation of the HOM experiment with plane waves. The input state is symmetrized to describe two indistinguishable particles. We calculate, for a given delay of the HOM beam splitter, the joint probability of measuring an atom in each output mode $\mathcal{P}_{+-} = \mathcal{P}(p,-q) + \mathcal{P}(q,-p)$ as a function of the velocity class using $\delta = -k_\mathrm{B}\Delta v$, and average it over a velocity box of width $\Delta = 2.5\,\mathrm{mms^{-1}}$, centered on resonance, to get $\tilde{\mathcal{P}}_{+-}$. The duration of the first free propagation is $T_1 = 800\,\mu\mathrm{s}$, and the two-photon Rabi frequency of each pulse is $\Omega_\mathrm{M} = 5\,\mathrm{kHz}$.

The results clearly show the emergence of an HOM dip for a certain value of T_2. We still find $\tilde{\mathcal{P}}_{+-} \approx 0$ for a given delay because when averaging the value of $\mathcal{P}_{+-}$ over a velocity range where the detuning does not vary too much, the average value of $\mathcal{P}_{+-}$ is approximately equal to its value at resonance, i.e., zero. On the other hand, for others values of T_2, if the detuning varies significantly within the integration volume, the average probability value is 0.5, and no HOM effect is observed. This occurs when the interferometer is not closed, meaning the phase terms due to the wave packets propagation induce a phase shift that strongly depends on the momentum class. The width of the HOM dip thus depends on the integration range: the smaller the integration range for pulse measurement, the larger the width of the dip.

Figure 5.4 shows that the interferometer is closed for $T_2 = 768\,\mu\mathrm{s}$. This result can be corroborated using the expression determined for the Bell phase, as we showed that it involves determining the value of T_2 for which Φ does not depend on δ. We have:

$$\Phi = 2\tan^{-1}\left[\frac{\delta}{\sqrt{\Omega^2+\delta^2}}\tan\left(\sqrt{\Omega^2+\delta^2}\frac{T_\mathrm{S}}{2}\right)\right] + 2\delta(T_2 - T_1) + \phi_0(\delta) \tag{5.24}$$

This result is valid only within a limited range of detuning, for which we can consider the mirror transmission coefficient to be zero. Therefore, we can expand the result in the limit where the detuning tends towards zero, especially for $\delta \ll \Omega$. We find, for the phase,

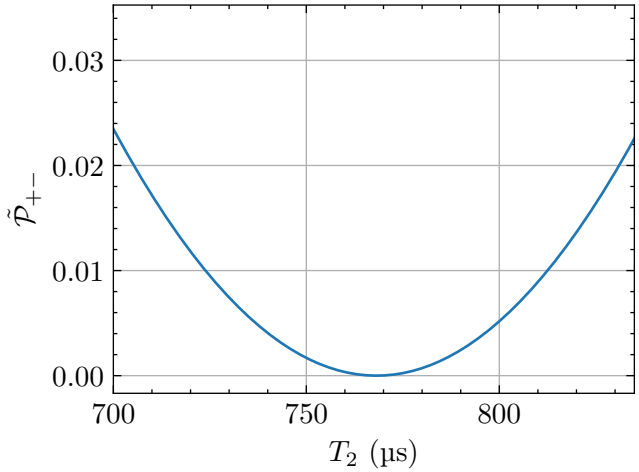

Figure 5.4: Simulation of the HOM experiment with plane waves. This is the same calculation as 5.3, plotted over a smaller beam splitter delay range.

using the fact that $\Omega T_\mathrm{S} = \pi/2$ (for a $\pi/2$ pulse):

$$\Phi \approx 2\frac{\delta}{\Omega} + 2\delta(T_2 - T_1) + \phi_0(\delta) = 2\delta\left(T_2 - T_1 + \frac{2T_\mathrm{S}}{\pi}\right) + \phi_0(\delta) \tag{5.25}$$

At first order, if we omit the phase term $\phi_0(\delta)$ associated with the pair source, the Bell phase varies linearly with the detuning, and the slope is proportional to a term which depends on the closure of the interferometer. In the vicinity of the resonance, we have $\phi_0(\delta) = 0$ since over the momentum range of one mode there is only the doublet $|p_0, -p_0\rangle$ which is considered. The relationship 5.25 determines the closure of the HOM interferometer when accounting for the phase shifts due to the interaction of atoms with light. We conclude that the interferometer is closed when

$$T_2 = T_1 - \frac{2T_\mathrm{S}}{\pi} \tag{5.26}$$

and we recover $T_2 = 768\,\mu\mathrm{s}$.

It is interesting to note that in this case,

$$\frac{T_\mathrm{M}}{2} + T_2 + \frac{T_\mathrm{S}}{2} = T_1 + T_\mathrm{M}\left(\frac{3}{4} - \frac{1}{\pi}\right) \approx T_1 + 0.43\,T_\mathrm{M} \tag{5.27}$$

which means that the duration between the middle of the beam splitter pulse and the middle of the mirror pulse ($T_\mathrm{M}/2 + T_2 + T_\mathrm{S}/2$) is not far from the duration between the start of the interferometer and the middle of the mirror pulse ($T_1 + T_\mathrm{M}/2$), as it is often commonly represented.

The results from this section show that, when the interferometer is closed (for T_2 in the HOM dip), the Bell phase at the vicinity of the resonance does not vary with detuning, which can be translated by

$$\frac{\mathrm{d}\Phi}{\mathrm{d}\delta}(\delta = 0) = 0 \tag{5.28}$$

We can use the closure condition 5.26 to look at what happens out of resonance when the interferometer is closed. We find the results shown in Figure 5.5, to be compared to

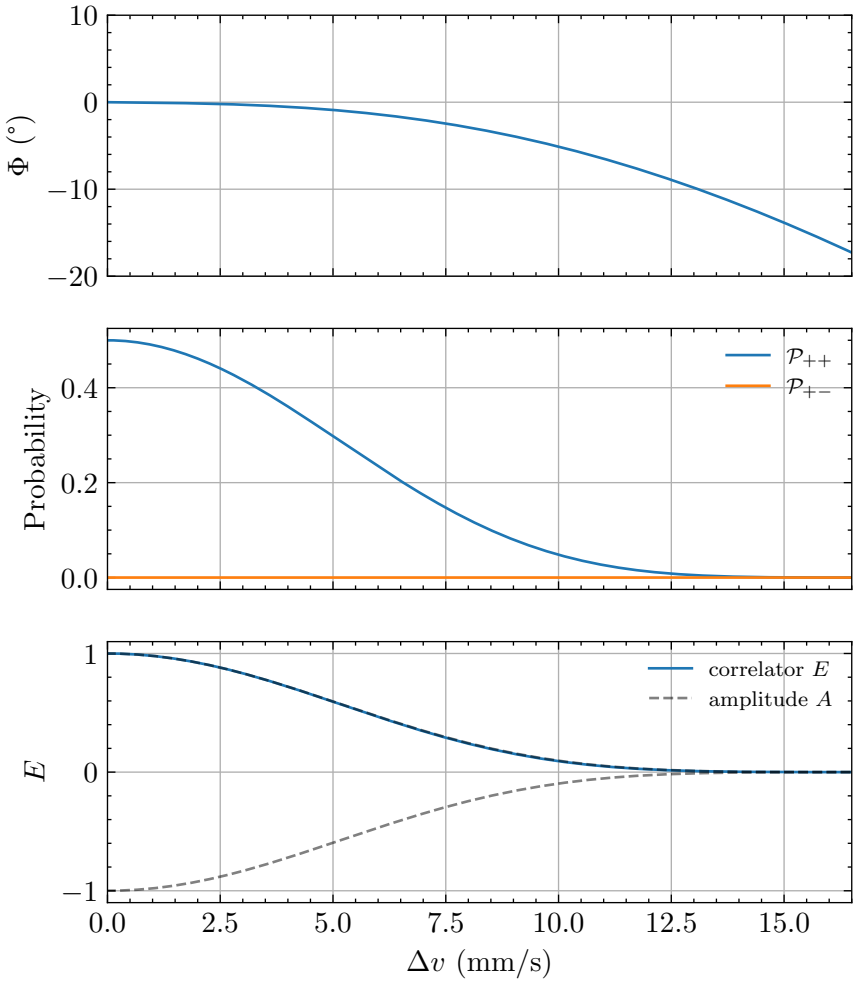

Figure 5.5: Analytical solution of the Bell interferometer for square pulses. The atoms transmitted by the mirror are not taken into account. We calculate the Bell phase Φ that appears in the Bell correlator, the joint probabilities $\mathcal{P}_{++} = \mathcal{P}(p,q) + \mathcal{P}(-p,-q)$ and $\mathcal{P}_{+-} = \mathcal{P}(p,-q) + \mathcal{P}(q,-p)$, and the Bell correlator E. Each value corresponds to the analytical solution at a fixed detuning, and the results are plotted as a function of the velocity class Δv using $\delta = -k_\mathrm{B}\Delta v$. The phase ϕ_0 between the pairs is supposed to be zero. The two-photon Rabi frequency of each pulse is $\Omega_\mathrm{M} = 5\,\mathrm{kHz}$, the duration of the first free propagation is $T_1 = 800\,\mu\mathrm{s}$, and the duration of the second free propagation is determined by the closure relation 5.26 such that $T_2 = 768\,\mu\mathrm{s}$.

Figure 5.2.

As expected, the tangent to the phase curve Φ at zero is zero because the interferometer is closed. As one moves away from resonance, the phase varies, but not rapidly enough for the variation to be significant in the velocity range where the correlator oscillation amplitude is non-zero. Therefore, without making a substantial error, one can consider that when the phase around resonance does not vary with detuning, the same holds true outside of resonance in the range of interest.

Thus, any observed variation of the Bell correlator as a function of the velocity class (for a closed interferometer) is either due to a decrease in signal amplitude or to the presence of a phase shift ϕ_0 that depends on the quadruplet used for the Bell calculation (only

the resonant "quadruplet" has $\phi_0 = 0$ since it is actually the $(p_0, -p_0)$ doublet that is used for HOM).

Note that the simulations of this section are incomplete for two main reasons, related to treating the atoms as plane waves. Firstly, spatial aspects, especially the effects of light on the center of mass, are neglected here. But we showed that the Bell phase depends on the center of mass when the interferometer is not closed. Therefore, additional phase shifts would need to be considered to calculate the true T_2 value where the wave packets overlap. Secondly, this model does not account for the coherence length of the source, which also affects the width of the HOM dip (this was actually the point of the historic Hong, Ou, and Mandel experiment[36]). The width of the HOM dip determined in our calculation is an ideal width assuming an infinite coherence length of the source. Nevertheless, this would not change our conclusions regarding the timing at which the interferometer is closed.

5.1.3 Numerical simulation

So far, we assumed that the mirror's transmission coefficient was strictly zero, regardless of the detuning. This strong assumption simplifies the expression of the phase involved in the Bell interferometer. However, it is also possible to express the Bragg transfer matrix associated with the mirror without forcing the diagonal terms to be zero. More generally, it is possible to numerically solve the Bragg coupling system 4.60, not only for a constant pulse but also for any temporal pulse shape. In this section, we will numerically calculate the output state of the interferometer and then the Bell correlator for a constant pulse, without neglecting the losses due to the imperfect reflectivity of the mirror pulse. Again, the spatial effects related to the center of mass of the wave packets are not taken into account.

Thus, for each Bragg doublet, we numerically solve the following system:

$$\begin{pmatrix} \dot{C}_0 \\ \dot{C}_2 \end{pmatrix} = \mathrm{i} \begin{pmatrix} \mathrm{e}^{-\mathrm{i}\omega_0 t} & \frac{\Omega_\mathrm{R}(t)}{2}\mathrm{e}^{\mathrm{i}\delta_0 t}\mathrm{e}^{-\mathrm{i}\omega_0 t} \\ \frac{\Omega_\mathrm{R}^*(t)}{2}\mathrm{e}^{-\mathrm{i}\delta_0 t}\mathrm{e}^{-\mathrm{i}\omega_2 t} & \mathrm{e}^{-\mathrm{i}\omega_2 t} \end{pmatrix} \begin{pmatrix} C_0 \\ C_2 \end{pmatrix} \tag{5.29}$$

which is the Bragg coupling system with propagation phases $\mathrm{e}^{\mathrm{i}\omega t}$. The two-photon Rabi frequency $\Omega_\mathrm{R}(t)$ is equal to zero during free propagation steps, and is constant and equal to 5 kHz otherwise. For doublet A, we have

$$\begin{cases} \delta_0 = \delta \\ \omega_0 = \omega_{-p} \\ \omega_2 = \omega_q \end{cases} \tag{5.30}$$

while for doublet B,

$$\begin{cases} \delta_0 = -\delta \\ \omega_0 = \omega_{-q} \\ \omega_2 = \omega_p \end{cases} \tag{5.31}$$

The input state is given by 5.22 with $\phi_0 = 0$. Note that a first step consists in solving equation 5.29 step by step by setting the mirror's transmission coefficient to zero, in order to verify that this numerical solution coincided with the analytical results. The numerical results are plotted in Figure 5.6 for $T_1 = 800\,\mu\mathrm{s}$ and T_2 satisfying the relation 5.26.

We can be observe that, unlike the case where there are no transmitted atoms, the probabilities (and consequently the correlator) start oscillating as one moves away from

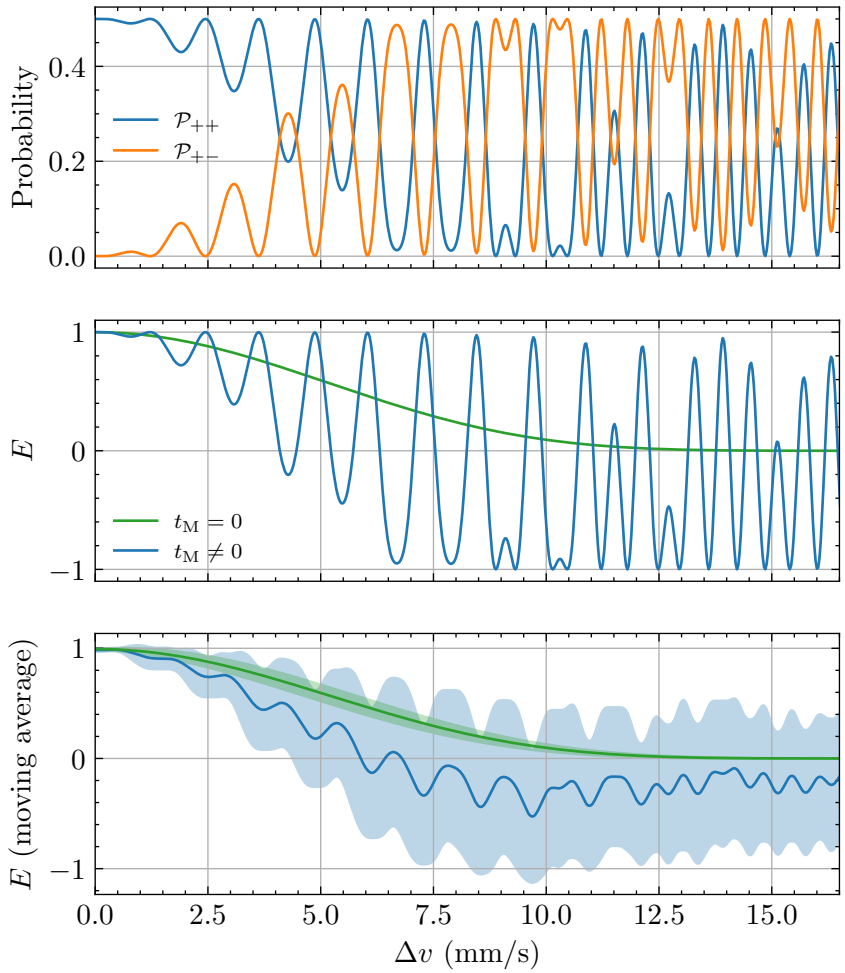

Figure 5.6: Numerical solution of the Bell interferometer for square pulses. The parameters are the same as Figure 5.5, except that the atoms transmitted by the mirror are taken into account. Top: Joint detection probabilities $\mathcal{P}_{++} = \mathcal{P}(p,q) + \mathcal{P}(-p,-q)$ and $\mathcal{P}_{+-} = \mathcal{P}(p,-q) + \mathcal{P}(q,-p)$. Middle: Bell correlator as a function of velocity class, numerically calculated taking into account atoms transmitted by the mirror ($t_M \neq 0$, in blue) and without taking them into account ($t_M = 0$ in green). The transmitted atoms interfere with the reflected atoms, leading to oscillations of the Bell correlator, with amplitudes increasing away from resonance. Bottom: Moving average of the correlator E, calculated by averaging over a velocity integration box of $2\,\mathrm{mm.s^{-1}}$, taking into account the transmitted atoms (in blue) and without considering them (in green). The shaded areas are error bars representing the standard deviation of the correlator in the considered box.

resonance. This can be explained by the fact that the atoms transmitted by the mirror will interfere with the atoms of the same momentum, resulting in a blurring of the Bell-type interference. Indeed, this interference occurs between wave packets with imperfect overlap: this interferometer is not closed, leading to a significant dependence on detuning of the added phase, hence a substantial oscillation of the correlator.

The importance of having good reflectivity, especially from the mirror, is evident: as soon as atoms are transmitted, parasitic interferences with the transmitted atoms can occur (Figure 5.7).

Experimentally, it is not possible to filter out these atoms, as they fall almost simultaneously with the atoms in the same momentum mode on the MCP. Thus, the signal received by the detector corresponds to the average over a certain integration volume of

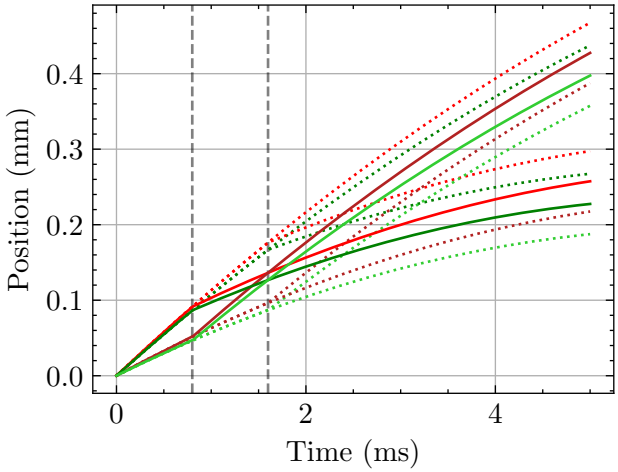

Figure 5.7: Atom trajectories in an imperfect interferometer, taking into account atom leakage through the mirror. Representation in the laboratory frame. Solid lines represent the trajectories of off-resonant atoms in the HOM interferometer, while dotted lines correspond to the trajectories of atoms transmitted by the mirror, and possibly reflected again by the beam splitter. These atoms form spurious interferences with the atoms that contribute to the observation of Bell correlations, resulting in the appearance of fringes in the correlator. We consider a HOM doublet at speeds $65\,\mathrm{mm.s^{-1}}$ and $115\,\mathrm{mm.s^{-1}}$ in the laboratory frame, and a Bell quadruplet with a velocity difference of $\pm 3\,\mathrm{mm.s^{-1}}$ relative to the HOM doublet. The typical free propagation time is $800\,\mu\mathrm{s}$ and Bragg pulses are considered to be infinitely thin.

the correlator. This is why the moving average of the correlator over a box of $2.0\,\mathrm{mm.s^{-1}}$ has also been plotted in Figure 5.6, in the ideal case without transmitted atoms (in green) and with transmitted atoms (in blue). The shaded area represents the standard deviation of the correlator in the box centered on the corresponding abscissa. It can be seen that the amplitude of the Bell signal decreases more rapidly and with a larger standard deviation when transmitted atoms are taken into account.

5.1.4 Discussion of previous results

We can now comment on the results obtained from the study of the 2016 HOM experiment. Measurements off-resonance were conducted on three quadruplets, integrated over a box of 2.0 $\mathrm{mm.s^{-1}}$, centered on $\Delta v = 2$, 4, and 6 $\mathrm{mm.s^{-1}}$, respectively. The joint detection probabilities were also plotted, to make sure that they vary simultaneously two by two. The results are given in Figure 5.8 as dots.

We observe a significant variation in the correlator across the three analyzed quadruplets. Additionally, the values of the joint detection probabilities have been plotted, revealing similar variations two by two, as expected. This ensures that the correlator variations are not due to measurement noise, which would result in random values for the probabilities. Each measurement point corresponds to 2218 repetitions of the experiment. On the same plot, we have included, for reference, the moving average of the correlator and of the joint probabilities (for a closed interferometer) integrated over a 2mm/s box, with a constant ϕ_0 value set at 107°, so that the average of the correlator and joint probabilities align with the measurement points for the box closest to resonance.

It is observed that assuming a constant ϕ_0, the model for the correlator varies relatively slowly with the velocity class, even when accounting for transmitted atoms. This fails to

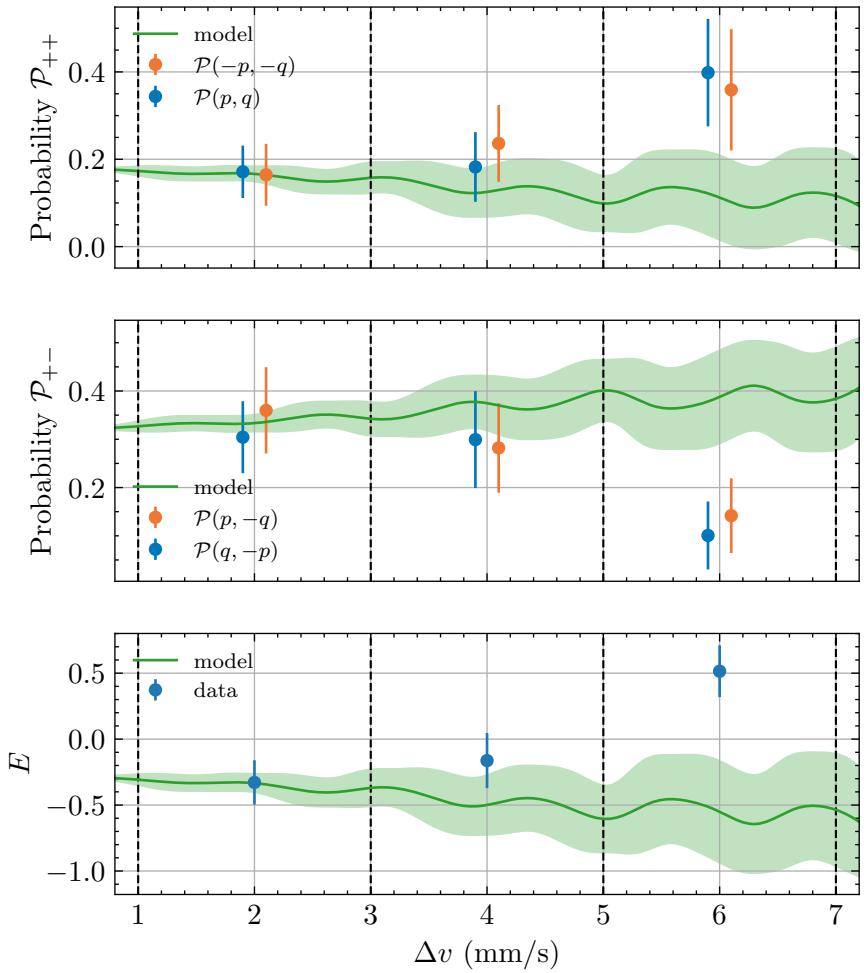

Figure 5.8: Joint probabilities and Bell correlator as a function of the velocity class, averaged over a velocity box of $2\,\mathrm{mm.s^{-1}}$. The experimental results are given as blue and orange dots, while the simulation results are represented in green solid lines. The green shaded areas represent the standard deviation of the corresponding computed quantity (probability or correlator) within the integration volume. The value of the calculation parameter ϕ_0, assumed to be constant for all velocity classes, is adjusted in order to fit the experimental results from the first experimental quadruplet considered, centered on $\Delta v = 2\,\mathrm{mm.s^{-1}}$. The significant deviation between the experimental data and the computed correlator suggests that a phase shift not considered in the calculation may be responsible for the variation of the Bell correlations observed experimentally.

explain the significant variations observed experimentally. The only plausible explanation is to consider that the phase ϕ_0 depends on the specific momentum quadruplet under consideration. This would introduce an offset to the correlator from one quadruplet to another, providing an explanation for the observed variations in E.

For the quadruplet centered on $\Delta v = 6\,\mathrm{mm.s^{-1}}$, the measured value of the correlator is 0.51 ± 0.20, providing hope for the future observation of a correlator oscillation (once the control of the phase imprinted on the atoms is achieved) with a significant amplitude. Even if a correlator amplitude greater than 0.71 is required to demonstrate a violation of the Bell inequality, exhibiting an oscillation of the Bell correlator would be a promising first step.

The main problem in this measurement using HOM data lies in the inability to control

the phase imprinted on the atoms, making it impossible to vary it to observe a Bell correlator oscillation. Nevertheless, the previously obtained results by the team are promising and allow us to assert that it is possible to achieve a non-zero Bell correlator for a given momentum quadruplet.

In the next section, we will present the strategy devised to carry out a genuine Bell test by controlling the relative phase imprinted on A and B.

5.2 Bell phase control

As mentioned earlier, we aim to use the fact that doublets A and B of the Bell interferometer do not have the same resonance frequency to control the imprinted phase. In this section, we will show that this can be done by modulating the two-photon Rabi frequency. We will first theoretically analyze the desired pulse shape and then discuss its experimental implementation.

5.2.1 Principle: two-frequency pulses

Since doublets A and B do not share the same Bragg resonance frequency, the idea is to send a two-frequency Bragg beam splitter pulse on the atoms. Let us consider the following pulse:

$$\Omega_{\mathrm{R}}(t) = \Omega_{\mathrm{M}} \mathrm{e}^{\mathrm{i}\Delta\varphi} \left(\mathrm{e}^{\frac{\mathrm{i}\Omega_{\mathrm{D}} t}{2}} + \mathrm{e}^{-\frac{\mathrm{i}\Omega_{\mathrm{D}} t}{2}} \right) \tag{5.32}$$

where Ω_{M} is the amplitude of the two-photon Rabi frequency, and $\Delta\varphi = \varphi_2 - \varphi_1$ is the phase difference between the lasers, assumed to be constant during the pulse, whose duration is noted T. The two additional terms make it possible to shift the resonance condition by $\pm\Omega_{\mathrm{D}}/2$.

In a first approximation, it can be considered that this pulse is equivalent to two independent pulses: the left term has a resonance shifted by $-\Omega_{\mathrm{D}}/2$ while the right term has a resonance shifted by $+\Omega_{\mathrm{D}}/2$. This can be easily understood by injecting one of these terms in the two-level Bragg system 4.60:

$$\begin{pmatrix} \dot{C}_0 \\ \dot{C}_2 \end{pmatrix} = \frac{\mathrm{i}}{2} \begin{pmatrix} 0 & \Omega_{\mathrm{M}} \mathrm{e}^{\mathrm{i}\Delta\varphi} \mathrm{e}^{\mathrm{i}\left(\delta_0 + \frac{\Omega_{\mathrm{D}}}{2}\right)t} \\ \Omega_{\mathrm{M}} \mathrm{e}^{-\mathrm{i}\Delta\varphi} \mathrm{e}^{-\mathrm{i}\left(\delta_0 + \frac{\Omega_{\mathrm{D}}}{2}\right)t} & 0 \end{pmatrix} \begin{pmatrix} C_0 \\ C_2 \end{pmatrix} \tag{5.33}$$

This expression, which is valid for a two-photon Rabi frequency $\Omega_{\mathrm{R}}(t) = \Omega_{\mathrm{M}} \mathrm{e}^{\mathrm{i}\Delta\varphi} \mathrm{e}^{\frac{\mathrm{i}\Omega_{\mathrm{D}} t}{2}}$, can be analytically solved with a variable change indicating a resonance frequency shift. However, when summing two such pulses, the system cannot be analytically resolved anymore because the pulse depends non-trivially on time. Nevertheless, the system can be solved numerically, giving, for example, a plot of the reflection coefficient associated with this pulse.

We consider a two-frequency pulse with a two-photon Rabi frequency amplitude of $\Omega_{\mathrm{M}} = 1\,\mathrm{kHz}$. The pulse duration is $T = \pi/2\Omega_{\mathrm{M}} = 250\,\mu\mathrm{s}$. The Bragg coupling system from equation 4.60 was solved numerically using $C_0(0) = 1$ and $C_2(0) = 0$. In Figure 5.9, the reflectivity profiles (i.e., $|C_2(T)|^2$) are plotted against the detuning for various values of Ω_{D}.

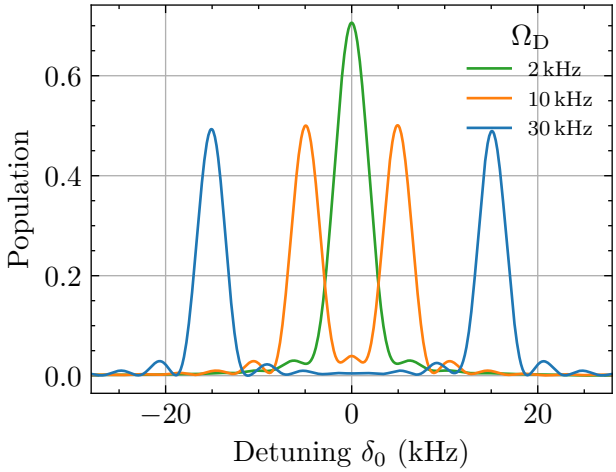

Figure 5.9: Bragg reflectivity profiles as a function of the detuning for two-frequency Bragg beam splitters. $|C_2|^2$ is plotted for several values of Ω_D. The bragg system 4.60 is solved with $C_0(0) = 1$ and $C_2(0) = 0$ as initial conditions, for a Rabi frequency $\Omega_M = 1\,\text{kHz}$.

It can be observed that when Ω_D is significantly larger than Ω_M, there are two distinct reflectivity peaks, corresponding to two well-defined beam splitters with resonances effectively shifted by $\pm\Omega_D/2$. The reflectivity profile of each beam splitter has a sinc^2 shape, similar to that of a single pulse. In this case, the two-frequency pulse is equivalent to implementing two independent beam splitters. As Ω_D decreases, the peaks approach each other until partial and then complete overlap occurs, making them indistinguishable. The resonant reflectivity is then different from 0.5, due to some interference between the two beam splitters. This situation with two overlapped pulses is not suitable for implementing a two-frequency Bell pulse, where the goal is to achieve two independent beam splitters.

Now, let us suppose that we are in the case where Ω_D is much larger than Ω_M , allowing us to consider the two beam splitters as independent. We introduce a different phase for each resonance so that the two-photon Rabi frequency is given by:

$$\Omega_R(t) = \Omega_M e^{i\Delta\varphi}\left(e^{i\left(\frac{\Omega_D t}{2}+\frac{\theta}{2}\right)} + e^{-i\left(\frac{\Omega_D t}{2}+\frac{\theta}{2}\right)}\right) \tag{5.34}$$

As seen previously, for a single-frequency square pulse, the phase imprinted on the resonant atoms is equal to the phase difference $\Delta\varphi$ between the lasers. Adding these additional terms, we see that it is possible to imprint a phase $\Delta\varphi + \theta/2$ for the doublet resonating at $-\Omega_D/2$ (left term) and a phase of $\Delta\varphi - \theta/2$ for the doublet resonating at $+\Omega_D/2$ (right term).

Thus, if we choose Ω_D so that the two resonant doublets are the doublets A and B involved in the Bell interferometer, we can imprint a different phase on doublets A and B, such that, at resonance, the Bell phase is:

$$\Phi = \phi_A - \phi_B + \phi_0 = \Delta\varphi + \frac{\theta}{2} - (\Delta\varphi - \frac{\theta}{2}) + \phi_0 = \theta + \phi_0 \tag{5.35}$$

Therefore, in principle, at resonance, we may be able to control the phase difference between A and B that plays a role in the Bell correlator, allowing us to observe an oscillation. If the amplitude of this oscillation is large enough, it could lead to the violation of

Bell's inequality predicted by quantum mechanics.

The importance of studying what happens for non-resonant velocity classes has been emphasized multiple times. This is particularly crucial because, during an experiment, we will average the signal over a certain range of momentum. In the following, we will determine the specific parameters to be employed for the Bragg beam splitter and plot reflectivity and phase profiles as functions of the detuning.

5.2.2 Experimental implementation

Now, arises the question arises of how to implement these two-frequency pulses. The basic experimental setup for realizing a two-photon Bragg transition involves an initial laser beam split into two to form Bragg beams 1 and 2 (Figure 5.10). Each beam is prepared with the appropriate power and polarization. The frequency of each beam is controlled using an acousto-optic modulator, to which an RF signal of frequency ω_i is applied. This signal shifts the frequency of the light wave through the diffraction of light by acoustic waves. The phase of the RF signal determines the phase of the light beam used for the Bragg transition. The beams are then mixed spatially with a different polarization before being separated again while being sent to the atoms with different angles.

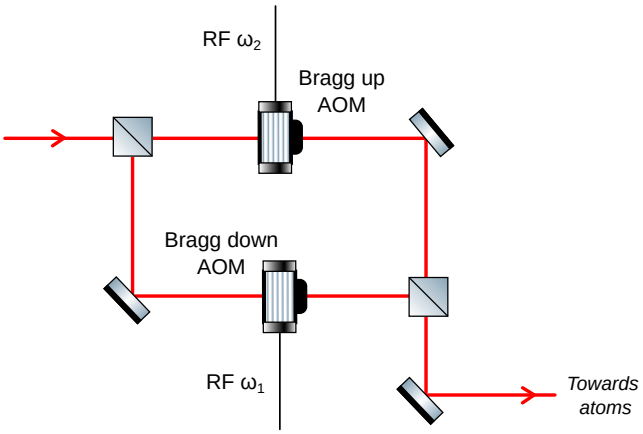

Figure 5.10: Experimental setup for a two-photon transition. A laser beam is split into two by a beam splitter. Each beam passes through an acousto-optic modulator, which allows, using an RF signal, control over the laser frequency and power. The beams are then recombined on a second beam splitter before being sent to the atoms.

Three ways of implementing two-frequency Bragg pulses were investigated in our team over the years. Here, we will provide only a brief introduction to the first two, which are discussed in more detail in the respective theses of M. Perrier[104] and A. Imanaliev[147] .

- The Bragg resonance frequency is determined by the δ_0. To select a specific momentum class, a given frequency difference $\omega_1 - \omega_2$ between lasers is required. Thus, the first idea for implementing a two-frequency Bragg pulse involves splitting the initial beam into three parts and using not two but three acousto-optic modulators: one with a frequency ω_1 and the other two with frequencies $\omega_{2A} = \omega_2 - \Omega_D/2$ and $\omega_{2B} = \omega_2 + \Omega_D/2$, respectively (Figure 5.11). This way, by recombining beams A and B, one can obtain light comprising two distinct resonance frequencies.

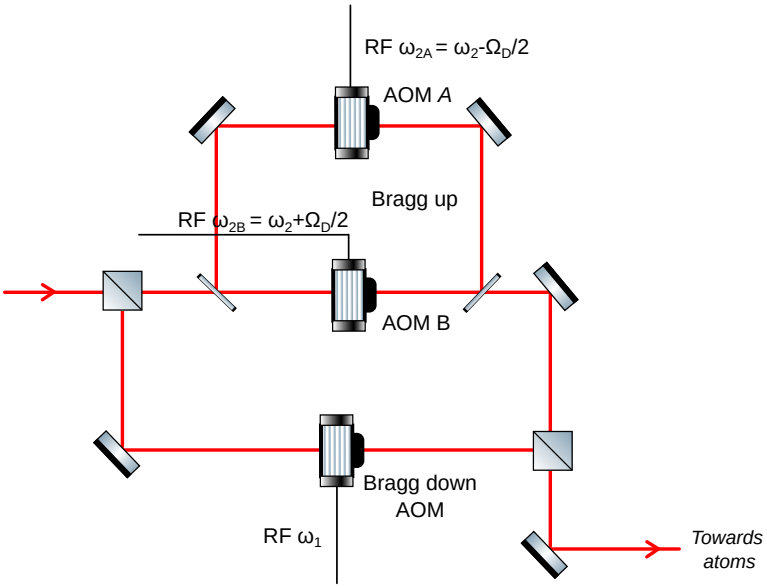

Figure 5.11: First experimental solution to implement two-frequency Bragg pulses. One of the two Bragg beams is itself split into two beams, going each through an acousto-optic modulator, whose frequency is tuned so that a portion of the light is resonant with doublet A while another portion is resonant with doublet B.

Although this solution enables the emission of two-frequency pulses, its main drawback lies in the fact that, since two different beams and two different acousto-optic modulators are used for doublet A and doublet B, the phase difference imprinted on the lasers will not be the same. As $\Delta\varphi_A$ and $\Delta\varphi_B$ are distinct, these two terms must be taken into account in the Bell phase. It is still possible to ensure $\Delta\varphi_A = \Delta\varphi_B$ by using the same RF source with an adjustable relative phase, or by adding a phase locking procedure, but this approach remains restrictive as it is sensitive to phase fluctuations and vibrations that occur when beams A and B are separate.

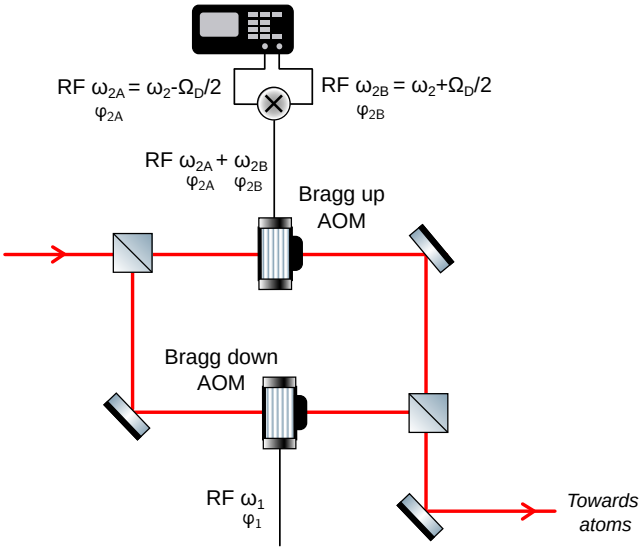

Figure 5.12: Second experimental solution to implement two-frequency Bragg pulses. Only two acousto-optic modulators are used, but one of them receives a two-frequency RF signal.

- The second possibility involves mixing two RF signals at different frequencies and phases, sending the combined signal into a single acousto-optic modulator (Figure 5.12). This AOM would then exhibit two resonance frequencies, each resonant with a doublet. This technique enables the generation of a two-frequency pulse. To control the phase imprinted on each loop of the interferometer, it is necessary for both signals to originate from the same RF source with an adjustable relative phase between the two output channels.

  This technique was implemented in the experiment and yielded initial promising results[147]. However, despite this, the solution was not chosen at the time because the AOM used operated in a double-pass configuration, resulting in a more complex frequency spectrum on the atoms, i.e., a crosstalk phenomenon that could degrade signal quality. Transitioning to a single-pass configuration provided an opportunity to explore the third possibility for implementing the Bragg two-frequency beam splitter, an option that was chosen and will be presented in the following sections of this manuscript.

The third possibility consists in noticing that implementing two-frequency pulses is equivalent to performing amplitude modulation of a constant pulse. Indeed, the expression 5.34 of the two-photon Rabi frequency we aim to realize can be written in the following form:

$$\Omega_{\mathrm{R}}(t) = 2\,\Omega_{\mathrm{M}} \mathrm{e}^{\mathrm{i}\Delta\varphi} \cos\left(\frac{\Omega_{\mathrm{D}} t}{2} + \frac{\theta}{2}\right) \tag{5.36}$$

As we can see, it would be sufficient to multiply a constant pulse with a Rabi frequency Ω_{M}, and a phase difference between the lasers $\Delta\varphi$, by a periodic signal with a frequency $\Omega_{\mathrm{D}}/2$ and an initial phase $\theta/2$. This can be implemented experimentally if two essential elements are put in place. Firstly, it is necessary to control the power emitted by the acousto-optic modulators to give the Rabi frequency (proportional to light intensity) the desired sinusoidal shape. Secondly, we need to add π phase shifts between the two lasers phases whenever the modulation signal is negative.

- Regarding the power control, it is possible to control the optical power at the output of an acousto-optic modulator by adjusting the amplitude of the RF signal sent to the AOM. Nevertheless, the relationship between the amplitude of the electrical signal and the diffracted optical power is not linear. Therefore, it is preferable to implement a feedback control system rather than an open-loop control.

  This requires generating a reference signal with the desired shape (which can be achieved with a computer-controllable signal generator), extracting a portion of the optical power (using a beam sampler, for example), and providing feedback on the signal sent to the AOM with a Proportional-Integral (PI) controller. The performance of the PI controller must be sufficient to ensure that the power follows well the setpoint signal.

  Of course, the required PI controller bandwidth depends on the modulation frequency and the chosen duration of the Bragg pulses, which will be determined in the following. Typically, a bandwidth of a few hundred of kHz would be sufficient in our range of applications. This bandwidth is accessible in the laboratory thanks to the PID controllers developed by the electronics workshop of the Laboratoire Charles Fabry.

To ensure that the light intensity on the atoms has the correct shape, it is necessary to modulate the power of both beams. Instead of implementing two separate feedback controls on each arm, we can do it on an upstream acousto-optic modulator, before the separation of the two Bragg beams, which we use to control the total power allocated to the Bragg and Raman beams (the Raman beams originate from the same laser and are separated beforehand). Therefore, a power feedback control system on this AOM is sufficient to control the shape of the absolute value of the two-photon Rabi frequency.

- Regarding the phase control, assuming that the phase difference $\Delta\varphi$ remains constant during the duration of a pulse, an electronic component called a phase shifter can be used to add π phase shifts. This device, given an input RF signal, produces an output signal with a certain phase shift determined by a set voltage.

  This phase shifter can be placed on one of the two RF signals sent to a Bragg AOM. The idea is to generate a set voltage synchronized with the power setpoint to ensure that π phase shifts occur when the two-photon Rabi frequency should be negative (Figure 5.13). Similarly, the response bandwidth of the phase shifter must be greater than a few kHz to make sure that when the phase setpoint is varied, a π phase jump occurs.

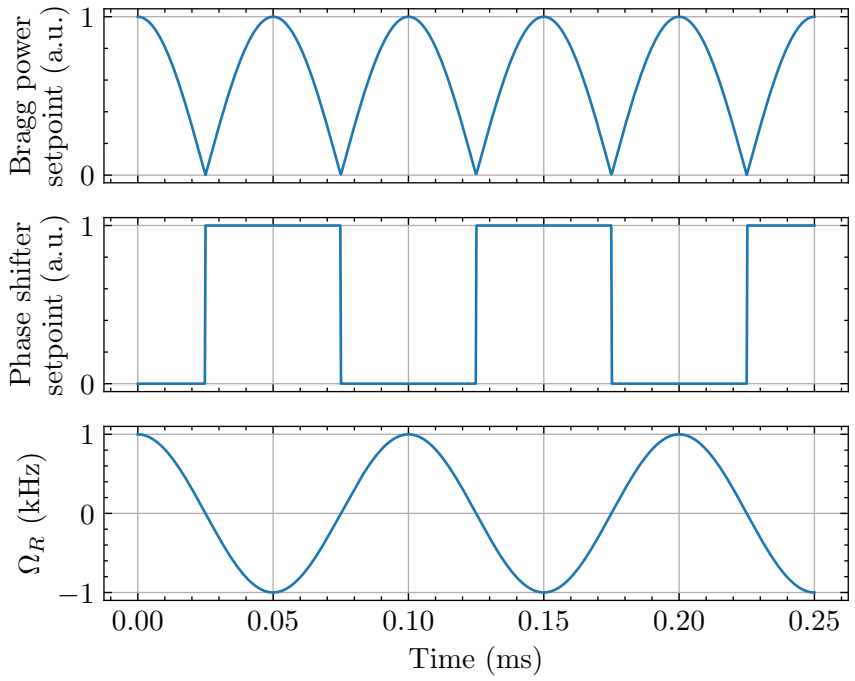

Figure 5.13: Voltage setpoints and two-photon Rabi frequency for a modulated Bragg pulse. The Bragg power setpoint, combined with π phase shifts, makes it possible to have a negative two-photon Rabi frequency, so that the modulated Bragg pulse is resonant with two velocity classes. The phase shifter setpoint is calibrated such that the phase shifter adds a π phase shift in the RF signal of a Bragg AOM whenever the two-photon Rabi frequency must be negative.

Then, we can shape the two-photon Rabi frequency so that we have:

$$\Omega_{\mathrm{R}}(t) = 2\,\Omega_{\mathrm{M}} \mathrm{e}^{\mathrm{i}[\varphi_2 - \varphi_1 + \mathrm{sgn}(\Omega_{\mathrm{R}}(t))]} \left| \cos\left(\frac{\Omega_{\mathrm{D}} t}{2} + \frac{\theta}{2}\right) \right| \tag{5.37}$$

where $\mathrm{sgn}(\Omega_\mathrm{R}(t))$ is a function that equals zero when $\Omega_\mathrm{R}(t)$ is positive and π when $\Omega_\mathrm{R}(t)$ is negative. This is the expression 5.34 of the two-photon Rabi frequency that selectively imprints a phase $\pm\theta/2$ depending on the resonant doublet. Thus, experimentally, to vary the Bell phase, it will be sufficient to vary the phase at the origin of this modulation function.

It is important to note that with this technique, we do not precisely control the absolute phase imprinted on each doublet but rather the phase difference imprinted between these two doublets. Indeed, the phase imprinted on doublet A, for example, is given by $\phi_A = \varphi_2 - \varphi_1 + \theta/2$.

While θ is a fully tunable parameter, $\varphi_2 - \varphi_1$ is a parameter to which we do not have direct access. This does not pose a problem for observing oscillations in the Bell correlator since this term does not come into play. However, to claim that a rigorous Bell test is conducted, one must be able to independently control ϕ_A *and* ϕ_B, which, in our case, vary jointly with $\varphi_2 - \varphi_1$.

A stronger version of the Bell test, incorporating independent control of φ_A and φ_B, is currently under investigation in our team. Such a project requires phase control between the two lasers, which is not necessary in our weaker version. One idea involves observing the two beams beating and locking this signal to a set value to fix the value of $\varphi_2 - \varphi_1$, enabling control of φ_A and φ_B at will. Since the frequency of the two beams varies during the Bragg pulses (due to the frequency sweep which compensates for gravity), it would be necessary to lock the beat *before* the pulse emission and release the lock at the moment of the pulse, relying on the assumption that the phase does not vary on the timescale of the interferometer. We will describe in Chapter 6 experiments showing that this assumption is well verified.

Let us conclude regarding the experimental implementation of the two-frequency pulses. By adding the power feedback control and the phase shifter, the resulting two-photon Rabi frequency that we are able to shape can be expressed in a general form as:

$$\Omega_\mathrm{R}(t) = |\Omega_\mathrm{R}(t)| \mathrm{e}^{\mathrm{i}[\varphi_2 - \varphi_1 + \Delta\varphi(t)]} \tag{5.38}$$

where the optical power control shapes the profile of the absolute value $|\Omega_\mathrm{M}(t)|$ of the two-photon Rabi frequency, and the setpoint of the phase shifter controls the phase $\Delta\varphi(t)$ term imprinted on the atoms over time.

The implementation of the complete setup, as depicted in Figure 5.14, makes it possible to have a two-photon Rabi frequency of any shape. It can be not only negative, if we restrict ourselves to π jumps, but also complex if we allow continuous phase variation of $\Delta\varphi(t)$. This ability to shape the two-photon Rabi frequency as desired is known as pulse shaping. This practice, increasingly prevalent in the community, enables the generation of Bragg pulses with characteristics optimized for specific cases. In particular, as discussed later in this chapter, pulse shaping can be employed to enhance the reflectivity of Bragg pulses, improving the visibility of interferometric signals. To our knowledge, there is no example in the literature where the temporal profile of a Bragg pulse is modulated to have two resonance frequencies, as is the case here. Although this method was developed in a specific context of a Bell interferometer, it would be interesting to reuse the concepts and tools developed within this framework for application in other contexts.

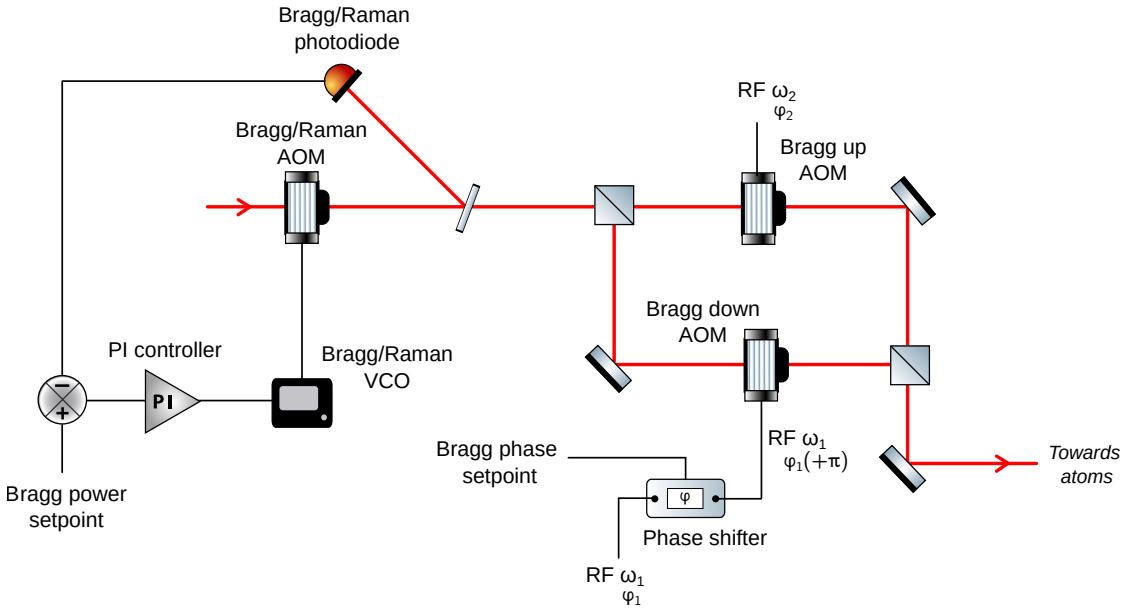

Figure 5.14: Experimental setup for pulse shaping. A first AOM is used to control the intensity of the Bragg beams, using a power feedback loop. The setpoint voltage is digitally generated and controls the amplitude of the RF signal sent to the AOM. In parallel, a phase shifter receives a setpoint voltage such that a phase jump of π is added to the RF signal sent to an AOM on the path of one of the Bragg beams, when the two-photon Rabi frequency is supposed to be negative. The RF signals of frequencies ω_1 and ω_2 are generated by the same device.

5.2.3 Reflectivity and phase of Bragg pulses for a Bell test

We can now attempt to determine the characteristics of the Bragg pulses that we should use for a Bell test. To do this, it is necessary to establish specifications given the performance we aim to achieve. Let us recall that the Bell correlator we aim at measuring can be expressed as

$$E(\Delta v) = A(\Delta v)\,\cos(\Phi(\Delta v)) \tag{5.39}$$

where Δv determines a momentum quadruplet.

Experimentally, we will average this signal for a given quadruplet over a velocity range corresponding to a mode, approximately in the order of $1\,\mathrm{mm.s^{-1}}$. Optimizing the performances of the Bragg pulses has a dual purpose: firstly, to ensure that the reflectivity is sufficiently high so that the interference amplitude $A(\Delta v)$ is maximized for our given population; secondly, to ensure that the imprinted phase $\Phi((\Delta v)$ does not vary too much on the scale of a mode to avoid blurring the interference.

Regarding the mirror:

- We aim to generate a one-frequency pulse with a resonance broad enough for the reflectivity to be closest to 1 over a velocity range corresponding to several pairs of modes, around $10\,\mathrm{mm.s^{-1}}$ (i.e., $5\,\mathrm{mm.s^{-1}}$ on either side of resonance). Otherwise, atoms transmitted through the mirror start to interfere with the useful signal.

- We have observed that the phase imprinted by the mirror on the atoms plays a role in the Bell phase expression. Therefore, we also want the phase imprinted by the

mirror to vary minimally over a velocity range corresponding to a mode, around 1mm/s.

Regarding the beam splitter:

- We aim to create a pulse at two frequencies, each with a resonance broad enough for the reflectivity to be close to 0.5 over a velocity range corresponding to several modes. The two resonance peaks must be sufficiently separated to avoid cross talk that would harm the reflectivity of the beam splitters.
- Similar to the mirror, we want the phase imprinted by the beam splitter to the atoms to not vary significantly over a velocity range corresponding to a mode.

Since we only have an estimate of the atom population per mode due to significant uncertainty in the quantum efficiency of the MCP, it is challenging to provide a concrete quantitative criterion for the reflectivity needed to observe the Bell inequality violation predicted by quantum mechanics. Therefore, we will assume that the input state of the Bell interferometer is a so called "Bell" state, maximally entangled, rather than a superposition of TMS states. In this manner, the subsequent study will focus on examining the effects of a decrease in Bell contrast solely attributed to the interaction with light, independently of the quality of the input state.

In the following, we will separately study the mirror and beam splitter pulses to analyze these different criteria. To achieve this, it is sufficient to solve the coupled Bragg system of equations 4.51, taking into account the possibility of diffraction towards higher orders. To analyze the performance of each pulse, we initially assume that the input state is composed solely of mode p to numerically determine the reflectivity and phase profiles of a given pulse as a function of detuning. Subsequently, we will plot the Bell correlator for the selected pulses.

We now turn to the phase imprinted on the atoms. The phase that matters for us is the Bell phase, which includes not only the Bragg pulses but also free propagation. Nevertheless, we can examine the phase imprinted by a given pulse by studying the phase difference between the transmitted and reflected atoms. Indeed, as seen in equation 5.12, the phase of the Bell correlator depends on such a phase difference for a given pulse.

For constant pulses, we have derived an analytical expression for the reflectivity and phases profiles in the framework of a two-level system, using the evolution operator 4.63. If we assume that the initial state is $(C_0(0), C_2(0)) = (1, 0)$ and that the duration of the pulse is T, we get:

$$\begin{pmatrix} C_0(T) \\ C_2(T) \end{pmatrix} = \begin{pmatrix} \left[\cos\left(\frac{\Omega T}{2}\right) - \mathrm{i}\frac{\delta_0}{\Omega}\sin\left(\frac{\Omega T}{2}\right)\right] \mathrm{e}^{\frac{\mathrm{i}\delta_0 T}{2}} \\ \mathrm{i}\frac{\Omega_\mathrm{M}}{\Omega}\mathrm{e}^{-\mathrm{i}\Delta\varphi}\sin\left(\frac{\Omega T}{2}\right)\mathrm{e}^{-\frac{i\delta_0 T}{2}} \end{pmatrix} = \begin{pmatrix} t\mathrm{e}^{\mathrm{i}\phi'} \\ \mathrm{i}r\mathrm{e}^{-\mathrm{i}\phi} \end{pmatrix} \tag{5.40}$$

with $\Omega = \sqrt{\Omega_\mathrm{M}^2 + \delta_0^2}$.

If we omit the contribution of the laser difference $\Delta\varphi$ (which cancels out in the Bell phase since it is the same for A and B), the imprinted phase by a constant pulse can therefore be written

$$\Delta\phi = \arg(C_2) - \arg(C_0) = -\phi - \phi' = -\frac{\delta_0 T}{2} + \tan^{-1}\left[\frac{\delta_0}{\Omega}\tan\left(\frac{\Omega T}{2}\right)\right] - \frac{\delta_0 T}{2} \tag{5.41}$$

When the detuning δ_0 is significantly larger than the two-photon Rabi frequency Ω_M, we have $\delta_0/\Omega \approx 1$, so the imprinted phase is, far from resonance:

$$\Delta\phi \underset{\delta_0 \gg \Omega}{\approx} -\delta_0 T + \frac{\Omega T}{2} = -\delta_0 T + \frac{\delta_0 T}{2} = -\frac{\delta_0 T}{2} \tag{5.42}$$

This phase, linear with detuning, has no physical significance since far from resonance, there is no interaction between atoms and light, and thus no imprinted phase. In fact, this term cancels out when considering free propagation terms. Here, to study the phase imprinted on the atoms by such a pulse, we will add $\delta_0 T/2$ to neglect this "dynamic" phase. The idea is to compare the phase imprinted by the light to the situation where there is no light. Therefore, when solving numerically the n-level system 4.51, we will plot

$$\phi_\mathrm{impr} = \arg(C_2) - \arg(C_0) + \frac{\delta_0 T}{2} \tag{5.43}$$

This relationship can be generalized to any type of pulse, not necessarily constant, as the dynamic phase comes from the $\delta_0 t/2$ terms that are always present in the differential equation. Regardless of the temporal pulse shape, we will subtract this dynamic phase term in the study of the imprinted phase.

Finally, since the phase imprinted on the transmitted atoms by the mirror is not relevant for the Bell phase, we will only plot the phase term from the reflected atoms:

$$\phi_\mathrm{impr,mir} = \arg(C_2) + \frac{\delta_0 T}{2} \tag{5.44}$$

Square Bragg mirror

Initially, we can use the mirror chosen for HOM, which is a constant pulse with a two-photon Rabi frequency $\Omega_\mathrm{M} = 5\,\mathrm{kHz}$ (and hence, the duration is $T_\mathrm{M} = \pi/\Omega_\mathrm{M} = 100\,\mu\mathrm{s}$). It is worth noting that a larger Rabi frequency results in a broader Bragg resonance, but it also increases the rate of diffraction towards higher orders, leading to losses in terms of signal-to-noise ratio. The chosen value of 5 kHz represents a good compromise between these two aspects.

We will plot the reflectivity and phase graphs as a function of the initial velocity class, which varies linearly with the detuning via the relation $\Delta v\ (\mathrm{mm.s^{-1}}) = -2\delta\ (\mathrm{kHz})$. The objective is to verify that the performance of the chosen pulse is satisfactory for a given quadruplet, and if possible, for multiple quadruplets. This assumes the possibility of multiplexing by conducting several Bell experiments in parallel on various quadruplets, with each mode represented by a velocity "box" over which to integrate the signal. A quadruplet is thus formed by two modes symmetric with respect to $\Delta v = 0$ and by two other modes shifted by v_B. The modes represented in green are the modes for loop A, while the modes in red are the modes for loop B (Figure 5.15). In the following, we will consider five $1\,\mathrm{mm.s^{-1}}$ wide quadruplets, labeled by their center which is respectively equal to $\Delta v = 1$, 2, 3, 4, and $5\,\mathrm{mm.s^{-1}}$.

The results for the reflectivity and phase are given in Figure 5.16. We observe that the phase imprinted on the reflected atoms varies little with the velocity class, and it can be considered constant for integration over a given mode. However, as previously observed, the reflectivity decreases quite rapidly with Δv. By the fifth box, the reflectivity of the mirror is already only 80%. Consequently, it will not be useful to calculate the signal beyond this point, because of the interferences with the transmitted atoms.

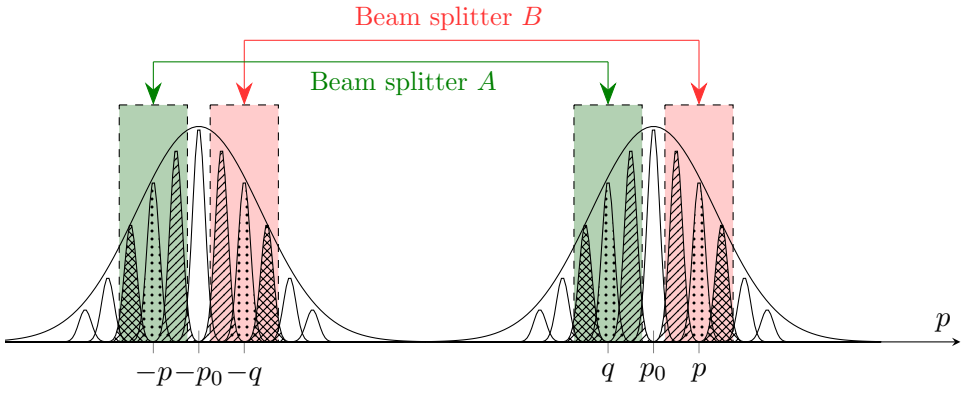

Figure 5.15: Schematic representation of the modes involved in the Bell interferometer. The pulse modes are depicted as Gaussians within a density envelope that characterizes the pair creation process. Modes within the same quadruplet are characterized by the same filling pattern. The green area corresponds to the modes resonant with beam splitter A, while the red area corresponds to the modes resonant with beam splitter B. The Bragg resonance is wide enough to allow coupling of multiple quadruplets.

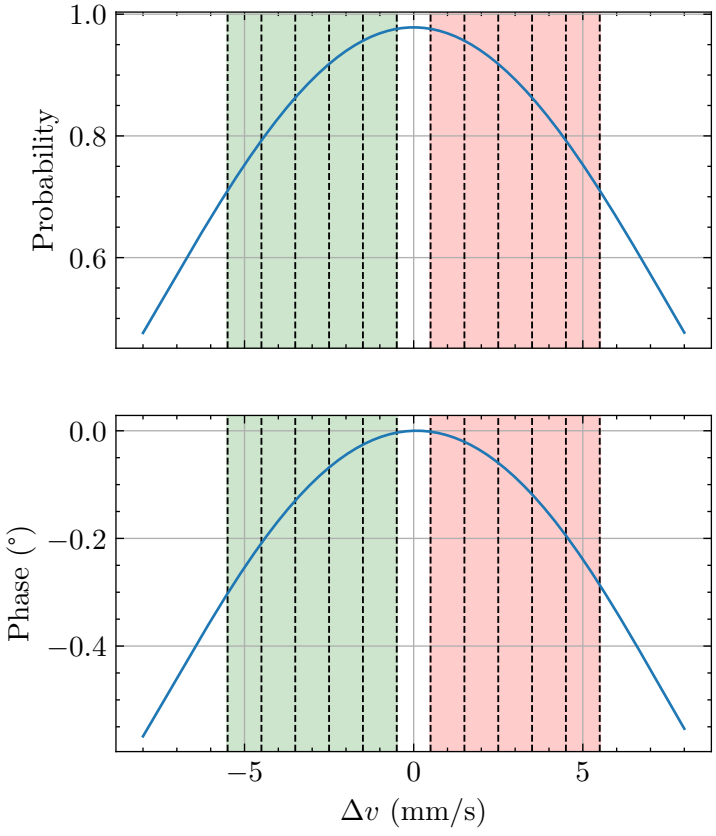

Figure 5.16: Reflectivity and phase profiles of a Bragg mirror. The Bragg coupling system 4.51 was solved for a square pulse with $\Omega_{\mathrm{M}} = 5\,\mathrm{kHz}$ and $T = \pi/\Omega_{\mathrm{M}}$ in order to get the probability $|C_2|^2$ and the imprinted phase $\phi_{\mathrm{impr,mir}}$ as a function of the detuning, converted in velocity. The shaded areas correspond to the five quadruplets considered: the green modes correspond to loop A doublets while the red modes correspond to loop B doublets.

Modulated Bragg beam splitter

Let us now turn our attention to the Bragg beam splitter. Unlike the HOM beam splitter, we aim to apply the amplitude modulation method to imprint a different phase on doublets A and B. The two-photon Rabi frequency is therefore:

$$\Omega_{\mathrm{R}}(t) = 2\,\Omega_{\mathrm{M}} \cos\left(\frac{\Omega_{\mathrm{D}} t}{2} + \frac{\theta}{2}\right) \tag{5.45}$$

where we omit the global phase $\mathrm{e}^{\mathrm{i}\Delta\varphi}$ caused by the laser difference, which ultimately cancels out in our configuration.

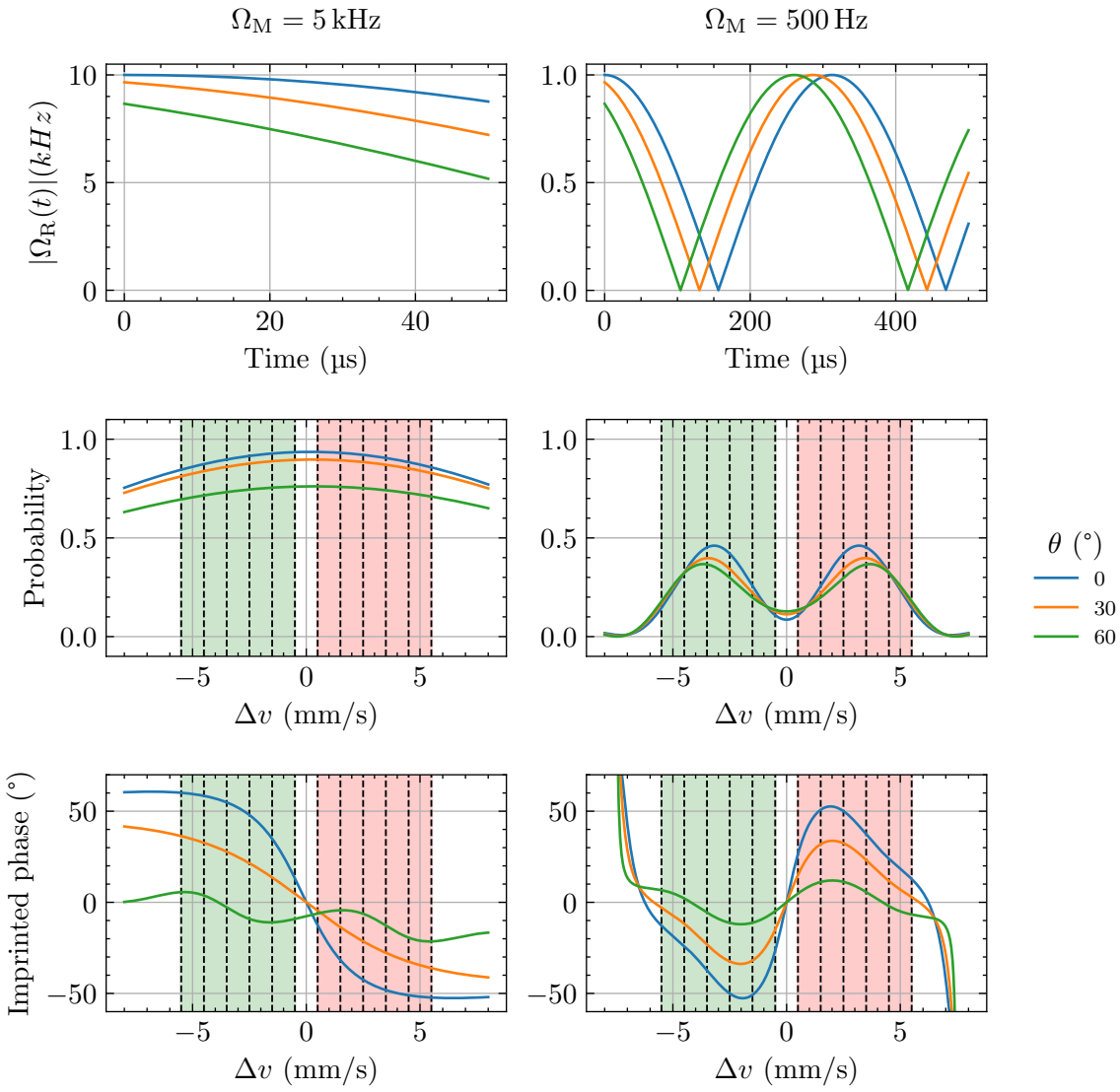

Figure 5.17: Temporal profile, reflectivity and phase profiles of a Bragg beam splitter. The Bragg coupling system 4.51 was solved for a square pulse with $\Omega_{\mathrm{M}} = 5\,\mathrm{kHz}$ (left) and $\Omega_{\mathrm{M}} = 500\,\mathrm{Hz}$ (left) with $T = \pi/\Omega_{\mathrm{M}}$ and $\Omega_{\mathrm{D}} = 3\,\mathrm{kHz}$, in order to get the probability $|C_2|^2$ and the imprinted phase ϕ_{impr} as a function of the detuning, converted in velocity.

It quickly becomes apparent that it is not possible to use this method while maintaining a Rabi frequency amplitude of $\Omega_{\mathrm{M}} = 5\,\mathrm{kHz}$. The duration of such a beam splitter pulse is $T = \pi/2\Omega_{\mathrm{M}} = 50\,\mu\mathrm{s}$. However, our Bragg doublets are separated by approximately

6 mm/s, equivalent to 3 kHz. Therefore, we must use a modulation frequency on the order of $\Omega_D = 3\,\text{kHz}$. The modulation period for such a frequency is about 300 µs, which is significantly higher than the pulse duration. This prevents the modulation from being adequately defined, resulting in the method's failure and, consequently, a reflectivity that does not exhibit two distinct peaks for the resonant velocities, as shown in Figure 5.17, where pulse profile, reflectivity and imprinted phase graphs are plotted for two different Rabi frequencies and three values of θ.

The only solution to increase the "resolution" of the modulation is to extend the duration of the beam splitter. This has the effect of allowing the appearance of two resonance peaks centered on modes A and B, respectively. Another consequence is that the resonance peaks are also narrower, which determines the lower limit of the Rabi frequency that cannot be surpassed if one wishes the reflectivity to be around 0.5 for two or three quadruplets. In Figure 5.17, two resonance peaks are clearly visible for $\Omega_M = 500\,\text{Hz}$, but they are not sufficiently separated to be considered independent. This causes a decrease in reflectivity compared to the desired value of 0.5, which may result in a reduction in the contrast of the Bell correlator oscillation. However, it is noticeable that the imprinted phase difference between doublets A and B depends on the initial phase value θ of the modulation function.

Due to the interference between the two resonance peaks, the imprinted phase difference between doublets A and B (symmetric with respect to $\Delta v = 0$) is not equal to θ. However, a significant variation in this phase difference is noted when θ varies. Additionally, on a box scale, the phase only varies by approximately ten degrees. To assess the effectiveness of phase control using this method, one can plot the averaged phase difference between A and B over a box of $1\,\text{mm.s}^{-1}$ as a function of θ (Figure 5.18).

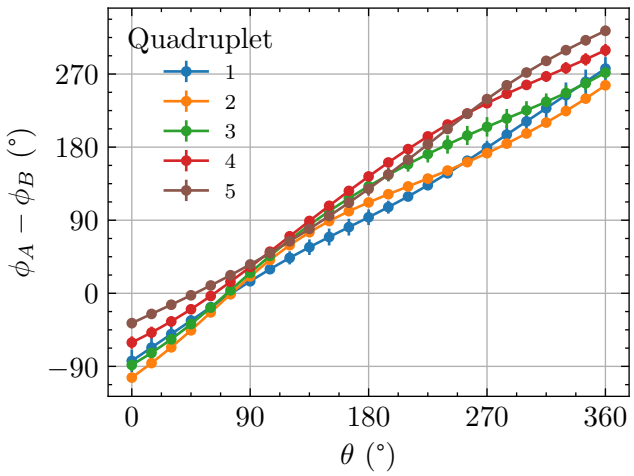

Figure 5.18: Imprinted phase as a function of the control parameter θ. For a given value of θ and a given quadruplet, i.e. a $1\,\text{mm.s}^{-1}$ wide velocity box labeled by the value of its velocity center Δv (in mm.s^{-1}), we plot the imprinted phase difference between the doublet A (in green in Figure 5.17) and the doublet B (in red in Figure 5.17), averaged over the velocity range of the box. The error bars are given by the standard deviation of the imprinted phase difference within the box.

The curves plotted for the five successive quadruplet boxes demonstrate that phase control operates as intended: there is a one-to-one mapping between θ and the imprinted phase. The relationship is not as linear as desired due to cross-talk between the two

resonances, but the imprinted phase can still be controlled using the phase at the origin of the modulation function.

5.2.4 Bell correlator

With these two pulses, the Bell correlator can be calculated and used as a criterion for the relevance of the selected Bragg pulses for exhibiting a violation of Bell's inequality. Similar to the approach used for the HOM interferometric sequence, we numerically solve the Bragg coupling equation 5.29 for each doublet to compute the output state. It is worth noting that determining the appropriate delay for the beam splitter pulse is not straightforward now that its duration has been changed compared to HOM. Experimentally, the ideal approach would be to conduct an HOM experiment using a beam splitter with the same duration intended for the Bell experiment.

Assuming that a preliminary HOM experiment is performed with a 5 kHz mirror (100 µs long), a 500 Hz beam splitter (500 µs long), and with $T_1 = 800\,\mu s$, we use the closure relation 5.26 analytically determined for square pulses to calculate the value of T_2 for which the HOM interferometer is closed. We find $T_2 = T_1 - 2T_S/\pi = 482\,\mu s$, which we use as a parameter for the Bell simulation.

Now, these timings can be used to simulate the proper Bell experiment: this time, T_2 is fixed, but the correlator is calculated for different values of θ. We take into account the atoms transmitted by the Bragg mirror.

The simulation results for the Bell correlator are presented in Figure 5.19 for three values of θ. A noticeable variation of the correlator with respect to this control parameter is observed. However, within a quadruplet, the correlator varies significantly, potentially reducing the interference contrast during integration over this velocity range.

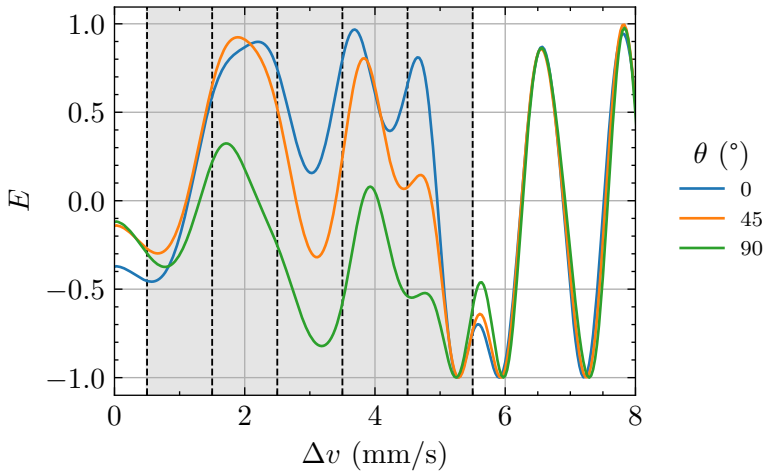

Figure 5.19: Bell correlator as a function of the velocity class for different values of the control parameter θ. The Bell correlator is computed for a given interferometric profile, corresponding here to one square mirror and one modulated beam splitter. The two-photon Rabi frequency of the mirror is $\Omega_M = 5\,kHz$ and the one of the beam splitter is $\Omega_M = 500\,Hz$. The free propagation durations are $T_1 = 800\,\mu s$ et $T_2 = 482\,\mu s$. Varying θ only consists in changing the phase at the origin of the modulated Bragg beam splitter. For the non-resonant quadruplets (beyond $\Delta v = 6\,mm.s^{-1}$), the rapid oscillation of the correlator is due to additional phases from atoms transmitted by the mirror (as discussed in section 5.1.3) but no longer depends on θ, which explains the superposition of the curves.

Our main concern is to calculate the average value of the correlator within a specified box as a function of θ. The obtained results are plotted in Figure 5.20 for the five quadruplets considered. The error bars correspond to the standard deviation of the Bell correlator in the considered integration box for each value of θ.

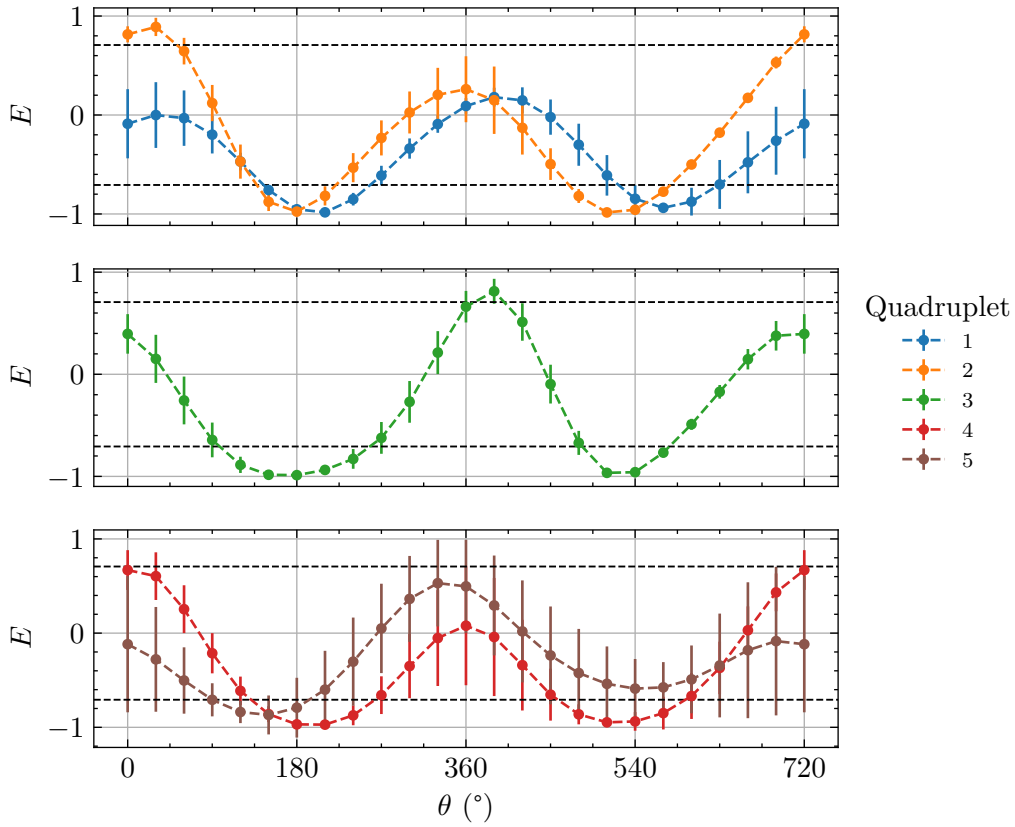

Figure 5.20: Oscillation of the Bell correlator as a function of the control parameter θ. For a given value of θ, we compute the correlator E as a function of the velocity class, as shown in Figure 5.19. Then, we average its value within a velocity box corresponding to a quadruplet, labeled by the value of its center Δv (in mm.s^{-1}). The error bars equal the standard deviation of the Bell correlator within the corresponding integration box.

A clear oscillation of the correlator can be observed as a function of θ for the various quadruplets. However, it is interesting to note that the interferometric sequence used to compute these results exhibits several drawbacks and deviations from the ideal case initially presented.

- Firstly, the observed oscillation is not exactly sinusoidal. This was actually expected based on the results from the previous section on phase control, which already indicated that the phase imprinted on the atoms does not vary linearly with θ (5.18). This is because the two beam splitters are not independent, so atoms from doublet A also experience an imprinted phase that is preferentially imprinted on doublet B.

- For the same reasons, although the correlator's oscillation has a period of approximately 2π, it can be observed that the correlator is not strictly 2π periodic but rather 4π periodic, despite the initial prediction of an oscillation in the form of $E = A\cos(\theta)$. This is due to the modulation function in $\cos(\Omega_D t/2 + \theta/2)$, which is itself 4π periodic. Because of the cross talk between the beam splitters, the reflec-

tivity and the phase imprinted on the atoms differ for a phase $\theta = 0$ compared to a phase $\theta = 2\pi$.

- The amplitude of the oscillation is indicative of the quality of the mirror and the beam splitter in the considered box: it is maximal for the 3rd quadruplet, corresponding to the center of resonance. It degrades for boxes 1 and 2, where the reflectivity of the beam splitter deviates significantly from 0.5, and similarly for boxes 4 and 5, where the quality of the mirror and the beam splitter degrades compared to the resonance.

- Similarly, as one moves away from the resonance, the reflectivity of the mirror decreases. For the quadruplets farthest from the resonance, there are many transmitted atoms interfering with the useful signal, inducing a significant variation of the correlator with the velocity class. This is reflected in the graph by increasingly large error bars. This situation is not desirable experimentally as it significantly decreases the signal-to-noise ratio.

Recall that, for a sinusoidal Bell correlator, the amplitude of the oscillation should be greater than $1/\sqrt{2} = 0.71$ if one hopes to observe a violation of Bell's inequality. But when the correlator is not sinusoidal, the angles θ for which the maximum value of the Bell parameter S can be reached are not obvious, so this condition on the oscillation amplitude does not hold.

Instead, it is possible to numerically determine the maximum value of S which can be achieved given a Bell correlator, by trying many sets of phases. The Bell parameter is defined as

$$S = E(\phi_{A1} - \phi_{B1}) - E(\phi_{A1} - \phi_{B2}) + E(\phi_{A2} - \phi_{B1}) + E(\phi_{A2} - \phi_{B2}) \tag{5.46}$$

Numerically, we enumerate all sets of four phases (ϕ_{A1}, ϕ_{A2}, ϕ_{B1}, ϕ_{B2}) where each value of ϕ is within the range of 0 to 355° with a 5° increment, and we calculate S knowing the value of E for all corresponding $\theta = \phi_A - \phi_B$ values. We repeat the same procedure for θ between 360 and 720°. The highest value $S_{\max}$ of S that can be achieved for each quadruplet is given in Table 5.1. We also calculate an estimation of the error bar on S using the errorbar ΔE on E, with

$$\Delta S = \sqrt{\sum_{i,j} \left(\Delta E(\phi_i - \phi_j)\right)^2} \tag{5.47}$$

We note $\theta_1 = \phi_{A1} - \phi_{B1}$, $\theta_2 = \phi_{A1} - \phi_{B2}$, $\theta_3 = \phi_{A2} - \phi_{B2}$ and $\theta_4 = \phi_{A2} - \phi_{B2}$. The results are to be compared with the value S_{th} that we get by using the optimal angles for a sinusoidal correlator[1].

Two quadruplets can produce a Bell parameter exceeding 2, with a relatively low error bar. These are the quadruplets for which the correlator has the largest oscillation amplitude. The values of $\phi_A - \phi_B$ that optimize S differ from the ones typically considered, due to the unusual shape of the correlator.

It is important to note that this model only accounts for the effects of Bragg pulses on the correlator amplitude; in a real experiment, there are additional causes for the decrease of the amplitude of E (and of S, subsequently), especially due to the initial state of the interferometer not being maximally entangled. We have seen that for a two-mode squeezed

[1] That is to say $\phi_{A1} - \phi_{B1} = 45°$, $\phi_{A1} - \phi_{B2} = 135°$, $\phi_{A2} - \phi_{B1} = 315°$ and $\phi_{A2} - \phi_{B2} = 45°$.

Quadruplet	$S_{\max}$	θ_1	θ_2	θ_3	θ_4	S_{th}
1	0.90 ± 0.30	445°	530°	360°	445°	0.41 ± 0.45
2	2.60 ± 0.27	65°	130°	0°	65°	2.46 ± 0.32
3	2.58 ± 0.24	400°	495°	665°	400°	0.82 ± 0.41
4	2.00 ± 0.62	0°	325°	35°	0°	1.48 ± 0.57
5	1.82 ± 0.94	355°	45°	305°	355°	0.56 ± 0.80

Table 5.1: Values for the Bell parameter.

state, the Bell oscillation amplitude decreases with the atom population per mode. Furthermore, our source of pairs does not truly provide two-mode squeezed states; although we model the initial state as a superposition of TMS, the $g^{(2)}$ correlation measurements suggest the state is likely more complex. For these reasons, we will delve a bit further into the analysis in the next section, in order to bring the Bell parameter even closer to the ideal value of $2\sqrt{2}$, with an even smaller variation of the correlator within a quadruplet.

In conclusion, it has been demonstrated that modulating a constant signal by a sinusoidal function allows, through the phase at the origin of this function, the control of the Bell correlator. Although the double-frequency beam splitter used is not ideal, as the phase imprinted on doublets A and B is not independent, one can still hope to observe a correlator variation with sufficient amplitude to exhibit a violation of Bell's inequality for several momentum quadruplets.

In the following, efforts will be made to improve these results by leveraging the fact that the techniques employed to create a double-frequency beam splitter (laser power lock and π phase shifts) can also be used to optimize the reflectivity and phase profiles of the mirror and the beam splitter.

5.3 Bragg pulse shaping

5.3.1 State of the art, motivation and criteria

Pulse shaping

The perturbative development carried out in section 4.2.3 has demonstrated that, in the limit where the transfer rate is small, the reflectivity profile as a function of detuning is equal to the Fourier transform of the temporal profile of the pulse. We will use this idea to shape a pulse with the most rectangular reflectivity profile possible by examining pulses whose temporal profiles have the form of a sinc function. Such pulses can be experimentally realized using the same techniques employed for phase control, enabling access to negative or even complex two-photon Rabi frequencies. By extending our parameter space in this manner, we can relax some constraints imposed by square pulses and achieve improved reflectivity profiles in the desired velocity ranges.

It is important to note that this Fourier transform relationship is not valid when the transfer rate is significant, which is obviously the case for beam splitters and even more so for mirrors. Therefore, we will observe significant deviations in the reflectivity profiles from rectangular shapes. However, the obtained profiles with sinc pulses still improve both the velocity range with excellent reflectivity and the sharpness of the resonance compared to square pulses. These aspects are crucial for achieving high-quality Bragg mirrors and

beam splitters.

As mentioned before, this technique is referred to as pulse shaping. In the literature, there are some examples where this method is suggested to enhance contrast in atomic interferometers. In the early 2010s, inspired by techniques used in NMR for manipulating quantum states[148][149], theoretical work emerged with the aim of enhancing and shaping the reflectivity profile of two-photon transitions in a controlled manner[150]. The idea is to generate composite pulses, i.e., a series of pulses with varying phases. In the context of NMR, these pulses have demonstrated significant robustness to variations in interaction parameters such as pulse amplitude and frequency, along with the suppression of excitation sidebands which justifies the growing interest in these methods for atom interferometry and quantum processing. Indeed, not only can the transfer rate over a given range of velocity be tuned by shaping the pulse intensity and shape, increasing the interference contrast, but the temporal shape is expected to affect the response of the interferometer to phase fluctuations, which is a major source of instability in most atom interferometers.

The first experimental results for studying the reflectivity profiles of these composite pulses on cold thermal clouds were promising[151]. Such pulses have quickly found applications in atomic Mach-Zehnder interferometers [152] demonstrating their importance, especially in interferometers where multiple consecutive transitions are performed to impart a large momentum transfer to the atoms[153]. This led to the development of new procedures to shape the temporal profile of Raman and Bragg pulses by tuning both the phase and power of the pulses. In particular, Luo et al.[154] proposed using sinc-shaped pulse profiles to make the reflectivity profile rectangular, while other authors have investigated the possibility of using Gaussian-shaped pulses[155][156]. Note that there are pulses that are potentially better than sinc-shaped pulses for the mirror in particular[154], which belong to the BURP family used in NMR[157]. The study of such pulses would constitute a logical continuation of this work.

A first experimental attempt to use sinc-shaped pulses on thermal cold atoms was reported by Fang et al.[158] in 2018, introducing the π shifts technique to achieve negative Rabi oscillations. The authors demonstrated that sinc-shaped profiles (peak Rabi frequency of 12 kHz, duration 300 µs), although challenging to implement, exhibit a broader resonance width compared to other tested profiles (Gaussian and rectangular). It is worth noting that the shaped pulses do not lead to an improvement in resonance transfer efficiency but rather an increase in the width of the resonance, so the performance of the beam splitters and mirrors remained low (up to 0.35 and 0.8 transfer efficiency, respectively).

To our knowledge, there is no other experimental example that specifically employs pulse shaping techniques for atomic interferometers. Indeed, the pulse shaping approach falls within the broader scope of seeking to improve the contrast of interferometric signals. In recent years, another technique has been gaining prominence: optimal control. The principle involves using an algorithm that, given constraints in terms of reflectivity or phase, optimizes the temporal profile of a pulse to meet these specifications[159][160]. This is often achieved by decomposing the profiles into bases of reference functions. The optimization is performed with respect to a cost function that contains information about the criteria to be met, and the algorithm aims to minimize this function. Beyond constraints related to interferometric performance, it is also crucial for the algorithm to consider technical constraints, such as power lock and phase bandwidth, or pulse duration, to ensure that the pulse profile towards the algorithm converges is experimentally accessible.

Such optimal control resulting pulses were successfully implemented in Mach-Zehnder interferometers[161], exhibiting an enhanced contrast and resonance width. With the rise of interferometers with large momentum transfer, this technique is increasingly being studied[162][163][164][165] and experimentally applied with promising results[166]. It serves not only to improve the contrast of interferometric signals but also to enhance their robustness to phase fluctuations.

Application to our case: sinc-shaped pulses

In our case, the highly specific constraints on phase and reflectivity make it challenging to use existing algorithms to determine the optimal profile for conducting our Bell inequality test. However, it would be an interesting project to focus on the use or creation of an optimal control code. The cost function could be the difference between the Bell correlator and a sinusoidal function, or even directly related to the Bell parameter S (which would require a few additional code steps since, if the correlator E is not sinusoidal but takes another form, the phase values that optimize the Bell parameter must be determined given the shape of E).

Nevertheless, it is worth noting that one of the advantages of using sinc pulses lies in the ease of determining the role of various free parameters. This allows convenient modification of these parameters to alter the profile as desired. It is a user-friendly tool compared to an optimal control algorithm, the outcome of which would be specific to a predetermined set of specifications.

Let us express the sinc pulse in the form, for $t \in [0, T]$:

$$\Omega_{\mathrm{R}}(t) = \Omega_{\mathrm{M}} \operatorname{sinc}\left(\Omega_{\mathrm{S}}(t - T/2)\right) \tag{5.48}$$

The parameters Ω_{M} (depth of the lattice), T (duration of the pulse), and Ω_{S} (sinc frequency) are free, and we aim to determine them using the criteria mentioned earlier. Initially, we will seek to establish the relationship between these parameters that enables the creation of mirror and beam splitter pulses. To achieve this, we cannot retain conditions $\Omega_{\mathrm{R}}T = \pi$ and $\Omega_{\mathrm{R}}T = \pi/2$, which are only valid for square pulses. Therefore, we rewrite these conditions in integral form:

$$\int_0^T \Omega_{\mathrm{R}}(t)\,\mathrm{d}t = \alpha\pi \tag{5.49}$$

where $\alpha = 1$ for a mirror and $\alpha = 1/2$ for a beam splitter. This condition can be rewritten in a dimensionless form by involving the sine integral function, denoted as Si:

$$\int_0^T \Omega_{\mathrm{R}}(t)\mathrm{d}t = 2\frac{\Omega_{\mathrm{M}}}{\Omega_{\mathrm{S}}}\mathrm{Si}\left(\frac{\Omega_{\mathrm{S}}T}{2}\right) = \alpha\pi \tag{5.50}$$

where

$$\mathrm{Si}(x) = \int_0^x \frac{\sin t}{t}\,\mathrm{d}t \tag{5.51}$$

The graph of the sine integral function is provided in Figure 5.21. It is observed that this function rapidly approaches $\pi/2$ when x is sufficiently large. We will use this asymptote to satisfy condition 5.50. By assuming that the product $\Omega_{\mathrm{S}}T/2$ is large, we indeed have $\mathrm{Si}\left(\Omega_{\mathrm{S}}T/2\right) \approx \pi/2$. This leads to a relationship between Ω_{S} and Ω_{M} that must be satisfied to achieve a beam splitter or a mirror:

- For a mirror ($\alpha = 1$), we must use $\Omega_S = \Omega_M$;
- for a beam splitter ($\alpha = 1/2$), we must use $\Omega_S = 2\Omega_M$.

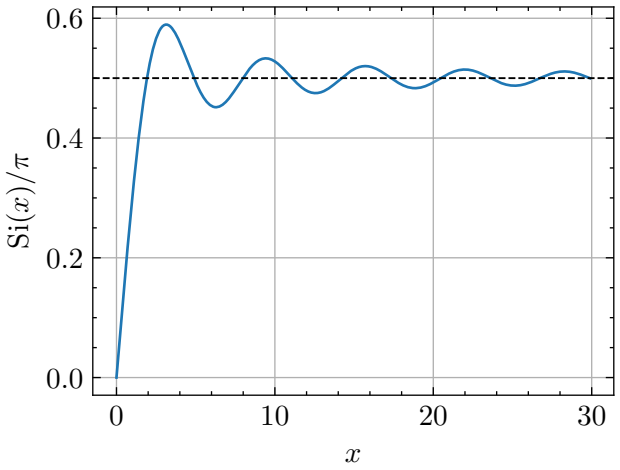

Figure 5.21: Graph of the sine integral function.

These conditions determine the parameter Ω_S. In the following, we will aim to manipulate T and Ω_M to meet the specifications in terms of reflectivity and phase described in section 5.2.3.

5.3.2 Sinc-shaped mirror

In this section, we will study the reflectivity and phase profile of sinc pulses defined in equation 5.48. For a mirror pulse, we have $\Omega_S = \Omega_M$. Two examples of reflectivity profiles are provided in Figure 5.22 for $\Omega_M = 5\,\text{kHz}$ sinc pulses with respective durations of $T = 0.4$ and 1 ms. The reflectivity associated to a constant 5 kHz pulse is shown in dashed lines.

For a sinc pulse, the full-width at half-maximum of the resonance is mainly determined by the Rabi frequency amplitude Ω_M, provided that the pulse duration T is long enough for the sinc to be "resolved", i.e., the duration must be sufficient for the rebounds of the sinc to appear. The longer the duration, the more rebounds the sinc exhibits, and the better the reflectivity resembles a rectangular profile. However, significant deviations from a perfect rectangular reflectivity profile are observed, as expected, since the Fourier relationship between reflectivity and the temporal shape no longer holds when the transfer rate is high.

Thus, reflectivity rebounds are observed, more centered on the resonance as T increases. Similarly, the sharpness of the profile increases with the pulse duration. To compare the different profiles, the following observables are defined, focusing on the width and sharpness of each profile: $W_{50\%}$ and $W_{90\%}$ which correspond to the width of the resonance at 50% and 90% reflectivity, respectively, and $\mathcal{S}_\pm(50\%)$ which represents the slope of the reflectivity curve at 50%:

$$\mathcal{S}_\pm = \frac{\mathrm{d}|C_2|^2}{\mathrm{d}\Delta v}(50\%) \tag{5.52}$$

Quantitative comparison of the results obtained for different reflectivity profiles can be made (Table 5.2). For the pulses considered here, it is observed that the sinc pulse

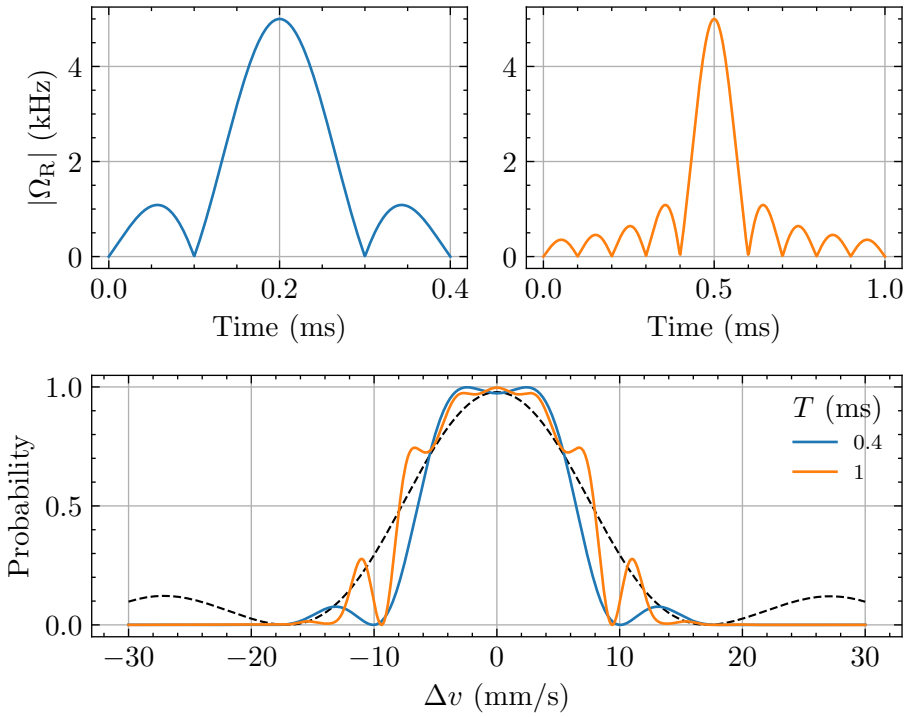

Figure 5.22: Pulse shape and reflectivity profile of sinc-shaped mirror pulses. The reflectivity profile $|C_2|^2$ is computed as a function of the velocity class from system 4.51 for the two profiles depicted at the top of the figure for two different pulse durations ($T = 0.4$ and 1 ms), with a two-photon Rabi frequency$\Omega_M = 5$ kHz. For comparison, the reflectivity profile of a square pulse with the same two-photon Rabi frequency is shown as a black dashed line.

not only improved the velocity range for which reflectivity is very good ($W_{90\%}$ increased by a factor of 1.3) but also enhanced the sharpness $\mathcal{S}_\pm$ of the profile by a factor of 2 to 4 depending on the pulse duration. As we will see in the next section, this improvement will hold particular significance for beam splitter pulses.

Pulse		**Width** (mm.s^{-1})		**Sharpness** (%/mm.s^{-1})
Shape	T (ms)	$W_{50\%}$	$W_{90\%}$	$\mathcal{S}_\pm(50\%)$
square	0.1	15.5	5.7	$\pm$9.6
sinc	0.4	12.9	8.7	$\pm$23.3
sinc	1	15.9	8.0	$\pm$43.1
sinc	2	14.8	7.1	$\pm$28.2

Table 5.2: Bragg mirror performances for $\Omega_M = 5$ kHz.

However, the interest in the sinc pulse for the mirror remains limited. To further increase the resonance quality over a broader velocity range, increasing the two-photon Rabi frequency would be necessary. But this would lead to an increase in population in higher diffraction orders, which is not desirable in our case as it would decrease our signal-to-noise ratio. Nevertheless, quantifying this effect would be interesting, as there might be a compromise between reducing the signal-to-noise ratio and increasing the mirror quality. This would require a detailed model of the expected signal-to-noise ratio given the atomic population per mode, the quantum efficiency of the detector, and the quality of the Bragg

pulses. Establishing such a model is an ongoing project.

Note that the reflectivity profile not only exhibits rebounds but also small additional peaks (especially when T is large), which can be likened to Gibbs oscillations that appear when truncating a signal and calculating its Fourier transform. A simple way to smooth the signal is through apodization, which involves multiplying the sinc by a windowing function. This has the effect of reducing Gibbs oscillations by decreasing the amplitude of the sinc rebounds, making the truncation less abrupt. Smoothing the reflectivity profile within the velocity range relevant for Bell will also result in smoothing the Bell correlator within a given integration bin, thus reducing its standard deviation within that quadruplet, aiming for an improved signal-to-noise ratio.

Thus, one can multiply the sinc by a function written in the form:

$$w(t) = \sin^{\beta}\left(\frac{\pi t}{T}\right) \tag{5.53}$$

where β denotes the degree of apodization. For $\beta = 0$, we have $w(t) = 1$, while for $\beta = 1$, the window is sinusoidal. For $\beta = 2$, it is a Hann-type window, well-known in signal processing. The reflectivity plots are provided in Figure 5.23 for $T = 2\,\mathrm{ms}$.

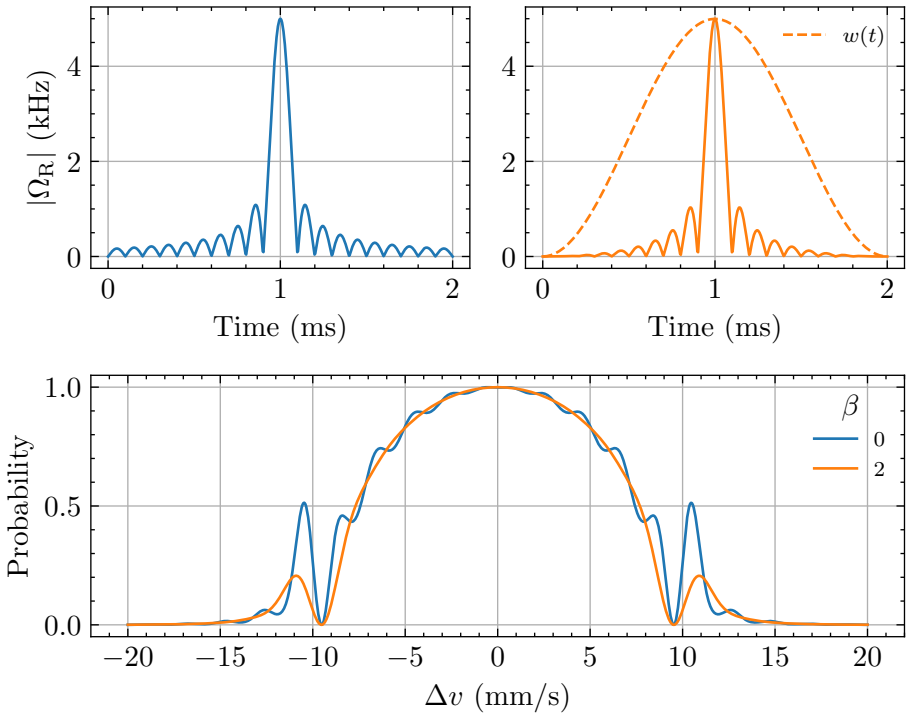

Figure 5.23: Comparison between the reflectivity profiles of the sinc-shaped pulses, with and without apodization. The pulse parameters are the same ($T = 2\,\mathrm{ms}$, $\Omega_M = 5\,\mathrm{kHz}$), except for the degree of apodization β, which equals 0 (in blue) or 2 (in orange).

Apodization might also have the effect of deteriorating the sharpness of the reflectivity profile. For $T = 2\,\mathrm{ms}$ and $\beta = 2$, we find $W_{90\%} = 7.7\,\mathrm{mm.s^{-1}}$, $W_{50\%} = 15.4\,\mathrm{mm.s^{-1}}$ and $\mathcal{S}_{\pm} = \pm 20.6\%/\mathrm{mm.s^{-1}}$, so the performances of the mirror are similar than those of the pulse without apodization. However, it is noticeable that when T is shorter, the windowing becomes less beneficial and may even tend to degrade the mirror's performance. For

$T = 1\,\text{ms}$ and $\beta = 2$, we find for instance $W_{90\%} = 7.9\,\text{mm.s}^{-1}$, $W_{50\%} = 14.3\,\text{mm.s}^{-1}$ and $\mathcal{S}_{\pm} = \pm 23.4\%/\text{mm.s}^{-1}$, which is slighlty lower than the values for $\beta = 0$.

Finally, it should be noted that experimentally, it is not particularly relevant to choose arbitrarily long pulse durations. First, decoherence that can occur if the light-atom interaction is prolonged (due to spontaneous emission). Of course, this is even more true when the laser intensity is high; hence, the decoherence rate for a sinc-shaped pulse with duration T remains much lower than for a constant signal of the same duration. In fact, a sinc shaped pulse can often be considered equivalent to a constant pulse with the same two-photon Rabi frequency since it is the area under these two temporal signals that is conserved for a mirror. Furthermore, an excessively long mirror or beam splitter duration would lead to a significant duration of the Bell interferometer. Since atoms fall freely during the interferometer, there is a risk of them leaving the beams if the interferometric sequence is too long.

For all these reasons, we will consider in the following a sinc mirror pulse of two-photon Rabi amplitude $\Omega_{\text{M}} = 5\,\text{kHz}$ with a duration $T = 1\,\text{ms}$ without apodization. The reflectivity and phase profiles over the velocity range of interest for Bell are provided in Figure 5.24, and exhibit a slight improvement compared to the square pulse.

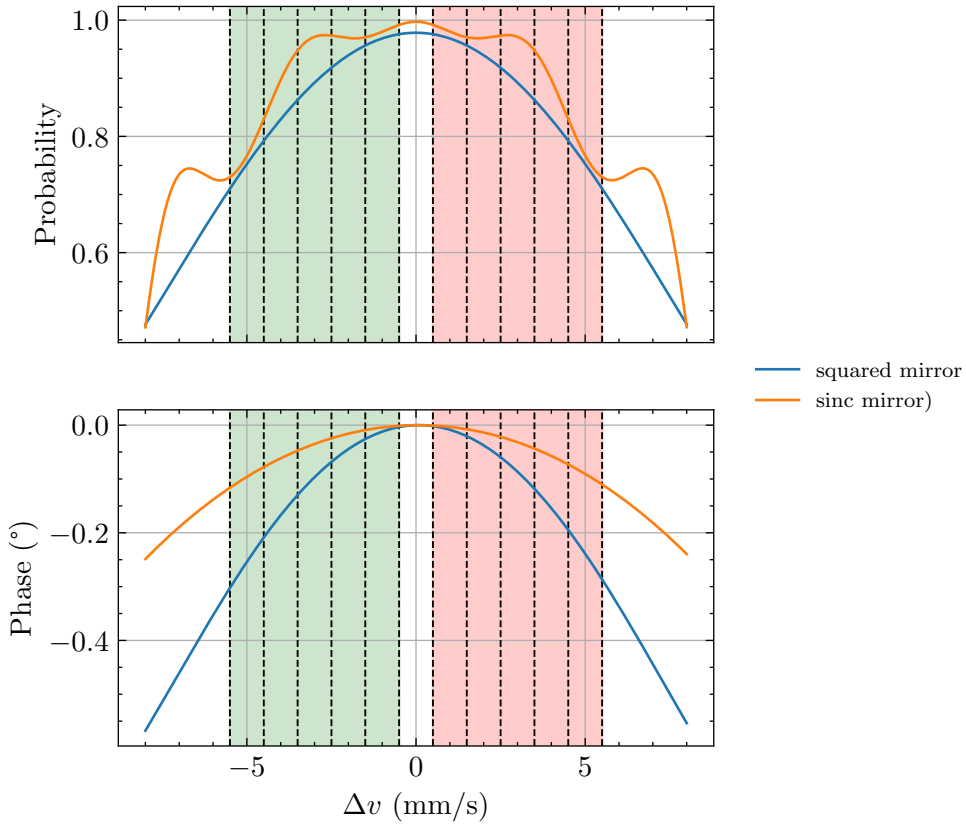

Figure 5.24: Reflectivity and phase profiles of a Bragg sinc-shaped mirror. The Bragg coupling system 4.51 was solved for a pulse with $\Omega_{\text{M}} = 5\,\text{kHz}$ and $T = 1\,\text{ms}$ in order to get the probability $|C_2|^2$ and the imprinted phase $\phi_{\text{impr,mir}}$ as a function of the detuning, converted in velocity. Again, the shaded areas correspond to the five quadruplets considered: the green modes correspond to loop A doublets while the red modes correspond to loop B doublets.

5.3.3 Modulated sinc-shaped beam splitter

The same ideas can be applied to the beam splitter. Rather than multiplying the constant pulse with a modulation function to create a two-frequency splitter, we will modulate a sinc function. The idea is to take advantage of the flexibility we have over the duration of the sinc pulses to resolve the modulation function without deteriorating the reflectivity of each splitter. The sharpness of the resonance peaks of the sinc pulses is an advantage in avoiding interference between the two splitters, which will make it possible to approach the ideal case where the two splitters are independent. To this end, the expression of the beam splitter is:

$$\Omega_{\mathrm{R}}(t) = 2\,\Omega_{\mathrm{M}}\,\mathrm{sinc}\left(\Omega_{\mathrm{S}}(t - T/2)\right)\cos\left(\frac{\Omega_{\mathrm{D}}t}{2} + \frac{\theta}{2}\right) \tag{5.54}$$

with $\Omega_{\mathrm{S}} = 2\,\Omega_{\mathrm{M}}$.

Let us first consider the case of a single-frequency beam splitter without modulation to compare the performance of a Bragg splitter with a sinc-shaped splitter against a constant splitter. The reflectivity graphs for $\Omega_{\mathrm{M}} = 5\,\mathrm{kHz}$ are plotted Figure 5.25.

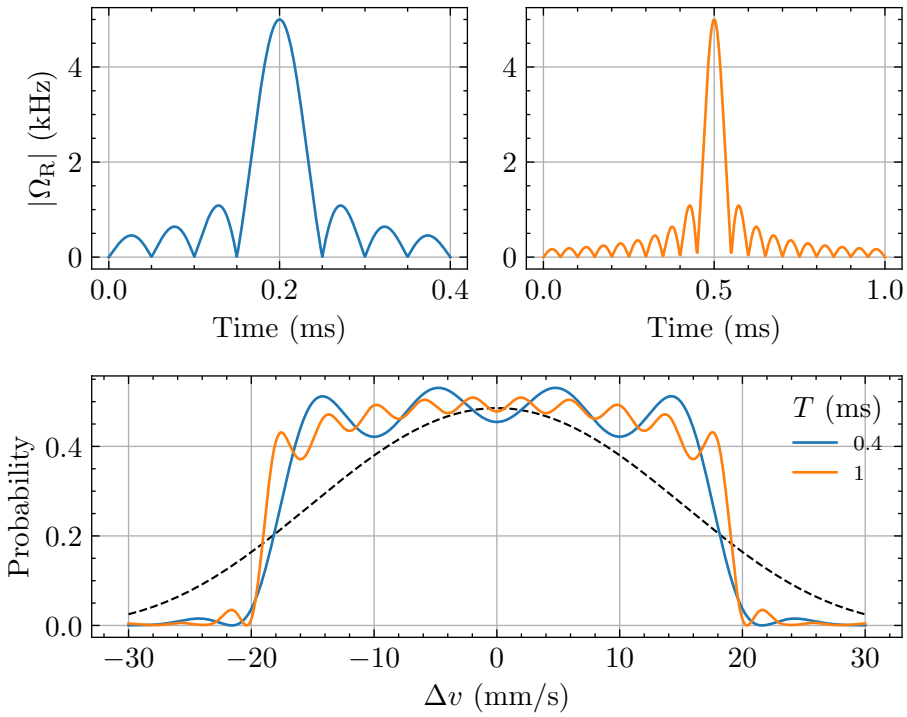

Figure 5.25: Pulse shape and reflectivity profile of sinc-shaped beam splitter pulses. The reflectivity profile $|C_2|^2$ is computed as a function of the velocity class from system 4.51 for the two profiles depicted at the top of the figure for two different pulse durations ($T = 0.4$ and $1\,\mathrm{ms}$), with a two-photon Rabi frequency $\Omega_{\mathrm{M}} = 5\,\mathrm{kHz}$. For comparison, the reflectivity profile of a square pulse with the same two-photon Rabi frequency is shown as a black dashed line.

This time, a truly significant difference is observed between the reflectivity profile obtained for a constant pulse and that obtained for the sinc. This is due to the fact that the relationship describing reflectivity as the Fourier transform of the temporal signal is better satisfied for the beam splitter than for the mirror. The considerations regarding the pulse duration are the same as for the mirror: the longer the duration, the better the

resolution of the sinc, which has more rebounds, resulting in a more rectangular reflectivity profile. However, additional small peaks appear in the reflectivity, also due to the rather abrupt truncation of the sinc. Even more than for the mirror, these Gibbs oscillations induce a variation in reflectivity at resonance, which will, in turn, lead to a variation in the correlator. As before, this reflectivity can be smoothed by multiplying the sinc by an apodization window as defined in equation 5.53. To quantify this effect, one can define the smoothness s of the pulse reflectivity at resonance as the standard deviation of the reflectivity profile in a velocity range for which the reflection probability remains within 90% of the desired value of 0.5:

$$s_{90\%} = \mathrm{std}(|C_2(\Delta v)|)_{90\%} \tag{5.55}$$

We also use the previous definitions of the width at 50% and 90%, as well as the sharpness at 50%, by redefining them with respect to a probability of 0.5 (which corresponds to calculating the width at 25% and 45%, and the slope of the reflectivity when it reaches 25%). This allows for a quantitative comparison of the performance of different pulses. The results are provided in Table 5.3.

Pulse			**Width** ($\mathrm{mm.s^{-1}}$)		**Sharpness** ($\%/\mathrm{mm.s^{-1}}$)	**Smoothness** (%)
Shape	T (ms)	β	$W_{50\%}$	$W_{90\%}$	$\mathcal{S}_{\pm}(50\%)$	$s_{45\%}$
square	0.05	0	32.1	11.3	$\pm$2.3	1.1
sinc	0.4	0	35.5	31.8	$\pm$12.1	3.4
sinc	1	0	37.7	28.9	$\pm$25.9	1.9
sinc	2	0	38.6	26.7	$\pm$41.7	1.4
sinc	0.4	2	33.2	23.6	$\pm$5.9	1.0
sinc	1	2	36.2	25.6	$\pm$12.2	1.2

Table 5.3: Bragg performances for $\Omega_{\mathrm{M}} = 5\,\mathrm{kHz}$

Recall that the sharpness parameter is important because we aim to ensure that the reflectivity profiles of the two Bragg beam splitters separated by Ω_{D} do not overlap: the greater the sharpness, the more it ensures that the two beam splitters for A and B will be independent.

It can be observed that the sinc widens the velocity range with excellent reflectivity by a factor of approximately 3, representing a significant gain. Additionally, the resonance slope is greater by a factor of at least 5 (up to 20 depending on the pulse duration), which is a great advantage for subsequently realizing a two-frequency pulse with independent resonance peaks. Moreover, as expected, the apodization function smoothens the signal over the resonant range but significantly reduces both the resonant range and the sharpness of the resonance. In the following, we will not seek to smoothen the reflectivity profile.

Let us now return to the two-frequency pulses. We choose a modulation frequency Ω_{D} of around 3 kHz, corresponding to two resonance peaks centered at $\Delta v = 3\,\mathrm{mm.s^{-1}}$ and $\Delta v = -3\,\mathrm{mm.s^{-1}}$. These values correspond to the center of the two velocity zones we aim to address. Similar to a constant splitter, the resonance for a 5 kHz pulse is currently too broad, which would lead to interference between the two resonance peaks A and B. To avoid this, the two-photon Rabi frequency needs to be decreased to narrow the resonance

width. The primary advantage of the sinc shaped pulse is that this reduction does not come with a significant decrease in the performance of each splitter.

We choose pulses with a Rabi frequency of $\Omega_M = 800\,\text{Hz}$ to maintain good reflectivity for the five considered quadruplets. We take $\Omega_D = 3.5\,\text{kHz}$ and $T = 1\,\text{ms}$. The results are plotted in Figure 5.26 for different values of θ. They are to be compared with those from Figure 5.17 obtained using a two-frequency beam splitter without a sinc-shaped form.

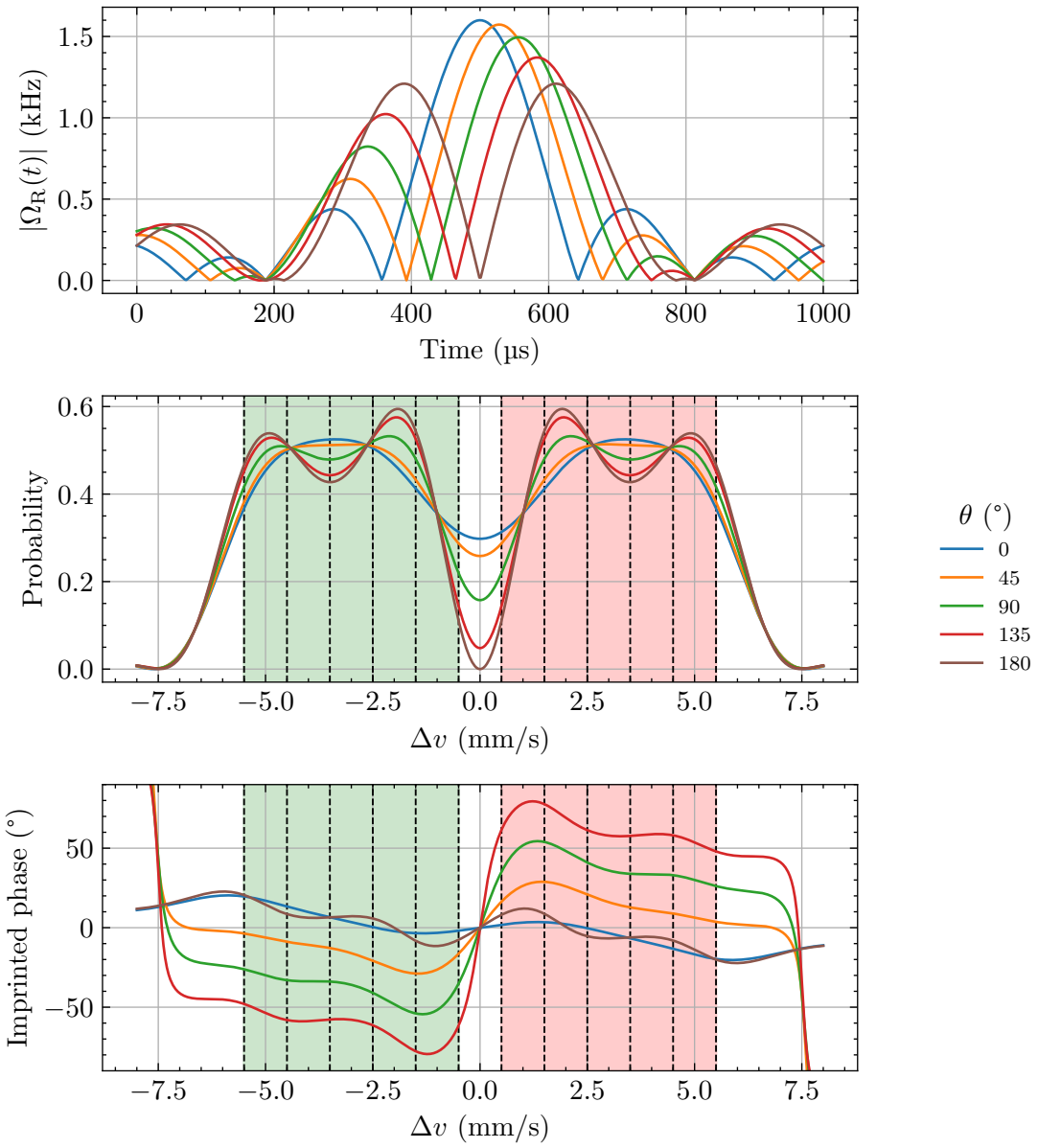

Figure 5.26: Temporal profile, reflectivity and phase profiles of a sinc-shaped Bragg beam splitters, for different values of θ. The Bragg coupling system 4.51 was solved for a sinc pulse with $\Omega_M = 800\,\text{Hz}$, $\Omega_D = 3.5\,\text{kHz}$ and $T = 1\,\text{ms}$, in order to get the probability $|C_2|^2$ and the imprinted phase ϕ_{impr} as a function of the detuning, converted in velocity.

It can be observed that there is still an influence of θ on the reflectivity profiles, but it remains minor. The reflectivity profile is good (i.e. close to 0.5) and constant for each quadruplet, except for the quadruplet centered on 1 mm/s, where there is a small inter-

ference between the two beam splitters. Overall, the reflectivity is much better than with the square two-frequency pulses, and this is the major advantage afforded by the sinc-shaped beam splitters. It is also noteworthy that the imprinted phase behaves in a more controlled manner than with two-frequency constant pulses: the phase difference between two doublets is constant over the width of a mode and equals to θ, suggesting that the phase control will be improved.

As done previously, in order to study the quality of phase control, one can examine the influence of θ on the difference of imprinted phase between doublet A and doublet B within a given quadruplet, averaged over a mode (Figure 5.27). As expected, the relationship between these two quantities is linear. The most significant deviation from a linear relationship is observed for the quadruplet centered on 1 mm/s; this is where the variation in imprinted phase is the most pronounced due to cross talk between the two beam splitters, arising from a lack of sharpness of the resonance peaks. For the other quadruplets, however, the phase difference imprinted by light on the doublets A and B is well controlled by the modulation function's phase at the origin θ.

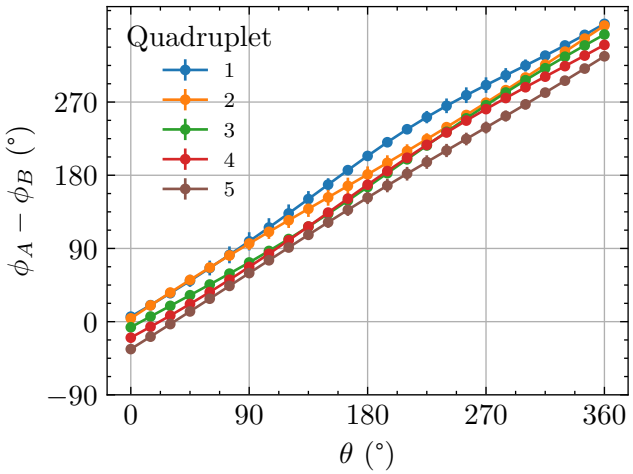

Figure 5.27: Imprinted phase as a function of the control parameter θ for sinc-shaped beam splitter pulses. For a given value of θ and a given quadruplet, i.e. a 1 mm.s^{-1} wide velocity box labeled by the value of its velocity center Δv (in mm.s^{-1}), we plot the imprinted phase difference between the doublet A (in green in Figure 5.26) and the doublet B (in red in Figure 5.26), averaged over the velocity range of the box. The error bars are given by the standard deviation of the imprinted phase difference within the box.

Thanks to pulse shaping, we have successfully designed pulse profiles that meet our initial specifications: flat reflectivity and imprinted phase across multiple quadruplets. Phase control is finely ensured by a parameter that is experimentally easy to manipulate. Therefore, these pulses can be used to simulate the Bell experiment to determine the correlator that can be achieved with these pulses.

5.3.4 Oscillation of the Bell correlator

The next step involves simulating a Hong-Ou-Mandel experiment. Indeed, experimentally, we will begin by conducting an HOM experiment to determine the timings ensuring the closure of the interferometer. As discussed before, if this condition is not met, the phase of the correlator will exhibit phase terms that potentially vary rapidly with the

detuning, i.e., with the velocity class considered. This could degrade the quality of the phase control we aim to achieve.

Since we have increased the pulse durations by switching to sinc-shaped pulses, new timings must be chosen for the interferometer. In the following, we will assume a free propagation duration of $T_1 = 1\,\mathrm{ms}$ between the start of the interferometer and the mirror. It is worth noting that experimentally, the instant corresponding to the start of the interferometer is not clearly defined since the pair creation process takes several hundred microseconds, which highlights the importance of conducting a HOM experiment.

Thus, we consider a sinc mirror of $T_\mathrm{M} = 1\,\mathrm{ms}$ duration with a Rabi frequency of 5 kHz, and a sinc beam splitter (at a single frequency) of the same duration and Rabi frequency (with the idea of conducting afterwards a Bell experiment using a Bell two-frequency splitter that also lasts 1 ms, even if the amplitude and profile are different).

We proceed like in section 5.1.2 to simulate a HOM experiment: given an interferometric sequence corresponding to a certain delay for the beam splitter, we calculate the probability $\mathcal{P}_{+-}$ of measuring two atoms in two different output modes as a function of the velocity class, and average the result over a box centered on $\Delta v = 0$. By varying the beam splitter delay, or equivalently, the free propagation time T_2, we can then observe a HOM dip when the interferometer is closed.

Note that, since we are not using constant pulses, we no longer have an analytical expression for the correlator phase and, consequently, for the joint probabilities. Similar to a Bell calculation, we perform a numerical resolution of the Bragg coupled equations 5.29 for each considered doublet. We then calculate the two-particle output state and, subsequently, the joint detection probabilities.

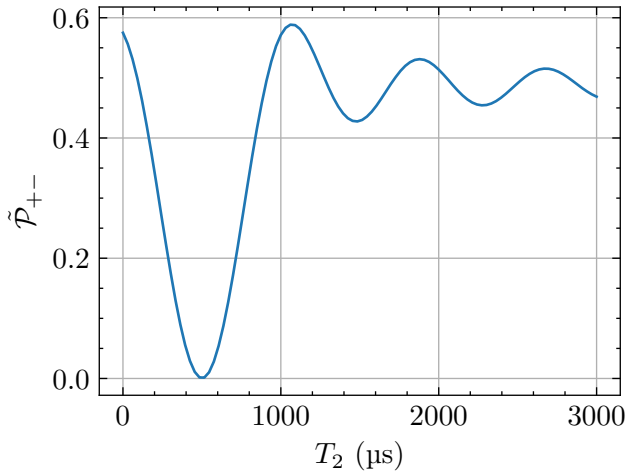

Figure 5.28: Simulation of the HOM experiment with sinc-shaped pulses. The input state is symmetrized to describe two indistinguishable particles. We calculate, for a given delay of the HOM beam splitter, the joint probability of measuring an atom in each output mode $\mathcal{P}_{+-} = \mathcal{P}(p,-q) + \mathcal{P}(q,-p)$ as a function of the velocity class using $\delta = -k_\mathrm{B}\Delta v$, and average it over a velocity box of width $\Delta = 2.5\,\mathrm{mms}^{-1}$, centered on resonance, to get $\tilde{\mathcal{P}}_{+-}$. The duration of the first free propagation is $T_1 = 1\,\mathrm{ms}$, as well as the duration of each pulse. The Rabi frequency of each pulse is $\Omega_\mathrm{M} = 5\,\mathrm{kHz}$.

Interestingly, we observe a HOM dip for a duration $T_2 = 500\,\mu\mathrm{s}$. This precisely corresponds to the delay for which the center of the beam splitter and the initial instant are symmetrical with respect to the center of the mirror: the closure condition involves the center of the pulses. We had previously demonstrated for a constant pulse that the delay

between the initial instant and the center of the mirror pulse was not exactly equal to the delay between the center of the mirror and the midpoint of the beam splitter.

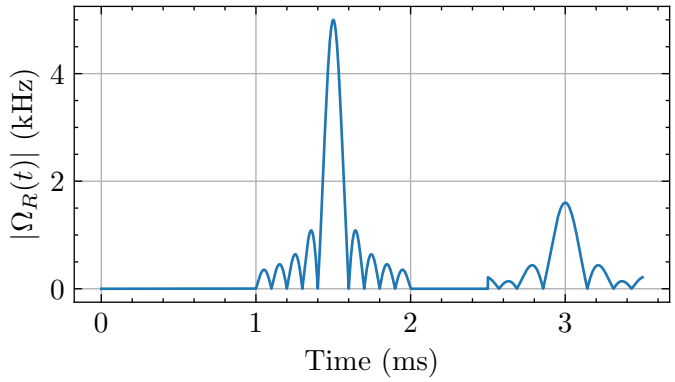

Figure 5.29: Absolute value of the two-photon Rabi frequency used for the Bell interferometer as a function of time. The first propagation duration is $T_1 = 1\,\text{ms}$, while the second propagation duration is $T_2 = 0.5\,\text{ms}$. The mirror is a 1 ms long sinc-shaped pulse of Rabi frequency $\Omega_\text{M} = 5\,\text{kHz}$, the beam splitter is a 1 ms long modulated sinc-shaped pulse of Rabi frequency $\Omega_\text{M} = 0.8\,\text{kHz}$, with a modulation frequency $\Omega_\text{D} = 1.3\,\text{kHz}$.

One can then use these timings to simulate the Bell experiment, this time using a two-frequency pulse. The interferometric sequence is depicted in Figure 5.29 for $\theta = 0$. We calculate the Bell correlator with respect to the velocity class for different values of θ (Figure 5.30).

We can observe that the correlator varies less on the scale of a box than in the case of square pulses, which will enhance the amplitude of the correlator oscillation as well as the signal-to-noise ratio. Again, the sinc-shaped mirror did not significantly improve reflectivity, as previously noted, and this is reflected in the observation that once again, the dynamics of the correlator evolution with velocity are dictated by interferences with transmitted atoms as one moves away from $\Delta v = 0$.

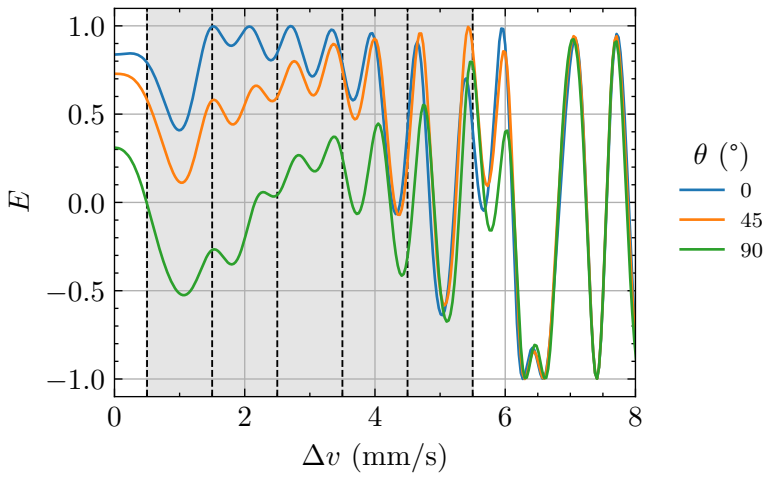

Figure 5.30: Bell correlator as a function of the velocity class for different values of the control parameter θ. The Bell correlator is computed for the interferometric profile represented in Figure 5.29.

Now, let us plot the oscillation of the Bell correlator as a function of θ, which was the main goal of the two previous chapters. The results of the simulation are given in Figure 5.31. We can observe a clear oscillation of the Bell correlator as a function of θ for all five quadruplets. This oscillation is much closer to a cosine function than what was observed with the square pulses. The amplitude of the oscillation remains good for the five considered quadruplets, or at least for the first three. Beyond that, we are affected by the poor reflectivity of the mirror, leading to a decrease in reflectivity and, consequently, a reduction in the contrast of the oscillations. Additionally, there is an increase in transmitted atoms that interfere with the useful signal, resulting in a decrease in the signal-to-noise ratio. However, the sinc-shaped pulses have still highlighted very favorable conditions for demonstrating a violation of Bell inequalities.

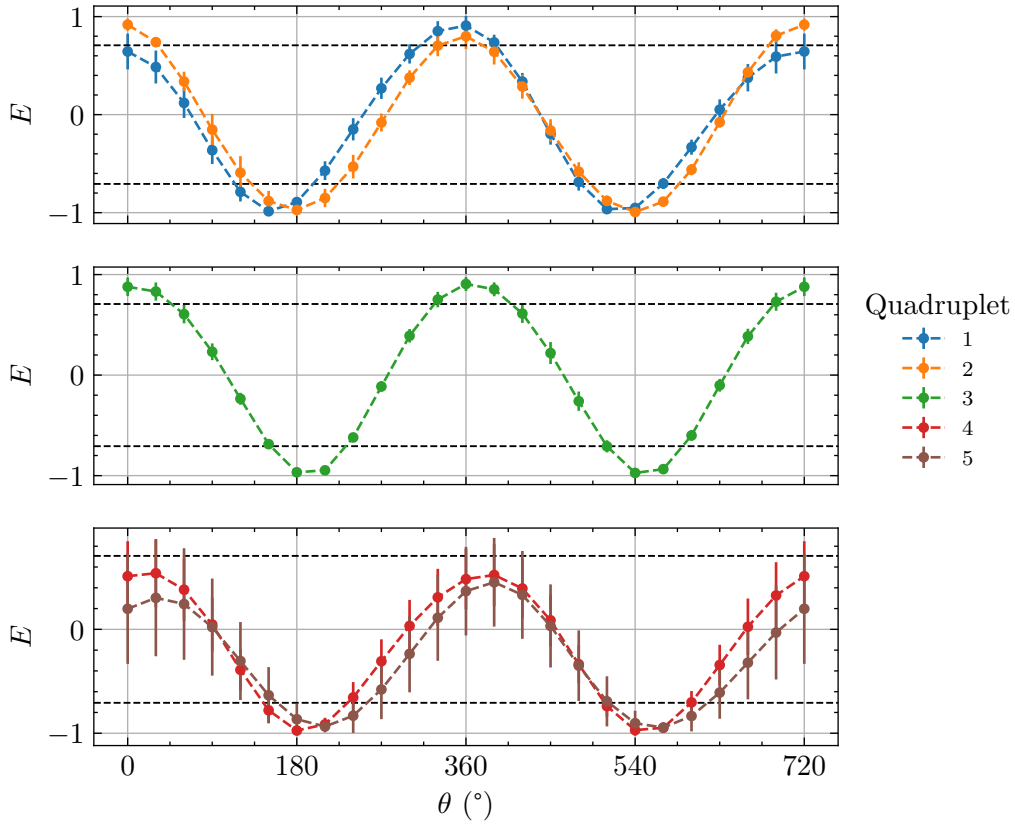

Figure 5.31: Oscillation of the Bell correlator as a function of the control parameter θ for sinc-shaped pulses. For a given value of θ, we compute the correlator E as a function of the velocity class, as shown in Figure 5.30. Then, we average its value within a velocity box corresponding to a quadruplet, labeled by the value of its center Δv (in mm.s^{-1}). The error bars equal the standard deviation of the Bell correlator within the corresponding integration box.

It is worth noting that, a priori, averaging all quadruplets together to improve the signal-to-noise ratio may not be possible. Indeed, the results of the off-resonance HOM experiment for measuring the Bell correlator as a function of the velocity class have shown that there might be an additional phase ϕ_0 for each quadruplet that we did not consider here. This would shift the oscillations of each correlator relative to the others. Nevertheless, if we manage to spot several quadruplets for which there is a clear oscillation of the Bell correlator, we could consider averaging these results (after recentering them on the same phase at the origin) depending on the oscillation amplitude, in order to enhance the signal-to-noise ratio during the measurement of the optimal Bell parameter S.

Again, it is possible to numerically determine the values of θ which will optimize S for a given correlator. Knowing $E(\theta)$, we calculate S for every set of phases $(\phi_{A1}, \phi_{A2}, \phi_{B1}, \phi_{B2})$ by path of 5° and between 0° and 355° on the one hand, and 360° and 715° on the other hand. The highest values are given in Table 5.4.

Quadruplet	$S_{\max}$	θ_1	θ_2	θ_3	θ_4	S_{th}
1	2.56 ± 0.18	390°	490°	650°	390°	2.33 ± 0.25
2	2.52 ± 0.16	680°	590°	405°	675°	2.44 ± 0.20
3	2.78 ± 0.14	325°	225°	60°	320°	2.55 ± 0.15
4	1.87 ± 0.52	425°	520°	690°	425°	1.75 ± 0.54
5	1.46 ± 0.76	435°	510°	360°	435°	1.01 ± 0.94

Table 5.4: Values for the Bell parameter.

The results indicate that with sinc-shaped pulses, three quadruplets would now yield a Bell parameter exceeding 2. The maximum value of S, obtained for the quadruplet centered on 3 mm.s^{-1}, is 2.78, which is very close to the maximum value of $2\sqrt{2}$. More importantly, due to the correlator's reduced variation with the velocity class for each quadruplet, the error bars on S have been reduced by a factor of 2 compared to square pulses, potentially enhancing the accuracy of the measurement.

Thus, it has been observed that the pulse shaping technique has improved the performances of the Bragg pulses, especially the beam splitter, leading to a correlator oscillation whose sinusoidal shape is closer to the theoretically expected one. The amplitude of this oscillation may result in S measurements very close to $2\sqrt{2}$, suggesting that these pulses could unequivocally highlight a Bell inequality violation.

Chapter 6

Experimental preparation of the Bragg pulses: interferometric experiments

6.1 Setup of the Bragg pulses . . . 220
6.1.1 Optical setup . . . 220
6.1.2 Alignment and two-photon resonances . . . 221
6.1.3 Compensating gravity . . . 222
6.1.4 Rabi oscillations . . . 223
6.1.5 Bragg diffraction in the Kapitza-Dirac regime . . . 225
6.1.6 Experimental setup for the pulses shaping . . . 226
6.2 Ramsey interferometer . . . 228
6.2.1 Principle . . . 228
6.2.2 Calculation . . . 229
6.2.3 Experimental results . . . 234
6.2.4 Phase shifter calibration . . . 237
6.3 Shaped Bragg pulses . . . 239
6.3.1 Sinc pulses . . . 239
6.3.2 Shaped pulse equivalent time . . . 243
6.3.3 Modulated pulses . . . 245
6.3.4 Phase control . . . 247
6.4 Mach-Zehnder gravimeter . . . 250
6.4.1 Principle . . . 250
6.4.2 Gravity measurement attempt . . . 251
6.5 Conclusion and outlook . . . 253

This chapter is dedicated to the experimental implementation of the Bragg beams and the description of interferometric measurements that were realized as proofs of principle. The majority of the results presented in this chapter were obtained from April to August 2023 (see Appendix A).

In a first section, we describe the implementation of the experimental setup for the pulse shaping. To calibrate the phase shifter and ensure that the correct phase is imprinted onto the atoms, we conduct a series of Ramsey-type interference experiment, which involve two successive beam splitter pulses, such that the interference pattern between two overlapping BECs allows us to determine the relative phase between them. This experiment enables us to calibrate the phase shifter and ensure the proper functioning of the phase control achieved by modulating the two-photon Rabi frequency. The performance of sinc-shaped pulses will be compared to square pulses by transferring atoms from a BEC in the magnetic trap. Finally, we conduct a Mach-Zehnder interferometer to ensure that the sinc-shaped pulses can lead to the observation of interferences.

6.1 Setup of the Bragg pulses

In this section, we will briefly present the procedure used to set up the Bragg beams.

6.1.1 Optical setup

As for Raman beams, we use the 1083 nm laser diode locked 400 MHz away from the $2^3S_1 \rightarrow 2^3P_0$ transition by a saturation absorption spectroscopy setup using a helium discharge cell. The beam is amplified by a 1 W fiber amplifier and further red-detuned from the atomic resonance by an additional 200 MHz through a first Acousto-Optic Modulator (AOM), which acts as a gate for Bragg and Raman light. An optical fiber carries the beam to a breadboard which is described in Figure 6.1.

Following the fiber, a polarization beam splitter splits the beam in two, such that one of them is used as a Raman beam. A beam sampler then takes 8% of the power of the remaining beam and sends it to a photodiode. Then, the beam is split again by two successive polarization beam splitters to form the second Raman beam on the one hand, and the two Bragg beams on the other hand. Each Bragg beam passes through an acousto-optical modulator which adds about 200 MHz detuning. The RF signal is sent to the AOMs by a 2-output Aim-TTI® TGF4242 signal generator which makes it possible to control the detuning and phase between the two beams. The two Bragg beams with an orthogonal polarization are then spatially recombined after a non polarizing beam splitter and directed towards the vacuum chamber, where they are once again separated before being sent to the atoms, with a relative angle $\theta_B \approx 32\,^\circ$ along the vertical axis. Just before their separation, a portion of the power is used to observe the beating between the two beams on a photodiode. The whole point of this optical setup is to make sure that the optical path taken by each beam is as much as possible the same so that the dephasing between the two is minimal.

The waists of the beams are the same, equal to 2.8 mm and the power of the beams is chosen to be equal. The detuning to the atomic transition is $\Delta = 800$ MHz since the light passes successively through four 200 MHz AOMs. The polarization axis is determined by a bias magnetic field which shifts the $m = \pm 1$ magnetic levels by a few MHz.

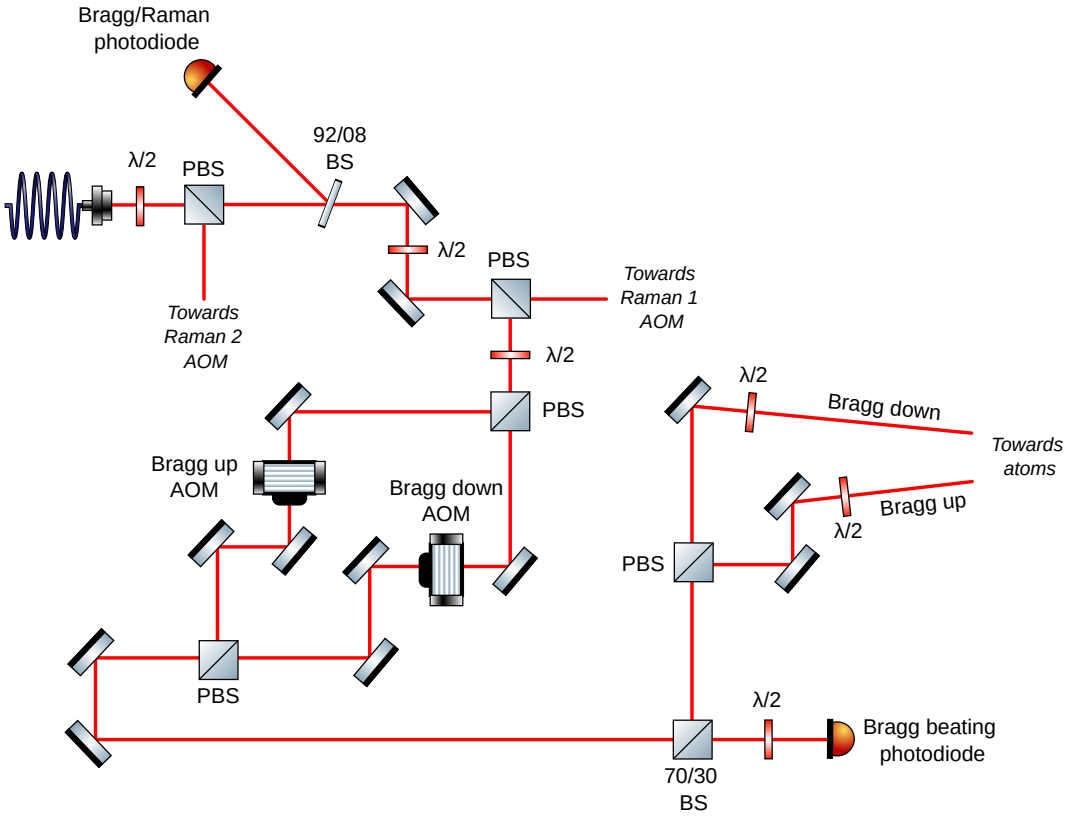

Figure 6.1: Optical setup for the Bragg beams. AOM stands for Acousto-Optic Modulator, PBS (respectively BS) stands for Polarizing Beam-Splitter Cube (respectively Beam-Splitter Cube).

6.1.2 Alignment and two-photon resonances

To achieve initial alignment for each beam, a long and powerful Bragg pulse (typically a few tenths of milliseconds and a few mW) is directed to the atoms from the magnetic trap, in order to transfer them in non-trapped states by spontaneous emission, thus reducing the number of atoms in the trap. The temperature of the cloud used for the alignment is typically a few μK. This way, each beam is aligned by optimizing the number of atoms removed from the trap. Once the beams are pre-aligned, a two-photon transition towards the nth diffraction order should be observed for a detuning δ_{2n} corresponding to the equation derived in section 4.2.1:

$$\hbar\delta_{2n} = \hbar(\omega_1 - \omega_2) - \left(\frac{\hbar^2 k_{\mathrm{B}}^2}{2m}(2n+1) + \frac{\hbar k_{\mathrm{B}}}{m}p\right) \tag{6.1}$$

where p is the selected momentum along the vertical axis. In our case, at first the Bragg pulse is performed right after the atoms are released from the trap, which corresponds to a momentum $p = 0$. The atoms, initially in the 0 order diffraction, can then be transferred into the $2\hbar k = \hbar k_{\mathrm{B}}$ momentum state ($n = 0$), or into the $-2\hbar k$ momentum state ($n = -1$). The corresponding resonances are

$$(\omega_1 - \omega_2) = \pm\frac{\hbar k_{\mathrm{B}}^2}{2m} = \pm 2\pi \times 12.4\,\mathrm{kHz} \tag{6.2}$$

Experimentally, we obtain the resonances showed in Figure 6.2 by counting the atoms falling on the MCP as a function of time. Since the atoms transferred have a different speed $\pm\frac{\hbar k_{\mathrm{B}}}{m}$, they fall at a different time $t_{\pm 1} \approx t_0 \pm 5\,\mathrm{ms}$ (with $t_0 \approx 308\,\mathrm{ms}$), so counting the

atoms within a given time range makes it possible to distinguish the different diffraction orders and count the atoms number (up to a certain level because of the saturation of the detector when the atomic flux is too high).

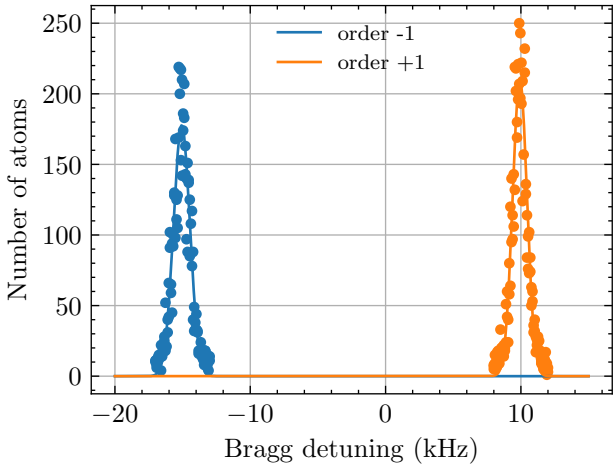

Figure 6.2: Bragg resonances towards orders ± 1. The figure is obtained for a Bragg pulse of $2\pi \times 500\,\mathrm{Hz}$ and $1\,\mathrm{ms}$. The relationship between the velocity and the detuning is given by $\Delta\delta = -k_\mathrm{B}\Delta v$.

Figure 6.2 shows that the resonance towards order -1 is $\delta_{-2} = -2\pi \times 15.1 \pm 0.1\,\mathrm{kHz}$, and the resonance towards order $+1$ is $\delta_{+2} = 2\pi \times 9.9 \pm 0.1\,\mathrm{kHz}$. Although the detuning difference between the two resonances corresponds to what is expected ($\delta_{+2} - \delta_{-2} = 2\pi \times 25.0\,\mathrm{kHz}$), the two resonances values are not symmetric. This resonance shift of $2.7\,\mathrm{kHz}$ suggests that the momentum of the atoms at the time of the Bragg pulse is about $3.4\,\mathrm{mm.s^{-1}}$ instead of zero.

Such an initial speed may be due to the fact that (1) the atoms are not at equilibrium in the optical dipole trap, leading to an initial speed when the trap is switched off, (2) the atoms are accelerated between the release of the trap and the Bragg pulse. The first hypothesis can be easily tested by varying the duration of the holding duration in the optical dipole trap, and it was found that the resonance is not affected. The second hypothesis is more likely, since the cloud, initially in the $m = 1$ magnetic level, can be accelerated due to a remnant magnetic field before being transferred in the $m = 0$ thanks to the Raman beams. A slight misalignment of the Raman beams could also be responsible for a momentum transfer along the vertical direction, and this is currently our main lead to explain the observed shift of the resonances.

6.1.3 Compensating gravity

During their fall, the atoms are accelerated due to gravity. This affects the resonance condition as a Doppler shift which needs to be taken into account: the detuning towards a given diffraction order then linearly depends on the time at which the Bragg pulse is sent to the atoms. In order to stay resonant with the atoms during their fall, a frequency sweep is applied to one of the Bragg beams so that the Doppler shift is compensated. At a given time t after the trap cutoff, the speed of the atoms (initially at zero speed) is $-gt$, therefore the resonance condition 6.1 is shifted by

$$\delta_\mathrm{Dopp} = -k_\mathrm{B} g t \tag{6.3}$$

To this end, we control the RF signal generator to add a frequency sweep on one of the RF signals sent to the Bragg AOMs. The slope α of the sweep is

$$\alpha = -gk_{\mathrm{B}} = -2\pi \times 4,87\,\mathrm{kHz.ms}^{-1} \tag{6.4}$$

In our standard use of the Bragg pulses, the resonance is typically a few kHz large. The previous equation shows that after 1 ms, the resonance has shifted by about 5 kHz, which shows how quickly the beam would be out of resonance without adding the frequency sweep.

Adding the sweep corresponds to placing the Bragg lattice formed by the interference of the two beams in an accelerated frame. It is worth noting that the slope of the chirp only depends on the Bragg momentum k_B and the value of the gravity acceleration g. Finding the right slope to compensate gravity is therefore a way of measuring g, and this is actually the principle of Mach-Zehnder gravimeters which will be discussed later in this manuscript (section 6.4).

Experimentally, we check that the sweep applied to the atoms is the right one by performing a series of Bragg resonance measurements like the one in Figure 6.2 at different times after the release of the trap, so that the detuning value for a given resonance remains the same independently of the Bragg delay[115].

Since the atoms cover a distance $z(t) = -\frac{1}{2}gt^2$ and the waist of the beams are $w = 2.8\,\mathrm{mm}$, it can be considered that the light intensity seen by the atoms remains the same for about 20 ms (for which $z(t) = 2\,\mathrm{mm}$), which gives an upper limit for the application of the Bragg pulse.

6.1.4 Rabi oscillations

It is possible to observe Rabi oscillations by scanning the duration of a pulse resonant with a given diffraction order. Recall that the transfer probability $\mathcal{P}(t)$ is expressed as follows:

$$\mathcal{P}(t) = \frac{\Omega_{\mathrm{M}}}{\sqrt{\delta^2 + \Omega_{\mathrm{M}}^2}} \sin^2\left(\sqrt{\delta^2 + \Omega_{\mathrm{M}}^2}\,\frac{t}{2}\right) \tag{6.5}$$

where δ is the detuning, and Ω_{M} the amplitude of the (constant) two-photon Rabi frequency. At resonance, in particular, the number of diffracted atoms should oscillate as a function of the Bragg duration with the best contrast. By defining the transfer efficiency $\eta_B = N_0/(N_0 + N_{\mathrm{d}})$, where N_0 and N_{d} are respectively the number of atoms in the BEC and the number of atoms in the diffracted order, we have

$$\eta_{\mathrm{B}}(t) = \sin^2\left(\frac{\Omega_{\mathrm{M}}\,t}{2}\right) \tag{6.6}$$

Figure 6.3 shows a Rabi oscillation between the diffraction orders 0 and 1. Experimental data are fitted with a damped oscillating function $f(t) = A\sin^2(2\pi f_0 t)\exp(-t/\tau)$. The exponential decay comes from any decoherence effect which is not included in the Rabi 2-level model.

We find in this example that the amplitude of the two-photon Rabi frequency is $\Omega_{\mathrm{M}} = 2\pi \times 1.21 \pm 0.9\,\mathrm{kHz}$. The transfer efficiency is $99.6 \pm 0.5\,\%$ after a π pulse. In

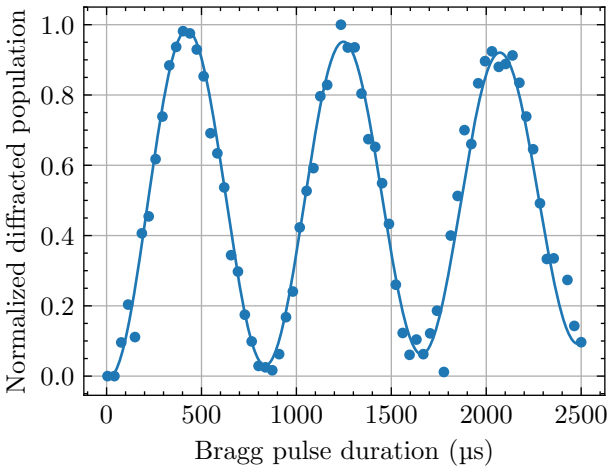

Figure 6.3: Rabi oscillations. The normalized diffracted population correspond to the number of atoms N_1 detected in a 0.5 mm.s^{-1} box centered on the second diffraction order, normalized by the $N_0 + N_1$ where N_0 is the number of atoms detected in a 0.5 mm.s^{-1} box centered on the BEC.

this configuration, a Bragg mirror would correspond to a pulse duration of 413 µs while a 50/50 splitter would correspond to a pulse duration of 207 µs.

For a 2.5 ms long pulse with a two-photon Rabi frequency of 1.21 kHz, the full width at half maximum of the resonance is of the order of 1.5 kHz, which corresponds to 3 mm/s. In order to plot the result from Figure 6.3, only a small part of the full momentum distribution was selected, that is to say the atoms were counted within boxes of 0.5 mm/s size in momentum separated by $\hbar k_{\mathrm{B}}$. Otherwise, counting the atoms within boxes containing the whole momentum distribution of the BEC would correspond to averaging over momentum classes which are not all at resonance with the pulse, leading to a higher damping as well as a decrease in the fitted two-photon Rabi oscillation.

The typical damping time is $\tau = 11.6 \pm 1.3$ ms from Figure 6.3, partly attributed to spontaneous emission. Indeed, the spontaneous emission rate for a two-level system is

$$\Gamma_{\mathrm{sp}} = \frac{\Gamma}{2} \frac{s}{1+s} \tag{6.7}$$

with $s = \dfrac{1}{2} \dfrac{|\Omega|^2}{\Delta^2 + \Gamma^2/4}$ the saturation parameter, where Ω is the (one-photon) Rabi frequency, Γ the natural width of the excited state. In our case, assuming that both beams have the same intensity, the one-photon Rabi frequency is $\Omega = \sqrt{2\Delta\Omega_{\mathrm{M}}}$. The spontaneous emission rate towards one specific magnetic sub-level must also be multiplied by 2 since there are two π beams to consider, and by 3 since there can be spontaneous emission towards the three magnetic sub-levels. Finally, we find $s = 1.51 \times 10^{-6}$ and therefore $\Gamma_{\mathrm{sp}} = 46.2\,\mathrm{s}^{-1}$, leading to $\tau_{\mathrm{sp}} = 21.6$ ms. There is still a factor of 2 with the measured value, which suggests that there may be other decoherence effects which cause the observed damping. Still, the typical decoherence time is high compared to the duration of a π or $\pi/2$ Bragg pulse of a few kHz.

These results are very encouraging and even better than what was reported by A. Imanaliev[147], PhD student in the team at the time of the first HOM experiment, who

found a decoherence time of 5.2 ms and a transfer efficiency of 95%.

6.1.5 Bragg diffraction in the Kapitza-Dirac regime

In order to measure precisely the Bragg momentum as well as checking the vertical alignment of the beams, it is possible to perform Bragg diffraction in a specific regime of short and intense pulses called the Kapitza-Dirac regime. The idea is the following: in these specific conditions, the resonance of the Bragg diffraction is very large in terms of momentum, which means that the BEC will be resonant with several diffraction orders, leading to the emission of multiple clouds, each having a momentum separated by $\hbar k_{\mathrm{B}}$. This way, one can check the velocity of every diffracted cloud, which makes it possible to precisely measure the Bragg velocity transferred to the atoms along the vertical direction. Note that this is also a way to verify the alignment of the beams, because if the Bragg beams are not perfectly aligned along this axis, there will also be a momentum shift along the other directions.

Figure 6.4b shows the results obtained with an intense pulse of 10 µs. One can see 7 diffraction orders, whose intensity is modulated by a Bessel envelop $|J_n(\Omega_{\mathrm{M}}t)|^2$, as shown in section 4.2.2.

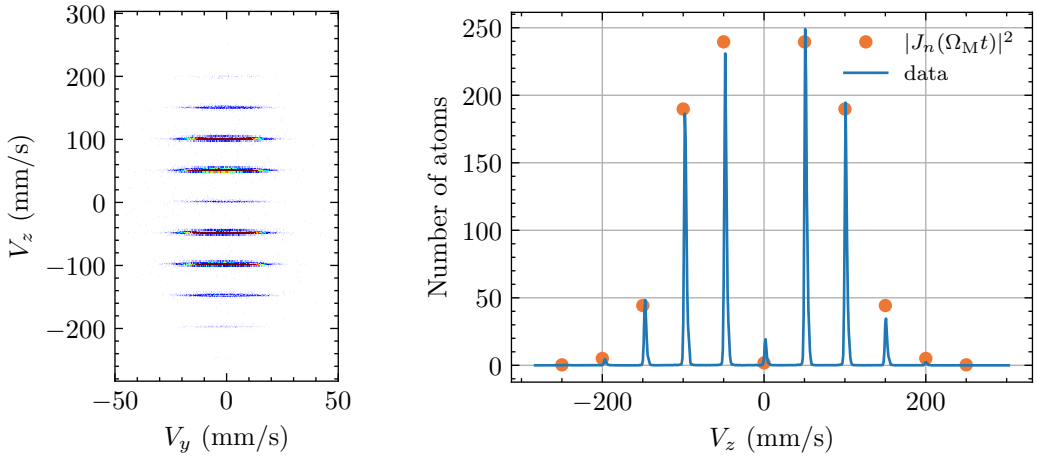

(a) 2D histogram.

(b) 1D histogram along z.

Figure 6.4: Bragg diffraction in the Kapitza-Dirac regime. Density profiles obtained for a 10 µs Kapitza-Dirac pulse. A fit on the diffraction orders is shown in orange, and gives a Rabi frequency of $\Omega_{\mathrm{M}} = 36.9 \pm 1.2\,\mathrm{kHz}$.

By fitting the momentum of each cloud in every direction, we find a Bragg speed

$$v_{\mathrm{B}} = \frac{\hbar k_{\mathrm{B}}}{m} = 49.58 \pm 0.03\,\mathrm{mm.s^{-1}} \tag{6.8}$$

The momentum fit in the others directions gives negligible relative angles of $\theta_x = -0.08 \pm 0.03\,^\circ$ and $\theta_y = -0.04 \pm 0.02\,^\circ$, which validates the alignment of the beams.

There is another way of measuring the Bragg velocity by transferring atoms into many diffraction orders. The idea is to realize a long Bragg pulse with a frequency sweep whose

slope such that the atoms, once transferred from the diffraction order 0 to the order 1, are at some point resonant again, this time with order 2 and thus partly transferred to this order, and so on. With this method, which is related to Bloch oscillations[167], we were able to observe up to 36 diffraction orders, transferring atoms from zero velocity to a maximum velocity of $1.5\,\mathrm{m.s^{-1}}$ in 4 ms. This process will not be described in this manuscript.

6.1.6 Experimental setup for the pulses shaping

As seen in the previous chapter, we want to implement the possibility to have a negative (or even complex) two-photon Rabi frequency by adding a phase between the two beams. To this end, we use a Mini-Circuits® SPHSA-251+ phase shifter, which adds a controllable dephasing between 0 and 180 ° on a RF signal. After an electronic calibration voltage-dephasing, the phase shifter is added on the RF voltage sent to one of the Bragg AOMs (Figure 6.5).

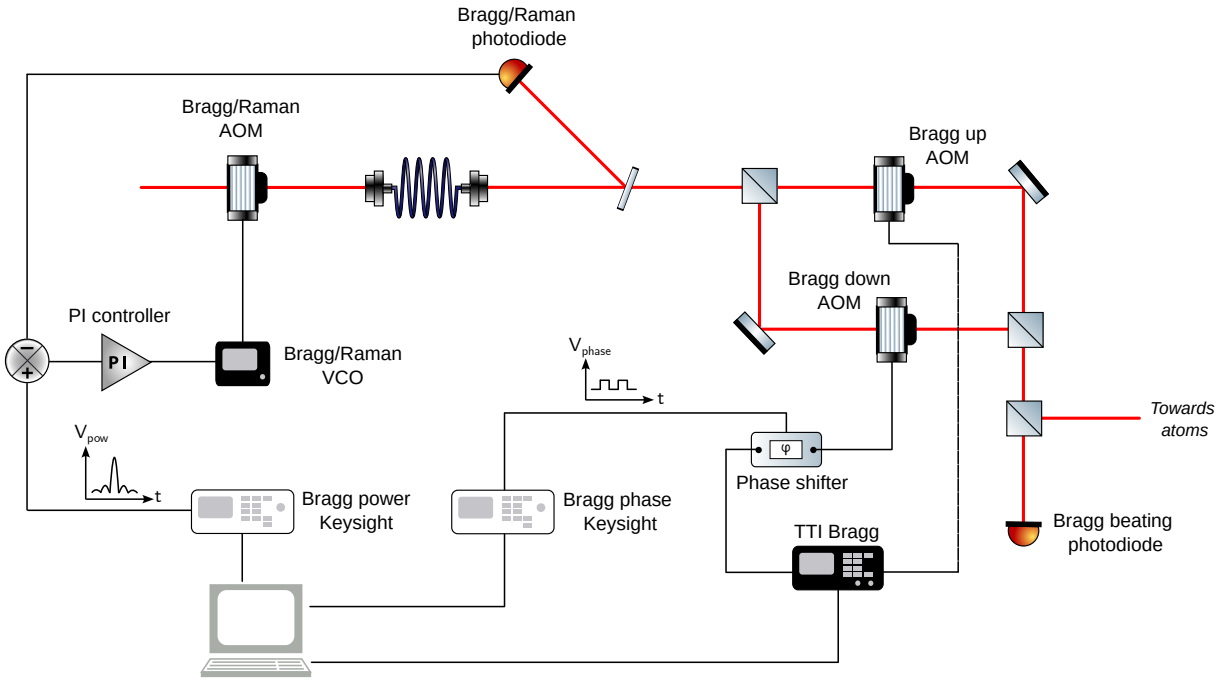

Figure 6.5: Experimental setup for the complex Bragg pulses.VCO stands for Voltage Controlled Oscillator. Keysight® and TTI® are the brands of the devices.

As we also want to shape the Bragg pulse, the power of the Bragg laser must be locked on a reference signal because of the non-linearity of the power control of a beam by a Voltage-controlled oscillator. We chose to shape the intensity of the laser by locking the signal from the Bragg-Raman photodiode to a setpoint voltage signal. We therefore use a Proportional-Integral (PI) controller after comparing the Bragg photodiode feedback with the setpoint signal. Then, the output of the corrector is used as input for the VCO which sends the RF signal to the Bragg-Raman AOM. The voltage setpoints for both Bragg up and Bragg down AOMs remain constant and maximal during the pulse.

The Bode plot of the power feedback loop is provided in Figure 6.6, showing that the power closely follows the setpoint as long as the frequency remains below 50 kHz. Beyond this point, the phase lag between the input and output signals begins to increase, and the output signal amplitude also rises until it becomes completely distorted around 100 kHz.

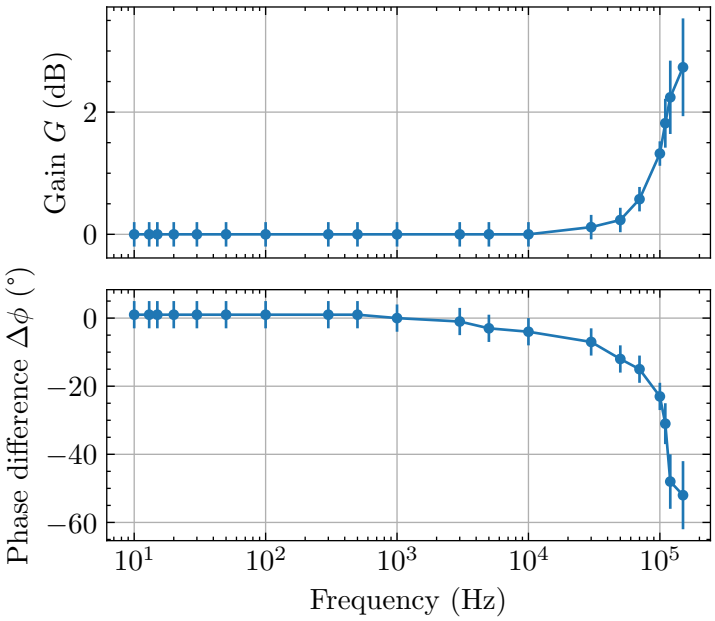

Figure 6.6: Bode diagram of the power feedback loop. Results obtained using sinusoidal signals. The gain is defined by $G = 20 \log \frac{A_{\text{out}}}{A_{\text{in}}}$ where A_{in} and A_{out} are the oscillation amplitudes of the input and output signals, respectively. $\Delta\phi$ is the phase difference between these two signals.

The voltage setpoint for the Bragg-Raman power as well as the phase shifter setpoint are generated numerically as lists of points, which are sent by SCPI (Standard Commands for Programmable Instruments) to two Agilent® signal generators with a maximum of 80000 points. Both devices are triggered at the same time by a logical signal of the ADWIN® controller when a Bragg pulse is sent to the atoms.

For instance, the voltage setpoint and the phase shifter setpoint are plotted in Figure 6.7 for a 1.5 ms long sinc shaped Bragg beam splitter pulse of 5 kHz. The parameters of the waveform were determined in section 5.3. The expected Bragg two-photon Rabi frequency is

$$\Omega_{\text{R}}(t) = \Omega_{\text{M}} \operatorname{sinc}\left(\Omega_{\text{S}}(t - T/2)\right) \tag{6.9}$$

where $t = 0$ is the beginning of the pulse and T its duration. Recall that in order to have a beam splitter, we need to have $\Omega_{\text{S}} = 2\,\Omega_{\text{M}}$. In our case, in order to imprint the waveform to the laser beams, the power setpoint needs to correspond to the absolute value of the signal, and the phase shifter must add a dephasing of π each time the two-photon Rabi frequency becomes negative.

Now remains the question of the calibration. Regarding the voltage setpoint, getting the relation between the voltage setpoint and the effective two-photon Rabi frequency is easy as one only needs to send a constant pulse and make Rabi oscillations, which gives immediately the Rabi frequency. Besides, the relation between the two quantities is linear because the two-photon Rabi frequency is proportional to the power of the beam.

Regarding the calibration of the phase shifter setpoint, it is easy to get an electronic calibration curve by comparing the phase of an input RF signal with the output signal. But finding a way to check that the phase imprinted on the atoms depends indeed on the

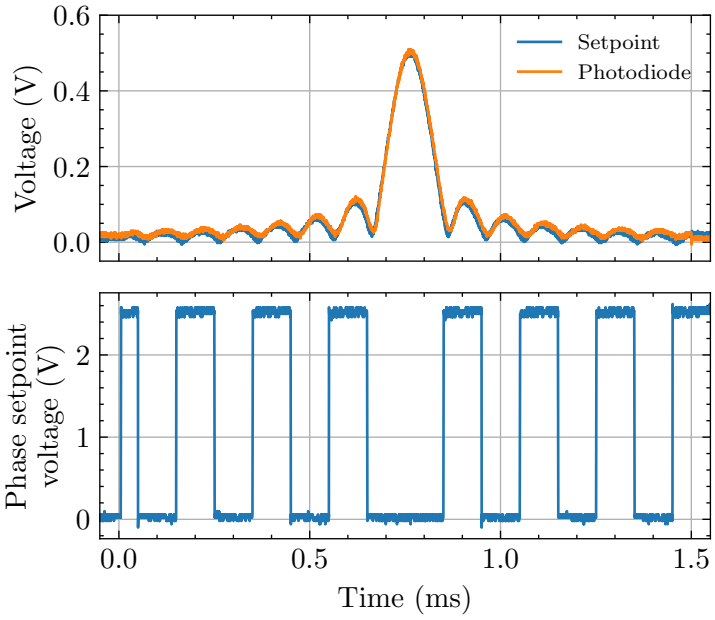

Figure 6.7: Voltage setpoints and measurement of the optical power (top) and phase shifter setpoint (bottom) for a sinc-shaped Bragg pulse.

voltage setpoint of the phase shifter would represent a valuable advantage.

In order to be able to evaluate the phase imprinted on the atoms using the phase shifter, an interference experiment is needed.

6.2 Ramsey interferometer

6.2.1 Principle

The idea of this experiment is to superpose two clouds which do not have the same phase, and which will therefore interfere. To do so, we perform two successive Bragg 50/50 splitters pulses ($\pi/2$ pulses resonant with the BEC) after the atoms are released from the trap (Figure 6.8). This interferometric scheme using two successives $\pi/2$ pulses is named a Ramsey interferometer.

The first splitter makes a copy of the first cloud by transferring half the atoms (with initial momentum p) to a momentum state $p + \hbar k_{\mathrm{B}}$. Then a second splitter also makes a copy of each cloud, so that in the end there are two clouds falling with momentum p and two clouds falling with momentum $p+\hbar k_{\mathrm{B}}$. If the duration between the two pulses is small enough, the two clouds with the same velocity overlap on the MCP and interfere along the vertical direction, because due to gravity they did not accumulate the same phase between the two splitters. This results in an interference pattern as a function of the arrival time on the MCP.

The observed interfringe should only depend on g and the duration τ between the two pulses. Now, one should not forget that there is also a phase imprinted on the reflected atoms by the Bragg splitter. We will show in the next section that a relative phase between the two beam splitters results in shifting the interference pattern along the vertical direction.

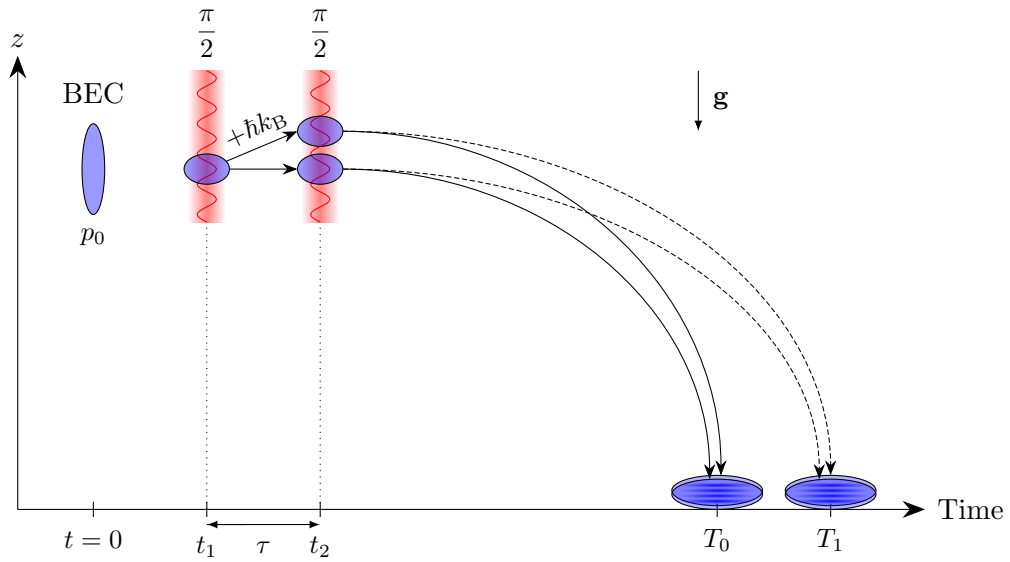

Figure 6.8: Principle of the Ramsey interferometer. Starting from a BEC, two successive Bragg beam splitters are applied to the atoms, resulting in four output clouds. Two clouds with the same momentum will interfere on the MCP after time of flight when they overlap.

Assuming that the phase imprinted by the Bragg splitter to the reflected atoms remains the same for both splitters, then the interference pattern should not shift from one experimental run to the other, and the contrast of the interference is expected to be optimal in these conditions.

On the contrary, if the imprinted phase by the Bragg lasers varies between the two pulses, then it will result in shifting the interference pattern. Since this variation is unwanted and uncontrolled (it may be due to an optical path difference between the two beams, caused for instance by the vibration of a mirror) it is reasonable to assume that it would result in a random shift in the interference pattern between each run, which will lead to a decrease of contrast after averaging over many experimental runs.

This last point has two important consequences:

- First, averaging over many runs will make it possible to determine the phase stability of the beam splitter between the two pulses, separated by typically a few ms, which corresponds to the timescale of the Bell interferometer. Let us note that this only gives an information about the phase difference stability over a few milliseconds.
- Second, using a phase shifter allows us to imprint a different phase between the first and the second pulse, only by adding a constant voltage setpoint between the two. This way, we can calibrate the phase shifter on the atoms by measuring the shift in the interference pattern (which corresponds to the phase difference imprinted to the atoms between each pulse) as a function of the voltage setpoint.

6.2.2 Calculation

In this section, we will reuse the formalism introduced in Chapter 4 to describe interferometers. The Ramsey interferometer is particularly noteworthy in that it is not a closed interferometer, as we will see, resulting in the appearance of a phase term related to the propagation of wave packets to the MCP.

First, let us consider the interferometer depicted in Figure 6.9. We neglect the duration of the Bragg pulses and focus only on the resonant case. Let us calculate first the phase terms related to the light-matter interaction during the Bragg pulses.

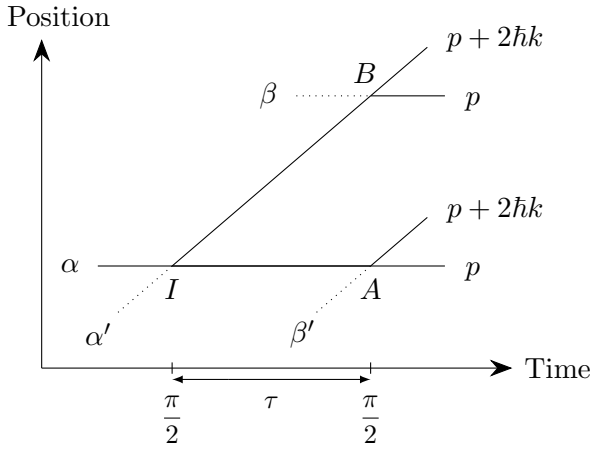

Figure 6.9: Momentum modes involved in the Ramsey interferometer.

This interferometer involves two momentum modes, p and $p + 2\hbar k$, each of which, at the interferometer output, is found in two different spatial modes. Like in section 4.4.1 with the Mach-Zehnder interferometer, we will separately describe each mode, indicating them by α, α', β and β'. The first beam splitter thus couples $(p)_\alpha$ and $(p + 2\hbar k)_{\alpha'}$, while the second beam splitter couples modes $(p)_\alpha$ and $(p+2\hbar k)_{\beta'}$ in A and $(p)_\beta$ and $(p+2\hbar k)_{\alpha'}$ in B. We can thus write, for the first beam splitter:

$$\begin{pmatrix} C_{0,\alpha}(t) \\ C_{2,\alpha'}(t) \\ C_{0,\beta}(t) \\ C_{2,\beta'}(t) \end{pmatrix} = \frac{\sqrt{2}}{2} \begin{pmatrix} 1 & \mathrm{i}e^{\mathrm{i}\phi_1} & 0 & 0 \\ \mathrm{i}e^{-\mathrm{i}\phi_1} & 1 & 0 & 0 \\ 0 & 0 & 0 & 0 \\ 0 & 0 & 0 & 0 \end{pmatrix} \begin{pmatrix} C_{0,\alpha}(0) \\ C_{2,\alpha'}(0) \\ C_{0,\beta}(0) \\ C_{2,\beta'}(0) \end{pmatrix} \tag{6.10}$$

where ϕ_1 is the phase imprinted by the first pulse. This defines the matrix U_{S1} of the first beam splitter. In the same basis, the second beam splitter matrix writes

$$U_{\mathrm{S2}} = \frac{\sqrt{2}}{2} \begin{pmatrix} 1 & 0 & 0 & \mathrm{i}e^{\mathrm{i}\phi_{2A}} \\ 0 & 1 & \mathrm{i}e^{-\mathrm{i}\phi_{2B}} & 0 \\ 0 & \mathrm{i}e^{\mathrm{i}\phi_{2B}} & 1 & 0 \\ \mathrm{i}e^{-\mathrm{i}\phi_{2A}} & 0 & 0 & 1 \end{pmatrix} \tag{6.11}$$

Let us consider an input state for which $C_{0,\alpha}(0) = 1$ while the other modes are not populated. After the first beam splitter, the state is

$$\begin{pmatrix} C_{0,\alpha} \\ C_{2,\alpha'} \\ C_{0,\beta} \\ C_{2,\beta'} \end{pmatrix} = \frac{\sqrt{2}}{2} \begin{pmatrix} 1 \\ \mathrm{i}e^{-\mathrm{i}\phi_1} \\ 0 \\ 0 \end{pmatrix} \tag{6.12}$$

Then, both clouds accumulated a phase related to the propagation of the wavepackets in different paths and at different velocities. Let us write $\phi_{\text{path},A}$ and $\phi_{\text{path},B}$ these propagation phases. Before the first second splitter, the state is therefore

$$\begin{pmatrix} C_{0,\alpha} \\ C_{2,\alpha'} \\ C_{0,\beta} \\ C_{2,\beta'} \end{pmatrix} = \frac{\sqrt{2}}{2} \begin{pmatrix} \mathrm{e}^{\mathrm{i}\phi_{\text{path},A}} \\ \mathrm{i}\mathrm{e}^{-\mathrm{i}\phi_1}\mathrm{e}^{\mathrm{i}\phi_{\text{path},B}} \\ 0 \\ 0 \end{pmatrix} \tag{6.13}$$

Using U_{S2}, we can now determine the state ofthe system after the second beam splitter:

$$\begin{pmatrix} C_{0,\alpha} \\ C_{2,\alpha'} \\ C_{0,\beta} \\ C_{2,\beta'} \end{pmatrix} = \frac{1}{2} \begin{pmatrix} \mathrm{e}^{\mathrm{i}\phi_{\text{path},A}} \\ \mathrm{i}\mathrm{e}^{-\mathrm{i}\phi_1}\mathrm{e}^{\mathrm{i}\phi_{\text{path},B}} \\ -\mathrm{e}^{\mathrm{i}(\phi_{2B}-\phi_1)}\mathrm{e}^{\mathrm{i}\phi_{\text{path},B}} \\ \mathrm{i}\mathrm{e}^{-\mathrm{i}\phi_{2A}}\mathrm{e}^{\mathrm{i}\phi_{\text{path},A}} \end{pmatrix} \tag{6.14}$$

This time, we cannot stop the calculation here, since the modes with the same velocity interfere after time of flight when they overlap. We need to take into account the propagation phases between the second beam splitter pulse and the arrival time of the clouds on the MCP, which is obviously not the same for the modes of different velocity.

Let us write T_0 the arrival time of the initial BEC center of mass, in the 0 diffraction order, and T_1 the arrival time of the center of mass of the diffracted atoms in the first diffraction order. If we neglect the fact that the initial position of the clouds with the same velocity is not exactly the same, we have the equations:

$$\begin{cases} z(T_0) &= z_0 - \dfrac{1}{2}gT_0^2 = 0 \\ z(T_1) &= z_0 - \dfrac{1}{2}gT_1^2 + v_{\text{B}}T_1 = 0 \end{cases} \tag{6.15}$$

If we write $T_1 = T_0 + \Delta T$, and neglect v_{B} compared to gt_0 after time of flight ($t_0 \approx 308\,\text{ms}$), we get from system 6.15 that $\Delta T = T_1 - T_0 = v_{\text{B}}/g$. In order to take into account all velocity classes and not only the center of mass, we will write T the arrival time of the atoms from the 0 diffraction order, whose histogram is a density envelop centered on T_0, and T' the arrival time of the atoms from the first diffraction order, whose histogram is a density envelop centered on T_1

The propagation phases accumulated after the second beam splitter differ for each mode, because the initial position and the velocity are not the same. The corresponding phases will be written $\phi^{(0)}_{A\to T}$, $\phi^{(0)}_{B\to T}$ for the atoms in modes p[1] and $\phi^{(2)}_{A\to T'}$, $\phi^{(2)}_{B\to T'}$ for the atoms in modes $p + 2\hbar k$. Finally, on the MCP, the state of the system is

$$\begin{pmatrix} C_{0,\alpha} \\ C_{2,\alpha'} \\ C_{0,\beta} \\ C_{2,\beta'} \end{pmatrix} = \frac{1}{2} \begin{pmatrix} \mathrm{e}^{\mathrm{i}\left(\phi_{\text{path},A}+\phi^{(0)}_{A\to T}\right)} \\ \mathrm{i}\mathrm{e}^{-\mathrm{i}\phi_1}\,\mathrm{e}^{\mathrm{i}\left(\phi_{\text{path},B}+\phi^{(2)}_{B\to T'}\right)} \\ -\mathrm{e}^{\mathrm{i}(\phi_{2B}-\phi_1)}\,\mathrm{e}^{\mathrm{i}\left(\phi_{\text{path},B}+\phi^{(0)}_{B\to T}\right)} \\ \mathrm{i}\mathrm{e}^{-\mathrm{i}\phi_{2A}}\,\mathrm{e}^{\mathrm{i}\left(\phi_{\text{path},A}+\phi^{(0)}_{A\to T'}\right)} \end{pmatrix} \tag{6.16}$$

[1] Or, strictly speaking, $p - mgt$.

After time of flight, the total population in modes p and $p+2\hbar k$ can then be expressed as

$$\begin{cases} |C_0|^2 = |C_{0,\alpha} + C_{0,\beta}|^2 = \sin^2\left(\dfrac{\Delta\Phi_0}{2}\right) \\ |C_2|^2 = |C_{2,\alpha'} + C_{2,\beta'}|^2 = \cos^2\left(\dfrac{\Delta\Phi_2}{2}\right) \end{cases} \tag{6.17}$$

where

$$\begin{cases} \Delta\Phi_0 = \phi_B - \phi_1 + \phi_{\text{path},B} - \phi_{\text{path},A} + \phi^{(0)}_{B\to T} - \phi^{(0)}_{A\to T} \\ \Delta\Phi_2 = \phi_A - \phi_1 + \phi_{\text{path},B} - \phi_{\text{path},A} + \phi^{(2)}_{B\to T'} - \phi^{(2)}_{A\to T'} \end{cases} \tag{6.18}$$

Each phase term can be calculated easily. Let us consider at first the phase imprinted by the lasers. Recall that each phase ϕ due to the interaction with light includes a term related to the center of mass of the wavepacket and another related to the phase difference between the lasers, such that

$$\begin{cases} \phi_1 = -k_{\text{B}} z_I + \Delta\varphi_1 + \alpha\dfrac{t_1^2}{2} \\ \phi_{2A} = -k_{\text{B}} z_A + \Delta\varphi_2 + \alpha\dfrac{t_2^2}{2} \\ \phi_{2B} = -k_{\text{B}} z_B + \Delta\varphi_2 + \alpha\dfrac{t_2^2}{2} \end{cases} \tag{6.19}$$

where z is the position of the center of mass of each wavepacket, $\Delta\varphi_1$ and $\Delta\varphi_2$ the laser phase differences during the first and the second beam splitter, respectively. α is the slope of the frequency ramp used to compensate gravity. and t_1 and $t_2 = t_1 + \tau$ the instant at which the Bragg pulses occur. Let us consider that the velocity of the cloud is v_0 (with $v_0 \approx 0$): we can deduce z_A and z_B such that

$$\begin{cases} z_A = z_I + v_0\tau - \dfrac{1}{2}g\tau^2 \\ z_B = z_I + (v_0 + v_{\text{B}})\tau - \dfrac{1}{2}g\tau^2 \end{cases} \tag{6.20}$$

From these expressions, we get

$$\begin{cases} \phi_B - \phi_1 = -k_{\text{B}}(v_0 + v_{\text{B}})\tau + \Delta\varphi_2 - \Delta\varphi_1 \\ \phi_A - \phi_1 = -k_{\text{B}} v_0\tau + \Delta\varphi_2 - \Delta\varphi_1 \end{cases} \tag{6.21}$$

So there is a difference of $-k_{\text{B}} v_{\text{B}}\tau$ between the two phases.

Now, let us consider the phase terms related to the propagation of the wave packets after time of flight. According to the results of Chapter 4, when two atoms fall with the same velocity from different initial position, the corresponding phase difference, for the two overlapping clouds in mode p, is given by:

$$\phi^{(0)}_{B\to T} - \phi^{(0)}_{A\to T} = \frac{m}{\hbar}\left(\frac{v_0^2}{2} + g z_B\right)T - \frac{m}{\hbar}\left(\frac{v_0^2}{2} + g z_A\right)T \tag{6.22}$$

from which we get

$$\phi^{(0)}_{B\to T} - \phi^{(0)}_{A\to T} = \frac{m}{\hbar} g T (z_B - z_A) = \frac{m}{\hbar} g T v_{\text{B}}\tau \tag{6.23}$$

where τ is the duration between the two Bragg pulses. Similarly, we have, for the overlapping clouds in modes $p + 2\hbar k$:

$$\phi^{(2)}_{B\to T'} - \phi^{(2)}_{A\to T'} = \frac{m}{\hbar} g T' (z_B - z_A) = \frac{m}{\hbar} g T' v_{\mathrm{B}} \tau \tag{6.24}$$

Thus, the atoms density, both in modes p and $p + 2\hbar k$, oscillates along the vertical axis since there is a phase term linearly dependent on the arrival time T (and T' for the diffracted clouds). The interfringe depends on the duration τ between the two beam splitter pulses.

Note that, if we consider the center of mass of each cloud, we have

$$\begin{cases} \phi^{(0)}_{B\to T_0} - \phi^{(0)}_{A\to T_0} = \dfrac{m}{\hbar} g T_0 v_{\mathrm{B}} \tau \\ \phi^{(2)}_{B\to T_1} - \phi^{(2)}_{A\to T_1} = \dfrac{m}{\hbar} g T_1 v_{\mathrm{B}} \tau = \dfrac{m}{\hbar} g \left(T_0 + \dfrac{v_{\mathrm{B}}}{g} \right) v_{\mathrm{B}} \tau = \dfrac{m}{\hbar} g T_0 v_{\mathrm{B}} \tau + k_{\mathrm{B}} v_{\mathrm{B}} \tau \end{cases} \tag{6.25}$$

The phase difference between the two is $+k_{\mathrm{B}} v_{\mathrm{B}} \tau$.

As a result, when we compare $\Delta\Phi_0(T_0)$ and $\Delta\Phi_2(T_1)$, the phase shift $k_{\mathrm{B}} v_{\mathrm{B}} \tau$ originating from the different arrival time of both clouds compensates exactly the term $-k_{\mathrm{B}} v_{\mathrm{B}} \tau$ which arised from the phase difference imprinted by the lasers as seen in equation 6.21. Thus, $\Delta\Phi_0(T_0) = \Delta\Phi_2(T_1)$, meaning that the population of the centers of mass of the two clouds at different velocities oscillate with opposite phase.

As a conclusion, if we consider (for instance) only the atoms in mode p, the population is given by

$$|C_0|^2 = \sin^2 \left(\frac{\Delta\Phi_0}{2} \right) \tag{6.26}$$

where

$$\Delta\Phi_0 = \frac{m}{\hbar} g T v_{\mathrm{B}} \tau + \Delta\varphi_2 - \Delta\varphi_1 + \phi_{\mathrm{prop,others}} \tag{6.27}$$

where $\phi_{\mathrm{prop,others}}$ is a term which encompasses the terms related to the propagation of the clouds that do not depend on the arrival time (but depend on τ).

Thus, when the atoms fall onto the MCP, we observe an population oscillation as a function of the arrival time T. This interference pattern is modulated by a density envelope representing the overlap between the two wave packets.

The atoms with momentum p do not arrive at the same time as the atoms with momentum $p + 2\hbar k$; therefore, we should observe two successive interfering clouds, each presenting an interference pattern whose interfringe T_{i} ultimately depends only on k_{B}, g and τ:

$$T_{\mathrm{i}} = \frac{2\pi}{k_{\mathrm{B}} g \tau} \tag{6.28}$$

A particularly interesting point for us is that the laser phase difference between the two Bragg beam splitters acts as a phase origin of the interference term: by changing this quantity, we can shift the interference pattern.

Note that the centers of the wave packets of each cloud are in phase opposition, so the number of atoms arriving at time t writes:

$$\begin{cases} N_p(T) & = A_0(T)(1 + \cos(k_{\mathrm{B}} g \tau (T - T_0) + \Delta\varphi_2 - \Delta\varphi_1)) \\ N_{p+2\hbar k}(T) & = A_1(T)(1 - \cos(k_{\mathrm{B}} g \tau (T - T_1) + \Delta\varphi_2 - \Delta\varphi_1)) \end{cases} \tag{6.29}$$

where, for each cloud, $A_0(T)$ and $A_1(T)$ are density envelopes centered on T_0 and T_1, respectively, which are the arrival times of the centers of each wave packet. Note that, if τ is too large, the two wave packets of same momentum start separating, resulting ultimately in a vanishing of the interference when they do not overlap.

6.2.3 Experimental results

The Ramsey interference experiment was performed using a constant Bragg 50/50 splitter of 1 kHz two-photon Rabi frequency (corresponding to a duration of 250 µs). It was first conducted without using any phase shifter, so that we expect to have $\Delta\varphi_2 = \Delta\varphi_1$. If it is not the case due to phase fluctuations between the lasers during the interferometer, this will result in a loss of contrast of the interferences.

The duration τ between each splitter is typically a few milliseconds (typically $\tau = 1$ ms corresponds to an interfringe of 0.2 ms in terms of arrival time of the cloud on the MCP). The range of τ is limited: if τ is too small, then the interfringe is equal to the width of the cloud and the interference cannot be seen anymore ; if τ is too large, then the interfringe reaches the resolution limit of the detector along this axis. Moreover, as τ increases, the separation between the two interfering clouds increases too, leading to a smaller overlap between them after time of flight and therefore to a loss of contrast.

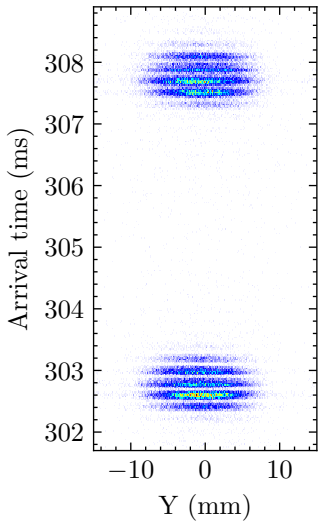

Figure 6.10: Ramsey interferences. Data averaged over 24 experimental runs, showing two interfering clouds with the same interfringe. Here, the BEC is diffracted into the -1 diffraction order, whose arrival time is ≈ 303 ms.

As expected, interference fringes can be seen on both the BEC and the diffracted cloud, with a nice contrast, as shown in figure 6.10.

Figure 6.11 shows the interference observed for $\tau = 1$ ms on the diffracted cloud, averaged over 24 runs. A fit of the interference pattern gives access to the interfringe, which corresponds to the interfringe expected from equation 6.28. The good contrast suggests that over 24 runs, there was no variation of the phase difference between the first and the second beam splitter, meaning that the phase difference variation is small over one millisecond.

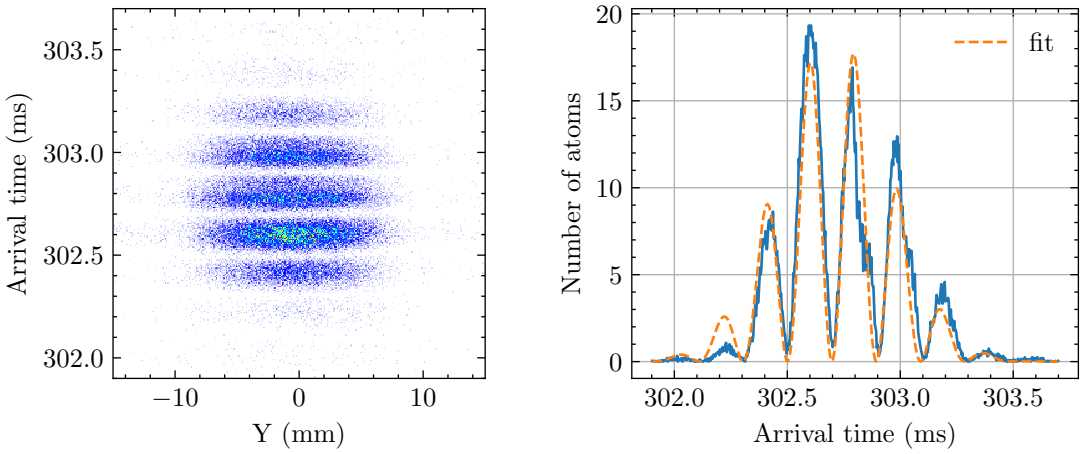

(a) 2D histogram.

(b) 1D histogram along the vertical axis.

Figure 6.11: Ramsey interferences obtained for $\tau = 1\,\text{ms}$. Data averaged over 24 experimental runs. The 1D data is fitted with a sinusoidal function modulated by a gaussian envelope, in order to measure the interfringe.

The experiment was conducted for different values of τ (as showed in Figure 6.12 for $\tau = 2\,\text{ms}$), within a range of 1 to 5 ms. As expected, the contrast of the interference pattern decreases as τ increases due to the fact that the clouds only partially overlap. At some point when τ increases, it is even possible to distinguish two envelops corresponding to the two interfering clouds. In all cases, the observed interfringe corresponds to what is expected theoretically, as shown in Figure 6.13.

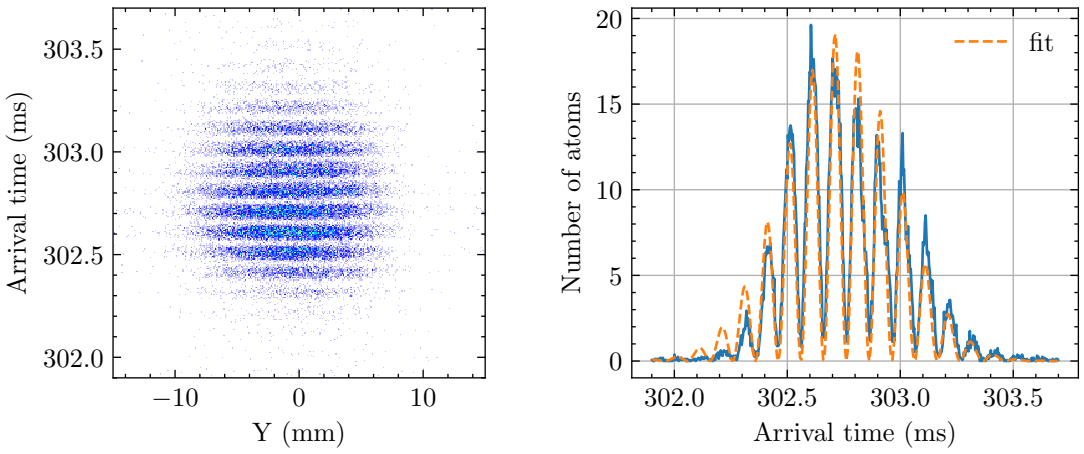

(a) 2D histogram.

(b) 1D histogram along the vertical axis.

Figure 6.12: Ramsey interferences obtained for $\tau = 2\,\text{ms}$. Data averaged over 24 experimental runs. The 1D data is fitted with a sinusoidal function modulated by a gaussian envelope.

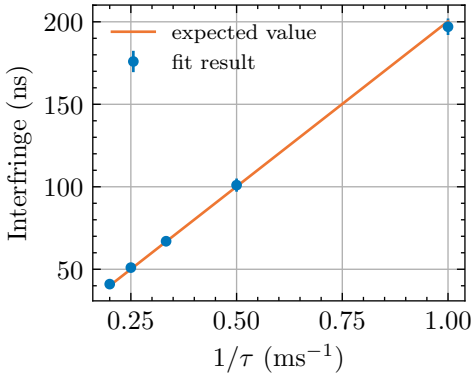

Figure 6.13: Interfringe of the Ramsey interference. The experimental results are represented as blue dots, while the expected value from equation 6.28 is shown in orange.

The Ramsey interference was also conducted on a BEC from the magnetic trap (Figure 6.14). Because the confinement along the vertical direction is more important with the magnetic trap than with the optical dipole trap, the momentum width of the cloud after time of flight is higher in the vertical direction, leading to the possibility to observe more interference fringes. To this end, the two-photon Rabi frequency used for the experiment (5 kHz) was chosen in order to ensure a broad resonance.

In this situation with $\tau = 2\,\text{ms}$, about 45 fringes are visible, while only a dozen were observed from a BEC of the optical dipole trap. The contrast also decreased compared to the one from a BEC of the optical dipole trap, which might be due to the imperfect reflectivity of the beam splitter over such a wide range of momentum.

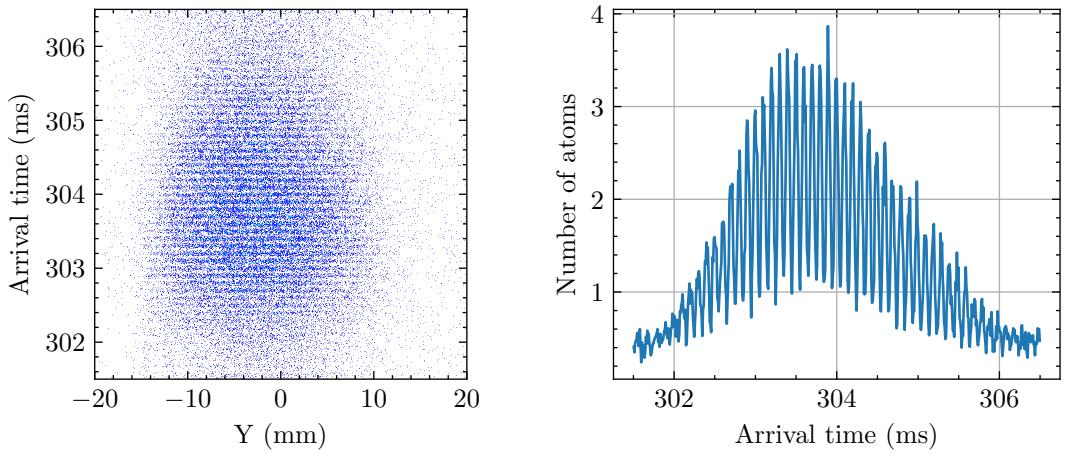

(a) 2D histogram **(b)** 1D histogram

Figure 6.14: Ramsey interferences on a BEC from the magnetic trap. Data averaged over 120 runs.

In order to determine whether the phase difference between the interference patterns of both clouds corresponds to what is expected (i.e. a π dephasing at the center of mass), the density profile of the interfering clouds can be plotted from equations 6.29 in the conditions of the experiment. The result was plotted for a Gaussian cloud, whose width in

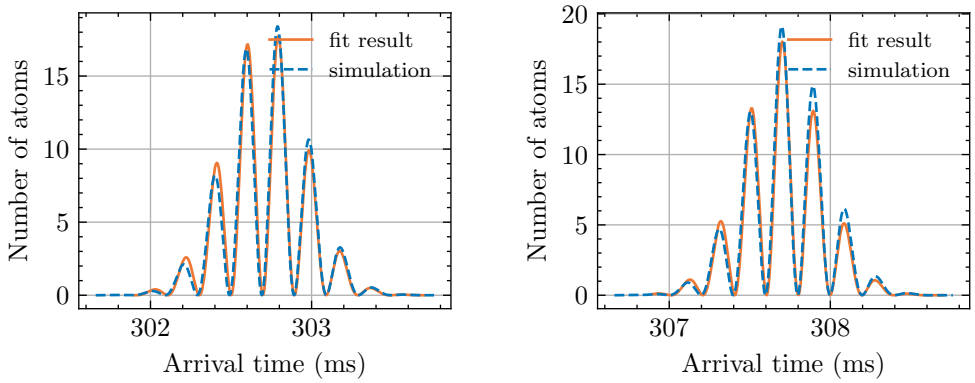

(a) Clouds interfering in the -1 diffraction order.

(b) Clouds interfering in the 0 diffraction order.

Figure 6.15: Density profiles of interfering clouds in two diffraction orders. The interference pattern of each cloud is fitted (in orange) by a sinusoidal signal modulated by a density envelope. The fit results (cloud width, amplitude, center) are provided as parameters of the analytical function given by equation 6.29, depicted in blue. The only unfitted parameter is the phase difference between the interference pattern of the -1 order clouds and the interference pattern of the 0 order clouds, which is fixed such that the centers of both wave packets oscillate in opposite phase. The good match between the fit result and the simulated interference indicates that the centers of mass have a phase difference of π.

terms of arrival time is 0.35 ms. The density fit of the interference patterns returns the arrival time of the center of both clouds, as well as the amplitude of the signal. These values, and the duration τ between each splitter, are used as parameters in the plot depicted in Figure 6.15. The superposition of the simulated density profiles, whose phase difference is π at the center of mass, with the fitted density profile confirms the expected result.

The Ramsey interferometer was repeated for $\tau = 2\,\text{ms}$, and averaged over 350 runs (corresponding to an hour and a half), in order to make a contrast analysis. For the first run, the contrast is evaluated to be 91%. We find that there is no significant loss of contrast, which is equal to 86% after averaging over the 350 runs. This means that there is no drift of the phase difference between the two pulses separated by 2 ms. Since this experiment is only sensitive to the difference of phases $\Delta\varphi_2 - \Delta\varphi_1$ imprinted on the atoms by each beam splitter, we cannot conclude about the stability of the absolute phase $\Delta\varphi$ between the two Bragg beams, which cancels out in this experiment.

6.2.4 Phase shifter calibration

The second goal of the Ramsey interferometric experiment is to add a tunable phase between the two splitters in order to shift the interference pattern. It is a way to make sure that the phase imprinted on the atoms indeed corresponds to the phase difference between the two lasers. Thus, by adding a π phase shift, it will be possible to implement negative two-photon Rabi frequencies.

To calibrate the phase shifter, we will use the fact that the interference pattern can be

expressed as:

$$\Delta\Phi_0 = \frac{m}{\hbar} g t v_\mathrm{B} \tau + \Delta\varphi_2 - \Delta\varphi_1 + \phi_\mathrm{prop,others} \tag{6.30}$$

Until now, without a phase shifter, we had $\Delta\varphi_2 = \Delta\varphi_1$. By sending a non-zero setpoint to the phase shifter between the first and second beam splitters, we can control the phase difference $\Delta\varphi_2 - \Delta\varphi_1$, which will shift the interference pattern. We can thus identify the voltage value for which the pattern has been shifted by π.

The Ramsey sequence was therefore conducted as previously, with the only difference consisting in adding a constant voltage setpoint to the phase shifter after the first pulse, for which the setpoint is zero. By scanning the value of the setpoint, the interference pattern was shifted. The experiment was repeated several times for each value of phase shifter setpoint, making it possible to fit the data in order to determine the relative phase imprinted to the atoms between the two pulses. This is a calibration of the phase shifter for which the phase is evaluated directly on the atoms.

The obtained curve is given in Figure 6.16a. Remarkably, it fits well the electronic curve which was made only by comparing the phase of the RF output signal with the RF input signal of the phase shifter. In particular, the voltage setpoint correspond to a π phase shift was determined. With this value, the interference pattern was shifted by half an interfringe, as seen in Figure 6.16b.

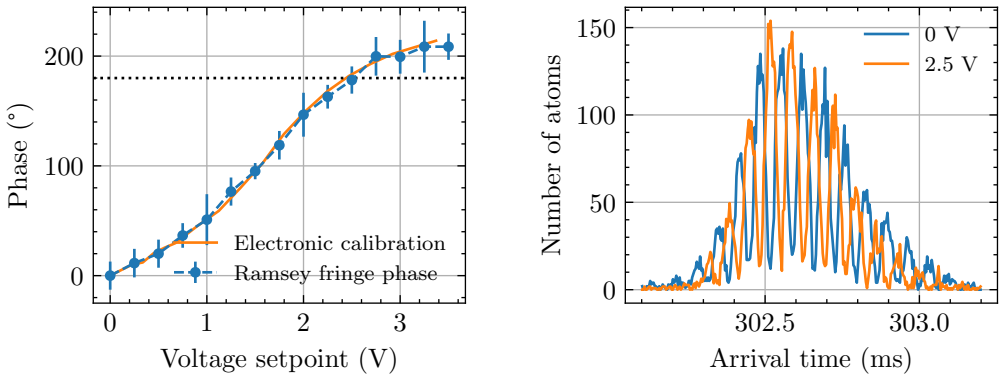

(a) Calibration curve of the phase shifter.

(b) Ramsey interferences shifted by π.

Figure 6.16: Phase shifter calibration. The phase of the interference was fitted from the density profiles along the vertical direction, for a given phase shifter voltage setpoint. Each point is averaged over 12 experimental runs.

6.3 Shaped Bragg pulses

6.3.1 Sinc pulses

The previous calibration shows that the implementation of the phase shifter makes it possible to add a π phase shift on one of the laser beams, and this phase will be imprinted on the atoms, leading to the possibility of realizing a negative two-photon frequency. As discussed in the previous chapter (see section 5.3), an interesting shape for the temporal pulse is a sinc shape, given by :

$$\Omega_{\mathrm{R}}(t) = \Omega_{\mathrm{M}} \operatorname{sinc}\left(\Omega_{\mathrm{S}}(t - T/2)\right) \tag{6.31}$$

where Ω_{M} is the two-photon Rabi frequency amplitude, T is the duration of the pulse and Ω_{S} is the sinc frequency, which equals Ω_{M} for a mirror and $2\Omega_{\mathrm{M}}$ for a beam splitter.

Using the phase shifter and the power control of the Bragg beams, we have performed a series of sinc-shaped Bragg pulses in order to test the performances of these pulses compared with constant pulses. The resonance width of the pulses we want to test is greater than the momentum range of the BEC from the optical dipole trap. In order to get the reflectivity profile, one solution would be to scan the detuning and measuring the respective number of atoms reflected and transmitted in a small momentum box. But we chose a more direct way, which consists in using a BEC from the magnetic trap.

As discussed before, the BEC from the magnetic trap has a broad momentum width along the vertical axis compared to the BEC from the optical dipole trap. The two-photon Rabi frequency is such that the width of the resonance is smaller than the width of the BEC, and the detuning is chosen so that the atoms are transferred into a momentum state which is initially unpopulated. This way, the profile of the transferred cloud corresponds to the reflectivity profile, modulated by the initial Thomas-Fermi density profile of the cloud.

However, this method has drawbacks inherent to using a BEC from the magnetic trap. Significant fluctuations in atom number and arrival time, along with the presence of a non-condensed thermal fraction, result in a reduced transfer efficiency when averaging over multiple cycles, as there are occasionally atoms within the supposedly unpopulated momentum range where the diffracted atoms are transferred.

The obtained density profiles will be compared with Bragg simulations solving the Schrödinger equation. So far in this manuscript, the Bragg simulations did not take into account the initial population of the atoms. Indeed, assuming that all the atoms are initially in the momentum state $p = 0$ and plotting the result as a function of the momentum (or, equivalently, as a function of the detuning) is a good way to determine the reflectivity profile of a given Bragg pulse, but it does not allow to determine the density profile of a cloud (with a given initial momentum distribution) after the Bragg pulse.

The simulations were made using a parabolic fit of the cloud density profile as input. The resonant momentum and the number of atoms are free parameters which were adjusted to fit the output density profile with the experimental data. However, the Bragg wavevector and the pulse shape (power, waveform and duration) are fixed, to best represent the pulse sent to the atoms.

The obtained density profiles with a two-photon Rabi frequency of 5 kHz are represented in Figure 6.17 for a sinc-shaped beam splitter, and in Figure 6.18 for a constant beam splitter. In both cases, the experimental results are in very good agreement with

the expected profiles. The differences between the simulated profile and the experimental one may arise from thermally populated atoms initially present in the momentum range corresponding to diffracted atoms, control loop imperfections smoothing the temporal profile of the pulse, or imperfect calibration of the power used to generate a 5 kHz pulse.

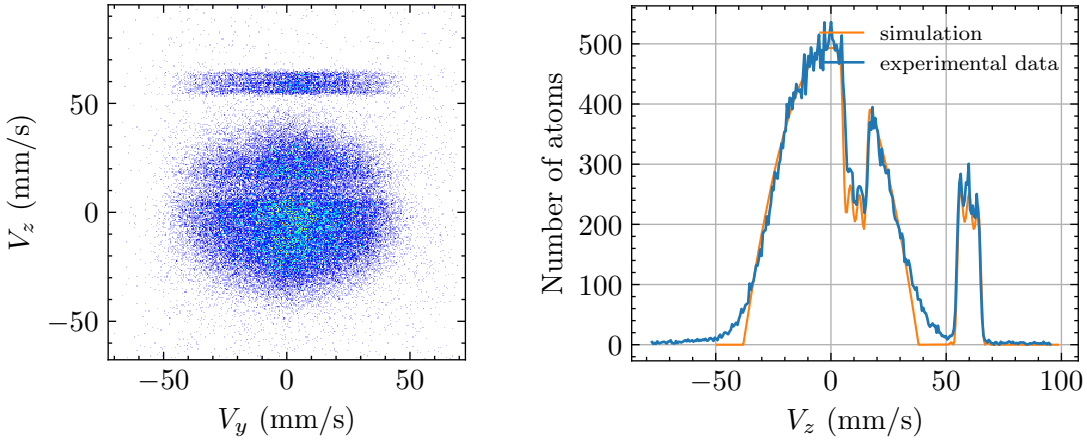

(a) 2D histogram.

(b) 1D histogram along the vertical axis.

Figure 6.17: Bragg sinc beam splitter. The parameters chosen for the Bragg pulse are $\Omega_M = 5\,\text{kHz}$, $T = 1\,\text{ms}$. Data averaged over 50 runs.

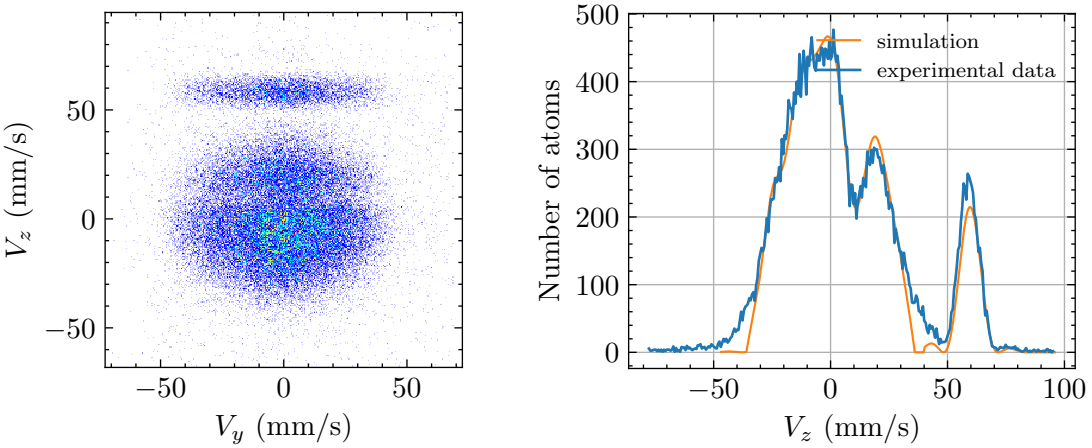

(a) 2D histogram.

(b) 1D histogram along the vertical axis.

Figure 6.18: Bragg constant beam splitter. The parameters chosen for the Bragg pulse are $\Omega_M = 5\,\text{kHz}$, $T = \pi/2\Omega_M$. Data averaged over 50 runs.

Similarly, figures 6.19 and 6.20 represent the density profiles obtained for a 1.5 kHz sinc-shaped mirror and a 1.5 kHz constant mirror, respectively. Again, the experimental results align well with the expected profiles.

To quantitatively express the performances of these different pulses, we arbitrarily defined parameters to account for the experimental characteristics of Bragg transfer. Firstly,

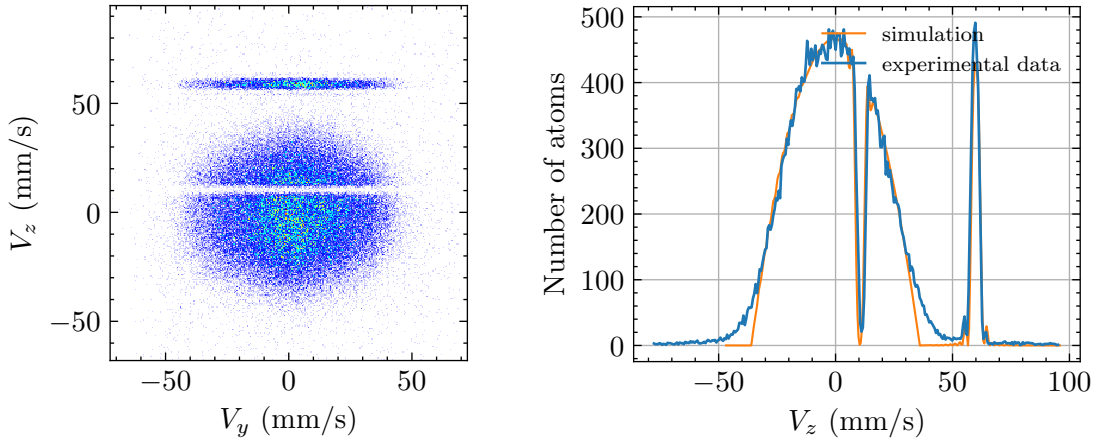

(a) 2D histogram.

(b) 1D histogram along the vertical axis.

Figure 6.19: Bragg sinc mirror. The parameters chosen for the Bragg pulse are $\Omega_M = 1.5\,\text{kHz}$, $T = 1\,\text{ms}$. Data averaged over 50 runs.

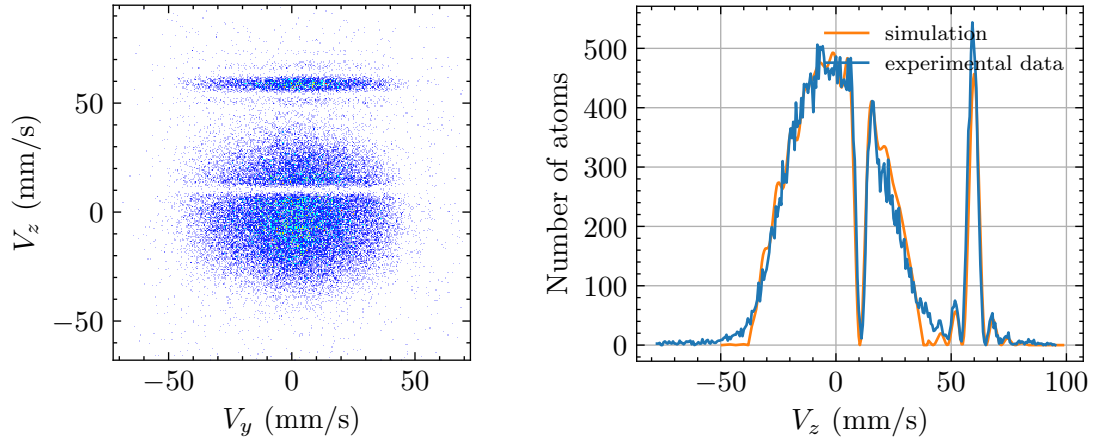

(a) 2D histogram.

(b) 1D histogram along the vertical axis.

Figure 6.20: Bragg constant mirror. The parameters chosen for the Bragg pulse are $\Omega_M = 1.5\,\text{kHz}$, $T = 1\,\text{ms}$. Data averaged over 50 runs.

the resonance transfer efficiency η_{eff} is defined as the ratio of transferred atoms to the initially populated atoms at resonance :

$$\eta_{\text{eff}} = \frac{N_{\text{init}} - N_{\text{transferred}}}{N_{\text{init}}} \tag{6.32}$$

In order to reflect the width of the resonance, we define, on one hand, the half-maximum width ($W_{50\%}$) of the peak corresponding to the transferred atoms, and on the other hand, the width at 90% of the same peak ($W_{90\%}$). Finally, to quantify the sharpness $\mathcal{S}$ of the resonance, density profiles were fitted at half-maximum to define a slope, in % per mm.s^{-1} :

$$\mathcal{S}_{\pm} = \frac{\mathrm{d}N}{\mathrm{d}V_z}(50\%) \tag{6.33}$$

Pulse	**Efficiency**(%)	**Width** ($\mathrm{mm.s^{-1}}$)		**Sharpness**($\%/\mathrm{mm.s^{-1}}$)	
	η_{eff}	$W_{50\%}$	$W_{90\%}$	$\mathcal{S}_+$	$\mathcal{S}_-$
Exp. sinc splitter	46 ± 2	10.4 ± 0.2	8.8 ± 0.4	26.3 ± 2.0	-23.8 ± 2.0
Sim. sinc splitter	50	10.5	9.2	32.9 ± 0.5	-28.9 ± 0.5
Exp. constant splitter	45.6 ± 2.0	10.0 ± 0.2	4.0 ± 0.4	6.6 ± 2.0	-5.8 ± 2.0
Sim. constant splitter	50	10.3	4.4	7.2 ± 0.5	-6.8 ± 0.5
Exp. sinc mirror	94.4 ± 2.0	4.2 ± 0.2	1.9 ± 0.4	40.6 ± 2.0	-45.1 ± 2.0
Sim. sinc mirror	100	4.0	2.0	41.6 ± 0.5	-42.8 ± 0.5
Exp. constant mirror	96.6 ± 2.0	5.0 ± 0.2	1.5 ± 0.4	26.3 ± 2.0	-31.8 ± 2.0
Sim. constant mirror	100	4.8	1.9	29.8 ± 0.5	-29.0 ± 0.5

Table 6.1: Bragg performances for 1.5 kHz mirrors and beam splitters.

The results are given in Table 6.1, both for the simulated profile and the experimental one. The results confirm a good agreement between the two. A noticeable difference lies in the transfer efficiency, slightly lower by a few percent than expected. However, this is mainly explained by the fact that the experiment was conducted using the magnetic trap. Better efficiencies can be achieved using the optical dipole trap. The measured widths correspond to the simulated widths. The sharpness values are within the right order of magnitude, although the measured values sometimes deviate significantly from the expected slopes. These parameters are, in any case, sensitive to the chosen velocity range for fitting and the atoms number fluctuations.

Now, let us compare the performance of the constant pulse with that of the sinc pulse. First, we observe that the full width at half maximum is minimally affected by the pulse type, which was expected since this width is determined by the integral of the time profile of the pulse $\Omega_{\mathrm{R}}(t)$. However, the width at 90% is almost doubled for a sinc-shaped pulse, which was the primary goal of the pulse shaping. The mirror width is slightly increased with the pulse shaping, which is of interest even though it's less pronounced than in the case of the separator. Once again, this was expected, as we have seen that the relationship between the reflectivity profile and the Fourier transform of the time profile becomes less accurate as the population of diffracted atoms increases.

Although the better performances of the sinc-shaped pulse compared to the square pulse was expected theoretically, it is worth noting that our experimental data match very well with the expected profiles, even for shaped pulses. Indeed, the performance difference between the experimental measures and the simulated profiles is similar with square and sinc pulses. This means the experimental setup we implemented for pulse shaping did not cause a significant deviation from a perfect sinc-shaped two-photon Rabi frequency.

A similar analysis was conducted with various two-photon Rabi frequencies (from 350 Hz to 8 kHz), as seen in Figures 6.21 and 6.22 for 5 kHz beam splitter and mirror, respectively. As seen earlier, changing the two-photon Rabi frequency modifies the resonance width: the higher Ω_{R}, the broader the resonant momentum range becomes. The conclusions of the analysis remain the same: there is no significant loss of contrast when using shaped pulses, the obtained density profiles are very similar to what we expect theoretically and lead to a better width at 90%.

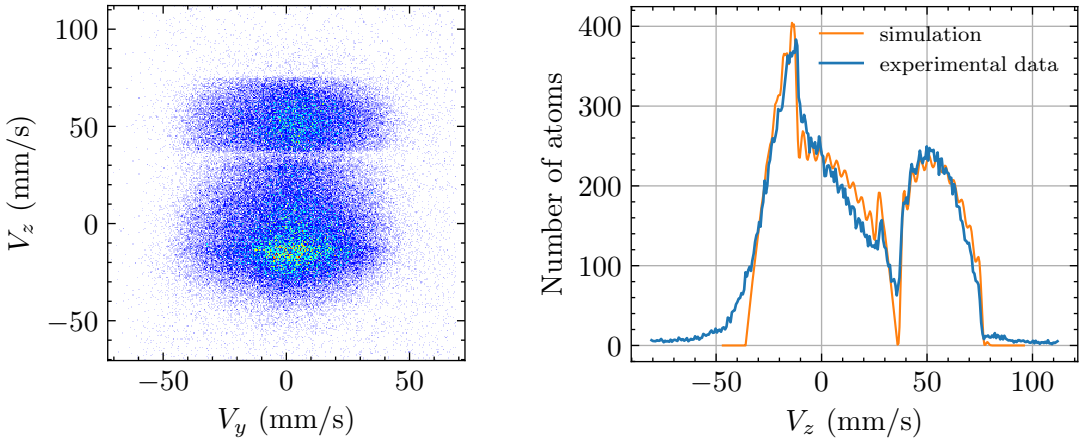

(a) 2D histogram.

(b) 1D histogram along the vertical axis.

Figure 6.21: Bragg sinc beam splitter. The parameters chosen for the Bragg pulse are $\Omega_M = 5\,\text{kHz}$, $T = 1\,\text{ms}$. Data averaged over 50 runs.

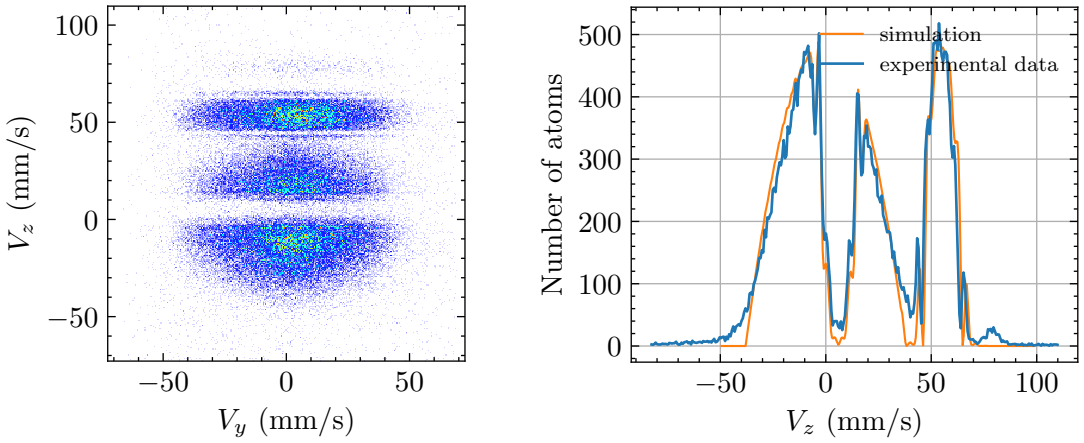

(a) 2D histogram

(b) 1D histogram along the vertical axis.

Figure 6.22: Bragg sinc mirror. The parameters chosen for the Bragg pulse are $\Omega_M = 5\,\text{kHz}$, $T = 1\,\text{ms}$. Data averaged over 50 runs.

In conclusion, this section demonstrates how implementing sinc-shaped Bragg pulses has provided us with an effective tool to enhance the reflectivity of Bragg pulses within a resonant range which can be tuned by the two-photon Rabi frequency.

6.3.2 Shaped pulse equivalent time

In most atomic interferometers discussed in the literature, the duration of a single pulse is significantly shorter compared to the interval between two pulses. For instance, in cold atom gravimeters, the duration of a pulse is typically around 10 µs, whereas the interval between two pulses could be 60 ms[168]. In the HOM interferometer[92], the mirror duration was 100 µs, the beam splitter duration was 50 µs, while the free propagation

interval between these two pulses was 500 µs.

With shaped pulses, whose duration is long compared to the duration of a constant pulse, one can wonder to what extent the duration of the pulse will impact the interferometric performance. What happens when the duration of the pulse is of the same order of magnitude or even longer than the free propagation time between two pulses? As an initial insight for a sinc-shaped pulse, it can be affirmed that although the total duration of the pulse is indeed longer, the power delivered to the atoms is very low for a significant duration (corresponding to the small rebounds of the sinc function), resulting in a very weak transfer of atoms to the diffracted state. Therefore, it is possible to evaluate an effective period of time, smaller than the total duration, within which most of the transfer occurs.

It is easy to determine numerically the population of the resonant diffracted atoms during the application of a pulse, as the dynamics is given by the Schrödinger equation for a two-level system. Experimentally, we can measure the number of diffracted atoms as a function of the application duration of the pulse by truncating it. The results for a sinc mirror are given in Figure 6.23, along with the temporal profile of the pulse which was used for the measurement (5 kHz, 1 ms).

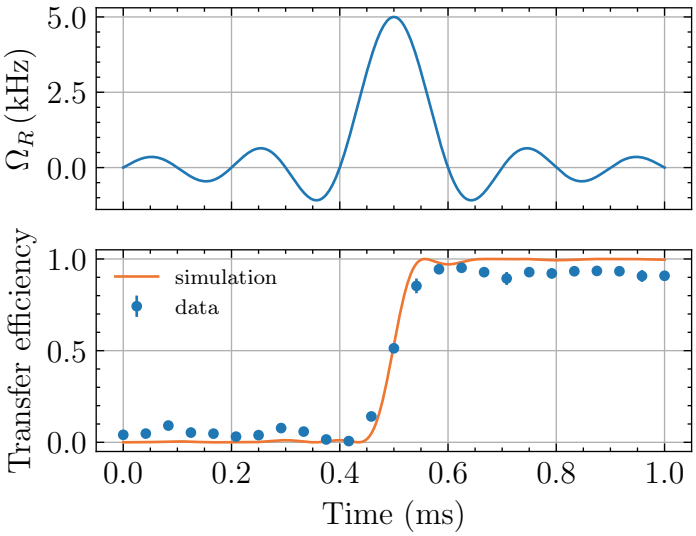

Figure 6.23: Transfer of atoms during a sinc-shaped pulse. Initially, all the atoms are in the BEC. A 5 kHz sinc-shaped mirror is applied. The pulse is truncated so that we can determine the transfer efficiency at a given time. The experimental results are depicted as blue dots, while a numerical resolution of the Schrödinger equation at resonance is represented in orange.

Both the experimental results and the simulation confirm that the main transfer dynamics are restricted to a duration of about 100-200 µs. This typical duration actually corresponds to the duration of a constant π pulse at the same two-photon Rabi frequency (100 µs for a 5 kHz constant mirror), which makes sense as two equivalent pulses need to have the same area under the curve, as discussed in section 5.3. In the case of the sinc pulse, most of the transfer occurs during the main lobe of the sinc function. Noticeably, there is a slight broadening of the equivalent duration in the experimental measurements, possibly due to imperfections in the power lock or because the atoms were counted within a momentum box that includes atoms slightly off-resonance.

Hence, as a first approximation, one can consider a sinc-shaped pulse to be equivalent to a constant pulse with a duration set by the two-photon Rabi frequency ($T_{\mathrm{eq}} = \pi/\Omega_{\mathrm{M}}$ for a mirror), and temporally centered on the main lobe of the sinc function, i.e., the half-duration of the sinc pulse.

6.3.3 Modulated pulses

After confirming that the sinc-shaped pulses behave as expected, the second step in designing the Bragg pulses for the Bell test is to investigate whether modulating the pulse's amplitude enables addressing two distinct momentum classes, as shown theoretically in section 5.2.3. The experimental setup remains unchanged, the only difference lies in the voltage setpoints sent to the phase shifter and the Bragg/Raman power lock, as shown in Figure 6.24. We want to generate a two-photon Rabi-frequency such that:

$$\Omega_{\mathrm{R}}(t) = \Omega_{\mathrm{M}} \operatorname{sinc}\left(\Omega_{\mathrm{S}}(t - T/2)\right) \cos(\Omega_{\mathrm{D}} t/2) \tag{6.34}$$

This setpoint has more angular points, but since Ω_{S} and Ω_{D} are of the same order of magnitude, there is no particular issue related to the bandwidth of the lock.

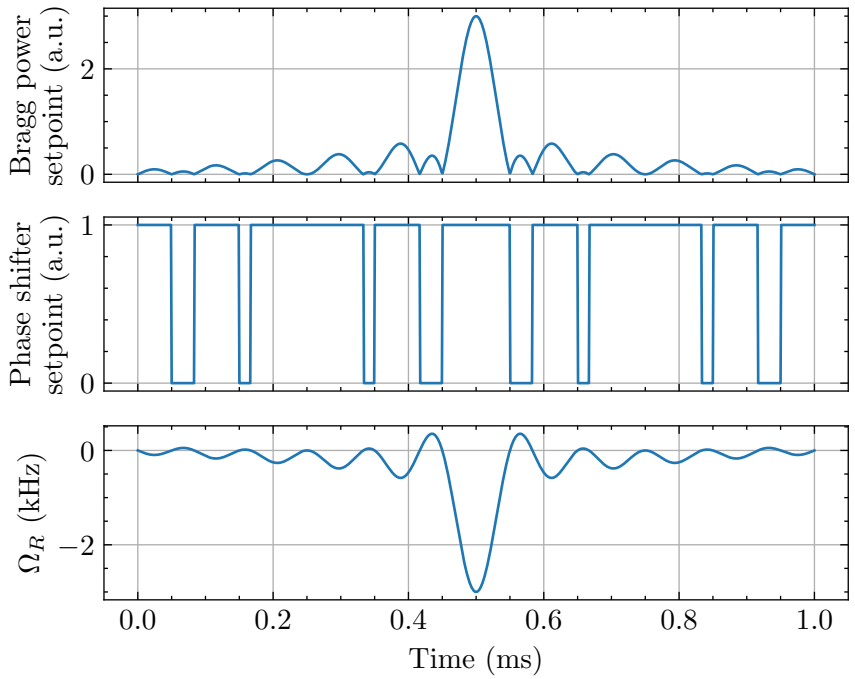

Figure 6.24: Voltage setpoint for the Bragg power and the phase shifter, in order to obtain a modulated sinc-shaped two-photon Rabi frequency. In the pulse represented here, $\Omega_{\mathrm{M}} = 3\,\mathrm{kHz}$, $\Omega_{\mathrm{D}} = 2.5\,\mathrm{kHz}$, $T = 1\,\mathrm{ms}$.

With this kind of pulses, we expect to find two different resonant momentum classes, separated by $\Delta v = \Omega_{\mathrm{D}}/k_{\mathrm{B}}$. For a same two-photon Rabi frequency, it is necessary to send twice the power for a modulated pulse than for a simple pulse, due to the relationship $\cos\theta = (\mathrm{e}^{i\theta} + \mathrm{e}^{-i\theta})/2$. Again, we performed such pulses by transferring atoms from the magnetic trap, since its momentum width makes it possible to directly observe the reflectivity profile, modulated by the initial momentum profile. Alternatively, one could plot

the reflectivity profile from a BEC with a thinner momentum width only by scanning the detuning.

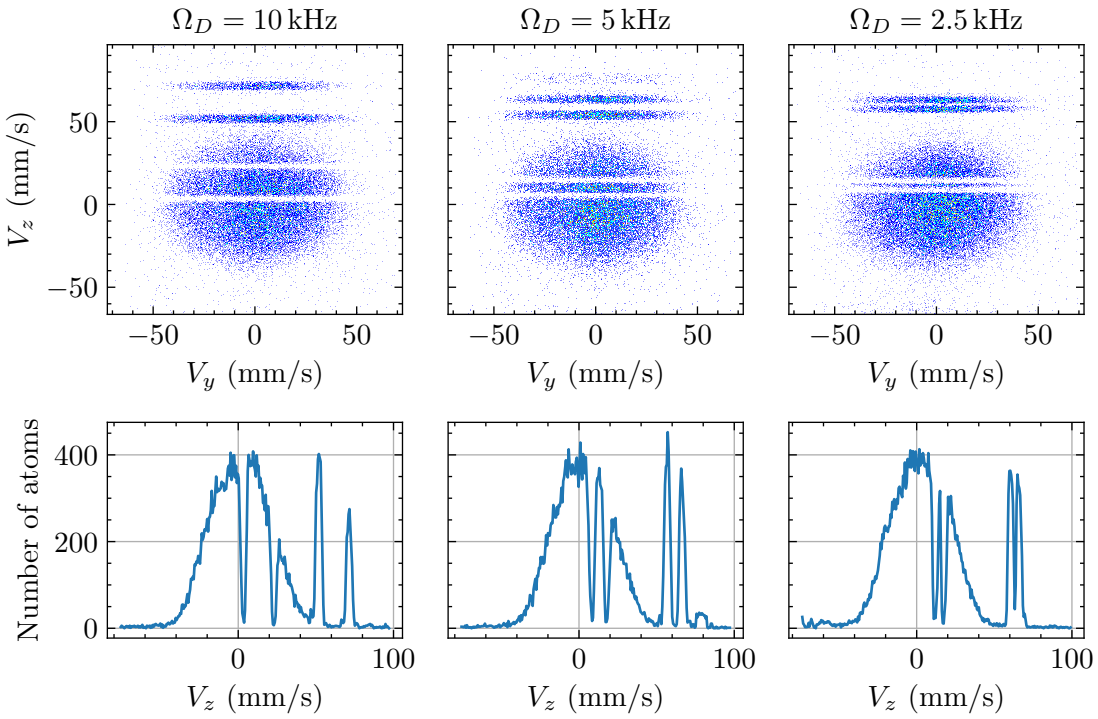

Figure 6.25: Density profiles obtained with modulated sinc-shaped mirrors, for different values of Ω_D.

The obtained profiles are plotted in Figure 6.25 for three values of Ω_D from modulated sinc-shaped Bragg pulses. In all three cases, the obtained profiles clearly exhibit two distinct resonant momentum classes. As anticipated, the separation between the resonant momentum ranges decreases as Ω_D decreases. The additional modulation applied to generate these two-frequency pulses did not induce any contrast loss. Similar outcomes were achieved for modulated square pulses: the results once again display two distinct resonance peaks separated by a velocity controlled by the parameter Ω_D. The difference from the sinc pulses lies in the peak profile, demonstrating rebounds and a narrower 90% width in the case of the square pulse.

These preliminary results confirm that modulating a pulse corresponds to addressing two different momentum classes, separated by $\Delta v = \Omega_\mathrm{D}/k_\mathrm{B}$. It is worth noting that if the modulation period becomes comparable to the pulse duration, the double resonance is no longer resolved, resulting in the merging of the two peaks. This theoretically predicted outcome is experimentally verified: achieving the density profile from Figure 6.25 with $\Omega_\mathrm{D} = 2.5\,\mathrm{kHz}$ has necessitated increasing the Bragg pulse duration from 1 ms to 2 ms.

To be more quantitative, we conducted a measurement using atoms from the dipole trap, scanning the Bragg detuning for each value of Ω_D to determine the resonance frequency associated with each peak as a function of Ω_D. The idea is to verify that the modulation frequency indeed corresponds to the frequency difference between the two resonances.

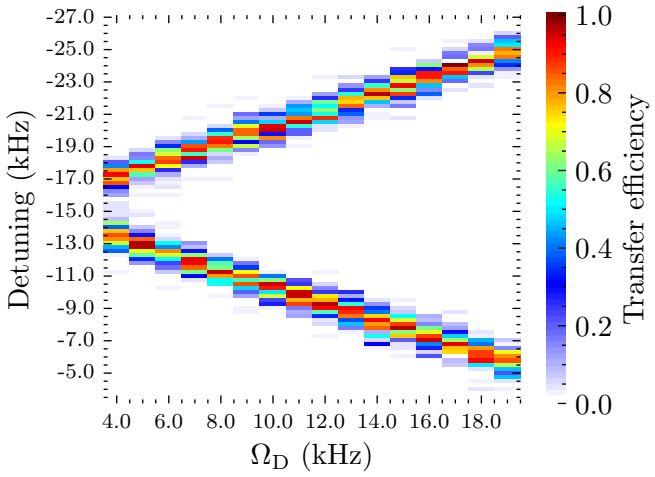

Figure 6.26: Transfer efficiency as a function of the detuning for several values of Ω_D. Starting from a BEC in the optical dipole trap, we realize a modulated sinc-shaped mirror of 1 kHz. It is possible to determine the Bragg transfer efficiency for a given detuning by counting the relative population in the BEC and in the diffracted cloud. Due to the modulation of the Bragg pulse at a frequency Ω_D, we find two resonance peaks separated by Ω_D.

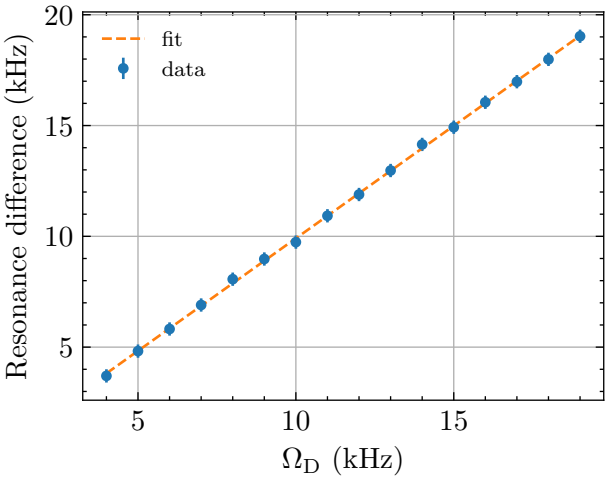

Figure 6.27: Frequency difference between the resonance peaks as a function of Ω_D.

The results are shown in Figure 6.26. Two distinct resonances are clearly visible, and linearly move away from each other as Ω_D increases. In Figure 6.27, we plot the difference between the two resonances, determined by a density fit, as a function of Ω_D. We obtain a straight line with a slope of 1.02 ± 0.04, providing evidence that the method works: by modulating a Bragg pulse at a frequency Ω_D, we obtain two resonances separated by Ω_D.

6.3.4 Phase control

As presented in section 5.2.3, implementing modulated pulses is crucial since this is how we aim to imprint a phase on the atoms through the phase at the origin of the modulation function. Confirming that the density profile exhibits two resonances is an initial step in validating the principle of the modulated pulse. However, this does not provide us any information about the phase imprinted on the atoms. In order to study the phase

imprinted on the atoms, conducting interferometric experiments is necessary. Similarly to the phase shifter calibration, Ramsey-type interferences were performed for this purpose.

The Ramsey experiment was conducted by using two modulated sinc-shaped splitters separated by a few milliseconds, without varying θ at first, such that each pulse is defined by:

$$\Omega_{\mathrm{R}}(t) = \Omega_{\mathrm{M}} \operatorname{sinc}\left(\Omega_{\mathrm{S}}(t - T/2)\right) \cos\left(\Omega_{\mathrm{D}} t/2\right) \tag{6.35}$$

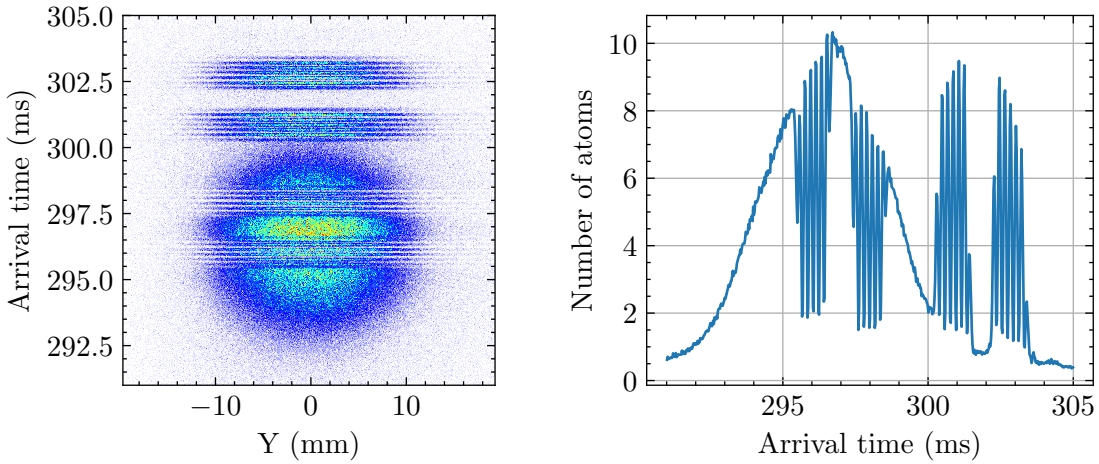

(a) 2D histogram **(b)** 1D histogram

Figure 6.28: Ramsey interferences with a modulated Bragg pulse. Data averaged over 350 experimental runs, conducted with sinc-shaped pulses of $\Omega_{\mathrm{M}} = 5\,\mathrm{kHz}$. The Bragg modulation at Ω_{D} is responsible for the observation of four interference zones, corresponding to the two velocity classes resonant with A (at 296 and 301 ms of arrival time), and the two other resonant with B (at 298 and 303 ms of arrival time).

We were able to observe interferences in four momentum areas, separated by v_{B} two by two, meaning that once again the modulation behaves as expected by splitting the resonance into two terms. Figure 6.28 shows the density profile obtained from a BEC of the magnetic trap with $\Omega_{\mathrm{R}} = 5\,\mathrm{kHz}$.

Now, we want to determine the impact of a phase $\theta/2$ at the origin of the modulation term:

$$\Omega_{\mathrm{R}}(t) = \Omega_{\mathrm{M}} \operatorname{sinc}\left(\Omega_{\mathrm{S}}(t - T/2)\right) \cos\left(\Omega_{\mathrm{D}} t/2 + \theta/2\right) \tag{6.36}$$

We expect the phase imprinted to the atoms to be equal to $+\theta/2$ for the atoms resonant with speed $+\Omega_{\mathrm{D}}/2k_{\mathrm{B}}$ and to $-\theta/2$ for the atoms resonant with speed $-\Omega_{\mathrm{D}}/2k_{\mathrm{B}}$. As explained earlier, the Ramsey experiment does not make it possible to directly measure the phase imprinted to the atoms, since the interfering term actually corresponds to the difference between the phase imprinted by the first splitter and the phase imprinted by the second one. But it is possible to proceed similarly to the phase shifter calibration to verify that one of the two splitters effectively imprints, for each resonance peak, an equal but opposite phase.

To describe the corresponding Ramsey interferometer, we can use the same formalism as in section 6.2.2, except that now the Bragg beam splitter has two resonance frequencies.

Provided that the width of the resonance is small compared to the frequency difference Ω_{D}, then each resonance can be described independently. We denote by A and B the velocity doublets resonant with $-\Omega_{\mathrm{D}}/2k_{\mathrm{B}}$ and $+\Omega_{\mathrm{D}}/2k_{\mathrm{B}}$, respectively.

We want to shift the interference pattern as a function of the phase at the origin θ. To do so, we will perform two successive sinc-shaped beam splitter pulses, such that:

$$\begin{cases} \Omega_{\mathrm{R1}}(t) = \Omega_{\mathrm{M}}\,\mathrm{sinc}\left(\Omega_{\mathrm{S}}(t-T/2)\right)\,\cos\left(\Omega_{\mathrm{D}}t/2\right) \\ \Omega_{\mathrm{R2}}(t) = \Omega_{\mathrm{M}}\,\mathrm{sinc}\left(\Omega_{\mathrm{S}}(t-T/2)\right)\,\cos\left(\Omega_{\mathrm{D}}t/2+\theta/2\right) \end{cases} \tag{6.37}$$

The reasoning from section 6.2.2 can be applied to describe the interference, provided that an additional phase term $\pm\theta/2$ is added to the phase imprinted by the light. The sign $\pm$ depends on the doublet A or B considered. In this case, the phase involved in the Ramsey experiment becomes:

$$\begin{cases} \Delta\Phi_A = \dfrac{m}{\hbar} g t v_{\mathrm{B}} \tau + \theta/2 + \phi_{\mathrm{prop,others}} \\ \Delta\Phi_B = \dfrac{m}{\hbar} g t v_{\mathrm{B}} \tau - \theta/2 + \phi_{\mathrm{prop,others}} \end{cases} \tag{6.38}$$

where we assumed that the phase difference between the lasers $\Delta\varphi$ remains the same for the two Bragg pulses. As we can see, by scanning the value of θ, we should observe a shift of the interference pattern, in opposite direction for the A doublet and the B doublet.

In order to have the best contrast when fitting the interference pattern to determine the differential phase imprinted on the atoms, the experiment was performed from a BEC of the optical dipole trap. Since the momentum distribution of the BEC is small compared to the resonance width used for the experiment, we adjusted the detuning by $\pm\Omega_{\mathrm{D}}/2$ so that the BEC is resonant either with the v_{B} peak, either with the $-v_{\mathrm{B}}$ one. Thus, the experiment was performed twice, one for each resonance, and each time the phase offset of the interference pattern was determined using a fit averaged over 15 runs and plotted as a function of θ (Figure 6.29).

The obtained results show without ambiguity what was expected from the theory. The slopes of the linear fits of $\Delta\Phi_A$ and $\Delta\Phi_B$ as a function of θ are $+0.50 \pm 0.02$ for A and -0.51 ± 0.02 for B, which shows that the differential phase imprinted by the second splitter adds a phase $\pm\theta/2$ to the atoms, where the sign depends on the resonant doublet considered.

As a consequence, the phase difference between A and B is given by $\Delta\Phi_A - \Delta\Phi_B = \theta$. Experimentally, this is the parameter we want to control for our Bell test. Although this experiment is an indirect measurement of this phase difference, since it is necessary to realize an initial beam splitter pulse to observe such interferences, this is a promising result regarding the phase control we want to realize in a Bell interferometer.

This is an important result from this thesis and my work in the team in general, which shows experimentally that we can control the phase imprinted on the atoms only by tuning the phase at the origin of the modulation fonction. This is a proof of principle which validates the way we chose to control the phase in the Bell experiment.

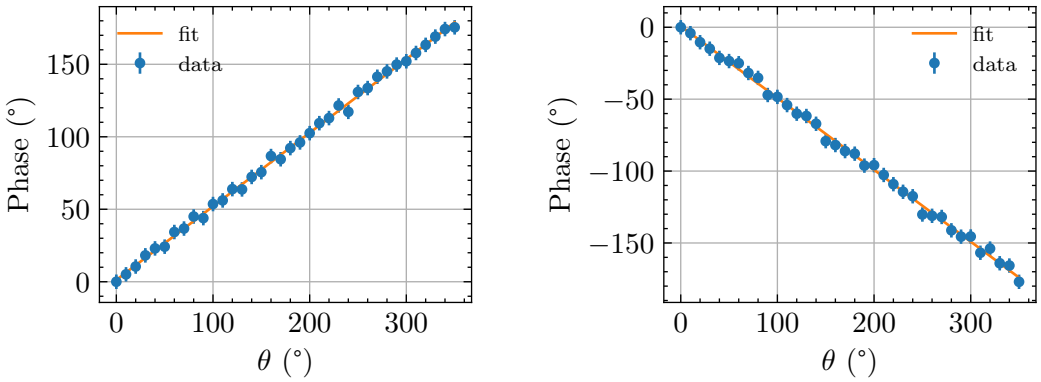

(a) Fitted phase of the interference pattern for the cloud resonant with A.

(b) Fitted phase of the interference pattern for the cloud resonant with B.

Figure 6.29: Proof of principle for phase control. The interference pattern of a Ramsey experiment was shifted by scanning the phase at the origin $\theta/2$ of the modulation function. For both a cloud resonant with A (such that its resonance frequency is $-\Omega_D/2$) and a cloud resonant with B (such that its resonance frequency is $+\Omega_D/2$), the interference pattern was fitted to determine the phase. The results show that the fitted phase of the interference pattern shift in opposite directions for A and B.

6.4 Mach-Zehnder gravimeter

6.4.1 Principle

To ensure that the sinc-shaped Bragg pulses behave as expected, we opted to realize a Mach-Zehnder interferometer. The goal is to exhibited one-atom interferences in the population of the different modes at the output of the interferometer.

Constituted by three successive Bragg pulses, respectively $\pi/2$, π, and then $\pi/2$, this setup shares significant similarities with a HOM or a Bell-type interferometer. Indeed, the initial beam splitter acts as a "source" for a two-input interferometer. The second pulse acts as a mirror to close the interferometer. Finally, the last splitter allows for the actual interference to occur. As with a Bell or HOM-type interference, proper closure of the interferometer is crucial to optimize interference contrast.

In section 4.4, we have shown that starting from a BEC (considered as the zero diffraction order), the phase involved in the Mach-Zehnder interferometer along a vertical direction is given by

$$\Phi = (k_B g + \alpha)T^2 + \Delta\varphi_1 - 2\Delta\varphi_2 + \Delta\varphi_3 \tag{6.39}$$

where $\Delta\varphi$ are the laser phase differences during each pulse, and α is the value of the slope of a frequency sweep, aiming at compensating gravity.

The population at the output of the interferometer are therefore:

$$\begin{cases} N_0 = \dfrac{N}{2}(1 - \cos\Phi) \\ N_1 = \dfrac{N}{2}(1 + \cos\Phi) \end{cases} \tag{6.40}$$

where N_0 and N_1 are the number of atoms in the order 0 of diffraction, and in the first order of diffraction, respectively. N is the total number of atoms.

There are several ways to use a Mach-Zehnder interferometer. For instance, one can add a phase shifter on the second splitter and vary the phase $\Delta\varphi_3$ imprinted at this stage to shift the interference fringes, altering the relative proportions of the two momentum classes coupled by Bragg diffraction. However, the current phase shifter at our disposal only allows for a variation from 0 to π, not from 0 to 2π. Therefore, we decided to perform a Mach-Zehnder gravimeter, the operation and principles of which are well-documented in literature[146][169][170].

The principle is as follows[168]: when the interferometer is suitably closed, we scan the slope α of the frequency sweep and measure the populations N_0 and N_1. This makes it possible to observe fringes. By repeating the experiment for different values of T, defined here as the time between two pulses, fringes with another period become observable. Independently of the value of T, a fringe will always have the same shade when the frequency slope compensates perfectly for gravity such as $\alpha_0 = -k_B g$. Thus, by determining with precision the slope α_0 corresponding to this zero-order fringe, one can deduce the value of the gravitational acceleration, g.

6.4.2 Gravity measurement attempt

The experiment was conducted using 1 ms sinc pulses at 5 kHz for various values of T. For instance, for respective delays after the trap cutoff of 1.1, 6.1, and 9.1 ms, corresponding to $T = 5$ ms (see Figure 6.30), clear fringes are visible when the frequency sweep slope α is scanned. The observed period matches well with the expected one. The contrast is high (0.8), and, as anticipated, it decreases as the duration T between two pulses increases.

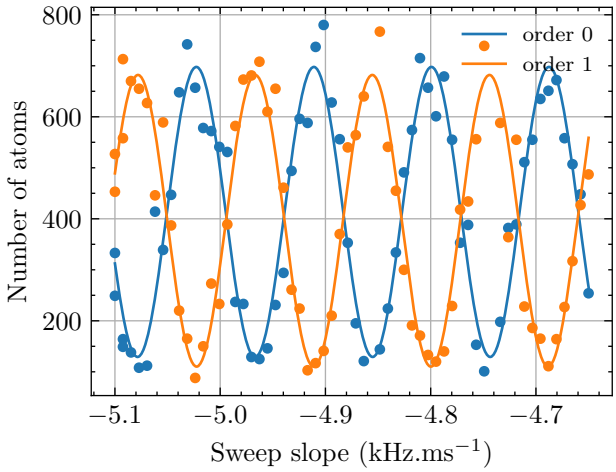

Figure 6.30: Mach-Zehnder interference fringes.

Such oscillations have been observed for a T ranging between 3 and 8.25 ms. As expected, the contrast decreases as T increases, indicating that the longer the delay between two pulses, the more the atoms move away from the region where the beams have a constant intensity, which affects the quality of the Bragg mirror and beam splitters.

The interference fringes were plotted for several values of T, in order to identify the zero-order fringe, independant of T and corresponding to a slope $\alpha_0 = -gk_B$. For a small

range of T between 5 and 6 ms, it is possible to identify such a fringe (Figure 6.31). We find $g = 9.823 \pm 0.006\,\mathrm{m.s^{-2}}$, but this value does not match the known value of g in Paris ($g = 9.8089\,\mathrm{m.s^{-2}}$).

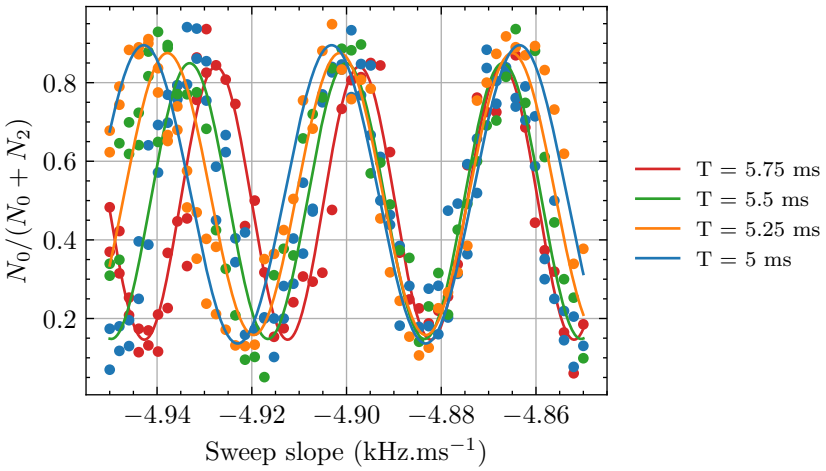

Figure 6.31: Mach-Zehnder gravimeter. N_0 is the number of atoms in the 0th diffraction order, while N_2 is the number of atoms in the 1st diffraction order. The Mach-Zehnder oscillations are obtained for different values of T, defined as the duration between the beginning of two successive pulses.

Moreover, we found that the slope corresponding to the fringe that we identified as the zero-order fringe was not constant as T varied. The plot illustrating the slope value of the zero-order fringe against T is presented in Figure 6.32. The interpretation of this curve has not yet been definitively established. Two distinct asymptotic behaviors are noteworthy, suggesting the presence of two terms dependent on T in the expression of the slope. Note that, as α_0 seems to depend on T, it is not even obvious to determine where the 0th order fringe is located.

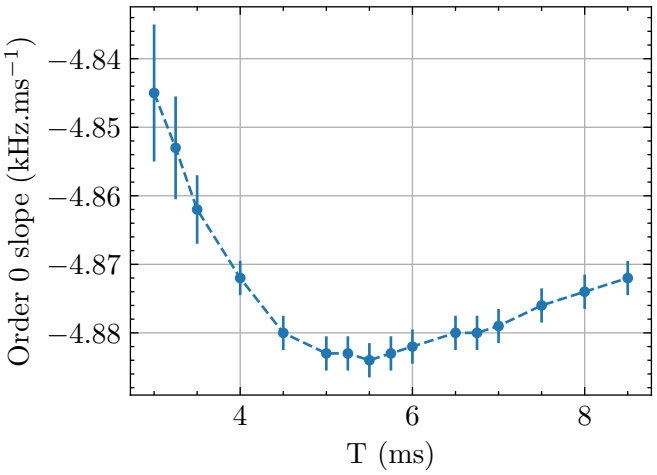

Figure 6.32: Order 0 fringe slope.

The reasons behind this unexpected behavior are not well understood yet. For a given duration between the pulses, the measurements are well reproducible. Recent results

suggest that we may be more sensitive than we first thought to the combined effects of a slight error in the detuning and an imperfect closure of the interferometer. These two imperfect settings might add a phase term which can shift the interference pattern for different values of T. Moreover, there might be some unexpected phase exchanges between the momentum modes when dealing with pulses with a large two-photon Rabi frequency. Since 5 kHz is not far from the threshold at which there is diffraction into higher orders, this could also be responsible for a shift in the interference pattern, so no 0th order fringe can be identified.

Note that an additional phase term is not an obstacle to the successful implementation of a Bell test conducted at a fixed T, as long as it remains independent of the velocity class considered. Therefore, we have decided to perform a Hong-Ou-Mandel interferometer.

6.5 Conclusion and outlook

In this chapter, we discussed the experimental implementation of intensity-modulated Bragg pulses to achieve negative two-photon Rabi oscillations. To do so, we introduced a power feedback control for the Bragg beams and a phase shifter adding a π phase shift between the phases of the two laser beams when the Rabi oscillation needs to be negative. The phase shifter was calibrated using a Ramsey interferometer, for which the interference pattern could be shifted by the phase difference imposed by the two successive beam splitters.

Intensity-modulated sinc-shaped Bragg pulses were successfully implemented, and the obtained density profiles are very promising since we were able to increase the momentum resonance range without decreasing the transfer performances. Furthermore, modulating the intensity of a Bragg pulse at a frequency Ω_{D} makes it possible to perform two distinct resonant pulses whose speed is separated by $\Omega_{\mathrm{D}}/k_{\mathrm{B}}$. By controlling the phase at the origin of the modulation function, two different phases can be imprinted on the two resonant classes, as confirmed by a Ramsey interference where the fringes of each resonance shift in opposite directions.

The sinc-shaped Bragg pulses were used to conduct a gravity measurement with a Mach-Zehnder interferometer. Although we observed interferences with good contrast, we did not manage to measure g due to additional phase terms depending on the duration T between the Bragg pulses, making it impossible to precisely identify the zeroth-order fringe needed to measure gravity. Further investigations must be conducted to identify the reasons for the observed effect, which appears to be reproducible when the value of T is fixed. This, a priori, allows us to proceed with the Bell experiment.

These results can be leveraged for the Bell experiment we aim to conduct, as the improved transfer efficiency broadens the momentum range within which we can perform the Bell test. In a more general context, although we limited ourselves here to a sinc-shaped modulation as a proof of concept, it will be interesting to explore other modulation functions to further enhance the mirror quality[154], either using analytical functions or custom profiles derived from optimal control algorithms[161].

Chapter 7

Hong-Ou-Mandel experiment and Bell inequality test

7.1 The Hong-Ou-Mandel effect with atoms 255
7.1.1 Generalization for any input state 255
7.1.2 Tuning indistinguishability 257
7.2 Observation of an atomic Hong-Ou-Mandel effect 259
7.2.1 Experimental preparation 259
7.2.2 Results: analysis of the HOM dip 262
7.2.3 Ramsey fringes 267
7.3 First Bell test attempt 268
7.3.1 Parameters and procedure 268
7.3.2 Sensitivity to the interferometer closure 270
7.3.3 Sensitivity to the detuning 272
7.3.4 Sensitivity to the initial cloud position 273

7.1 The Hong-Ou-Mandel effect with atoms

Since the historic experiment[36], the HOM effect has become a textbook example of quantum interference that cannot be explained by classical or semi-classical models. It has been observed in various quantum systems using particles emitted in pairs, including atoms in our team[92] (an example that will be discussed in the following) and phonons in trapped ions[171]. Notably, in order to observe a HOM dip, it is not necessary for the two interfering particles to be emitted in pairs, nor even by the same source, as they only need to be indistinguishable at the beam splitter. The HOM interference has then become a standard method for characterizing the purity of single-particle sources or the indistinguishability of particles. The HOM effect was reported with single photons emitted one after the other by a quantum dot[172], as well as photons emitted by independant sources, such as through spontaneous emission by independently trapped atoms[173], or even with one photon emitted by a quantum dot and one emitted by the Sun[174], which were made indistinguishable by a series of filtering and post-selection methods.

An experiment aiming to exhibit a violation of the Bell inequality must rely on a closed interferometer, otherwise, additional phase terms will blur the interference signal, as discussed in Chapter 4. Thus, the first step to conduct a Bell test with our setup is to close the interferometer by performing an atomic Hong-Ou-Mandel interference experiment. In our case, the indistinguishability between the input particles is tuned by controlling the moment at which the Bragg splitter is applied. When the particles are indistinguishable, the atoms' wavepackets overlap on the beam splitter and a HOM dip is observed, which corresponds to the case where the interferometer is said to be closed. Our team first demonstrated the quantum HOM dip in 2014[92] and subsequently replicated it in 2016[93]. This step is crucial towards a Bell test, since the extended duration of the pair creation lattice leads to an uncertainty about the moment when pairs are created, which can be resolved by determining the beam-splitter delay closing the interferometer thanks to the HOM dip.

Observing a Hong-Ou-Mandel dip with sufficient contrast serves as evidence for the quantum nature of the interferometer's input state. While not displaying correlations as strong as those in a Bell interferometer, this experiment validates the state's quantum nature, along with the quality of the sinc-shaped Bragg pulses and therefore confirm the feasibility of the Bell test.

7.1.1 Generalization for any input state

So far, we have only described the HOM effect between two individual particles, meaning we have considered the input state as the twin Fock state $|1,1\rangle$. It is possible to generalize the HOM effect to an input state with any two modes. We will see that the visibility of the signal decreases rapidly with the population, that is, with the number of atoms per mode.

Let us consider a two-particle input state which can be written in the basis of the twin Fock states:

$$|\Psi_{\text{in}}\rangle = \sum_n \mathcal{P}(n)\,|n,n\rangle \tag{7.1}$$

It was shown[92][175] that the second-order correlation function $G^{(2)}_{cd}$ can be expressed

as:

$$G^{(2)}_{cd,\mathrm{Ind}} = \frac{1}{4}\left(G^{(2)}_{aa} + G^{(2)}_{bb}\right) \qquad \text{for indistinguishable particles} \tag{7.2}$$

$$G^{(2)}_{cd,\mathrm{Dis}} = \frac{1}{4}\left(G^{(2)}_{aa} + G^{(2)}_{bb} + 2G^{(2)}_{ab}\right) \qquad \text{for distinguishable particles} \tag{7.3}$$

leading to a visibility

$$V = 1 - \frac{G^{(2)}_{aa} + G^{(2)}_{bb}}{G^{(2)}_{aa} + G^{(2)}_{bb} + 2G^{(2)}_{ab}} \tag{7.4}$$

In the particular case of a two-mode squeezed state, we have:

$$|\Psi_{\mathrm{in}}\rangle = \sum_n \frac{\tanh^n(\lambda)}{\cosh(\lambda)} |n, n\rangle \tag{7.5}$$

as seen in chapter 3, where λ is related to the mean number of particles $\langle N\rangle$ through the relationship $\langle N\rangle = \sinh^2(\lambda)$. In this case, we get

$$\begin{cases} G^{(2)}_{aa} = G^{(2)}_{bb} = 2\langle N\rangle^2 \\ G^{(2)}_{ab} = \langle N\rangle (1 + 2\langle N\rangle) \end{cases} \tag{7.6}$$

and therefore

$$\begin{cases} G^{(2)}_{cd,\mathrm{Ind}} = \langle N\rangle^2 \\ G^{(2)}_{cd,\mathrm{Dis}} = 2\langle N\rangle^2 + \dfrac{\langle N\rangle}{2} \end{cases} \tag{7.7}$$

This leads to the visibility

$$V = 1 - \frac{1}{2 + \frac{1}{2\langle N\rangle}} \tag{7.8}$$

The graph of the visibility of the HOM dip as a function of the population $\langle N\rangle$ is given in Figure 7.1a.

We can see that, for a TMS, the visibility of the HOM dip is maximal when the mean number of particles is minimal. It then decreases as $\langle N\rangle$ increases, until approaching 0.5,which corresponds to the classical limit. In fact, one can show that even for a Fock state $|2, 2\rangle$, the visibility of the HOM dip is only 0.66[115]. The HOM interference is a *two*-particle effect, and its visibility decreases rapidly with the number of particles. For a TMS, the probability of having more than two particles at the input increases rapidly, as illustrated in Figure 7.1b, showing the evolution of the probability $\mathcal{P}(n, \langle N\rangle)$ of having n particles in each input port as a function of the average number of particles $\langle N\rangle$. For a TMS, we have:

$$\mathcal{P}(n, \langle N\rangle) = \left(\frac{\tanh^n\left[\sinh^{-1}\left(\sqrt{\langle N\rangle}\right)\right]}{\cosh\left[\sinh^{-1}\left(\sqrt{\langle N\rangle}\right)\right]}\right)^2 \tag{7.9}$$

This is why, in order to exhibit a clear two-photon interference signal far from the classical threshold, one needs to work in a regime where the particle population is low.

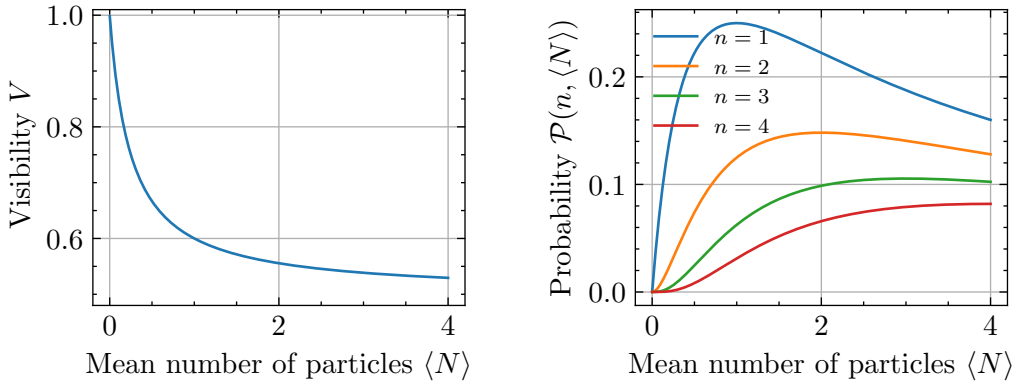

(a) Visibility of the HOM interference as a function of population.

(b) Probability of having n particles in each input port

Figure 7.1: Visibility of the HOM dip and probability of having n particles at the input of the HOM interferometer as a function of the mean number of particles $\langle n \rangle$ for a two-mode squeezed state.

From an experimental point of view, this also reduces the signal-to-noise ratio, as working with a very low population means that most events will correspond to cases where there are no particles. Therefore, it becomes necessary to conduct the experiment on a large statistical sample.

One should note that the visibility of the HOM dip is related to the Cauchy-Schwarz inequality, as discussed in references [175] and [115]: the visibility of the dip can be rewritten

$$V = 1 - \frac{1}{1 + \mathcal{C}} \tag{7.10}$$

where, if we assume that $G^{(2)}_{aa} = G^{(2)}_{bb}$,

$$\mathcal{C} = \frac{G^{(2)}_{ab}}{\sqrt{G^{(2)}_{aa} G^{(2)}_{bb}}} \tag{7.11}$$

The parameter $\mathcal{C}$ should be smaller than 1 in any classical model. We retrieve the classical threshold, since $\mathcal{C} = 1$ leads to a maximal visibility of 0.5. But for stronger correlations as those expected with quantum mechanics, we expect to have $\mathcal{C} > 1$: this violation of the Cauchy-Schwarz inequality leads to a HOM visibility smaller than 0.5.

7.1.2 Tuning indistinguishability

The previous results apply to bosons. The historical experiments were conducted with photons since, historically, it has been easier to manipulate individual photons than single atoms. Now that Bose-Einstein condensates are widely used as coherent sources of atoms, atom optics experiments have successfully replicated some of the major results achieved in photonics, this time with atoms, and the HOM effect is no exception. The challenges of transitioning from photons to atoms to exhibit a HOM interference with external degrees of freedom are detailed in the thesis of R. Lopes[115], and we will only summarize here

the most important points.

- To perform a HOM experiment with atoms, we have, thanks to the optical lattice (as discussed in Chapter 3), a multimode atom pair source, emitting pairs that can be modeled as a sum of TMS states. Such an input state, if the population is low enough, is sufficient to expect a HOM dip with a visibility exceeding the classical limit.
- The second essential element is the beam splitter. To send atoms, initially moving in opposite directions in the lattice reference frame, onto the same beam splitter, mirrors must first be implemented so that atoms can interfere on the beam splitter. Thanks to Bragg pulses, we are able to realize coherent atom mirrors and beam splitters with reflectivity properties that are very good over a momentum range larger than the width of a mode from the source.
- Next, we must be capable of detecting individual atoms and their joint detection probabilities. This is made possible thanks to the MCP and the delay lines, enabling the detection of atoms and correlations between them. It is worth noting that this single detector allows the detection of individual atoms in all modes emitted by the atom source. In the study of cross-correlations for HOM, we will restrict the analyses to the modes coupled by Bragg diffraction.

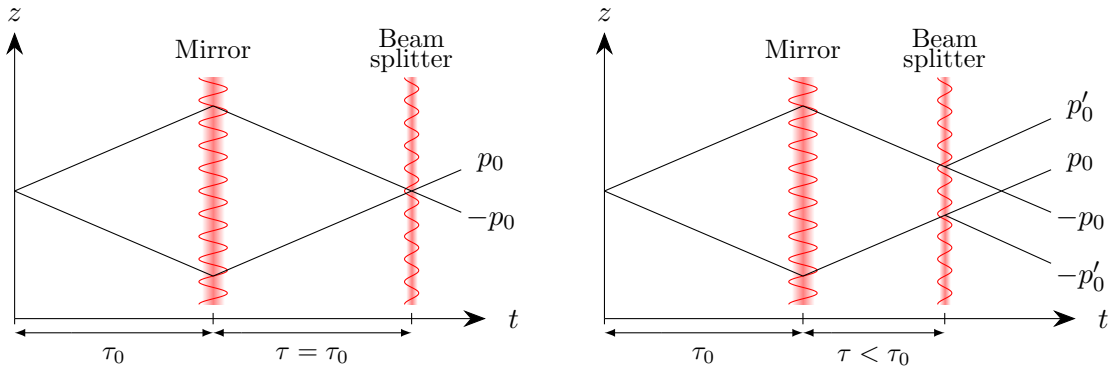

Figure 7.2: Schematic representation of the atomic Hong-Ou-Mandel interferometer in the falling frame. The delay of the second beam splitter is scanned. When the interferometer is closed (left), the wavepackets of the clouds overlap when the beam splitter is realized, and there is no way to determine which path was followed by the measured atoms, which are indistinguishable. When the interferometer is not closed (right), atoms are distinguishable.

- Finally, similarly to the historic 1987 experiment, a means of tuning the distinguishable or indistinguishable character of particles is required. In the historic experiment, this was achieved by controlling the position of the beam splitter. Similarly, in our case where the beam splitter is in momentum space, tuning the timing at which the beam splitter is applied allows us to control indistinguishability. Indeed, if the interferometer is closed, the wavepackets associated to each atom overlap on the beam splitter, and there is no way to determine, at the output of the beam splitter, which atoms come from which input port (Figure 7.2). Conversely, if the interferometer is not closed, the wavepackets do not overlap on the beam splitter, and the output modes vary slightly according to the input mode, eliminating destructive interference and providing any observation of the HOM dip.

In our case, implementing a HOM interferometer has a dual purpose: in the event of observing a HOM dip deep enough to signify purely quantum interference, it serves, on one hand, to verify that the newly designed sinc-shaped pulses are indeed suitable for conducting a Bell-type interferometric experiment. It also makes it possible to determine the beam-splitter timing at which particles are indistinguishable, another key element for observing oscillations of the Bell parameter.

7.2 Observation of an atomic Hong-Ou-Mandel effect

7.2.1 Experimental preparation

We now have all the necessary experimental components to implement an HOM experiment. The optical lattice enables the emission of correlated pairs of atoms. The Bragg mirror and beam splitter allow us to set up an interferometer with controllable timings. Specifically, the delay of the beam splitter can be scanned to tune the indistinguishability of the atoms. Subsequently, the analysis will consist in examining the cross-correlations $G^{(2)}_{cd}$ as a function of the beam splitter delay in order to look for a HOM dip.

The choice of the experimental parameters is important. In accordance with the analysis of the pair correlations emitted by the lattice, we opted to operate in a regime with a low pair density to achieve a significant visibility of the HOM dip. The population of the pairs is mainly controlled by the duration of the lattice and the initial number of atoms in the BEC during the lattice, which can be adjusted without modifying the trap confinement by tuning the holding duration of the ODT before the application of the lattice. The chosen population regime allowed the observation of satisfactory cross-correlations and sub-shot noise variance, and is estimated at 0.28 atoms per mode (0.14 atoms per mode were measured, and we assume a quantum efficiency of the MCP of 50%). Note that this population would not be enough to exhibit a violation of Bell inequality, as we showed in section 4.1.2 that the average number of atoms, for a TMS, has to be smaller than 0.26. Unlike the 2014 experiment conducted by the team, the primary goal here is not to maximize the visibility but to determine the timing of the beam splitter for detecting the closure of the interferometer. Hence, we chose not to further decrease the population to avoid sacrificing the signal-to-noise ratio.

The depth of the lattice is $0.49\,E_{\mathrm{lat}}$, and the detuning between the two beams of the lattice ($\delta = 101.8\,\mathrm{kHz}$) was chosen to ensure that the velocity difference between the two peaks of population density corresponds to the increment of velocity from the two-photon Bragg transfer. This way, the momentum modes coupled by Bragg diffraction are those with the highest population, which has a favorable impact on the signal-to-noise ratio (the mode population values presented in this manuscript hold at peak density).

Regarding the choice of the Bragg pulses, we selected sinc-shaped pulses, with a duration of 1 ms and a two-photon Rabi frequency of $2\pi \times 5\,\mathrm{kHz}$. This frequency corresponds to the Rabi frequency used in the previous experiments conducted in the team with square pulses. If a sinc-shaped Bragg pulse is equivalent to a constant Bragg pulse with the same two-photon Rabi frequency, one should expect to have a similar result in terms of the width of the HOM dip (an assumption that will be discussed later).

Another important parameter to set correctly is the Bragg resonance frequency. It must be ensured that the mirror and the beam splitter couple correlated momentum modes

(Figure 7.3). One can consider that the width of the mirror pulse resonance (narrower compared to that of the beam splitter pulse) is sufficient to efficiently couple around 5 pulse modes, each being $1\,\mathrm{mm.s^{-1}}$ large. We assume that, due to the strict conservation of momentum during the two-photon transition, two coupled modes are systematically separated by $v_\mathrm{B} = 49.6\,\mathrm{mm/s}$. Thus, it is necessary for us to ensure that the error on the detuning does not exceed 3 pulse modes, corresponding to 1.5 kHz.

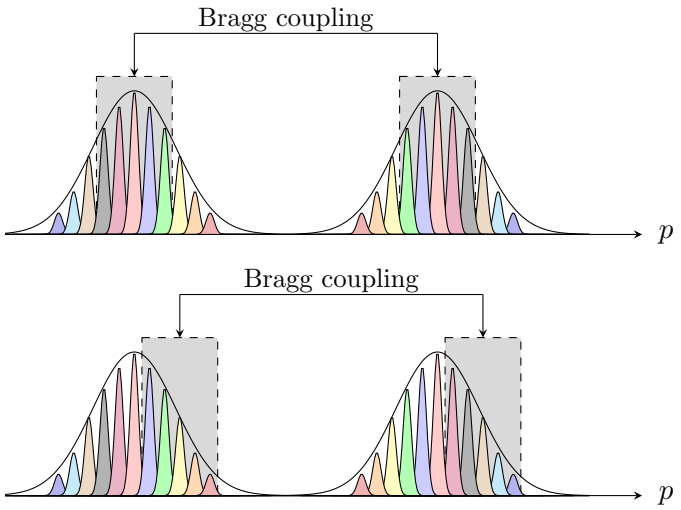

Figure 7.3: Schematic representation of the Bragg coupling for two resonance frequencies. The goal is to couple the correlated momentum modes whose velocity difference equals the Bragg velocity, represented in pink in the center of each Gaussian (top). If we make an error on the Bragg detuning such that the resonance is shifted by more than the resonance width (bottom), the correlated modes we are interested in are not coupled and we cannot observe a HOM interference.

To this end, we use the linear relationship between the detuning and the resonant velocity. Initially, correlation data (presented in Chapter 3) are used to determine the velocities V_{z1} and V_{z2} (in the reference frame of the BEC, for instance) for which the cross-correlation is maximum. The average between these two velocities corresponds to the lattice speed v_lat, i.e., the axis of symmetry between the coupled modes. Having precisely determined beforehand (within 0.5 kHz) the detuning corresponding to the BEC resonance towards the -2 diffraction order, we then have to shift this detuning value in order to be in resonance with the mode located at $v_\mathrm{lat} + v_\mathrm{B}/2$:

$$\delta_\mathrm{HOM} = \delta_\mathrm{BEC}^{(-2)} + k_B\,(v_\mathrm{lat} + v_\mathrm{B}/2) \tag{7.12}$$

The interferometric sequence used for HOM is illustrated in Figure 7.4. The optical lattice is adiabatically ramped up for 200 µs and then held for 500 µs. Subsequently, it is adiabatically turned off in approximately 100 µs, after which both the optical dipole trap and the lattice are switched off, thus releasing the atoms. After a delay of 1 ms, the Raman beams are applied to the atoms, transferring them to the $m = 0$ state, insensitive to the possible remnant magnetic fields. The duration of the Raman pulse is 14 µs. Then, 1.1 ms after the trap is switched off, the 1 ms long Bragg mirror pulse begins. Finally, the timing at which the Bragg beam splitter is applied is randomly scanned between 2100

and 3300 µs, with more points between 2600 µs and 3100 µs. Simultaneously, we took some data without any Bragg pulse in order to be able to properly determine the pair properties directly on the dataset used for HOM.

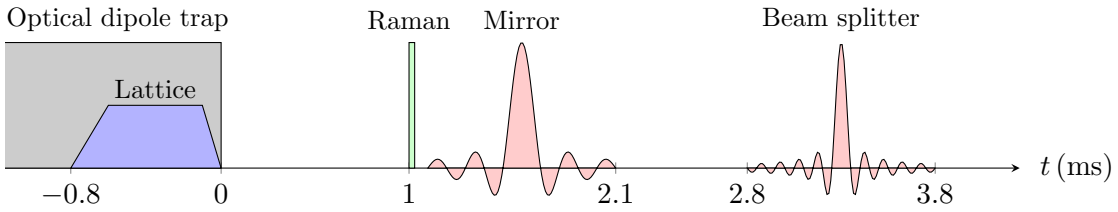

Figure 7.4: Interferometric sequence used for HOM.

It is noteworthy that these temporal parameters significantly differ from those employed in the two previous reported realizations of the HOM experiment. The details are documented in Table 7.1. The longer duration of the sinc-shaped Bragg pulses inherently requires a longer interferometer than what has been done previously. This implies a greater uncertainty in estimating the delay of the beam splitter for closing the interferometer.

Parameter	**This work**	**2014 experiment**[92]	**2016 experiment**[93]
Lattice delay (µs)	0	-150	0
Lattice rise time (µs)	200	300	100
Lattice duration (µs)	500	350	600
Lattice fall time (µs)	100	50	100
Raman delay (µs)	1000	0	0
Raman duration (µs)	14	300	300
Bragg mirror delay (µs)	1100	300	300
Bragg mirror duration (µs)	1000	100	100
Bragg splitter duration (µs)	1000	50	50
Estimated atoms per mode	0.28(5)	0.8(2)	0.33(7)
Expected visibility	0.74(2)	0.62(2)	0.72(2)

Table 7.1: Comparison of the HOM interferometers. The time reference ($t = 0$), from which the delays are defined, corresponds to the time when the trap is switched off. In particular, the lattice delay corresponds to a waiting time between the end of the lattice and the end of the optical dipole trap.

The experiment was conducted in September 2023 after several unsuccessful attempts for which no dip was observed. The reasons for the experiment's failure are not yet clearly established, but a significant drift in the intensity of the Bragg beams over the few days required for acquiring the HOM signals is suspected. This drift results in a substantial degradation of the dip visibility. The likely cause of this drift, despite the power lock before the separation of the Bragg beams, is the emergence of power fluctuations at the Bragg AOMs due to thermal effects.

7.2.2 Results: analysis of the HOM dip

In order to observe the HOM effect, correlations between output modes are studied by calculating the second-order correlation $G^{(2)}_{CD}$. This is done in the same manner as presented in Chapter 3: for a given beam splitter delay τ, the atoms are counted in boxes in momentum space at each experimental cycle. The $G^{(2)}$ function is the average of the product $N_C \times N_D$:

$$G^{(2)}_{CD}(\tau) = \langle N_C(\tau) N_D(\tau) \rangle \tag{7.13}$$

where N_C is the number of atoms counted in the box centered on one output mode and N_D is the number of atoms counted in the box centered on the other output mode.

The size of the box should correspond to the size of a mode. If the box is smaller, the signal-to-noise ratio decreases, and the correlation increases. On the other hand, if it is larger, averaging over several mode pairs occurs, and visibility decreases. Indeed, only the mode pair with a velocity difference corresponding to v_{B} will yield maximum visibility.

Since our source is multimode, it is necessary to identify the mode pair that interferes. This pair is determined by the Bragg resonance and the lattice reference frame. To this end, correlation maps $G^{(2)}(V_{z_1}, V_{z_2})$ were plotted, varying V_{z1} and V_{z2}. We work in the lattice reference frame, and we expect to observe a decrease in $G^{(2)}$ when the interferometer is closed, between two modes separated by $v_{\mathrm{B}} = 49.65\,\mathrm{mm/s}$. To ensure that the results are not affected by differences in density between different delays, we normalize $G^{(2)}$ by the product of the average number of atoms in each box to plot the normalized correlation function $g^{(2)}$:

$$g^{(2)}_{CD}(\tau) = \frac{\langle N_C(\tau) N_D(\tau) \rangle}{\langle N_C(\tau) \rangle \langle N_D(\tau) \rangle} \tag{7.14}$$

Finally, it is important to keep in mind that the atoms numbers provided here are the number of *detected* atoms, reduced by a factor of η compared to the actual number of atoms involved in the experiment. Normalizing the correlation function renders the result independent of quantum efficiency.

The maps obtained are shown in Figure 7.5 for three different delays. On these plots, each point corresponds to the value of $g^{(2)}$ for two boxes of $0.8\,\mathrm{mm/s}$ along z and $8\,\mathrm{mm/s}$ along x and y, centered respectively on V_{z_1} and V_{z_2}. The speed coordinates along x and y, identical for both boxes, are chosen to correspond to the density maximum. The plots are oversampled (as the number of points exceeds the size of the box) to determine the optimal values of V_{z_1} and V_{z_2} for which the correlation decreases. The typical size of the box is shown in black. These data correspond to a bit more than 1000 experimental runs for each delay, which took 3 days of data acquisition.

We observe a specific delay ($\tau = 2800\,\mu\mathrm{s}$) for which a region exhibits a lower correlation function $g^{(2)}$ than the background. This region corresponds notably to pairs V_{z1} and V_{z2} separated by a speed of approximately $v_{\mathrm{B}} = 49.65\,\mathrm{mm.s^{-1}}$. The reason why the low correlation area has an elongated shape along the anti-diagonal is a unknown. Indeed, the corresponding modes ($V_{z1} = -25.6\,\mathrm{mm.s^{-1}}$ and $V_{z2} = 25.6\,\mathrm{mm.s^{-1}}$) are correlated modes, but they should not be coupled by Bragg diffraction if we consider a strict momentum correlation in the two-photon process.

From these correlation map data, one can calculate, for a given pair V_{z1} and V_{z2}, the evolution of $G^{(2)}$ and $g^{(2)}$ as a function of the delay. The graphs presented in Figure 7.6

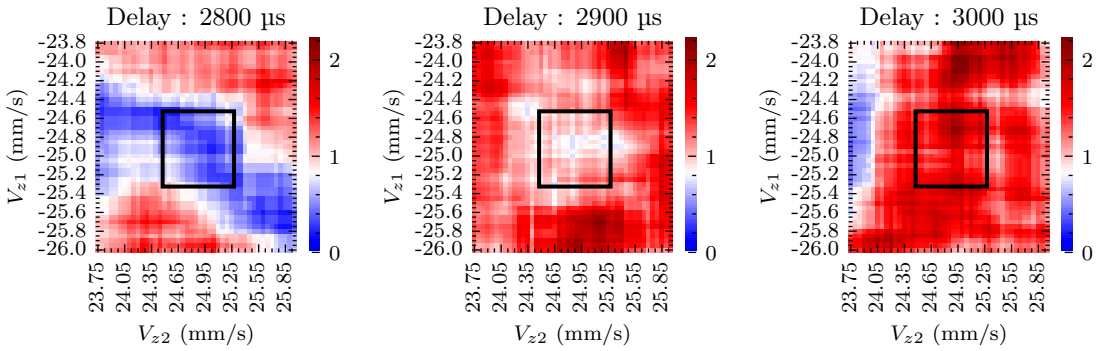

Figure 7.5: $g^{(2)}_{CD}(\tau)$ correlation maps for different beam splitter delays τ. The results are plotted for boxes whose size is given by $\Delta V_z = 0.8\,\mathrm{mm.s^{-1}}$ and $\Delta V_{x,y} = 8\,\mathrm{mm.s^{-1}}$. A typical box is represented in black. We expect $g^{(2)}_{CD}(\tau)$ to decrease when the interferometer is closed.

show a distinctive HOM dip. The graphs were calculated with boxes of $0.8\,\mathrm{mm.s^{-1}}$ along z (which corresponds to the estimated size of a momentum mode), for $V_{z1} = -24.65\,\mathrm{mm.s^{-1}}$ and $V_{z2} = 24.65\,\mathrm{mm.s^{-1}}$, which optimized the dip visibility. The speed difference between these modes is $\Delta v = 49.3\,\mathrm{mm.s^{-1}}$, which is in good agreement with the two-photon Bragg speed ($v_\mathrm{B} = 49.65\,\mathrm{mm.s^{-1}}$). A difference of 3% is also reported in the thesis of R. Lopes[115] who also optimized the visibility by selecting boxes separated by 0.97% of v_B. This point will be discussed in section 7.3.4.

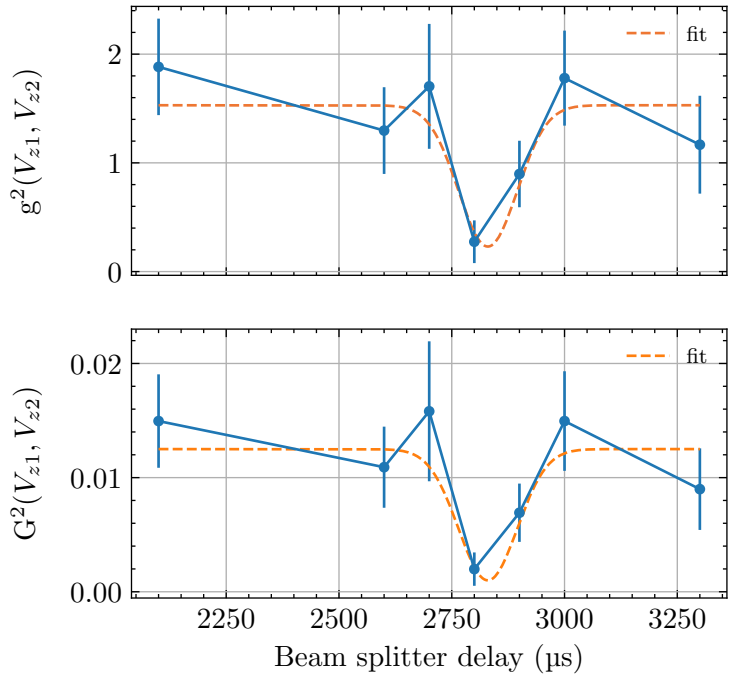

Figure 7.6: HOM dip. The cross-correlation between V_{z_1} and V_{z_2} is plotted as a function of the beam splitter delay. The center of the boxes are $V_{z1} = -24.65\,\mathrm{mm.s^{-1}}$, $V_{z2} = 24.65\,\mathrm{mm.s^{-1}}$,and the size of the boxes are $\Delta V_z = 0.8\,\mathrm{mm.s^{-1}}$ and $\Delta V_{x,y} = 8\,\mathrm{mm.s^{-1}}$.

The error bars were evaluated by bootstrap after 300 random draws. The evolution of the bootstrap-estimated error bar was plotted as a function of the number of draws to ensure the convergence of the bootstrapping technique. In general, the error bar varies as

the square root of the number of draws.

We obtain similar results with a box width of $1\,\mathrm{mm.s^{-1}}$ instead of 0.8 (Figure 7.7). Again, a significant HOM dip can be observed. If the size of the box is further increased, the visibility of the dip decreases significantly (as expected when averaging coincidences over a speed range larger than the size of a mode). Conversely, if the box size is reduced, the signal-to-noise ratio decreases, making it challenging to define a background from which to calculate the visibility.

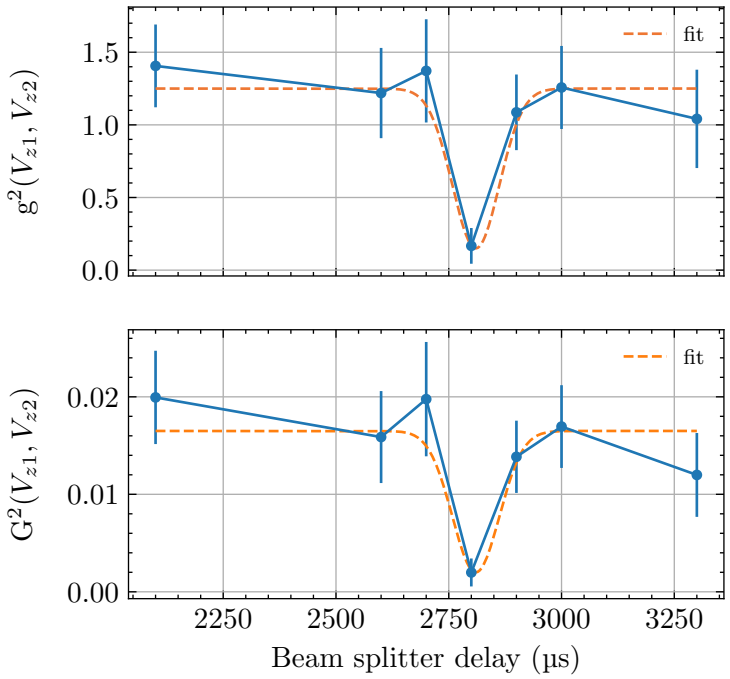

Figure 7.7: HOM dip. The cross-correlation between V_{z_1} and V_{z_2} is plotted as a function of the beam splitter delay. The center of the boxes are $V_{z1} = -24.65\,\mathrm{mm.s^{-1}}$, $V_{z2} = 24.65\,\mathrm{mm.s^{-1}}$,and the size of the boxes are $\Delta V_z = 1\,\mathrm{mm.s^{-1}}$ and $\Delta V_{x,y} = 8\,\mathrm{mm.s^{-1}}$.

An exhaustive analysis of the HOM dip can be found in R. Lopes' thesis[115]. The HOM dip was fitted with a Gaussian function to deduce the visibility, width, and especially the center of the dip, that is to say the beam splitter delay corresponding to the situation where the interferometer is closed. The results of the fit are given in Table 7.2. There is a trend in which the contrast slightly decreases with the size of the box, while the width decreases, but it is not statistically significant.

Box width ($\mathrm{mm.s^{-1}}$)	**Correlation function**	**Visibility**	**Width** (µs)	**Center** (µs)
1.0	$g^2(\tau)$	0.88(9)	52(15)	2810(30)
	$G^2(\tau)$	0.88(9)	55(15)	2816(30)
0.8	$g^2(\tau)$	0.85(13)	65(25)	2832(50)
	$G^2(\tau)$	0.86(13)	67(25)	2830(50)

Table 7.2: Fit results of the HOM dip on the $G^{(2)}$ correlation function. The time reference ($t = 0$), from which the delays are defined, corresponds to the time when the trap is switched off.

At this stage, we emphasize that these preliminary data should be approached with caution. In contrast to the previously reported HOM experiments, only one data point, obtained for a delay of 2800 µs, stands out due to its significant visibility leading to the HOM dip. In a somewhat less clear manner, it can be added that the data point at 2900 should also be considered in this context, since the correlation function appears to be lower than the background value when considering a box size of $0.8\,\mathrm{mm.s^{-1}}$. Despite all other indicators suggesting the observation of the HOM dip, these limited data must therefore be considered cautiously, as suggested by the significant error bars which prevent us from providing a comprehensive quantitative analysis.

The results are compared to those obtained with the previous HOM experiments reported in the team in Table 7.3.

Parameter	**This work**	**2014 experiment** [92]	**2016 experiment** [93]
Visibility	0.88(9)	0.65(7)	0.78(6)
Width (µs)	55(15)	70(40)	85(23)
Beam splitter delay (µs)	2816(30)	875(50)	1150(30)
Box width $\Delta V_z\,(\mathrm{mm.s^{-1}})$	1.0	2.8	2.6
Box width $\Delta V_{x,y}\,(\mathrm{mm.s^{-1}})$	8.0	4.8	4.0

Table 7.3: Comparison of the results of the HOM dip on the $G^{(2)}$ correlation function. The time reference ($t = 0$), from which the delays are defined, corresponds to the time when the trap is switched off.

With a box size of 0.8 mm/s, a visibility of $85 \pm 13\,\%$ is observed. The expected visibility is 74 % for a population estimated at 0.28 atoms per mode, which is a bit lower but remains within the error bar. If the number of atoms per mode was not overestimated, it is possible that taking more data would lead to the detection of more atoms in the dip which will decrease the visibility.

The width of the dip is 53 ± 17 µs, which is smaller than in previous experiments. This is not surprising, as we are now working in a more anisotropic trap than a few years ago. This implies that the size of a mode is smaller, as evidenced by both the width of the dip and the size of the integration box required to observe a signal. Furthermore, it should be noted that for the larger box, the width of the dip is smaller, as previously observed. This is consistent with the HOM dip model developed in Chapter 5: without considering the size of a mode and assuming it has an infinite coherence length, then the HOM experiment is equivalent to averaging the Bell correlator in a box centered on resonance. The larger the averaging box, the more the correlator varies with detuning as one moves away from the interferometer closure, and thus the HOM dip is narrower.

Finally, we find that the delay (relative to the trap cutoff) at which we observe the dip is equal to 2813 ± 33 µs for the 1 mm/s box and 2831 ± 51 µs for the 0.8 mm/s box. We can try to interpret this delay in terms of interferometer closure, particularly to determine the time at which the initial state is emitted. From experimental analysis, we have seen that for a sinc-shaped pulse, most atoms are transferred by Bragg diffraction at the time of the central lobe of the sinc function. Additionally, the study of HOM interferometer closure based on a plane wave model from Chapter 5 has established that for two sinc-shaped

pulses, the center of the beam splitter and the initial instant are symmetrical with respect to the center of the mirror.

In the conducted experiment, the delay of the mirror is 1.1 ms (corresponding to a central lobe at 1.6 ms, see Figure 7.4), and the delay of the beam splitter is 2.8 ms for the interferometer to be closed, corresponding to a central lobe at 3.3 ms. Hence, by subtracting the time interval between the mirror and the beam splitter to the central lobe of the mirror, we estimate that the initial instant of the interferometer would correspond to a delay of -0.1 ms, i.e. 100 µs before the trap cutoff. This precisely aligns with the end of the lattice application, at the moment when its intensity begins to decrease (Figure 7.8). This result provides reassurance regarding the validity of the observed HOM dip: since the number of created pairs grows exponentially with the lattice duration, we expect that most pairs are created at the end of the lattice, so the beginning of the interferometer corresponds precisely to this value. A similar time had been determined during the first experiment in 2014, but this was not the case in 2016, for unknown reasons.

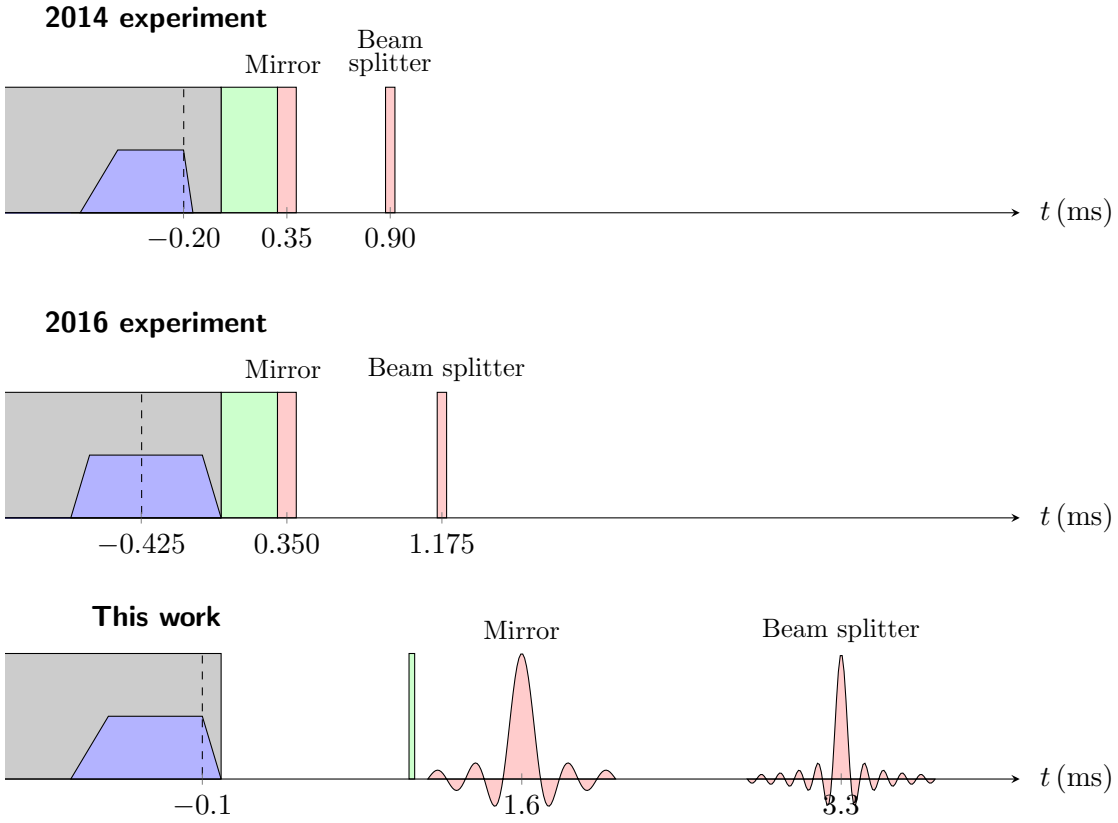

Figure 7.8: Comparison between the measured closures of the HOM interferometer. In gray: optical dipole trap is on. In blue: pairs creation lattice. In green: Raman pulse. In red: Bragg pulses.

In order to get more precise results with smaller error bars, we aimed to add points to the obtained curve, by conducting the same experiment and adding beam splitter delays. However, after adding the new data to the dataset, the HOM dip lost a significant visibility, preventing us from completing the analysis. At this stage, we became aware of the power drift of the Bragg beams mentioned earlier, leading to an important decrease in the mirror and beam splitter reflectivity. This problem was later corrected through

digital feedback on the setpoint power at the output of the Bragg/Raman AOM. This was achieved after calibrating the photodiode that we use to observe the beating between the two Bragg beams. We were able to exhibit a clear correlation between the measured power on the amplitude of the beating signal and the number of atoms transferred by a Bragg mirror. This calibration enabled us to adjust the setpoint power in order to maintain the good reflectivity of the Bragg pulses.

7.2.3 Ramsey fringes

The next step, like in the 2017 article, is to conduct a study of the correlator's evolution not as a function of a control parameter, but of detuning (or, equivalently, the speed class out of resonance). This would ensure that, like it was the case before, a significantly non-zero value of the correlator can be distinguished when looking at the out of resonance quadruplets when performing an HOM interferometer (see section 5.1).

However, we have observed the presence of density fringes along the z-axis in the velocity profile of the pairs at the output of the interferometer (Figure 7.9). The amplitude of these fringes seems to increase as we move away from resonance doublet $(p_0, -p_0)$, naturally leading to Ramsey fringes, which are observed when two successive beam splitters are applied to a coherent cloud. Of course, this phenomenon exhibits maximum contrast when two beam splitters are used, but it remains possible even when a pulse does not have a reflectivity of 1, which is the case for our mirror that is not perfect out of resonance. Thus, we attribute the appearance of these fringes to the decreased reflectivity of the mirror off resonance. The measured fringe spacing is $1.4\,\mathrm{mm.s^{-1}}$, which is consistent with the expected fringe spacing between two pulses separated by 1.7 ms, as is the case for Figure 7.9.

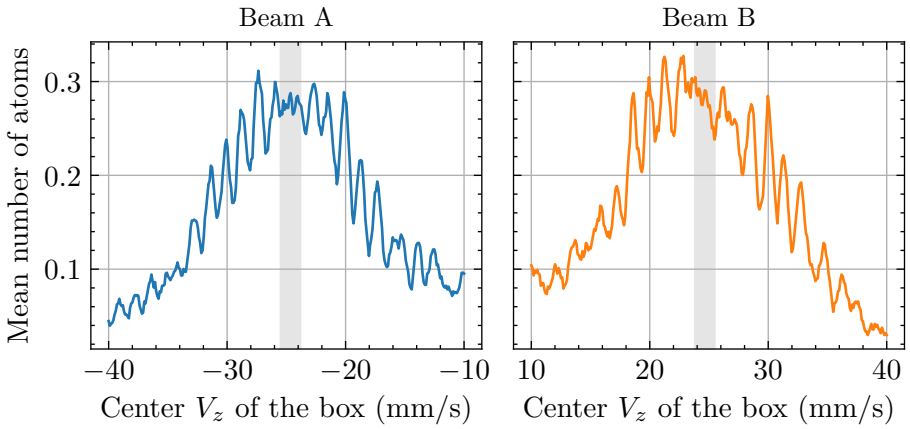

Figure 7.9: Density profile along the vertical direction for $\tau = 2800\,\mu\mathrm{s}$. The box width is $\Delta V_z = 1.6\,\mathrm{mm.s^{-1}}$ and $\Delta V_{x,y} = 8\,\mathrm{mm.s^{-1}}$, which corresponds to approximately two modes.

This phenomenon was not noticed at first because when plotting the density profiles of the HOM dataset, we were averaging the data for different delays, resulting in different fringe contrasts that were smoothed out.

Importantly, this density issue leads to correlations when examining the joint detection probabilities. Indeed, to plot the Bell correlator as a function of momentum out of

resonance, we compute the probabilities

$$\mathcal{P}(p,q) = \frac{\langle N(p)N(q)\rangle}{\langle N(p)N(q)\rangle + \langle N(-p)N(-q)\rangle + \langle N(p)N(-q)\rangle + \langle N(q)N(-p)\rangle} \tag{7.15}$$

and so on for $\mathcal{P}(-p,-q)$, $\mathcal{P}(p,-q)$ and $\mathcal{P}(q,-p)$, where $p = p_0 + \Delta p$ and $q = p_0 - \Delta p$.

Since the density varies on a scale similar to that of the size of the box, which is taken to be equal to that used to observe the HOM dip, the density fringes are visible in the joint probabilities. As a consequence, plotting the correlator as a function of Δp results in the observation of correlations that are not related to the expected Bell interference effect, or at least not exclusively. The variation of the correlator evidently exhibits correlations associated with this undesirable effect of density fringes, rendering the analysis conducted in 2017 impossible.

It would be interesting to understand why this effect was not observed previously: it was not detected in the analysis of the off-resonance correlator in 2016 but also not reported during the study of the HOM dip in 2014. This is actually an expected phenomenon when the reflectivity of the mirror decreases. The quality of the mirror used in the previous HOM experiments was not superior to that used for the dataset presented in this manuscript. It is possible that larger phase fluctuations at that time blurred the phenomenon, or that it was present but a misalignment in the vertical direction of the Bragg beams led to fringes not only along the z-axis but also along an axis inclined along x or y. This would make it more difficult to detect if the density profile was traced only in one direction, integrating over the other two.

Note that this effect is particularly undesirable in the state of the correlator as a function of Δp. Nevertheless, it is not problematic for a Bell test in its version where a control parameter is varied for a given quadruplet. Indeed, when Δp is fixed, even if there are fringes when looking at different velocity classes, there is no Ramsey fringes related variations in density when varying the phase.

7.3 First Bell test attempt

7.3.1 Parameters and procedure

Despite the reservations expressed earlier, the results of the HOM dip were deemed promising enough for a decision to be made in October 2023 to launch a first Bell test. The parameters chosen for the delays of the Bragg pulses correspond to those for observing the HOM dip. The mirror is similar to that used in the HOM experiment, while the beam splitter is the one determined in Chapter 5. The Bragg parameters are given in Table 7.4. We use sinc-shaped pulses to optimize the reflectivity of the Bragg pulses, and modulate the beam splitter to control the phase imprinted on each loop of the interferometer. Recall that the expressions of the sinc Bragg pulses write, between τ and $\tau + T$,

$$\begin{cases} \Omega_{\mathrm{R}}(t) = \Omega_{\mathrm{M}}\,\mathrm{sinc}\left[\Omega_{\mathrm{S}}\left(t-\tau-\dfrac{T}{2}\right)\right] \mathrm{e}^{\mathrm{i}\Delta\varphi} & \text{for the mirror} \\ \Omega_{\mathrm{R}}(t) = \Omega_{\mathrm{M}}\,\mathrm{sinc}\left[\Omega_{\mathrm{S}}\left(t-\tau-\dfrac{T}{2}\right)\right] \cos\left[\dfrac{\Omega_{\mathrm{D}}}{2}(t-\tau)+\dfrac{\theta}{2}\right] \mathrm{e}^{\mathrm{i}\Delta\varphi} & \text{for the beam splitter} \end{cases} \tag{7.16}$$

where $\Delta\varphi$ is the phase difference between the two lasers, which does not need to be locked in our weak version of a Bell test where we control the phase *difference* between A and B but not the absolute phase imprinted on A or B.

The control parameter θ, which is related to the phase at the origin of the modulation function for the beam splitter, is scanned iteratively for 12 values between 0° and 330°.

Parameter	Mirror	Beam splitter
Shape	sinc	sinc
Delay τ (ms)	1.1	2.8
Duration T (ms)	1	1
Two-photon Rabi frequency Ω_{M} (kHz)	5	0.8
sinc frequency Ω_{S} (kHz)	5	1.6
Modulation frequency Ω_{D}(kHZ)	–	1.3

Table 7.4: Bragg pulses experimental parameters used for the first Bell test attempt.

The width of the beam splitter is such that four to five Bell interferometers are run in parallel, meaning that as many quadruplets are coupled by the Bragg pulse and thus potentially allow the observation of a Bell parameter oscillation. A beat setup between the two Bragg beams allows for logging of the temporal profile of the beating during the Bragg pulses. This signal serves both to verify the Bragg power, enabling correction of power drift effects using a feedback loop, and to fit the beating signal to determine the global phase ϕ_{G} between the two lasers, which is the only parameter not under control at this stage.

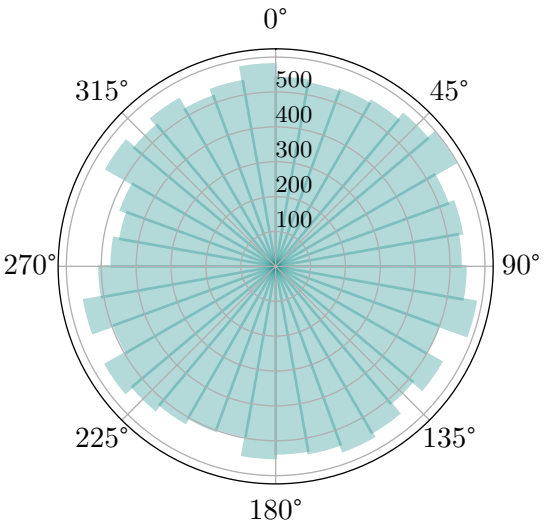

Figure 7.10: Histogram of the laser phase difference $\Delta\varphi$ measured during the Bell experiment. Data collected over 20 000 experimental runs. $\Delta\varphi$ was fitted from a beating setup just before the beams are directed to the atoms.

A total of approximately 20 000 experimental runs were conducted, with roughly 1200 runs per value of θ. Fits of the global phase show a difference of less than 5° between the phase determined at the mirror and at the beam splitter, indicating good stability of $\Delta\varphi$ throughout the interferometer duration. However, from one run to another, this phase

varies significantly, as shown in the histogram in Figure 7.10. The uniform distribution of this global phase ensures that it does not introduce any particular bias into our analysis.

A thorough analysis of the results was conducted, but unfortunately did not reveal any oscillation of the Bell parameter. For all considered quadruplets, the joint detection probabilities did not exhibit similar pairwise evolutions, as one would expect to have $\mathcal{P}(p,q) = \mathcal{P}(-p,-q)$ and $\mathcal{P}(p,-q) = \mathcal{P}(-p,q)$. In the following, we will seek to provide some insights to explain why the test failed.

7.3.2 Sensitivity to the interferometer closure

The only parameter that changed between the Bell and the HOM experiments is the delay of the Raman pulse. It was 1 ms for HOM and was decreased for the Bell test so that the atoms would be immediately transferred into $m = 0$ at the trap cutoff.

The typical delay for the Raman pulse we use to transfer atoms from $m = 1$ to $m = 0$ in a BEC is indeed on the order of 1 ms. This is because we wait several hundred microseconds for the cloud to become less dense before transferring it into $m = 0$, where the rate of Penning collisions is much higher. A too-dense cloud in the $m = 0$ state indeed leads to significant losses, which is why we prefer to wait for an expansion of the cloud in time of flight before the Raman pulse.

While this is true for the atoms in the BEC, there is no reason to expect collision effects on the pairs, which are particularly dilute. Therefore, the Raman delay was reduced. But this may have had significant consequences on the interferometer. Indeed, if there is an undesirable magnetic force that accelerates the atoms in a particular direction when they are in $m = 1$ during their fall, this will result in unexpected propagation terms in the interferometer, leading to a modification of the interferometer closure condition. Modifying the Raman delay between two experiments thus may be responsible for changing the closure condition. It has been observed in section 5.1 that if the interferometer is not closed, the correlator tends to vary more rapidly within a given velocity range, resulting in decreased visibility and increased error bars.

This effect can be quantified using numerical resolution of the Bell interferometer presented in Chapter 5 for the case of plane waves. Here, we neglect any spatial effects related to the propagation of wave packets (which may deviate from reality) and focus on calculating the Bell correlators for different quadruplets separated from the HOM resonance by $\Delta v = 1$, 3, and 5 $\mathrm{mm.s^{-1}}$. The calculation is similar to that used to plot the correlators with sinc pulses as a function of the control parameter θ, except that this time we also scan the delay τ of the Bell beam splitter to investigate the consequences of an imperfect interferometer closure on the oscillation of the Bell parameter. We observe that while imperfect closure does not affect the shape of the oscillation, it does, as expected, affect its amplitude and variation within a given momentum range.

Recall that, for a given momentum quadruplet, the Bell oscillation can be written

$$E(\theta) = A\,\cos(\theta + \phi_0) \pm \Delta E(\theta) \tag{7.17}$$

where $E(\theta)$ and $\Delta E(\theta)$ are respectively the mean and standard deviation of the Bell correlator $E(p,\theta)$ averaged over a given momentum quadruplet.

In Figure 7.11 is plotted the oscillation amplitude A as a function of the closure delay $\Delta\tau_\mathrm{c} = \tau - \tau_\mathrm{c}$, which corresponds to the difference between the delay τ of the beam splitter

(scanned) and the delay τ_c for which we established that the interferometer was closed. The error bars correspond to the average variation $\langle \Delta E(\theta) \rangle_\theta$ of the correlator over a velocity box for the various values of θ.

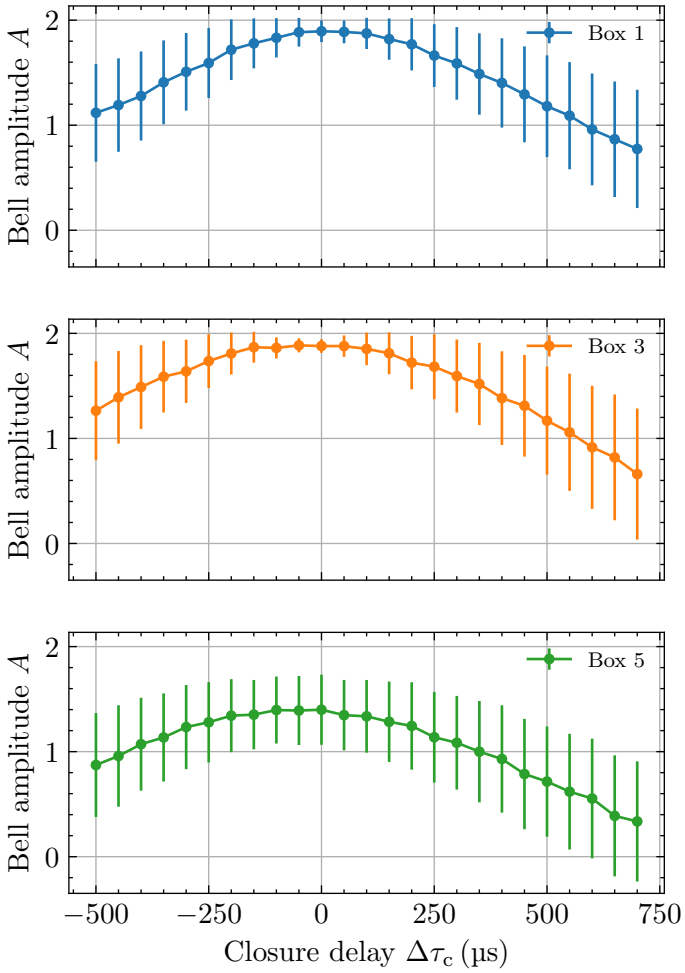

Figure 7.11: Simulated amplitude of the Bell correlator oscillation as a function of the closure delay. For each delay of the beam splitter, a Bell correlator was calculated as a function of θ, along with the standard deviation of E for each value of θ within an integration box of $1\,\mathrm{mm.s^{-1}}$. Here, we represent the amplitude of $E(\theta)$. The error bars correspond to the mean value of the standard deviation $\Delta E(\theta)$ within the integration box. This was done for three velocity quadruplets, labeled by their velocity center $\Delta v = 1$, 3 and $5\,\mathrm{mm.s^{-1}}$ (where $\Delta v = 0$ corresponds to the HOM resonance).

The results show that the amplitude decreases relatively slowly with the closure delay, while the error bar, which characterizes the typical variation of the correlator within a box, also increases relatively slowly compared to the delays involved in the interferometer. The effects worsen as the considered quadruplet is far from resonance, which makes sense as the variation of the correlator with the detuning (and thus the velocity class) increases as one moves away from resonance. In this case, it is the imperfect reflectivity of the mirror for the Bragg quadruplets that is responsible for this effect.

One could consider that the oscillation of the correlator becomes impossible to detect when the error bar is of the order of the amplitude of the oscillation, which occurs for a closure delay $\Delta\tau_c$ on the order of 500 µs. Thus, it seems that in this model, only

a significant deviation from interferometer closure would result in a total loss of the signal.

It seems unlikely that the change in the Raman delay would result in such a high closure delay, so this change may not be the only effect responsible for the fact that no Bell signal was observed. Nevertheless, since we suspect a misalignment of the Raman beams, responsible for an additional momentum transfer along the vertical direction, a change in the Raman delay could also lead to a change in the resonance with the pairs when choosing the Bragg detuning. It should be noted that to avoid suspecting this effect, it will be important in future tests to keep the same Raman delay for Bell as was used for HOM.

Note also that the previous model only takes into account the visibility loss due to the Bragg pulses, for a perfect Bell state. Therefore, as our input state is supposed to be a TMS and not a Bell state, the expected amplitude of the oscillation is actually lower than what was plotted in Figure 7.11 (as discussed in Chapter 4). This negative effect on the signal detection due to an imperfect input state must be added to those that are taken into account in the model (imperfect Bragg pulses, imperfect closure of the interferometer).

7.3.3 Sensitivity to the detuning

In the section on the preparation of the HOM experiment, it was mentioned that it was necessary to precisely determine the Bragg detuning in order to couple the correct momentum classes. This is even more crucial in a Bell test.

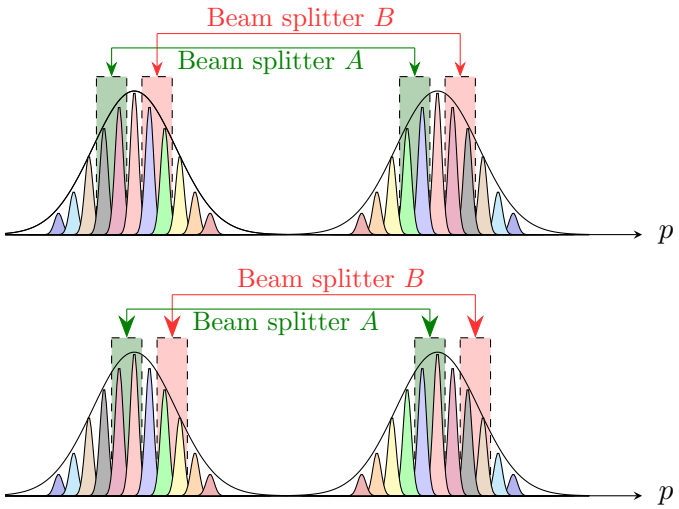

Figure 7.12: Schematic representation of the Bragg coupling for two resonance frequencies. The goal is to couple a momentum quadruplet, where modes are correlated two by two. This implies that two correlated modes must be coupled by two different beam splitters. This is the case in the top scheme, where the detuning is such that the center of the two beam splitters resonances corresponds to the HOM doublet. If the detuning is shifted by only one mode (bottom scheme), then the beam splitters do not couple the same modes and no correlation can be observed.

For a Bell test, it is necessary to adjust the detuning between the two lasers so that the resonant doublet couples the modes used for HOM. For the HOM experiment, it was acceptable to be off by a few modes on the resonance, as long as the doublet $(p_0, -p_0)$ was within the resonance width of the mirror and beam splitter Bragg pulses. In the case of a

Bell experiment, the error made on the detuning must be smaller than the size of a mode (Figure 7.12).

Indeed, it is necessary for the Bell beam splitter to be effective that the correct modes are coupled. It is imposed in the temporal profile of the beam splitter pulse that the two resonances of A and B are separated by Ω_D, so we need to correctly determine the right detuning to couple p_0 and $-p_0$. Even though the width of each beam splitter resonance (A or B) is wider than the size of a mode, a shift of one mode inevitably leads to the Bragg coupling of uncorrelated modes, which would result in a complete loss of signal. Since a mode has a width of $1\,\mathrm{mm.s^{-1}}$, which corresponds to a detuning range of $0.5\,\mathrm{kHz}$, the detuning must be smaller than this quantity. This is experimentally challenging to achieve since, so far, even by locating the pair reference frame by studying the center of the cross-correlations, the uncertainty in the fit center result remains larger than this value.

7.3.4 Sensitivity to the initial cloud position

Of course, the previous Bragg detuning setup also requires precise knowledge of the value of the Bragg velocity, as shown by relation 7.12. This velocity has been determined experimentally using Bragg pulses in the Kapitza-Dirac regime as well as Bloch oscillations with a good precision.

However, we have recently found out that our velocity measurements exhibited a systematic error stemming from an effect that we had previously neglected. This systematic error can be highlighted with a simple experiment, which consists solely of making a short Bragg beam splitter, resonant with the condensate, for different delays after the trap cut-off. We can then make a density fit of the two clouds detected on the MCP, and convert the temporal difference between the two peak centers into velocity, thus determining the Bragg velocity as a function of the delay. The results are given in Figure 7.13.

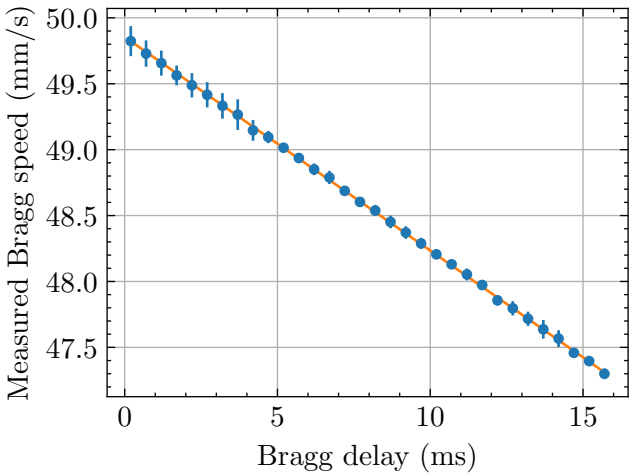

Figure 7.13: Measured Bragg speed as a function of the Bragg delay. The graph indicates a systematic error when calculating the velocity of atoms, by neglecting their initial position before time of flight.

We find that the Bragg velocity we measure depends linearly on the application delay of the beam splitter, which is, of course, not supposed to be the case. In reality, it is not the Bragg velocity that depends on the delay, but rather our method of calculating the velocity from the arrival times that was incorrect. This linear dependence can be

explained using a simple reasoning.

Let us consider a BEC, whose initial velocity is 0 in the laboratory frame. Again, we consider that the initial time correspond to the optical dipole trap cutoff while the space origin is the center of the MCP. The trajectory over time of the cloud is:

$$z(t) = -\frac{gt^2}{2} + L \tag{7.18}$$

where $L = gt_{\mathrm{BEC}}^2/2$ is the distance between the trapped cloud and the MCP, with t_{BEC} being the arrival time of the condensate on the MCP. Atoms detected at time T have an initial velocity V_z such that

$$V_z = \frac{1}{2}gt - \frac{L}{t} \tag{7.19}$$

For the mean velocity of the condensate, we find of course $V_z = 0$.

Now, at $t = \tau$, we apply a Bragg beam splitter pulse to transfer half of the atoms to the first diffraction order. The transmitted cloud is not affected by the pulse, and we can apply the previous result. The reflected cloud follows a trajectory that can be written as, for $t > \tau$:

$$\begin{aligned} z(t) &= z(\tau) - \frac{1}{2}g(t-\tau)^2 + (v(\tau) + v_{\mathrm{B}})(t-\tau) \\ &= -\frac{gt^2}{2} + v_{\mathrm{B}}t + L - v_{\mathrm{B}}\tau \end{aligned} \tag{7.20}$$

This second cloud falls on the MCP at time t_1 such that $z(t_1) = 0$. From this relation, we get

$$v_{\mathrm{B}} = \frac{1}{2}gt_1 - \frac{L}{t_1} + \frac{v_{\mathrm{B}}\tau}{t_1} \tag{7.21}$$

Thus, when we calculate the velocity from the equation

$$V_z = v_{\mathrm{B}}^{(\mathrm{mes})} = \frac{1}{2}gt_1 - \frac{L}{t_1} = v_{\mathrm{B}}^{(\mathrm{mes})} = v_{\mathrm{B}} - \frac{v_{\mathrm{B}}\tau}{t_1} \tag{7.22}$$

we miss a corrective term related to the position of the cloud after the pulse, equal to $v_{\mathrm{B}}\tau/t_1$. This term is actually not negligible when the application time of the pulse equals a few milliseconds: it is equal to $0.8\,\mathrm{mm.s^{-1}}$ for $\tau = 5\,\mathrm{ms}$, which is approximately the size of a momentum mode.

In Figure 7.13, the data were fitted with a corrective function $\tilde{v}(t)$, defined as

$$\tilde{v}(t) = v_{\mathrm{B}}\left(1 - \frac{\tau}{t_1}\right) \tag{7.23}$$

where $t_1 \approx t_{\mathrm{BEC}}$ is fixed and v_{B} is a fit parameter. This provides a measurement of v_{B}, which does not vary as a function of the Bragg delay.

As a result, the velocities of atoms that have been subjected to Bragg pulses are systematically calculated incorrectly. This can have important consequences, notably on the determination of the detuning for the Bell experiment if a false value of v_{B} is used. This must be added to the imprecision of the lattice velocity determination, and both effects possibly explain why no Bell correlation signal could be observed. In future analyses, it will be necessary to include these corrections when calculating velocities from arrival times, particularly when analyzing datasets from HOM or Bell interferometers.

In this respect, it should be noted that while we found a HOM doublet for velocities v_0 and $-v_0$ whose difference was indeed very close to the measured value for v_B, a difference of a few percent between the box centers and v_B had been reported in 2014, probably due to an incorrect estimate of the Bragg velocity, calculated via the Kapitza-Dirac regime of Bragg diffraction.

Conclusion and outlook

The aim of this manuscript has been to provide a detailed overview of our quest for realizing a Bell's inequality test with momentum correlated atoms.

After several years of experimental problems, the metastable helium experiment I worked on for my thesis has been improved and modernized, and has yielded promising results for launching a Bell inequality test, from the stability of condensates to the correlation properties of pairs created by four-wave mixing. Although the strength of the correlations observed is not as significant as hoped, we have succeeded in observing purely quantum correlations, such as a violation of the Cauchy-Schwarz inequality and a sub-Poissonian variance.

I personally contributed to develop an original strategy to control the phase imprinted on the two momentum doublets involved in the Bell interferometer, leveraging the fact that the pairs of modes A and B do not have the same Bragg resonance frequency, allowing the use of a two-frequency beam splitter to be selectively resonant with A and B. An important point to avoid sensitivity to laser phase fluctuations is to use the same beams for A and B and modulate their intensity. I have implemented the appropriate hardware and conducted experiments that provide proof of concept using Ramsey fringes, whose interference pattern was shifted in opposite directions for A and B, validating this method.

Although the first Bell test we conducted was not successful, we remain confident in the forthcoming observation of correlation signals, the amplitude of which may be sufficient to provide the first direct evidence of Bell inequality violation with massive particles entangled in momentum. Nevertheless, some points still require clarification and improvement.

Towards new Bell tests

At the end of 2023, new experimental issues prevented us from continuing interferometric experiments. We would like to conduct an HOM experiment again, and then perform a new Bell test, taking into account the errors that have been recently identified, particularly in our method of calculating velocities from arrival times. Including corrective terms related to the delay of the Bragg pulses in the datasets analysis poses no significant issues and would help avoid systematic errors, in the estimation of the Bragg velocity for instance.

In Chapter 4, we highlighted the advantages of our setup compared to the one used by the team of A. Truscott to demonstrate Bell correlations[94]. While our setup is much less sensitive to phase fluctuations, this comes at a certain cost because we need to use two different resonance frequencies for doublet A and doublet B, which requires precise

adjustment of the Bragg detuning. In order to be less sensitive to the adjustment of this parameter, required to couple the correct momentum modes, we would like to increase the size of the modes along z. As we have seen, this is directly related to the size of the condensate, and thus to the shape of the optical dipole trap. In recent weeks, an adjustable telescope has been implemented on the path of the horizontal beam of the trap. The objective is to be able to tune its waist and thus decrease the trap's anisotropy, in order to increase the size of the modes along z. Datasets of pairs should be collected soon to study the correlations obtained with this new setup.

Recall that, in the weak version of the Bell test we conducted, we only control the phase difference between loops A and B. The demonstration of Bell's inequality strictly involves independent degrees of freedom for A and B. A genuine Bell test would therefore require an independent control of the phase imprinted on A and B. This means that we should control the global phase involved in the Bell test, a phase which is currently left unconstrained. Implementing such a setup is not particularly challenging. We already have a beat system in place to measure this global phase, which is the relative phase between the two Bragg beams. This phase was shown to remain approximately constant at the timescale of the interferometer. It would be feasible to add a phase-locking system to control its value. Experimental details are provided in Appendix C.

Interferometric measurements

Some results obtained with the Bragg pulses require further analysis. In particular, although the Mach-Zehnder experiment we performed aimed at making sure that sinc pulses could lead to the observation of a significant interference, which was successful, we would like to understand why the Mach-Zehnder interferometer did not allow us to determine the value of g properly. It will be necessary to repeat the experiment described in Chapter 6, comparing the results obtained with a sinc pulse and with a square pulse to see if the pulse shaping has an impact on the experiment outcome. It would be interesting to vary the duration of the pulses to determine their influence.

Note that the measuring the interfringe of the interference pattern in the Ramsey experiment also provides another way of determining gravity. We would like to conduct such an analysis and compare it with the Mach-Zehnder gravimeter.

Characterization of the detector

The correlations measured between atom pairs are not as strong as expected. In particular, it is surprising that the normalized variance of the difference in the number of atoms in pairs does not decrease below 0.85. One would indeed expect it to decrease to $1-\eta$, where η is the quantum efficiency of the detector, estimated at 50%. Is it because of the bad quality of our quantum state? Is there a mechanism which decreases the strength of the correlations? Is the quantum efficiency lower than expected?

To verify the last point, we would like to conduct a precise study of the quantum efficiency of the MCP. Such a study requires calibration of the number of atoms by absorption for a given cloud, from which a very small known fraction of atoms would be extracted via Raman to avoid saturating the MCP. The ratio between the number of detected atoms and the number of transferred atoms then directly provides an estimation of the quantum efficiency of the detector. Preliminary work has been done in this direction but needs to be continued.

Furthermore, the size of a mode ($\approx 0.8 - 1\,\mathrm{mm.s^{-1}}$) corresponds to an arrival time difference of $\Delta t \approx 80 - 100\,\mu\mathrm{s}$ on the MCP. This is not far from the alleged longitudinal resolution of the MCP, estimated around 10 µs by geometric considerations. It is obviously important for our velocity measurements that the width of a mode remains greater than the resolution, which has not been measured yet. This is why it would be interesting to experimentally determine the resolution limit of the MCP, in the vertical direction in particular. This can be done by performing a genuine HBT experiment, using thermal clouds to determine the width of the second order function correlation. In the case where the correlation length in one direction is very small, then the width of the measured $g^{(2)}$ function is dominated by the resolution, which can therefore be measured[59][176]. Using clouds of very different geometries from the magnetic trap and the optical dipole trap, we have access to the resolution in every direction, which would provide a valuable characterization of the MCP regarding the precision of our measurements.

Probing strong correlations

A low quantum efficiency would not explain why the normalized second order correlation function is not as high as we expect. Again, it is not obvious to identify the cause of the decrease in crossed correlation and its broadening. Recent numerical simulations of the four-wave mixing process with fewer assumptions as possible did not identify any mechanism which would be responsible for the weak correlations we observe. One last important hypothesis that remains to be investigated is the fact that the atoms are in a harmonic trap. Most analytical and even numerical results for BECs in a lattice are performed in an uniform potential.

We are currently investigating the possibility to implement a Digital Micromirror Device (DMD) on the experiment in order to trap the atoms in a uniform potential (of finite size). This would also open up a wide range of possibilities for experiments on metastable helium condensates, as we could create potentials of arbitrary shape. The environment around the science chamber is already quite constrained due to the numerous optomechanical elements already in use, but the addition of a DMD remains feasible.

The addition of a copper plate beam dump to protect the MCP has allowed us to carry out interferometry experiments successfully, thus advancing toward achieving our objective of exhibiting Bell correlations. However, this is not the better solution in the long term. Indeed, we are depriving ourselves of a significant portion of the detector, which restricts us to working in a reduced area. Furthermore, as observed on the MCP detectivity maps, the copper plate and its stainless steel arm disturb the electromagnetic environment of the MCP, resulting in spatial dependence of detectivity around the "shadow" of the beam dump, potentially reducing the detection efficiency in these areas. For these reasons, it seems necessary to come up with a strategy for removing the beam dump without damaging the center of the MCP with a powerful laser beam.

There exists MCPs with a central hole, through which beams can pass. This solution would enable us to maintain the same transfer and evaporation strategy in the vertical dipole trap, without the risk of burning the channels around the center. However, it also deprives us of a potentially interesting central zone. This is why we think about elaborating a new strategy by changing the orientation of the optical dipole trap. We could, for example, transfer the atoms from the magnetic trap to an optical trap tilted by 7 degrees with respect to the vertical, using the same axis as for the lattice beams, so as to bring the powerful beam out of the chamber without damaging the detector. We could then either maintain the condensate in this geometry that does not correspond to

the experiment's axes, or transfer the atoms to a strictly vertical beam after evaporation, ensuring that the beam's power is low. These different possibilities are currently being studied for a change in the next few years.

Outlook: towards a Bell test at larger scale

In a longer-term perspective, it would be interesting to implement a Bell test similar to the one proposed in this manuscript, but with the atoms placed further apart at the time of the beam splitter pulse. As we have seen, the very small distance between the place the wave packets overlap during the beam splitter, on the order of 20 µm, prevents us from truly probing the non-local properties of quantum mechanics. However, it would not be impossible to go further by transferring a large momentum to the atoms in one of the loops in order to spatially separate it from the first loop. Of course, this process of large momentum transfer must remain coherent. In recent years, the emergence of enhanced Bragg pulses has made it possible to achieve such significant momentum transfers. Two main strategies exist to increase the momentum transferred to the atoms by more than $2\hbar k$.

- The first strategy involves performing Bloch oscillations, which consist in loading the atoms into a Bragg optical lattice, where a frequency ramp between the two beams allows for adiabatic acceleration of the atoms[167]. This method has recently been used to transfer momentum up to $408\hbar k$ to rubidium atoms[177].

- The second strategy is to perform multiple successive Bragg pulses, gradually accelerating the atoms. To optimize the momentum transfer of each pulse, it is possible to work between the Bragg regime and the Kapitza-Dirac regime, in what is known as the quasi-Bragg regime[178]. This regime allows for the transfer of atoms into a high diffraction order with a good efficiency using an optimized shaped temporal profile. Recently, it has been shown that rubidium atoms could be transferred to a momentum state by more than $200\hbar k$[179].

The development of interferometers with large momentum transfer represents a significant metrological challenge, as substantial spatial separation enhances the sensitivity of interferometric measurements in many contexts (gravimetry, measurement of fundamental constants, tests of general relativity). Most interferometers demonstrating large momentum transfer use a large number of atoms and do not allow probing of quantum states. A first test of quantum superposition between wavepackets separated by a large distance was reported in 2015[180], but in a single-particle interferometer, which does not settle the debate on the observation of entanglement in the system[181]. Our setup would solve this issue by performing a genuine Bell test on spatially separated particles.

In a first step, a spatial separation on the order of a centimeter seems feasible with our current setup (the atoms must remain within the range of the Bragg beams for the Bell separator to be applicable, so they should not stray too far beyond the waist of the beams). We recently achieved what we believe to be the first achievement of large momentum transfer on helium atoms, which have a very low mass leading to a significant recoil velocity. Starting from a BEC, we observed 36 orders of diffraction in a regime of Bloch oscillations, thus transferring to the atoms a velocity on the order of $1.5\,\mathrm{m.s^{-1}}$ within 4 ms. So far, this phenomenon has been used to precisely measure the Bragg velocity in a context where many diffraction modes were populated, but we could explore more efficient transfers to a specific diffraction order. In order to selectively transfer a large momentum

to atoms from one of the two doublets of the Bell interferometer, we can once again exploit the fact that the Bragg resonance frequency of this doublet is different from that of the other.

Thus, we could perform a large momentum transfer pulse after the emission of the pairs to move the atoms from one doublet away from the atoms of the other doublet, getting closer to a Bell test probing locality. Demonstrating a violation of Bell inequalities would unequivocally confirm the observation of entanglement between spatially separated massive particles, paving the way for new tests of quantum gravitation.

Appendices

A. Experimental sequences used for the figures 282
B. Timeline 283
C. Experimental setup for a Bell test with global phase control 288

A. Experimental sequences used for the figures

Figure	Title	Day	Sequences
1.13	Scattering halo resulting from the collision of two BEC	2019/08/06	72
2.10	Bose-Einstein Condensation in the Magnetic Trap	2020/09/18	13
2.13	Detectivity map of the MCP with the copper plate (MOT)	2022/07/15	7
2.13	Detectivity map of the MCP with the copper plate ($m = 0$)	2022/07/07	9
2.16	Rabi oscillations with the Raman beams	2023/09/08	143, 150, 152
2.18	Stability histograms for the BEC	2023/04/03	55
2.19	Average BEC after time of flight	2023/04/03	55
3.6	Density profile along the vertical direction	2023/08/01	18
3.7	Density profile of the emitted pairs	2023/08/01	18
3.8	Experimental phase-matching diagram	2022/05/19	12-54
3.9	Correlation map	2022/05/17	40
3.10	Local normalized correlation functions	2022/05/17	40
3.11	Effect of the integration thresholds on the correlation	2022/05/17	40
3.12	Crossed correlation map	2022/05/17	40
3.13	1D crossed correlation	2022/05/17	40
3.14	Counting statistics	2022/05/17	40
3.15	Mean population per mode	2022/05/17	40
3.21	Maps of normalized variance and Cauchy-Schwarz coefficient	2023/08/04	28
3.22	Normalized variance and Cauchy-Schwarz coefficient	2023/08/04	28
6.2	Bragg resonances towards orders ± 1	2023/10/23	6, 8
6.3	Rabi oscillations	2023/04/24	36
6.4	Bragg diffraction in the Kapitza-Dirac regime	2023/04/19	68
6.10	Ramsey interferences	2023/04/12	12
6.11	Ramsey interferences, $\tau = 1\,\mathrm{ms}$	2023/04/12	12
6.12	Ramsey interferences, $\tau = 2\,\mathrm{ms}$	2023/04/12	13
6.14	Ramsey interferences on a BEC from the magnetic trap	2023/04/12	84
6.13	Interfrange of the Ramsey interference	2023/04/12	12-16
6.15	Simulation of the interference pattern and density fit	2023/04/12	12
6.16a	Calibration curve of the phase shifter	2023/05/10	22-38
6.16b	Ramsey interferences shifted by π	2023/05/10	31, 38
6.17	Bragg sinc splitter	2023/08/23	64
6.18	Bragg constant splitter	2023/08/23	67
6.19	Bragg sinc mirror	2023/08/23	65
6.20	Bragg constant mirror	2023/08/23	68
6.21	Bragg sinc splitter	2023/08/23	56
6.22	Bragg sinc mirror	2023/08/23	57
6.23	Classical time for a Bragg pulse	2023/06/30	82
6.25	Bragg modulation	2023/08/23	69, 70, 72
6.26	Bragg modulation	2024/01/11	30
6.27	Bragg modulation	2024/01/11	30
6.28	Ramsey interferences with a modulated Bragg pulse	2023/06/02	27
6.29	Phase calibration	2023/07/06	22, 23
6.30	Mach-Zehnder interference fringes	2023/08/23	12
6.31	Mach-Zehnder gravimeter	2023/08/23	29, 33, 34, 35
6.32	Order 0 fringe slope	2023/08/23	29-49
7.13	Bragg speed measured as a function of the Bragg delay	2024/01/23	33, 46, 47

HOM dataset (Chapter 7): 2023/09/12 - Sequences 37, 39, 40 ; 2023/09/13 - Sequences 13, 16 ; 2023/09/14 - Sequences 12, 13.

B. Timeline

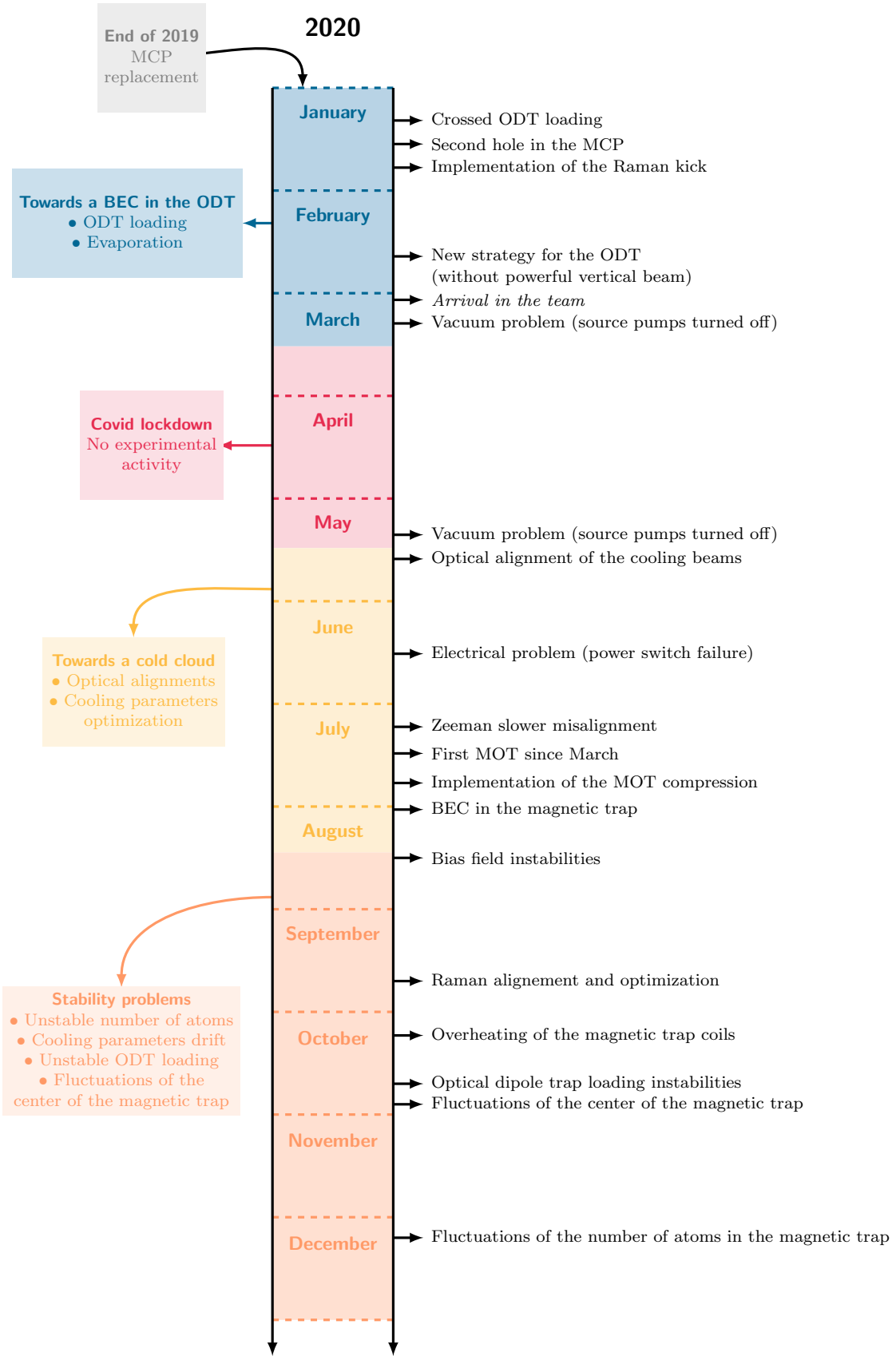
End of 2019
MCP
replacement
2020
January
Crossed ODT loading
Second hole in the MCP
Implementation of the Raman kick
Towards a BEC in the ODT
• ODT loading
• Evaporation
February
New strategy for the ODT
(without powerful vertical beam)
March
Arrival in the team
Vacuum problem (source pumps turned off)
Covid lockdown
No experimental
activity
April
May
Vacuum problem (source pumps turned off)
Optical alignment of the cooling beams
June
Towards a cold cloud
• Optical alignments
• Cooling parameters
optimization
Electrical problem (power switch failure)
July
Zeeman slower misalignment
First MOT since March
Implementation of the MOT compression
BEC in the magnetic trap
August
Bias field instabilities
September
Raman alignement and optimization
Stability problems
• Unstable number of atoms
• Cooling parameters drift
• Unstable ODT loading
• Fluctuations of the
center of the magnetic trap
October
Overheating of the magnetic trap coils
Optical dipole trap loading instabilities
Fluctuations of the center of the magnetic trap
November
December
Fluctuations of the number of atoms in the magnetic trap

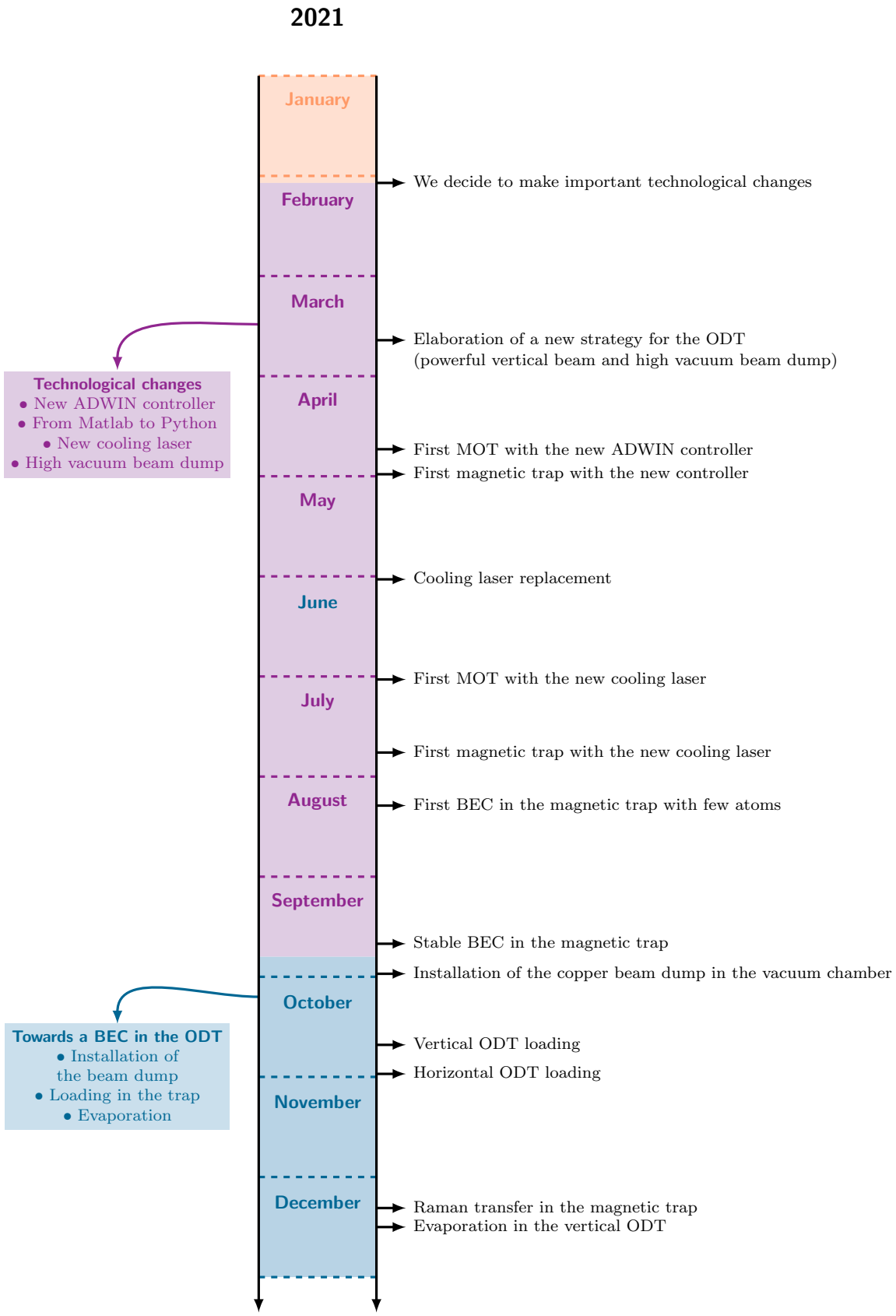
2021
January
February
March
April
May
June
July
August
September
October
November
December
We decide to make important technological changes
Elaboration of a new strategy for the ODT
(powerful vertical beam and high vacuum beam dump)
First MOT with the new ADWIN controller
First magnetic trap with the new controller
Cooling laser replacement
First MOT with the new cooling laser
First magnetic trap with the new cooling laser
First BEC in the magnetic trap with few atoms
Stable BEC in the magnetic trap
Installation of the copper beam dump in the vacuum chamber
Vertical ODT loading
Horizontal ODT loading
Raman transfer in the magnetic trap
Evaporation in the vertical ODT
Technological changes
• New ADWIN controller
• From Matlab to Python
• New cooling laser
• High vacuum beam dump
Towards a BEC in the ODT
• Installation of
the beam dump
• Loading in the trap
• Evaporation

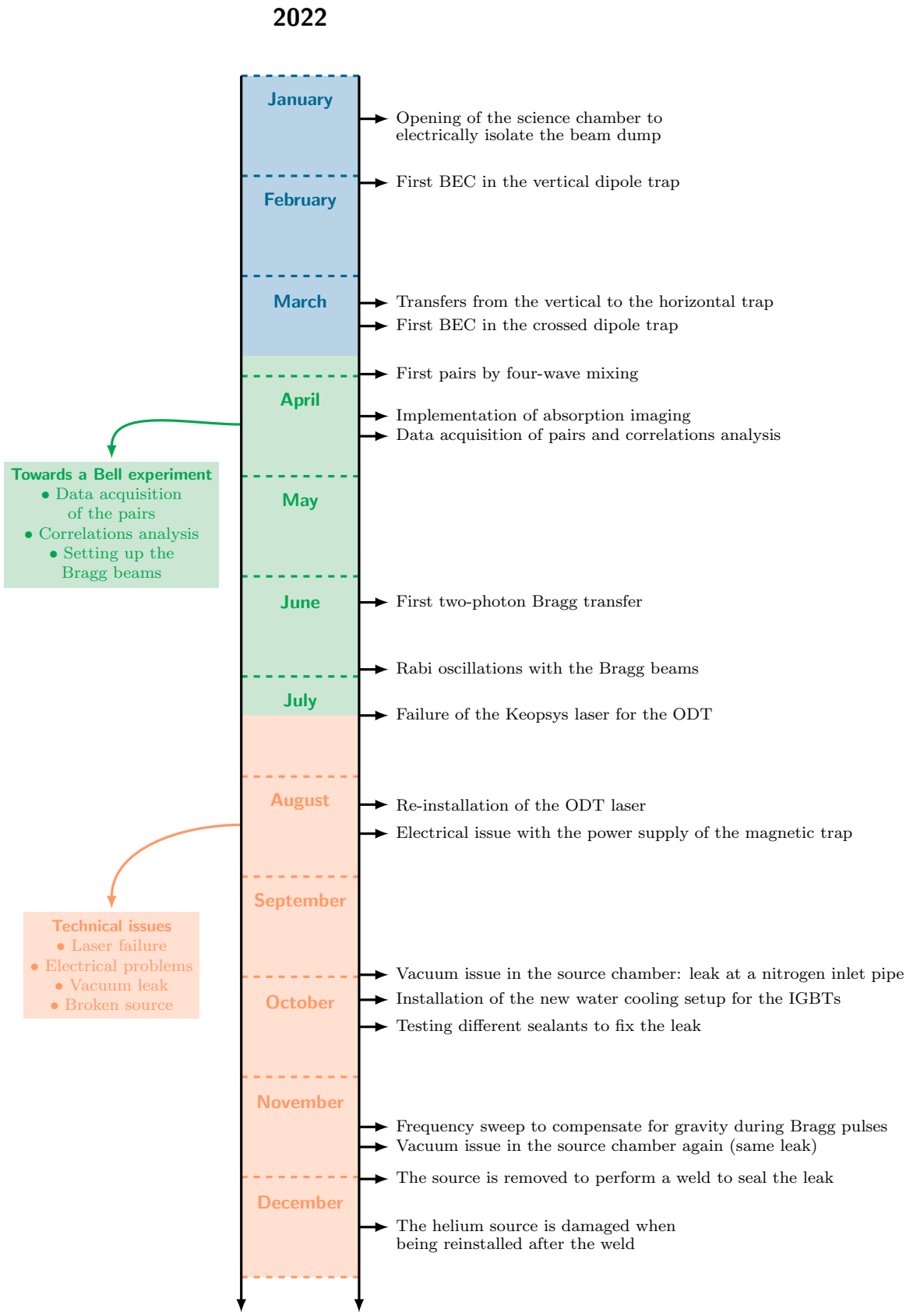
2022
January
Opening of the science chamber to electrically isolate the beam dump
February
First BEC in the vertical dipole trap
March
Transfers from the vertical to the horizontal trap
First BEC in the crossed dipole trap
April
First pairs by four-wave mixing
Implementation of absorption imaging
Data acquisition of pairs and correlations analysis
Towards a Bell experiment
• Data acquisition of the pairs
• Correlations analysis
• Setting up the Bragg beams
May
June
First two-photon Bragg transfer
Rabi oscillations with the Bragg beams
July
Failure of the Keopsys laser for the ODT
August
Re-installation of the ODT laser
Electrical issue with the power supply of the magnetic trap
September
Technical issues
• Laser failure
• Electrical problems
• Vacuum leak
• Broken source
October
Vacuum issue in the source chamber: leak at a nitrogen inlet pipe
Installation of the new water cooling setup for the IGBTs
Testing different sealants to fix the leak
November
Frequency sweep to compensate for gravity during Bragg pulses
Vacuum issue in the source chamber again (same leak)
December
The source is removed to perform a weld to seal the leak
The helium source is damaged when being reinstalled after the weld

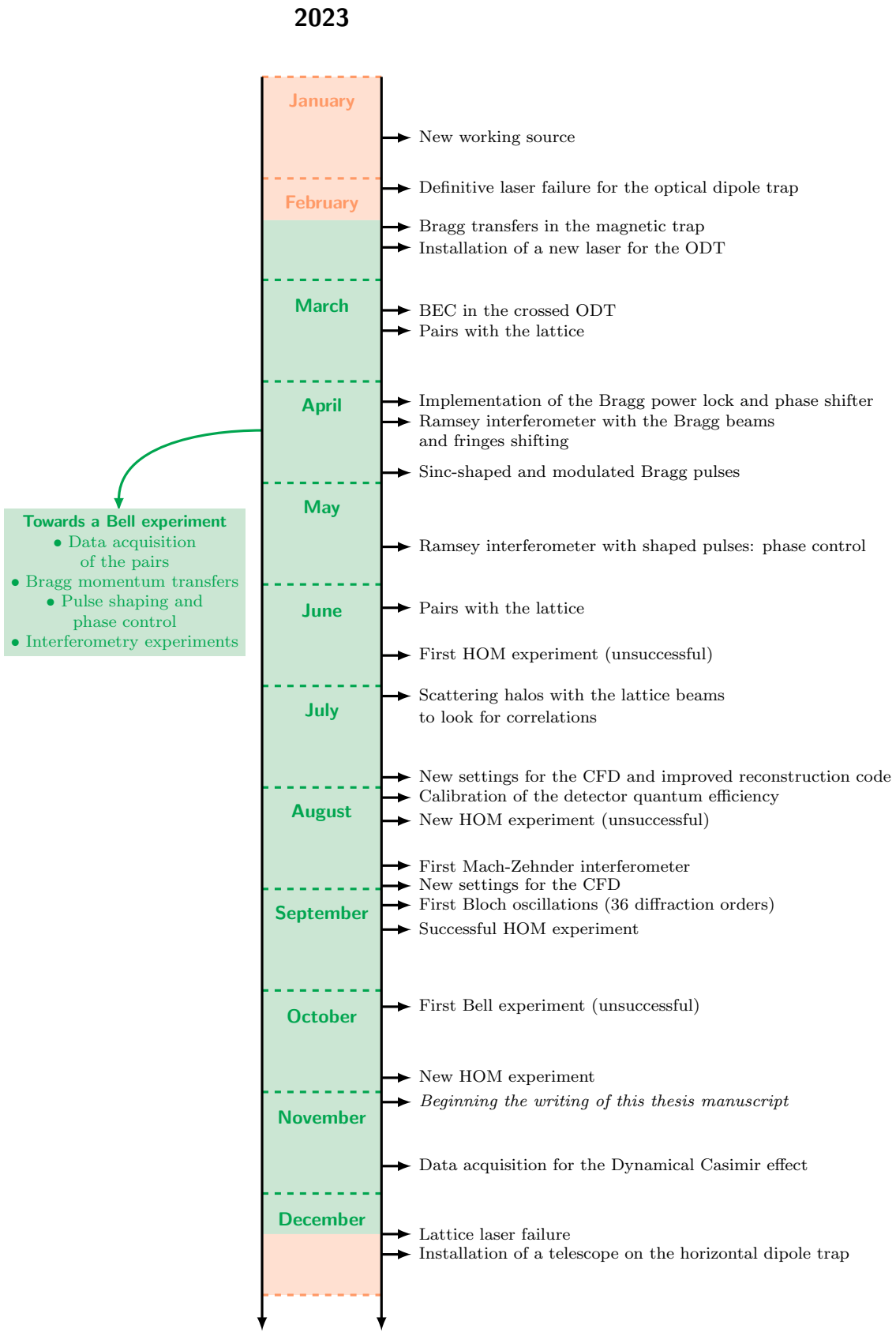
2023
January
New working source
February
Definitive laser failure for the optical dipole trap
Bragg transfers in the magnetic trap
Installation of a new laser for the ODT
March
BEC in the crossed ODT
Pairs with the lattice
April
Implementation of the Bragg power lock and phase shifter
Ramsey interferometer with the Bragg beams and fringes shifting
Sinc-shaped and modulated Bragg pulses
May
Ramsey interferometer with shaped pulses: phase control
June
Pairs with the lattice
First HOM experiment (unsuccessful)
July
Scattering halos with the lattice beams to look for correlations
New settings for the CFD and improved reconstruction code
Calibration of the detector quantum efficiency
August
New HOM experiment (unsuccessful)
First Mach-Zehnder interferometer
New settings for the CFD
September
First Bloch oscillations (36 diffraction orders)
Successful HOM experiment
October
First Bell experiment (unsuccessful)
New HOM experiment
November
Beginning the writing of this thesis manuscript
Data acquisition for the Dynamical Casimir effect
December
Lattice laser failure
Installation of a telescope on the horizontal dipole trap
Towards a Bell experiment
• Data acquisition of the pairs
• Bragg momentum transfers
• Pulse shaping and phase control
• Interferometry experiments

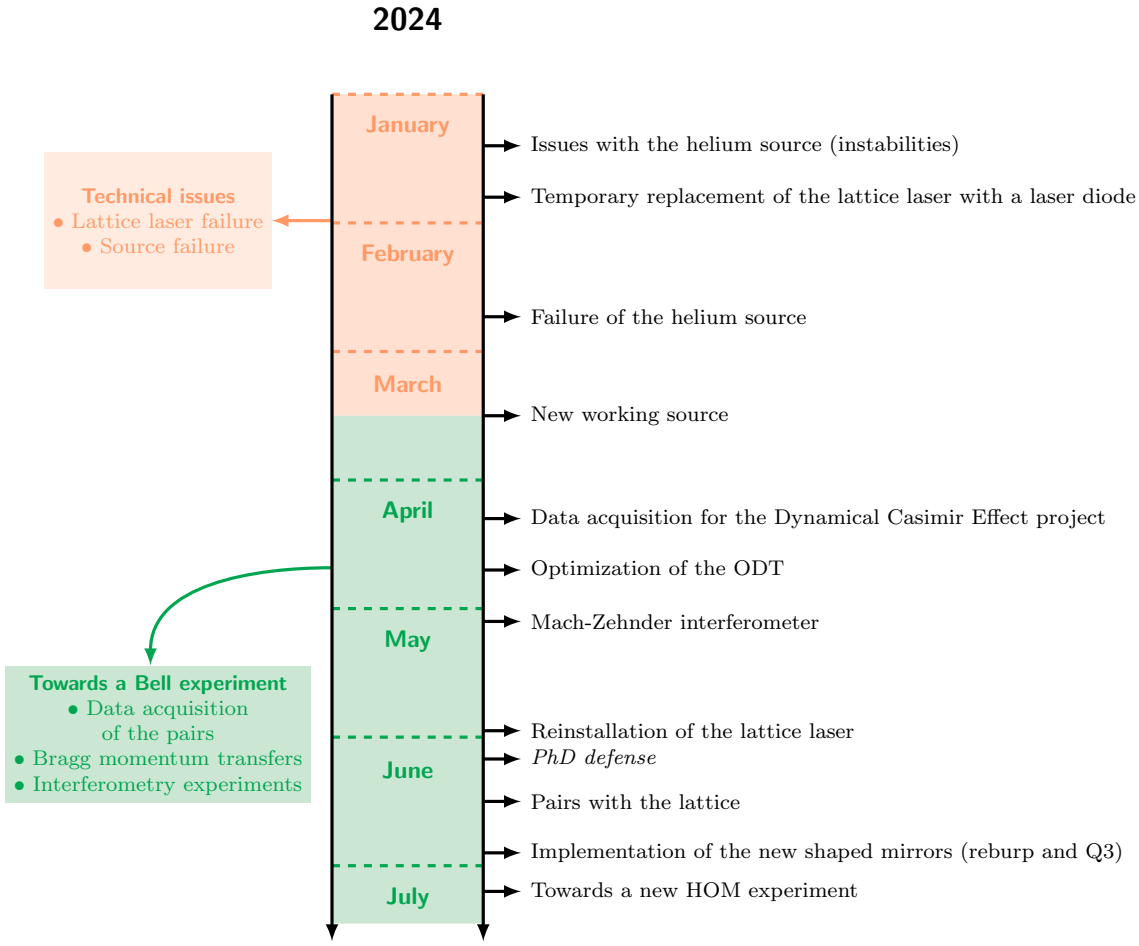
2024
January
February
March
April
May
June
July
Technical issues
• Lattice laser failure
• Source failure
Towards a Bell experiment
• Data acquisition of the pairs
• Bragg momentum transfers
• Interferometry experiments
Issues with the helium source (instabilities)
Temporary replacement of the lattice laser with a laser diode
Failure of the helium source
New working source
Data acquisition for the Dynamical Casimir Effect project
Optimization of the ODT
Mach-Zehnder interferometer
Reinstallation of the lattice laser
PhD defense
Pairs with the lattice
Implementation of the new shaped mirrors (reburp and Q3)
Towards a new HOM experiment

C. Experimental setup for a Bell test with global phase control

In this section, we provide some details for a future Bell interferometer experiment allowing independent phase control of A and B. The realization of such a Bell test, in its more rigorous formulation, does not pose a major experimental challenge.

The expression of the beam splitter pulse is

$$\Omega_{\mathrm{R}}(t) = \Omega_{\mathrm{M}} \operatorname{sinc}\left[\Omega_{\mathrm{S}}\left(t - \frac{T}{2}\right)\right] \cos\left[\frac{\Omega_{\mathrm{D}}}{2}t + \frac{\theta}{2}\right] \mathrm{e}^{\mathrm{i}\Delta\varphi} \tag{1}$$

where Ω_{M} is the two-photon Rabi frequency of the pulse, Ω_{S} is the sinc frequency and equals $2\Omega_{\mathrm{M}}$, and T is the duration of the beam splitter. Ω_{D} is the modulation frequency which makes it possible to have a two-frequency pulse since it shifts the Bragg detuning by $\pm\Omega_{\mathrm{D}}/2$, each frequency being resonant with one or the other of the A and B momentum doublets. θ is the Bell control parameter, and $\Delta\varphi$ is the phase difference between the two lasers. The imprinted phases on doublets A, resonant with $+\Omega_{\mathrm{D}}/2$, and B, resonant with $-\Omega_{\mathrm{D}}/2$, are therefore

$$\begin{cases} \phi_A = \dfrac{\theta}{2} + \Delta\varphi \\ \phi_B = -\dfrac{\theta}{2} + \Delta\varphi \end{cases} \tag{2}$$

The Bell phase involved the phase difference $\phi_A - \phi_B = \theta$, so an oscillation of the Bell correlator would only depend on θ and not $\Delta\varphi$: this is a common mode rejection proper to our configuration. Although this is an advantage in terms of sensitivity to phase fluctuations, a genuine Bell test requires an independant control of the phases imprinted on A and B.

The global phase $\Delta\varphi$ can be measured using the beating between the two Bragg beams. The beating signal can be used to lock the value of the global phase on a setpoint value using a PID controller.

Since the frequency and the temporal profile of the Bragg pulses vary during the mirror and beam splitter, we are planning to maintain the power and frequency of the beams constant for the majority of the experiment duration before the interferometer, while a beam dump would ensure that no Bragg light is received by the atoms. The beat signal between the Bragg beams could then be locked onto a voltage setpoint to fix the global phase. This could be achieved by providing feedback on the phase using a phase shifter added to the current setup, allowing adjustment of the phase of one of the RF signals used to generate the frequency of a Bragg beam via an acousto-optic modulator (Figure 1).

The feedback loop would then be interrupted during the Bragg pulses. Determining the global phase from a fit of the beat signal during the pulses would ensure that it remains at the desired value during the interferometer (it has been observed that the global phase vary by less than five degrees between the two pulses, so it can be considered constant between the interruption of the feedback loop and the beam splitter). A device enabling intermittent feedback based on a TTL voltage value has been developed by the electronics workshop of the Institut d'Optique and is currently undergoing testing phase.

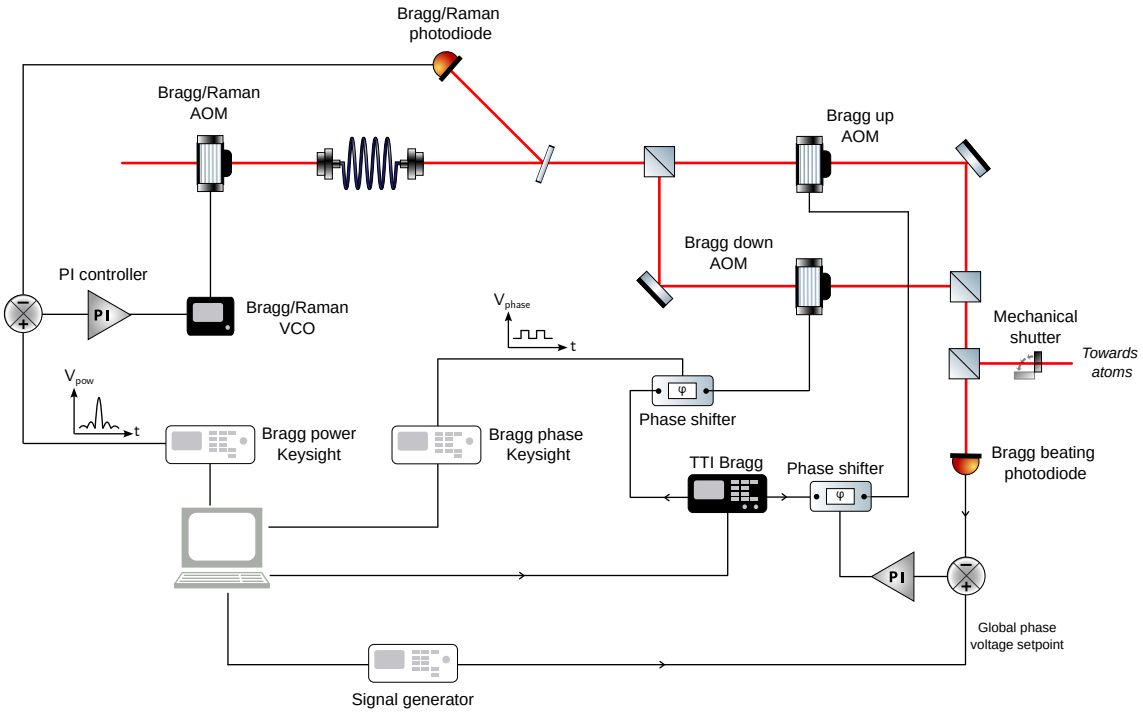

Figure 1: Optical setup for the Bragg beams.

Bibliography

[1] Max Planck. Ueber das gesetz der energieverteilung im normalspectrum. *Annalen der Physik*, 309(3):553–563, January 1901. ISSN 1521-3889. doi: 10.1002/andp.19013090310. URL http://dx.doi.org/10.1002/andp.19013090310.

[2] A. Einstein. Über einen die erzeugung und verwandlung des lichtes betreffenden heuristischen gesichtspunkt. *Annalen der Physik*, 322(6):132–148, January 1905. ISSN 1521-3889. doi: 10.1002/andp.19053220607. URL http://dx.doi.org/10.1002/andp.19053220607.

[3] N. Bohr. Xxxvii. on the constitution of atoms and molecules. *The London, Edinburgh, and Dublin Philosophical Magazine and Journal of Science*, 26(153):476–502, September 1913. ISSN 1941-5990. doi: 10.1080/14786441308634993. URL http://dx.doi.org/10.1080/14786441308634993.

[4] A. Einstein, B. Podolsky, and N. Rosen. Can quantum-mechanical description of physical reality be considered complete? *Phys. Rev.*, 47:777–780, May 1935. doi: 10.1103/PhysRev.47.777. URL https://link.aps.org/doi/10.1103/PhysRev.47.777.

[5] J. S. Bell. On the einstein podolsky rosen paradox. *Physics*, 1:195–200, Nov 1964. doi: 10.1103/PhysicsPhysiqueFizika.1.195. URL https://link.aps.org/doi/10.1103/PhysicsPhysiqueFizika.1.195.

[6] John F. Clauser, Michael A. Horne, Abner Shimony, and Richard A. Holt. Proposed experiment to test local hidden-variable theories. *Phys. Rev. Lett.*, 23:880–884, Oct 1969. doi: 10.1103/PhysRevLett.23.880. URL https://link.aps.org/doi/10.1103/PhysRevLett.23.880.

[7] Stuart J. Freedman and John F. Clauser. Experimental test of local hidden-variable theories. *Phys. Rev. Lett.*, 28:938–941, Apr 1972. doi: 10.1103/PhysRevLett.28.938. URL https://link.aps.org/doi/10.1103/PhysRevLett.28.938.

[8] Edward S. Fry and Randall C. Thompson. Experimental test of local hidden-variable theories. *Phys. Rev. Lett.*, 37:465–468, Aug 1976. doi: 10.1103/PhysRevLett.37.465. URL https://link.aps.org/doi/10.1103/PhysRevLett.37.465.

[9] Alain Aspect, Philippe Grangier, and Gérard Roger. Experimental tests of realistic local theories via bell's theorem. *Phys. Rev. Lett.*, 47:460–463, Aug 1981. doi: 10.1103/PhysRevLett.47.460. URL https://link.aps.org/doi/10.1103/PhysRevLett.47.460.

[10] Alain Aspect, Philippe Grangier, and Gérard Roger. Experimental realization of einstein-podolsky-rosen-bohm gedankenexperiment: A new violation of bell's inequalities. *Phys. Rev. Lett.*, 49:91–94, Jul 1982. doi: 10.1103/PhysRevLett.49.91. URL https://link.aps.org/doi/10.1103/PhysRevLett.49.91.

[11] Alain Aspect, Jean Dalibard, and Gérard Roger. Experimental test of bell's inequalities using time-varying analyzers. *Phys. Rev. Lett.*, 49:1804–1807, Dec 1982. doi: 10.1103/PhysRevLett.49.1804. URL https://link.aps.org/doi/10.1103/PhysRevLett.49.1804.

[12] J. G. Rarity and P. R. Tapster. Experimental violation of bell's inequality based on phase and momentum. *Phys. Rev. Lett.*, 64:2495–2498, May 1990. doi: 10.1103/PhysRevLett.64.2495. URL https://link.aps.org/doi/10.1103/PhysRevLett.64.2495.

[13] Michael A. Horne, Abner Shimony, and Anton Zeilinger. Two-particle interferometry. *Phys. Rev. Lett.*, 62:2209–2212, May 1989. doi: 10.1103/PhysRevLett.62.2209. URL https://link.aps.org/doi/10.1103/PhysRevLett.62.2209.

[14] Gregor Weihs, Thomas Jennewein, Christoph Simon, Harald Weinfurter, and Anton Zeilinger. Violation of bell's inequality under strict einstein locality conditions. *Phys. Rev. Lett.*, 81:5039–5043, Dec 1998. doi: 10.1103/PhysRevLett.81.5039. URL https://link.aps.org/doi/10.1103/PhysRevLett.81.5039.

[15] B. Hensen, H. Bernien, A. E. Dréau, A. Reiserer, N. Kalb, M. S. Blok, J. Ruitenberg, R. F. L. Vermeulen, R. N. Schouten, C. Abellán, W. Amaya, V. Pruneri, M. W. Mitchell, M. Markham, D. J. Twitchen, D. Elkouss, S. Wehner, T. H. Taminiau, and R. Hanson. Experimental loophole-free violation of a Bell inequality using entangled electron spins separated by 1.3 km. *Nature*, 526:682–686, October 2015. doi: 10.4121/uuid:6e19e9b2-4a2d-40b5-8dd3-a660bf3c0a31. URL https://www.nature.com/articles/nature15759. arXiv:1508.05949 [quant-ph].

[16] Lynden K. Shalm, Evan Meyer-Scott, Bradley G. Christensen, Peter Bierhorst, Michael A. Wayne, Martin J. Stevens, Thomas Gerrits, Scott Glancy, Deny R. Hamel, Michael S. Allman, Kevin J. Coakley, Shellee D. Dyer, Carson Hodge, Adriana E. Lita, Varun B. Verma, Camilla Lambrocco, Edward Tortorici, Alan L. Migdall, Yanbao Zhang, Daniel R. Kumor, William H. Farr, Francesco Marsili, Matthew D. Shaw, Jeffrey A. Stern, Carlos Abellán, Waldimar Amaya, Valerio Pruneri, Thomas Jennewein, Morgan W. Mitchell, Paul G. Kwiat, Joshua C. Bienfang, Richard P. Mirin, Emanuel Knill, and Sae Woo Nam. Strong loophole-free test of local realism. *Phys. Rev. Lett.*, 115:250402, Dec 2015. doi: 10.1103/PhysRevLett.115.250402. URL https://link.aps.org/doi/10.1103/PhysRevLett.115.250402.

[17] Marissa Giustina, Marijn A. M. Versteegh, Sören Wengerowsky, Johannes Handsteiner, Armin Hochrainer, Kevin Phelan, Fabian Steinlechner, Johannes Kofler, Jan-Åke Larsson, Carlos Abellán, Waldimar Amaya, Valerio Pruneri, Morgan W. Mitchell, Jörn Beyer, Thomas Gerrits, Adriana E. Lita, Lynden K. Shalm, Sae Woo Nam, Thomas Scheidl, Rupert Ursin, Bernhard Wittmann, and Anton Zeilinger. Significant-loophole-free test of bell's theorem with entangled photons. *Phys. Rev. Lett.*, 115:250401, Dec 2015. doi: 10.1103/PhysRevLett.115.250401. URL https://link.aps.org/doi/10.1103/PhysRevLett.115.250401.

[18] M. H. Anderson, J. R. Ensher, M. R. Matthews, C. E. Wieman, and E. A. Cornell. Observation of bose-einstein condensation in a dilute atomic vapor. *Science*, 269(5221):198–201, 1995. doi: 10.1126/science.269.5221.198. URL https://www.science.org/doi/abs/10.1126/science.269.5221.198.

[19] O Jagutzki, V Mergel, K Ullmann-Pfleger, L Spielberger, U Spillmann, R Dörner, and H Schmidt-Böcking. A broad-application microchannel-plate detector system for advanced particle or photon detection tasks: large area imaging, precise multi-hit timing information and high detection rate. *Nuclear Instruments and Methods in Physics Research Section A: Accelerators, Spectrometers, Detectors and Associated Equipment*, 477(1–3): 244–249, January 2002. ISSN 0168-9002. doi: 10.1016/s0168-9002(01)01839-3. URL http://dx.doi.org/10.1016/S0168-9002(01)01839-3.

[20] M. Bonneau, J. Ruaudel, R. Lopes, J.-C. Jaskula, A. Aspect, D. Boiron, and C. I. Westbrook. Tunable source of correlated atom beams. *Physical Review A*, 87(6), June 2013. ISSN 1094-1622. doi: 10.1103/physreva.87.061603. URL http://dx.doi.org/10.1103/PhysRevA.87.061603.

[21] K. V. Kheruntsyan, J.-C. Jaskula, P. Deuar, M. Bonneau, G. B. Partridge, J. Ruaudel, R. Lopes, D. Boiron, and C. I. Westbrook. Violation of the Cauchy-Schwarz inequality with

matter waves. *Physical Review Letters*, 108(26):260401, June 2012. ISSN 0031-9007, 1079-7114. doi: 10.1103/PhysRevLett.108.260401. URL https://link.aps.org/doi/10.1103/PhysRevLett.108.260401. arXiv:1204.0058.

[22] Roger Penrose. On gravity's role in quantum state reduction. *General Relativity and Gravitation*, 28(5):581–600, May 1996. ISSN 1572-9532. doi: 10.1007/bf02105068. URL http://dx.doi.org/10.1007/BF02105068.

[23] R. Hanbury Brown and R. Q. Twiss. Correlation between photons in two coherent beams of light. *Nature*, 177(4497):27–29, January 1956. ISSN 1476-4687. doi: 10.1038/177027a0. URL http://dx.doi.org/10.1038/177027a0.

[24] Alain Aspect. *Hanbury Brown and Twiss, Hong Ou and Mandel effects and other landmarks in quantum optics: from photons to atoms*, page 428–449. Oxford University Press, May 2019. doi: 10.1093/oso/9780198837190.003.0012. URL http://dx.doi.org/10.1093/oso/9780198837190.003.0012.

[25] U. Fano. Quantum theory of interference effects in the mixing of light from phase-independent sources. *American Journal of Physics*, 29(8):539–545, August 1961. ISSN 1943-2909. doi: 10.1119/1.1937827. URL http://dx.doi.org/10.1119/1.1937827.

[26] Christopher Gerry and Peter Knight. *Introductory Quantum Optics*. Cambridge University Press, October 2004. ISBN 9780511791239. doi: 10.1017/cbo9780511791239. URL http://dx.doi.org/10.1017/CBO9780511791239.

[27] Roy J. Glauber. Photon correlations. *Phys. Rev. Lett.*, 10:84–86, Feb 1963. doi: 10.1103/PhysRevLett.10.84. URL https://link.aps.org/doi/10.1103/PhysRevLett.10.84.

[28] Jean-Louis Basdevant, Jean Dalibard, and Manuel Joffre. *Mécanique quantique*. Editions Ecole Polytechnique, 2002.

[29] Ling-An Wu, H. J. Kimble, J. L. Hall, and Huifa Wu. Generation of squeezed states by parametric down conversion. *Physical Review Letters*, 57(20):2520–2523, November 1986. ISSN 0031-9007. doi: 10.1103/physrevlett.57.2520. URL http://dx.doi.org/10.1103/PhysRevLett.57.2520.

[30] R. E. Slusher, L. W. Hollberg, B. Yurke, J. C. Mertz, and J. F. Valley. Observation of squeezed states generated by four-wave mixing in an optical cavity. *Physical Review Letters*, 55(22):2409–2412, November 1985. ISSN 0031-9007. doi: 10.1103/physrevlett.55.2409. URL http://dx.doi.org/10.1103/PhysRevLett.55.2409.

[31] Henning Vahlbruch, Moritz Mehmet, Karsten Danzmann, and Roman Schnabel. Detection of 15 db squeezed states of light and their application for the absolute calibration of photoelectric quantum efficiency. *Phys. Rev. Lett.*, 117:110801, Sep 2016. doi: 10.1103/PhysRevLett.117.110801. URL https://link.aps.org/doi/10.1103/PhysRevLett.117.110801.

[32] Roman Schnabel. Squeezed states of light and their applications in laser interferometers. *Physics Reports*, 684:1–51, April 2017. ISSN 0370-1573. doi: 10.1016/j.physrep.2017.04.001. URL http://dx.doi.org/10.1016/j.physrep.2017.04.001.

[33] X.Y. Zou, L.J. Wang, and L. Mandeļ. Violation of classical probability in parametric down-conversion. *Optics Communications*, 84(5–6):351–354, August 1991. ISSN 0030-4018. doi: 10.1016/0030-4018(91)90101-i. URL http://dx.doi.org/10.1016/0030-4018(91)90101-I.

[34] M. D. Reid and D. F. Walls. Violations of classical inequalities in quantum optics. *Phys. Rev. A*, 34:1260–1276, Aug 1986. doi: 10.1103/PhysRevA.34.1260. URL https://link.aps.org/doi/10.1103/PhysRevA.34.1260.

[35] Xavier Busch and Renaud Parentani. Quantum entanglement in analogue hawking radiation: When is the final state nonseparable? *Phys. Rev. D*, 89:105024, May 2014. doi: 10.1103/PhysRevD.89.105024. URL https://link.aps.org/doi/10.1103/PhysRevD.89.105024.

[36] C. K. Hong, Z. Y. Ou, and L. Mandel. Measurement of subpicosecond time intervals between two photons by interference. *Physical Review Letters*, 59(18):2044–2046, November 1987. ISSN 0031-9007. doi: 10.1103/PhysRevLett.59.2044. URL https://link.aps.org/doi/10.1103/PhysRevLett.59.2044.

[37] E. Bocquillon, V. Freulon, J.-M. Berroir, P. Degiovanni, B. Plaçais, A. Cavanna, Y. Jin, and G. Fève. Coherence and Indistinguishability of Single Electrons Emitted by Independent Sources. *Science*, 339(6123):1054–1057, March 2013. ISSN 0036-8075, 1095-9203. doi: 10.1126/science.1232572. URL https://www.science.org/doi/10.1126/science.1232572.

[38] D. Bohm and Y. Aharonov. Discussion of experimental proof for the paradox of einstein, rosen, and podolsky. *Physical Review*, 108(4):1070–1076, November 1957. ISSN 0031-899X. doi: 10.1103/physrev.108.1070. URL http://dx.doi.org/10.1103/PhysRev.108.1070.

[39] Alain Aspect. *Bell's Theorem: The Naive View of an Experimentalist*, page 119–153. Springer Berlin Heidelberg, 2002. ISBN 9783662050323. doi: 10.1007/978-3-662-05032-3_9. URL http://dx.doi.org/10.1007/978-3-662-05032-3_9.

[40] John F. Clauser, Michael A. Horne, Abner Shimony, and Richard A. Holt. Proposed experiment to test local hidden-variable theories. *Phys. Rev. Lett.*, 23:880–884, Oct 1969. doi: 10.1103/PhysRevLett.23.880. URL https://link.aps.org/doi/10.1103/PhysRevLett.23.880.

[41] Quentin Marolleau. *Quantum atom optics with metastable helium atoms*. PhD thesis, Université Paris-Saclay, 2022. URL http://www.theses.fr/2022UPASP166. Thèse de doctorat dirigée par Denis Boiron, Palaiseau, Université Paris-Saclay, Institut d'optique graduate School, 2022.

[42] Gregor Weihs, Thomas Jennewein, Christoph Simon, Harald Weinfurter, and Anton Zeilinger. Violation of bell's inequality under strict einstein locality conditions. *Physical Review Letters*, 81(23):5039–5043, December 1998. ISSN 1079-7114. doi: 10.1103/physrevlett.81.5039. URL http://dx.doi.org/10.1103/PhysRevLett.81.5039.

[43] Jérôme Wenger, Mohammad Hafezi, Frédéric Grosshans, Rosa Tualle-Brouri, and Philippe Grangier. Maximal violation of bell inequalities using continuous-variable measurements. *Physical Review A*, 67(1), January 2003. ISSN 1094-1622. doi: 10.1103/physreva.67.012105. URL http://dx.doi.org/10.1103/PhysRevA.67.012105.

[44] Alain Aspect. Bell's inequality test: more ideal than ever. *Nature*, 398(6724):189–190, March 1999. ISSN 1476-4687. doi: 10.1038/18296. URL http://dx.doi.org/10.1038/18296.

[45] Y. H. Shih and C. O. Alley. New type of einstein-podolsky-rosen-bohm experiment using pairs of light quanta produced by optical parametric down conversion. *Physical Review Letters*, 61(26):2921–2924, December 1988. ISSN 0031-9007. doi: 10.1103/physrevlett.61.2921. URL http://dx.doi.org/10.1103/PhysRevLett.61.2921.

[46] Z. Y. Ou and L. Mandel. Violation of bell's inequality and classical probability in a two-photon correlation experiment. *Physical Review Letters*, 61(1):50–53, July 1988. ISSN 0031-9007. doi: 10.1103/physrevlett.61.50. URL http://dx.doi.org/10.1103/PhysRevLett.61.50.

[47] Daniel M. Greenberger, Michael A. Horne, and Anton Zeilinger. Going Beyond Bell's Theorem. In Menas Kafatos, editor, *Bell's Theorem, Quantum Theory and Conceptions of the Universe*, pages 69–72. Springer Netherlands, Dordrecht, 1989. ISBN 978-94-017-0849-4. doi: 10.1007/978-94-017-0849-4_10. URL https://doi.org/10.1007/978-94-017-0849-4_10.

[48] N. David Mermin. Quantum mysteries revisited. *American Journal of Physics*, 58(8):731–734, August 1990. ISSN 1943-2909. doi: 10.1119/1.16503. URL http://dx.doi.org/10.1119/1.16503.

[49] Albert Bramon and Marek Nowakowski. Bell inequalities for entangled pairs of neutral kaons. *Physical Review Letters*, 83(1):1–5, July 1999. ISSN 1079-7114. doi: 10.1103/physrevlett.83.1. URL http://dx.doi.org/10.1103/PhysRevLett.83.1.

[50] M. A. Rowe, D. Kielpinski, V. Meyer, C. A. Sackett, W. M. Itano, C. Monroe, and D. J. Wineland. Experimental violation of a bell's inequality with efficient detection. *Nature*, 409(6822):791–794, February 2001. ISSN 1476-4687. doi: 10.1038/35057215. URL http://dx.doi.org/10.1038/35057215.

[51] D. L. Moehring, M. J. Madsen, B. B. Blinov, and C. Monroe. Experimental bell inequality violation with an atom and a photon. *Physical Review Letters*, 93(9), August 2004. ISSN 1079-7114. doi: 10.1103/physrevlett.93.090410. URL http://dx.doi.org/10.1103/PhysRevLett.93.090410.

[52] D. L. Moehring, P. Maunz, S. Olmschenk, K. C. Younge, D. N. Matsukevich, L.-M. Duan, and C. Monroe. Entanglement of single-atom quantum bits at a distance. *Nature*, 449 (7158):68–71, September 2007. ISSN 1476-4687. doi: 10.1038/nature06118. URL http://dx.doi.org/10.1038/nature06118.

[53] G. Waldherr, P. Neumann, S. F. Huelga, F. Jelezko, and J. Wrachtrup. Violation of a temporal bell inequality for single spins in a diamond defect center. *Physical Review Letters*, 107(9), August 2011. ISSN 1079-7114. doi: 10.1103/physrevlett.107.090401. URL http://dx.doi.org/10.1103/PhysRevLett.107.090401.

[54] Daniel Carney, Philip C E Stamp, and Jacob M Taylor. Tabletop experiments for quantum gravity: a user's manual. *Classical and Quantum Gravity*, 36(3):034001, January 2019. ISSN 1361-6382. doi: 10.1088/1361-6382/aaf9ca. URL http://dx.doi.org/10.1088/1361-6382/aaf9ca.

[55] Harold J. Metcalf and Peter van der Straten. *Laser Cooling and Trapping*. Springer New York, 1999. ISBN 9781461214700. doi: 10.1007/978-1-4612-1470-0. URL http://dx.doi.org/10.1007/978-1-4612-1470-0.

[56] Massimo Inguscio and Leonardo Fallani. *Atomic Physics: Precise Measurements and Ultracold Matter*. Oxford University Press, September 2013. ISBN 9780198525844. doi: 10.1093/acprof:oso/9780198525844.001.0001. URL http://dx.doi.org/10.1093/acprof:oso/9780198525844.001.0001.

[57] T. Gys. Micro-channel plates and vacuum detectors. *Nuclear Instruments and Methods in Physics Research Section A: Accelerators, Spectrometers, Detectors and Associated Equipment*, 787:254–260, July 2015. ISSN 0168-9002. doi: 10.1016/j.nima.2014.12.044. URL http://dx.doi.org/10.1016/j.nima.2014.12.044.

[58] A. Robert, O. Sirjean, A. Browaeys, J. Poupard, S. Nowak, D. Boiron, C. I. Westbrook, and A. Aspect. A bose-einstein condensate of metastable atoms. *Science*, 292(5516):461–464, April 2001. ISSN 1095-9203. doi: 10.1126/science.1060622. URL http://dx.doi.org/10.1126/science.1060622.

[59] M. Schellekens, R. Hoppeler, A. Perrin, J. Viana Gomes, D. Boiron, A. Aspect, and C. I. Westbrook. Hanbury brown twiss effect for ultracold quantum gases. *Science*, 310(5748): 648–651, October 2005. ISSN 1095-9203. doi: 10.1126/science.1118024. URL http://dx.doi.org/10.1126/science.1118024.

[60] F. Pereira Dos Santos, J. Léonard, Junmin Wang, C. J. Barrelet, F. Perales, E. Rasel, C. S. Unnikrishnan, M. Leduc, and C. Cohen-Tannoudji. Bose-einstein condensation of metastable helium. *Physical Review Letters*, 86(16):3459–3462, April 2001. ISSN 1079-7114. doi: 10.1103/physrevlett.86.3459. URL http://dx.doi.org/10.1103/PhysRevLett.86.3459.

[61] S. Charles Doret, Colin B. Connolly, Wolfgang Ketterle, and John M. Doyle. Buffer-gas cooled bose-einstein condensate. *Physical Review Letters*, 103(10), September 2009. ISSN 1079-7114. doi: 10.1103/physrevlett.103.103005. URL http://dx.doi.org/10.1103/PhysRevLett.103.103005.

[62] Michael Keller, Mateusz Kotyrba, Florian Leupold, Mandip Singh, Maximilian Ebner, and Anton Zeilinger. Bose-einstein condensate of metastable helium for quantum correlation experiments. *Physical Review A*, 90(6), December 2014. ISSN 1094-1622. doi: 10.1103/physreva.90.063607. URL http://dx.doi.org/10.1103/PhysRevA.90.063607.

[63] A. H. Abbas, X. Meng, R. S. Patil, J. A. Ross, A. G. Truscott, and S. S. Hodgman. Rapid generation of metastable helium bose-einstein condensates. *Physical Review A*, 103(5), May 2021. ISSN 2469-9934. doi: 10.1103/physreva.103.053317. URL http://dx.doi.org/10.1103/PhysRevA.103.053317.

[64] Q. Bouton, R. Chang, A. L. Hoendervanger, F. Nogrette, A. Aspect, C. I. Westbrook, and D. Clément. Fast production of bose-einstein condensates of metastable helium. *Physical Review A*, 91(6), June 2015. ISSN 1094-1622. doi: 10.1103/physreva.91.061402. URL http://dx.doi.org/10.1103/PhysRevA.91.061402.

[65] A. M. Kaufman, B. J. Lester, and C. A. Regal. Cooling a single atom in an optical tweezer to its quantum ground state. *Physical Review X*, 2(4), November 2012. ISSN 2160-3308. doi: 10.1103/physrevx.2.041014. URL http://dx.doi.org/10.1103/PhysRevX.2.041014.

[66] A. M. Kaufman, B. J. Lester, C. M. Reynolds, M. L. Wall, M. Foss-Feig, K. R. A. Hazzard, A. M. Rey, and C. A. Regal. Two-particle quantum interference in tunnel-coupled optical tweezers. *Science*, 345(6194):306–309, July 2014. ISSN 1095-9203. doi: 10.1126/science.1250057. URL http://dx.doi.org/10.1126/science.1250057.

[67] F. Borselli, M. Maiwöger, T. Zhang, P. Haslinger, V. Mukherjee, A. Negretti, S. Montangero, T. Calarco, I. Mazets, M. Bonneau, and J. Schmiedmayer. Two-particle interference with double twin-atom beams. *Physical Review Letters*, 126(8), February 2021. ISSN 1079-7114. doi: 10.1103/physrevlett.126.083603. URL http://dx.doi.org/10.1103/PhysRevLett.126.083603.

[68] R. J. Lewis-Swan and K. V. Kheruntsyan. Atomic twin beams and violation of a motional-state bell inequality from a phase-fluctuating quasicondensate source. *Physical Review A*, 101(4), April 2020. ISSN 2469-9934. doi: 10.1103/physreva.101.043615. URL http://dx.doi.org/10.1103/PhysRevA.101.043615.

[69] Marie Bonneau, William J. Munro, Kae Nemoto, and Jörg Schmiedmayer. Characterizing twin-particle entanglement in double-well potentials. *Physical Review A*, 98(3), September 2018. ISSN 2469-9934. doi: 10.1103/physreva.98.033608. URL http://dx.doi.org/10.1103/PhysRevA.98.033608.

[70] F. Anders, A. Idel, P. Feldmann, D. Bondarenko, S. Loriani, K. Lange, J. Peise, M. Gersemann, B. Meyer-Hoppe, S. Abend, N. Gaaloul, C. Schubert, D. Schlippert, L. Santos, E. Rasel, and C. Klempt. Momentum entanglement for atom interferometry. *Physical Review Letters*, 127(14), September 2021. ISSN 1079-7114. doi: 10.1103/physrevlett.127.140402. URL http://dx.doi.org/10.1103/PhysRevLett.127.140402.

[71] Stuart S. Szigeti, Onur Hosten, and Simon A. Haine. Improving cold-atom sensors with quantum entanglement: Prospects and challenges. *Applied Physics Letters*, 118(14), April 2021. ISSN 1077-3118. doi: 10.1063/5.0050235. URL http://dx.doi.org/10.1063/5.0050235.

[72] Fabian Finger, Rodrigo Rosa-Medina, Nicola Reiter, Panagiotis Christodoulou, Tobias Donner, and Tilman Esslinger. Spin- and momentum-correlated atom pairs mediated by photon exchange and seeded by vacuum fluctuations. *Physical Review Letters*, 132(9), February

2024. ISSN 1079-7114. doi: 10.1103/physrevlett.132.093402. URL http://dx.doi.org/10.1103/physrevlett.132.093402.

[73] J.-C. Jaskula, G. B. Partridge, M. Bonneau, R. Lopes, J. Ruaudel, D. Boiron, and C. I. Westbrook. Acoustic analog to the dynamical casimir effect in a bose-einstein condensate. *Physical Review Letters*, 109(22), November 2012. ISSN 1079-7114. doi: 10.1103/physrevlett.109.220401. URL http://dx.doi.org/10.1103/physrevlett.109.220401.

[74] Logan W. Clark, Anita Gaj, Lei Feng, and Cheng Chin. Collective emission of matter-wave jets from driven bose–einstein condensates. *Nature*, 551(7680):356–359, November 2017. ISSN 1476-4687. doi: 10.1038/nature24272. URL http://dx.doi.org/10.1038/nature24272.

[75] R. Ghosh and L. Mandel. Observation of nonclassical effects in the interference of two photons. *Physical Review Letters*, 59(17):1903–1905, October 1987. ISSN 0031-9007. doi: 10.1103/physrevlett.59.1903. URL http://dx.doi.org/10.1103/PhysRevLett.59.1903.

[76] J. F. Ward and G. H. C. New. Optical third harmonic generation in gases by a focused laser beam. *Physical Review*, 185(1):57–72, September 1969. ISSN 0031-899X. doi: 10.1103/physrev.185.57. URL http://dx.doi.org/10.1103/PhysRev.185.57.

[77] A. Perrin, H. Chang, V. Krachmalnicoff, M. Schellekens, D. Boiron, A. Aspect, and C. I. Westbrook. Observation of atom pairs in spontaneous four-wave mixing of two colliding bose-einstein condensates. *Physical Review Letters*, 99(15), October 2007. ISSN 1079-7114. doi: 10.1103/physrevlett.99.150405. URL http://dx.doi.org/10.1103/PhysRevLett.99.150405.

[78] J.-C. Jaskula, M. Bonneau, G. B. Partridge, V. Krachmalnicoff, P. Deuar, K. V. Kheruntsyan, A. Aspect, D. Boiron, and C. I. Westbrook. Sub-poissonian number differences in four-wave mixing of matter waves. *Physical Review Letters*, 105(19), November 2010. ISSN 1079-7114. doi: 10.1103/physrevlett.105.190402. URL http://dx.doi.org/10.1103/PhysRevLett.105.190402.

[79] K. V. Kheruntsyan, J.-C. Jaskula, P. Deuar, M. Bonneau, G. B. Partridge, J. Ruaudel, R. Lopes, D. Boiron, and C. I. Westbrook. Violation of the cauchy-schwarz inequality with matter waves. *Physical Review Letters*, 108(26), June 2012. ISSN 1079-7114. doi: 10.1103/physrevlett.108.260401. URL http://dx.doi.org/10.1103/PhysRevLett.108.260401.

[80] Karen Marie Hilligsøe and Klaus Mølmer. Phase-matched four wave mixing and quantum beam splitting of matter waves in a periodic potential. *Physical Review A*, 71(4), April 2005. ISSN 1094-1622. doi: 10.1103/physreva.71.041602. URL http://dx.doi.org/10.1103/PhysRevA.71.041602.

[81] Gretchen K. Campbell, Jongchul Mun, Micah Boyd, Erik W. Streed, Wolfgang Ketterle, and David E. Pritchard. Parametric amplification of scattered atom pairs. *Physical Review Letters*, 96(2), January 2006. ISSN 1079-7114. doi: 10.1103/physrevlett.96.020406. URL http://dx.doi.org/10.1103/PhysRevLett.96.020406.

[82] Peter Martin, Bruce Oldaker, Andrew Miklich, and David Pritchard. Bragg scattering of atoms from a standing light wave. *Physical Review Letters*, 60(6):515–518, February 1988. ISSN 0031-9007. doi: 10.1103/physrevlett.60.515. URL http://dx.doi.org/10.1103/PhysRevLett.60.515.

[83] M. Kozuma, L. Deng, E. W. Hagley, J. Wen, R. Lutwak, K. Helmerson, S. L. Rolston, and W. D. Phillips. Coherent splitting of bose-einstein condensed atoms with optically induced bragg diffraction. *Physical Review Letters*, 82(5):871–875, February 1999. ISSN 1079-7114. doi: 10.1103/physrevlett.82.871. URL http://dx.doi.org/10.1103/PhysRevLett.82.871.

[84] D. M. Stamper-Kurn, A. P. Chikkatur, A. Görlitz, S. Gupta, S. Inouye, J. Stenger, D. E. Pritchard, and W. Ketterle. Probing bose-einstein condensates with optical bragg scattering. In *Recent Progress in Many-Body Theories*. WORLD SCIENTIFIC, September 2000. doi: 10.1142/9789812792754_0039. URL http://dx.doi.org/10.1142/9789812792754_0039.

[85] F. Riehle, Th. Kisters, A. Witte, J. Helmcke, and Ch. J. Bordé. Optical ramsey spectroscopy in a rotating frame: Sagnac effect in a matter-wave interferometer. *Physical Review Letters*, 67(2):177–180, July 1991. ISSN 0031-9007. doi: 10.1103/physrevlett.67.177. URL http://dx.doi.org/10.1103/PhysRevLett.67.177.

[86] Mark Kasevich and Steven Chu. Atomic interferometry using stimulated Raman transitions. *Physical Review Letters*, 67(2):181–184, July 1991. ISSN 0031-9007. doi: 10.1103/PhysRevLett.67.181. URL https://link.aps.org/doi/10.1103/PhysRevLett.67.181.

[87] David M. Giltner, Roger W. McGowan, and Siu Au Lee. Atom interferometer based on bragg scattering from standing light waves. *Physical Review Letters*, 75(14):2638–2641, October 1995. ISSN 1079-7114. doi: 10.1103/physrevlett.75.2638. URL http://dx.doi.org/10.1103/PhysRevLett.75.2638.

[88] Alexander D. Cronin, Jörg Schmiedmayer, and David E. Pritchard. Optics and interferometry with atoms and molecules. *Reviews of Modern Physics*, 81(3):1051–1129, July 2009. ISSN 1539-0756. doi: 10.1103/revmodphys.81.1051. URL http://dx.doi.org/10.1103/RevModPhys.81.1051.

[89] Onur Hosten, Nils J. Engelsen, Rajiv Krishnakumar, and Mark A. Kasevich. Measurement noise 100 times lower than the quantum-projection limit using entangled atoms. *Nature*, 529(7587):505–508, January 2016. ISSN 1476-4687. doi: 10.1038/nature16176. URL http://dx.doi.org/10.1038/nature16176.

[90] Johannes Kofler, Mandip Singh, Maximilian Ebner, Michael Keller, Mateusz Kotyrba, and Anton Zeilinger. Einstein-podolsky-rosen correlations from colliding bose-einstein condensates. *Physical Review A*, 86(3), September 2012. ISSN 1094-1622. doi: 10.1103/physreva.86.032115. URL http://dx.doi.org/10.1103/PhysRevA.86.032115.

[91] S. S. Hodgman, W. Bu, S. B. Mann, R. I. Khakimov, and A. G. Truscott. Higher-order quantum ghost imaging with ultracold atoms. *Physical Review Letters*, 122(23), June 2019. ISSN 1079-7114. doi: 10.1103/physrevlett.122.233601. URL http://dx.doi.org/10.1103/PhysRevLett.122.233601.

[92] R. Lopes, A. Imanaliev, A. Aspect, M. Cheneau, D. Boiron, and C. I. Westbrook. Atomic Hong–Ou–Mandel experiment. *Nature*, 520(7545):66–68, April 2015. ISSN 0028-0836, 1476-4687. doi: 10.1038/nature14331. URL https://www.nature.com/articles/nature14331.

[93] Pierre Dussarrat, Maxime Perrier, Almazbek Imanaliev, Raphael Lopes, Alain Aspect, Marc Cheneau, Denis Boiron, and Christoph Westbrook. A two-particle, four-mode interferometer for atoms. *Physical Review Letters*, 119(17):173202, October 2017. ISSN 0031-9007, 1079-7114. doi: 10.1103/PhysRevLett.119.173202. URL https://link.aps.org/doi/10.1103/PhysRevLett.119.173202.

[94] Kieran F. Thomas, Bryce M. Henson, Yu Wang, Robert J. Lewis-Swan, Karen V. Kheruntsyan, Sean S. Hodgman, and Andrew G. Truscott. A matter wave Rarity-Tapster interferometer to demonstrate non-locality. *The European Physical Journal D*, 76(12):244, December 2022. ISSN 1434-6060, 1434-6079. doi: 10.1140/epjd/s10053-022-00551-y. URL https://epjd.epj.org/articles/epjd/abs/2022/12/10053_2022_Article_551/10053_2022_Article_551.html. arXiv:2206.08560.

[95] Donald C Morton, Qixue Wu, and G WF Drake. Energy levels for the stable isotopes of atomic helium(4he i and3he i). *Canadian Journal of Physics*, 84(2):83–105, February 2006. ISSN 1208-6045. doi: 10.1139/p06-009. URL http://dx.doi.org/10.1139/p06-009.

[96] S. S. Hodgman, R. G. Dall, L. J. Byron, K. G. H. Baldwin, S. J. Buckman, and A. G. Truscott. Metastable helium: A new determination of the longest atomic excited-state lifetime. *Physical Review Letters*, 103(5), July 2009. ISSN 1079-7114. doi: 10.1103/physrevlett.103.053002. URL http://dx.doi.org/10.1103/PhysRevLett.103.053002.

[97] David R Lide, editor. *CRC handbook of chemistry and physics, 90th edition*. CRC Press, Boca Raton, FL, 90 edition, May 2009.

[98] William C. Martin. Energy levels and spectrum of neutral helium (4he i). *Journal of Research of the National Bureau of Standards Section A: Physics and Chemistry*, 64A(1):19, January 1960. ISSN 0022-4332. doi: 10.6028/jres.064a.003. URL http://dx.doi.org/10.6028/jres.064A.003.

[99] M. W. Muller, A. Merz, M. W. Ruf, H. Hotop, W. Meyer, and M. Movre. Experimental and theoretical studies of the bi-excited collision systems he*(23 s) + he*(23 s, 21 s) at thermal and subthermal kinetic energies. *Zeitschrift fur Physik D Atoms, Molecules and Clusters*, 21(2):89–112, June 1991. ISSN 1434-6079. doi: 10.1007/bf01425589. URL http://dx.doi.org/10.1007/BF01425589.

[100] H. C. Mastwijk, J. W. Thomsen, P. van der Straten, and A. Niehaus. Optical collisions of cold, metastable helium atoms. *Physical Review Letters*, 80(25):5516–5519, June 1998. ISSN 1079-7114. doi: 10.1103/physrevlett.80.5516. URL http://dx.doi.org/10.1103/PhysRevLett.80.5516.

[101] Wim Vassen, Claude Cohen-Tannoudji, Michele Leduc, Denis Boiron, Christoph I. Westbrook, Andrew Truscott, Ken Baldwin, Gerhard Birkl, Pablo Cancio, and Marek Trippenbach. Cold and trapped metastable noble gases. *Reviews of Modern Physics*, 84 (1):175–210, February 2012. ISSN 1539-0756. doi: 10.1103/revmodphys.84.175. URL http://dx.doi.org/10.1103/RevModPhys.84.175.

[102] S. Seidelin, J. Viana Gomes, R. Hoppeler, O. Sirjean, D. Boiron, A. Aspect, and C. I. Westbrook. Getting the elastic scattering length by observing inelastic collisions in ultracold metastable helium atoms. *Physical Review Letters*, 93(9), August 2004. ISSN 1079-7114. doi: 10.1103/physrevlett.93.090409. URL http://dx.doi.org/10.1103/PhysRevLett.93.090409.

[103] F. B. Dunning, R. D. Rundel, and R. F. Stebbings. Determination of secondary electron ejection coefficients for rare gas metastable atoms. *Review of Scientific Instruments*, 46(6): 697–701, June 1975. ISSN 1089-7623. doi: 10.1063/1.1134291. URL http://dx.doi.org/10.1063/1.1134291.

[104] Maxime Perrier. *Interférences multiples avec atomes froids*. PhD thesis, Université Paris-Saclay, 2018. URL http://www.theses.fr/2018SACLO004. Thèse de doctorat dirigée par Denis Boiron, Palaiseau, Université Paris-Saclay, Institut d'optique graduate School, 2018.

[105] W. Lu, M. D. Hoogerland, D. Milic, K. G. H. Baldwin, and S. J. Buckman. A bright metastable atom source at 80 k. *Review of Scientific Instruments*, 72(6):2558–2561, June 2001. ISSN 1089-7623. doi: 10.1063/1.1372169. URL http://dx.doi.org/10.1063/1.1372169.

[106] Antoine Browaeys. *Piegeage magnetique d'un gaz d'helium metastable : vers la condensation de bose-einstein*. PhD thesis, Université Paris 6, 2000. URL http://www.theses.fr/2000PA066081. Thèse de doctorat dirigée par Alain Aspect, Université Paris 6, 2000.

[107] J. Dalibard. *Une brève histoire des atomes froids*. Cours du Collège de France, 2015. URL https://pro.college-de-france.fr/jean.dalibard/index.html.

[108] Guillaume Labeyrie. *Deux outils pour l'optique atomique : jet intense d'helium metastable et miroir a onde evanescente exaltee*. PhD thesis, Université Paris XI Orsay, 1998. URL

http://www.theses.fr/1998PA112063. Thèse de doctorat dirigée par Alain Aspect, Orsay, Université Paris XI Orsay, Institut d'optique théorique et appliquée, 1998.

[109] Wolfgang Petrich, Michael H. Anderson, Jason R. Ensher, and Eric A. Cornell. Behavior of atoms in a compressed magneto-optical trap. *Journal of the Optical Society of America B*, 11(8):1332, August 1994. ISSN 1520-8540. doi: 10.1364/josab.11.001332. URL http://dx.doi.org/10.1364/JOSAB.11.001332.

[110] M.-O. Mewes, M. R. Andrews, N. J. van Druten, D. M. Kurn, D. S. Durfee, and W. Ketterle. Bose-einstein condensation in a tightly confining dc magnetic trap. *Physical Review Letters*, 77(3):416–419, July 1996. ISSN 1079-7114. doi: 10.1103/physrevlett.77.416. URL http://dx.doi.org/10.1103/PhysRevLett.77.416.

[111] Piet O. Schmidt, Sven Hensler, Jörg Werner, Thomas Binhammer, Axel Görlitz, and Tilman Pfau. Doppler cooling of an optically dense cloud of magnetically trapped atoms. *Journal of the Optical Society of America B*, 20(5):960, May 2003. ISSN 1520-8540. doi: 10.1364/josab.20.000960. URL http://dx.doi.org/10.1364/JOSAB.20.000960.

[112] Ziyad Amodjee. *Création et caractérisation de paires d'atomes corrélées : vers des tests de la mécanique quantique*. PhD thesis, Université Paris-Saclay, 2020. URL http://www.theses.fr/2020UPASP049. Thèse de doctorat dirigée par Christoph Westbrook, Palaiseau, Université Paris-Saclay, Institut d'optique graduate School, 2020.

[113] Clothilde Lamirault. Détermination du nombre d'atomes d'un gaz d'hélium par imagerie d'absorption. Internship report, Université Paris-Saclay, Institut d'Optique Graduate School, Laboratoire Charles Fabry, Palaiseau, France, July 2023. Supervised par Denis Boiron.

[114] Antoine Ténart. *Momentum-space correlations in the depletion of weakly interacting lattice Bose gases*. PhD thesis, Université Paris-Saclay, 2021. URL http://www.theses.fr/2021UPASP128. Thèse de doctorat dirigée par David Clément, Palaiseau, Université Paris-Saclay, Institut d'optique graduate School, 2021.

[115] Raphael Lopes. *An atomic Hong-Ou-Mandel experiment*. PhD thesis, Université Paris-Saclay, 2015. URL http://www.theses.fr/2015IOTA0001. Thèse de doctorat dirigée par Denis Boiron, Palaiseau, Université Paris-Saclay, Institut d'optique graduate School, 2015.

[116] Tomasz M Brzozowski, Maria Maczynska, Michal Zawada, Jerzy Zachorowski, and Wojciech Gawlik. Time-of-flight measurement of the temperature of cold atoms for short trap-probe beam distances. *Journal of Optics B: Quantum and Semiclassical Optics*, 4(1):62–66, January 2002. ISSN 1741-3575. doi: 10.1088/1464-4266/4/1/310. URL http://dx.doi.org/10.1088/1464-4266/4/1/310.

[117] Y. Castin and R. Dum. Bose-einstein condensates in time dependent traps. *Physical Review Letters*, 77(27):5315–5319, December 1996. ISSN 1079-7114. doi: 10.1103/physrevlett.77.5315. URL http://dx.doi.org/10.1103/PhysRevLett.77.5315.

[118] Yu. Kagan, E. L. Surkov, and G. V. Shlyapnikov. Evolution of a bose gas in anisotropic time-dependent traps. *Physical Review A*, 55(1):R18–R21, January 1997. ISSN 1094-1622. doi: 10.1103/physreva.55.r18. URL http://dx.doi.org/10.1103/PhysRevA.55.R18.

[119] W. Ketterle, D. S. Durfee, and D. M. Stamper-Kurn. Making, probing and understanding bose-einstein condensates, 1999. URL https://arxiv.org/abs/cond-mat/9904034.

[120] A. Perrin, H. Chang, V. Krachmalnicoff, M. Schellekens, D. Boiron, A. Aspect, and C. I. Westbrook. Observation of atom pairs in spontaneous four wave mixing of two colliding Bose-Einstein Condensates. *Physical Review Letters*, 99(15):150405, October 2007. ISSN 0031-9007, 1079-7114. doi: 10.1103/PhysRevLett.99.150405. URL https://link.aps.org/doi/10.1103/PhysRevLett.99.150405. arXiv:0704.3047.

[121] Pierre Dussarrat. *Expériences d'Optique Atomique Quantique, Interféromètres à 2 et 4 modes*. Theses, Université Paris Saclay (COmUE), November 2017. URL https://pastel.hal.science/tel-01686709. Thèse de doctorat dirigée par Denis Boiron, Palaiseau, Université Paris-Saclay, Institut d'optique graduate School, 2017.

[122] Josselin Ruaudel. *Création et caractérisation d'une source ajustable de paires d'atomes corrélés*. PhD thesis, Université Paris-Sud, 2013. URL http://www.theses.fr/2013IOTA0003. Thèse de doctorat dirigée par Denis Boiron, Palaiseau, Institut d'optique théorique et appliquée, 2013.

[123] Paul Paquiez. Etude du processus de mélange à 4 ondes pour un condensat de bose-einstein dans un réseau optique. Internship report, Université Paris-Saclay, Institut d'Optique Graduate School, Laboratoire Charles Fabry, Palaiseau, France, July 2023. Supervised par Denis Boiron.

[124] Martijn Schellekens. *L'effet Hanbury Brown et Twiss pour les atomes froids*. PhD thesis, Université Paris XI Orsay, 2007. URL http://www.theses.fr/2007PA112086. Thèse de doctorat dirigée par Christoph Westbrook, Université Paris XI Orsay, 2007.

[125] Hugo Cayla. *Measuring the momentum distribution of a lattice gas at the single-atom level*. PhD thesis, Université Paris Saclay (COmUE), 2018. URL http://www.theses.fr/2018SACLO005. Thèse de doctorat dirigée par Christoph Westbrook, Université Paris-Saclay (ComUE), 2018.

[126] Cécile Carcy, Hugo Cayla, Antoine Tenart, Alain Aspect, Marco Mancini, and David Clément. Momentum-space atom correlations in a mott insulator. *Physical Review X*, 9(4), November 2019. ISSN 2160-3308. doi: 10.1103/physrevx.9.041028. URL http://dx.doi.org/10.1103/PhysRevX.9.041028.

[127] Bradley Efron and R.J. Tibshirani. *An Introduction to the Bootstrap*. Chapman and Hall/CRC, May 1994. ISBN 9780429246593. doi: 10.1201/9780429246593. URL http://dx.doi.org/10.1201/9780429246593.

[128] Maxime Perrier, Ziyad Amodjee, Pierre Dussarrat, Alexandre Dareau, Alain Aspect, Marc Cheneau, Denis Boiron, and Christoph I. Westbrook. Thermal counting statistics in an atomic two-mode squeezed vacuum state. *SciPost Phys.*, 7:002, 2019. doi: 10.21468/SciPostPhys.7.1.002. URL https://scipost.org/10.21468/SciPostPhys.7.1.002.

[129] B. Yurke and M. Potasek. Obtainment of thermal noise from a pure quantum state. *Physical Review A*, 36(7):3464–3466, October 1987. ISSN 0556-2791. doi: 10.1103/physreva.36.3464. URL http://dx.doi.org/10.1103/PhysRevA.36.3464.

[130] Joseph W Goodman. *Statistical Optics*. Wiley Series in Pure and Applied Optics. John Wiley & Sons, Nashville, TN, March 1985.

[131] Jonas Kitzinger, Xin Meng, Matteo Fadel, Valentin Ivannikov, Kae Nemoto, William J. Munro, and Tim Byrnes. Bell correlations in a split two-mode-squeezed bose-einstein condensate. *Physical Review A*, 104(4), October 2021. ISSN 2469-9934. doi: 10.1103/physreva.104.043323. URL http://dx.doi.org/10.1103/physreva.104.043323.

[132] R. J. Lewis-Swan and K. V. Kheruntsyan. Proposal for a motional-state Bell inequality test with ultracold atoms. *Physical Review A*, 91(5):052114, May 2015. ISSN 1050-2947, 1094-1622. doi: 10.1103/PhysRevA.91.052114. URL https://link.aps.org/doi/10.1103/PhysRevA.91.052114.

[133] S. S. Hodgman, R. I. Khakimov, R. J. Lewis-Swan, A. G. Truscott, and K. V. Kheruntsyan. Solving the quantum many-body problem via correlations measured with a momentum microscope. *Phys. Rev. Lett.*, 118:240402, Jun 2017. doi: 10.1103/PhysRevLett.118.240402. URL https://link.aps.org/doi/10.1103/PhysRevLett.118.240402.

[134] J. Dalibard. *Des cages de lumière pour les atomes: la physique des pièges et des réseaux optiques*. Cours du Collège de France, 2013. URL https://pro.college-de-france.fr/jean.dalibard/index.html.

[135] Ashley Beguin. *Interférométrie atomique à grands transferts d'impulsion dans le régime de quasi-Bragg*. PhD thesis, Université Toulouse 3 - Paul Sabatier, 2023. URL http://www.theses.fr/2023TOU30056. Thèse de doctorat dirigée par David Guéry-Odelin, et Alexandre Gauguet, Université Toulouse 3 - Paul Sabatier, 2023.

[136] P. L. Kapitza and P. A. M. Dirac. The reflection of electrons from standing light waves. *Mathematical Proceedings of the Cambridge Philosophical Society*, 29(2):297–300, May 1933. ISSN 0305-0041, 1469-8064. doi: 10.1017/S0305004100011105. URL https://www.cambridge.org/core/journals/mathematical-proceedings-of-the-cambridge-philosophical-society/article/abs/reflection-of-electrons-from-standing-light-waves/482DA4D6EFA5C067CC6990F936EA3F04.

[137] K. Bongs, R. Launay, and M.A. Kasevich. High-order inertial phase shifts for time-domain atom interferometers. *Applied Physics B*, 84(4):599–602, September 2006. ISSN 0946-2171, 1432-0649. doi: 10.1007/s00340-006-2397-5. URL https://doi.org/10.1007/s00340-006-2397-5.

[138] A Peters, K Y Chung, and S Chu. High-precision gravity measurements using atom interferometry. *Metrologia*, 38(1):25–61, February 2001. ISSN 0026-1394. doi: 10.1088/0026-1394/38/1/4. URL https://dx.doi.org/10.1088/0026-1394/38/1/4.

[139] Ch. J. Bordé. Theoretical tools for atom optics and interferometry. *Comptes Rendus De L'Académie Des Sciences, Série IV - Physique Astrophysique*, 2:509–530, 2001. URL https://api.semanticscholar.org/CorpusID:54770732.

[140] Ch Antoine and Ch J Bordé. Quantum theory of atomic clocks and gravito-inertial sensors: an update. *Journal of Optics B: Quantum and Semiclassical Optics*, 5(2):S199, apr 2003. doi: 10.1088/1464-4266/5/2/380. URL https://dx.doi.org/10.1088/1464-4266/5/2/380.

[141] Hibbs A. R. Feynman R. P. *Quantum Mechanics and Path Integrals*. New York, McGraw-Hill, 1965.

[142] Pippa Storey and Claude Cohen-Tannoudji. The Feynman path integral approach to atomic interferometry. A tutorial. *Journal de Physique II*, 4(11):1999–2027, November 1994. ISSN 1155-4312, 1286-4870. doi: 10.1051/jp2:1994103. URL https://doi.org/10.1051/jp2:1994103.

[143] Jason M. Hogan, David M. S. Johnson, and Mark A. Kasevich. Light-pulse atom interferometry, June 2008. URL http://arxiv.org/abs/0806.3261. arXiv:0806.3261 [physics].

[144] David M. Giltner, Roger W. McGowan, and Siu Au Lee. Atom Interferometer Based on Bragg Scattering from Standing Light Waves. *Physical Review Letters*, 75(14):2638–2641, October 1995. ISSN 0031-9007, 1079-7114. doi: 10.1103/PhysRevLett.75.2638. URL https://link.aps.org/doi/10.1103/PhysRevLett.75.2638.

[145] Yoshio Torii, Yoichi Suzuki, Mikio Kozuma, Toshiaki Sugiura, Takahiro Kuga, Lu Deng, and E. W. Hagley. Mach-Zehnder Bragg interferometer for a Bose-Einstein condensate. *Physical Review A*, 61(4):041602, February 2000. ISSN 1050-2947, 1094-1622. doi: 10.1103/PhysRevA.61.041602. URL https://link.aps.org/doi/10.1103/PhysRevA.61.041602.

[146] M. Kasevich and S. Chu. Measurement of the gravitational acceleration of an atom with a light-pulse atom interferometer. *Applied Physics B Photophysics and Laser Chemistry*, 54(5):321–332, May 1992. ISSN 0721-7269, 1432-0649. doi: 10.1007/BF00325375. URL https://link.springer.com/article/10.1007/BF00325375.

[147] Almazbek Imanaliev. *Towards testing Bell's inequality using atoms correlated in momentum.* PhD thesis, Université Paris-Saclay, 2016. URL http://www.theses.fr/2016SACLO003. Thèse de doctorat dirigée par Denis Boiron, Palaiseau, Université Paris-Saclay, Institut d'optique graduate School, 2016.

[148] William G. Alway and Jonathan A. Jones. Arbitrary precision composite pulses for NMR quantum computing. *Journal of Magnetic Resonance*, 189(1):114–120, 2007. ISSN 1090-7807. doi: 10.1016/j.jmr.2007.09.001. URL https://doi.org/10.1016/j.jmr.2007.09.001.

[149] Sylvia McDonald and Warren S. Warren. Uses of shaped pulses in nmr: A primer. *Concepts in Magnetic Resonance*, 3(2):55–81, 1991. doi: 10.1002/cmr.1820030202. URL https://onlinelibrary.wiley.com/doi/abs/10.1002/cmr.1820030202.

[150] Boyan T. Torosov and Nikolay V. Vitanov. Smooth composite pulses for high-fidelity quantum information processing. *Physical Review A*, 83(5):053420, May 2011. ISSN 1050-2947, 1094-1622. doi: 10.1103/PhysRevA.83.053420. URL https://link.aps.org/doi/10.1103/PhysRevA.83.053420.

[151] Alexander Dunning, Rachel Gregory, James Bateman, Nathan Cooper, Matthew Himsworth, Jonathan A. Jones, and Tim Freegarde. Composite pulses for interferometry in a thermal cold atom cloud. *Physical Review A*, 90(3):033608, September 2014. ISSN 1050-2947, 1094-1622. doi: 10.1103/PhysRevA.90.033608. URL https://link.aps.org/doi/10.1103/PhysRevA.90.033608.

[152] P. Berg, S. Abend, G. Tackmann, C. Schubert, E. Giese, W. P. Schleich, F. A. Narducci, W. Ertmer, and E. M. Rasel. Composite-Light-Pulse Technique for High-Precision Atom Interferometry. *Physical Review Letters*, 114(6):063002, February 2015. ISSN 0031-9007, 1079-7114. doi: 10.1103/PhysRevLett.114.063002. URL https://link.aps.org/doi/10.1103/PhysRevLett.114.063002.

[153] David L. Butts, Krish Kotru, Joseph M. Kinast, Antonije M. Radojevic, Brian P. Timmons, and Richard E. Stoner. Efficient broadband raman pulses for large-area atom interferometry. *J. Opt. Soc. Am. B*, 30(4):922–927, Apr 2013. doi: 10.1364/JOSAB.30.000922. URL https://opg.optica.org/josab/abstract.cfm?URI=josab-30-4-922.

[154] Yukun Luo, Shuhua Yan, Qingqing Hu, Aiai Jia, Chunhua Wei, and Jun Yang. Contrast enhancement via shaped Raman pulses for thermal coldatom cloud interferometry. *The European Physical Journal D*, 70(12):262, December 2016. ISSN 1434-6060, 1434-6079. doi: 10.1140/epjd/e2016-70428-6. URL https://link.springer.com/article/10.1140/epjd/e2016-70428-6.

[155] Xu Zhao, Xiaoyan Liu, Jianfang Sun, Zhen Xu, Zhengfeng Hu, and Xihua Yang. Optimized Gaussian pulse for mirrors and beam splitters in atom interferometry. *The European Physical Journal D*, 76(3):39, March 2022. ISSN 1434-6060, 1434-6079. doi: 10.1140/epjd/s10053-022-00368-9. URL https://link.springer.com/article/10.1140/epjd/s10053-022-00368-9.

[156] Holger Müller, Sheng-wey Chiow, and Steven Chu. Atom-wave diffraction between the Raman-Nath and the Bragg regime: Effective Rabi frequency, losses, and phase shifts. *Physical Review A*, 77(2):023609, February 2008. ISSN 1050-2947, 1094-1622. doi: 10.1103/PhysRevA.77.023609. URL https://link.aps.org/doi/10.1103/PhysRevA.77.023609.

[157] Helen Geen and Ray Freeman. Band-selective radiofrequency pulses. *Journal of Magnetic Resonance (1969)*, 93(1):93–141, June 1991. ISSN 0022-2364. doi: 10.1016/0022-2364(91)90034-q. URL http://dx.doi.org/10.1016/0022-2364(91)90034-Q.

[158] Bess Fang, Nicolas Mielec, Denis Savoie, Matteo Altorio, Arnaud Landragin, and Remi Geiger. Improving the phase response of an atom interferometer by means of temporal pulse shaping. *New Journal of Physics*, 20(2):023020, February 2018. ISSN 1367-2630.

doi: 10.1088/1367-2630/aaa37c. URL https://iopscience.iop.org/article/10.1088/1367-2630/aaa37c.

[159] Navin Khaneja, Timo Reiss, Cindie Kehlet, Thomas Schulte-Herbrüggen, and Steffen J. Glaser. Optimal control of coupled spin dynamics: Design of NMR pulse sequences by gradient ascent algorithms. *Journal of Magnetic Resonance*, 172(2):296–305, February 2005. ISSN 10907807. doi: 10.1016/j.jmr.2004.11.004. URL https://doi.org/10.1016/j.jmr.2004.11.004.

[160] Tommaso Caneva, Tommaso Calarco, and Simone Montangero. Chopped random-basis quantum optimization. *Physical Review A*, 84(2):022326, August 2011. ISSN 1050-2947, 1094-1622. doi: 10.1103/PhysRevA.84.022326. URL https://link.aps.org/doi/10.1103/PhysRevA.84.022326.

[161] Jack Saywell, Max Carey, Mohammad Belal, Ilya Kuprov, and Tim Freegarde. Optimal control of Raman pulse sequences for atom interferometry. *Journal of Physics B: Atomic, Molecular and Optical Physics*, 53(8):085006, April 2020. ISSN 0953-4075, 1361-6455. doi: 10.1088/1361-6455/ab6df6. URL https://doi.org/10.1088/1361-6455/ab6df6.

[162] Zilin Chen, Garrett Louie, Yiping Wang, Tejas Deshpande, and Tim Kovachy. Enhancing strontium clock atom interferometry using quantum optimal control. *Physical Review A*, 107(6):063302, June 2023. ISSN 2469-9926, 2469-9934. doi: 10.1103/PhysRevA.107.063302. URL https://link.aps.org/doi/10.1103/PhysRevA.107.063302.

[163] Nikolaos Dedes, Jack Saywell, Max Carey, Ilya Kuprov, and Tim Freegarde. Optimizing beam-splitter pulses for atom interferometry: A geometric approach. *Physical Review A*, 108(5):053319, November 2023. ISSN 2469-9926, 2469-9934. doi: 10.1103/PhysRevA.108.053319. URL https://link.aps.org/doi/10.1103/PhysRevA.108.053319.

[164] Michael H. Goerz, Mark A. Kasevich, and Vladimir S. Malinovsky. Quantum optimal control for atomic fountain interferometry. In Selim M. Shahriar and Jacob Scheuer, editors, *Optical and Quantum Sensing and Precision Metrology*, page 3, Online Only, United States, March 2021. SPIE. ISBN 978-1-5106-4235-5 978-1-5106-4236-2. doi: 10.1117/12.2587002. URL https://quantum-journal.org/papers/q-2022-12-07-871/.

[165] Garrett Louie, Zilin Chen, Tejas Deshpande, and Timothy Kovachy. Robust atom optics for Bragg atom interferometry. *New Journal of Physics*, 25(8):083017, August 2023. ISSN 1367-2630. doi: 10.1088/1367-2630/aceb15. URL https://iopscience.iop.org/article/10.1088/1367-2630/aceb15.

[166] Jack C. Saywell, Max S. Carey, Philip S. Light, Stuart S. Szigeti, Alistair R. Milne, Karandeep S. Gill, Matthew L. Goh, Viktor S. Perunicic, Nathanial M. Wilson, Calum D. Macrae, Alexander Rischka, Patrick J. Everitt, Nicholas P. Robins, Russell P. Anderson, Michael R. Hush, and Michael J. Biercuk. Enhancing the sensitivity of atom-interferometric inertial sensors using robust control. *Nature Communications*, 14(1):7626, November 2023. ISSN 2041-1723. doi: 10.1038/s41467-023-43374-0. URL https://www.nature.com/articles/s41467-023-43374-0.

[167] Pierre Cladé, Saida Guellati-Khélifa, François Nez, and François Biraben. Large momentum beam splitter using bloch oscillations. *Physical Review Letters*, 102(24), June 2009. ISSN 1079-7114. doi: 10.1103/physrevlett.102.240402. URL http://dx.doi.org/10.1103/PhysRevLett.102.240402.

[168] Vincent Ménoret, Pierre Vermeulen, Nicolas Le Moigne, Sylvain Bonvalot, Philippe Bouyer, Arnaud Landragin, and Bruno Desruelle. Gravity measurements below 10-9 g with a transportable absolute quantum gravimeter. *Scientific Reports*, 8(1):12300, August 2018. ISSN 2045-2322. doi: 10.1038/s41598-018-30608-1. URL https://www.nature.com/articles/s41598-018-30608-1.

[169] Franck Pereira dos Santos and Sylvain Bonvalot. *Cold-Atom Absolute Gravimetry*, page 1–6. Springer International Publishing, 2016. ISBN 9783319023700. doi: 10.1007/978-3-319-02370-0_30-2. URL http://dx.doi.org/10.1007/978-3-319-02370-0_30-2.

[170] Guglielmo M Tino. Testing gravity with cold atom interferometry: results and prospects. *Quantum Science and Technology*, 6(2):024014, March 2021. ISSN 2058-9565. doi: 10.1088/2058-9565/abd83e. URL http://dx.doi.org/10.1088/2058-9565/abd83e.

[171] Kenji Toyoda, Ryoto Hiji, Atsushi Noguchi, and Shinji Urabe. Hong–Ou–Mandel interference of two phonons in trapped ions. *Nature*, 527(7576):74–77, November 2015. ISSN 0028-0836, 1476-4687. doi: 10.1038/nature15735. URL https://www.nature.com/articles/nature15735.

[172] Charles Santori, David Fattal, Jelena Vučković, Glenn S. Solomon, and Yoshihisa Yamamoto. Indistinguishable photons from a single-photon device. *Nature*, 419(6907):594–597, October 2002. ISSN 0028-0836, 1476-4687. doi: 10.1038/nature01086. URL https://www.nature.com/articles/nature01086.

[173] J. Beugnon, M. P. A. Jones, J. Dingjan, B. Darquié, G. Messin, A. Browaeys, and P. Grangier. Quantum interference between two single photons emitted by independently trapped atoms. *Nature*, 440(7085):779–782, April 2006. ISSN 0028-0836, 1476-4687. doi: 10.1038/nature04628. URL https://www.nature.com/articles/nature04628.

[174] Yu-Hao Deng, Hui Wang, Xing Ding, Z.-C. Duan, Jian Qin, M.-C. Chen, Yu He, Yu-Ming He, Jin-Peng Li, Yu-Huai Li, Li-Chao Peng, E. S. Matekole, Tim Byrnes, C. Schneider, M. Kamp, Da-Wei Wang, Jonathan P. Dowling, Sven Höfling, Chao-Yang Lu, Marlan O. Scully, and Jian-Wei Pan. Quantum Interference between Light Sources Separated by 150 Million Kilometers. *Physical Review Letters*, 123(8):080401, August 2019. ISSN 0031-9007, 1079-7114. doi: 10.1103/PhysRevLett.123.080401. URL https://link.aps.org/doi/10.1103/PhysRevLett.123.080401.

[175] R. J. Lewis-Swan and K. V. Kheruntsyan. Proposal for demonstrating the Hong–Ou–Mandel effect with matter waves. *Nature Communications*, 5(1):3752, April 2014. ISSN 2041-1723. doi: 10.1038/ncomms4752. URL https://www.nature.com/articles/ncomms4752.

[176] J. Viana Gomes, A. Perrin, M. Schellekens, D. Boiron, C. I. Westbrook, and M. Belsley. Theory for a hanbury brown twiss experiment with a ballistically expanding cloud of cold atoms. *Physical Review A*, 74(5), November 2006. ISSN 1094-1622. doi: 10.1103/physreva.74.053607. URL http://dx.doi.org/10.1103/PhysRevA.74.053607.

[177] Martina Gebbe, Jan-Niclas Siemß, Matthias Gersemann, Hauke Müntinga, Sven Herrmann, Claus Lämmerzahl, Holger Ahlers, Naceur Gaaloul, Christian Schubert, Klemens Hammerer, Sven Abend, and Ernst M. Rasel. Twin-lattice atom interferometry. *Nature Communications*, 12(1), May 2021. ISSN 2041-1723. doi: 10.1038/s41467-021-22823-8. URL http://dx.doi.org/10.1038/s41467-021-22823-8.

[178] A. Béguin, T. Rodzinka, J. Vigué, B. Allard, and A. Gauguet. Characterization of an atom interferometer in the quasi-bragg regime. *Physical Review A*, 105(3), March 2022. ISSN 2469-9934. doi: 10.1103/physreva.105.033302. URL http://dx.doi.org/10.1103/PhysRevA.105.033302.

[179] A. Béguin, T. Rodzinka, L. Calmels, B. Allard, and A. Gauguet. Atom interferometry with coherent enhancement of bragg pulse sequences. *Physical Review Letters*, 131(14), October 2023. ISSN 1079-7114. doi: 10.1103/physrevlett.131.143401. URL http://dx.doi.org/10.1103/PhysRevLett.131.143401.

[180] T. Kovachy, P. Asenbaum, C. Overstreet, C. A. Donnelly, S. M. Dickerson, A. Sugarbaker, J. M. Hogan, and M. A. Kasevich. Quantum superposition at the half-metre scale. *Nature*, 528(7583):530–533, December 2015. ISSN 1476-4687. doi: 10.1038/nature16155. URL http://dx.doi.org/10.1038/nature16155.

[181] D. M. Stamper-Kurn, G. E. Marti, and H. Müller. Verifying quantum superpositions at metre scales. *Nature*, 537(7618):E1–E2, August 2016. ISSN 1476-4687. doi: 10.1038/nature19108. URL `http://dx.doi.org/10.1038/nature19108`.

université PARIS-SACLAY

ÉCOLE DOCTORALE
Ondes et matière (EDOM)

Titre : Contrôle de phase et façonnage d'impulsion de la diffraction de Bragg pour l'optique atomique quantique

Mots clés : Hélium métastable, Condensat de Bose-Einstein, Inégalités de Bell, Interférométrie atomique, Diffraction de Bragg

Résumé : La mécanique quantique prédit le phénomène d'intrication, qui prévoit que pour un système de deux particules dites intriquées, on observe de très fortes corrélations entre les propriétés des particules.

Une façon de caractériser un système intriqué est de réaliser un test d'inégalité de Bell. Le projet décrit dans cette thèse se propose de mettre en place un interféromètre de Bell mettant en jeu des atomes d'hélium métastables intriqués en impulsion. A partir d'atomes préparés dans un condensat de Bose-Einstein, des paires d'atomes fortement corrélées sont émises à des impulsions différentes par le processus de mélange à quatre ondes, puis les atomes sont envoyés dans un interféromètre à deux particules et quatre modes d'impulsion. Pour cela, on utilise la diffraction de Bragg, pour transférer de l'impulsion aux atomes de façon cohérente et ainsi former des miroirs et séparatrices à atomes.

Dans cette thèse, on étudie en détails la diffraction de Bragg et son influence dans la réalisation d'un interféromètre de Bell. On propose une méthode originale pour contrôler la différence de phase imprimée sur les atomes entre les deux doublets d'impulsion en jeu, en modulant temporellement l'amplitude de la pulsation de Rabi. Cette technique est également mise à profit pour façonner le profil temporel des miroirs et séparatrices Bragg afin d'améliorer leurs propriétés de réflectivité et de phase. De premiers tests interférométriques sont reportés (interféromètres de type Mach-Zehnder, Ramsey, Hong-Ou-Mandel), validant la technique de contrôle de phase notamment et donnant des résultats prometteurs quant à la réalisation prochaine d'un test de Bell.

Title : Phase control and pulse shaping in Bragg diffraction for quantum atom optics

Keywords : Metastable helium, Bose-Einstein Condensate, Bell's inequality, Atom interferometer, Bragg diffraction

Abstract : Quantum mechanics predicts the phenomenon of entanglement, which predicts thatthat for a system of two entangled particles, very strong correlations can be observed.

One way to characterize an entangled system is to perform a Bell inequality test. The project described in this thesis aims to set up a Bell interferometer involving metastable helium atoms entangled in momentum. Starting with atoms in a Bose-Einstein condensate, pairs of highly correlated atoms are emitted at different momenta through the four-wave mixing process. These atoms are then sent through a two-particle, four-momentum mode interferometer using Bragg diffraction to coherently transfer momentum to the atoms and create atom mirrors and beam splitters.

In this thesis, we study in detail Bragg diffraction and its influence on the realization of a Bell interferometer. We propose an original method to control the phase difference imprinted on the atoms between the two involved momentum doublets by temporally modulating the amplitude of the Rabi frequency. This technique is also used to shape the temporal profile of Bragg mirrors and beam splitters to improve their reflectivity and phase properties. Initial interferometric tests are reported (Mach-Zehnder, Ramsey, Hong-Ou-Mandel interferometers), validating the phase control technique in particular and showing promising results for the upcoming realization of a Bell test.